frontiers | Research Topics

Targeting ion channels for drug discovery: Emerging challenges for high throughput screening technologies

Edited by
Ciria Hernandez, Luis Eduardo Diaz Gimenez, Jean-Marc Taymans, Tim Strassmaier and Marc Rogers

Published in
Frontiers in Molecular Neuroscience

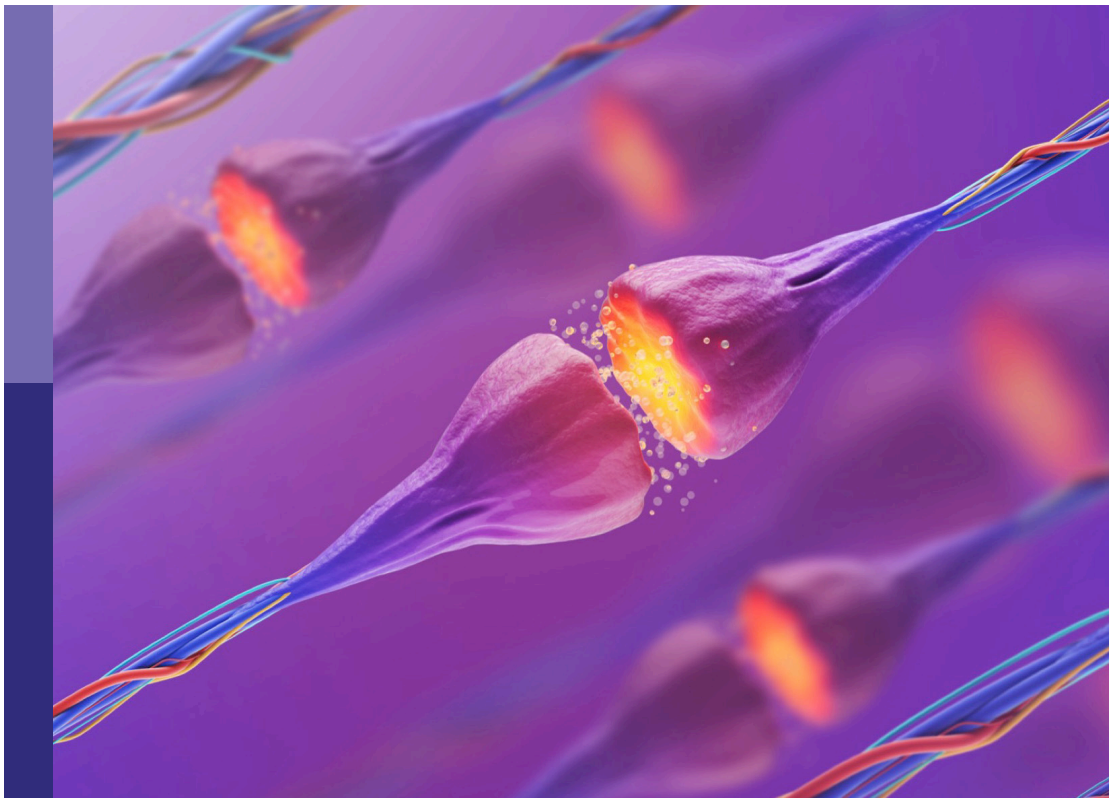

ISSN 1664-8714
ISBN 978-2-8325-5016-8
DOI 10.3389/978-2-8325-5016-8

About Frontiers

Frontiers is more than just an open access publisher of scholarly articles: it is a pioneering approach to the world of academia, radically improving the way scholarly research is managed. The grand vision of Frontiers is a world where all people have an equal opportunity to seek, share and generate knowledge. Frontiers provides immediate and permanent online open access to all its publications, but this alone is not enough to realize our grand goals.

Frontiers journal series

The Frontiers journal series is a multi-tier and interdisciplinary set of open-access, online journals, promising a paradigm shift from the current review, selection and dissemination processes in academic publishing. All Frontiers journals are driven by researchers for researchers; therefore, they constitute a service to the scholarly community. At the same time, the *Frontiers journal series* operates on a revolutionary invention, the tiered publishing system, initially addressing specific communities of scholars, and gradually climbing up to broader public understanding, thus serving the interests of the lay society, too.

Dedication to quality

Each Frontiers article is a landmark of the highest quality, thanks to genuinely collaborative interactions between authors and review editors, who include some of the world's best academicians. Research must be certified by peers before entering a stream of knowledge that may eventually reach the public - and shape society; therefore, Frontiers only applies the most rigorous and unbiased reviews. Frontiers revolutionizes research publishing by freely delivering the most outstanding research, evaluated with no bias from both the academic and social point of view. By applying the most advanced information technologies, Frontiers is catapulting scholarly publishing into a new generation.

What are Frontiers Research Topics?

Frontiers Research Topics are very popular trademarks of the *Frontiers journals series*: they are collections of at least ten articles, all centered on a particular subject. With their unique mix of varied contributions from Original Research to Review Articles, Frontiers Research Topics unify the most influential researchers, the latest key findings and historical advances in a hot research area.

Find out more on how to host your own Frontiers Research Topic or contribute to one as an author by contacting the Frontiers editorial office: frontiersin.org/about/contact

Targeting ion channels for drug discovery: Emerging challenges for high throughput screening technologies

Topic editors

Ciria Hernandez — University of Michigan, United States
Luis Eduardo Diaz Gimenez — University of Michigan, United States
Jean-Marc Taymans — Institut National de la Santé et de la Recherche Médicale (INSERM), France
Tim Strassmaier — Nanion Technologies GmbH, Germany
Marc Rogers — Albion Drug Discovery Services Ltd, United Kingdom

Citation

Hernandez, C., Gimenez, L. E. D., Taymans, J.-M., Strassmaier, T., Rogers, M., eds. (2024). *Targeting ion channels for drug discovery: Emerging challenges for high throughput screening technologies*. Lausanne: Frontiers Media SA.
doi: 10.3389/978-2-8325-5016-8

Table of contents

frontiers | Frontiers in Molecular Neuroscience

TYPE Editorial
PUBLISHED 31 May 2024
DOI 10.3389/fnmol.2024.1414816

OPEN ACCESS

EDITED AND REVIEWED BY
Robert J. Harvey,
University of the Sunshine Coast, Australia

*CORRESPONDENCE
Ciria C. Hernandez
ciria@umich.edu

RECEIVED 09 April 2024
ACCEPTED 14 May 2024
PUBLISHED 31 May 2024

CITATION
Hernandez CC, Gimenez LE, Strassmaier T, Rogers M and Taymans J-M (2024) Editorial: Targeting ion channels for drug discovery: emerging challenges for high throughput screening technologies.
Front. Mol. Neurosci. 17:1414816.
doi: 10.3389/fnmol.2024.1414816

Editorial: Targeting ion channels for drug discovery: emerging challenges for high throughput screening technologies

Ciria C. Hernandez[1]*, Luis E. Gimenez[1], Tim Strassmaier[2], Marc Rogers[3] and Jean-Marc Taymans[4]

[1]Life Sciences Institute, University of Michigan, Ann Arbor, MI, United States, [2]Nanion Technologies Inc., Livingston, NJ, United States, [3]Albion Drug Discovery Services Ltd., Cambridge, United Kingdom, [4]Univ. Lille, Inserm, CHU Lille, UMR-S 1172 - LilNCog - Lille Neuroscience & Cognition, Lille, France

KEYWORDS

ion channel, high throughput screening (HTS), drug discovery and development, automated patch clamp (APC), channelopathy

Editorial on the Research Topic
Targeting ion channels for drug discovery: emerging challenges for high throughput screening technologies

Cellular functions are regulated by complex signaling networks that determine gene expression and cellular behavior. Membrane receptors transmit various types of information from the external environment to be processed at the membrane, cytoplasmic, or nuclear level (Ullo and Case, 2023). Among these receptors are the ligand and voltage-gated ion channels, which are highly regulated proteins that control ion flow and cellular excitability (Catterall and Swanson, 2015). Some ion channels are also membrane "sensors" like receptors, such as ASIC channels (pH) and TRPx receptors (Storozhuk et al., 2021; Zhang et al., 2023), triggering cellular responses in excitable tissues, such as neurons and muscle cells (Hille, 1978). Dysregulation of ion channels can lead to a wide range of disorders, including neuropathies, cardiac arrhythmias, muscle disorders, and metabolic diseases (Harraz and Delpire, 2024). With over 1.5% of the human genome represented by ion channels and a sizable (15 to 18%) proportion of small molecule drugs focusing on either sensor-, voltage-, or ligand-gated ion channels (Santos et al., 2017), this protein class is the second-largest category of pharmacologically targetable proteins after G protein-coupled receptors (Kaczorowski et al., 2008; Alexander et al., 2019), highlighting their clinical potential.

The first ion channel-targeting drugs date back to the last decade of the 19th century with the discovery of cocaine-derived amino ester Na^+ channel blockers leading to the discovery of the topical anesthetic lidocaine (c. 1943) and the class Ia antiarrhythmic procainamide (Cox, 2014). These discoveries paved the way for the FDA-approved drugs currently used in the clinic, including L-type voltage-gated Ca^{2+} channel blockers for treating hypertension (e.g., amlodipine, nifedipine, and verapamil), stroke (e.g., nimodipine), and arrhythmias (e.g., verapamil and diltiazem), and N- and T-type Ca^{2+} channel blockers for analgesic or anti-convulsant activity, and anti-convulsant Na^+ channel inhibitors and KCNQ2/Kv7 K^+ channel openers (e.g., retigabine) for treating epilepsy, to name a few.

The field has undergone considerable progress in the past 15 years, fueled by advancements in rodent and human genetic target detection and validation, structure-based drug design, high throughput computational modeling and disease modeling at the cellular level. With the acknowledgment of ion channels as quintessential drug targets, a deeper understanding of their pharmacology and structure has paved the way for substantial breakthroughs. Functional assays and instrumentation have significantly improved, leading to high-throughput screening (HTS) technologies designed explicitly for ion channels. Nonetheless, these targets present a challenging puzzle, and developing a successful *in vitro* drug profile for ion channel modulators remains a formidable goal. The current Research Topic showcases cutting-edge HTS technologies for various classes of ion channels, offering a glimpse into the forefront of research and innovation in this dynamic and vital field.

The first part of this Research Topic is devoted to the optimization of automated patch clamp (APC) and optogenetic screening platforms to accurately capture the nuances of ion channel activity and modulation. Ridley et al. focus on acid-sensing ion channels (ASIC), ligand-gated receptors playing a crucial role in detecting inflammation, tissue injury, and hypoxia-induced acidosis, and are thus considered promising targets for drug discovery in areas such as pain, oncology, and ischemia. The research outlines the development, optimization, and validation of various fast perfusion protocols for studying ligand-gated ion channels across multiple APC platforms using the hASIC1a channel as a case study. On the other hand, Rapedius et al. challenge the use of fluoride as a seal enhancer in APC experiments, which has been a longstanding practice for achieving optimal voltage control due to the criticality of seal and access resistance. The authors have developed APC recording substrates for high-throughput fluoride-free recordings on a 384-well APC system, achieving success rates exceeding 40% for GΩ seals.

The studies brought by Govorunova et al. and Borja et al. describe the combination of high-throughput, optical systems and reagents capable of collecting information-dense data from patch clamp and optogenetic assays in both heterologous and induced pluripotent stem cell-derived models. Govorunova et al. utilize a high-throughput APC platform to demonstrate the potential for discovery of new cation- and anion-selective channelrhodopsins (ChRs), discussing the advantages and limitations of employing the APC platform for ChR-coupled HTS. Borja et al. introduced Swarm^{TM}, a custom-designed all-optical instrument addressing the critical need for a compatible technology to enhance the application of optogenetic assays in drug screening. With variable-intensity blue-light optogenetic stimulation, Swarm^{TM} facilitates membrane depolarization and enables fluorescence detection of changes in membrane potential or calcium levels.

Finally, Rosholm et al. review the state of APC techniques applied to the study of pluripotent stem cells (PSC). In particular, the authors posit that high-throughput electrophysiological profiling of human PSCs as cells differentiate will find application in personalized medicine based on stem-cell therapeutics.

In contrast to the high-throughput approaches described above, Mayar et al. showed the direct effect of cannabinoids on hyperpolarization-activated cyclic-nucleotide-gated (HCN1) channels using the two-electrode voltage clamp technique. The authors propose that cannabinoid-related drugs can directly affect channel function by bypassing GPCR activation, which may impact the use of these drugs as therapeutic entities.

Two additional articles focused on developing more effective drugs. The first review by Clement et al. discussed the neurological roles of ATP-sensitive potassium (KATP) channels and highlighted the potential for blocking the Kir6.1/SUR2B subtype as a promising approach to developing drugs to treat migraines. On the other hand, Melancon et al. delve into the limitlessness of chemical space and the intricacies of ion channels, presenting hurdles in identifying potential drug candidates and providing a comprehensive overview of cutting-edge computational chemistry methodologies for screening extensive compound libraries.

Further, in a cutting-edge study, Tsortouktzidis et al. used CRISPR activation and interference/inhibition systems (CRISPRa/i) to target promoter sequences and modulate gene expression in a highly specific manner. The study focused on the *Cacna1h* gene, which encodes the low-voltage-activated T-type calcium channel CaV3.2 linked to channelopathies associated with epileptic seizures. The researchers demonstrated the feasibility of a newly developed CRISPRa/i toolbox in manipulating the promoter activity of Cacna1h in various cell types, providing a promising approach to studying the functional effects of gain-of-function or loss-of-function variants in the *Cacna1h* gene. Following this channelopathy topic, it remains crucial to accurately profile the functional effects of patient-derived and disease-linked ion channel mutations and polymorphisms to determine their pathogenic potential. Accordingly, Ye et al. conducted a comprehensive analysis of 11 *de novo* KCNQ2 Kv7.2 variants linked to epileptic encephalopathies using manual patch clamp. The team used different combinations of homomeric KCNQ2 and heteromeric KCNQ2/KCNQ3 channels in a semi-high throughput manner.

In conclusion, the work presented in this Research Topic on ion channels as drug targets has highlighted novel approaches for drug screening and strategies to improve ion channel drug targeting. Technological progress in the field will no doubt spawn further work to discover drugs to modulate this yet underexploited class of drug targets, the ion channels.

Author contributions

CH: Conceptualization, Investigation, Project administration, Supervision, Validation, Writing – original draft, Writing – review & editing. LG: Conceptualization, Investigation, Project administration, Supervision, Validation, Writing – original draft, Writing – review & editing. TS: Conceptualization, Investigation, Project administration, Supervision, Writing – original draft, Writing – review & editing. MR: Conceptualization, Investigation, Project administration, Supervision, Writing – original draft, Writing – review & editing. J-MT: Conceptualization, Investigation, Project administration, Supervision, Writing – original draft, Writing – review & editing.

Funding

The author(s) declare that no financial support was received for the research, authorship, and/or publication of this article.

Conflict of interest

LG and the University of Michigan have equity in Courage Therapeutics. TS was employed by Nanion Technologies Inc. and MR was employed by Albion Drug Discovery Services Ltd.

The remaining authors declare that the research was conducted in the absence of any commercial or financial relationships that could be construed as a potential conflict of interest.

The author(s) declared that they were an editorial board member of Frontiers, at the time of submission. This had no impact on the peer review process and the final decision.

Publisher's note

References

Alexander, S. P. H., Mathie, A., Peters, J. A., Veale, E. L., Striessnig, J., Kelly, E., et al. (2019). The concise guide to pharmacology 2019/20: ion channels. *Br. J. Pharmacol.* 176, S142–S228. doi: 10.1111/bph.14749

Catterall, W. A., and Swanson, T. M. (2015). Structural basis for pharmacology of voltage-gated sodium and calcium channels. *Mol. Pharmacol.* 88, 141–150. doi: 10.1124/mol.114.097659

Cox, B. (2014). "Ion channel drug discovery: a historical perspective," in *Ion Channel Drug Discovery RSC drug discovery* (Cambridge: The Royal Society of Chemistry), 1–15. doi: 10.1039/9781849735087-00001

Harraz, O. F., and Delpire, E. (2024). Recent insights into channelopathies. *Physiol. Rev.* 104, 23–31. doi: 10.1152/physrev.00022.2023

Hille, B. (1978). Ionic channels in excitable membranes. Current problems and biophysical approaches. *Biophys. J.* 22, 283–294. doi: 10.1016/s0006-3495(78)85489-7

Kaczorowski, G. J., McManus, O. B., Priest, B. T., and Garcia, M. L. (2008). Ion channels as drug targets: the next GPCRs. *J. Gen. Physiol.* 131, 399–405. doi: 10.1085/jgp.200709946

Santos, R., Ursu, O., Gaulton, A., Bento, A. P., Donadi, R. S., Bologa, C. G., et al. (2017). A comprehensive map of molecular drug targets. *Nat. Rev. Drug Discov.* 16, 19–34. doi: 10.1038/nrd.2016.230

Storozhuk, M., Cherninskyi, A., Maximyuk, O., Isaev, D., and Krishtal, O. (2021). Acid-sensing ion channels: focus on physiological and some pathological roles in the brain. *Curr. Neuropharmacol.* 19, 1570–1589. doi: 10.2174/1570159X19666210125151824

Ullo, M. F., and Case, L. B. (2023). How cells sense and integrate information from different sources. *WIREs Mech. Dis.* 15:e1604. doi: 10.1002/wsbm.1604

Zhang, M., Ma, Y., Ye, X., Zhang, N., Pan, L., and Wang, B. (2023). TRP (transient receptor potential) ion channel family: structures, biological functions and therapeutic interventions for diseases. *Signal Transduct. Target. Ther.* 8:261. doi: 10.1038/s41392-023-01464-x

frontiers in Molecular Neuroscience

BRIEF RESEARCH REPORT
published: 06 January 2022
doi: 10.3389/fnmol.2021.667143

A Versatile Clustered Regularly Interspaced Palindromic Repeats Toolbox to Study Neurological $Ca_V3.2$ Channelopathies by Promoter-Mediated Transcription Control

Despina Tsortouktzidis[1], Anna R. Tröscher[1,2], Herbert Schulz[3], Thoralf Opitz[4], Susanne Schoch[1], Albert J. Becker[1†] and Karen M. J. van Loo[1,5†]*

[1] Institute of Neuropathology, Medical Faculty, Section for Translational Epilepsy Research, University of Bonn, Bonn, Germany, [2] Department of Neurology, Kepler University Hospital, Johannes Kepler University Linz, Linz, Austria, [3] Department of Microgravity and Translational Regenerative Medicine, Clinic for Plastic, Aesthetic and Hand Surgery, Otto von Guericke University, Magdeburg, Germany, [4] Institute of Experimental Epileptology and Cognition Research, Medical Faculty, University of Bonn, Bonn, Germany, [5] Department of Epileptology and Neurology, RWTH Aachen University, Aachen, Germany

OPEN ACCESS

Edited by:
Felix Viana, Institute of Neurosciences, Spanish National Research Council (CSIC), Spain

Reviewed by:
Arnaud Monteil, Centre National de la Recherche Scientifique (CNRS), France
Luis Quintino, Lund University, Sweden

***Correspondence:**
Karen M. J. van Loo
kvanloo@ukaachen.de

† These authors have contributed equally to this work

Specialty section:
This article was submitted to Methods and Model Organisms, a section of the journal Frontiers in Molecular Neuroscience

Received: *12 February 2021*
Accepted: *15 December 2021*
Published: *06 January 2022*

Citation:
Tsortouktzidis D, Tröscher AR, Schulz H, Opitz T, Schoch S, Becker AJ and van Loo KMJ (2022) A Versatile Clustered Regularly Interspaced Palindromic Repeats Toolbox to Study Neurological $Ca_V3.2$ Channelopathies by Promoter-Mediated Transcription Control. Front. Mol. Neurosci. 14:667143. doi: 10.3389/fnmol.2021.667143

Precise genome editing in combination with viral delivery systems provides a valuable tool for neuroscience research. Traditionally, the role of genes in neuronal circuits has been addressed by overexpression or knock-out/knock-down systems. However, those techniques do not manipulate the endogenous loci and therefore have limitations. Those constraints include that many genes exhibit extensive alternative splicing, which can be regulated by neuronal activity. This complexity cannot be easily reproduced by overexpression of one protein variant. The CRISPR activation and interference/inhibition systems (CRISPRa/i) directed to promoter sequences can modulate the expression of selected target genes in a highly specific manner. This strategy could be particularly useful for the overexpression of large proteins and for alternatively spliced genes, e.g., for studying large ion channels known to be affected in ion channelopathies in a variety of neurological diseases. Here, we demonstrate the feasibility of a newly developed CRISPRa/i toolbox to manipulate the promoter activity of the *Cacna1h* gene. Impaired, function of the low-voltage-activated T-Type calcium channel $Ca_V3.2$ is involved in genetic/mutational as well as acquired/transcriptional channelopathies that emerge with epileptic seizures. We show CRISPR-induced activation and inhibition of the *Cacna1h* locus in NS20Y cells and primary cortical neurons, as well as activation in mouse organotypic slice cultures. In future applications, the system offers the intriguing perspective to study functional effects of gain-of-function or loss-of-function variations in the *Cacna1h* gene in more detail. A better understanding of $Ca_V3.2$ channelopathies might result in a major advancement in the pharmacotherapy of $Ca_V3.2$ channelopathy diseases.

Keywords: ion channelopathies, Cacna1h promoter modulation, CRISPR-induced activation, CRISPR-induced inhibition, T-Type calcium channel $Ca_V3.2$

INTRODUCTION

The human genome encodes approximately 400 ion channel genes, encompassing both voltage-gated and ligand-gated ion channels (Hutchings et al., 2019). Ion channels are pore forming membrane proteins that allow ionic flows across membranes and are crucial for normal functioning of many tissues, including the central and peripheral nervous system, heart, kidney, and liver (Cannon, 2007). Ion channel dysfunctions, also coined as ion "channelopathies," have been associated with a large variety of diseases. Besides disorders of the nervous system (e.g., epilepsy, ataxia, Alzheimer's disease, and Autism spectrum disorders), also cardiac arrhythmia and several muscle, endocrine, and renal disorders are linked to dysfunction of ion channels (Wang et al., 1996; Heeringa et al., 2009; Ryan et al., 2010). Still, many molecular and structural mechanisms of how channelopathies convert cells from a health to disease state are not fully understood, including critical time-windows during development as well as the potential reversibility by reconstituting normal expression/function of affected molecules. Major obstacles to manipulate ion channels are given by their large size, which limits options for widespread and *in vivo* overexpression and their diversification by alternative splicing.

Genetic editing using a modified CRISPR (clustered regularly interspaced palindromic repeats) system could be a powerful approach for the manipulation of large proteins that cannot be done by conventional techniques. Recently, substantial progress has been made in genomic editing by using specific applications of the CRISPR technique, including the CRISPR *activation* (CRISPRa) and CRISPR *interference/inhibition* (CRISPRi) technology. CRISPRa uses a catalytically dead Cas9 (dCas9) enzyme fused with a highly efficient transcriptional activator complex consisting of the tripartite transcriptional activator VP64-p65-Rta (VPR), shown to increase target gene expression even up to 320-fold (Chavez et al., 2015). CRISPRi also uses the dCas9 enzyme and is fused with the transcriptional repressor KRAB (Krüppel-associated box) protein, which results in up to 60–80% reduction in the expression of endogenous eukaryotic genes (Gilbert et al., 2013). Using these enhanced CRISPR technology systems, the expression of genes can be modified in their native context with utmost precision. Therefore, this strategy will be particularly useful for (a) the overexpression of large proteins, which is difficult to accomplish by conventional techniques and (b) for alternatively spliced genes.

In this study, we have developed a CRISPRa/i toolbox for manipulating the expression of a well-described ion channelopathy gene, *Cacna1h,* encoding the low-voltage-activated T-Type calcium channel $Ca_V3.2$. Ion channelopathies for *Cacna1h* have been described particularly for epilepsy variants (Khosravani et al., 2004, 2005; Powell et al., 2009; Souza et al., 2019), but were also reported for other neurological diseases including autism spectrum disorders (Splawski et al., 2006), amyotrophy lateral sclerosis (ALS; Rzhepetskyy et al., 2016) and pain disorders (Souza et al., 2016). By using the unique CRISPRa/i toolbox, we demonstrate to specifically modulate *Cacna1h* gene expression in different cell types in order to closely recapitulate $Ca_V3.2$ channelopathies.

MATERIALS AND METHODS

Design of sgRNAs

sgRNA design was performed using the computational software Benchling (Cloud-Based Informatics Platform for Life Sciences R&D | Benchling, 2021). The previously validated *Cacna1h* promoter (Van Loo et al., 2012) was used to set the sgRNAs targeting sequence. The sgRNAs were selected based on their local off-target scores, proximity to the start-ATG, a distance of at least 50 bp between each other and a 100% match in targeting both the mouse and rat genome.

Cloning

All primer sequences used for cloning are shown in **Supplementary Table 1**. As a basis for our cloning strategies, we exchanged the hybrid cytomegalovirus-actin-globin promoter of pAAV-MCS (Agilent) by the human synapsin (hSyn) promoter (Kügler et al., 2003) using the *Mlu*I/*Bsu*15I restriction sites. In order to generate the pAAV-U6-sgRNA plasmids, we cloned a U6-*Bbs*I/*Bbs*I cassette into the pAAV-hSyn-MCS backbone. For this, the U6-*Bbs*I/*Bbs*I cassette was PCR-amplified from px458 [Addgene #48138, Ran et al. (2013)] and inserted by in-fusion cloning (IFC; Takara Bio Europe/Clontech) into *Mlu*I/*Asi*SI-digested pAAV-hSyn-MCS. Next, the polyA was removed by digestion with *Afe*I/*Pml*I and subsequent self-ligation. Finally, the sgRNAs were annealed and cloned into the *Bbs*I sites (Cloud-Based Informatics Platform for Life Sciences R&D | Benchling, 2021). Briefly, the annealing was performed using 10 μM of each oligo, 1X T4 ligation buffer and 5U of T4 PNK in a total volume of 10 μL, following an incubation at 37°C for 30 min and 95°C for 5 min, the reaction was cooled at room temperature. The annealed oligos (1 μL) were cloned using 25 ng of construct, 1X T4 ligation buffer, T4 ligase (200 U) and *Bbs*I (2.5 U) in a total volume of 10 μL, the reaction was performed by 30 cycles at 37°C for 5 min and 23°C for 5 min.

The all-in-one CRISPRa lentiviral system was generated by replacing the promoter of pLenti-Ef1a-dCas9-VPR [Addgene#114195, Savell et al. (2019)] by the hSyn promoter using IFC. For this, pAAV-hSyn-MCS was used as PCR template for the hSyn promoter and cloned into *Afe*I/*Kpn*I-digested pLenti-Ef1a-dCas9-VPR. In a second step, the *Cacna1h* and *LacZ* sgRNA sequences from the pAAV-U6-sgRNA plasmids (see above) were cloned by IFC into the *Pac*I site of pLenti-syn-dCas9-VPR, resulting in pLenti-U6-sgRNA$_{(Cacna1h/LacZ)}$-Syn-dCas9-VPR.

The all-in-one CRISPRi lentiviral system was produced by replacing the hU6-sgRNA-hUbC cassette of pLenti-hU6-sgRNA-hUbC-dCas9-KRAB-T2a-eGFP [Addgene#71237, Thakore et al. (2015)] for the hSyn promoter by IFC. The backbone was digested with *Xba*I/*Pac*I and the hSyn promoter PCR amplified from pAAV-hSyn-MCS, resulting in pLenti-hSyn-dCas9-KRAB-T2A-eGFP. Subsequently, the U6-sgRNA$_{Cacna1h/LacZ}$ cassettes from the pAAV-U6-sgRNA plasmids (see above) were inserted into the *Pac*I site of pLenti-hSyn-dCas9-KRAB-T2A-eGFP by IFC.

pTRE-dCas9-VPR was generated by replacing the promoter of pLenti-Ef1a-dCas9-VPR [Addgene#114195, Savell et al. (2019)] for the tetracycline response element (TRE) of the pK031.TRE-Cre [Addgene#69136 (Mizuno et al., 2014)] by IFC using the *Afe*I/*Kpn*I restriction sites. pTRE-dCas9-KRAB-T2A-eGFP was produced by replacing the promoter of the previously generated pLenti-hSyn-dCas9-KRAB-T2A-eGFP with the TRE of pK031.TRE-Cre [Addgene#69136 (Mizuno et al., 2014)] by IFC, using the *Pac*I/*Xba*I restriction sites. pAAV-hSyn-rtTA was generated by IFC using *Eco*RI/*Sal*I-digested pAAV-hSyn-MCS and the rtTA sequence PCR-amplified from mCreb1 in pInducer20, kindly provided by Dasgupta and co-workers (Chhipa et al., 2018).

Cell Culture, Transfection, and Luciferase Assay

NS20Y cells (Sigma, #08062517) were maintained at 37°C and 5% CO_2 in DMEM (Sigma, D6546) supplemented with 10% (v/v) heat inactivated FBS, 2 mM L-Glutamine, 100 units/mL penicillin/streptomycin. Cells were transfected in 24 well plates using Lipofectamine (Invitrogen) following the manufacturer's instructions. The DNA concentration used per well: *Cacna1h*-Luciferase or *Cacna1h*-mRuby 100 ng, CMV-VPR [Addgene# 63798, (Chavez et al., 2015)] or CMV-KRAB [Addgene#110821, (Yeo et al., 2018)] 200 ng, pAAV-sgRNA 200 ng and hypB-CAG-2A-eGFP 100 ng. Following 48 h after transfection, the cells were imaged or collected for luciferase assays. Luciferase assays were performed using the Dual Luciferase Reporter Assay System (Promega) according to the manufacturer's specifications. Firefly luciferase activity was determined using the Glomax Luminometer (Promega).

Viral Production and Neuronal Transduction

AAV1/2 viruses were produced by large-scale triple $CaPO_4$ transfection of HEK293-AAV cells (Agilent, #240073) as described previously (Van Loo et al., 2012). Lentiviruses were produced in HEK293T cells using a second-generation lentiviral packaging system. The procedure was performed as described before (Van Loo et al., 2019). Dissociated primary neurons were prepared from mouse cortex (C57Bl6/N) at embryonic day 15–19 as described before (Woitecki et al., 2016). All animals were handled according to government regulations as approved by local authorities (LANUV Recklinghausen). All procedures were planned and performed in accordance with the guidelines of the University Hospital Bonn Animal-Care-Committee as well as the guidelines approved by the European Directive (2010/63/EU) on the protection of animals used for experimental purposes. Cells were kept in BME medium (Gibco) supplemented with 1% FBS, 0.5 mM L-glutamine, 0.5% glucose and 1X B27 at 37°C and 5% CO_2. Neuronal transduction was performed at days *in vitro* (DIV) 4 in 24 well plates containing 70,000 cells/well with a multiplicity of infection (MOI) of approximately 14. Cells were collected on DIV15 in lysis/binding buffer (Invitrogen, A33562) and stored at −80°C until mRNA extraction or at DIV20 for Western blot.

RNA Isolation and Real Time RT-PCR

RNA isolation and cDNA production was performed using Dynabeads mRNA Direct Micro Kit (Invitrogen, 61021) and RevertAid H Minus First strand cDNA Synthesis Kit (Thermo Fisher Scientific, K1632) following the manufacturer's instructions. Quantitative PCR was performed in a Thermal Cycler (BioRad C1000 Touch, CFX384 Real-Time system). The reaction was performed using 1X Maxima SYBR Green/Rox qPCR Master Mix (Thermo Fisher Scientific, K0223), 0.3 μM of each primer (for primer sequences see **Supplementary Table 2**) and 1/10 synthesized cDNA (for NS20Y and 1/2 for Neurons) for a total volume of 6.25 μL. The qPCR conditions were as follow: 2 min at 50°C, 10 min at 95°C, 40 cycles of 15 s at 95°C and 1 min at 59°C. mRNA quantification was performed by real-time RT-PCR using the ΔΔCt-method. Quantification was based on synaptophysin (Chen et al., 2001).

Protein Extraction and Western Blotting

Transduced cortical neurons (4,20,000 cells) were lysed in RIPA buffer (150 mM sodium chloride, 1% NP40, 0.5% sodium deoxycholate, 0.1% SDS, 50 mM Tris–HCl, pH8, protease inhibitor 1X, and phosphatase inhibitor 1X), loaded on 8% SDS polyacrylamide gels and transferred onto nitrocellulose membranes. Blots were blocked in 5% milk for 1 h and incubated overnight with a primary antibody against $Ca_V3.2$ (1:200, Sigma C1868). Following washing steps in PBS-T (0.1% Tween) the membrane was incubated with IRDye800 Goat anti-Rabbit (1:10,000, LI-COR Biosciences) for 45 min, washed and imaged. The membrane was subsequently incubated with anti-Tubulin antibody (1:5,000, ab6160) for 2 h at RT, washed and incubated with IRDye680 Goat anti-Rat (1:10,000, LI-COR Biosciences). Bands were detected with infrared Odyssey system (LI-COR Biosciences) and quantified using the software Image Studio Lite.

Mouse Organotypic Slices

Organotypic hippocampal slices were prepared from mice (C57Bl6/N) at postnatal day 3–6 as described before (Biermann et al., 2014). In brief, the hippocampus was isolated and cut in 350 μM thickness using a McIllwain tissue chopper. The slices were cultured in 6 well plates containing cell culture inserts 0.4 μM, 30 mm (Millipore) and medium (50% Neurobasal medium, 25% Hank's balanced salt solution (without $MgCl_2$, without $CaCl_2$), 25% horse serum, 0.65% D(+)-glucose, 0.01 M Hepes, 2 mM L-glutamine and 0.5X B27). Cultured slices were kept at 37°C, 5% CO_2.

Cell Imaging

Images were obtained using an inverted phase contrast fluorescent microscope (Zeiss Axio Observer A1 with objectives 20X, LD A-Plan and 5X, Fluar) and processed using Fiji. The cell surface area, set by the GFP fluorescence, was determined using the Weka trainable segmentation plugging. The integrated density, determined by the mRuby fluorescence was normalized to the cell surface area to obtain the reported values of integrated density/cell surface (IntDE/cell surfase).

Statistical Analyses

Statistical analyses were performed using GaphPad software. One sample *t*-test, Student *t*-test, and two way ANOVA followed by multiple comparison tests were used to compare significance of the results. Values were considered significant a $p < 0.05$. For all graphs data are displayed as mean ± SEM.

RESULTS

To modulate the promoter activity of the *Cacna1h* gene, we first designed sgRNAs sequences targeting the mouse and rat *Cacna1h* gene. Using the Benchling computational tool, we selected two sgRNAs binding 66 (sgRNA1) and 131 (sgRNA2) base pairs (bp) upstream of the start-ATG of the *Cacna1h* gene (**Figure 1A**). Next, we tested the efficiency of the two sgRNAs to target the *Cacna1h* promoter and regulate its activity in neuroblastoma NS20Y cells. For this, we transfected the two sgRNAs together with (i) a minimal reporter unit expressing mRuby under control of the rat *Cacna1h* promoter, (ii) a ubiquitous promoter expressing eGFP, and (iii) either a CRISPRa construct [dCas9-VPR, Chavez et al. (2015)] or a CRISPRi construct [dCas9-KRAB, (Yeo et al., 2018)] in NS20Y cells and analyzed the fluorescence intensity 2 days after transfection (**Figures 1B,C**). A strong activation of the *Cacna1h* promoter was observed after co-transfection with the CRISPRa construct and an inhibition after co-transfection with the CRISPRi construct (**Figure 1C**). No modulation was observed for the ubiquitous CAG-eGFP construct, indicating that the sgRNAs only affected the activity of the *Cacna1h* promoter (**Figure 1C**).

Next, we compared the modulatory effects of the two sgRNAs in both the CRISPRa and CRISPRi systems. A significant increase in *Cacna1h*-mRuby fluorescence activity was observed for the two single sgRNAs in the CRISPRa system (mean ± SEM = sgRNA1: 3.41 ± 0.26-fold increase, $p = 0.0026$; sgRNA2: 2.93 ± 0.16-fold increase, $p = 0.0012$), and reached similar levels as observed for the combination of the two sgRNAs (**Figure 1D**, left panel; mean ± SEM = sgRNA1 + 2: 3.60 ± 0.51-fold increase, $p = 0.015$). Also for the CRISPRi system, comparable modulatory effects were observed for sgRNA1 (mean ± SEM = 0.52 ± 0.078-fold decrease, $p = 0.0088$), sgRNA2 (0.51 ± 0.046-fold decrease, $p = 0.0017$) and the combination of the two sgRNAs (0.52 ± 0.10-fold decrease, $p = 0.017$; **Figure 1D**, middle panel). A control sgRNA targeting *Lac*Z did not have an effect on *Cacna1h* fluorescence intensity in the CRISPRa or CRISPRi system (**Figure 1D**, right panel), indicating that the modulatory effects observed for the two *Cacna1h*-sgRNAs were highly specific.

To confirm and precisely quantify the *Cacna1h*-specific CRISPRa and CRISPRi regulation, we next exchanged the mRuby reporter for a luciferase reporter gene (**Figure 1E**, left panel). As expected, transfection of the CRISPRa and CRISPRi components into NS20Y cells, resulted in an increase of luciferase activity for the CRISPRa system (**Figure 1E**, middle panel; sgRNA1: 5.44 ± 0.84-fold increase, $p = 0.034$; sgRNA2: 4.79 ± 0.80-fold increase, $p = 0.042$; sgRNA1 + 2: 6.75 ± 0.45-fold increase, $p = 0.006$) and a decrease for the CRISPRi system (**Figure 1E**, right panel; sgRNA1: 0.26 ± 0.087-fold decrease, $p = 0.013$; sgRNA2: 0.24 ± 0.039-fold decrease, $p = 0.0026$; sgRNA1 + 2: 0.12 ± 0.014-fold decrease, $p = 0.0003$). Also here, no significant differences were observed between the two sgRNAs or the combination of the two sgRNAs.

We next examined the endogenous *Cacna1h* mRNA expression levels after manipulation with the CRISPRa and CRISPRi systems using quantitative real-time RT-PCR. Since both sgRNAs showed similar effects on the *Cacna1h* reporter constructs (**Figures 1D,E**) we decided to use the combination of the two sgRNAs for this experiment. Activation of the system in NS20Y cells, resulted in augmentation of endogenous *Cacna1h* mRNA expression levels, whereas inhibition significantly decreased the *Cacna1h* mRNA expression levels (**Figure 1F**, right panel; CRISPRa: 2.69 ± 0.33-fold increase, $p = 0.036$; CRISPRi: 0.69 ± 0.018-fold decrease, $p = 0.0034$). No changes in *Cacna1h* expression were observed for the CRISPRa and CRISPRi controls (no sgRNA; **Figure 1F**, left panel). Altogether, these results confirmed that the present *Cacna1h*-CRISPR modulatory toolbox successfully can activate or inhibit endogenous *Cacna1h* expression in NS20Y cells.

We then probed whether the modulatory effects observed in NS20Y cells could also be observed in primary cultured neurons. For this, we transduced primary mouse cortical neurons at DIV4 with all-in-one CRISPRa/i lentiviruses (**Figure 2A**) and measured endogenous *Cacna1h* mRNA expression levels at DIV15 and protein levels at DIV20. Since the two sgRNAs displayed similar effects in NS20Y cells (**Figures 1D,E**), we decided to proceed with only one sgRNA (sgRNA2) to minimize unspecific effects in the neuronal cultures. Intriguingly, a strong activation was observed after transduction with CRISPRa lentiviruses both at the mRNA (**Figure 2B**, left panel, 4.37 ± 0.37-fold increase, $p = 0.0016$) and at the protein level (**Figure 2C**, 2.18 ± 0.42-fold increase, $p = 0.0046$). In addition, also inhibition of the system using CRISPRi in neuronal cultures resulted in a reduced *Cacna1h* expression at the mRNA (**Figure 2B**, right panel, 0.12 ± 0.049-fold change, $p = 0.032$) as well as at the protein level (**Figure 2D**, 0.39 ± 0.14-fold change, $p = 0.042$), indicating that sgRNA2 can efficiently modulate *Cacna1h* promoter activity in primary neurons. Although we observed additional non-specific bands in our Western blot experiments (**Supplementary Figure 1**), only the band of approximately 260 kDa corresponding to $Ca_V3.2$ increases or decreases in intensity after treatment with *Cacna1h*-CRISPRa and *Cacna1h*-CRISPRi, respectively.

To prove unequivocally that the *Cacna1h*-CRISPRa/i toolbox is specific for *Cacna1h* modulation, we next examined the mRNA expression levels of other calcium channel family members (*Cacna1g*, *Cacna1i,* and *Cacna1e*) after *Cacna1h*-CRISPRa/i targeting using quantitative real-time RT-PCR. No alterations were observed for any of the other calcium channels tested (**Figure 2E**), indicating that our newly developed *Cacna1h*-CRISPRa/i toolbox is highly specific for *Cacna1h* modulation.

In order to test if our system has the potential to be delivered in neuronal network structures *in vivo* we infected mouse organoptypic hippocampal slices with recombinant adeno-associated (rAAV) and lentiviruses encoding our *Cacna1h*-CRISPRa toolbox and a fluorescent reporter. After

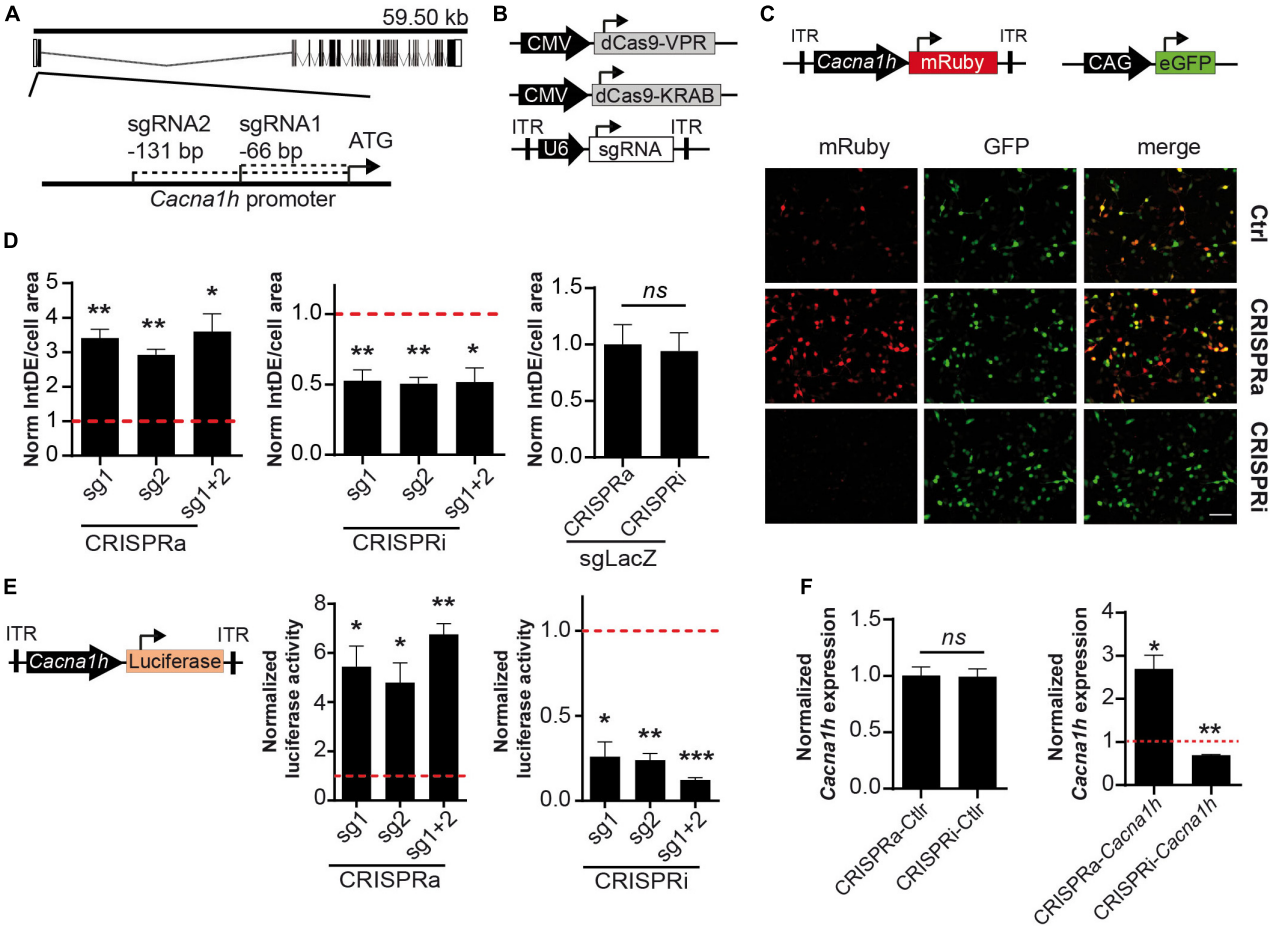

FIGURE 1 | Validation of the CRISPRa/i system for modulating *Cacna1h* expression. **(A)** Schematic representation of the *Cacna1h* mouse gene. Exons and introns are shown as boxes and dash lines, respectively. The position of sgRNA1 and sgRNA2 are indicated respective to the start-ATG (bp: base pairs). **(B)** Schematic illustration of the CRISPRa (CMV-dCas9-VPR), CRISPRi (CMV-dCas9-KRAB), and the sgRNA (pAAV-U6-sgRNA) constructs. **(C)** NS20Y co-transfected with CRISPRa or CRISPRi, the two sgRNAs targeting *Cacna1h* (or *LacZ* as control), the reporter pAAV-*Cacna1h*-mRuby, and a CAG-eGFP construct as internal control for transfection. Scale bar = 100 μm. **(D)** Quantification of integrated density (IntDE) of mRuby per cell surface area (defined by CAG-eGFP positive cells). Values of IntDE/cell area were normalized to the controls of each treatment: CRSIPRa-*LacZ* for CRISPRa and CRISPRi-*LacZ* for CRISPRi (One sample *t*-test, $N = 4$), $^*p \leq 0.05$, $^{**}p \leq 0.01$. **(E)** Luciferase activity of cells co-transfected with pAAV-*Cacna1h*-luciferase, CRISPRa or CRISPRi and sgRNAs targeting *Cacna1h* (or *LacZ* as control). Data normalized to each control: CRISPRa-*LacZ* for CRISPRa treatment and CRISPRi-*LacZ* for CRISPRi treatment (One sample *t*-test, $N = 3$), $^*p \leq 0.05$, $^{**}p \leq 0.01$, $^{***}p \leq 0.001$. **(F)** *Cacna1h* mRNA expression in NS20Y cells co-transfected with CRISPRa or CRISPRi. Left panel: Cells transfected with CRISPRa and CRISPRi without sgRNAs ($N = 3$, *t*-test). Right panel: *Cacna1h* mRNA expression levels in NS20Y cells transfected with CRISPRa or CRISPRi and sgRNAs targeting *Cacna1h* (sgRNA1 + 2). Values were normalized to the mean of CRISPRa and CRISPRi controls (lacking sgRNA) (One sample *t*-test, $N = 3$), $^*p \leq 0.05$, $^{**}p \leq 0.01$.

co-transduction with AAV-sgRNA, lenti-EF1a-dCas9-VPR (Savell et al., 2019) and the reporter AAV-*Cacna1h*-mRuby we observed a stronger signal of the red fluorescent protein when using the sgRNA targeting *Cacna1h* than in the control indicating an activation of the *Cacna1h* promoter *in vivo* (**Figure 2F**).

The *Cacna1h*-CRISPR toolbox we describe here was made for constitutive activation or inhibition of the *Cacna1h* transcripts. We next adapted the system for induced gene expression control by incorporating doxycycline-controlled Tet-On gene expression systems (Colasante et al., 2019; Zhang et al., 2019). In this way, *Cacna1h* expression can be activated or inhibited at a precise temporal resolution. We tested the system in primary cortical neurons with a combination of viruses that allow doxycycline-inducible CRISPR-*Cacna1h* activation (denoted as TET-ON-CRISPRa-*Cacna1h*; **Figure 3A**) or doxycycline-inducible CRISPR-*Cacna1h* inhibition (denoted as TET-ON-CRISPRi-*Cacna1h*; **Figure 3B**). Doxycycline was administered 4 days after viral transduction and mRNA was analyzed at DIV15. Interestingly, we observed an increase in *Cacna1h* expression after transduction with the TET-ON-CRISPRa-*Cacna1h* system following doxycycline treatment (**Figure 3C**; 1.85 ± 0.12-fold change, $p = 0.0015$), and a decrease in *Cacna1h* expression after TET-ON-CRISPRi-*Cacna1h* transduction and doxycycline treatment (**Figure 3D**; 0.28 ± 0.11-fold change, $p = 0.027$). No effect on *Cacna1h* expression was observed when using a control sgRNA targeting *LacZ* (**Supplementary Figure 2**). We thus present a proof of principle that *Cacna1h* expression can be activated or inhibited at a precise temporal resolution.

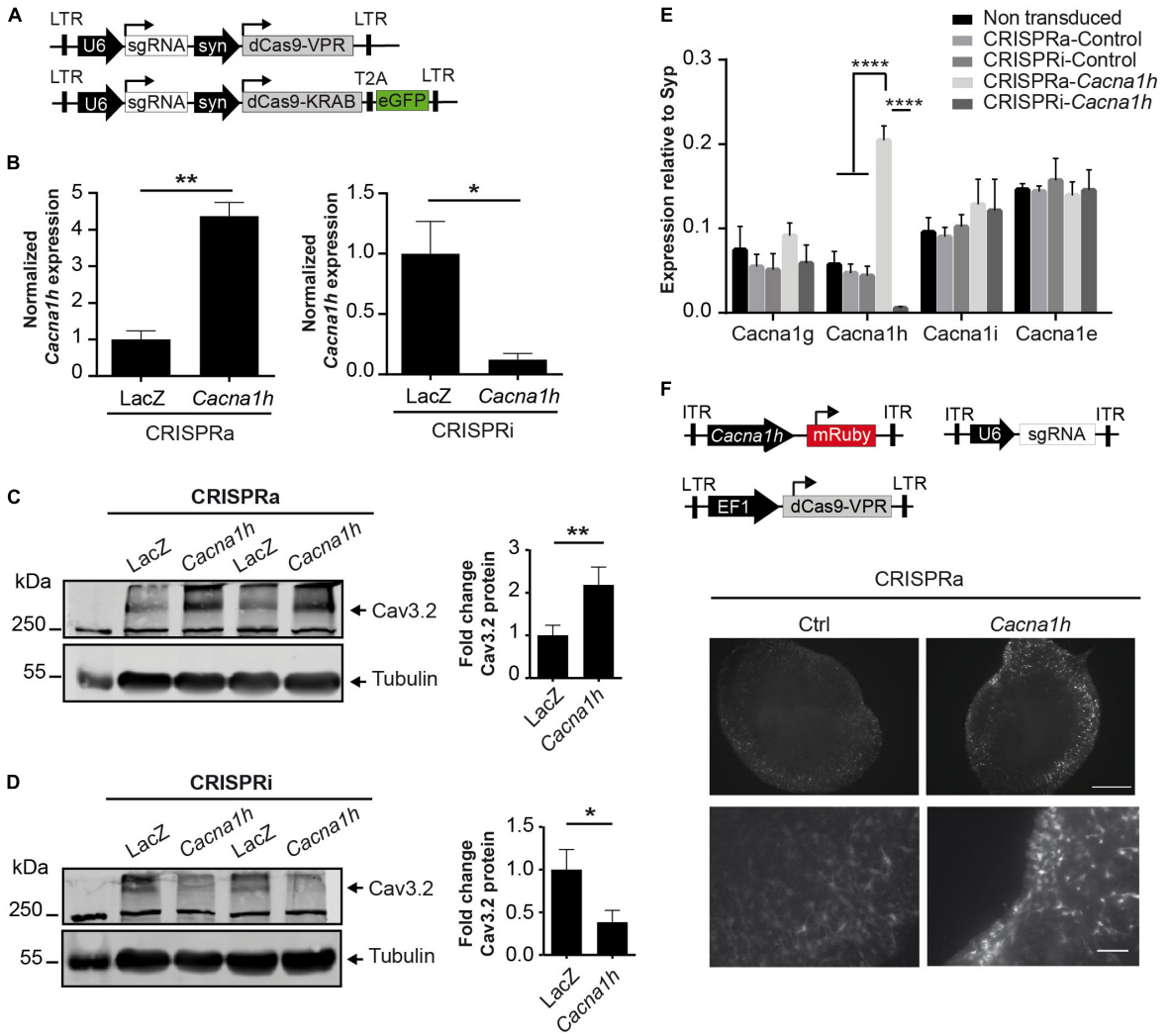

FIGURE 2 | CRISPRa/i modulates the endogenous expression of *Cacna1h* in primary neurons. **(A)** Schematic representation of the all-in-one lentiviral constructs for CRISPRa (Lenti-U6-sgRNA-syn-dCas9-VPR) and CRISPRi (Lenti-U6-sgRNA-syn-dCas9-KRAB-EGFP). **(B)** mRNA expression of *Cacna1h* in cultured neurons after transduction with the all-in-one lentivirus targeting either *Cacna1h* or the control (*LacZ*). Expression levels of *Cacna1h* relative to Synaptophysin in every treatment were normalized to the controls (CRISPRa-*LacZ* and CRISPRi-*LacZ*), $N = 3$, unpaired *t*-test, $^{*}p \leq 0.05$, $^{**}p \leq 0.01$. **(C)** Representative western blot and quantification of Cav3.2 protein levels in cortical neurons transduced with the all in one lentivirus for CRISPRa-*Cacna1h* (or *LacZ*, as control) ($N = 6$, paired *t*-test), $^{**}p \leq 0.01$. **(D)** Representative western blot and quantification of Cav3.2 protein levels in cortical neurons transduced with the all in one lentivirus for CRISPRi-*Cacna1h* (or *LacZ*, as control) ($N = 5$, paired *t*-test), $^{*}p \leq 0.05$. **(C,D)** Tubulin was used as loading control. Values of Cav3.2/Tubulin were normalized to the controls of each treatment: CRSIPRa-*LacZ* for CRISPRa and CRISPRi-*LacZ* for CRISPRi. **(E)** mRNA expression of different calcium channels in neurons transduced with the all-in-one lentiviral constructs targeting *Cacna1h*. Expression relative to synaptophysin ($N = 3$, Two way ANOVA, Tukey's multiple comparison test, $^{****}p \leq 0.0001$). **(F)** Mouse organotypic hippocampal slices transduced with the CRISPRa lentivirus, the AAV-U6-sgRNA and the reporter AAV-*Cacna1h*-mRuby (Scale bar of 500 μM for upper and 100 μM for lower panel).

DISCUSSION

Detailed analyses of the dynamic contribution of individual ion channels in the context of neuronal network function remains challenging, particularly in the context of mutational and transcriptional "channelopathies," in which for example the fine-tuned regulation of mRNA expression levels of affected genes, including *Cacna1h* plays a major role. Traditionally, the functional characterization of individual ion channels in terms of gain- and loss-of-function approaches has been addressed by the exogenous overexpression of genetically encoded proteins and by knock-down systems *via* RNA interference (RNAi)/genetic gene ablation (knock-out), respectively. Although very valuable, the applicability of these techniques has limitations (Kampmann, 2018).

Here, we present a modular method using a CRISPRa/i system that allows to manipulate the endogenous expression of *Cacna1h in vitro* and *in vivo*. This CRISPRa/i system applies specific sgRNAs directed to the *Cacna1h* promoter and a dCas9 fused to the transcriptional activator VPR or the transcriptional

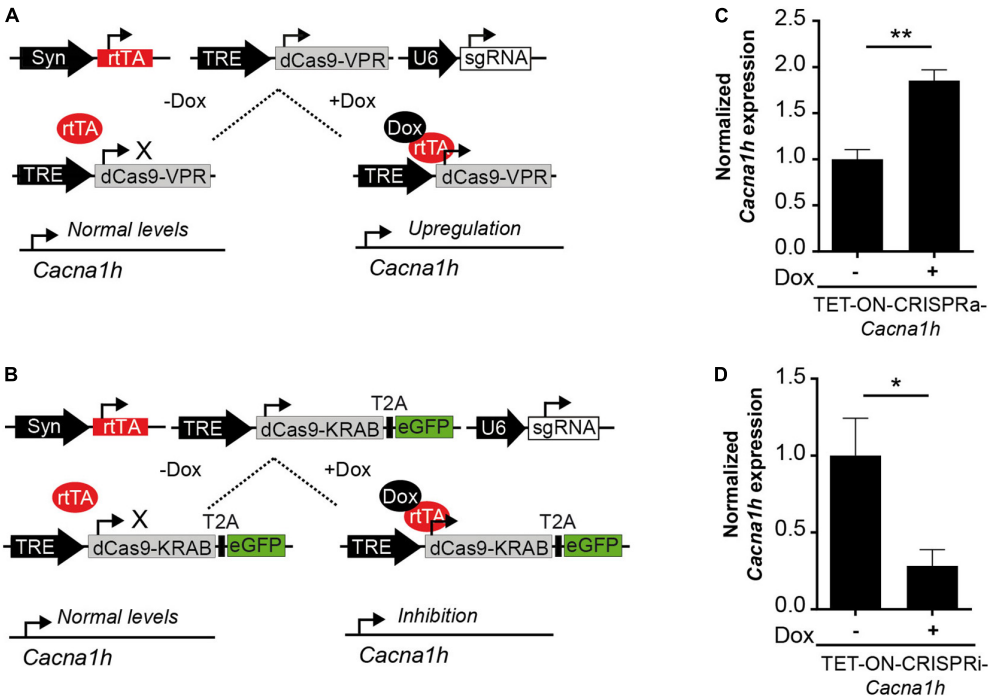

FIGURE 3 | Future perspectives to study *Cacna1h*-channelopathies. **(A)** Schematic representation of a TET-ON system for the conditional expression of CRISPRa (TRE-dCas9-VPR). Only in the presence of doxycycline (Dox) the reverse tetracycline-controlled transactivator (rtTA) binds to the tetracycline response element (TRE) inducing the expression of *Cacna1h*-CRISPRa resulting in augmented endogenous *Cacna1h* expression. **(B)** Schematic representation of a TET-ON system for the conditional expression of CRISPRi (TRE-dCas9-KRAB). Only in the presence of Dox, endogenous *Cacna1h* expression is inhibited. **(C)** *Cacna1h* mRNA expression levels of cultured neurons after transduction with the TET-ON-CRISPRa-*Cacna1h* system (pTRE-dCas9-VPR, pAAV-hSyn-rtTA and pAAV-sgRNA-*Cacna1h*) in the presence or absence of doxycycline (1 μg/mL) ($N = 4$, *t*-test), $^{**}p \leq 0.01$. **(D)** *Cacna1h* mRNA expression of cultured neurons after transduction with the TET-ON-CRISPRi-*Cacna1h* system (pTRE-KRAB-T2A-eGFP, pAAV-hSyn-rtTA, and pAAV-sgRNA-*Cacna1h*) in the presence or absence of doxycycline (1 μg/mL) ($N = 5$, *t*-test), $^{*}p \leq 0.05$.

inhibitor KRAB (Gilbert et al., 2013; Chavez et al., 2015) to induce changes in the endogenous expression of the *Cacna1h* gene. We provide evidence that both the CRISPRa and CRISPRi systems can specifically manipulate the endogenous expression of *Cacna1h* in dividing cells as well as in primary neuronal cultures. In addition, we demonstrate the possibility to activate the *Cacna1h* promoter in mouse organotypic hippocampal slices. Interestingly, the fold-change induction by CRISPRa occurred within a range also observed for $Ca_V3.2$ channelopathies (Becker et al., 2008), making our *Cacna1h*-CRISPR system highly suitable for analyzing this particular and also other channelopathies at the functional level.

Increasing the gene expression levels of *Cacna1h* in a high percentage of cultured cells, which is required for many downstream analyses, or *in vivo* requires the application of viral transduction systems. Here, our *Cacna1h*-CRISPRa toolbox has a clear advantage over conventional virally mediated overexpression approaches, where the limiting packaging capacity of the commonly used and easily applicable recombinant adeno-associated- and lenti-viruses, excludes the possibility to overexpress large proteins like *Cacna1h*. On the other hand, recombinant viruses with a higher packaging capacity, like Adeno- and Herpes Simplex virus, cannot be easily generated in the lab and are expensive to purchase. Since augmentation of proteins using the CRISPRa system is independent of their transcript size, even the large *Cacna1h* gene (mRNA transcript length up to 8.2 Kb) can be easily augmented using rAAV and lentiviruses, which can be produced in most molecular biology labs. Another advantage of the *Cacna1h*-CRISPRa system over conventional gain-of-function approaches is the endogenous modulation of the *Cacna1h* genomic locus, providing the opportunity to study the effects of abundant alternative splicing variants of *Cacna1h*. For *Cacna1h*, at least 12–14 alternative splicing sites have been described, resulting in the possibility to generate more than 4,000 alternative *Cacna1h* transcripts (Zhong et al., 2006). Such a complexity cannot be achieved by conventional overexpression of only one variant of *Cacna1h*. Also in terms of loss-of-function approaches, our *Cacna1h*-CRISPRi has clear advantages over conventional shRNA/siRNA approaches. A siRNA approach for *Cacna1h* in mouse embryonic stem cells reduced *Cacna1h* expression levels to approximately 40% but also caused a non-specific decrease in *Cacna1g* mRNA expression levels (Rodríguez-Gómez et al., 2012). By interfering directly with gene promoters, CRISPRa/i modifies corresponding transcript abundance in a way that strongly recapitulates physiological promoter regulation – compared to the above mentioned molecular manipulations, which typically target one specific mRNA variant only. In contrast, CRISPRa/i leads to abundance changes of the respective RNA, which will then be subjected to alternative splicing. Thereby, the abundance

of the full complement of alternatively spliced variants will be increased.

The fact that we did not observe any alterations in the mRNA expression levels of the calcium channel family members *Cacna1g*, *Cacn1i,* and *Cacna1e* clearly indicates that our newly developed *Cacna1h*-CRISPRa/i toolbox is highly specific for *Cacna1h* modulation. Importantly, since the catalytic inactive Cas9 (dCas9) used in our system does not cleave the DNA, the possible off-target effects are more likely to be less deleterious than using the conventional Cas9 to induce a genetic knock-out (Colasante et al., 2020). Compared to genetic knock-out approaches, the *Cacna1h*-CRISPRa/i toolbox, which is based on viral-transduction, allows to decrease *Cacna1h* expression in selected neuron types, by putting dCas expression under the control of cell type specific promoters, in localized brain regions and under temporal control, without time consuming breeding of animals.

Our Tet-On C*acna1h*-CRISPR toolbox system might open new roads for investigating the role of *Cacna1h* in several channelopathies in more detail. Our present study has some limitations. Firstly, we did not test the present CRISPRa/i systems parallel to cell culture in an *in vivo* approach. However, AAV-constructs acting properly in cultured neurons have been successfully translated into *in vivo* applications (Van Loo et al., 2012, 2015). Secondly, we could not scrutinize the effects of CRISPRa/i on a functional level such as by T-type Ca^{2+}-current density or neuronal discharge analyses. Although neuronal cultures constitute a well-known system for studying electrophysiological properties, measuring calcium currents is challenging, especially after modulation of the system. However, all of our previous studies indicate that cellular changes of $Ca_V3.2$ mRNA expression are reflected on the protein level and by changes of current densities and neuronal discharge behavior (Su et al., 2002; Becker et al., 2008; Van Loo et al., 2015).

Also in the context of mutational/genetic ion channelopathies, the potential of inducible *Cacna1h*-CRISPR approaches are immense. For example, in the Genetic Absence Epilepsy Rat from Strasburg (GAERS) a mutation in C*acna1h* has been described, which augments the expression of $Ca_v3.2$ at the cell surface and increases calcium influx (Proft et al., 2017). Here, the *Cacna1h*-CRISPRa could be used as a gain-of-function approach to mimic the enhanced expression seen in GEARS. In addition, a transient inhibition of *Cacna1h via* the Tet-on inducible *cacna1h*-CRISPRi system in the GAERS rats at different stages during development could also reveal potentially interesting time windows for *Cacna1h*-associated channelopathies.

Taken together, our here described *Cacna1h*-CRISPRa/i modular approach could thus be used to model transient gain-of-function or loss-of-function effects in the *Cacna1h* gene and to study $Ca_V3.2$ channelopathies in more detail *in vivo*.

DATA AVAILABILITY STATEMENT

The original contributions presented in the study are included in the article/**Supplementary Material**, further inquiries can be directed to the corresponding author.

ETHICS STATEMENT

The animal study was reviewed and approved by the LANUV Recklinghausen, Leibnizstr. 10, 45659 Recklinghausen.

AUTHOR CONTRIBUTIONS

DT, SS, AB, and KL conceived and planned the study. DT and AT carried out the molecular and cellular experiments. HS, TO, and SS contributed to the study design and analysis. DT wrote the initial draft. AB, SS, and KL contributed to the review and editing. All authors contributed to the article and approved the submitted version.

FUNDING

Our work was supported by the Deutsche Forschungsgemeinschaft (SFB 1089 to AB, SS, and KL, FOR 2715 to AB and HS, SCHO 820/7-2; SCHO 820/5-2; SCHO 820/6-1; SCHO 820/4-1; SCHO 820 5-2 to SS) and BONFOR. AT was supported by the Humboldt Foundation.

ACKNOWLEDGMENTS

We thank Sabine Optiz for excellent technical assistance.

SUPPLEMENTARY MATERIAL

The Supplementary Material for this article can be found online at: https://www.frontiersin.org/articles/10.3389/fnmol.2021.667143/full#supplementary-material

REFERENCES

Becker, A. J., Pitsch, J., Sochivko, D., Opitz, T., Staniek, M., Chen, C. C., et al. (2008). Transcriptional upregulation of Cav3.2 mediates epileptogenesis in the pilocarpine model of epilepsy. *J. Neurosci.* 28, 13341–13353. doi: 10.1523/JNEUROSCI.1421-08.2008

Biermann, B., Sokoll, S., Klueva, J., Missler, M., Wiegert, J. S., Sibarita, J. B., et al. (2014). Imaging of molecular surface dynamics in brain slices using single-particle tracking. *Nat. Commun.* 5:3024. doi: 10.1038/ncomms4024

Cannon, S. C. (2007). Physiologic Principles Underlying Ion Channelopathies. *Neurotherapeutics* 4, 174–183. doi: 10.1016/j.nurt.2007.01.015

Chavez, A., Scheiman, J., Vora, S., Pruitt, B. W., Tuttle, M., Iyer, E. P. R., et al. (2015). Highly efficient Cas9-mediated transcriptional programming. *Nat. Methods* 12, 326–328. doi: 10.1038/nmeth.3312

Chen, J., Sochivko, D., Beck, H., Marechal, D., Wiestler, O. D., and Becker, A. J. (2001). Activity-induced expression of common reference genes in individual CNS neurons. *Lab. Investig.* 81, 913–916. doi: 10.1038/labinvest.3780300

Chhipa, R. R., Fan, Q., Anderson, J., Muraleedharan, R., Huang, Y., Ciraolo, G., et al. (2018). AMP kinase promotes glioblastoma bioenergetics and tumour growth. *Nat. Cell. Biol.* 20, 823–835. doi: 10.1038/s41556-018-0126-z

Cloud-Based Informatics Platform for Life Sciences R&D | Benchling (2021). Available online at: https://www.benchling.com/ [Accessed February 10, 2021].

Colasante, G., Lignani, G., Brusco, S., Di Berardino, C., Carpenter, J., Giannelli, S., et al. (2019). dCas9-Based Scn1a Gene Activation Restores Inhibitory Interneuron Excitability and Attenuates Seizures in Dravet Syndrome Mice. *Mol. Ther.* 28, 235–253. doi: 10.1016/j.ymthe.2019.08.018

Colasante, G., Qiu, Y., Massimino, L., Di Berardino, C., Cornford, J. H., Snowball, A., et al. (2020). In vivo CRISPRa decreases seizures and rescues cognitive deficits in a rodent model of epilepsy. *Brain* 143, 891–905. doi: 10.1093/brain/awaa045

Gilbert, L. A., Larson, M. H., Morsut, L., Liu, Z., Brar, G. A., Torres, S. E., et al. (2013). CRISPR-mediated modular RNA-guided regulation of transcription in eukaryotes. *Cell* 154, 442–451. doi: 10.1016/j.cell.2013.06.044

Heeringa, S. F., Möller, C. C., Du, J., Yue, L., Hinkes, B., Chernin, G., et al. (2009). A novel TRPC6 mutation that causes childhood FSGS. *PLoS One* 4:e7771. doi: 10.1371/journal.pone.0007771

Hutchings, C. J., Colussi, P., and Clark, T. G. (2019). Ion channels as therapeutic antibody targets. *MABS* 11, 265–296. doi: 10.1080/19420862.2018.1548232

Kampmann, M. (2018). CRISPRi and CRISPRa Screens in Mammalian Cells for Precision Biology and Medicine. *ACS Chem. Biol.* 13, 406–416. doi: 10.1021/acschembio.7b00657

Khosravani, H., Altier, C., Simms, B., Hamming, K. S., Snutch, T. P., Mezeyova, J., et al. (2004). Gating Effects of Mutations in the Cav3.2 T-type Calcium Channel Associated with Childhood Absence Epilepsy. *J. Biol. Chem.* 279, 9681–9684. doi: 10.1074/jbc.C400006200

Khosravani, H., Bladen, C., Parker, D. B., Snutch, T. P., McRory, J. E., and Zamponi, G. W. (2005). Effects of Cav3.2 channel mutations linked to idiopathic generalized epilepsy. *Ann. Neurol.* 57, 745–749. doi: 10.1002/ana.20458

Kügler, S., Kilic, E., and Bähr, M. (2003). Human synapsin 1 gene promoter confers highly neuron-specific long-term transgene expression from an adenoviral vector in the adult rat brain depending on the transduced area. *Gene. Ther.* 10, 337–347. doi: 10.1038/sj.gt.3301905

Mizuno, H., Luo, W., Tarusawa, E., Saito, Y. M., Sato, T., Yoshimura, Y., et al. (2014). NMDAR-regulated dynamics of layer 4 neuronal dendrites during thalamocortical reorganization in neonates. *Neuron* 82, 365–379. doi: 10.1016/j.neuron.2014.02.026

Powell, K. L., Cain, S. M., Ng, C., Sirdesai, S., David, L. S., Kyi, M., et al. (2009). A Cav3.2 T-type calcium channel point mutation has splice-variant-specific effects on function and segregates with seizure expression in a polygenic rat model of absence epilepsy. *J. Neurosci.* 29, 371–380. doi: 10.1523/JNEUROSCI.5295-08.2009

Proft, J., Rzhepetskyy, Y., Lazniewska, J., Zhang, F. X., Cain, S. M., Snutch, T. P., et al. (2017). The Cacna1h mutation in the GAERS model of absence epilepsy enhances T-type Ca2+ currents by altering calnexin-dependent trafficking of Cav3.2 channels. *Sci. Rep.* 7:11513. doi: 10.1038/s41598-017-11591-5

Ran, F. A., Hsu, P. D., Wright, J., Agarwala, V., Scott, D. A., and Zhang, F. (2013). Genome engineering using the CRISPR-Cas9 system. *Nat. Protoc.* 8, 2281–2308. doi: 10.1038/nprot.2013.143

Rodríguez-Gómez, J. A., Levitsky, K. L., and López-Barneo, J. (2012). T-type Ca 2+ channels in mouse embryonic stem cells: modulation during cell cycle and contribution to self-renewal. *Am. J. Physiol.* 302, C494–C504. doi: 10.1152/ajpcell.00267.2011

Ryan, D. P., Dias da Silva, M. R., Wah Soong, T., Fontaine, B., Donaldson, M. R., Kung, A. W. C., et al. (2010). Mutations in a potassium channel (Kir2.6) causes susceptibility to thyrotoxic hypokalemic periodic paralysis. *Cell* 140, 88–98. doi: 10.1016/j.cell.2009.12.024

Rzhepetskyy, Y., Lazniewska, J., Blesneac, I., Pamphlett, R., and Weiss, N. (2016). CACNA1H missense mutations associated with amyotrophic lateral sclerosis alter Cav3.2 T-type calcium channel activity and reticular thalamic neuron firing. *Channels* 10, 466–477. doi: 10.1080/19336950.2016.1204497

Savell, K. E., Bach, S. V., Zipperly, M. E., Revanna, J. S., Goska, N. A., Tuscher, J. J., et al. (2019). A neuron-optimized CRISPR/dCas9 activation system for robust and specific gene regulation. *Eneuro* 6, ENEURO.0495–18.2019. doi: 10.1523/ENEURO.0495-18.2019

Souza, I. A., Gandini, M. A., Wan, M. M., and Zamponi, G. W. (2016). Two heterozygous Cav3.2 channel mutations in a pediatric chronic pain patient: recording condition-dependent biophysical effects. *Pflugers Arch. Eur. J. Physiol.* 468, 635–642. doi: 10.1007/s00424-015-1776-3

Souza, I. A., Gandini, M. A., Zhang, F. X., Mitchell, W. G., Matsumoto, J., Lerner, J., et al. (2019). Pathogenic Cav3.2 channel mutation in a child with primary generalized epilepsy. *Mol. Brain* 12:86. doi: 10.1186/s13041-019-0509-5

Splawski, I., Yoo, D. S., Stotz, S. C., Cherry, A., Clapham, D. E., and Keating, M. T. (2006). CACNA1H mutations in autism spectrum disorders. *J. Biol. Chem.* 281, 22085–22091. doi: 10.1074/jbc.M603316200

Su, H., Sochivko, D., Becker, A., Chen, J., Jiang, Y., Yaari, Y., et al. (2002). Upregulation of a T-Type Ca2+ Channel Causes a Long-Lasting Modification of Neuronal Firing Mode after Status Epilepticus. *J. Neurosci.* 22, 3645–3655. doi: 10.1523/jneurosci.22-09-03645.2002

Thakore, P. I., D'Ippolito, A. M., Song, L., Safi, A., Shivakumar, N. K., Kabadi, A. M., et al. (2015). Highly specific epigenome editing by CRISPR-Cas9 repressors for silencing of distal regulatory elements. *Nat. Methods* 12, 1143–1149. doi: 10.1038/nmeth.3630

Van Loo, K. M. J., Rummel, C. K., Pitsch, J., Müller, J. A., Bikbaev, A. F., Martinez-Chavez, E., et al. (2019). Calcium channel subunit α2σ4 is regulated by early growth response 1 and facilitates epileptogenesis. *J. Neurosci.* 39, 3175–3187. doi: 10.1523/JNEUROSCI.1731-18.2019

Van Loo, K. M. J., Schaub, C., Pernhorst, K., Yaari, Y., Beck, H., Schoch, S., et al. (2012). Transcriptional regulation of T-type calcium channel CaV3.2: bi-directionality by early growth response 1 (Egr1) and repressor element 1 (RE-1) protein -silencing transcription factor (REST). *J. Biol. Chem.* 287, 15489–15501. doi: 10.1074/jbc.M111.310763

Van Loo, K. M. J., Schaub, C., Pitsch, J., Kulbida, R., Opitz, T., Ekstein, D., et al. (2015). Zinc regulates a key transcriptional pathway for epileptogenesis via metal-regulatory transcription factor 1. *Nat. Commun.* 6, 1–12. doi: 10.1038/ncomms9688

Wang, Q., Curran, M. E., Splawski, I., Burn, T. C., Millholland, J. M., VanRaay, T. J., et al. (1996). Positional cloning of a novel potassium channel gene: kVLQT1 mutations cause cardiac arrhythmias. *Nat. Genet.* 12, 17–23. doi: 10.1038/ng0196-17

Woitecki, A. M. H., Müller, J. A., van Loo, K. M. J., Sowade, R. F., Becker, A. J., and Schoch, S. (2016). Identification of synaptotagmin 10 as effector of NPAS4-mediated protection from excitotoxic neurodegeneration. *J. Neurosci.* 36, 2561–2570. doi: 10.1523/JNEUROSCI.2027-15.2016

Yeo, N. C., Chavez, A., Lance-Byrne, A., Chan, Y., Menn, D., Milanova, D., et al. (2018). An enhanced CRISPR repressor for targeted mammalian gene regulation. *Nat. Methods* 15, 611–616. doi: 10.1038/s41592-018-0048-5

Zhang, J., Chen, L., Zhang, J., and Wang, Y. (2019). Drug Inducible CRISPR/Cas Systems. *Comput. Struct. Biotechnol. J.* 17, 1171–1177. doi: 10.1016/j.csbj.2019.07.015

Zhong, X., Liu, J. R., Kyle, J. W., Hanck, D. A., and Agnew, W. S. (2006). A profile of alternative RNA splicing and transcript variation of CACNA1H, a human T-channel gene candidate for idiopathic generalized epilepsies. *Hum. Mol. Genet.* 15, 1497–1512. doi: 10.1093/hmg/ddl068

Conflict of Interest: The authors declare that the research was conducted in the absence of any commercial or financial relationships that could be construed as a potential conflict of interest.

Publisher's Note: All claims expressed in this article are solely those of the authors and do not necessarily represent those of their affiliated organizations, or those of the publisher, the editors and the reviewers. Any product that may be evaluated in this article, or claim that may be made by its manufacturer, is not guaranteed or endorsed by the publisher.

frontiers | Frontiers in Molecular Neuroscience

ORIGINAL RESEARCH
published: 06 April 2022
doi: 10.3389/fnmol.2022.848540

Direct Regulation of Hyperpolarization-Activated Cyclic-Nucleotide Gated (HCN1) Channels by Cannabinoids

*Sultan Mayar, Mina Memarpoor-Yazdi, Ahmad Makky, Romina Eslami Sarokhalil and Nazzareno D'Avanzo**

Département de Pharmacologie et Physiologie, Université de Montréal, Montréal, QC, Canada

Cannabinoids are a broad class of molecules that act primarily on neurons, affecting pain sensation, appetite, mood, learning, and memory. In addition to interacting with specific cannabinoid receptors (CBRs), cannabinoids can directly modulate the function of various ion channels. Here, we examine whether cannabidiol (CBD) and Δ9-tetrahydrocannabinol (THC), the most prevalent phytocannabinoids in *Cannabis sativa*, can regulate the function of hyperpolarization-activated cyclic-nucleotide-gated (HCN1) channels independently of CBRs. HCN1 channels were expressed in *Xenopus* oocytes since they do not express CBRs, and the effects of cannabinoid treatment on HCN1 currents were examined by a two-electrode voltage clamp. We observe opposing effects of CBD and THC on HCN1 current, with CBD acting to stimulate HCN1 function, while THC inhibited current. These effects persist in HCN1 channels lacking the cyclic-nucleotide binding domain (HCN1ΔCNBD). However, changes to membrane fluidity, examined by treating cells with TX-100, inhibited HCN1 current had more pronounced effects on the voltage-dependence and kinetics of activation than THC, suggesting this is not the primary mechanism of HCN1 regulation by cannabinoids. Our findings may contribute to the overall understanding of how cannabinoids may act as promising therapeutic molecules for the treatment of several neurological disorders in which HCN function is disturbed.

Keywords: HCN channel, cannabinoids, cannabidiol, Δ9-THC, ion channel

OPEN ACCESS

Edited by:
Stephan Kellenberger, University of Lausanne, Switzerland

Reviewed by:
Lei Zhou, Virginia Commonwealth University, United States
Bin Pan, Medical College of Wisconsin, United States
John Bankston, University of Colorado Anschutz Medical Campus, United States

****Correspondence:***
Nazzareno D'Avanzo
nazzareno.d.avanzo@umontreal.ca

Specialty section:
This article was submitted to Pain Mechanisms and Modulators, a section of the journal Frontiers in Molecular Neuroscience

Received: *04 January 2022*
Accepted: *21 February 2022*
Published: *06 April 2022*

Citation:
Mayar S, Memarpoor-Yazdi M, Makky A, Eslami Sarokhalil R and D'Avanzo N (2022) Direct Regulation of Hyperpolarization-Activated Cyclic-Nucleotide Gated (HCN1) Channels by Cannabinoids. Front. Mol. Neurosci. 15:848540. doi: 10.3389/fnmol.2022.848540

INTRODUCTION

Hyperpolarization-activated cyclic-nucleotide-gated (HCN) channels are widely expressed in the central and peripheral nervous systems. All four isoforms (HCN1-4) are expressed in the brain (Pape, 1996; Santoro et al., 1997, 1998; Ludwig et al., 1998; Moosmang et al., 2001) where they play a role in setting the resting membrane potential, dendritic integration, neuronal pacemaking, and establishing the action potential threshold (Pape, 1996). HCN channels are important for learning and memory, pain sensation, sour taste sensation, and vision. $HCN1^{-/-}$ mice show impaired motor learning but enhanced spatial learning and memory (Nolan et al., 2003, 2004) and enhanced susceptibility to kainic acid-induced seizures (Huang et al., 2009). $HCN2^{-/-}$ mice presented symptoms of absence epilepsy and tremoring (Ludwig et al., 2003). Gain and loss of function mutations in HCN1 and HCN2 have also been identified in patients with various forms of

epilepsy (Tang et al., 2008; Dibbens et al., 2010; DiFrancesco et al., 2011; Nakamura et al., 2013; Nava et al., 2014). Altered HCN-cAMP signaling in prefrontal cortex networks also appears to contribute to the working memory deficits in schizophrenia and stress (Arnsten, 2011; Paspalas et al., 2013; Gamo et al., 2015). HCN channels are also highly expressed in primary afferent (sensory) neurons such as the dorsal root ganglion (Scroggs et al., 1994; Villiere and McLachlan, 1996; Yagi and Sumino, 1998; Cardenas et al., 1999; Abdulla and Smith, 2001; Chaplan et al., 2003; Yao et al., 2003; Tu et al., 2004; Masuda et al., 2006; Onoda et al., 2006) with HCN1 and HCN2 predominant in large and small-sized neurons, respectively (Moosmang et al., 2001; Chaplan et al., 2003; Tu et al., 2004). $HCN2^{-/-}$ mice do not demonstrate neuropathic pain in response to mechanical or thermal stimuli (Emery et al., 2011) suggesting that I_h drives action potential firing to initiate neuropathic pain in nociceptors. Mutations in the scaffolding protein SHANK3 may predispose people to autism by inducing an I_h channelopathy with increased neuronal input resistance, enhanced neuronal excitability, and reduced synaptic transmission (Yi et al., 2016).

Cannabinoids are a broad class of molecules that act primarily on neurons, affecting pain sensation, appetite, mood, learning, and memory. There are 3 classes of cannabinoids: (1) endocannabinoids produced naturally by the body, (2) phytocannabinoids from some plants, and (3) synthetic cannabinoids. Cannabinoids may provide effective treatments for addiction, pain, epilepsy, major mood disorders, anxiety, post-traumatic stress disorder, spasticity in multiple sclerosis, Parkinson's disease, and Huntington's disease (Cunha et al., 1980; Hill et al., 2012; The Health Effects of Cannabis Cannabinoids, 2017; Russo, 2018). However, to use them therapeutically, without negative side effects, we must understand exactly how they interact with their targets to affect nerve function.

Cannabinoids bind to cannabinoid receptors (CB1R or CB2R). However, activating CBRs cannot directly alter electrical excitability in neurons, since CBRs do not generate electrical signals on their own. Instead, membrane potential and electrical signaling in all excitable cells, including neurons, are generated by ion channels embedded in the cell membrane. Recently, it has been shown that the synthetic cannabinoid WIN55,212-2 affects memory by activating CB1 receptors, leading to intracellular signaling changes that affect the I_h current generated by hyperpolarization-activated HCN channels (Maroso et al., 2016) (**Figure 1**). The CB1R–I_h pathway does not involve adenylyl cyclase/cAMP formation, since CB1Rs decrease cAMP levels through $G\alpha_i$. Instead, CB1R activation involves JNK-mediated increases in activated nitric oxide synthase (NOS), resulting in increased guanylyl cyclase activity and, in turn, cGMP.

In addition to activating CBRs, cannabinoids can also directly bind ion channels, or affect their function by altering the physiochemical properties of the cell membrane. WIN 55,212–2, Δ^9-tetrahydrocannabinol (THC) and cannabidiol (CBD) alter the voltage-dependence of activation and inactivation in several Nav channels (Okada et al., 2005; Ghovanloo et al., 2018). THC and CBD also inhibit T-type calcium channels (Ross et al., 2008). Some TRP channel subfamilies, including TRPV1, are activated and desensitized by CBD, while TRPM8 is inhibited (De Petrocellis et al., 2011, 2012; Iannotti et al., 2014). On the other hand, anandamide, THC, and CBD potentiate homomeric and heteromeric glycine receptors (Hejazi et al., 2006; Ahrens et al., 2009). Given the important role of HCNs in synaptic integration, mood, pain sensation, and memory, and the knowledge that cannabinoids may have therapeutic potential for these same disorders and can directly regulate the function of several ion channels, we aimed to determine if cannabinoids have direct effects on HCN channels that are independent CBR activation.

MATERIALS AND METHODS

Drugs and Reagents

Drugs, cannabidiol (CBD), and Δ9-THC (Sigma-Aldrich, USA) were prediluted in 99.8% methanol at a concentration of 1.0 mg/ml. Detergent, Triton™ X-100 (Sigma-Aldrich, USA) was diluted to a working concentration of 10 mM with distilled water from a stock solution.

Molecular Biology and Cell Expression

cDNA coding for the mouse HCN1 gene was previously subcloned into expression vector pGH19 (provided by Dr. William N. Zagotta, University of Washington, Seattle, Washington). The mouse HCN1-CX5 construct (denoted as HCN1-ΔCNBD in this article) was previously subcloned into expression vector pGH19 (provided by Bina Santoro, Columbia University, New York). To obtain RNA, NheI (New England Biolabs) was used to linearize both cDNA constructs of mHCN1 and ∼1.0 μg of linearized cDNA was used for *in vitro* transcription synthesis using the mMESSAGE mMACHINE™ T7 Transcription kit (Thermo Fisher Scientific, Life Technologies, USA).

All the experiments were performed using unfertilized *Xenopus* oocytes, extracted from anesthetized female *Xenopus laevis*. Once extracted, oocytes were injected with 4.6 ng of mHCN1 using a Drummond Nanoject II injector (Drummond Scientific Company). Prior to injection, oocytes were subject to a controlled temperature of 17–19°C and placed in vials containing Barth antibiotic solution (mM): 90 NaCl, 3 KCl, 0.82 $MgSO_4.7H_2O$, 0.41 $CaCl_2.2H_2O$, 0.33 $Ca(NO_3)_2.4H_2O$, and 5 HEPES supplemented with 100 U/ml of penicillin-streptomycin and 10 mg/ml of kanamycin stock (10 mg/ml). Post injection cells were incubated in Barth antibiotic serum solution supplemented with ∼5% horse serum. Cells were expressed and ready to be used in electrophysiological recordings 1–3 days post injection.

Electrophysiological Recordings

Electrophysiological studies were conducted using the two-electrode voltage clamp (TEVC) technique. Borosilicate rapid fill microelectrode pipettes (1.0 mm OD × 0.5 mm ID/Fiber from FHC Inc., USA) were filled with filtered 1 M KCL solution. Oocytes expressing wild-type HCN1 and HCN1-ΔCNBD were recorded in a bath solution containing (in mM) 89 KCl, 15 HEPES, 0.4 $CaCl_2$, and 0.8 $MgCl_2$, pH = 7.4. Macroscopic currents were recorded using Oocyte Voltage Clamp (OC-725C) amplifier (Warner Instruments, USA) and digitized using the

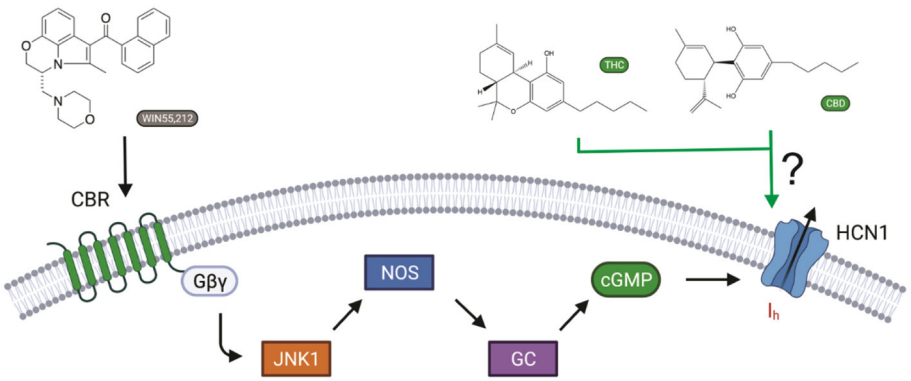

FIGURE 1 | Cannabinoid regulation of I_h in neurons. The synthetic cannabinoid WIN55,212-2 affects memory *via* increasing I_h by activating CB1 receptors, leading to JNK-mediated increases in activated nitric oxide synthase (NOS), resulting in increased guanylyl cyclase activity and, in turn, cGMP (Hill et al., 2012). However, cannabinoids have also been shown to modify the function of several ion channels independently of cannabinoid receptors (CBRs) activation. Here, we ask if hyperpolarization-activated cyclic-nucleotide-gated (HCN1) channels can be directly modulated by cannabidiol (CBD) and Δ9-tetrahydrocannabinol (THC) (Maroso et al., 2016).

Digidata 1322A data acquisition apparatus (Molecular Devices). All the data were acquired using the software Clampex 10.5 at a sampling rate of 5 KHz with a filter of 1 KHz. Repetitive pulse protocols involved 2 s pulses to −130 mV hyperpolarized voltage every 30 s from a holding potential (V_H) of 0 mV. HCN1 activation was assessed by 3.5 s test-steps between −160 and −30 mV (ΔV = +10 mV) from a V_H = 0 mV, followed by a 3 s step to −160 mV. Deactivation was assessed by applying a 1.75 s prepulse to −130 mV, followed by test pulses from +50 to −70 mV (ΔV = −10 mV). Hysteresis was also monitored by applying voltage ramps from 0 to −150 mV and back to 0 mV at varying speeds. In all recordings, cells were held at the holding potential for an inter-pulse time of 27 s to allow the channels to fully recover between sweeps. Cannabinoids were added to the bath solution in 10 μM increments only after recordings of the previous condition had stabilized (i.e., current density remained unchanged between recordings at that concentration; typically, 15–30 min after their addition). Equimolar quantities of methanol used to solvate the cannabinoids to their listed concentrations were used as controls. Therefore, where presented, MeOH (X μM) represents the quantity of methanol used to dilute CBD or THC to X μM, and not X μM of methanol. All recordings were conducted at room temperature.

Data Analysis and Statistics

All recordings were analyzed offline using the Clampfit (Molecular Devices) software. Data were analyzed and plotted using Origin 8.0 software (Northampton, MA, USA) or GraphPad Prism (Version 8.1.1, San Diego, CA). Current-voltage (I–V) relationships were analyzed using built-in software in pClamp, taking each respective voltage to an inquired current. The I–V relationship was fit with the Boltzman I–V equation:

$$I = \frac{(V_m - V_{rev})g_{\max}}{1 + e^{\frac{V_m - V_{\frac{1}{2}}}{k}}} \quad (1)$$

Activation and deactivation kinetics were determined with mono-exponential fits of test pulses after the initial lag period. Steady-state activation curves were fit with a standard Boltzmann equation:

$$\frac{G}{G_{Max}} = \frac{1}{1 + e^{\frac{V_m - V_{\frac{1}{2}}}{k}}} \quad (2)$$

where V_m corresponds to the test pulse, $V_{1/2}$ is the midpoint of activation, and k is the slope factor. EC_{50}/IC_{50} values were determined by fitting concentration dependence curves with the Hill equation:

$$\frac{I}{I_0} = \frac{1}{1 + \left(\frac{EC_{50}\ or\ IC_{50}}{[A]}\right)^n}, \quad (3)$$

where I_0 is the baseline current for HCN1 prior to treatment.

Data are presented as means (±) standard error. Statistical significance for I–V curves was measured using two-way ANOVA with Tukey HSD *post-hoc* analysis. $V_{1/2}$'s of steady-state dependencies were determined for each recording and pooled for a given treatment then analyzed by one-way ANOVA with Tukey *post-hoc* analysis. Mean activation and deactivation kinetics (from −20 to −70 mV) were analyzed using the Zar method for significance (Zar, 1984).

RESULTS

Unfertilized *Xenopus oocytes* lack CBRs (Xenbase.org) (Karimi et al., 2018) and thus, provide an ideal system to examine the direct effects of cannabinoids on HCN channels by two-electrode voltage-clamp (TEVC). Using a repetitive pulse protocol to hyperpolarized potentials (−130 mV from a holding potential V_H = 0 mV), we assessed the effects of adding CBD or THC to the bath solution at increasing concentrations (**Figure 1**). To ensure the effects of CBD and THC could be differentiated from the vehicle (methanol), we first examined the effects of equimolar

quantities of methanol used to solvate the cannabinoids to their listed concentrations. We saw a negligible change (<5%) in overall current over the course of nearly 2 h at varying concentrations (**Figures 2F,G**). We observed a concentration-dependent increase in HCN1 current with the addition of CBD, which can then be inhibited by a saturating concentration of ZD7288 (**Figures 2A,C,D**). At −130 mV, the concentration dependence of CBD activation of HCN1 shows 50% max response (EC_{50}) at 28.5 μM (slope = 0.1) with up to 91% maximal increase in current (**Figure 2B**). This effect is observed even in the presence of the CB1 receptor antagonist AM-251 (**Figure 2B**), providing further support that CBRs are not functionally expressed in *Xenopus* oocytes. Furthermore, the addition of CBD to uninjected oocytes does not stimulate the activation of a "background" current (**Figure 2C**), indicating that the observed changes are only due to the effect on HCN1 currents.

We then studied the effect of Δ^9- THC on HCN1. Contrary to the effect of CBD, THC has an inhibitory effect on HCN1 (**Figure 2E**). Using repetitive pulses to −130 mV, we observe a concentration-dependent inhibition by THC with a maximal inhibitory response of THC of 63% (**Figure 2G**) and a half-maximal response (relative IC_{50}) at 21.8 μM (slope = −0.1). A total of 50% block of HCN1 current by THC (absolute IC_{50}) occurs at 28.9 μM.

To assess the effects of CBD and THC on HCN1 currents in more detail, we examined the relative I–V relationship, steady-state voltage-dependencies, and gating kinetics. Cannabinoids were added to the bath solution in 10 μM increments only after currents at the previous concentration had stabilized, and for each cell, currents were normalized to the amount of current −160 mV under control (0 μM) conditions. We observed a concentration-dependent increase in HCN1 current with the addition of CBD above 10 μM, with no statistically significant changes in steady-state voltage-dependence and gating kinetics (**Figures 3A–E**). On the other hand, the addition of THC in the bath induces a concentration-dependent decrease in the current (**Figures 3F,G**). However, THC also does not affect steady-state voltage-dependence or gating kinetics (**Figures 3G,H**). Equivalent amounts of methanol used to dissolve CBD or THC have no effect on current, voltage-dependence, or gating kinetics (**Supplementary Figure 1**).

HCN channels have been shown to undergo a hysteresis or mode-shifting in their voltage-dependence where the voltage sensitivity of gating charge movement depends on the previous state (Mannikko et al., 2005; Elinder et al., 2006; Xiao et al., 2010). Voltage-hysteresis is thought to play an important role in preventing cardiac arrhythmias (Mannikko et al., 2005; Elinder et al., 2006; Xiao et al., 2010), and for short-term, activity-dependent memory (Bruening-Wright and Larsson, 2007). We quantified the degree of hysteresis using ramp protocols of various rates between 600 and 37.5 mV/s and measuring the difference in area between the curves of the forward and reverse direction as performed previously (Furst and D'Avanzo, 2015) (**Figure 4A**). We observe that HCN1 hysteresis in oocytes decreases with slower ramp speeds (**Figure 4A**), and that methanol has no concentration-dependent effect on HCN1 hysteresis (**Figure 4B**). We observe that at all concentrations and ramp speeds, CBD had no significant effect on HCN1 hysteresis (**Figures 4C–E**). On the other hand, at concentrations above 10 μM, THC decreases the degree of hysteresis at faster ramp speeds (**Figures 4C–E**). Notably, the impact of THC on HCN1 hysteresis also appears to be concentration-dependent with a greater range of ramp speeds affected as THC concentrations increase.

To address the mechanism(s) by which CBD and THC modulate HCN1 channels, we first examined the role of the CNBD, by performing similar experiments on an mHCN1 construct lacking the cyclic-nucleotide binding domain (HCN1ΔCNBD) (Santoro et al., 2011). Similar to full-length channels, methanol has no effect on HCN1ΔCNBD properties (**Supplementary Figures 1E–H**). The application of CBD to HCN1ΔCNBD channels increases the current in a concentration-dependent manner, with a 35% maximal increase in current above 40 μM (**Figure 5A**). Steady-state voltage dependence and activation kinetics are unaffected by treatment with CBD (**Supplementary Figures 2B,C**). Intriguingly, the lack of CNBD uncovered an effect of CBD on slowing the deactivation kinetics of HCN1 (**Figure 5B**). On the other hand, HCN1ΔCNBD current decreases following treatment with THC, although the effect on slope conductance (**Figure 5C**) is less than what was observed for full-length HCN1 (**Figure 3G**). Again, similar to full-length channels, THC does not affect HCN1 steady-state voltage-dependence and gating kinetics (**Supplementary Figures 2F–H**). Hysteresis in HCN1ΔCNBD channels is also unaffected by methanol and CBD, however, similarly to what we observed for full-length channels, HCN1ΔCNBD hysteresis also decreases with elevated levels of THC at faster ramp speeds (**Figures 5D,E**). These results suggest that the primary effects of CBD and THC on HCN1 function do not directly involve the CNBD, though this domain may fine tune their modulation.

Our results suggest that the CBR-independent regulation of HCN1 channels by CBD and THC does not involve the CNBD and thus likely involves the transmembrane regions. The functions of numerous membrane proteins are regulated by the physiochemical properties of the membrane bilayer, including membrane fluidity (Caires et al., 2017; Yoshida et al., 2019; Ghovanloo et al., 2021). CBD and THC have both been shown to alter membrane fluidity. THC increases membrane fluidity in the hydrophobic core of brain membranes (Hillard et al., 1985; Beiersdorf et al., 2020), while CBD decreases membrane fluidity (increases membrane stiffness) (Ghovanloo et al., 2021). To assess whether the mechanism of cannabinoid regulation of HCN1 involves changes to membrane fluidity, we performed experiments using Triton X-100, a non-ionic surfactant that has been shown to increase membrane fluidity (Ingolfsson et al., 2010). Similar to THC, TX-100 rapidly decreases HCN1 current at −130 mV using a repetitive pulse protocol (**Figure 6A**). However, while the effects of cannabinoid treatment on HCNs were slow (15–40 min), the effects of TX-100 treatment occurred much more rapidly (<5 min). TX-100 also decreases HCN1 current using step protocols (**Figure 6B**), however, the effects on steady-state activation and gating kinetics are significantly

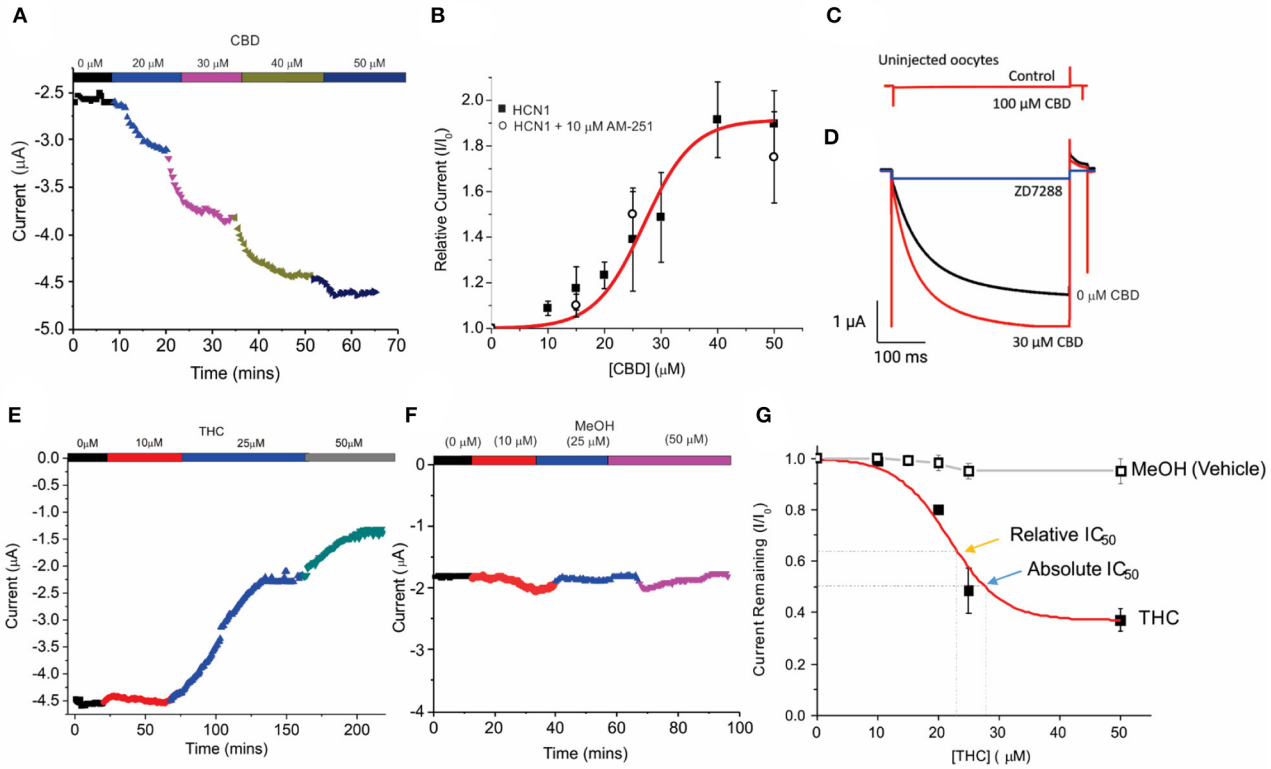

FIGURE 2 | Concentration-dependent regulation of HCN1 current by THC and CBD. **(A)** Steady-state current values from a representative cell following repetitive pulses to −130 mV from V_H = 0 mV with the addition of 0, 10, 20, 30, and 50 μM CBD. **(B)** Concentration dependence of HCN1 activation by CBD (■) at −130 mV (n = 13). This activation of HCN1 persists in the presence of the CB1R antagonist 10 μM AM-251 (○) (n = 5). A total of 50% Max response (EC_{50}) for CBD is elicited at 28.5 μM, with a 91% maximal increase in current. **(C)** CBD has no effects on uninjected oocytes, indicating that we are not observing effects on background currents. **(D)** CBD activated currents can be fully inhibited by 500 μM ZD7288. This indicates that CBD is only activating HCN1 currents, and not activating a background current in oocytes. **(E)** Steady-state currents from a representative cell following repetitive pulses to −130 mV in 0, 10, 25, and 50 μM THC. **(F)** Steady-state currents from a representative cell following repetitive pulses to −130 mV in the presence of the quantity of methanol used as a vehicle for 0, 10, 25, and 50 μM CBD/THC. **(G)** Concentration dependence of HCN1 inhibition by THC (■) or methanol (□) at −130 mV (n = 5). THC induces a 63% maximal block of HCN1 currents, with a half-maximal response (Relative IC_{50}) of 21.8 μM. 50% block of total current (Absolute IC_{50}) occurs at 28.9 μM. Methanol induces <a 5% decrease in current at concentrations above 20 μM (n = 4).

different compared with THC (e.g., $P < 0.05$ for $V_{1/2}$ of 30 μM THC vs. TX-100 by two-sample unpaired t-test). We see a leftward shift from −10 to −15 mV in the steady-state, meaning increasing membrane fluidity makes it more difficult for HCN1 channels to open (**Figure 6C** and **Supplementary Table 3**). In addition, we see a change in the slope of the activation time constants, indicating that the channel opens slower at more hyperpolarized voltages (**Figure 6D**). This change in slope of the activation time constants was not observed in cannabinoid treated cells. Thus, since the effects of TX-100 do not resemble the modulation seen by either CBD or THC, it appears that the mechanism of HCN1 regulation by either of these cannabinoids cannot be completely described by the effects of altered membrane fluidity.

DISCUSSION

Phytocannabinoids CBD and THC have been shown to interact with numerous ion channels independently of CBRs (Okada et al., 2005; Hejazi et al., 2006; Ross et al., 2008; Ahrens et al., 2009; De Petrocellis et al., 2011, 2012; Iannotti et al., 2014; Ghovanloo et al., 2018). Here, we demonstrate that HCN1 currents are enhanced by CBD and inhibited by THC (**Figures 2**, **3**). Using standard step protocols, the effects of both CBD and THC were limited to changes in current density with no observed changes in steady-state activation or gating kinetics. This is similar to the effects that modulating membrane cholesterol content has on HCN1 current (Furst and D'Avanzo, 2015). Some of the effects of THC and CBD on voltage-dependence may be obscured by the non-saturating voltage-dependence curve we report, as a result of our use of a high K^+ bath solution. However, if the basis of the increase in HCN1 current observed following treatment with CBD was caused a shift in voltage-dependence, we would expect the $V_{1/2}$ to be more depolarized and thus saturation to be more apparent. From our traces and the data, we see this is not the case. On the other hand, it is possible that a further hyperpolarized shift in $V_{1/2}$ may cause the effect of decreased HCN1 currents by THC. However, this is also unlikely since we were able to detect such a hyperpolarizing shift with TX-100 but not THC. Thus, it is more likely that the number of channels at the membrane, or the unitary conductance, are affected by treatment by these cannabinoids.

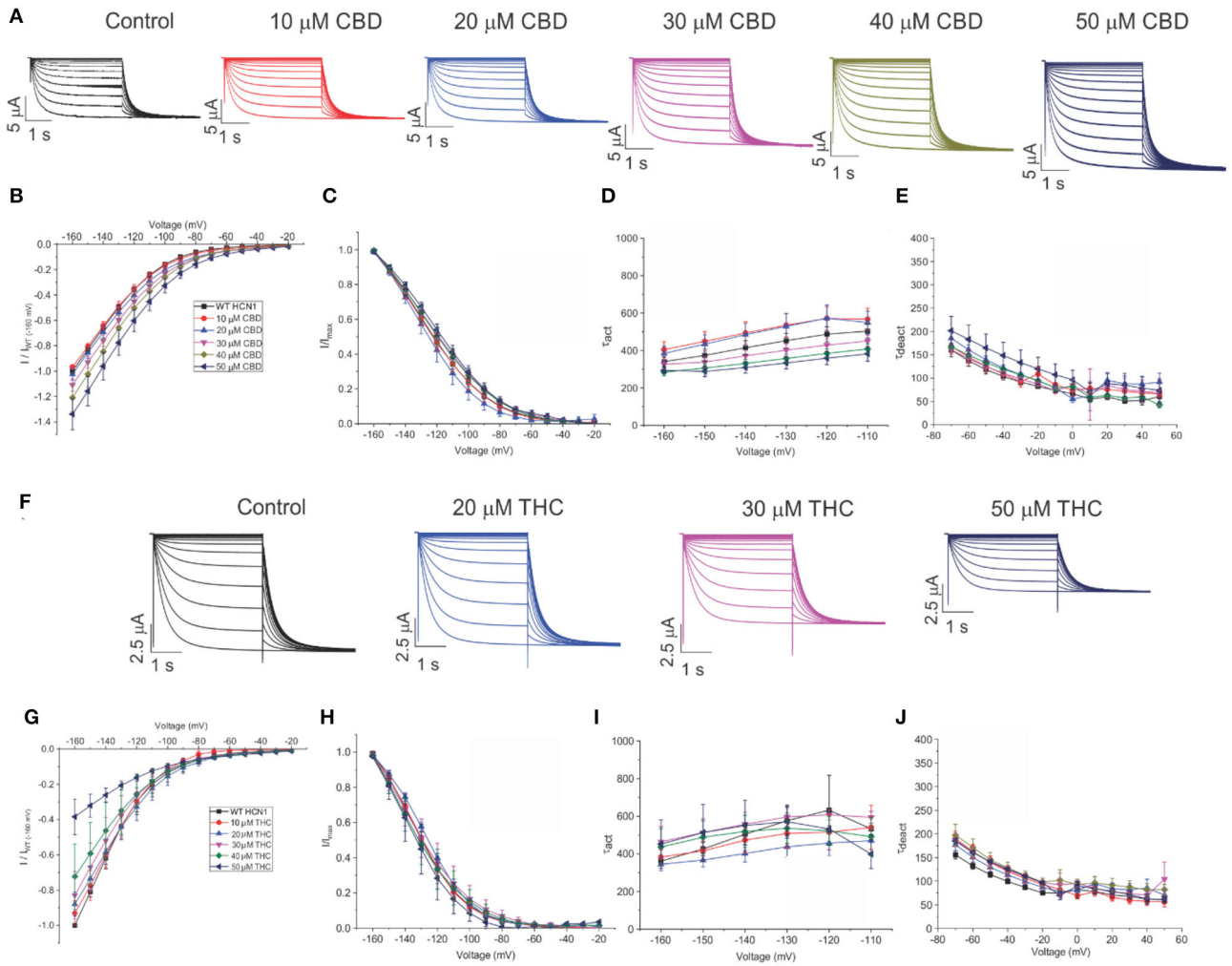

FIGURE 3 | Regulation of HCN1 by cannabidiol (CBD) and Δ^9-tetrahydrocannabidiol (THC). **(A)** Representative traces from a paired experiment following the addition of increasing concentrations of CBD to oocytes expressing full-length HCN1. **(B)** Current–voltage (I/V) relationship in presence of CBD normalized to maximal current ($I_{WT(-160\,mV)}$) ($5 < n < 18$ per condition; $P < 0.05$ for 30–50 μM). **(C)** Steady state activation in presence of CBD ($P = 0.81$ for $V_{1/2}$). **(D)** Activation time constant (τ) kinetics in presence of CBD ($0.21 < P < 0.71$). **(E)** Deactivation time constant (τ) kinetics in presence of CBD ($3 < n < 7$ per condition; $0.09 < P < 0.65$). **(F)** Representative traces from a paired experiment following the addition of increasing concentrations of THC to oocytes expressing full-length HCN1. **(G)** (I/V) relationship in presence of THC normalized to maximal current ($I_{WT(-160\,mV)}$) ($4 < n < 8$ per condition; $P < 0.05$ for Gmax (slope between −120 and −160 mV) of 20–50 μM). **(H)** Steady-state activation in presence of THC ($P = 0.49$ for $V_{1/2}$). **(I)** Activation time constant (τ) kinetics in presence of THC ($0.21 < P < 0.90$). **(J)** Deactivation time constant (τ) kinetics in presence of THC ($3 < n < 8$ per condition; $0.11 < P < 0.45$).

We also observed that THC alters the non-equilibrium gating properties of the HCN1, since they undergo less hysteresis following treatment with that cannabinoid, particularly with faster ramps (**Figure 4**). This means THC makes HCN1 channels less responsive to the rate of membrane potential changes (i.e., firing rate). The CNBD domain does not appear to be critical for cannabinoid regulation of HCN function, since these changes are also observed in recordings of HCN1ΔCNBD channels (**Figure 5**). This also indicates that CBD and THC do not alter HCN1 channels through changes in intracellular cyclic-nucleotide signaling. However, the lack of the CNBD did unmask the effects of CBD on the HCN deactivation kinetics (**Figure 5B**), indicating that CBD in the membrane slows channel closure. Since cannabinoids are lipids that are embedded in the lipid bilayer, they can alter channel function by altering membrane properties and/or directly binding the channel. Both mechanisms appear to be important for the regulation of Nav's by CBD (Ghovanloo et al., 2018, 2021; Sait et al., 2020) while TRPV2 directly binds CBD in the transmembrane helices (Pumroy et al., 2019). Changes to membrane fluidity were induced by the treatment of cells by TX-100, a non-ionic surfactant that has been shown to increase membrane fluidity (Ingolfsson et al., 2010). TX-100 decreases HCN1 function, indicating that membrane fluidity is an important modulator of this channel. However, the rate of action and the changes in voltage-dependent activation and gating kinetics did not reflect the effects of CBD or THC

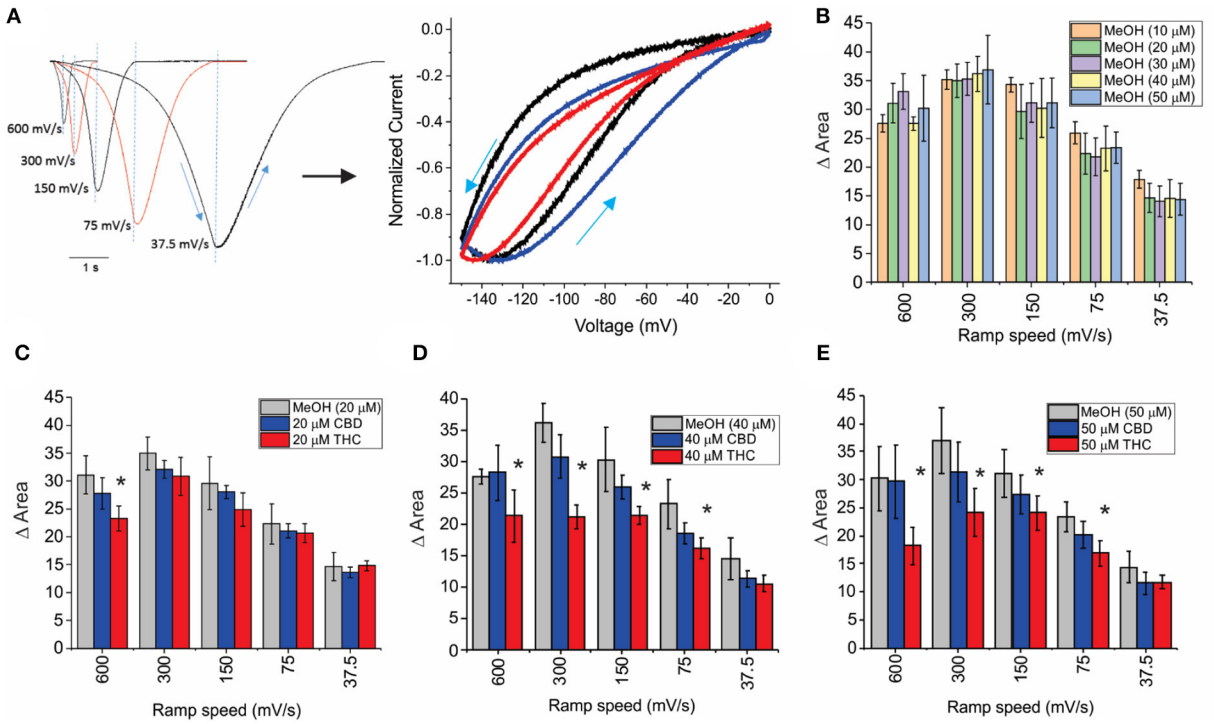

FIGURE 4 | Effects of CBD and THC on HCN1 hysteresis. **(A)** Ramps from 0 to −150 mV and back to 0 mV at speeds of 600, 300, 150, 75, and 37.5 mV/s. The degree of hysteresis was quantified by the area between the forward and backward current traces when plotted vs. the membrane voltage. **(B)** Histogram of HCN1 hysteresis for HCN1 treated with different concentrations of methanol used as vehicles for the cannabinoids at concentrations listed in parentheses. Hysteresis is unaffected by increasing concentrations of methanol. **(C–E)** THC reduces the degree of hysteresis at fast ramp speeds, with a greater range of ramp speeds affected as THC concentration increases. CBD did not affect HCN1 hysteresis ($3 < n < 10$ for each condition; $^*P < 0.05$).

on HCN1 that we observe. While it is possible that TX-100 has greater effects on membrane fluidity than THC at the concentrations used, even at low (15 μM) concentrations, the effects of TX-100 on HCN1 currents are faster than THC, a −10 mV change in $V_{1/2}$ is observed, and the slopes of the activation kinetics are in the opposite direction. THC does not induce these effects even at the highest concentrations used, and thus their effects appear qualitatively different. Therefore, it appears that the primary mechanism of action on HCN1 channels is not through altered membrane fluidity, though it may still be a secondary contributor to the effects observed. However, at this time, we cannot conclude that these phytocannabinoids directly bind HCN channels without further experimentation. Other mechanisms, such as changes in bilayer thickness/hydrophobic matching, lipid organization, or other membrane properties may contribute to the modulation by cannabinoids. Since the macroscopic current is a function of the unitary conductance, the number of channels, and the open probability, we did not observe changes in steady-state voltage dependence (i.e., open probability), meaning THC and CBD may alter the single-channel properties of these channels. Alternatively, given the slow time courses involved in the observed effects, it is possible that these cannabinoids alter protein turnover at the membrane, altering the number of channels at the membrane with time.

The concentrations of CBD and THC necessary to affect HCN1 channels (in the mid-micromolar range) may be considered high for these molecules to have therapeutic actions through these channels. However, additional considerations may prove such concerns to be unwarranted. At first, various other ion channels have been shown to be modulated by CBD and THC within the concentration ranges used in this study. Direct activation of chloride ion channels (α_1 and $\alpha_2\beta$ glycine receptors) by CBD has been reported with an EC_{50} of 132.4 and 144.3 μM (Ahrens et al., 2009). Sodium channel, NavMs, and α_7 -nicotinic acethylcholine (α_7 nACh) are inhibited by CBD with an IC_{50} of 17.8 (Sait et al., 2020) and 11.3 μM (Mahgoub et al., 2013), respectively. Kv1.2 channels are inhibited by THC with an IC_{50} of 2.4 μM (Poling et al., 1996), while human ether-à-go-go (hERG) channels are inhibited with an IC_{50} of 10.3 μM (Orvos et al., 2020). In addition, single-dose administration of 10 mg CBD and THC generate serum levels of 3.0 ± 3.1μg/L (= 9.1–19.4 μM) (Guy and Flint, 2004; Guy and Robson, 2004). Anticonvulsant effects of THC and CBD have an ED_{50} ∼120 mg/kg (Devinsky et al., 2014). Depending on the mode of administration, 120 mg/kg of CBD leads to concentrations of 7 μM in serum and 1.3 μg/g in the brain; increased with IP administration to 45 μM in serum and 6.9 μg/g in the brain (Deiana et al., 2012). Because of their high lipophilicity ($K_{octanol-water}$ ∼ 6–7), there is a preferential distribution to fat with rapid distribution in the

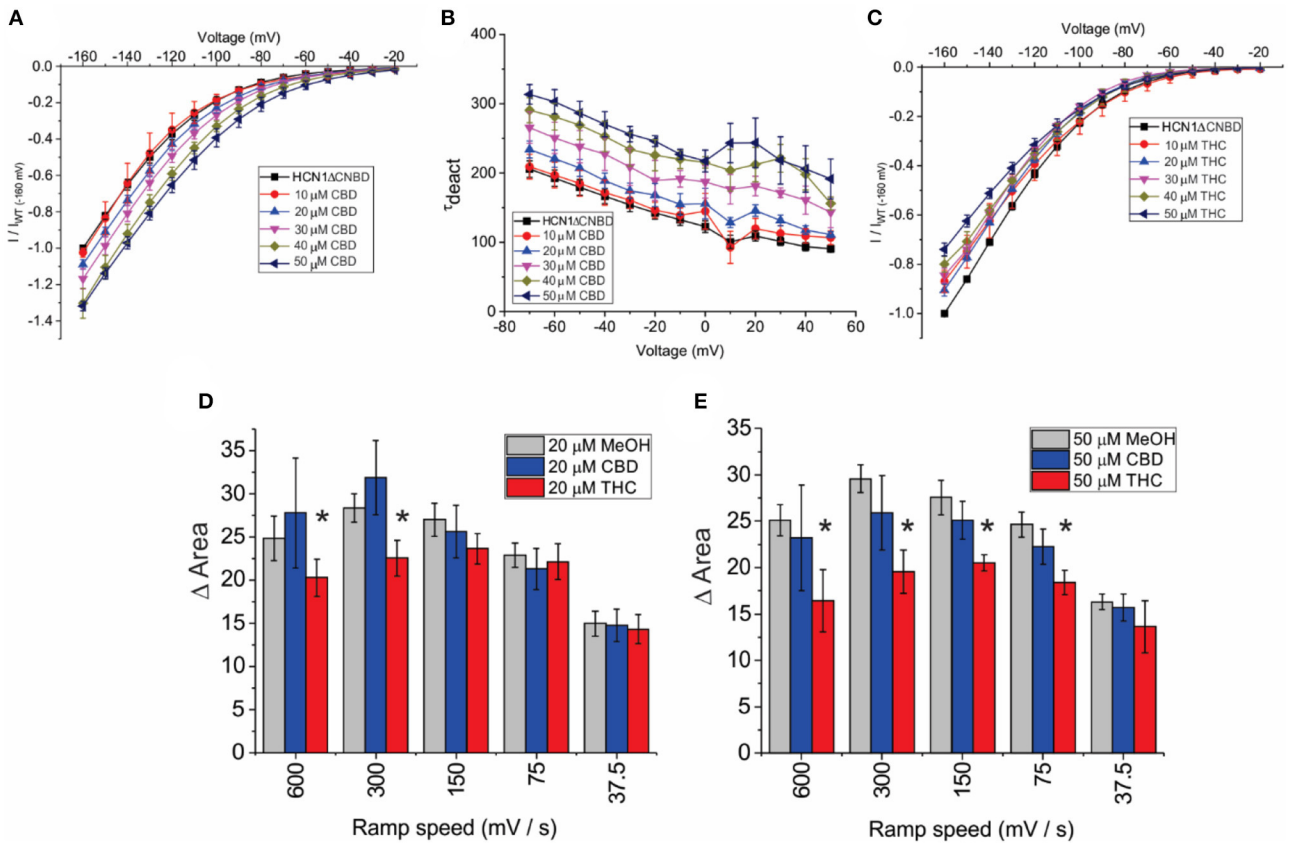

FIGURE 5 | Effects of CBD and THC on HCN1 do not require the CNBD. **(A)** Current-voltage (I/V) relationship of HCN1ΔCNBD in the presence of increasing concentrations of CBD normalized to maximal current ($I_{WT(-160\,mV)}$) ($4 < n < 13$ per condition; $P < 0.05$ for 20–50 μM). **(B)** Deactivation time constant (τ) kinetics of HCN1ΔCNBD following treatment with CBD ($4 < n < 10$ per condition; $P < 0.05$ for 20–50 μM). **(C)** Current-voltage (I/V) relationship of HCN1ΔCNBD in the presence of increasing concentrations of THC normalized to maximal current ($I_{WT(-160\,mV)}$) ($4 < n < 12$ per condition; $P < 0.05$ for 10–50 μM). **(D,E)** THC reduces the degree of HCN1ΔCNBD hysteresis at fast ramp speeds, with a greater range of ramp speeds affected as THC concentration increases. CBD did not affect HCN1ΔCNBD hysteresis ($3 < n < 10$ for each condition; $^*P < 0.05$).

brain, adipose tissue, and other organs (Ohlsson et al., 1984) with only 10% of administered CBD bound to circulating red blood cells (Williamson, 2004). Chronic administration may lead to further accumulation. It is important to also note the relative differences in IC_{50} and EC_{50} values between mammalian cell lines such as HEK or CHO cells and *Xenopus* oocytes observed for some drugs, including cannabinoids. Previous studies reveal IC_{50} and EC_{50} values which are significantly higher in *Xenopus* oocytes when compared with mammalian cells. Potassium channel (Kv1.1) blocker, aminopyridine (4-AP), was shown to inhibit channels expressed in mammalian Sol-8 cells with an IC_{50} value of 88 ± 5 μM (Castle et al., 1994). This value was more than 10 times higher in oocytes with IC_{50} values closer to 1 mM. Another study monitoring the efficacy of various blocking agents on hERG potassium channels showed 5–100 times higher IC_{50} values in *Xenopus* oocytes when compared with the mammalian HEK293 and CHO cells (Lacerda et al., 2001). K2P10.1 channels are blocked by carvedilol with an IC_{50} of 24 μM in oocytes and 7.6 μM in HEK cells (Kisselbach et al., 2014). In our experiments, TRPV1 channels in oocytes required more than 10 μM CBD before activation could be observed (**Supplementary Figure 3**) whereas an EC_{50} of 1.0 ± 0.1 μM was reported in HEK-293 cells (De Petrocellis et al., 2011). These differences between cell types might be attributed to differences in basal properties of the cells (e.g., differences in levels of cAMP, or phosphorylation) or to differences in the membrane composition which may modify the equilibrium of cannabinoid insertion into the bilayers. For example, *Xenopus* oocytes membranes possess higher levels of sphingomyelin (∼25% of lipids) (Stith et al., 2000; Hermansson et al., 2005; Hill et al., 2005; Pike et al., 2005) in their external leaflet than mammalian cells (4–18%) (Post et al., 1995; Hamplova et al., 2004; Hermansson et al., 2005; Pike et al., 2005). Moreover, some drugs have been shown to also bind the follicular layer of oocytes, with as much as a 90% reduction in membrane availability and increases of the IC_{50} values up to 30-fold (Madeja et al., 1997). Therefore, the general effect of the ligand still holds true, and variations between cell types are generally limited to 1 order of magnitude. Taking this into

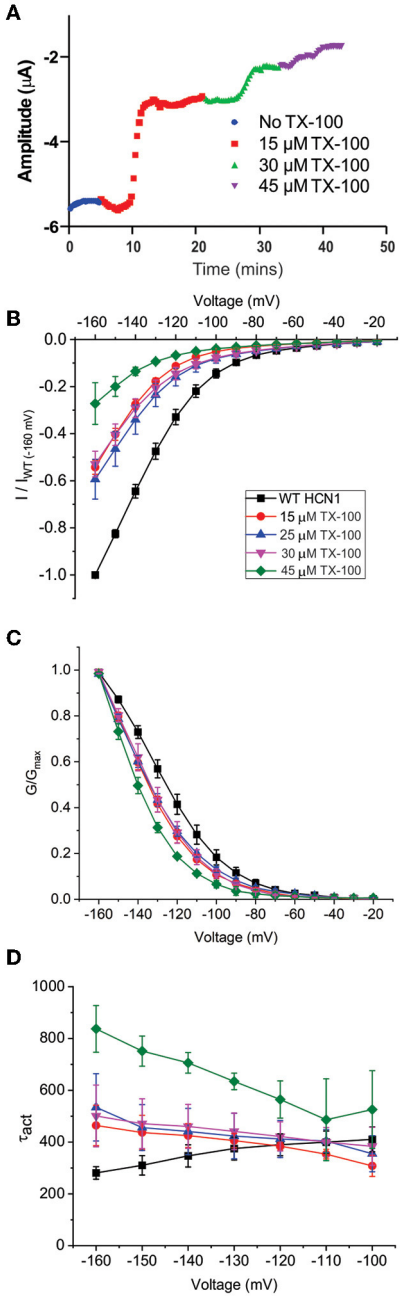

FIGURE 6 | Changes in membrane fluidity do not account for cannabinoid regulation of HCN1. Membrane fluidity was altered by the addition of Triton X-100 (TX-100) to the bath solution. **(A)** Representative time course of the steady-state current following the application of TX-100 at different concentrations, indicating that increasing membrane fluidity decreases HCN1 channel activity. However, this decrease in HCN1 current occurs more rapidly (within 1–2 min) than the decline observed with THC (which occurs over the course of 10–30 min). **(B)** Current-voltage relationship of HCN1 upon the addition of 0, 15, 25, 30, and 45 μM TX-100 normalized to maximal current ($I_{WT(-160\,mV)}$). **(C)** TX-100 induces a −10 to −15 mV hyperpolarizing shift in the steady-state voltage-dependence of HCN1, which does not occur when THC or CBD is applied. **(D)** HCN1 activation kinetics are uniquely affected by TX-100, with membrane fluidity having a greater impact on slowing channel activation with more hyperpolarization of the membrane potential ($3 < n < 9$ per condition; $P < 0.05$).

account, it is likely the effects of CBD and THC we observe for HCN1 channels in oocytes are not outside the therapeutic range, especially since they are comparable to those observed for other channels and receptors, and that the IC_{50} and EC_{50} values are likely to be the same, if not even lower, in the mammalian cells.

Cannabinoids are already being examined for the therapeutic potential of various neurological disorders, including neuropathic pain and epileptic seizures (Jones et al., 2010). Similarly, HCN channels are promising targets for neuropathic pain and epilepsy (Tibbs et al., 2013; Dini et al., 2018; Balducci et al., 2021). Activation of HCN1 current may contribute to the overall reduction of neuronal hyperactivity in epilepsy with CBD treatment (Iannotti et al., 2014; Maroon and Bost, 2018), similar to the reduced neuronal firing observed in CA1 pyramidal neurons resulting from lamotrigine stimulated I_h (Peng et al., 2010). There is also growing evidence that CBD exerts promising analgesic effects in different models of inflammatory and chronic pain including nerve injury, chemotherapy-induced peripheral neuropathy, and diabetes (Costa et al., 2007; Xiong et al., 2012; Casey et al., 2017; Finn et al., 2021). THC also significantly attenuates pain-related behaviors in nerve injury models (Soliman et al., 2021). In addition to animal studies, clinical studies have demonstrated that a combination of THC and CBD can be an effective therapeutic option for patients with neuropathic and other types of chronic pain (Nurmikko et al., 2007; Turcotte et al., 2010; Lynch and Campbell, 2011). Since HCN1 expression and I_h in HCN1/2-rich sensory neurons increase following their injury (Momin et al., 2008) and antineoplastics treatment (Descoeur et al., 2011), or HCN pore blockers (ZD7288 or ivabradine) reverse spontaneous discharges in injured nerve fibers and are anti-hyperalgesic for late-phase inflammatory pain, nerve injury-induced mechanical allodynia, as well as chemotherapy-induced mechanical and thermal hyperalgesia (Tibbs et al., 2016), we anticipate that CBD and THC effects on HCN1 currents may contribute to their role in reducing pain though through different mechanisms. Inhibition of HCN1 current by THC would be expected to reduce excitability in those neurons, as has been demonstrated for other HCN blockers. On the other hand, stimulation of HCN1 by CBD may reduce pain by depleting neurotransmitter release in sensory neurons similar to capsaicin stimulation of TRPV channels (Willis, 1997; Yan et al., 2006) or by stimulating inhibition by GABAergic interneurons. On the other hand, activation of HCN channels by CBD may not be directly involved in analgesia, but rather may help limit the decrease in excitability induced by action on other channels, including Nav's, whose conductance is inhibited up to 90% (Ghovanloo et al., 2018, 2021).

DATA AVAILABILITY STATEMENT

The raw data supporting the conclusions of this article will be made available by the authors, without undue reservation.

AUTHOR CONTRIBUTIONS

Experiments were performed and analyzed by SM, MM-Y, AM, RE, and ND'A. The manuscript was prepared by SM and ND'A. All authors contributed to the article and approved the submitted version.

FUNDING

This work was supported by a Discovery Grant (RGPIN-2019-00373) from the National Science and Engineering Research Council (NSERC) and a Project Grant from the Canadian Institutes of Health Research (CIHR) (FRN 173388) awarded to ND'A.

SUPPLEMENTARY MATERIAL

The Supplementary Material for this article can be found online at: https://www.frontiersin.org/articles/10.3389/fnmol.2022.848540/full#supplementary-material

REFERENCES

Abdulla, F. A., and Smith, P. A. (2001). Axotomy- and autotomy-induced changes in Ca2+ and K+ channel currents of rat dorsal root ganglion neurons. *J. Neurophysiol.* 85, 644–658. doi: 10.1152/jn.2001.85.2.644

Ahrens, J., Demir, R., Leuwer, M., de la Roche, J., Krampfl, K., Foadi, N., et al. (2009). The nonpsychotropic cannabinoid cannabidiol modulates and directly activates alpha-1 and alpha-1-beta glycine receptor function. *Pharmacology* 83, 217–222. doi: 10.1159/000201556

Arnsten, A. F. (2011). Prefrontal cortical network connections: key site of vulnerability in stress and schizophrenia. *Int. J. Dev. Neurosci.* 29, 215–223. doi: 10.1016/j.ijdevneu.2011.02.006

Balducci, V., Credi, C., Sacconi, L., Romanelli, M. N., Sartiani, L., and Cerbai, E. (2021). The HCN channel as a pharmacological target: why, where, and how to block it. *Prog. Biophys. Mol. Biol.* 166, 173–181. doi: 10.1016/j.pbiomolbio.2021.07.010

Beiersdorf, J., Hevesi, Z., Calvigioni, D., Pyszkowski, J., Romanov, R., Szodorai, E., et al. (2020). Adverse effects of Delta9-tetrahydrocannabinol on neuronal bioenergetics during postnatal development. *JCI Insight* 5:e135418. doi: 10.1172/jci.insight.135418

Bruening-Wright, A., and Larsson, H. P. (2007). Slow conformational changes of the voltage sensor during the mode shift in hyperpolarization-activated cyclic-nucleotide-gated channels. *J. Neurosci.* 27, 270–278. doi: 10.1523/JNEUROSCI.3801-06.2007

Caires, R., Sierra-Valdez, F. J., Millet, J. R. M., Herwig, J. D., Roan, E., Vasquez, V., et al. (2017). Omega-3 fatty acids modulate TRPV4 function through plasma membrane remodeling. *Cell Rep.* 21, 246–258. doi: 10.1016/j.celrep.2017.09.029

Cardenas, C. G., Mar, L. P., Vysokanov, A. V., Arnold, P. B., Cardenas, L. M., Surmeier, D. J., et al. (1999). Serotonergic modulation of hyperpolarization-activated current in acutely isolated rat dorsal root ganglion neurons. *J. Physiol.* 518, 507–523. doi: 10.1111/j.1469-7793.1999.0507p.x

Casey, S. L., Atwal, N., and Vaughan, C. W. (2017). Cannabis constituent synergy in a mouse neuropathic pain model. *Pain* 158, 2452–2460. doi: 10.1097/j.pain.0000000000001051

Castle, N. A., Fadous, S., Logothetis, D. E., and Wang, G. K. (1994). Aminopyridine block of Kv1.1 potassium channels expressed in mammalian cells and Xenopus oocytes. *Mol. Pharmacol.* 45:1242.

Chaplan, S. R., Guo, H. Q., Lee, D. H., Luo, L., Liu, C., Kuei, C., et al. (2003). Neuronal hyperpolarization-activated pacemaker channels drive neuropathic pain. *J. Neurosci.* 23, 1169–1178. doi: 10.1523/JNEUROSCI.23-04-01169.2003

Costa, B., Trovato, A. E., Comelli, F., Giagnoni, G., and Colleoni, M. (2007). The non-psychoactive cannabis constituent cannabidiol is an orally effective therapeutic agent in rat chronic inflammatory and neuropathic pain. *Eur. J. Pharmacol.* 556, 75–83. doi: 10.1016/j.ejphar.2006.11.006

Cunha, J. M., Carlini, E. A., Pereira, A. E., Ramos, O. L., Pimentel, C., Gagliardi, R., et al. (1980). Chronic administration of cannabidiol to healthy volunteers and epileptic patients. *Pharmacology* 21, 175–185. doi: 10.1159/000137430

De Petrocellis, L., Ligresti, A., Moriello, A. S., Allara, M., Bisogno, T., Petrosino, S., et al. (2011). Effects of cannabinoids and cannabinoid-enriched Cannabis extracts on TRP channels and endocannabinoid metabolic enzymes. *Br. J. Pharmacol.* 163, 1479–1494. doi: 10.1111/j.1476-5381.2010.01166.x

De Petrocellis, L., Orlando, P., Moriello, A. S., Aviello, G., Stott, C., Izzo, A. A., et al. (2012). Cannabinoid actions at TRPV channels: effects on TRPV3 and TRPV4 and their potential relevance to gastrointestinal inflammation. *Acta Physiol.* 204, 255–266. doi: 10.1111/j.1748-1716.2011.02338.x

Deiana, S., Watanabe, A., Yamasaki, Y., Amada, N., Arthur, M., Fleming, S., et al. (2012). Plasma and brain pharmacokinetic profile of cannabidiol (CBD), cannabidivarine (CBDV), Δ?-tetrahydrocannabivarin (THCV) and cannabigerol (CBG) in rats and mice following oral and intraperitoneal administration and CBD action on obsessive-compulsive behaviour. *Psychopharmacology* 219, 859–873. doi: 10.1007/s00213-011-2415-0

Descoeur, J., Pereira, V., Pizzoccaro, A., Francois, A., Ling, B., Maffre, V., et al. (2011). Oxaliplatin-induced cold hypersensitivity is due to remodelling of ion channel expression in nociceptors. *EMBO Mol. Med.* 3, 266–278. doi: 10.1002/emmm.201100134

Devinsky, O., Cilio, M. R., Cross, H., Fernandez-Ruiz, J., French, J., Hill, C., et al. (2014). Cannabidiol: pharmacology and potential therapeutic role in epilepsy and other neuropsychiatric disorders. *Epilepsia* 55, 791–802. doi: 10.1111/epi.12631

Dibbens, L. M., Reid, C. A., Hodgson, B., Thomas, E. A., Phillips, A. M., Gazina, E., et al. (2010). Augmented currents of an HCN2 variant in patients with febrile seizure syndromes. *Ann. Neurol.* 67, 542–546. doi: 10.1002/ana.21909

DiFrancesco, J. C., Barbuti, A., Milanesi, R., Coco, S., Bucchi, A., Bottelli, G., et al. (2011). Recessive loss-of-function mutation in the pacemaker HCN2 channel causing increased neuronal excitability in a patient with idiopathic generalized epilepsy. *J. Neurosci.* 31, 17327–17337. doi: 10.1523/JNEUROSCI.3727-11.2011

Dini, L., Del Lungo, M., Resta, F., Melchiorre, M., Spinelli, V., Di Cesare Mannelli, L., et al. (2018). Selective Blockade of HCN1/HCN2 channels as a potential pharmacological strategy against pain. *Front. Pharmacol.* 9:1252. doi: 10.3389/fphar.2018.01252

Elinder, F., Mannikko, R., Pandey, S., and Larsson, H. P. (2006). Mode shifts in the voltage gating of the mouse and human HCN2 and HCN4 channels. *J Physiol.* 575, 417–431. doi: 10.1113/jphysiol.2006.110437

Emery, E. C., Young, G. T., Berrocoso, E. M., Chen, L., and McNaughton, P. A. (2011). HCN2 ion channels play a central role in inflammatory and neuropathic pain. *Science* 333, 1462–1466. doi: 10.1126/science.1206243

Finn, D. P., Haroutounian, S., Hohmann, A. G., Krane, E., Soliman, N., and Rice, A. S. C. (2021). Cannabinoids, the endocannabinoid system, and pain: a review of preclinical studies. *Pain* 162, S5–S25. doi: 10.1097/j.pain.0000000000002268

Furst, O., and D'Avanzo, N. (2015). Isoform dependent regulation of human HCN channels by cholesterol. *Sci. Rep.* 5:14270. doi: 10.1038/srep14270

Gamo, N. J., Lur, G., Higley, M. J., Wang, M., Paspalas, C. D., Vijayraghavan, S., et al. (2015). Stress impairs prefrontal cortical function via D1 dopamine receptor interactions with hyperpolarization-activated cyclic nucleotide-gated channels. *Biol. Psychiatry* 78, 860–870. doi: 10.1016/j.biopsych.2015.01.009

Ghovanloo, M. R., Choudhury, K., Bandaru, T. S., Fouda, M. A., Rayani, K., Rusinova, R., et al. (2021). Cannabidiol inhibits the skeletal muscle Nav1.4 by blocking its pore and by altering membrane elasticity. *J. Gen. Physiol.* 153:e202012701. doi: 10.1085/jgp.202012701

Ghovanloo, M. R., Shuart, N. G., Mezeyova, J., Dean, R. A., Ruben, P. C., and Goodchild, S. J. (2018). Inhibitory effects of cannabidiol on voltage-dependent sodium currents. *J. Biol. Chem.* 293, 16546–16558. doi: 10.1074/jbc.RA118.004929

Guy, G. W., and Flint, M. E. (2004). A single centre, placebo-controlled, four period, crossover, tolerability study assessing, pharmacodynamic effects, pharmacokinetic characteristics and cognitive profiles of a single dose of three formulations of Cannabis Based Medicine Extracts (CBMEs) (GWPD9901), plus a two period tolerability study comparing pharmacodynamic effects and pharmacokinetic characteristics of a single dose of a cannabis based medicine extract given via two administration routes (GWPD9901 EXT). *J. Cannabis Ther.* 3, 35–77. doi: 10.1300/J175v03n03_03

Guy, G. W., and Robson, P. J. (2004). A phase I, open label, four-way crossover study to compare the pharmacokinetic profiles of a single dose of 20 mg of a Cannabis Based Medicine Extract (CBME) Administered on 3 different areas of the buccal mucosa and to investigate the pharmacokinetics of CBME per oral in healthy male and female volunteers (GWPK0112). *J. Cannabis Ther.* 3, 79–120. doi: 10.1300/J175v03n04_01

Hamplova, B., Pelouch, V., Novakova, O., Skovranek, J., Hucin, B., and Novak, F. (2004). Phospholipid composition of myocardium in children with normoxemic and hypoxemic congenital heart diseases. *Physiol. Res.* 53, 557–560.

Hejazi, N., Zhou, C., Oz, M., Sun, H., Ye, J. H., and Zhang, L. (2006). Delta9-tetrahydrocannabinol and endogenous cannabinoid anandamide directly potentiate the function of glycine receptors. *Mol. Pharmacol.* 69, 991–997. doi: 10.1124/mol.105.019174

Hermansson, M., Uphoff, A., Kakela, R., and Somerharju, P. (2005). Automated quantitative analysis of complex lipidomes by liquid chromatography/mass spectrometry. *Anal. Chem.* 77, 2166–2175. doi: 10.1021/ac048489s

Hill, A. J., Williams, C. M., Whalley, B. J., and Stephens, G. J. (2012). Phytocannabinoids as novel therapeutic agents in CNS disorders. *Pharmacol. Ther.* 133, 79–97. doi: 10.1016/j.pharmthera.2011.09.002

Hill, W. G., Southern, N. M., MacIver, B., Potter, E., Apodaca, G., Smith, C. P., et al. (2005). Isolation and characterization of the Xenopus oocyte plasma membrane: a new method for studying activity of water and solute transporters. *Am. J. Physiol. Renal Physiol.* 289, F217–F224. doi: 10.1152/ajprenal.00022.2005

Hillard, C. J., Harris, R. A., and Bloom, A. S. (1985). Effects of the cannabinoids on physical properties of brain membranes and phospholipid vesicles: fluorescence studies. *J. Pharmacol. Exp. Ther.* 232, 579–588.

Huang, Z., Walker, M. C., and Shah, M. M. (2009). Loss of dendritic HCN1 subunits enhances cortical excitability and epileptogenesis. *J. Neurosci.* 29, 10979–10988. doi: 10.1523/JNEUROSCI.1531-09.2009

Iannotti, F. A., Hill, C. L., Leo, A., Alhusaini, A., Soubrane, C., Mazzarella, E., et al. (2014). Nonpsychotropic plant cannabinoids, cannabidivarin (CBDV) and cannabidiol (CBD), activate and desensitize transient receptor potential vanilloid 1 (TRPV1) channels in vitro: potential for the treatment of neuronal hyperexcitability. *ACS Chem. Neurosci.* 5, 1131–1141. doi: 10.1021/cn5000524

Ingolfsson, H. I., Sanford, R. L., Kapoor, R., and Andersen, O. S. (2010). Gramicidin-based fluorescence assay; for determining small molecules potential for modifying lipid bilayer properties. *J. Vis. Exp.* 44:e2131. doi: 10.3791/2131

Jones, N. A., Hill, A. J., Smith, I., Bevan, S. A., Williams, C. M., Whalley, B. J., et al. (2010). Cannabidiol displays antiepileptiform and antiseizure properties *in vitro* and *in vivo*. *J. Pharmacol. Exp. Ther.* 332, 569–577. doi: 10.1124/jpet.109.159145

Karimi, K., Fortriede, J. D., Lotay, V. S., Burns, K. A., Wang, D. Z., Fisher, M. E., et al. (2018). Xenbase: a genomic, epigenomic and transcriptomic model organism database. *Nucleic Acids Res.* 46, D861–D868. doi: 10.1093/nar/gkx936

Kisselbach, J., Seyler, C., Schweizer, P. A., Gerstberger, R., Becker, R., Katus, H. A., et al. (2014). Modulation of K2P 2.1 and K2P 10.1 K(+) channel sensitivity to carvedilol by alternative mRNA translation initiation. *Br. J. Pharmacol.* 171, 5182–5194. doi: 10.1111/bph.12596

Lacerda, A. E., Kramer, J., Shen, K. Z., Thomas, D., and Brown, A. M. (2001). Comparison of block among cloned cardiac potassium channels by non-antiarrhythmic drugs. *Eur. Heart J. Suppl.* 3, K23–K30. doi: 10.1016/S1520-765X(01)90003-3

Ludwig, A., Budde, T., Stieber, J., Moosmang, S., Wahl, C., Holthoff, K., et al. (2003). Absence epilepsy and sinus dysrhythmia in mice lacking the pacemaker channel HCN2. *EMBO J.* 22, 216–224. doi: 10.1093/emboj/cdg032

Ludwig, A., Zong, X., Jeglitsch, M., Hofmann, F., and Biel, M. (1998). A family of hyperpolarization-activated mammalian cation channels. *Nature* 393, 587–591. doi: 10.1038/31255

Lynch, M. E., and Campbell, F. (2011). Cannabinoids for treatment of chronic non-cancer pain; a systematic review of randomized trials. *Br. J. Clin. Pharmacol.* 72, 735–744. doi: 10.1111/j.1365-2125.2011.03970.x

Madeja, M., Musshoff, U., and Speckmann, E. J. (1997). Follicular tissues reduce drug effects on ion channels in oocytes of Xenopus laevis. *Eur. J. Neurosci.* 9, 599–604. doi: 10.1111/j.1460-9568.1997.tb01636.x

Mahgoub, M., Keun-Hang, S. Y., Sydorenko, V., Ashoor, A., Kabbani, N., Al Kury, L., et al. (2013). Effects of cannabidiol on the function of α7-nicotinic acetylcholine receptors. *Eur. J. Pharmacol.* 720, 310–319. doi: 10.1016/j.ejphar.2013.10.011

Mannikko, R., Pandey, S., Larsson, H. P., and Elinder, F. (2005). Hysteresis in the voltage dependence of HCN channels: conversion between two modes affects pacemaker properties. *J. Gen. Physiol.* 125, 305–326. doi: 10.1085/jgp.200409130

Maroon, J., and Bost, J. (2018). Review of the neurological benefits of phytocannabinoids. *Surg. Neurol. Int.* 9:91. doi: 10.4103/sni.sni_45_18

Maroso, M., Szabo, G. G., Kim, H. K., Alexander, A., Bui, A. D., Lee, S. H., et al. (2016). Cannabinoid control of learning and memory through HCN Channels. *Neuron* 89, 1059–1073. doi: 10.1016/j.neuron.2016.01.023

Masuda, N., Hayashi, Y., Matsuyoshi, H., Chancellor, M. B., de Groat, W. C., and Yoshimura, N. (2006). Characterization of hyperpolarization-activated current (Ih) in dorsal root ganglion neurons innervating rat urinary bladder. *Brain Res.* 1096, 40–52. doi: 10.1016/j.brainres.2006.04.085

Momin, A., Cadiou, H., Mason, A., and McNaughton, P. A. (2008). Role of the hyperpolarization-activated current Ih in somatosensory neurons. *J Physiol.* 586, 5911–5929. doi: 10.1113/jphysiol.2008.163154

Moosmang, S., Stieber, J., Zong, X., Biel, M., Hofmann, F., and Ludwig, A. (2001). Cellular expression and functional characterization of four hyperpolarization-activated pacemaker channels in cardiac and neuronal tissues. *Eur. J. Biochem.* 268, 1646–1652. doi: 10.1046/j.1432-1327.2001.02036.x

Nakamura, Y., Shi, X., Numata, T., Mori, Y., Inoue, R., Lossin, C., et al. (2013). Novel HCN2 mutation contributes to febrile seizures by shifting the channel's kinetics in a temperature-dependent manner. *PLoS ONE.* 8:e80376. doi: 10.1371/journal.pone.0080376

Nava, C., Dalle, C., Rastetter, A., Striano, P., de Kovel, C. G., Nabbout, R., et al. (2014). De novo mutations in HCN1 cause early infantile epileptic encephalopathy. *Nat. Genet.* 46, 640–645. doi: 10.1038/ng.2952

Nolan, M. F., Malleret, G., Dudman, J. T., Buhl, D. L., Santoro, B., Gibbs, E., et al. (2004). A behavioral role for dendritic integration: HCN1 channels constrain spatial memory and plasticity at inputs to distal dendrites of CA1 pyramidal neurons. *Cell* 119, 719–732. doi: 10.1016/S0092-8674(04)01055-4

Nolan, M. F., Malleret, G., Lee, K. H., Gibbs, E., Dudman, J. T., Santoro, B., et al. (2003). The hyperpolarization-activated HCN1 channel is important for motor learning and neuronal integration by cerebellar Purkinje cells. *Cell* 115, 551–564. doi: 10.1016/S0092-8674(03)00884-5

Nurmikko, T. J., Serpell, M. G., Hoggart, B., Toomey, P. J., Morlion, B. J., and Haines, D. (2007). Sativex successfully treats neuropathic pain characterised by allodynia: a randomised, double-blind, placebo-controlled clinical trial. *Pain.* 133, 210–220. doi: 10.1016/j.pain.2007.08.028

Ohlsson, A., Lindgren, J. E., Andersson, S., Agurell, S., Gillespie, H., and Hollister, L. E. (1984). Single dose kinetics of cannabidiol in Man. In: Agurell S, Dewey WL, Willette RE, editors. *The Cannabinoids: Chemical, Pharmacologic, Therapeutic Aspects* (Academic Press), pp. 219–225. doi: 10.1016/B978-0-12-044620-9.50020-8

Okada, Y., Imendra, K. G., Miyazaki, T., Hotokezaka, H., Fujiyama, R., Zeredo, J. L., et al. (2005). Biophysical properties of voltage-gated Na+ channels in frog parathyroid cells and their modulation by cannabinoids. *J. Exp. Biol.* 208, 4747–4756. doi: 10.1242/jeb.01967

Onoda, S., Masuda, N., Seto, T., Eguchi, K., Takiguchi, Y., Isobe, H., et al. (2006). Thoracic oncology research group. phase ii trial of amrubicin for treatment of refractory or relapsed small-cell lung cancer: thoracic oncology research group study 0301. *J. Clin. Oncol.* 24, 5448–53. doi: 10.1200/JCO.2006.08.4145

Orvos, P., Pászti, B., Topal, L., Gazdag, P., Prorok, J., Polyák, A., et al. (2020). The electrophysiological effect of cannabidiol on hERG current and in guinea-pig and rabbit cardiac preparations. *Sci. Rep.* 10:16079. doi: 10.1038/s41598-020-73165-2

Pape, H. C. (1996). Queer current and pacemaker: the hyperpolarization-activated cation current in neurons. *Annu. Rev. Physiol.* 58, 299–327. doi: 10.1146/annurev.ph.58.030196.001503

Paspalas, C. D., Wang, M., and Arnsten, A. F. (2013). Constellation of HCN channels and cAMP regulating proteins in dendritic spines of the primate prefrontal cortex: potential substrate for working memory deficits in schizophrenia. *Cereb. Cortex*. 23, 1643–1654. doi: 10.1093/cercor/bhs152

Peng, B.-W., Justice, J. A., Zhang, K., He, X. H., and Sanchez, R. M. (2010). Increased basal synaptic inhibition of hippocampal area CA1 pyramidal neurons by an antiepileptic drug that enhances IH. *Neuropsychopharmacology* 35, 464–472. doi: 10.1038/npp.2009.150

Pike, L. J., Han, X., and Gross, R. W. (2005). Epidermal growth factor receptors are localized to lipid rafts that contain a balance of inner and outer leaflet lipids: a shotgun lipidomics study. *J. Biol. Chem*. 280, 26796–26804. doi: 10.1074/jbc.M503805200

Poling, J. S., Rogawski, M. A., Salem, N., and Vicini, S. (1996). Anandamide, an endogenous cannabinoid, inhibits shaker-related voltage-gated K+ channels. *Neuropharmacology* 35, 983–991. doi: 10.1016/0028-3908(96)00130-X

Post, J. A., Verkleij, A. J., and Langer, G. A. (1995). Organization and function of sarcolemmal phospholipids in control and ischemic/reperfused cardiomyocytes. *J. Mol. Cell. Cardiol*. 27, 749–760. doi: 10.1016/0022-2828(95)90080-2

Pumroy, R. A., Samanta, A., Liu, Y., Hughes, T. E., Zhao, S., Yudin, Y., et al. (2019). Molecular mechanism of TRPV2 channel modulation by cannabidiol. *Elife* 8:e48792. doi: 10.7554/eLife.48792.045

Ross, H. R., Napier, I., and Connor, M. (2008). Inhibition of recombinant human T-type calcium channels by Delta9-tetrahydrocannabinol and cannabidiol. *J. Biol. Chem*. 283, 16124–16134. doi: 10.1074/jbc.M707104200

Russo, E. B. (2018). Cannabis therapeutics and the future of neurology. *Front. Integr. Neurosci*. 12:51. doi: 10.3389/fnint.2018.00051

Sait, L. G., Sula, A., Ghovanloo, M.-R., Hollingworth, D., Ruben, P. C., and Wallace, B. A. (2020). Cannabidiol interactions with voltage-gated sodium channels. *Elife* 9:e58593. doi: 10.7554/eLife.58593.sa2

Santoro, B., Grant, S. G., Bartsch, D., and Kandel, E. R. (1997). Interactive cloning with the SH3 domain of N-src identifies a new brain specific ion channel protein, with homology to eag and cyclic nucleotide-gated channels. *Proc. Natl. Acad. Sci. U.S.A*. 94, 14815–14820. doi: 10.1073/pnas.94.26.14815

Santoro, B., Hu, L., Liu, H., Saponaro, A., Pian, P., Piskorowski, R. A., et al. (2011). TRIP8b regulates HCN1 channel trafficking and gating through two distinct C-terminal interaction sites. *J. Neurosci*. 31, 4074–4086. doi: 10.1523/JNEUROSCI.5707-10.2011

Santoro, B., Liu, D. T., Yao, H., Bartsch, D., Kandel, E. R., Siegelbaum, S. A., et al. (1998). Identification of a gene encoding a hyperpolarization-activated pacemaker channel of brain. *Cell* 93, 717–729. doi: 10.1016/S0092-8674(00)81434-8

Scroggs, R. S., Todorovic, S. M., Anderson, E. G., and Fox, A. P. (1994). Variation in IH, IIR, and ILEAK between acutely isolated adult rat dorsal root ganglion neurons of different size. *J. Neurophysiol*. 71, 271–279. doi: 10.1152/jn.1994.71.1.271

Soliman, N., Haroutounian, S., Hohmann, A. G., Krane, E., Liao, J., Macleod, M., et al. (2021). Systematic review and meta-analysis of cannabinoids, cannabis-based medicines, and endocannabinoid system modulators tested for antinociceptive effects in animal models of injury-related or pathological persistent pain. *Pain* 162, S26–S44. doi: 10.1097/j.pain.0000000000002269

Stith, B. J., Hall, J., Ayres, P., Waggoner, L., Moore, J. D., and Shaw, W. A. (2000). Quantification of major classes of *Xenopus phospholipids* by high performance liquid chromatography with evaporative light scattering detection. *J. Lipid Res*. 41, 1448–1454. doi: 10.1016/S0022-2275(20)33457-X

Tang, B., Sander, T., Craven, K. B., Hempelmann, A., and Escayg, A. (2008). Mutation analysis of the hyperpolarization-activated cyclic nucleotide-gated channels HCN1 and HCN2 in idiopathic generalized epilepsy. *Neurobiol. Dis*. 29, 59–70. doi: 10.1016/j.nbd.2007.08.006

The Health Effects of Cannabis and Cannabinoids (2017). *The Current State of Evidence and Recommendations for Research* (Washington, DC), 85–126.

Tibbs, G. R., Posson, D. J., and Goldstein, P. A. (2016). Voltage-gated ion channels in the PNS: novel therapies for neuropathic pain? *Trends Pharmacol. Sci*. 37, 522–542. doi: 10.1016/j.tips.2016.05.002

Tibbs, G. R., Rowley, T. J., Sanford, R. L., Herold, K. F., Proekt, A., Hemmings, H. C. Jr, et al. (2013). HCN1 channels as targets for anesthetic and nonanesthetic propofol analogs in the amelioration of mechanical and thermal hyperalgesia in a mouse model of neuropathic pain. *J. Pharmacol. Exp. Ther*. 345, 363–373. doi: 10.1124/jpet.113.203620

Tu, H., Deng, L., Sun, Q., Yao, L., Han, J. S., and Wan, Y. (2004). Hyperpolarization-activated, cyclic nucleotide-gated cation channels: roles in the differential electrophysiological properties of rat primary afferent neurons. *J. Neurosci. Res*. 76, 713–722. doi: 10.1002/jnr.20109

Turcotte, D., Le Dorze, J. A., Esfahani, F., Frost, E., Gomori, A., and Namaka, M. (2010). Examining the roles of cannabinoids in pain and other therapeutic indications: a review. *Expert Opin. Pharmacother*. 11, 17–31. doi: 10.1517/14656560903413534

Villiere, V., and McLachlan, E. M. (1996). Electrophysiological properties of neurons in intact rat dorsal root ganglia classified by conduction velocity and action potential duration. *J. Neurophysiol*. 76, 1924–1941. doi: 10.1152/jn.1996.76.3.1924

Williamson, E. M. (2004). The Medicinal Uses of Cannabis Cannabinoids. Edited by Guy GW, Whittle BA, Robson PJ. Pharmaceutical Press: London, 2004. *Pages: 448. ISBN: 0-85369-517-2. Price £39.95. Human Psychopharmacology: Clinical and Experimental*. 19:589. doi: 10.1002/hup.631

Willis, W. D. (1997). Central sensitization following intradermal injection of capsaicin. *Behav. Brain Sci*. 20:471. doi: 10.1017/S0140525X97581490

Xiao, Y. F., Chandler, N., Dobrzynski, H., Richardson, E. S., Tenbroek, E. M., Wilhelm, J. J., et al. (2010). Hysteresis in human HCN4 channels: a crucial feature potentially affecting sinoatrial node pacemaking. *Sheng Li Xue Bao* 62, 1–13.

Xiong, W., Cui, T., Cheng, K., Yang, F., Chen, S. R., Willenbring, D., et al. (2012). Cannabinoids suppress inflammatory and neuropathic pain by targeting alpha3 glycine receptors. *J. Exp. Med*. 209, 1121–1134. doi: 10.1084/jem.20120242

Yagi, J., and Sumino, R. (1998). Inhibition of a hyperpolarization-activated current by clonidine in rat dorsal root ganglion neurons. *J. Neurophysiol*. 80, 1094–1104. doi: 10.1152/jn.1998.80.3.1094

Yan, J. Y., Sun, R. Q., Hughes, M. G., McAdoo, D. J., and Willis, W. D. (2006). Intradermal injection of capsaicin induces acute substance P release from rat spinal cord dorsal horn. *Neurosci. Lett*. 410, 183–186. doi: 10.1016/j.neulet.2006.09.072

Yao, H., Donnelly, D. F., Ma, C., and LaMotte, R. H. (2003). Upregulation of the hyperpolarization-activated cation current after chronic compression of the dorsal root ganglion. *J. Neurosci*. 23, 2069–2074. doi: 10.1523/JNEUROSCI.23-06-02069.2003

Yi, F., Danko, T., Botelho, S. C., Patzke, C., Pak, C., Wernig, M., et al. (2016). Autism-associated SHANK3 haploinsufficiency causes Ih channelopathy in human neurons. *Science*. 352:aaf2669. doi: 10.1126/science.aaf2669

Yoshida, K., Nagatoishi, S., Kuroda, D., Suzuki, N., Murata, T., and Tsumoto, K. (2019). Phospholipid membrane fluidity alters ligand binding activity of a G Protein-Coupled Receptor by shifting the conformational equilibrium. *Biochemistry* 58, 504–508. doi: 10.1021/acs.biochem.8b01194

Zar, J. H. (1984). *Biostatistical Analysis*. Englewood Cliffs, NJ: Prentice-Hall.

Conflict of Interest: The authors declare that the research was conducted in the absence of any commercial or financial relationships that could be construed as a potential conflict of interest.

Publisher's Note: All claims expressed in this article are solely those of the authors and do not necessarily represent those of their affiliated organizations, or those of the publisher, the editors and the reviewers. Any product that may be evaluated in this article, or claim that may be made by its manufacturer, is not guaranteed or endorsed by the publisher.

frontiers | Frontiers in Molecular Neuroscience

REVIEW
published: 22 June 2022
doi: 10.3389/fnmol.2022.898717

Adventures and Advances in Time Travel With Induced Pluripotent Stem Cells and Automated Patch Clamp

Kadla R. Rosholm[1], Beatrice Badone[1], Stefania Karatsiompani[1], David Nagy[2], Fitzwilliam Seibertz[3,4], Niels Voigt[3,4,5] and Damian C. Bell[1]*

[1] Sophion Bioscience A/S, Ballerup, Denmark, [2] Sophion Bioscience Inc., Woburn, MA, United States, [3] Institute of Pharmacology and Toxicology, University Medical Center Göttingen, Göttingen, Germany, [4] German Center for Cardiovascular Research (DZHK), Göttingen, Germany, [5] Cluster of Excellence "Multiscale Bioimaging: from Molecular Machines to Networks of Excitable Cells" (MBExC), University of Göttingen, Göttingen, Germany

In the Hollywood blockbuster "The Curious Case of Benjamin Button" a fantastical fable unfolds of a man's life that travels through time reversing the aging process; as the tale progresses, the frail old man becomes a vigorous, vivacious young man, then man becomes boy and boy becomes baby. The reality of cellular time travel, however, is far more wondrous: we now have the ability to both *reverse and then forward time* on mature cells. Four proteins were found to rewind the molecular clock of adult cells back to their embryonic, "blank canvas" pluripotent stem cell state, allowing these pluripotent stem cells to then be differentiated to fast forward their molecular clocks to the desired adult specialist cell types. These four proteins – the "Yamanaka factors" – form critical elements of this cellular time travel, which deservedly won Shinya Yamanaka the Nobel Prize for his lab's work discovering them. Human induced pluripotent stem cells (hiPSCs) hold much promise in our understanding of physiology and medicine. They encapsulate the signaling pathways of the desired cell types, such as cardiomyocytes or neurons, and thus act as model cells for defining the critical ion channel activity in healthy and disease states. Since hiPSCs can be derived from any patient, highly specific, personalized (or stratified) physiology, and/or pathophysiology can be defined, leading to exciting developments in personalized medicines and interventions. As such, hiPSC married with high throughput automated patch clamp (APC) ion channel recording platforms provide a foundation for significant physiological, medical and drug discovery advances. This review aims to summarize the current state of affairs of hiPSC and APC: the background and recent advances made; and the pros, cons and challenges of these technologies. Whilst the authors have yet to finalize a fully functional time traveling machine, they will endeavor to provide plausible future projections on where hiPSC and APC are likely to carry us. One future projection the authors are confident in making is the increasing necessity and adoption of these technologies in the discovery of the next blockbuster, this time a life-enhancing ion channel drug, not a fantastical movie.

Keywords: hiPSC, stem cells, automated patch clamp, cardiomyocytes, neurons, ion channels

OPEN ACCESS

Edited by:
Marc Rogers,
Metrion Biosciences Limited,
United Kingdom

Reviewed by:
Edward Humphries,
AstraZeneca, United Kingdom
Jessica Elaine Young,
University of Washington,
United States

****Correspondence:***
Kadla R. Rosholm
krr@sophion.com

Specialty section:
This article was submitted to Molecular Signalling and Pathways, a section of the journal Frontiers in Molecular Neuroscience

Received: *17 March 2022*
Accepted: *13 May 2022*
Published: *22 June 2022*

Citation:
Rosholm KR, Badone B, Karatsiompani S, Nagy D, Seibertz F, Voigt N and Bell DC (2022) Adventures and Advances in Time Travel With Induced Pluripotent Stem Cells and Automated Patch Clamp. Front. Mol. Neurosci. 15:898717. doi: 10.3389/fnmol.2022.898717

Abbreviations: APs, action potentials; APC, automated patch clamp; CMs, cardiomyocytes; hiPSC, human induced pluripotent stem cell; HT, high throughput; MPC, manual patch clamp; PSCs, pluripotent stem cells.

INTRODUCTION

When Takahashi and Yamanaka discovered four genes (*c-Myc, Oct3/4, Sox2,* and *Klf4*), whose protein products were shown to reprogram (induce) somatic cells into pluripotent stem cells (Takahashi and Yamanaka, 2006), these Yamanaka factors were heralded as a breakthrough in biomedical research (Press release, 2012). For the first time, pluripotency, the ability to form a range of specialized cell types from a pluripotent cell, was possible from mature, adult somatic cells, no longer requiring embryonic stem cells (Shi et al., 2017; Yoshida and Yamanaka, 2017).

The limited availability of embryonic tissue to derive embryonic stem cells coupled with legal and ethical regulations, always stymied stem cell research development and progress (Lo and Parham, 2009; Jha, 2011; Moradi et al., 2019). With the discovery of the Yamanaka factors, somatic cells could be taken from adult tissue and reprogrammed, turning back the clock on mature cells to an embryonic-like, pluripotent state. The processes where pluripotent stem cells (PSCs) are differentiated and matured, allows fast-forwarding of cells into specialized cell lines providing model cells for *in vitro* research (Rowe and Daley, 2019).

The use of human induced pluripotent stem cells (hiPSCs) has a number of advantages: it reduces the use of animal tissue; compared to cells overexpressing recombinant protein [e.g., Chinese hamster ovary (CHO)] human cells are more physiologically relevant and translatable models; in comparison with primary cells, such as tissue dissociated cardiomyocytes and neurons, they are easier to access (typically from a blood or skin sample) and to maintain in culture; hiPSCs can be derived from both healthy and patient populations, providing both human "wild type" control and diseased models; and, since hiPSCs can be derived from any of us, the options to study a personal genotype and phenotype are broad, allowing for truly personalized (also termed precision or stratified) medicines and interventions (Matsa et al., 2016; Hamazaki et al., 2017; Doss and Sachinidis, 2019). This technology, however, has limitations worth considering, such as: the fetal nature of hiPSCs; the lifespan in culture; the long-term maturation process (for details on the challenges and limitations see the following section "Maturity and Subtype Specificity of hiPSC-Derived Cell Lines").

Whilst these seminal developments in generating and differentiating hiPSCs were taking place, similar strides were being made in ion channel recording techniques. The dazzlingly brilliant but highly time consuming and technically challenging manual patch clamp (MPC) technique (Hamill et al., 1981) was simplified, made faster and more efficient, through a combination of planar patch clamp and automation (Bell and Dallas, 2018). By switching from manual micro-manipulation of a single recording electrode down onto an adherent cell in MPC, to the application of cell suspensions by robot pipettors to arrays of electrodes in automated patch clamp (APC), the technical hurdles were lowered whilst vastly increasing throughput of ion channel recordings.

Thus, with hiPSCs and APC, researchers now have the capabilities to characterize ion channel populations in hiPSCs and their differentiated cell lines, for instance exploring the effect of different reprogramming, differentiation and maturation conditions and introducing quantifiable metrics for quality assessment. Furthermore, as the hiPSC technology develops, APC will be applicable for safety pharmacology and drug screens in highly translatable hiPSC model cell lines from healthy and disease patient populations.

In this review, the authors aim to describe advances in the generation of mature hiPSC-derived cell lines; developments in cell suspension preparation for APC measurements; APC techniques and technologies that have made these once challenging ion channel recordings more successful, physiologically relevant, and amenable to high throughput screening; and the key challenges solved thus far and those to be faced. Finally, we provide examples of novel applications of hiPSCs and APC. These techniques offer huge potential to advance biomedical research and drug discovery, and the future they project looks to be bright and filled with many novel and exciting findings.

REPROGRAMMING, DIFFERENTIATION, AND MATURATION OF HUMAN INDUCED PLURIPOTENT STEM CELL DERIVED CELL LINES

During the last decade, substantial effort has gone into developing protocols for generating specialized hiPSC-derived cells and tissues for applications within a range of areas, such as blood, smooth muscle, liver, heart, and brain (Bellin et al., 2012; Shi et al., 2017; Rowe and Daley, 2019).

In general, the formation of different specialized hiPSC derived cells follow the same sequence of events: (1) the reprogramming (induction) of human unipotent somatic cells into hiPSCs by directed expression of certain transcriptional factors; and, (2) the differentiation and maturation of hiPSCs into specialized cells, typically by using signaling pathway agonists and antagonists in specific concentrations to induce stepwise progression through the embryonic development stages (Bellin et al., 2012; **Figure 1**).

In this section we aim to summarize the latest methodological advances of hiPSC generation and differentiation and discuss the key challenges in the field.

Genetic Variability of Human Induced Pluripotent Stem Cell Derived Cell Lines

A challenge with hiPSC-derived cell lines is the genetic variability existing within and between hiPSC populations, and an ongoing task is to control and maintain genome integrity during reprogramming and differentiation (Assou et al., 2018; Popp et al., 2018). An important development in this regard was the introduction of non-integrating methods, such as *Sendai* virus (Fusaki et al., 2009), for introducing reprogramming factors, which aim to reduce the risk of variability or spurious gene activation/inactivation in hiPSC-derived cell lines (Shi et al., 2017; Berry et al., 2019).

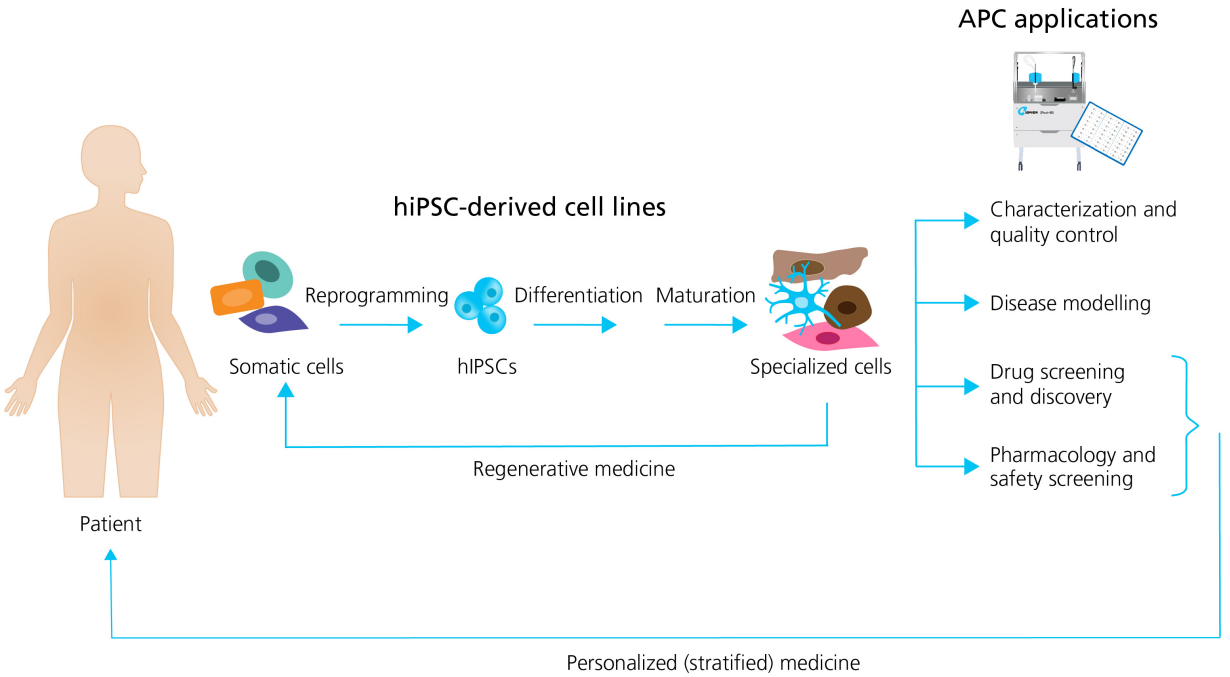

FIGURE 1 | Generation of specialized hiPSC-derived cells and APC applications. Somatic patient cells can be reprogrammed into hiPSCs, followed by the differentiation and maturation into specialized cells. The specialized cells can be used directly in regenerative medicine, or they can be employed together with APC for a range of applications including: characterization and quality control; disease modeling; drug screening and discovery; and pharmacology and safety screening. Patient hiPSCs can be used as personalized drug screening and pharmacology models in trials. Adapted from Bellin et al. (2012), with permission from publisher Springer Nature.

Another focus is the inherent biological variability between donors stemming from their individual genetic and epigenetic background (Berry et al., 2019; Rowe and Daley, 2019), which has been estimated to be responsible for up to 46% of phenotype variability and also influences differentiation efficiency (Kilpinen et al., 2017). A strategy for circumventing inter-donor variability is to apply gene-editing technologies, such as CRISPR/Cas9 (Jehuda et al., 2018) to generate isogenic controls, which allow the investigation of disease-causing mutations with control cells having the same genetic background (Yoshida and Yamanaka, 2017).

Maturity and Subtype Specificity of Human Induced Pluripotent Stem Cell-Derived Cell Lines

A further key challenge is to improve the maturity and subtype specificity of hiPSC-derived cell lines. Despite improved protocols for producing specific somatic cell types and subtypes, the vast majority of hiPSC-directed differentiations produce populations that most closely resemble fetal or neonatal cells (Berry et al., 2019), including the extensively studied hiPSC-derived cardiomyocytes (hiPSC-CMs; Kolanowski et al., 2017; Di Baldassarre et al., 2018; Ahmed et al., 2020), and hiPSC-derived neurons (hiPSC-neurons; Casalia et al., 2021; de Leeuw et al., 2021; Giacomelli et al., 2022). In both cases there is a further complexity in creating pure subtype populations, for example atrial or ventricular hiPSC-CMs (Cyganek et al., 2018; Feyen et al., 2020) or defining the desired hiPSC-neuron subtype (e.g., sensory, motor, or dopaminergic neurons; Davis-Dusenbery et al., 2014; Hartfield et al., 2014; Young et al., 2014).

Strategies to improve cell maturation during differentiation are many (see **Figure 2**) and include: the addition of specific chemical cues during differentiation (Burridge et al., 2012; Yoshida and Yamanaka, 2017; Ahmed et al., 2020); replacing the energy source, for instance the addition of fatty acids as a substitute for glucose in the culturing media, has been shown to improve hiPSC-CM maturation by activating the required metabolic pathways (Sharma et al., 2015; Yoshida and Yamanaka, 2017; Yang et al., 2019); prolonged time in culture which does, however, also increase the risk of contamination and mutation accumulation (Blokzijl et al., 2016; Odawara et al., 2016; Breckwoldt et al., 2017; Yoshida and Yamanaka, 2017; Biendarra-Tiegs et al., 2019; Ahmed et al., 2020); electrical and mechanical stimulation (pacing) have been reported as valid methods to improve the maturity and function of hiPSC-CMs and -neurons (Ahmed et al., 2020; Giacomelli et al., 2022); and finally modulating the chemical and spatial microenvironment of the differentiating cell culture, for example changing the adherence matrix (Feaster et al., 2015; Depalma et al., 2021), cell culture geometry, e.g., using 3D culture (Lemoine et al., 2017; Tiburcy et al., 2017; Di Baldassarre et al., 2018; de Leeuw et al.,

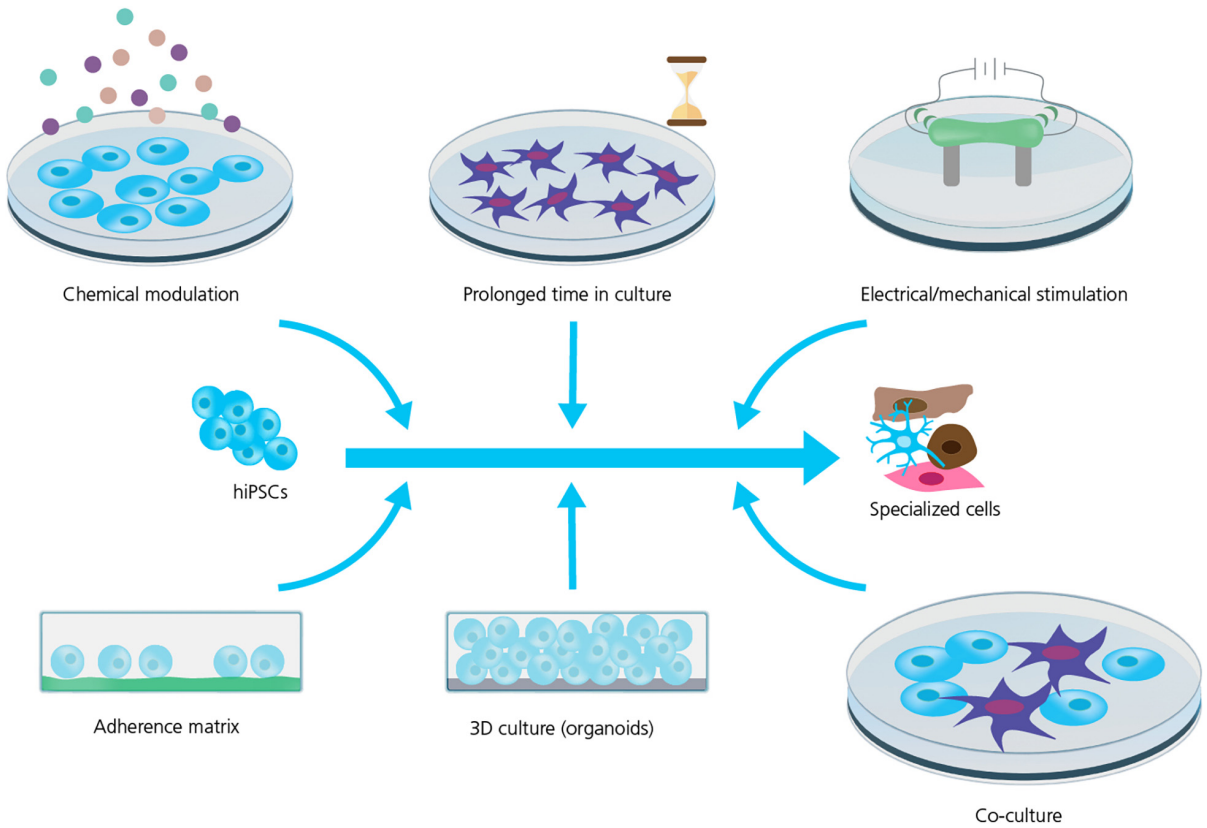

FIGURE 2 | Strategies for improving hiPSC maturity. Several strategies are used to improve the maturity and phenotype specificity of hiPSC-derived cell lines. However, the mechanism and efficiency of these strategies are still being explored and requires rigorous characterization and quality control. Adapted from Ahmed et al. (2020), with permission under Creative Commons Attribution License (CC BY).

2021) or preparing co-cultures with supportive cells (Odawara et al., 2016; Andersen et al., 2020; Zafeiriou et al., 2020).

Cell reprogramming, differentiation and maturation are manipulations that lead to many intracellular changes that can affect the lifespan of cells. Indeed, a somatic cell obtained from a patient which is "rejuvenated" into a stem-cell like phenotype, shows intracellular signatures such as an active telomerase activity and immature mitochondria, as well as a decrease in senescence markers [e.g., senescence marker p21, (Strässler et al., 2018)]. After differentiation, although the cellular aging process may restart, certain improved characteristics remain compared to the parent cell (e.g., longer telomeres).

Due to these intracellular changes, additional challenges arise when referring to how the age of patients could influence the functionality and maturity of hiPSC-derived models and whether it is feasible to apply this technology in age-related diseases. There is also an increasing need to perform safety pharmacology in "aged" senescent cells to functionally model and translate the complex physiology, pathophysiology and pharmacology of the aging, senior population, particularly in light of the growth of this demographic (Fermini and Bell, 2022).

In addressing these challenges, there is a need to define quality standards during hiPSC reprogramming and differentiation, as well as rigorous and statistically sound characterization of the final product (Engle et al., 2018). The specific composition of ion channels is an important marker of cell maturity and subtype specificity, for example in hiPSC-and -neurons (Jonsson et al., 2012; Bardy et al., 2016; Goversen et al., 2018b), rendering APC important as a high-throughput (HT) characterization method providing ion channel maturation metrics. Thus, we envision molecular and genetic approaches in combination with APC electrophysiological characterization will generate authentic, translatable and quantifiable hiPSC models for disease investigation and drug-screening.

ELECTROPHYSIOLOGICAL MEASUREMENTS OF HUMAN INDUCED PLURIPOTENT STEM CELL DERIVED CELL LINES USING AUTOMATED PATCH CLAMP

Ion channels represent attractive targets in hiPSC-derived cell lines, making electrophysiological studies of hiPSC-derived cell lines important not only for characterization (as mentioned above), but also for advances in biomedical research including drug discovery and development. The HT nature of APC

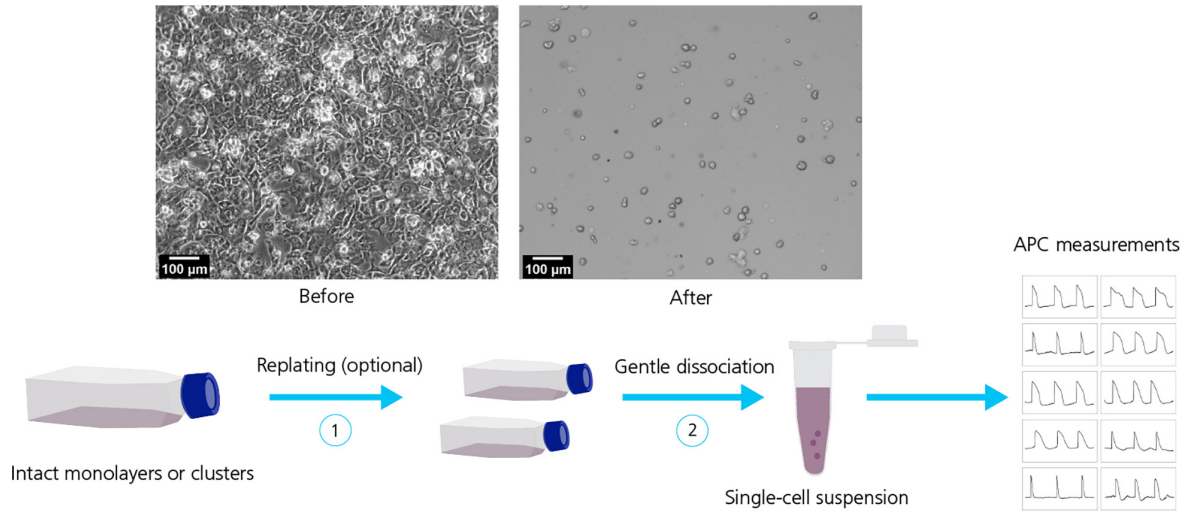

FIGURE 3 | Dissociation of hiPSC-derived cell lines. Top row: Micrographs of hiPSC-CMs before (left) and after (right) dissociation. Bottom row: Dissociation of hiPSC-derived cell lines typically include a sequence of steps for example replating (1) followed by gentle dissociation methods (2) to obtain a homogeneous, healthy single-cell suspension suitable for APC measurements. Adapted from Rajamohan et al. (2016), with permission under Creative Commons Attributions License (CC BY).

that enables recordings of large datasets within a few days or even hours, makes this method ideal for applications such as: quantification of inter-patient or inter-batch variability; identification of cell sub-populations within the same batch, based on their ion channel content; and HT drug screening.

In this section we summarize the latest advances and challenges toward making such APC measurements possible.

Advances and Recent Developments

Electrophysiological methods, such as MPC, have been extensively employed for characterization of hiPSC-derived cell lines over the years (Chen et al., 2014; Jones et al., 2014; Lemoine et al., 2017; Giannetti et al., 2021). However, the inherently labor intensive and low throughput nature of MPC, lead electrophysiologists to consider more time and resource efficient alternatives. Consequently, increasing efforts have gone into transferring MPC experimentation and measurements to APC systems (Haythornthwaite et al., 2012; Franz et al., 2017; Li et al., 2019; Jung et al., 2022). A key element that allows this transfer from MPC to APC is the provision of unicellular cell suspensions (see **Figure 3**). The quality (homogenous, unicellular populations) and health (minimal enzymatic and mechanical membrane damage and cytotoxicity) of cells in suspension are critical to achieving high success recording rates on APC. Using dissociated cell suspensions literally turns the ion channel current recording format on its head: in MPC the recording electrode is moved to an adherent cell, contrasting with APC where dissociated, single cells in suspension are moved by robotic pippetors to arrays of wells containing fixed, planar recording electrodes.

Initial with hiPSC-derived cell lines focused on APC assay development, including cell-handling on the machine; intra- and extra-cellular recording solutions; and, the suction protocols employed to position the cell and rupture the membrane, the so-called whole-cell conformation, to allow electrical access to the interior of the cell. However, progress has been slow, with only minor improvements in experiment success rate and reproducibility. It has become increasingly evident that working with hiPSC-derived cell lines demands a greater understanding of the cell population than working with clonal, homogenous immortalized cell lines. This includes the process of generating hiPSC-derived cell lines (as discussed in the section above), characterization and quality control of the final product and specialized dissociation methods for generating purer, more homogenous cell suspensions.

Whilst measurements on hiPSC-derived cell lines have progressed slowly, the technological development of APC features have advanced at a faster pace. This includes: the exchange of external and internal solutions; fast compound addition and wash out; perforated patch methods (Rosholm et al., 2021a); current clamp and dynamic clamp recordings, e.g., enabling measurements of action potentials (Becker et al., 2020; Rosholm, 2021); and temperature control for physiologically relevant temperature experimentation; all in a high throughput fashion that provides the statistical power necessary for drawing accurate and correct conclusions (Bell and Dallas, 2018; Bell and Fermini, 2021).

One major difference of APC compared to other methods typically used for hiPSC measurements, such as MPC, multielectrode-array (Odawara et al., 2016) or fluorescent plate readers (Sube and Ertel, 2017; Kilfoil et al., 2021), is that APC measures single cells that have been dissociated from 2D or 3D tissue culture. Whilst 2D/3D multi-cell or tissue recordings provide information on tissue/population behavior (including, e.g., morphology changes and network signaling), single cell APC recordings have increased temporal resolution providing crucial

information regarding inter-cell variability in, e.g., compound sensitivity, different ion channel expression levels and biological activity. It is imperative to be aware of and understand which questions can be answered using dissociated cells, because several important properties such as cell morphology and ion channel expression might change due to cell handling and dissociation from culture flasks (Raman and Bean, 1997). To fill this potential information gap that can arise in cell dissociated suspensions used in APC, a complementary technology would be single cell dye-based imaging of adherent cell populations (e.g., see Vala Sciences), though this, too, has its limitations: the dye(s) used can introduce new, non-biological variables to the imaging measurements and is an indirect, proxy measure of the ion channel activity.

The preferred harvest protocol will depend on the cell type, quality and culturing days and will likely evolve continuously (also, see **Figure 3**). Dissociating hiPSC-derived cell lines into single-cell suspensions is often challenging (especially CMs and neurons), due to the formation of tight cellular "tissue"-like structures and networks that must be disrupted. In general, the longer the cells have been cultured, the tighter the connections become, increasing the possibility of damage during cell harvest. For APC it is of utmost importance to work with a healthy, homogenous cell suspension that is free of debris. Improvements involve: using gentle dissociating enzymes (e.g., TrypLE^{TM}, Gibco, United States; Accutase^{TM}, Stemcell Technologies, United States; or Papain, Sigma-Aldrich, United States); cold-harvest and/or incubation; addition of protective chemicals to ensure membrane integrity (e.g., ROCK inhibitor, blebbistatin) and prevent stickiness (DNase); replating for 24 h – 1 week; filtering to remove aggregates and possibly positive selection based on surface markers (Rajamohan et al., 2016; Obergrussberger et al., 2017; Li et al., 2021b). Finally, the use of fluoride containing seal enhancing solutions on many APC platforms can be problematic for some measurements, e.g., cardiac action potentials, that rely on physiologically accurate calcium kinetics. Consequently, where possible, these measurements should be performed on systems using physiological recording solutions (Mann et al., 2019; Rosholm, 2021).

Even with the aforementioned challenges, the field is now rapidly advancing and with the existing cell quality and suspension preparation methods researchers have made significant progress in exploring and developing the possibilities of measuring hiPSC-derived cell lines using APC (Rajamohan et al., 2016; Mann et al., 2019; Potet et al., 2020; Toh et al., 2020; Li et al., 2021a).

NOVEL APPLICATIONS OF AUTOMATED PATCH CLAMP AND HUMAN INDUCED PLURIPOTENT STEM CELL DERIVED CELL LINES

Originally hiPSC-derived cell lines were mainly considered for applications in regenerative medicine (Laustriat et al., 2010; Doss and Sachinidis, 2019) but their extensive range of advantages have

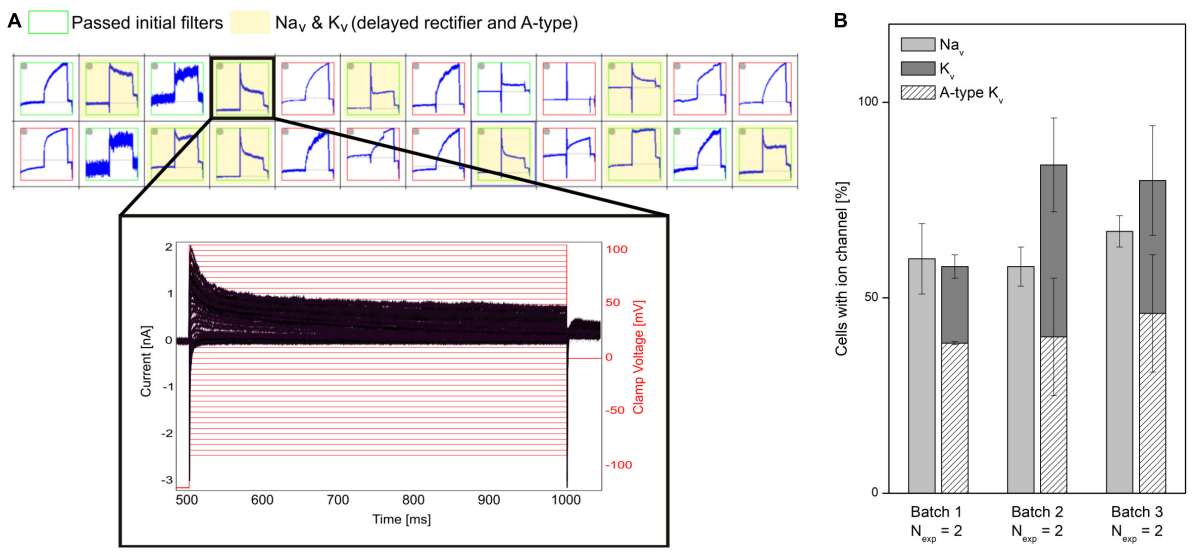

FIGURE 4 | Characterizing mixed ion channel populations in hiPSC-derived cortical neurons. **(A)** Quality control filters allow selection of cells expressing the ion channels of interest. Top: Cut-out of the measurement plate view showing 24 of 384 experiments. Red and green borders correspond to experiments that failed and passed, respectively, the initial filter criteria (R_{mem} > 500 MΩ, C_{cell} > 1.5 pF). The experiments highlighted in yellow passed filter criteria for Na_v and K_v currents. Bottom: Example of a population of current traces (black) elicited by + 5 mV voltage-steps (red) recorded from a neuron, expressing Na_v channels and a mixture of delayed rectifier and A-type K_v channels. **(B)** The percentage (average ± SEM) of investigated cells containing Na_v and K_v channels were displayed for three different differentiation batches of hiPSC cortical neurons (N_{exp} = 2 experiment days, with > 48 measurement sites per experiment). Of the cells expressing K_v channels, the percentage of K_v expressing cells also having A-type K_v currents are overlayed (diagonal pattern). No significant differences were observed between the three batches (Rosholm et al., 2021b). Adapted from Rosholm et al. (2021b), with permission from Sophion Bioscience A/S.

also made them interesting for the development of cell-based assays in the fields of drug-discovery, pharmaceutical research and personalized medicine (Yu et al., 2007; Di Baldassarre et al., 2018; Berry et al., 2019). Due to the improved quality and cell handling methods, ongoing development of APC features, and initiatives such as the Comprehensive *in vitro* Proarrhythmia Assay for cardiac ion channel safety pharmacology (Colatsky et al., 2016), the field is now making good progress developing new APC applications for the characterization and pharmacology of hiPSC-derived cell lines.

In this section we provide examples of some of these novel APC applications for studies of hiPSC-derived cell lines.

Ion Channel Analysis (Quality Control) in Human Induced Pluripotent Stem Cell Derived Cell Lines

A challenge of hiPSC-derived cells is that they typically display heterogeneous current expression. This might be due to different maturation states, different cell types, genetic, and/or biological variability. In APC, currents are recorded in parallel from many cells. This makes APC well suited to characterize cell populations and identify subpopulations (Haythornthwaite et al., 2012; Franz et al., 2017). A representative example is shown in **Figure 4** in which a subpopulation of hiPSC-derived cortical neurons is selected that expresses both Na_v and a mixture of delayed rectifier and A-type K_v channels. Properties of hiPSC-neurons, such as ion channel expression, AP firing characteristics and the resting membrane potential (RMP), have shown to approach that of mature adult neuronal cells by increased time in culture (Prè et al., 2014; Berry et al., 2015; Odawara et al., 2016). APC recordings can assist the evaluation of neuron population purity and maturity by comparing ion channel expression at different culturing time points or across different batches (see **Figure 4**).

Action Potential Measurements in Human Induced Pluripotent Stem Cells-Derived Cardiomyocytes and Neurons

Measurements of cardiac APs are of special interest for disease modeling, drug discovery and cardiac safety (Braam et al., 2009; Mummery, 2018; Rowe and Daley, 2019; Bell and Fermini, 2021). However, the immature phenotype and heterogeneous ion channel expression of hiPSC-derived CMs, as compared to acutely isolated, primary CMs has limited the physiological relevance of their electrophysiological characterization, in general, and high throughput measurements, in particular (Casini et al., 2017; Mann et al., 2019; Vaidyanathan et al., 2021). This includes the presence of the pacemaker current I_f (routinely expressed in immature CMs and lost in adult CMs) and reduced densities of hyperpolarizing current I_{K1} (Jonsson et al., 2012; Goversen et al., 2018b). Highlighting these differences, **Figure 5** provides a comparison between hiPSC-derived CMs and acutely isolated, primary adult CMs showing the relative size and contribution of ion channel currents that form the AP in each.

Different methods have been employed to compensate for missing currents. For example, a method that is increasingly being used is enhancing missing currents using viral transfection (Jones et al., 2014; Vaidyanathan et al., 2021). Another strategy that has been employed in APC is dynamic clamp, which is a method that models and electronically introduces ion currents into cells, to compensate for the lack of expression (Becker et al., 2013; Verkerk et al., 2017). For instance, this electronic compensation can be used to add the missing hyperpolarizing current I_{K1}, bringing the depolarized RMP often observed in dissociated hiPSC-CMs closer to the physiological, hyperpolarized potential, which results in AP durations and waveforms comparable to mature CMs (Li et al., 2019; Becker et al., 2020). Drawbacks of dynamic clamp are that the compensating current is only as accurate as the assumption-based model of the mature CM, and ideally each cell's current phenotype and derived model would need to be measured and performed individually with real-time compensation during experimentation, a potential computer processing bottleneck for the ms temporal resolution of 100 s of simultaneous recordings in APC.

Finally, the maturation of hiPSC-CMs has improved recently, and the paradigm of impaired I_{K1} expression in hiPSC-CMs has been challenged (Horváth et al., 2018). In **Figure 6** we display APC measurements of "mature" I_{K1} currents in hiPSC-CMs.

As observed with hiPSC-CMs, hiPSC-neurons (including several subtypes, such as motor neurons and sensory neurons) do not completely replicate the adult neuron phenotype in terms of morphology, electrical function, and critically, in resembling neurodegenerative disease features (Casalia et al., 2021; Giacomelli et al., 2022). Although iPSC-neurons fail to entirely capture all the characteristics of fully mature brain cells, they express functional ion channels and are capable of displaying primary neuronal functions such as firing action potentials (Franz et al., 2017). Recent developments of more sophisticated and reproducible differentiation protocols combined with advanced genome engineering, longer maturation in culture and improved dissociation procedures have improved iPSC-neurons which now constitute a promising cell model for APC recordings despite their relatively immature phenotype (Shi et al., 2017; Giacomelli et al., 2022).

The high throughput of APC allows sufficient data generation to accurately define heterogeneous ion channel populations in hiPSC-CMs, correlating channel levels to the resulting AP firing properties (Rosholm, 2021). Presently, optimized hiPSC-CM maturation and harvest protocols have made it possible to measure APs and capture compound effects in physiological solutions using APC (see **Figure 7**). The data were very similar to data obtained with a complementary optical assay (Seibertz et al., 2020). These advances hold great promise that robust and consistent AP assays for cardiac safety and compound screens will soon be feasible and routine.

Disease Modeling, Drug-Screening, and Personalized Medicine

As the quality of hiPSC-derived cell lines increases, an obvious next step will be to utilize the HT capability of APC for

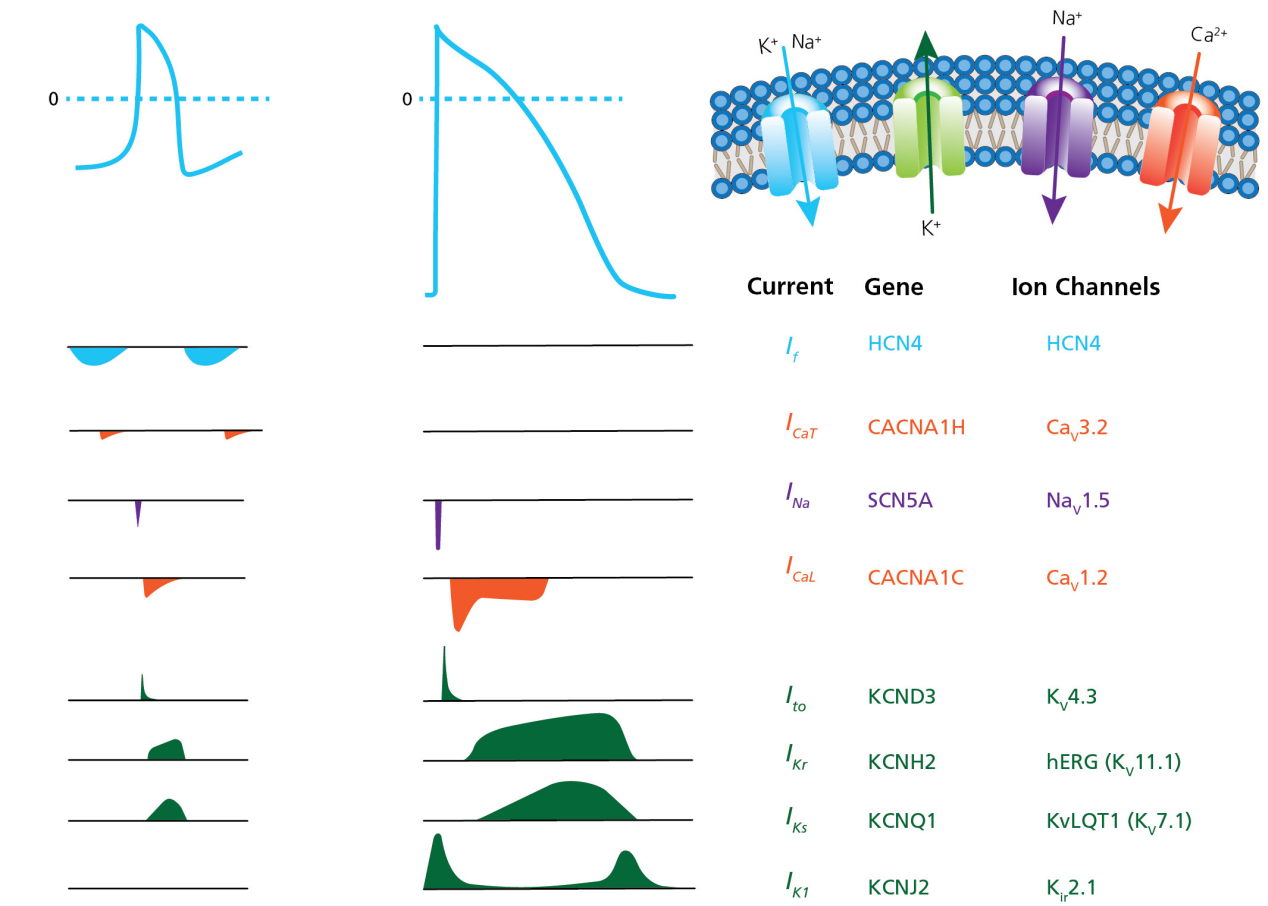

FIGURE 5 | Ion channel content in hiPSC-CMs versus human primary CMs. A comparison of action potential and ion channel currents recorded in **(A)** hiPSC-CMs and **(B)** human primary adult CMs. The associated genes and ion channels are listed on the right. From the top the currents are: I_f, pacemaker or funny current; I_{CaT}, T-type calcium channel current; I_{Na}, sodium current; I_{CaL}, L-type calcium channel current; I_{to}, transient outward potassium current; I_{Kr}, rapid delayed- rectifier potassium current; I_{Ks}, slow delayed-rectifier potassium current; and I_{K1}, inward-rectifier potassium current. The traces highlight differences traditionally observed in hiPSC-CMs, such as the presence of the pacemaker current I_f (routinely expressed in immature CMs and lost in adult CMs) and reduced densities of hyperpolarizing current I_{K1}. Adapted from Karbassi et al. (2020), with permission from publisher Springer Nature.

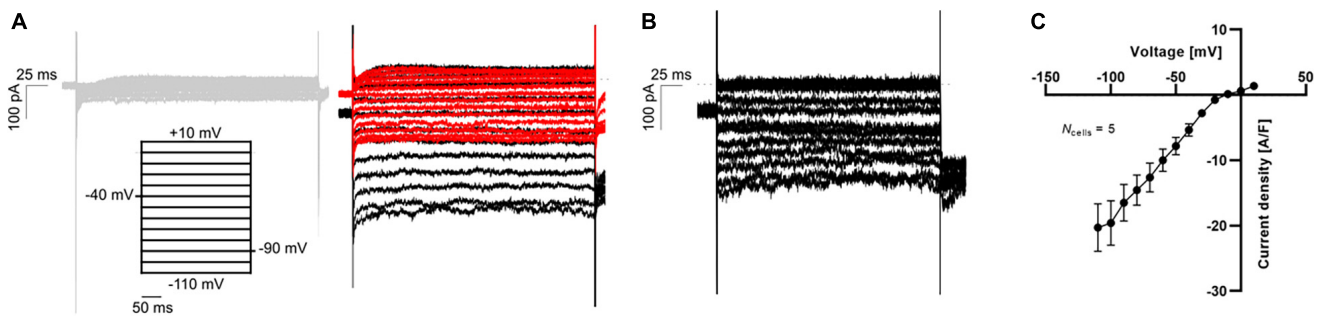

FIGURE 6 | APC measurements of I_{K1} current-voltage relationship in hiPSC-CMs using physiological solutions. **(A)** Representative K^+ current traces in response to a voltage step protocol from –110 mV to +10 mV with 10 mV increment step size (black). The current was measured in 5 mM extracellular K^+ (gray, left) and 75 mM extracellular K^+ before (black) and after (red) addition of 1 mM $BaCl_2$ (right). **(B)** The $BaCl_2$ sensitive I_{K1} was calculated by subtracting the insensitive current (red trace in **A**) from the total I_K (black trace in **A**). **(C)** The I_{K1} current-voltage relationship was plotted by extracting the average steady-state sensitive current (shown in **B**) and plotting as a function of step voltage. Adapted from Rosholm et al. (2022), with permission from Sophion Bioscience A/S.

studying disease models, drug-screening and personalized (or stratified) medicine (Chen et al., 2016). hiPSC disease models, characterization and drug-screening assays employing these cells have been developed for a range of diseases including neurodegenerative diseases (Kim, 2015; Lee and Huang, 2017) such as Alzheimer's Disease (Medda et al., 2016; Brownjohn et al., 2017), and cardiovascular diseases (Braam et al., 2009; Sube and Ertel, 2017; Mummery, 2018; Wu et al., 2020) such as long-QT syndrome (Friedrichs et al., 2015; Jouni et al., 2015; Chen et al., 2016).

Although examples of APC applications within personalized biomedicine are still scarce, their need and value mean they are in active development (Friedrichs et al., 2015; Goversen et al., 2018a), with expectations high that we will see more in the near future. For an example of such an application see Rosholm (2019) in which an hiPSC motor neuron disease model, derived from a Spinal Muscular Atrophy patient (Faravelli et al., 2015) was characterized together with control cells from healthy subjects. The results showed the expected overactivity of Na_v channels, which could be rescued by a Na_v antagonistic compound addition (SMN-C3), see **Figure 8**.

FUTURE PERSPECTIVES

As highlighted in this review, the advances made in our labs and amongst APC and stem cell researchers across the world in the last few years have catapulted this niche, often challenging, area of research into the limelight, and is becoming widely adopted amongst the stem cell and drug discovery communities (Rajamohan et al., 2016; Franz et al., 2017). With experimental success rates climbing, improved protocols and assays developed using physiological recording conditions, the large, objective data sets generated are furthering our understanding of ion channel physiology and pathophysiology. We believe these advances in APC *in vitro*

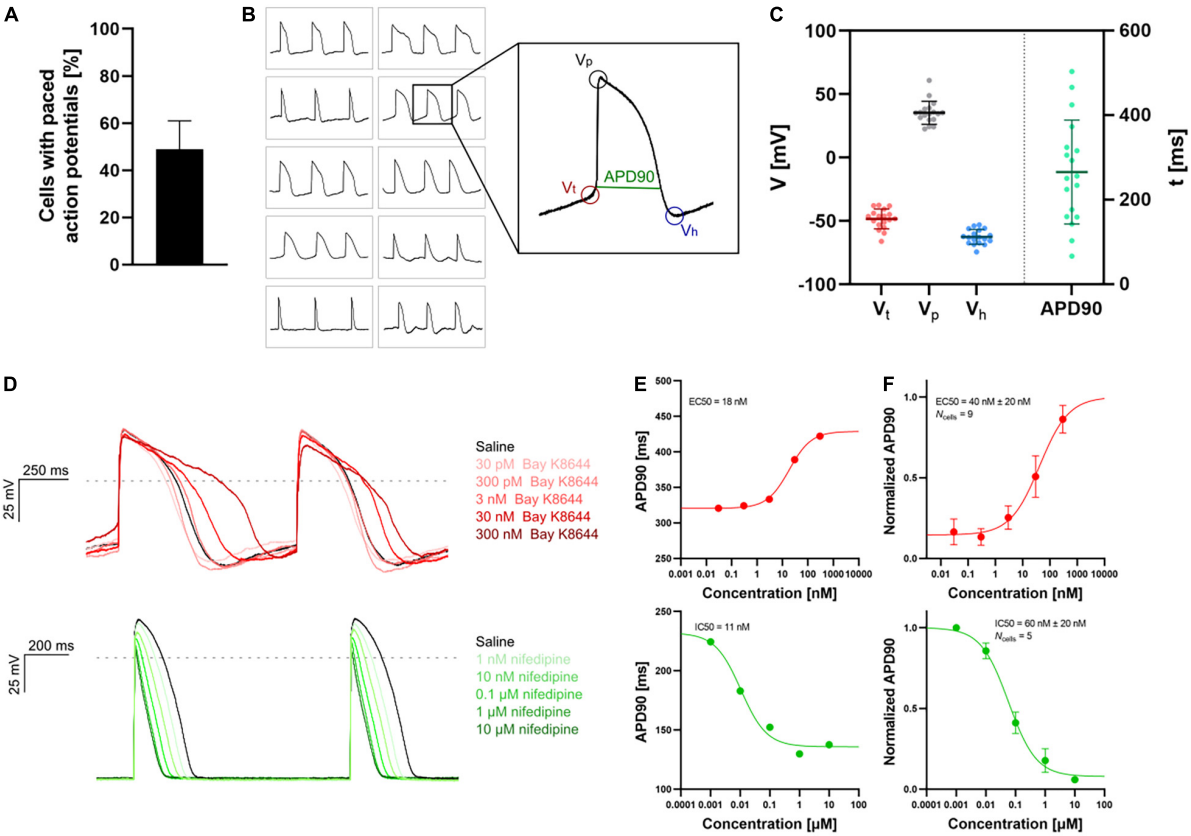

FIGURE 7 | APC current-clamp measurements of paced action potentials and APD90 concentration-response plots. **(A)** The percentage of successful experiments displaying paced action potentials [V_p > 0 mV, resting membrane potential (RMP) < –40 mV]. Data is avg ± SD of three measurement plates (each of 48 recording sites). Assay success rate was 10%–30% out of 48 sites. **(B)** Paced action potentials from 10 individual hiPSC-CMs within a single measurement plate (left) and an expanded action potential displaying the extracted parameters: threshold potential (V_t), peak potential (V_p), hyperpolarization potential (V_h), and action potential duration at 90% repolarization (APD90). **(C)** Plot of extracted parameters, V_t (red), V_p (gray), V_h (blue), and APD90 (green, ms) for 18 individual hiPSC-CMs with the avg ± SD (solid lines). **(D)** Paced action potentials for saline controls (black traces) and in response to increasing concentrations of Bay K8644 (top, traces in shades of red) and nifedipine (bottom, traces in shades of green). **(E)** Plots of APD90 versus compound concentration with Boltzmann fits including EC50 or IC50 calculated values, recorded in a single cell. **(F)** Cumulative concentration-response (average, APD90 normalized to pre compound concentration) relationships with Boltzmann fits including EC50 or IC50 calculated values. Data points are avg ± SEM of N_{cells}. Adapted from Rosholm (2021) and Rosholm et al. (2022), with permission from Sophion Bioscience A/S.

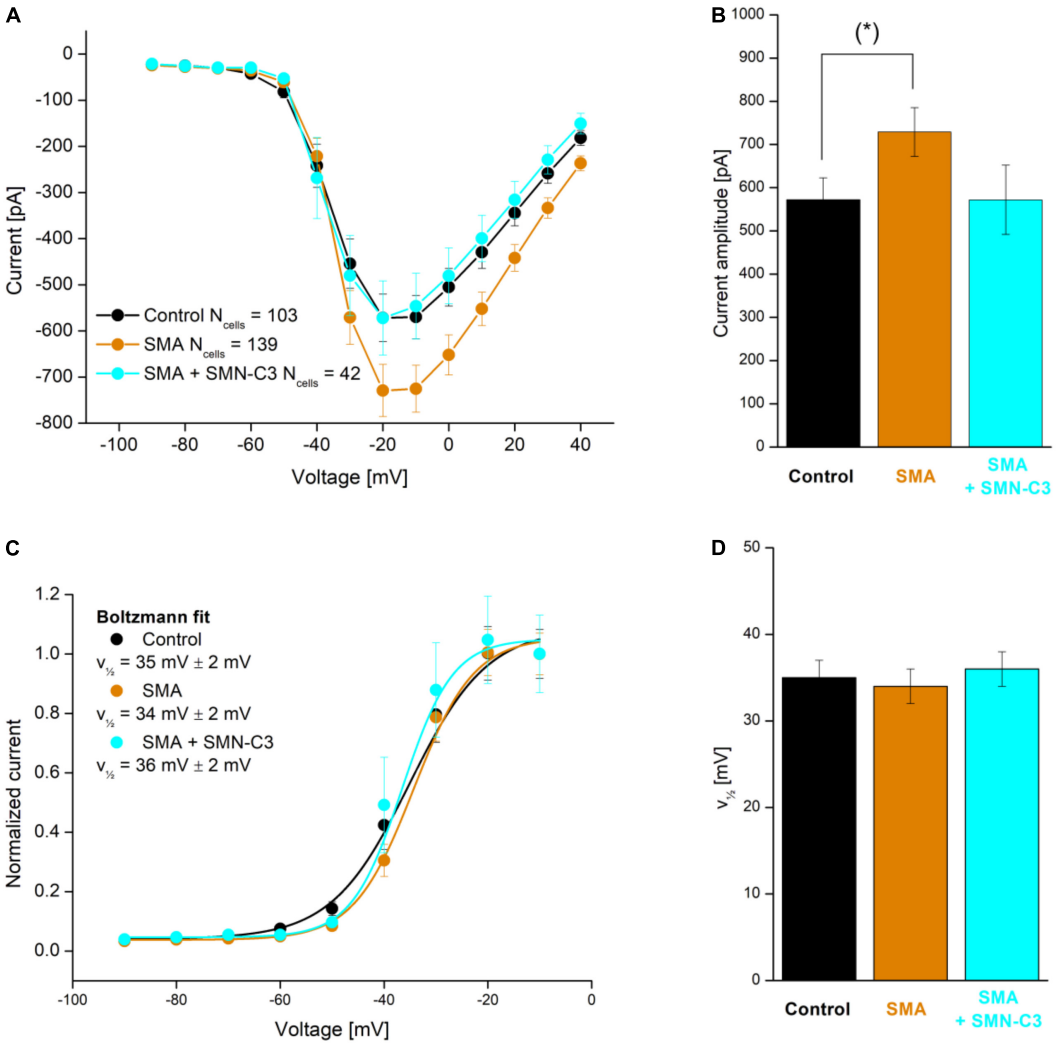

FIGURE 8 | APC evaluation of compound effects on Na_V channel properties in SMA hiPSC-neurons. Parallel recordings of control neurons (black), SMA neurons (orange), and SMA neurons treated with SMN-C3 during culturing (blue). **(A)** Average Na_V current versus step voltage. **(B)** Quantification of the current amplitude at –20 mV. The current amplitude is significantly larger in SMA cells than in control cells [Student's *t*-test, $p < 0.05$ (*), 95% confidence interval]. **(C)** Average Na_V current normalized to the current recorded at V = –20 mV. Fitting of a Boltzmann function (solid lines) yielded the half-activation voltage ($V_{\frac{1}{2}}$, mV). **(D)** Half-activation voltage ($V_{\frac{1}{2}}$) values. Error bars are SEM. Adapted from Rosholm (2019), with permission from Sophion Bioscience A/S.

electrophysiology, married with cross-correlated combinations of animal and human iPSC models, in time will reduce and circumvent the expensive use (and sometimes limited translatability) of primary animal organ, tissue and cell models (Ebert et al., 2012; Deng, 2017; Pessôa et al., 2020). The advances made to date are providing tools and assays for significant progress in the accuracy and efficiency of safety pharmacology, drug discovery and development, and regenerative and personalized medicines.

Jumping into the fabled time traveling DeLorean car and heading back to the future: one area that is likely to feature heavily in the future of stem cell and ion channel research are the possibilities afforded by patient-derived hiPSCs. Measuring and defining an individual patient's hiPSCs (such as their ion channel composition, pharmacology and biophysics) will allow the design of personalized, targeted medical interventions (Matsa et al., 2016; Hamazaki et al., 2017; Doss and Sachinidis, 2019), thus improving the efficacy of medicinal regimes and limiting side-effects.

Taking this concept of measuring and defining patient hiPSCs a step further: by identifying patient genotypes (by gene or genome sequencing) involved in a panel of potential health issues specific to the patient, these can be correlated to ion channel phenotypes determined using APC recordings of patient-derived hiPSCs, across a range of cell types. Such patient genotype/phenotype correlation ("phenotypic screening") will allow existing health issues to be identified and addressed (Muñoz-Martín and Matsa, 2021). Combining

this ion channel phenotypic screening with other typical phenotype screens (such as defining patient metabolic pathways or "metabolome") will allow potential future health issues to be flagged, enabling pre-emptive, prophylactic medical interventions or lifestyle changes to be implemented. In addition, high throughput APC would allow for the application of artificial intelligence (or machine learning) tools to study multidimensional high-volume data for particular phenotypes, which may allow for identification of novel cellular biomarkers as a basis for robust drug discovery research. With time and concomitant "big data" analyses, the correlation between genotype and phenotype is likely to become sufficiently predictive allowing gene sequencing alone to be used in forecasting the ion channel targeting medicinal regimes that best suit a designated genotype patient cohort or sub-group within the general population.

In conclusion, the marriage of hiPSC and APC offers much potential for ion channel biomedical research and drug discovery. The possibilities of defining ion channel activity, biophysics and pharmacology in specialized cells (like CMs and neuronal cells), including cells derived from healthy or diseased patients, provide model cells to efficiently perform APC driven *in vitro* studies and high throughput screens that increasingly translate to human clinical studies (Rowe and Daley, 2019; Muñoz-Martín and Matsa, 2021). In writing this review, the authors aim to convey the recent adventures and advances in cellular time travel and the vast potential for these techniques and technologies. After reading, we hope the reader, like us, is now flexing their muscles in the starting blocks for the bright biomedical future of the brave new world we are soon to be sprinting toward.

AUTHOR CONTRIBUTIONS

KR structured the manuscript and coordinated the writing process, and produced the experimental data included in the manuscript. KR, BB, and DB prepared the first version of the manuscript. SK, DN, NV, and FS reviewed the manuscript. All authors contributed to the article and approved the submitted version.

FUNDING

The work of NV is supported by the Deutsche Forschungsgemeinschaft (DFG; VO 1568/3-1, VO 1568/4-1, IRTG1816 project 12, SFB1002 project A13, and under Germany's Excellence Strategy – EXC 2067/1- 390729940) and the DZHK (German Center for Cardiovascular Research, 81X300189, 81X4300102, 81X4300115, and 81X4300112).

ACKNOWLEDGMENTS

The authors would like to acknowledge Jane Lucas for assistance with figure preparation. hiPSC-neurons were provided by Boston Children's Hospital and BrainXell. HiPSC-CMs were provided by NV, Göttingen.

REFERENCES

Ahmed, R. E., Anzai, T., Chanthra, N., and Uosaki, H. (2020). A brief review of current maturation methods for human induced pluripotent stem cells-derived cardiomyocytes. *Front. Cell Dev. Biol.* 8:178. doi: 10.3389/fcell.2020.00178

Andersen, J., Revah, O., Miura, Y., Thom, N., Amin, N. D., Kelley, K. W., et al. (2020). Generation of functional human 3D cortico-motor assembloids. *Cell* 183, 1913–1929.e26. doi: 10.1016/j.cell.2020.11.017

Assou, S., Bouckenheimer, J., and De Vos, J. (2018). Concise review: Assessing the genome integrity of human induced pluripotent stem cells: What quality control metrics? *Stem Cells* 36, 814–821. doi: 10.1002/stem.2797

Bardy, C., Van Den Hurk, M., Kakaradov, B., Erwin, J. A., Jaeger, B. N., Hernandez, R. V., et al. (2016). Predicting the functional states of human iPSC-derived neurons with single-cell RNA-seq and electrophysiology. *Mol. Psychiatry* 21, 1573–1588. doi: 10.1038/mp.2016.158

Becker, N., Horváth, A., De Boer, T., Fabbri, A., Grad, C., Fertig, N., et al. (2020). Automated dynamic clamp for simulation of IK1 in human induced pluripotent stem cell–derived cardiomyocytes in real time using patchliner dynamite8. *Curr. Protoc. Pharmacol.* 88, 1–23. doi: 10.1002/cpph.70

Becker, N., Stoelzle, S., Göpel, S., Guinot, D., Mumm, P., Haarmann, C., et al. (2013). Minimized cell usage for stem cell-derived and primary cells on an automated patch clamp system. *J. Pharmacol. Toxicol. Methods* 68, 82–87. doi: 10.1016/j.vascn.2013.03.009

Bell, D. C., and Dallas, M. L. (2018). Using automated patch clamp electrophysiology platforms in pain-related ion channel research: insights from industry and academia. *Br. J. Pharmacol.* 175, 2312–2321. doi: 10.1111/bph.13916

Bell, D. C., and Fermini, B. (2021). Use of automated patch clamp in cardiac safety assessment: past, present & future perspectives. *J. Pharmacol. Toxicol. Methods* 111:107114. doi: 10.1016/j.vascn.2021.107114

Bellin, M., Marchetto, M. C., Gage, F. H., and Mummery, C. L. (2012). Induced pluripotent stem cells: the new patient? *Nat. Rev. Mol. Cell Biol.* 13, 713–726. doi: 10.1038/nrm3448

Berry, B. J., Akanda, N., Smith, A. S. T., Long, C. J., Schnepper, M. T., Guo, X., et al. (2015). Morphological and functional characterization of human induced pluripotent stem cell-derived neurons (iCell Neurons) in defined culture systems. *Biotechnol. Prog.* 31, 1613–1622. doi: 10.1002/btpr.2160

Berry, B. J., Smith, A. S. T., Young, J. E., and Mack, D. L. (2019). Advances and current challenges associated with the use of human induced pluripotent stem cells in modeling neurodegenerative disease. *Cells Tissues Organs* 205, 331–349. doi: 10.1159/000493018

Biendarra-Tiegs, S. M., Li, X., Ye, D., Brandt, E. B., Ackerman, M. J., and Nelson, T. J. (2019). Single-Cell RNA-Sequencing and Optical Electrophysiology of Human Induced Pluripotent Stem Cell-Derived Cardiomyocytes Reveal Discordance between Cardiac Subtype-Associated Gene Expression Patterns and Electrophysiological Phenotypes. *Stem Cells Dev.* 28, 659–673. doi: 10.1089/scd.2019.0030

Blokzijl, F., De Ligt, J., Jager, M., Sasselli, V., Roerink, S., Sasaki, N., et al. (2016). Tissue-specific mutation accumulation in human adult stem cells during life. *Nature* 538, 260–264. doi: 10.1038/nature19768

Braam, S. R., Passier, R., and Mummery, C. L. (2009). Cardiomyocytes from human pluripotent stem cells in regenerative medicine and drug discovery. *Trends Pharmacol. Sci.* 30, 536–545. doi: 10.1016/j.tips.2009.07.001

Breckwoldt, K., Letuffe-Brenière, D., Mannhardt, I., Schulze, T., Ulmer, B., Werner, T., et al. (2017). Differentiation of cardiomyocytes and generation of human engineered heart tissue. *Nat. Protoc.* 12, 1177–1197. doi: 10.1038/nprot.2017.033

Brownjohn, P. W., Smith, J., Portelius, E., Serneels, L., Kvartsberg, H., De Strooper, B., et al. (2017). Phenotypic screening identifies modulators of amyloid precursor protein processing in human stem cell models of Alzheimer's Disease. *Stem Cell Rep.* 8, 870–882. doi: 10.1016/j.stemcr.2017.02.006

Burridge, P. W., Keller, G., Gold, J. D., and Wu, J. C. (2012). Production of de novo cardiomyocytes: human pluripotent stem cell differentiation and direct reprogramming. *Cell Stem Cell* 10, 16–28. doi: 10.1016/j.stem.2011.12.013

Casalia, M. L., Casabona, J. C., García, C., Cavaliere Candedo, V., Quintá, H. R., Farías, M. I., et al. (2021). A familiar study on self-limited childhood epilepsy patients using hIPSC-derived neurons shows a bias towards immaturity at the morphological, electrophysiological and gene expression levels. *Stem Cell Res. Ther.* 12:590. doi: 10.1186/s13287-021-02658-2

Casini, S., Verkerk, A. O., and Remme, C. A. (2017). Human iPSC-derived cardiomyocytes for investigation of disease mechanisms and therapeutic strategies in inherited arrhythmia syndromes: strengths and limitations. *Cardiovasc. Drugs Ther.* 31, 325–344. doi: 10.1007/s10557-017-6735-0

Chen, H., Qian, K., Du, Z., Cao, J., Petersen, A., Liu, H., et al. (2014). Modeling ALS with iPSCs reveals that mutant SOD1 misregulates neurofilament balance in motor neurons. *Cell Stem Cell* 14, 796–809. doi: 10.1016/j.stem.2014.02.004

Chen, I. Y., Matsa, E., and Wu, J. C. (2016). Induced pluripotent stem cells: at the heart of cardiovascular precision medicine. *Nat. Rev. Cardiol.* 13, 333–349. doi: 10.1038/nrcardio.2016.36

Colatsky, T., Fermini, B., Gintant, G., Pierson, J. B., Sager, P., Sekino, Y., et al. (2016). The comprehensive *in vitro* proarrhythmia assay (CiPA) initiative — Update on progress. *J. Pharmacol. Toxicol. Methods* 81, 15–20. doi: 10.1016/j.vascn.2016.06.002

Cyganek, L., Tiburcy, M., Sekeres, K., Gerstenberg, K., Bohnenberger, H., Lenz, C., et al. (2018). Deep phenotyping of human induced pluripotent stem cell-derived atrial and ventricular cardiomyocytes. *JCI Insight* 3:e99941. doi: 10.1172/jci.insight.99941

Davis-Dusenbery, B. N., Williams, L. A., Klim, J. R., and Eggan, K. (2014). How to make spinal motor neurons. *Development* 141, 491–501. doi: 10.1242/dev.097410

de Leeuw, S. M., Davaz, S., Wanner, D., Milleret, V., Ehrbar, M., Gietl, A., et al. (2021). Increased maturation of iPSC-derived neurons in a hydrogel-based 3D culture. *J. Neurosci. Methods* 360:109254. doi: 10.1016/j.jneumeth.2021.109254

Deng, B. (2017). Mouse models and induced pluripotent stem cells in researching psychiatric disorders. *Stem Cell Invest.* 4, 4–6. doi: 10.21037/sci.2017.06.10

Depalma, S. J., Davidson, C. D., Stis, A. E., Helms, A. S., and Baker, B. M. (2021). Microenvironmental determinants of organized iPSC-cardiomyocyte tissues on synthetic fibrous matrices. *Biomater. Sci.* 9, 93–107. doi: 10.1039/d0bm01247e

Di Baldassarre, A., Cimetta, E., Bollini, S., Gaggi, G., and Ghinassi, B. (2018). Human-induced pluripotent stem cell technology and cardiomyocyte generation: Progress and clinical applications. *Cells* 7:48. doi: 10.3390/cells7060048

Doss, M. X., and Sachinidis, A. (2019). Current Challenges of iPSC-Based Disease Modeling and Therapeutic Implications. *Cells* 8:403. doi: 10.3390/cells8050403

Ebert, A. D., Liang, P., and Wu, J. C. (2012). Induced pluripotent stem cells as a disease modeling and drug screening platform. *J. Cardiovasc. Pharmacol.* 60, 408–416. doi: 10.1097/FJC.0b013e318247f642

Engle, S. J., Blaha, L., and Kleiman, R. J. (2018). Best practices for translational disease modeling using human iPSC-derived neurons. *Neuron* 100, 783–797. doi: 10.1016/j.neuron.2018.10.033

Faravelli, I., Nizzardo, M., Comi, G. P., and Corti, S. (2015). Spinal muscular atrophy-recent therapeutic advances for an old challenge. *Nat. Rev. Neurol.* 11, 351–359. doi: 10.1038/nrneurol.2015.77

Feaster, T. K., Cadar, A. G., Wang, L., Williams, C. H., Chun, Y. W., Hempel, J. E., et al. (2015). A method for the generation of single contracting human-induced pluripotent stem cell-derived cardiomyocytes. *Circ. Res.* 117, 995–1000. doi: 10.1161/CIRCRESAHA.115.307580

Fermini, B., and Bell, D. C. (2022). On the perspective of an aging population and its potential impact on drug attrition and pre-clinical cardiovascular safety assessment. *J. Pharmacol. Toxicol. Methods.* doi: 10.1016/j.vascn.2022.107184

Feyen, D. A. M., McKeithan, W. L., Bruyneel, A. A. N., Spiering, S., Hörmann, L., Ulmer, B., et al. (2020). Metabolic maturation media improve physiological function of Human iPSC-Derived Cardiomyocytes. *Cell Rep.* 32:107925. doi: 10.1016/j.celrep.2020.107925

Franz, D., Olsen, H. L., Klink, O., and Gimsa, J. (2017). Automated and manual patch clamp data of human induced pluripotent stem cell-derived dopaminergic neurons. *Nat. Sci. Data* 4:170056. doi: 10.1038/sdata.2017.56

Friedrichs, S., Malan, D., Voss, Y., and Sasse, P. (2015). Scalable Electrophysiological Investigation of iPS Cell-Derived Cardiomyocytes Obtained by a Lentiviral Purification Strategy. *J. Clin. Med.* 4, 102–123. doi: 10.3390/jcm4010102

Fusaki, N., Ban, H., Nishiyama, A., Saeki, K., and Hasegawa, M. (2009). Efficient induction of transgene-free human pluripotent stem cells using a vector based on Sendai virus, an RNA virus that does not integrate into the host genome. *Proc. Jpn. Acad. Ser. B Phys. Biol. Sci.* 85, 348–362. doi: 10.2183/pjab.85.348

Giacomelli, E., Vahsen, B. F., Calder, E. L., Xu, Y., Scaber, J., Gray, E., et al. (2022). Human stem cell models of neurodegeneration: from basic science of amyotrophic lateral sclerosis to clinical translation. *Cell Stem Cell* 29, 11–35. doi: 10.1016/j.stem.2021.12.008

Giannetti, F., Benzoni, P., Campostrini, G., Milanesi, R., Bucchi, A., Baruscotti, M., et al. (2021). A detailed characterization of the hyperpolarization-activated "funny" current (I f) in human-induced pluripotent stem cell (iPSC)–derived cardiomyocytes with pacemaker activity. *Pflugers Arch.* 473, 1009–1021. doi: 10.1007/s00424-021-02571-w

Goversen, B., van der Heyden, M. A. G., van Veen, T. A. B., and de Boer, T. P. (2018b). The immature electrophysiological phenotype of iPSC-CMs still hampers *in vitro* drug screening: special focus on I K1. *Pharmacol. Ther.* 183, 127–136. doi: 10.1016/j.pharmthera.2017.10.001

Goversen, B., Becker, N., Stoelzle-Feix, S., Obergrussberger, A., Vos, M. A., van Veen, T. A. B., et al. (2018a). A hybrid model for safety pharmacology on an automated patch clamp platform: Using dynamic clamp to join iPSC-derived cardiomyocytes and simulations of Ik1 ion channels in real-time. *Front. Physiol.* 8:1094. doi: 10.3389/fphys.2017.01094

Hamazaki, T., El Rouby, N., Fredette, N. C., Santostefano, K. E., and Terada, N. (2017). Concise review: induced pluripotent stem cell research in the era of precision medicine. *Stem Cells* 35, 545–550. doi: 10.1002/STEM.2570

Hamill, O. P., Marty, A., Neher, E., Sakmann, B., and Sigworth, F. J. (1981). Improved patch-clamp techniques for high-resolution current recording from cells and cell-free membrane patches. *Pflügers Arch.* 391, 85–100. doi: 10.1007/BF00656997

Hartfield, E. M., Yamasaki-Mann, M., Ribeiro Fernandes, H. J., Vowles, J., James, W. S., Cowley, S. A., et al. (2014). Physiological characterisation of human iPS-derived dopaminergic neurons. *PLoS One* 9:e87388. doi: 10.1371/journal.pone.0087388

Haythornthwaite, A., Stoelzle, S., Hasler, A., Kiss, A., Mosbacher, J., George, M., et al. (2012). Characterizing human ion channels in induced pluripotent stem cell – derived neurons. *J. Biomol. Screen.* 17, 1264–1272. doi: 10.1177/1087057112457821

Horváth, A., Lemoine, M. D., Löser, A., Mannhardt, I., Flenner, F., Uzun, A. U., et al. (2018). Low resting membrane potential and low inward rectifier potassium currents are not inherent features of hiPSC-Derived Cardiomyocytes. *Stem Cell Rep.* 10, 822–833. doi: 10.1016/j.stemcr.2018.01.012

Jehuda, B. R., Shemer, Y., and Binah, O. (2018). Genome editing in induced pluripotent stem cells using CRISPR/Cas9. *Stem Cell Rev. Rep.* 14, 323–336. doi: 10.1007/s12015-018-9811-3

Jha, A. (2011). *Look, No Embryos! The Future of Ethical Stem Cells*. Guardian. Available online at: https://www.theguardian.com/science/2011/mar/13/ips-reprogrammed-stem-cells (accessed May 23, 2022).

Jones, D. K., Liu, F., Vaidyanathan, R., Eckhardt, L. L., Trudeau, M. C., and Robertson, G. A. (2014). hERG 1b is critical for human cardiac repolarization. *Proc. Natl. Acad. Sci. U.S.A.* 111, 18073–18077. doi: 10.1073/pnas.1414945111

Jonsson, M. K. B., Vos, M. A., Mirams, G. R., Duker, G., Sartipy, P., De Boer, T. P., et al. (2012). Application of human stem cell-derived cardiomyocytes in safety pharmacology requires caution beyond hERG. *J. Mol. Cell. Cardiol.* 52, 998–1008. doi: 10.1016/j.yjmcc.2012.02.002

Jouni, M., Si-Tayeb, K., Es-Salah-Lamoureux, Z., Latypova, X., Champon, B., Caillaud, A., et al. (2015). Toward personalized medicine: using cardiomyocytes differentiated from urine-derived pluripotent stem cells to recapitulate

electrophysiological characteristics of type 2 long QT syndrome. *J. Am. Heart Assoc.* 4, 1–13. doi: 10.1161/JAHA.115.002159

Jung, P., Seibertz, F., Ignatyeva, N., Sampathkumar, S., Ritter, M., Li, H., et al. (2022). Increased cytosolic calcium buffering contributes to a cellular arrhythmogenic substrate in iPSC-cardiomyocytes from patients with dilated cardiomyopathy. *Basic Res. Cardiol.* 117:5.

Karbassi, E., Fenix, A., Marchiano, S., Muraoka, N., Nakamura, K., Yang, X., et al. (2020). Cardiomyocyte maturation: advances in knowledge and implications for regenerative medicine. *Nat. Rev. Cardiol.* 17, 341–359. doi: 10.1038/s41569-019-0331-x

Kilfoil, P., Feng, S. L., Bassyouni, A., Lee, T., Leishman, D., Li, D., et al. (2021). Characterization of a high throughput human stem cell cardiomyocyte assay to predict drug-induced changes in clinical electrocardiogram parameters. *Eur. J. Pharmacol.* 912:174584. doi: 10.1016/j.ejphar.2021.174584

Kilpinen, H., Goncalves, A., Leha, A., Afzal, V., Alasoo, K., Ashford, S., et al. (2017). Common genetic variation drives molecular heterogeneity in human iPSCs. *Nature* 546, 370–375. doi: 10.1038/nature22403

Kim, C. (2015). iPSC technology-Powerful hand for disease modeling and therapeutic screen. *BMB Rep.* 48, 256–265. doi: 10.5483/BMBRep.2015.48.5.100

Kolanowski, T. J., Antos, C. L., and Guan, K. (2017). Making human cardiomyocytes up to date: derivation, maturation state and perspectives. *Int. J. Cardiol.* 241, 379–386. doi: 10.1016/j.ijcard.2017.03.099

Laustriat, D., Gide, J., and Peschanski, M. (2010). Human pluripotent stem cells in drug discovery and predictive toxicology. *Biochem. Soc. Trans.* 38, 1051–1057. doi: 10.1042/BST0381051

Lee, S., and Huang, E. J. (2017). Modeling ALS and FTD with iPSC-derived neurons. *Brain Res.* 1656, 88–97. doi: 10.1016/j.brainres.2015.10.003

Lemoine, M. D., Mannhardt, I., Breckwoldt, K., Prondzynski, M., Flenner, F., Ulmer, B., et al. (2017). Human iPSC-derived cardiomyocytes cultured in 3D engineered heart tissue show physiological upstroke velocity and sodium current density. *Sci. Rep.* 7:5464. doi: 10.1038/s41598-017-05600-w

Li, W., Luo, X., Ulbricht, Y., and Guan, K. (2021b). Blebbistatin protects iPSC-CMs from hypercontraction and facilitates automated patch-clamp based electrophysiological study. *Stem Cell Res.* 56:102565. doi: 10.1016/j.scr.2021.102565

Li, W., Luo, X., Ulbricht, Y., and Guan, K. (2021a). Applying automated patch-clamp to disease modeling: recapitulate phenotypes of Brugada syndrome using iPSC-CMs. *bioRvix* [Preprint]. doi: 10.1101/2021.06.07.447362

Li, W., Luo, X., Ulbricht, Y., Wagner, M., Piorkowski, C., El-Armouche, A., et al. (2019). Establishment of an automated patch-clamp platform for electrophysiological and pharmacological evaluation of hiPSC-CMs. *Stem Cell Res.* 41:101662. doi: 10.1016/j.scr.2019.101662

Lo, B., and Parham, L. (2009). Ethical issues in stem cell research. *Endocr. Rev.* 30, 204–213. doi: 10.1210/ER.2008-0031

Mann, S. A., Heide, J., Knott, T., Airini, R., Epureanu, F. B., Deftu, A. F., et al. (2019). Recording of multiple ion current components and action potentials in human induced pluripotent stem cell-derived cardiomyocytes via automated patch-clamp. *J. Pharmacol. Toxicol. Methods* 100:106599. doi: 10.1016/j.vascn.2019.106599

Matsa, E., Ahrens, J. H., and Wu, J. C. (2016). Human induced pluripotent stem cells as a platform for personalized and precision cardiovascular medicine. *Physiol. Rev.* 96, 1093–1126. doi: 10.1152/physrev.00036.2015

Medda, X., Mertens, L., Versweyveld, S., Diels, A., Barnham, L., Bretteville, A., et al. (2016). Development of a scalable, high-throughput-compatible assay to detect tau aggregates using iPSC-derived cortical neurons maintained in a three-dimensional culture format. *J. Biomol. Screen.* 21, 804–815. doi: 10.1177/1087057116638029

Moradi, S., Mahdizadeh, H., Šarić, T., Kim, J., Harati, J., Shahsavarani, H., et al. (2019). Research and therapy with induced pluripotent stem cells (iPSCs): social, legal, and ethical considerations. *Stem Cell Res. Ther.* 10:341. doi: 10.1186/s13287-019-1455-y

Mummery, C. L. (2018). Perspectives on the use of human induced pluripotent stem cell-derived cardiomyocytes in biomedical research. *Stem Cell Rep.* 11, 1306–1311. doi: 10.1016/j.stemcr.2018.11.011

Muñoz-Martín, N., and Matsa, E. (2021). Benefits & key considerations of using human iPSC-derived disease models in drug discovery. *Int. Biopharm. Ind.* 4, 26–29.

Obergrussberger, A., Haarmann, C., Stölzle-feix, S., Becker, N., Ohtsuki, A., Brüggemann, A., et al. (2017). "Automated patch clamp recordings of human stem cell- derived cardiomyocytes," in *Stem Cell-Derived Models in Toxicology*, eds M. Clements and L. Roquemore (New York, NY: Humana Press), 57–82. doi: 10.1007/978-1-4939-6661-5

Odawara, A., Katoh, H., Matsuda, N., and Suzuki, I. (2016). Physiological maturation and drug responses of human induced pluripotent stem cell-derived cortical neuronal networks in long-term culture. *Sci. Rep.* 6:26181. doi: 10.1038/srep26181

Pessôa, L. V., de, F., Pieri, N. C. G., Recchia, K., and Bressan, F. F. (2020). "Induced pluripotent stem cells from animal models: applications on translational research," in *Novel Perspectives of Stem Cell Manufacturing and Therapies*, eds D. Kitala and A. C. Maurício (Rijeka: IntechOpen). doi: 10.5772/INTECHOPEN.94199

Popp, B., Krumbiegel, M., Grosch, J., Sommer, A., Uebe, S., Kohl, Z., et al. (2018). Need for high-resolution Genetic Analysis in iPSC: results and lessons from the forips consortium. *Sci. Rep.* 8:17201. doi: 10.1038/s41598-018-35506-0

Potet, F., Egecioglu, D. E., Burridge, P. W., and George, A. L. (2020). GS-967 and eleclazine block sodium channels in human induced pluripotent stem cell-derived cardiomyocytes. *Mol. Pharmacol.* 98, 540–547. doi: 10.1124/MOLPHARM.120.000048

Prè, D., Nestor, M. W., Sproul, A. A., Jacob, S., Koppensteiner, P., Chinchalongporn, V., et al. (2014). A time course analysis of the electrophysiological properties of neurons differentiated from human induced Pluripotent Stem Cells (iPSCs). *PLoS One* 9:e103418. doi: 10.1371/journal.pone.0103418

Rajamohan, D., Kalra, S., Hoang, M. D., George, V., Staniforth, A., Russell, H., et al. (2016). Automated electrophysiological and pharmacological evaluation of human pluripotent stem cell-derived cardiomyocytes. *Stem Cells Dev.* 25, 439–452. doi: 10.1089/scd.2015.0253

Raman, I. M., and Bean, B. P. (1997). Resurgent sodium current and action potential formation in dissociated cerebellar Purkinje neurons. *J. Neurosci.* 17, 4517–4526. doi: 10.1523/jneurosci.17-12-04517.1997

Rosholm, K. R. (2019). *Electrophysiological Characterization of Human iPSC-Derived Motor Neurons Using Qube 384 and QPatch. Sophion Application Report*. Available online at: https://sophion.com/wp-content/uploads/2019/09/Electrophys-characterization-of-hiSPC-derived-motor-neurons-Qube-QPatch_AR_Public28033-5.pdf (accessed May 23, 2022).

Rosholm, K. R. (2021). *hiPSC-Derived Cardiomyocyte Recordings Using Physiological Solutions on QPatch II. Sophion Application Report*. Available online at: https://sophion.com/wp-content/uploads/2021/12/hiPSC-derived-cardiomyocyte-recordings-using-physiological-solutions-on-QPatch-II_AR_PUBLIC32856-3.pdf (accessed May 23, 2022).

Rosholm, K. R., Boddum, K., and Lindquist, A. (2021a). Perforated whole-cell recordings in automated patch clamp electrophysiology. *Methods Mol. Biol.* 2188, 93–108. doi: 10.1007/978-1-0716-0818-0_5

Rosholm, K. R., Chen, I. P., Sauter, D. R., Lindquist, A., Forman, T. E., Dwyer, S. A., et al. (2021b). *Electrophysiological Characterization of iPSC-derived Cortical Neurons Using Automated Patch Clamp*. Available online at: https://sophion.com/wp-content/uploads/2021/02/Electrophysiological-characterization-of-iPSC-derived-cortical-neurons-using-APC.pdf (accessed May 23, 2022).

Rosholm, K. R., Nagy, D., Liutkute, A., Seibertz, F., Voigt, N., and Lindquist, A. (2022). *Electrophysiological Characterization of hiPSC-Derived Cardiomyocytes, Including Voltage-Gated Ion Channels and Action Potential Measurements, Using Automated Patch Clamp*. Available online at: https://sophion.com/wp-content/uploads/2022/02/Electrophysiological-characterization-of-hiPSC-derived-CMs_BPS2022.pdf (accessed May 23, 2022).

Rowe, R. G., and Daley, G. Q. (2019). Induced pluripotent stem cells in disease modelling and drug discovery. *Nat. Rev. Genet.* 20, 377–388. doi: 10.1038/s41576-019-0100-z

Seibertz, F., Reynolds, M., and Voigt, N. (2020). Single-cell optical action potential measurement in human induced pluripotent stem cell-derived cardiomyocytes. *J. Vis. Exp.* 166:e61890. doi: 10.3791/61890

Sharma, A., Li, G., Rajarajan, K., Hamaguchi, R., Burridge, P. W., and Wu, S. M. (2015). Derivation of highly purified cardiomyocytes from human induced pluripotent stem cells using small molecule-modulated differentiation

and subsequent glucose starvation. *J. Vis. Exp.* 97:52628. doi: 10.3791/52628

Shi, Y., Inoue, H., Wu, J. C., and Yamanaka, S. (2017). Induced pluripotent stem cell technology: a decade of progress. *Nat. Rev. Drug Discov.* 16, 115–130. doi: 10.1038/nrd.2016.245

Strässler, E. T., Aalto-Setälä, K., Kiamehr, M., Landmesser, U., and Kränkel, N. (2018). Age is relative—Impact of donor age on induced pluripotent stem cell-derived cell functionality. *Front. Cardiovasc. Med.* 5:4. doi: 10.3389/fcvm.2018.00004

Sube, R., and Ertel, E. A. (2017). Cardiomyocytes derived from human induced pluripotent stem cells: an *in-vitro* model to predict cardiac effects of drugs. *J. Biomed. Sci. Eng.* 10, 527–549. doi: 10.4236/jbise.2017.1011040

Takahashi, K., and Yamanaka, S. (2006). Induction of pluripotent stem cells from mouse embryonic and adult fibroblast cultures by defined factors. *Cell* 126, 663–676. doi: 10.1016/j.cell.2006.07.024

Press release (2012). *The 2012 Nobel Prize in Physiology or Medicine – Press release – NobelPrize.Org*. Available online at: https://www.nobelprize.org/prizes/medicine/2012/press-release/ (accessed January 14, 2022).

Tiburcy, M., Hudson, J. E., Balfanz, P., Schlick, S., Meyer, T., Liao, M. L. C., et al. (2017). Defined engineered human myocardium with advanced maturation for applications in heart failure modeling and repair. *Circulation* 135, 1832–1847. doi: 10.1161/CIRCULATIONAHA.116.024145

Toh, M. F., Brooks, J. M., Strassmaier, T., Haedo, R. J., Puryear, C. B., Roth, B. L., et al. (2020). Application of High-Throughput Automated Patch-Clamp Electrophysiology to Study Voltage-Gated Ion Channel Function in Primary Cortical Cultures. *SLAS Discov.* 25, 447–457. doi: 10.1177/2472555220902388

Vaidyanathan, R., Markandeya, Y. S., Kamp, T. J., Makielski, J. C., January, C. T., and Eckhardt, L. L. (2021). I K1 -enhanced human-induced pluripotent stem cell-derived cardiomyocytes: an improved cardiomyocyte model to investigate inherited arrhythmia syndromes. *Am. J. Physiol. Heart Circ. Physiol.* 310, 1611–1621. doi: 10.1152/ajpheart.00481.2015

Verkerk, A. O., Veerman, C. C., Zegers, J. G., Mengarelli, I., Bezzina, C. R., and Wilders, R. (2017). Patch-clamp recording from human induced pluripotent stemcell-derived cardiomyocytes: improving action potential characteristics through dynamic clamp. *Int. J. Mol. Sci.* 18:1873. doi: 10.3390/ijms18091873

Wu, J. C., Garg, P., Yoshida, Y., Yamanaka, S., Gepstein, L., Hulot, J. S., et al. (2020). Towards precision medicine with human iPSCs for cardiac Channelopathies. *Circ. Res.* 125, 653–658. doi: 10.1161/CIRCRESAHA.119.315209

Yang, X., Rodriguez, M. L., Leonard, A., Sun, L., Fischer, K. A., Wang, Y., et al. (2019). Fatty acids enhance the maturation of cardiomyocytes derived from human pluripotent stem cells. *Stem Cell Reports* 13, 657–668. doi: 10.1016/j.stemcr.2019.08.013

Yoshida, Y., and Yamanaka, S. (2017). Induced pluripotent stem cells 10 years later. *Circ. Res.* 120, 1958–1968. doi: 10.1161/CIRCRESAHA.117.311080

Young, G. T., Gutteridge, A., Fox, H. D. E., Wilbrey, A. L., Cao, L., Cho, L. T., et al. (2014). Characterizing human stem cell-derived sensory neurons at the single-cell level reveals their ion channel expression and utility in pain research. *Mol. Ther.* 22, 1530–1543. doi: 10.1038/mt.2014.86

Yu, J., Vodyanik, M. A., Smuga-Otto, K., Antosiewicz-Bourget, J., Frane, J. L., Tian, S., et al. (2007). Induced pluripotent stem cell lines derived from human somatic cells. *Science* 318, 1917–1920. doi: 10.1126/science.1151526

Zafeiriou, M. P., Bao, G., Hudson, J., Halder, R., Blenkle, A., Schreiber, M. K., et al. (2020). Developmental GABA polarity switch and neuronal plasticity in Bioengineered Neuronal Organoids. *Nat. Commun.* 11:3791. doi: 10.1038/s41467-020-17521-w

Conflict of Interest: KR, BB, SK, and DB are employed by Sophion Bioscience A/S, Denmark. DN was employed by Sophion Bioscience Inc., United States.

The remaining authors declare that the research was conducted in the absence of any commercial or financial relationships that could be construed as a potential conflict of interest.

Publisher's Note: All claims expressed in this article are solely those of the authors and do not necessarily represent those of their affiliated organizations, or those of the publisher, the editors and the reviewers. Any product that may be evaluated in this article, or claim that may be made by its manufacturer, is not guaranteed or endorsed by the publisher.

frontiers | Frontiers in Molecular Neuroscience

ORIGINAL RESEARCH
published: 04 July 2022
doi: 10.3389/fnmol.2022.896320

Highly Parallelized, Multicolor Optogenetic Recordings of Cellular Activity for Therapeutic Discovery Applications in Ion Channels and Disease-Associated Excitable Cells

Gabriel B. Borja†, Hongkang Zhang†, Benjamin N. Harwood†, Jane Jacques, Jennifer Grooms, Romina O. Chantre, Dawei Zhang, Adam Barnett, Christopher A. Werley, Yang Lu, Steven F. Nagle, Owen B. McManus and Graham T. Dempsey**

Q-State Biosciences, Cambridge, MA, United States

Optogenetic assays provide a flexible, scalable, and information rich approach to probe compound effects for ion channel drug targets in both heterologous expression systems and associated disease relevant cell types. Despite the potential utility and growing adoption of optogenetics, there remains a critical need for compatible platform technologies with the speed, sensitivity, and throughput to enable their application to broader drug screening applications. To address this challenge, we developed the Swarm™, a custom designed optical instrument for highly parallelized, multicolor measurements in excitable cells, simultaneously recording changes in voltage and calcium activities at high temporal resolution under optical stimulation. The compact design featuring high power LEDs, large numerical aperture optics, and fast photodiode detection enables all-optical individual well readout of 24-wells simultaneously from multi-well plates while maintaining sufficient temporal resolution to probe millisecond response dynamics. The Swarm delivers variable intensity blue-light optogenetic stimulation to enable membrane depolarization and red or lime-light excitation to enable fluorescence detection of the resulting changes in membrane potential or calcium levels, respectively. The Swarm can screen ∼10,000 wells/day in 384-well format, probing complex pharmacological interactions *via* a wide array of stimulation protocols. To evaluate the Swarm screening system, we optimized a series of heterologous optogenetic spiking HEK293 cell assays for several voltage-gated sodium channel subtypes including Nav1.2, Nav1.5, and Nav1.7. The Swarm was able to record pseudo-action potentials stably across all 24 objectives and provided pharmacological characterization of diverse sodium channel blockers. We performed a Nav1.7 screen of 200,000 small molecules in a 384-well plate format with all 560 plates reaching a $Z' > 0.5$. As a demonstration of the versatility of the Swarm, we also developed an assay measuring cardiac action potential and calcium waveform properties simultaneously under paced conditions using human induced pluripotent stem (iPS) cell-derived cardiomyocytes as an additional counter screen for cardiac toxicity. In summary, the Swarm is a novel high-throughput all-optical system capable of collecting information-dense data from optogenetic assays in both

OPEN ACCESS

Edited by:
Marc Rogers,
Metrion Biosciences Limited,
United Kingdom

Reviewed by:
Angelika Lampert,
University Hospital RWTH Aachen, Germany
Christine E. Gee,
University of Hamburg, Germany
Shiqiang Gao,
University of Wuerzburg, Germany
Alexander Gottschalk,
Goethe University, Germany

***Correspondence:**
Graham T. Dempsey
graham.dempsey@qstatebio.com
Hongkang Zhang
hongkang.zhang@qstatebio.com

†These authors have contributed equally to this work and share first authorship

Specialty section:
This article was submitted to Molecular Signalling and Pathways, a section of the journal Frontiers in Molecular Neuroscience

Received: *14 March 2022*
Accepted: *06 June 2022*
Published: *04 July 2022*

Citation:
Borja GB, Zhang H, Harwood BN, Jacques J, Grooms J, Chantre RO, Zhang D, Barnett A, Werley CA, Lu Y, Nagle SF, McManus OB and Dempsey GT (2022) Highly Parallelized, Multicolor Optogenetic Recordings of Cellular Activity for Therapeutic Discovery Applications in Ion Channels and Disease-Associated Excitable Cells. Front. Mol. Neurosci. 15:896320. doi: 10.3389/fnmol.2022.896320

heterologous and iPS cell-derived models, which can be leveraged to drive diverse therapeutic discovery programs for nervous system disorders and other disease areas involving excitable cells.

Keywords: optogenetics, optopatch, high-throughput screening, ion channels, voltage-gated sodium channels, pain, human iPSC models, drug discovery

INTRODUCTION

The development of effective therapeutics for disorders of the nervous system has been challenging in comparison with other areas such as cancer and cardiovascular disease (Schoepp, 2011). Therapeutics for neurological disorders historically have had longer development periods and lower FDA approval rates compared to most other indication areas (Kaitlin, 2014; Dowden and Munro, 2019). For example, chronic pain is a neurological condition affecting more than one hundred million people in the United States and remains a major unmet medical need (Institute of Medicine of the National Academies, 2011). Individuals suffering from chronic pain often face significant loss of productivity and a decrease in overall quality of life (Connor, 2009). Opioid treatments, which are the most frequently prescribed treatment for chronic pain, have considerable undesirable side effects (Benyamin et al., 2008). The addictive properties of opioids create a substantial risk for the development of abuse disorders that can further negatively impact quality of life for patients. Existing non-opioid alternative drugs for chronic pain are less efficacious for a large subset of patients (Grosser et al., 2017). Despite the massive unmet medical and societal need, the pharmaceutical industry has yielded few new therapeutics for chronic pain patients and has similarly struggled for other nervous system disorders. As such, there remains a critical need for new technologies and approaches to support development of novel therapeutics for chronic pain and other neurological diseases with improved efficacy and safety profiles (Gribkoff and Kaczmarek, 2017).

Ion channels represent a promising class of drug targets for a variety of nervous system-based disorders (Waszkielewicz et al., 2013), as they are essential components in signal generation and propagation in neurons and other electrically excitable cell types. The characterization of pathogenic mutations in human ion channels has directly linked ion channel function to human disease pathologies, including "channelopathies" associated with severe genetic epilepsies, chronic pain conditions, and many others (Snowball and Schorge, 2015; Imbrici et al., 2016; Albury et al., 2017; Reid et al., 2017). Channel biophysical properties across the hundreds of ion channel targets have been deeply investigated, though the mechanisms that connect genetic and pharmacological modulation of ion channel properties to systems level outcomes in patients remains an area of active research. Bridging this knowledge gap is critical in the identification of effective therapeutics that target different ion channels. Despite the continued advancements in understanding ion channel properties, it remains a challenge to translate these findings to effective therapeutics.

One class of ion channels with strong genetic evidence for involvement in disease pathologies and broad recognition as important drug targets in the pharmaceutical industry are the voltage-gated sodium (Nav) channels (Wang et al., 2017). Nav channels are transmembrane proteins that are expressed and localized to the membranes of electrically excitable cells, such as neurons, and are responsible for the selective transport of Na^+ ions. There are nine members of the Nav channel class (Nav1.1–1.9), each with critical roles in diverse tissue types (de Lera Ruiz and Kraus, 2015). For example, Nav1.1, 1.2, 1.3, and 1.6 are expressed in the central nervous system, and dysfunction in these channels can lead to epilepsy, migraine, autism, and ataxias (Ogiwara et al., 2009). Nav1.7, 1.8, and 1.9 are expressed predominantly in dorsal root ganglion (DRG) sensory neurons, and dysfunction leads to pain disorders such as small fiber neuropathy (Eijkenboom et al., 2019) and congenital insensitivity to pain (Cox et al., 2006). Nav1.5 is expressed in heart muscle, and pathogenic mutations affecting this channel lead to Brugada syndrome, long QT syndrome, and atrial fibrillation (Keating and Sanguinetti, 2001; Splawski et al., 2002; Veerman et al., 2015). Our understanding of Nav channel biology has advanced dramatically over the last decade, however drug development for these targets remains a major challenge. Achieving the ideal molecular profile that balances selectivity, state dependence, and the preferred pharmacological activity in intact disease relevant cell types like neurons or cardiomyocytes is a key factor that has ultimately prevented the full realization of effective therapeutics for this class of targets.

A major challenge within Nav channels and, more generally, in ion channel drug discovery efforts is the limitations of the existing technologies, assays, and disease models, which lack either the throughput or the information content required to derive necessary insights into complex human biology and pharmacological responses that enable translation to efficacious therapies. Consequently, there remains a need to develop model systems that are both information-rich and high-throughput to enable rapid identification and optimization of novel drug templates. While methods such as manual patch clamp electrophysiology (E-phys) provide rich information content, high resolution, and flexibility to fine-tune assay conditions, this approach is severely limited by throughput in the context of drug discovery screening applications. Automated E-Phys development has made significant strides in achieving higher throughput than manual patch clamp, but still has lower throughput and is less affordable than optical assays, which are key considerations when conducting primary screening of large chemical libraries. First generation optical based technologies such as FLIPR and E-VIPR (Schroeder,

1996; Huang et al., 2006) are cost effective and well-adapted for high throughput screens (HTS), however they do not maintain high temporal resolution of single millisecond scale required to faithfully record electrical spiking, thus limiting information provided on complex drug mechanisms. In addition, most plate-based fluorescence assays rely on non-physiological stimuli that can alter pharmacological sensitivity and impact translation to therapeutic efficacy in humans. Given the limitations of current technologies, there is a clear need for new neuroscience drug discovery platforms applicable to ion channel targets that are capable of screening hundreds of thousands to millions of compounds while maintaining physiologically relevant assay conditions and providing information-rich data comparable to manual or automated patch clamp methods.

A promising solution to addressing current challenges in ion channel drug discovery lies in recent advances in optogenetic methodologies (Song and Knöpfel, 2016; Dempsey and Werley, 2017; Zhang and Cohen, 2017), which can enable high resolution all-optical electrophysiology achieving both dramatic improvements in throughput and deep information content measurements of excitable cells. One approach, called Optopatch^{TM} (Hochbaum et al., 2014), relies on genetically engineered optogenetic actuators such as the channelrhodopsin variant CheRiff that can be expressed in a variety of cell types to initiate cell depolarization and subsequent action potential (AP) initiation using a blue light stimulus (488 nm). Changes in membrane potential can be quantified with exquisite sensitivity using either a voltage sensitive fluorescent protein such as QuasAr (637 nm) (Hochbaum et al., 2014) or a voltage sensitive dye such as BeRST1 (635 nm) (Huang et al., 2015) by recording the changes in red fluorescence over time. When a blue-light driven actuator and red-light fluorescence voltage reporter are co-expressed, all-optical electrophysiology can be conducted with high spatial and temporal resolution. The achievable spatial and temporal resolution of optogenetic electrophysiology now enable the development of high throughput imaging systems to support drug discovery (Werley et al., 2017).

To translate the advances in optogenetic actuator and sensor technology to a robust, all-optical therapeutic discovery platform that can be leveraged for diverse drug targets such as ion channels we have developed the Swarm^{TM}, a novel high-throughput screening instrument for optogenetic assays. Here, we describe the physical and optical characteristics of the Swarm instrument. The Swarm can deliver blue-light stimuli across entire individual wells in a multi-well plate, eliciting changes in membrane potential and then recording cell depolarizations and firing *via* red-light excitation and fluorescence detection. To enable the high-throughput capacity of Swarm, the instrument stimulates and records from 24 wells simultaneously, which allows information from an entire 96-well or 384-well plate to be collected in 4 or 16 recordings, respectively. The system allows for optogenetic pacing and analysis of electrically excitable cell types in a multi-wavelength format with four input excitation channels (three independent wavelengths and one for patterned illumination) and three independent fluorescence channels for multicolor recording. We have also developed custom software to control the instrument and a suite of tools for automated data analysis.

To demonstrate the utility of the Swarm for ion channel drug discovery, we applied a set of custom optogenetic assays using HEK293 cell lines that heterologously express an optogenetic actuator and a series of voltage gated-sodium channel (Nav1.x) subtypes including Nav1.2, Nav1.5, and Nav1.7 (herein referred to as 'Nav1.x spiking HEK assays') and are compatible with a fluorescent voltage sensing dye BeRST1 (Zhang et al., 2016, 2020). In humans, Nav1.7 is a critical modulator of pain sensitivity and is expressed primarily in sensory neurons, playing a central role in neuronal action potential initiation (Gingras et al., 2014; Hameed, 2019). Nav1.7 is a genetically validated target for novel pain therapeutics with known loss- and gain-of-function mutations identified in humans that lead to dramatic hypo- or hyper-sensitivity to pain, respectively (Goldberg et al., 2007; Emery et al., 2016; Shields et al., 2018). Given the genetic validation of Nav1.7 as a drug target, significant effort has been devoted to identifying small molecule inhibitors that block Nav1.7. However, to date, none have demonstrated sufficient clinical efficacy to gain approval for pain related indications. Several challenges have hindered the development of small molecule inhibitors including a requirement for subtype selectivity to avoid adverse effects in the cardiovascular and nervous system resulting from block of other sodium channel subtypes such as Nav1.5 and Nav1.2, respectively (Mulcahy et al., 2019). Non-selective voltage-gated sodium blockers, such as lidocaine have clinical utility and are frequently used as local anesthetics, however systemic administration can cause side effects such as dizziness, shortness of breath, and nausea (Cherobin and Tavares, 2020). Compounds with high Nav1.7 subtype selectivity, such as PF-05089771, have shown limited efficacy in clinical pain studies, possibly due to a strong state-dependent blocking mechanism, lack of blood brain barrier penetrance, and poor performance in sensory neurons (McDonnell et al., 2018). These issues highlight a need to identify new classes of Nav1.7 inhibitors that meet the required characteristics to enable their use for treating chronic pain.

Using Nav1.x spiking HEK assays (Zhang et al., 2016, 2020) in a 384-well plate format, we show validation of the Swarm for high-throughput optogenetic screening. First, we demonstrate assay performance through uniform signal detection across all 24 detection channels and across whole 384-well control plates formatted with alternating columns of positive and negative control compounds. Next, we use an extensive panel of control pharmacology across Nav1.2, Nav1.5, and Nav1.7 spiking HEK assays to show that measured IC_{50} values and state dependence metrics are consistent with literature reports. We then use the Swarm to perform a HTS screen of 200,000 small molecules to identify novel inhibitors of Nav1.7. The demonstrated Z' (>0.5) and on-plate quality control metrics (IC_{50} of tetracaine) demonstrate high performance of the instrument and assay. We further report on potency, state dependence, and selectivity of confirmed hits from the screen along with tool compounds which are either clinically used or that have failed in clinical trials as comparators. Lastly, we show that the Swarm can also be used to record action potentials and calcium transients

simultaneously under paced conditions in human iPS cell-derived cardiomyocytes along with control pharmacological validation, enabling utilization of the Swarm instrument for counter screening for Nav channel programs or more broadly for screening applications in human cellular models.

MATERIALS AND METHODS

Swarm Instrument Design

The Swarm read head objective modules are made of custom-designed, CNC-machined, anodized aluminum (Protolabs, Maple Plain, MN). The 12-objective read heads are built as six independent 2-objective modules that hold the lenses, dichroics, and filters. The compact design of the read head module is dictated by the pitch between wells of a 96-well plate (9 mm) and complies with the optical design to maximize the light throughput, minimize stray light, and maximize positioning accuracy. A spring-loaded plate pusher is designed to hold 96-, 384-, or 1,536-well microplates. The plate pusher arm is articulated above the read-heads mounted flush to the top deck to provide smooth translation through a low-profile X-Y linear stage (Thorlabs, Newton, NJ), so that all wells can be measured, 24 wells at a time.

The Swarm read head comprises two banks of 12 objective modules, 24 in total, mounted to the top deck beneath the well plate. Each objective module houses more than 40 compact optics (lenses, filters, masks), LEDs, and photodiodes. Within the illumination path, there are 4 independent channels with high power LEDs (Luxeon, Alberta, Canada)—a red channel (627 nm), a lime channel (567 nm), an unpatterned blue channel (470 nm), and a patterned blue channel (470 nm with a chrome mask at the conjugate image plane). Light is delivered to the sample using a series of high numerical aperture aspheric relay lenses (LightPath, Orlando, FL) in 4-f configuration. The lens relay configuration was simulated and optimized with optical design software (Zemax, Kirkland, WA) to ensure maximum light delivery efficiency and to inform read head mechanical manufacturing tolerance. The designed focus spot size is 1 mm^2 at the sample after the final objective lens. A red (640/14 nm central wavelength/bandwidth nm), lime (563/9 nm), or blue (470/22 nm) bandpass filter (Semrock, Rochester, NY) is placed in front of each LED to narrow to the targeted excitation wavelengths. In the detection path, three output color channels are separated by dichroic mirrors (Semrock, Rochester, NY) detected simultaneously by three independent photodiodes (Hamamatsu, Hamamatsu, Japan): one photodiode is behind a red filter (736 nm long pass) for a voltage indicator, one behind an orange filter (600/14 nm) for a calcium indicator, and one behind a GFP filter (520/35 nm) for protein expression detection or other measurements.

We designed and fabricated custom-made printed circuit boards to hold the essential electronics components, collect/transmit signals, and deliver power to the Swarm. An LED board and 2 photodiode boards are attached to each two-objective module. Each LED board contains 8 high-power LEDs (2 x 4 LEDs per objective). The two photodiode boards contain 6 photodiodes (2 x 3 photodiodes per objective) and 6 independent picoammeter circuits that amplify the photodiode signal. Each two-objective module is also connected to a signal/driver board. The signal/driver board has two functions. First, it contains the LED driver circuitry that can deliver up to 1 A of low-noise constant current to the high-power LEDs in the LED board. Second, it collects the amplified signals from the photodiode boards and delivers them to a Compact Data Acquisition (DAQ) system (National Instruments, Austin, TX), which provides synchronized analog input for the 72 total photodiode channels and synchronized analog output control for the 96 LEDs. Each signal/driver board is connected to a power distribution bus board that delivers stable DC voltage from high-performance rugged power supplies (Acopian, Easton, PA).

Nav1.x Spiking HEK Cell Culture

Spiking HEK cells were used for Swarm instrument validation, the 200K small molecule screen, and tool compound pharmacological characterization. The spiking HEK cell lines consisted of HEK293 cells stably expressing human Nav.1.7, human Nav1.5, or human Nav1.2 co-expressed with the blue-shifted channelrhodopsin actuator CheRiff-EGFP. Spiking HEK cell lines and culture conditions are as previously described with slight modifications (Zhang et al., 2016, 2020). In brief, vials of Nav1.x spiking HEK cells were thawed and plated at 3 million cells/10 cm dish. Cell culture growth media contained DMEM, 10% FBS, 1% GluMax (Gibco, Waltham, MA) and MEM Non-Essential Amino Acids (ThermoFisher, Waltham, MA). To expand total cell numbers required for HTS, cells were grown at 37°C with 5% CO_2 for 48 h to approximately 70% confluence. After 48 h, 4 mL of cell culture medium was removed and 300 μL of Kir2.1 lentivirus was added to the 10 cm dish. Cells were incubated for 24 h to facilitate Kir2.1 lentivirus transduction. The following day, 384-well plates (789836, Greiner Bio-One) were treated with Poly-D-lysine (20 μg/mL) for 1 h at 37°C and aspirated. Kir2.1 transduced HEK293 cells were then trypsin treated (0.5%), resuspended, centrifuged, washed, and resuspended in fresh DMEM with serum. Cells were then replated in Poly-D-lysine treated 384-well plates at a density of 30,000 cells per well. Cells were then incubated at 37°C overnight to achieve 100% confluence prior to running spiking HEK assays.

Nav1.x Spiking HEK Assays

Imaging was performed on Nav1.x spiking HEK cells 24 h after plating on 384-well plates. Prior to compound addition, medium was removed from cells using a flick and tap method, and then 1 μM BeRST dye was added using a Janus Mini liquid handling robot (PerkinElmer, Waltham, MA). The cells were then incubated for 30 min at 30°C with no exposure to light. Following incubation, the cells were washed using Tyrode's solution (containing, 125 mM NaCl, 8 mM KCl, 3 mM $CaCl_2$, 1 mM $MgCl_2$, 30 mM glucose, 10 mM HEPES, pH 7.35) and compounds were added using a Janus Mini liquid handling robot (PerkinElmer, Waltham, MA). Compounds were prepared in 1 μL spots on a separate compound plate at a concentration of either 666-fold or 1,666-fold over screening concentration, with negative controls (DMSO) and positive controls (1 μM TTX), as

well as a reference compound (Tetracaine in a three-fold dilution series) on each plate. Following compound addition, plates were incubated for an additional 40 min at room temperature in the dark.

Each plate was read in two orientations throughout the studies to ensure data redundancy, first with well A1 designated as the top left corner of the plate, and then immediately again with well P24 as the top left corner. Instantaneous quality control metrics were generated using custom MATLAB (MathWorks, Natick, MA) software following each two-orientation plate read. Figures included heatmaps, signal-to-noise ratio, a list of traces indicating potentially problematic wells, and tetracaine concentration response curves (CRCs) with calculated IC_{50} values to ensure that the plate did not need to be imaged again due to user or instrument error. For Nav1.2 and Nav1.5 spiking HEK assays, imaging was performed using a process nearly identical to Nav1.7, with minor differences in potassium bath concentration and stimulus frequency (see Results Section for details).

Compound Libraries

Several small molecule libraries were used for instrument validation and our HTS campaign. For instrument validation, the commercially available Prestwick Chemical library™ (Prestwick Chemical Inc., Illkirch-Graffenstaden, France) was used. This library consists of 1,520 small molecules, most of which are FDA approved, prepared in 384-well plates at a stock concentration of 10 mM in DMSO. The 200,000 small molecule library screened for Nav1.7 inhibitors was compiled from a series of commercially available sources and internally assembled with three goals: diversity, CNS drug-like properties, and chemical scaffolds amenable to medicinal chemistry. Compound handling was performed using Janus and Janus Mini automated liquid handling instruments (PerkinElmer, Waltham, MA).

Nav1.x Spiking HEK Assay Data Analysis

For each well, the time course of fluorescence intensity was collected from a single objective and the collected raw trace was corrected for photobleaching by dividing the raw intensity time trace by the median filtered intensity. To reduce well-to-well variability, the photobleaching corrected trace was normalized to the steady state height of fluorescence plateau reached during the 500 ms long blue pulse (TP9), which is mainly determined by CheRiff depolarization, stable, and insensitive to sodium channel inhibitors. Next, for Nav1.7 and Nav.1.5, the peak amplitude during each blue light test pulse (TP) was extracted and the mean spike amplitude across all test pulses was used to calculate overall compound potency. For Nav1.2, mean spike areas under TP1, TP8, and TP10 were used to calculate compound potency. Since different regions within the same 384-well plate were imaged by different objectives, to further reduce the variability across different objectives, at the beginning of each imaging day, a sentinel plate with DMSO and a positive control compound (TTX for Nav1.2 and Nav1.7; tetracaine for Nav1.5) was imaged to establish the baseline and magnitude of Nav channel dependent signal from each objective. For each compound treated well, the key parameters such as spike amplitude and spike area under all the 10 test pulses were extracted using automated analysis in MATLAB. For all the following screening plates imaged on the same day, the extracted parameters from each well were normalized to the mean values of positive control and negative control wells imaged by the same objective from the sentinel plate. Since each plate was imaged using the regular orientation and the second orientation by rotating the plates by 180 degrees, each well was imaged by a pair of objectives and the mean values from these two objectives was used for next step of analysis. After objective-based normalization, to reduce plate-to-plate variability, each calculated parameter was further normalized based on the positive control wells and negative control wells from the same plate. For each plate, to evaluate assay quality, a Z′ factor was calculated as $Z' = 1-3(\sigma_p + \sigma_n)/(\mu_p - \mu_n)$, where σ_p is the standard deviation of all positive control wells, σ_n is the standard deviation of all negative control wells, μ_p is the mean of the positive controls, and μ_n is the mean of the negative controls. For IC_{50} values fitting, we define the Hill Equation in MATLAB as this syntax, sigmoid=@(beta,x) 1./(1+(x/beta(1)).beta(2)). Then we use MATLAB function nlinfit to derive IC_{50} values and we use MATLAB function nlparci (Non-linear regression parameter confidence intervals) to estimate the 95% confidence interval (CI) of the fitted IC_{50} values.

Cardiomyocyte Tissue Culture, Imaging, and Data Analysis

Human iPS cell-derived cardiomyocytes (Fujifilm Cellular Dynamics, Madison, WI) were cultured in clear 96-well Greiner COC plates which were plasma treated and coated with 0.1% gelatin (STEMCELL Technologies, Vancouver, Canada). iCell cardiomyocytes plating medium from the iCell Cardiomyocytes Media Kit was used to plate the cardiomyocytes at 60,000 cells/well and then exchanged with iCell Cardiomyocytes maintenance medium after 24 h. Four days after plating, the hiPSC-derived cardiomyocytes were transduced with lentiviral expression vectors for the blue light actuator CheRiff and the calcium indicator jRGECO1a. After 24 h, the medium was removed and exchanged for iCell maintenance medium to remove the virus. Medium (150 μL) was exchanged with fresh maintenance medium every 48 h. The cardiomyocytes imaging experiments were performed 9 days after plating.

Prior to imaging, maintenance medium was removed from the cells using a multichannel pipette, and then 150 μL of 1 μM BeRST1 dye was added to each well. The cells were incubated with BeRST1 dye for 30 min at 30°C in the dark. Following incubation, BeRST1 dye was washed out using 4 mM K^+ Tyrode's solution. The cells were incubated with the Tyrode's solution and preliminary recordings were made on the Swarm instrument with the enclosure temperature set at 30°C. Compounds were then added in a dilution series to three replicate wells per concentration. The compounds were incubated for 10 min before the second post-drug addition recordings were made. Cells were not treated with blebistatin or other agents to reduce cardiomyocyte contraction as cell movement does not affect the optical signals.

For the cardiomyocyte imaging, two separate photodiodes were used to simultaneously record both the BeRST1 voltage fluorescence and the jRGECO1a Ca^{2+} fluorescence. The photodiode voltage recordings were collected with an NI-9202 Analog Input module (National Instruments, Austin, TX) at 2,000 Hz. The raw voltage recordings were low-pass filtered with a moving average filter and then bleach corrected to report the change in fluorescence ($\Delta F/F$). Blue light stimulus artifacts were removed by linear interpolation between the data points immediately before and after the blue stimulus pulse. Post-drug addition traces were normalized to the maximum $\Delta F/F$ of the pre-drug addition traces for the same well. The max AP amplitude was extracted from each test pulse epoch and averaged across all 10 blue light test pulses to determine mean spike amplitude. AP70 width was calculated as the time between crossing 30% of maximum fluorescence between the upstroke and downstroke. The AP70 width was only calculated and averaged from epochs where the cardiomyocytes fired APs. The Ca^{2+} transients were quantified by computing the integrated area under the curve of the photobleach corrected jRGECO1a traces and averaged over all 10 test pulse epochs. Error bars represent the standard error of the mean (SEM) across three replicate wells each. Significance testing was performed using a one-way ANOVA with Dunnett's test and *p*-values were considered significant if <0.05. For the simultaneous voltage and calcium imaging experiments, the significance testing was conducted using a one-tailed *t*-test and *p*-values were considered significant if <0.05.

RESULTS

Swarm for Highly-Parallelized, Multicolor Optogenetic Recordings

We designed and built the Swarm instrument, which records both voltage and calcium activity in 24 wells simultaneously under optical simulation. The read head contains 24 objective modules, which enable flexibility in validation testing, optogenetic imaging, troubleshooting, and repair. Each objective module has over 40 optical elements comprised of low-cost molded aspheric lenses, low-noise photodiodes, high-power LEDs, and high-quality thin film filters and dichroics. Within each module, there are four excitation LED channels (637 nm red, 563 nm lime, 470 nm blue, and patterned 470 nm blue) optically cleaned by excitation filters, and three emission channels (736, 573, and 520 nm) collected by photodiode detectors (**Figure 1A**). The objective modules are aligned in parallel to form two banks of twelve modules that comprise the whole 24-objective read head. Each assay scan reported for this study requires approximately 9 s (3 s for imaging, 6 s of overhead, e.g., DAQ initialization, stage moving to read new wells, saving recordings). Imaging a 384-well plate requires 16 consecutive scans (∼2.5 min) using the read pattern shown in **Figure 1B**. We constructed custom printed circuit boards attached to each objective module as shown in **Figure 1C**: (1) A LED board containing four high power LEDs for the four excitation optical paths (red, lime, blue, and patterned blue). (2) Two photodiode boards containing three photodiodes and three independent picoammeter circuits to measure and amplify the signal collected in the three emission channels (Far Red, RFP, and GFP). The overall Swarm instrument and superstructure footprint on an "18 by 24" optical breadboard is shown in **Figure 1D**.

Optopatch Nav1.7 Spiking HEK Swarm Assay Validation

Nav1.x spiking HEK cells can fire sodium channel dependent pseudo-APs which afford robust signals reflecting Nav channel function and pharmacology. The basic components of Nav1.x spiking HEK cells are shown in **Figure 2A**. Nav1.x spiking HEK cells stably expressed a Nav1.x channel, the target of interest, and a modified channelrhodopsin (Zhang et al., 2016, 2020). In addition, an inwardly rectifying potassium channel (Kir2.1) was transiently expressed by lentiviral transduction. Kir channel expression was required to hyperpolarize the resting membrane potential in order to maintain Nav channels in a non-inactivated state and enable repolarization following stimulation. Expression of Kir channels also allowed tunable control of resting potential by adjusting extracellular potassium concentrations in imaging (Dai et al., 2008). For the primary Nav1.7 assays, we used 8 mM bath potassium to achieve a resting membrane potential of approximately −70 mV, which is near the physiological value in native sensory neurons (Liu et al., 2017). Cells were loaded with a bright far-red fluorescent membrane potential dye, BeRST1, prior to imaging to provide a rapid and linear fluorescence readout of membrane voltage, which is compatible with red LED levels from Swarm which can deliver a maximum intensity of $4 W/cm^2$. With this model, cells can be depolarized upon blue light stimuli leading to Nav1.x channel activation and the firing of pseudo-APs. The AP amplitude can be recorded by measuring BeRST1 fluorescence intensity and is sensitive to Nav channel inhibitor pharmacological modulation. For Nav1.7 spiking HEK cells, a 10 test-pulse blue light stimulus protocol ($125 mW/cm^2$) with nine 40 ms short pulses and one 500 ms long pulse was used and the mean spike amplitude across all the test pulses was applied to evaluate Nav1.7 inhibitor potency and efficacy (Zhang et al., 2020). **Figure 2B** shows all the 16 wells imaged by objective 1 from a zebra sentinel plate with alternating columns of wells containing a Nav1.7 blocker tetrodotoxin (TTX; 1 μM) as a positive control and dimethylsulfoxide (DMSO; 0.15%) as a negative vehicle control. For the single objective, the average waveform amplitudes for the eight DMSO treated wells showed excellent separation from those of the eight TTX treated wells. The 40% signal reduction is due to Nav1.7 inhibition and all residual signal is mediated by voltage actuator CheRiff-mediated depolarization. Since optogenetic assay results can be sensitive to light illumination intensity, we further validated the instrument homogeneity across different objectives by examining the DMSO and TTX traces collected from each objective. **Figure 2C** shows that after fine tuning of analog output voltages to each blue LED, the Swarm instrument generates a consistent TTX sensitive, Nav1.7 dependent signal amplitude across all the different objectives covering a full 384-well plate. To further reduce the assay variability resulting from subtle differences in LED intensity

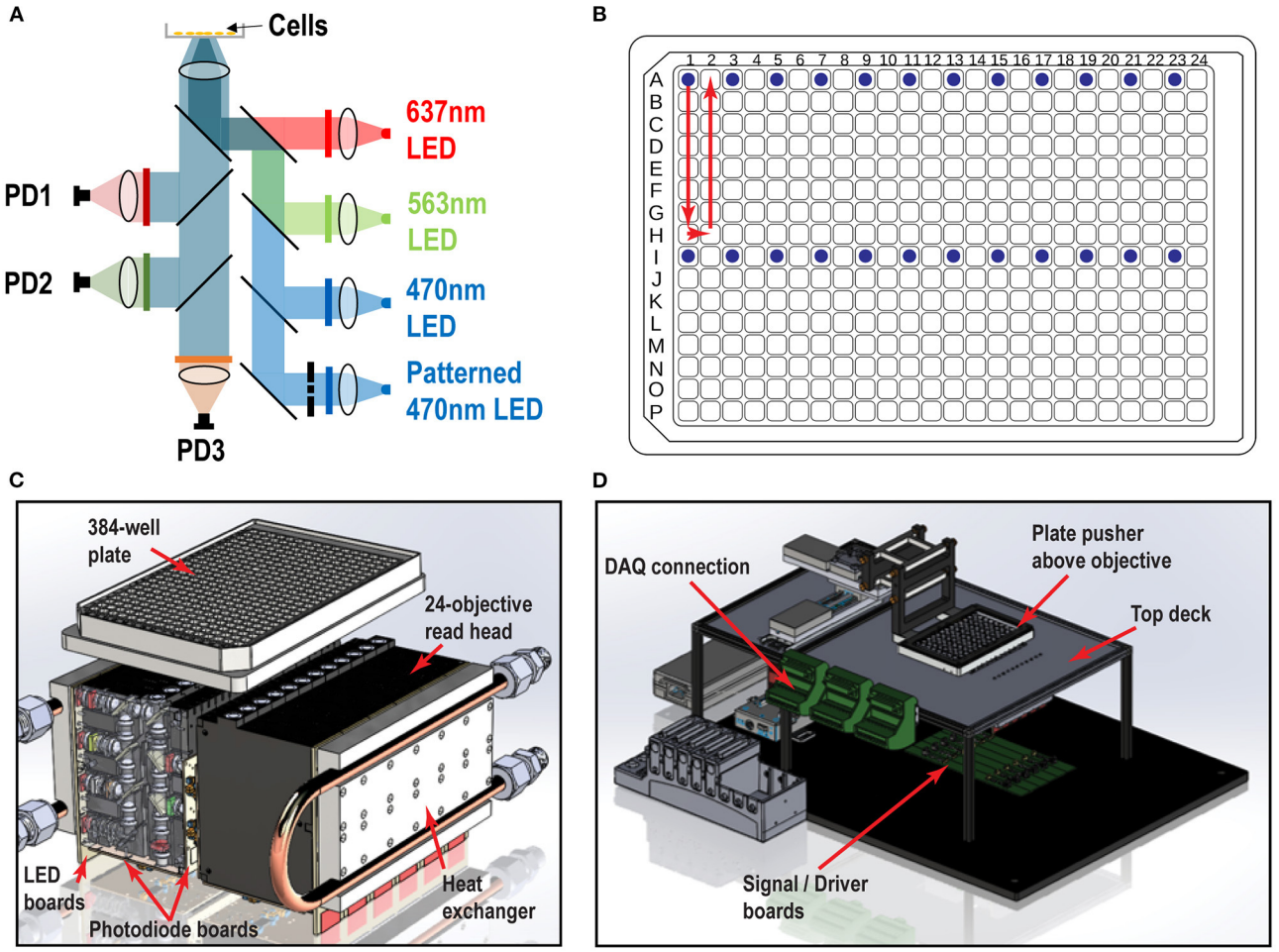

FIGURE 1 | Swarm instrument schematics. **(A)** Each objective module contains four excitation LED paths (637, 563, 470 nm, and patterned 470 nm) and three emission channels (736, 573, and 520 nm), which are collected by photodiode detectors. Chrome masks are placed on conjugate image planes to enable patterned blue light stimulation. Beam shaping optics are not shown. **(B)** 384-well plate and objective modules illuminating 24 wells (blue dots) and scan pattern (red arrow) to image the entire plate. **(C)** Each individual objective module has two banks of 12 modules that comprise the whole 24-objective read head. Each module contains multiple lenses, filters, and masks to deliver light from the LED board to the bottom of the well. The signal amplification picoammeters measure currents from the sample which are collected by each photodiode channel. Water cooled heat exchangers are fastened to the LED boards. **(D)** Surrounding superstructure of Swarm. A plate pusher arm articulates a 384-well plate over a 24-objective read head, which is fastened below the top deck. The DAQ connectors hang to the side of the top deck rails.

across different objectives, we also included an objective-wise normalization step in the analysis pipeline (see Materials and Methods section). **Figure 2D** shows a heatmap from a zebra sentinel plate in which DMSO and 1 μM of TTX were placed in alternating columns and no apparent objective or position biased effects were observed.

The Optopatch Nav1.7 spiking HEK assay, when run using a serial epifluorescence microscope, was reported to yield IC_{50} values comparable to an automated patch clamp platform such as IonWorks Barracuda (Zhang et al., 2020). The parallel recording feature of Swarm greatly reduces imaging time per plate and subsequently improves overall throughput while maintaining overall assay performance. When a diverse set of compounds were tested using both Swarm and a custom single-well compatible epifluorescence microscope, the instruments yielded IC_{50} values for each compound differing less than two-fold across the two platforms (**Supplementary Figure 1**).

Tool Compound Pharmacology for Swarm Assay Validation Across Different Nav Channels

In addition to Nav1.7, the Optopatch spiking HEK assay can be applied to study the pharmacology of other Nav subtypes, including Nav1.2 (a major Nav subtype in the brain) and Nav1.5 (dominant Nav subtype in the heart), both of which are important counter screen targets to confirm Nav1.7 selectivity. We established stable cell line expression of Nav1.2/CheRiff and

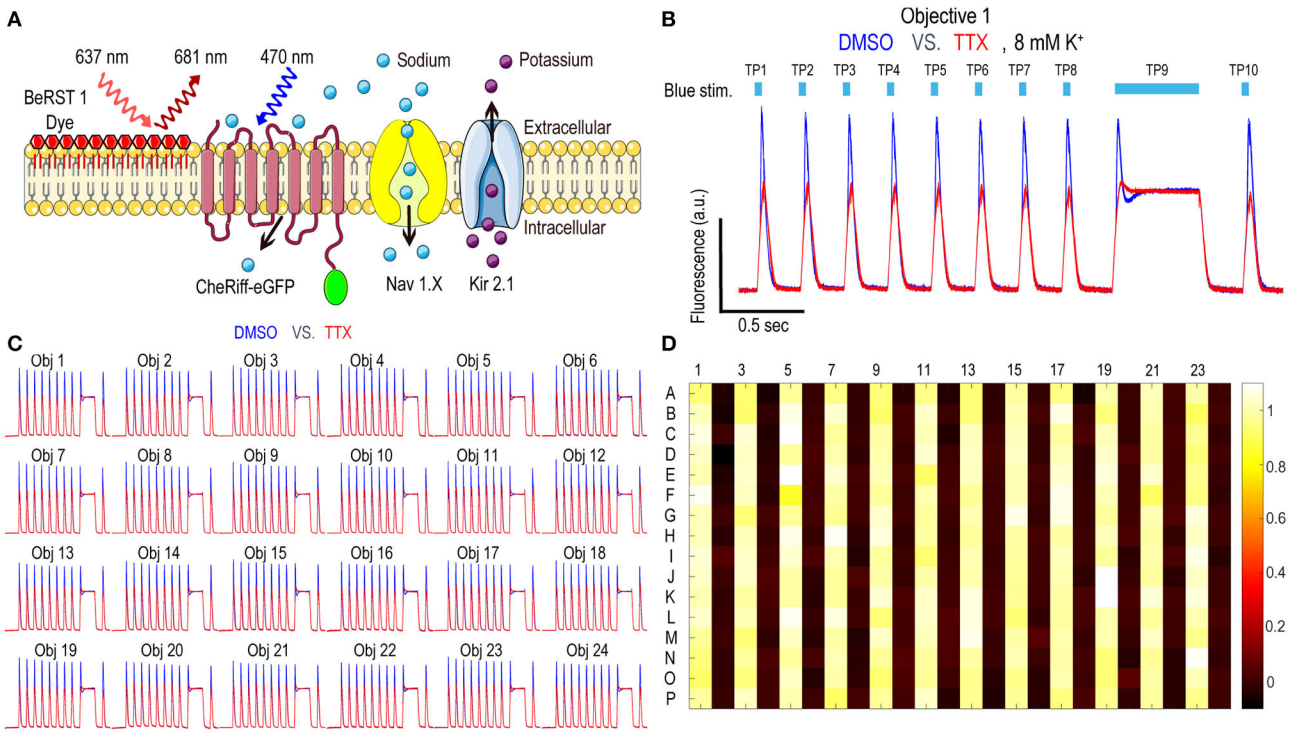

FIGURE 2 | Nav1.7 Spiking HEK assay performance with the Swarm instrument. **(A)** Diagram of key components in Nav1.x spiking HEK cells, including voltage sensitive dye BeRST1, CheRiff-eGFP, Kir2.1, and the target of interest, Nav1.x channel. **(B)** Representative fluorescence traces from eight wells of DMSO or 1 μM TTX treated Nav1.7 spiking HEK cells stimulated with a 10 test-pulse blue light stimulation protocol, imaged by Objective 1 of the Swarm instrument. The bath [K^+] is 8 mM. **(C)** Fluorescence traces collected from all the 24 objectives. The Nav1.7 spiking HEK cells were treated with either DMSO or 1 μM TTX and were stimulated by the protocol shown in **(B)**. Each trace was averaged based on 8 adjacent wells imaged by the same objective. **(D)** The heat map from a representative Nav1.7 spiking HEK 384-well sentinel plate. All the odd columns were treated with DMSO vehicle control, and all the even columns were treated with 1 μM TTX.

Nav1.5/CheRiff in HEK293 cells and Kir2.1 was introduced to the cells *via* lentiviral transduction prior to imaging. Similar to the Nav1.7 assay, upon blue light stimulation, Nav1.2 and Nav1.5 spiking HEK cells fire pseudo-APs and the spike amplitude and integrated spike area are sensitive to compound modulation (**Figure 3A**). The spike width is wider in Nav1.2 and Nav1.5 spiking HEK cells than Nav1.7 spiking HEK cells, possibly due to different Nav subtype channel gating properties or different background potassium current levels in different HEK cell lines (Ponce et al., 2018). It is also reported that exogenous expression of the beta subunit can alter Nav channel gating kinetics in Xenopus oocytes and thus potentially modulate AP width, but in HEK293 cells, Nav channel gating is much less impacted by exogenous beta subunit expression due to the endogenous expression of SCN1B (Moran et al., 2000; Walther et al., 2020). Different bath potassium concentrations were used for Nav1.2 (8 mM) and Nav1.5 (6 mM), based on the consideration that the cardiac Nav1.5 subtype has a more hyperpolarized half-inactivation voltage $V_{1/2}$ than the neuronal subtypes Nav1.2 and Nav1.7 (Vilin et al., 2012; Wang et al., 2015). Adjusting the bath potassium concentration to generate similar levels of channel inactivation across sodium channel subtypes enabled more consistent comparison of pharmacological effects. Like the Nav1.7 assay, we extracted parameters from multiple test pulses to comprehensively evaluate compound effects on Nav1.2 and Nav1.5 channels and then derive overall compound IC_{50} values. We validated the assay sensitivity and accuracy by performing concentration response experiments using a set of 15 Nav tool compounds covering a wide range of subtype specificities, mechanisms of action, and binding sites (**Table 1**, **Figure 3B**, and **Supplementary Figure 2**). Under current assay conditions, the non-selective Nav inhibitors amitriptyline, tetracaine, and vixotrigine can inhibit all the three Nav subtypes with similar potency (**Figure 3B**). The Nav subtype selective compounds JNJ63955918, PF-05089771, and tetrodotoxin demonstrated the expected subtype selectivity consistent with literature reports (Alexandrou et al., 2016; Flinspach et al., 2017; Tsukamoto et al., 2017). Only JNJ63955918 showed more than 50-fold Nav1.7 selectivity against both Nav1.2 and Nav1.5. While both tetrodotoxin and PF-05089771 potently blocked Nav1.7, they lacked or only had modest subtype specificity against Nav1.2 (**Figure 3B**). Also, a highly subtype selective Nav1.8 compound VX-150 (Hijma et al., 2021) has no effects on Nav1.2, Nav1.5 and Nav1.7 (**Table 1** and **Supplementary Figure 2**). In addition to assessing subtype selectivity profiles, Nav1.x spiking HEK assays on Swarm can be used to determine compound mechanism of action. The compound state dependence (Kr/Ki) was defined as the ratio Nav1.7 IC_{50} value at TP1 under 4 mM

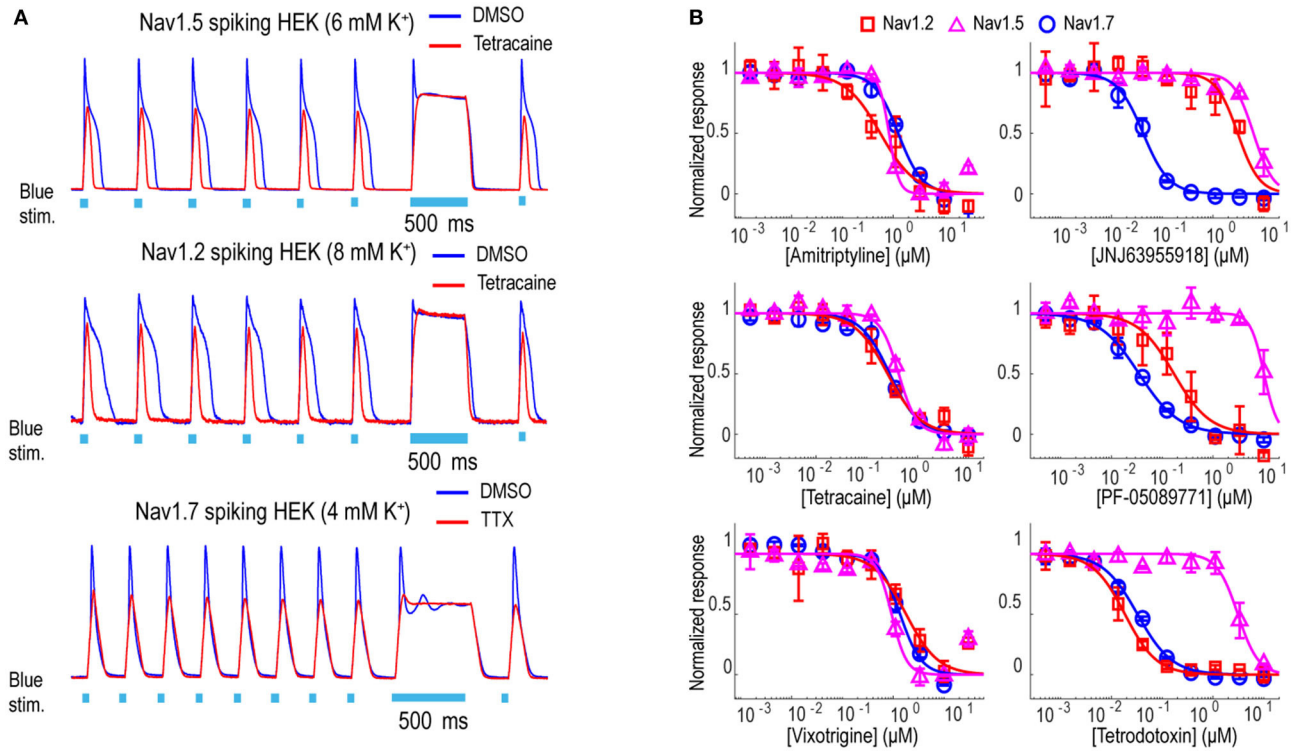

FIGURE 3 | Tool compound concentration-response curves on different Nav channel subtypes. **(A)** Representative fluorescence traces from DMSO, 1 μM TTX, or 10 μM tetracaine treated Nav1.2 spiking HEK cells (8 mM bath [K^+]), Nav1.5 spiking HEK cells (6 mM bath [K^+]), and Nav1.7 spiking HEK cells (4 mM bath [K^+]). For Nav1.2 and Nav1.5 spiking HEK assays, the cells were stimulated at 2 Hz. Eight test pulses were applied before the 500 ms long pulse and only action potentials triggered by the third to the eighth pulses were plotted for these two Nav channel subtypes; for Nav1.7 spiking HEK cells, the cells were stimulated at 4 Hz and all 10 triggered action potentials are plotted. **(B)** Concentration-response curves of 3 non-selective Nav channel blockers (Amitriptyline, Tetracaine, Vixotrigine) and 3 subtype-selective Nav channel blockers (JNJ63955918, PF-05089771, Tetrodotoxin) on Nav1.2 (8 mM bath [K^+]), Nav1.5 (6 mM bath [K^+]), and Nav1.7 (8 mM bath [K^+]). Error bars indicate SD based on measurements from 2 wells.

potassium (**Figure 3A**) over the IC_{50} value at TP10 under 8 mM potassium (**Figure 2B**). As expected, compounds that act on the voltage sensor domain IV (e.g., PF-05089771), as local anesthetics (e.g., lidocaine, tetracaine), and as prototypical anticonvulsants (e.g., carbamazepine, lamotrigine) show stronger state-dependent block than pore blockers (e.g., TTX) and peptide blockers (e.g., JNJ63955918). For example, both PF-05089771 and TTX have similar Ki (∼30 nM), but the ratio of Kr/Ki for a strong state-dependent blocker, PF-05089771 (43-fold) is at least 10 times greater than that of a weak state-dependent blocker TTX (four-fold), under our current assay conditions (**Supplementary Figure 3**).

Demonstration of Swarm Screening for Nav1.7 Small Molecule Inhibitors

To assess the platform readiness to support high-throughput screening, we first conducted a pilot screen using the Prestwick Chemical Library, which is a unique collection of 1,520 small molecules, many of which are approved drugs (approved by the FDA, EMA, JAN, and other agencies). Before imaging, Nav1.7 spiking HEK cells were loaded with BeRST1 dye and then incubated with the compounds at 1 μM for 30 min. Next, the cells were stimulated with a 10 test-pulse protocol and the resulting voltage waveforms were collected for compound pharmacology evaluation. The mean spike amplitude was used to calculate the Z′ factor for each plate. All four plates displayed Z′ values higher than 0.7 and the tetracaine in-plate control wells yielded consistent IC_{50} values across all four plates, which were 0.16, 0.18, 0.24, 0.20 μM, respectively (**Figure 4**). The hit rate was 9.3% when 0.5 mean spike amplitude was used as the cutoff for hit selection, which is consistent with the reported frequent occurrence of Nav channel inhibition for marketed approved drugs (Zhang et al., 2014). Since many Nav channel inhibitors are not subtype-selective, we chose a set of 75 reference compounds in the Prestwick Chemical Library also with reported IC_{50} values for Nav1.5 based on automated patch clamp recordings (Harmer et al., 2011). Fifteen out of sixteen compounds with Nav1.5 IC_{50} values < 3 μM also inhibited Nav1.7 spiking HEK signals by more than 50% indicating a lack of subtype selectivity (**Supplementary Table 1**). Many anti-depressant drugs are also Nav channel inhibitors (Huang et al., 2006) and the Prestwick Chemical Library identified hits which have been characterized as anti-depressant drugs, including nefazodone, doxepin, amitriptyline, nortriptyline, clomipramine, imipramine, trimipramine, and desipramine.

TABLE 1 | Tool compound results.

Compound name	Nav1.2 (μM)	Nav1.2 95% CI (μM)	Nav1.5 (μM)	Nav1.5 95% CI (μM)	Nav1.7 (μM)	Nav1.7 95% CI (μM)	State dependence*
Amitriptyline	0.56	0.33–0.79	0.82	0.71–0.94	1.25	1.08–1.43	9.6
Tetracaine	0.26	0.18–0.34	0.43	0.35–0.50	0.28	0.23–0.34	15.5
Vixotrigine	1.74	1.30–2.17	0.93	0.72–1.14	1.36	1.06–1.68	29.8
JNJ63955918	3.07	1.90–4.24	6.26	4.97–7.55	0.042	0.035–0.049	6.1
PF-05089771	0.17	0.087–0.25	10.1	8.58–11.6	0.035	0.030–0.040	42.9
Tetrodotoxin	0.019	0.016–0.021	3.08	2.45–3.71	0.033	0.028–0.037	4.0
Carbamazepine	139.4	115.3–163.4	37.1	26.7–47.5	52.6	40.0–65.3	39.9
Funapide	0.51	0.35–0.66	0.24	0.15–0.32	0.46	0.38–0.54	2.7
Mexiletine	28.8	19.2–38.5	21.0	15.6–26.5	13.0	9.1–16.9	9.2
Lacosamide	392.9	286.3–499.6	58.5	46.9–70.1	104.6	84.2–125.0	n.a.
Lamotrigine	72.4	60.9–83.9	20.6	14.7–26.6	32.8	23.5–42.0	24.3
MK-0759	1.50	0.91–2.10	1.61	1.28–1.93	2.05	1.56–2.54	18.8
Lidocaine	47.2	25.6–68.9	20.1	14.9–25.2	15.0	14.0–15.8	15.4
TC-N 1752	0.14	0.13–0.15	1.15	0.84–1.46	0.046	0.043–0.050	10.8
VX-150	Inactive	n.a	Inactive	n.a	Inactive	n.a	n.a

*Nav1.x IC_{50} values, Nav1.x IC_{50} 95% confidence intervals (CI), and state dependence from 15 tool compounds with different potencies and working mechanisms. *State dependence is defined as the ratio of IC_{50} values of Nav1.7 spiking HEK assay at TP1 at 4 mM K^+ over TP10 IC_{50} values at 8 mM K^+ (**Figure 2B**).*

Following the pilot screen, we next searched for Nav1.7 inhibitors with novel chemical scaffolds and desired molecular profiles by conducting a 200,000 small molecule library screen using the Nav1.7 spiking HEK assay on the newly engineered Swarm instrument. Five hundred and sixty 384-well plates were imaged with a throughput of ∼8,000 compounds/day (**Figure 5A**), though 10,000 compounds/day was readily achievable. The average Z′ for the entire screen was ∼0.8 (representative screening plate shown in **Figure 5B**) and the tetracaine in-plate control IC_{50} fluctuation was less than four-fold (**Figure 5C**) demonstrating assay robustness. Using 0.45 mean spike amplitude as the cutoff for hit selection, the hit rate was ∼1.4% (**Figure 5D**). 2,766 identified hit compounds were cherry-picked to advance into hit confirmation at 1 and 3 μM ($n = 2$). When tested at 3 μM, the hit confirmation rate was 60% when 0.5 mean spike amplitude was applied as the cutoff (**Supplementary Figure 4**) if we defined the confirmed hits as any compounds with IC_{50} values less than 3 μM. The hit confirmation rate was 54% when 0.45 mean spike amplitude cutoff was applied. The exact same cutoff threshold was used for hit cherry-picking and for hit confirmation. Among the hits confirmed at 3 μM, 352 compounds with confirmed activity at 1 μM were selected for 8-point concentration-response curve (CRC) analysis in Nav1.7 and Nav1.5 spiking HEK assays.

Validation studies were performed for 32 compounds using reordered powder samples and for activity confirmation in 10-point CRC analysis in spiking HEK assays. Reordered hit compounds were tested in Nav1.7, Nav1.5, and Nav1.2 assays for selectivity profiling and state-dependence determination (**Figure 6**). We benchmarked the properties of the newly identified hits against the 15 tool compounds selected in **Figure 3**. To mimic the genetic loss-of-function mechanism in congenital insensitivity to pain (CIP) patients, an ideal Nav1.7 inhibitor should have sufficient selectivity against both Nav1.2 and Nav1.5 and should display greater state-independent inhibition. Among the tested tool compounds, only JNJ63955918 demonstrated more than 10-fold subtype selectivity against both Nav1.2 (**Figure 6A**) and Nav1.5 (**Figure 6B**) and exhibited a state-dependence metric less than 10-fold (**Figure 6C**). However, JNJ63955918 is a small peptide that would require intrathecal delivery, which limits therapeutic applications. PF-05089771, a compound previously tested in Phase 2 clinical trials with limited success, lacked sufficient selectivity against Nav1.2 (**Figure 6A**) and it also displayed the strongest state-dependent block of the tested compounds (**Figure 6C**). Compound 1 was a promising internally identified hit from the Q-State screening library with ∼10-fold subtype selectivity against Nav1.2 (**Figure 6A**) and more than 10-fold subtype selectivity against Nav1.5 (**Figure 6B**) with improved state dependent properties compared to PF-05089771. Additional structure activity relationship and exploratory medicinal chemistry efforts may lead to further improvements in subtype selectivity and reduce the level of state-dependent inhibition to achieve the desired profile for a safe and effective Nav1.7 inhibitor therapeutic for chronic pain.

Simultaneous Voltage and Calcium Imaging of Human iPS Cell-Derived Cardiomyocytes Under Optogenetic Pacing Using the Swarm

We have previously demonstrated Optopatch compatibility with human iPS cell (hiPSC)-derived cardiomyocytes (Dempsey et al., 2016; Dempsey and Werley, 2017). Here we extended this approach by developing a Swarm-compatible counter screening assay in hiPSC-derived cardiomyocytes to assess cardiotoxicity of HTS hit compounds and validated the assay with pharmacological tool compounds. HiPSC-derived cardiomyocytes (CDI Cardiomyoctes^2) were plated on 96-well

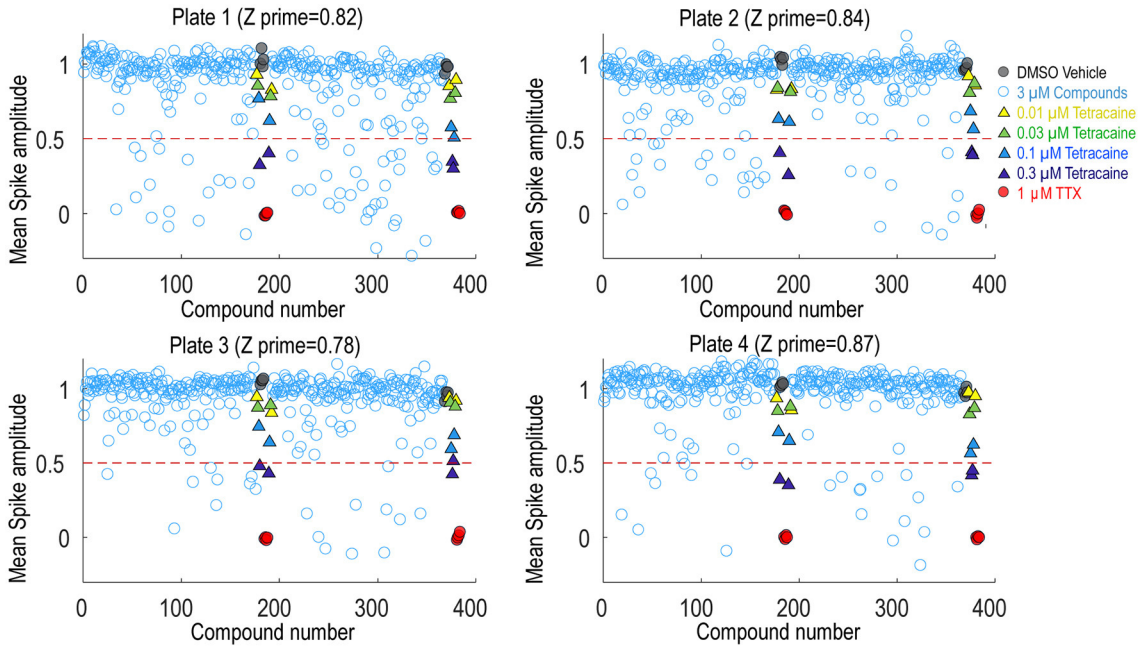

FIGURE 4 | Prestwick library pilot screen. Four 384-well plates from the Prestwick library were tested using Nav1.7 spiking HEK assay under 8 mM bath potassium. The mean spike amplitude of individual wells is shown in scatter plots for each individual plate. DMSO vehicle was used as the negative control and 1 μM TTX was used as the positive control. DMSO treated wells and TTX treated wells were used to calculate the Z′ factor. On each plate, a four-dose tetracaine titration series was also included to monitor assay variability across different plates.

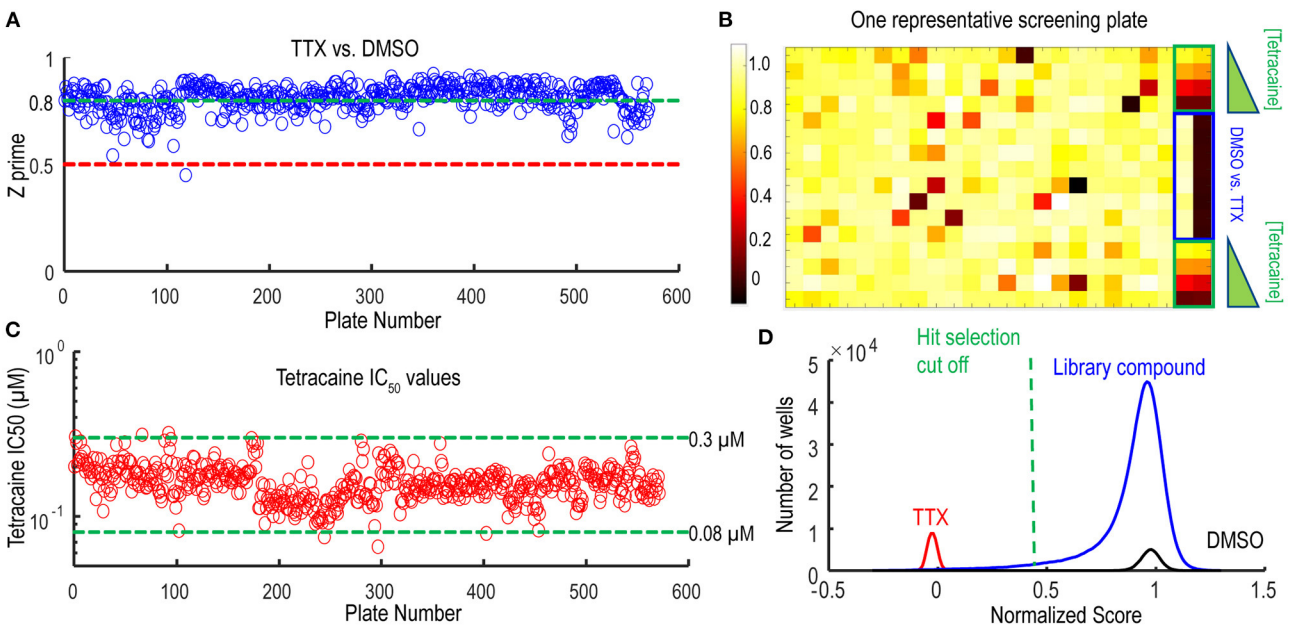

FIGURE 5 | Quality control metrics analysis for 200 K Nav1.7 spiking HEK Swarm screen. **(A)** The Z′ factor analysis for Nav1.7 Swarm screen. All 560 plates had Z′ factors at or above 0.5. **(B)** The heat map of one representative screening plate. Column 1 through Column 22 contained library compounds. Columns 23 and 24 contained control compounds, including 8 wells of TTX and 8 wells of DMSO for Z′ factor calculation and two 4-point titration series of tetracaine. **(C)** IC_{50} values derived from the 4-point tetracaine titration for each screening plate. The IC_{50} fluctuation was less than four-fold during the entire screen, indicating a high degree of assay consistency. **(D)** The histogram of library compounds and the control compounds. The normalized score of 0.45 was chosen for hit selection threshold, and based on this criterion, around 2,800 compounds were identified as hits from the 200 K Nav1.7 Swarm screen.

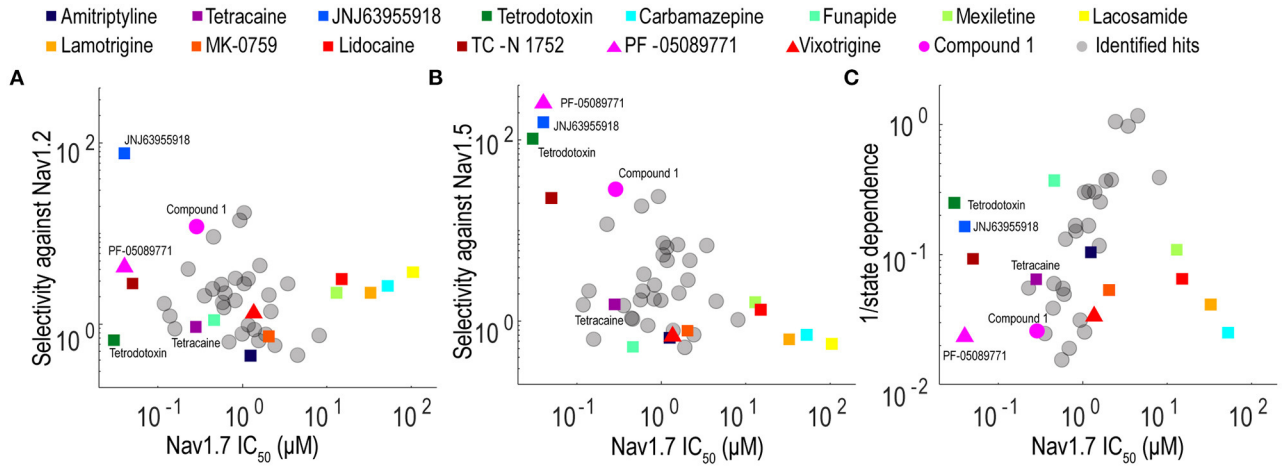

FIGURE 6 | Potency, selectivity, and state dependence of tool compounds and identified hits. **(A)** For each Nav1.7 inhibitor, its subtype selectivity against Nav1.2, defined as the ratio of Nav1.2 IC_{50} value over Nav1.7 IC_{50} value, was plotted against its Nav1.7 IC_{50} value. **(B)** For each Nav1.7 inhibitor, its subtype selectivity against Nav1.5, defined as the ratio of Nav1.5 IC_{50} value over Nav1.7 IC_{50} value, was plotted against its Nav1.7 IC_{50} value. **(C)** For each Nav1.7 inhibitor, its reciprocal of state dependence was plotted against its potency on Nav1.7. In all three panels, the compounds with desired properties (potent, subtype selective and less state-dependence) distribute to the upper left quadrant.

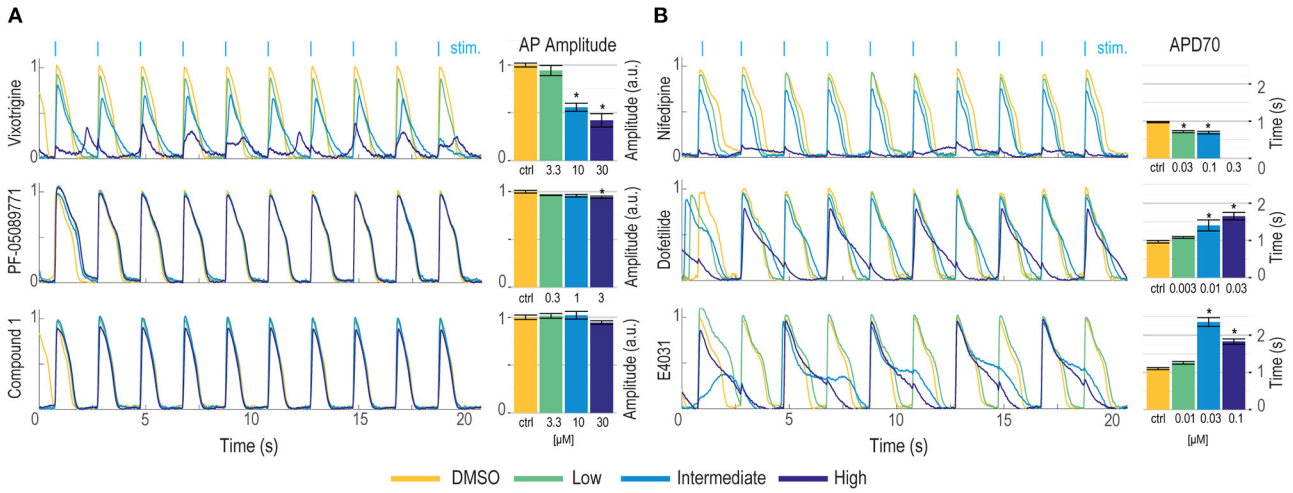

FIGURE 7 | Validation of hiPSC-derived cardiomyocyte counter-screening assay on Swarm instrument with pharmacological tool compounds and an identified screening hit. Representative BeRST1 voltage fluorescence traces are shown for 0.5 Hz paced cardiomyocytes treated with increasing concentrations of compound (yellow to dark blue). Cardiomyocytes were treated with **(A)** sodium channel blockers (Vixotrigine, PF-05089771, QS Compound 1) and **(B)** calcium channel and hERG channel blockers (Nifedipine, Dofetilide, E4031). Quantification of **(A)** action potential (AP) peak amplitude for sodium channel blockers and **(B)** AP70 width for calcium channel and hERG channel blockers are shown as mean ± SEM from triplicate wells. *$p < 0.05$ compared to DMSO control.

Greiner cyclic olefin copolymer (COC) plates and transfected with blue-light activated CheRiff channelrhodopsin and calcium reporter jRGECO1a (Dana et al., 2016). jRGECO1a has the largest SNR compared to other reported red-shifted genetically encoded calcium sensors, but is also prone to photoactivation, which may add confounding factors to interpret pharmacological results. To overcome this issue, we implemented two major strategies. (1) Minimize the blue light stimulation intensity and duration. (2) Perform the pre- and post-measurement on the same group of cells to assure that the magnitude of photophysical artifact is the same and any observed signal change is due to compound modulation. For voltage imaging, cardiomyocytes were also loaded with BeRST1 prior to imaging to record cell membrane potential. Cardiomyocytes were paced at 0.5 Hz with a ten-pulse 20 ms blue light stimulation protocol (125 mW/cm^2). Red light (2 W/cm^2) and lime light (980 mW/cm^2) were used to excite the sensors and BeRST membrane potential fluorescence and jRGECO1a calcium fluorescence were recorded. Optical stimulation *via* blue light activation of CheRiff enables controlled pacing which reduces variation in action potential frequency

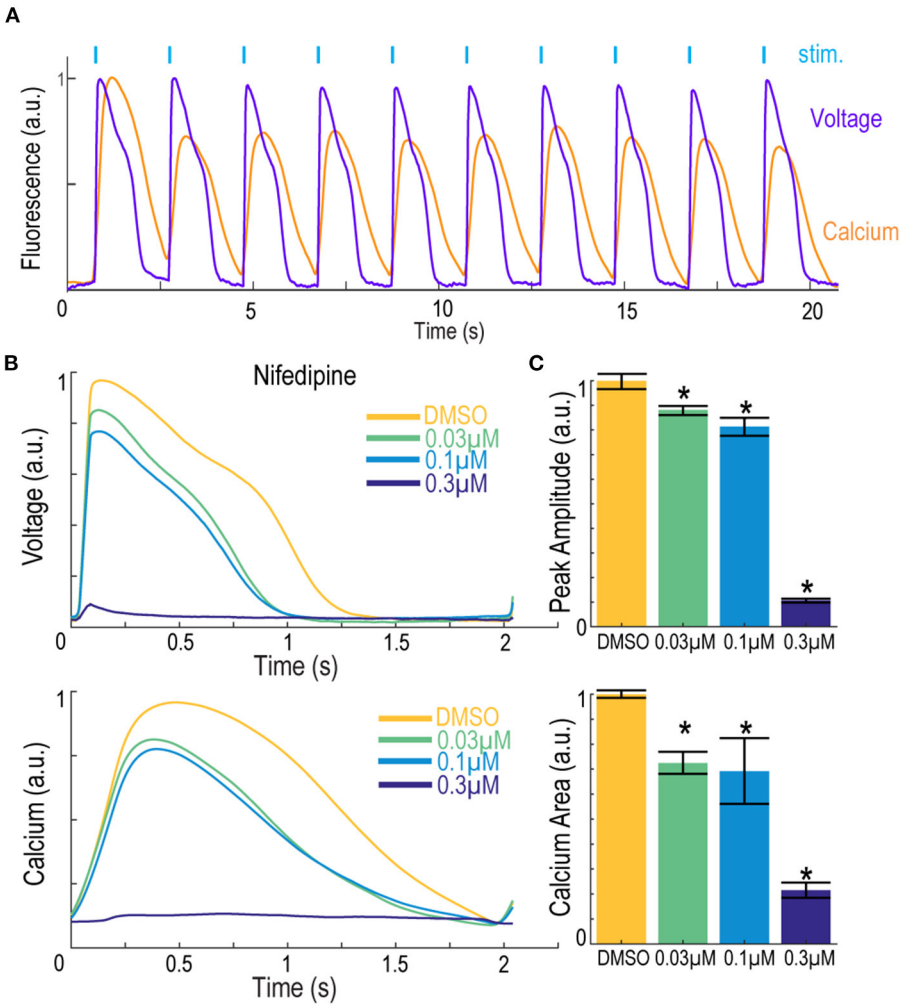

FIGURE 8 | Simultaneous voltage and calcium imaging with the Swarm instrument on hiPSC-derived cardiomyocytes. **(A)** Representative fluorescence traces from hiPSC-derived cardiomyocytes expressing jRGECO1a reporter and loaded with BeRST1 voltage sensitive dye. Cardiomyocytes were paced with ten 0.5 Hz, 20 ms blue pulses. **(B)** Average fluorescence waveforms for voltage and Ca^{2+} in hiPSC-derived cardiomyocytes treated with increasing concentrations of calcium channel blocker Nifedipine (yellow to dark blue). **(C)** Quantification of voltage AP peak amplitude and integrated Ca^{2+} waveform area. Data shown as mean from triplicate wells with ±SEM as error bars. *$p < 0.05$ compared to DMSO control.

that occurs across wells with spontaneous action potentials, leads to more uniform action potential properties, and more closely replicates conditions in ventricular myocytes. In some examples shown in **Figure 7**, spontaneous action potentials are seen at the left edge of each trace, prior to initiation of pacing. For the cardiomyocyte experiments, two recordings per well were made. One recording was made prior to compound treatment and a second recording was performed following compound addition with a 10-min compound incubation period. The post-compound treatment voltage traces were normalized to their corresponding pre-compound addition traces. Voltage traces from cardiomyocytes treated with sodium channel blockers vixotrigine, PF-05089771, and the HTS screening hit Q-State Compound 1 (QS Compound 1) are shown in **Figure 7A**. As a positive control, we tested the non-selective Nav channel blocker vixotrigine which showed dose-dependent reduction of the AP peak amplitude, with the AP waveform significantly distorted at the highest dose (30 μM, <25-fold above its Nav1.7 IC_{50}). In comparison, the Nav channel subtype-selective PF-05089771 and QS Compound 1 caused minimal effects at the highest doses tested (3 and 30 μM, respectively, >40-fold above their Nav1.7 IC_{50}). As additional control pharmacology, voltage traces for the calcium channel blocker nifedipine and hERG channel blockers dofetilide and E4031 were recorded (**Figure 7B**). Nifedipine shortened the AP width with increasing concentrations until the cardiac AP was completely extinguished at the highest 0.3 μM dose, consistent with previous reports (Dempsey et al., 2016). HERG channel blockers dofetilide and E4031 elongated APD70 with increasing concentrations, as expected (Dempsey et al., 2016; Millard et al., 2018). At the highest doses, the hERG

blockers altered the AP waveforms to such a degree that the cardiomyocytes failed to fire APs at the 0.5 Hz pacing frequency. Addition of dofetilide increased the APD70 from 1 to 1.75 s at 0.3 μM. Similarly, E4031 addition prolonged the AP waveform from 1 to 2.4 s at the intermediate dose of 0.03 μM.

The Swarm instrument is capable of recording from up to three emission wavelengths simultaneously. This makes the instrument ideally suited for recording both the far-red BeRST1 voltage fluorescence and red jRGECO1a Ca^{2+} transients on hiPSC-derived cardiomyocytes. **Figure 8A** shows representative fluorescence traces overlaid with the ten-pulse blue light stimulation protocol used to optically pace the cardiomyocytes. The cardiomyocytes were treated with the calcium channel blocker nifedipine, and voltage fluorescence and calcium transients were measured simultaneously (**Figure 8B**). At low and intermediate doses of 0.03 μM and 0.1 μM nifedipine, respectively, the voltage peak amplitude decreased by 33 ± 2.7% and 40 ± 7.0%, respectively, until the cardiomyocytes failed to fire APs at the highest 0.3 μM dose. Similarly, the calcium transients were quantified by taking the integrated area of the calcium signal. Addition of 0.03 μM nifedipine decreased the integrated calcium area by 28 ± 4.5% and 0.1 μM nifedipine decreased the integrated area by 31 ± 13% until it was completely extinguished at the highest 0.3 μM dose (**Figure 8C**). The results show that nifedipine altered both the AP waveform and calcium transients of iPS cell-derived cardiomyocytes, as expected (Dempsey and Werley, 2017; Millard et al., 2018). The Swarm instrument was able to capture the pharmacological effects of compounds with known activities in cardiomyocytes using both voltage and calcium readouts and can provide a platform for detailed pharmacological characterization using human cardiomyocytes.

DISCUSSION

Here we describe the design and validation of a novel optically-based instrument, the Swarm, for evaluating pharmacological effects of compounds on ion channels and excitable cells. Swarm enabled optical stimulation and simultaneous optical readout of multiple parameters including membrane voltage and intracellular calcium levels in cell-based assays. Optical stimulation *via* blue light stimulation of heterologously expressed channelrhodopsins allowed for precise and rapid stimulation with flexible control of stimulation protocols. Multiwavelength readouts of membrane voltage and calcium at red-shifted wavelengths enabled simultaneous stimulation and multiparameter readout with rapid response kinetics that are currently only limited by response times of the fluorescent voltage sensors. Swarm incorporated these capabilities in an instrument containing 24 individual objectives each having four optical input channels and three optical readout channels along with electronics for detection of the optical signals and control of LED-based stimulation. Swarm is designed for high throughput compound evaluation in 96- and 384-well plate formats and provides a new scalable technology for high-throughput screening of compounds targeting ion channels and excitable cells.

The Swarm instrument addresses key limitations in the current high-throughput instrument landscape. Current fluorescence plate readers such as FLIPR (Molecular Devices, San Jose, CA), FDSS6000, and FDSS/μCell (Hamamatsu, Hamamatsu, Japan) are high-throughput and cost-effective, but use non-physiological stimuli and have low temporal resolution. The Opto-plate96 (Bugaj and Lim, 2019) has 96 LED positions that can illuminate every well of a 96-well plate or 384-well plate simultaneously with 3 different wavelengths but has no built-in recording capability and needs to be coupled with a separate instrument or microscope to measure assay readouts. The ML8500 (Modulight Corporation, Tampere, Finland) is compatible with multiple well plates (24, 96, 384, and 1,536 well formats) and can use 6 different excitation colors but can only sequentially illuminate one well at a time, and has no recording capabilities. The Kinetic Imaging Cytometer (Vala Sciences, San Diego, CA) uses a sCMOS camera to acquire high-speed videos of fluorescent indicators and has multiple color excitation options but can only record from a single well at a time. The Bolt (Photoswitch Biosciences, Cleveland, OH) has fast simultaneous 96-channel stimulation and recording capabilities but has limited sensor options that are restricted to the far-red spectrum. Our Swarm platform is specifically designed to deliver highly parallelized optogenetic stimulation with 3 colors (red, lime, blue), and simultaneous recording in 3 distinct wavelengths (far-red, red, green) in order to fully leverage the Optopatch technology in a high throughput format.

Optical assays provide an advantageous path to develop scalable high throughput assays. Specialized and expensive consumable items are not typically required, and the screening format can be readily changed to match assay specific needs and throughput. Previous assays methods used for sodium channel screening have relied on flux of permeant ions (Trivedi et al., 2008; Du et al., 2015), fluorescence measurements of membrane potential (Dyes et al., 2004), and automated electrophysiology (Chambers et al., 2016; Li et al., 2017; Zhang et al., 2020). Flux assays and fluorescent membrane potential assays can provide a robust measure of cumulative sodium channel activity and can be tuned to detect specific pharmacological profiles, but they lack temporal resolution and generally require use of non-physiological triggering agents, such as veratridine, which can alter the pharmacological sensitivity of the assay. Binding assays typically use radiolabeled ligands which are less amenable to HTS and the readouts are not directly coupled to sodium channel function. Automated electrophysiology instruments provide a high-resolution linear readout of sodium channel function, but consumable costs and available assay formats currently limit use in HTS campaigns and position this technology as best used in conjunction with HTS fluorescent assays for medium throughput assays and downstream secondary confirmation of compound activity.

The optogenetic assays implemented on Swarm provide the throughput and scalability of conventional fluorescent sodium

channel assays such as FLIPR coupled with the information content, temporal resolution, activation by a physiological stimulus, and flexible control of channel activation obtained with automated E-Phys. In this work, we demonstrate the capabilities of Swarm to execute a Nav1.7 spiking HEK HTS campaign and to perform selectivity assays using Nav1.2 and Nav1.5 spiking HEK assays and hiPSC-derived cardiomyocyte counter screens along with a mechanistic classification of hit compounds. The subtype selectivity, state dependence, and cardiomyocyte toxicity information obtained from Swarm assays provide pharmacological profiles that can be readily generated and contain key information to drive chemical optimization efforts and to prioritize compound selection. The profiles generated for compounds listed in **Figure 3** and shown in **Figure 6** provide potential explanations for why some clinical stage compounds (e.g., vixotrigine and PF-05089771) demonstrated limited clinical success due to a lack of subtype selectivity (vixotrigine) or highly state-dependent inhibition (PF-05089771). The Swarm instrument provided a stable and reliable platform to execute a large-scale screen and downstream activities. We have also demonstrated that spiking HEK assays on Swarm provided reliable compound potency estimates of well-known reference compounds that matched values from previously published literature and from a similar assay performed using a single objective single well serial epifluorescence microscope (Zhang et al., 2020). Future developments of the instrument will implement laser-based illumination to enable the required intensities to fully leverage optogenetic voltage reporters coupled with novel sensing devices to enable extension to 1,536-well plate formats for yet higher throughput screening along with new multiplexing capabilities.

In this study, we focused on Nav channels to demonstrate the applicability to use the Swarm for ion channel drug discovery. However, other types of ion channels may be also compatible with the instrument and the optogenetic assay paradigm. For example, an optogenetic assay for a voltage-gated potassium channel has been previously reported (Zhang et al., 2016). Using optogenetic assays to screen for state-dependent modulators of Cav channels has also been reported and its assay format is compatible with the Swarm (Agus et al., 2015). In addition to channelrhodopsin, other types of light sensitive actuators may also be used to trigger channel activity. For example, a photo-activated adenylyl cyclase, bPAC (Stierl et al., 2011), can be used to induce cAMP concentration changes and trigger the opening of cyclic nucleotide gated (CNG) channels, which could be used for CNG channel modulator screening on the Swarm (Boddum et al., 2021).

Drug discovery projects require integrated use of a wide array of biophysical, biochemical, cell-based, and *in vivo* measurement modalities. Advances in drug discovery are often enabled by technological advances, and technology development can be motivated by drug discovery progress in a virtuous cycle. This relationship was highlighted more generally by Sidney Brenner, "Progress in science depends on new techniques, new discoveries and new ideas, probably in that order" (Brenner, 2002). More specifically, drug discovery for ion channels and excitable cells such as neurons and cardiomyocytes has been propelled by technical developments including patch clamp recordings (Hamill et al., 1981), fluorescence plate readers (Schroeder, 1996; Huang et al., 2006), and automated patch clamp (Fertig et al., 2002; Schroeder et al., 2003). In general, choice of assay methods aims to optimize information content, throughput, and relevance to disease pharmacology (McManus, 2014). Optogenetic assays implemented using the Swarm instrument enable a novel system that combines high information content, high throughput, and deep pharmacological characterization which can be leveraged to drive diverse therapeutic discovery programs for nervous system disorders and other disease areas involving excitable cells.

DATA AVAILABILITY STATEMENT

The datasets presented in this article are not readily available because of proprietary data sets. Requests to access the datasets should be directed to graham.dempsey@qstatebio.com.

AUTHOR CONTRIBUTIONS

GB, HZ, BH, CW, SN, OM, and GD designed the study. GB, YL, AB, and SN built the instrument and acquisition software. GB, HZ, BH, JJ, JG, RC, and DZ acquired the data. GB, HZ, and BH analyzed the data. GB, HZ, BH, YL, OM, and GD interpreted the results and prepared the manuscript. All authors contributed to manuscript revision and approved the submitted version.

FUNDING

This work was supported by funding from National Heart, Lung and Blood Institute grant number 2R44HL126314-02A1 and National Institute of Neurological Disorders and Stroke grant number 1R44NS107041-01.

ACKNOWLEDGMENTS

We would like to thank Steve Wasserman for input on instrumentation engineering and David Gerber for input on the manuscript.

SUPPLEMENTARY MATERIAL

The Supplementary Material for this article can be found online at: https://www.frontiersin.org/articles/10.3389/fnmol.2022.896320/full#supplementary-material

REFERENCES

Agus, V., Di Silvio, A., Rolland, J. F., Mondini, A., Tremolada, S., Montag, K., et al. (2015). Bringing the light to high throughput screening: use of optogenetic tools for the development of recombinant cellular assays. *Opt. Tech. Neurosurg. Neurophoton. Optogenet. II* 9305, 93052T. doi: 10.1117/12.2077579

Albury, C. L., Stuart, S., Haupt, L. M., and Griffiths, L. R. (2017). Ion channelopathies and migraine pathogenesis. *Mol. Genet. Genomics* 292, 729–739. doi: 10.1007/s00438-017-1317-1

Alexandrou, A. J., Brown, A. R., Chapman, M. L., Estacion, M., Turner, J., Mis, M. A., et al. (2016). Subtype-selective small molecule inhibitors reveal a fundamental role for Nav1.7 in nociceptor electrogenesis, axonal conduction and presynaptic release. *PLoS ONE* 11, e0152405. doi: 10.1371/journal.pone.0152405

Benyamin, R., Trescot, A., Datta, S., Buenaventura, R., Adllaka, R., Sehgal, N., et al. (2008). Opioid complications and side effects. *Pain Phys.* 11, S105–S120. doi: 10.36076/ppj.2008/11/s105

Boddum, K., Skafte-Pedersen, P., Rolland, J. -F., and Wilson, S. (2021). "Optogenetics and optical tools in automated patch clamping," in *Patch Clamp Electrophysiology: Methods in Molecular Biology, Vol. 2188*, eds M. Dallas and D. Bell (New York, NY: Springer), 311–330. doi: 10.1007/978-1-0716-0818-0_16

Brenner, S. (2002). Life sentences: detective rummage investigates. *Genome Biol.* 3, 1–2. doi: 10.1186/gb-2002-3-9-comment1013

Bugaj, L. J., and Lim, W. A. (2019). High-throughput multicolor optogenetics in microwell plates. *Nat. Protoc.* 14, 2205–2228. doi: 10.1038/s41596-019-0178-y

Chambers, C., Witton, I., Adams, C., Marrington, L., and Kammonen, J. (2016). High-throughput screening of NaV1.7 modulators using a giga-seal automated patch clamp instrument. *Assay Drug Dev. Technol.* 14, 93–108. doi: 10.1089/adt.2016.700

Cherobin, A. C. F. P., and Tavares, G. T. (2020). Safety of local anesthetics. *Anais Brasileiros de Dermatologia* 95, 82–90. doi: 10.1016/j.abd.2019.09.025

Connor, A. B. (2009). Neuropathic pain: quality-of-life impact, costs and cost effectiveness of therapy. *Pharmacoeconomics* 27, 95–112. doi: 10.2165/00019053-200927020-00002

Cox, J. J., Reimann, F., Nicholas, A. K., Thornton, G., Roberts, E., Springell, K., et al. (2006). An SCN9A channelopathy causes congenital inability to experience pain. *Nature* 444, 894–898. doi: 10.1038/nature05413

Dai, G., Haedo, R. J., Warren, V. A., Ratliff, K. S., Bugianesi, R. M., Rush, A., et al. (2008). A high-throughput assay for evaluating state dependence and subtype selectivity of Cav2 calcium channel inhibitors. *Assay Drug Dev. Technol.* 6, 195–212. doi: 10.1089/adt.2008.136

Dana, H., Mohar, B., Sun, Y., Narayan, S., Gordus, A., Jeremy, P., et al. (2016). Sensitive red protein calcium indicators for imaging neural activity. *eLife* 5, 1–24. doi: 10.7554/eLife.12727.002

de Lera Ruiz, M., and Kraus, R. L. (2015). Voltage-gated sodium channels: structure, function, pharmacology, and clinical indications. *J. Med. Chem.* 58, 7093–7118. doi: 10.1021/jm501981g

Dempsey, G. T., Chaudhary, K. W., Atwater, N., Nguyen, C., Brown, B. S., McNeish, J. D., et al. (2016). Cardiotoxicity screening with simultaneous optogenetic pacing, voltage imaging and calcium imaging. *J. Pharmacol. Toxicol. Methods* 81, 240–250. doi: 10.1016/j.vascn.2016.05.003

Dempsey, G. T., and Werley, C. A. (2017). "Optogenetic approach to cardiotoxicity screening: simultaneous voltage and calcium imaging under paced conditions," in *Stem Cell-Derived Models in Toxicology*, eds M. Clements and L. Roquemore (New York, NY: Springer), 109–134.

Dowden, H., and Munro, J. (2019). Trends in clinical success rates and therapeutic focus. *Nat. Rev. Drug Discov.* 18, 495–496. doi: 10.1038/D41573-019-00074-Z

Du, Y., Days, E., Romaine, I., Abney, K. K., Kaufmann, K., Sulikowski, G., et al. (2015). Development and validation of a thallium flux-based functional assay for the sodium channel NaV1.7 and its utility for lead discovery and compound profiling. *ACS Chem. Neurosci.* 6, 871–878. doi: 10.1021/acschemneuro.5b00004

Dyes, M. P., Felix, J. P., Williams, B. S., Priest, B. T., Brochu, R. M., Dick, I. E., et al. (2004). Functional assay of voltage-gated sodium channels using membrane potential-sensitive dyes. *Assay Drug Dev. Technol.* 2, 260–268. doi: 10.1089/1540658041410696

Eijkenboom, I., Sopacua, M., Hoeijmakers, J. G. J., De Greef, B. T. A., Lindsey, P., Almomani, R., et al. (2019). Yield of peripheral sodium channels gene screening in pure small fibre neuropathy. *J. Neurol. Neurosurg. Psychiatry*. 90, 342–352. doi: 10.1136/jnnp-2018-319042

Emery, E. C., Luiz, A. P., and Wood, J. N. (2016). Nav1.7 and other voltage-gated sodium channels as drug targets for pain relief. *Expert Opin. Therapeut. Targets* 20, 975–983. doi: 10.1517/14728222.2016.1162295

Fertig, N., Blick, R. H., and Behrends, J. C. (2002). Whole cell patch clamp recording performed on a planar glass chip. *Biophys. J.* 82, 3056–3062. doi: 10.1016/S0006-3495(02)75646-4

Flinspach, M., Xu, Q., Piekarz, A. D., Fellows, R., Hagan, R., Gibbs, A., et al. (2017). Insensitivity to pain induced by a potent selective closed-state Nav1.7 inhibitor. *Sci. Rep.* 7, 39662. doi: 10.1038/srep39662

Gingras, J., Smith, S., Matson, D. J., Johnson, D., Nye, K., Couture, L., et al. (2014). Global Nav1.7 knockout mice recapitulate the phenotype of human congenital indifference to pain. *PLoS ONE* 9, e105895. doi: 10.1371/journal.pone.0105895

Goldberg, Y. P., Macfarlane, J., Macdonald, M. L., Thompson, J., Dube, M. P., Mattice, M., et al. (2007). Loss-of-function mutations in the Nav1.7 gene underlie congenital indifference to pain in multiple human populations. *Clin. Genet.* 71, 311–319. doi: 10.1111/j.1399-0004.2007.00790.x

Gribkoff, V. K., and Kaczmarek, L. K. (2017). The need for new approaches in CNS drug discovery : why drugs have failed, and what can be done to improve outcomes. *Neuropharmacology* 120, 11–19. doi: 10.1016/j.neuropharm.2016.03.021

Grosser, T., Woolf, C. J., and FitzGerald, G. A. (2017). Time for nonaddictive relief of pain. *Science* 355, 1026–1027. doi: 10.1126/science.aan0088

Hameed, S. (2019). Nav1.7 and Nav1.8: role in the pathophysiology of pain. *Mol. Pain* 15. doi: 10.1177/1744806919858801

Hamill, O. P., Marty, A., Neher, E., Sakmann, B., and Sigworth, F. J. (1981). Improved patch-clamp techniques for high-resolution current recording from cells and cell-free membrane patches. *Pflugers Arch.* 391, 85–100. doi: 10.1007/BF00656997

Harmer, A. R., Valentin, J. P., and Pollard, C. E. (2011). On the relationship between block of the cardiac Na + channel and drug-induced prolongation of the QRS complex. *Brit. J. Pharmacol.* 164, 260–273. doi: 10.1111/j.1476-5381.2011.01415.x

Hijma, H. J., Siebenga, P. S., De Kam, M. L., and Groeneveld, G. J. (2021). A phase 1, randomized, double-blind, placebo-controlled, crossover study to evaluate the pharmacodynamic effects of VX-150, a highly selective NaV1.8 inhibitor, in healthy male adults. *Pain Med.* 22, 1814–1826. doi: 10.1093/PM/PNAB032

Hochbaum, D. R., Zhao, Y., Farhi, S. L., Klapoetke, N., Werley, C. A., Kapoor, V., et al. (2014). All-optical electrophysiology in mammalian neurons using engineered microbial rhodopsins. *Nat. Methods* 11, 825–833. doi: 10.1038/nmeth.3000

Huang, C.-J., Harootunian, A., Maher, M. P., Quan, C., Raj, C. D., McCormack, K., et al. (2006). Characterization of voltage-gated sodium-channel blockers by electrical stimulation and fluorescence detection of membrane potential. *Nat. Biotechnol.* 24, 439–446. doi: 10.1038/nbt1194

Huang, Y. L., Walker, A. S., and Miller, E. W. (2015). A photostable silicon rhodamine platform for optical voltage sensing. *J. Am. Chem. Soc.* 137, 10767–10776. doi: 10.1021/jacs.5b06644

Imbrici, P., Liantonio, A., Camerino, G. M., de Bellis, M., Camerino, C., Mele, A., et al. (2016). Therapeutic approaches to genetic ion channelopathies and perspectives in drug discovery. *Front. Pharmacol.* 7, 121. doi: 10.3389/fphar.2016.00121

Institute of Medicine of the National Academies (2011). *Relieving Pain in America: A Blueprint for Transforming Prevention, Care, Education, and Research*. National Academies Press. doi: 10.17226/13172

Kaitlin, K. I. (2014). CNS drugs take longer to develop, have lower success rates, than other drugs. *Tufts CSDD Impact Rep.* 16, 1–4. Available online at: http://csdd.tufts.edu/impact-reports#

Keating, M. T., and Sanguinetti, M. C. (2001). Molecular and cellular mechanisms of cardiac arrhythmias. *Cell* 104, 569–580. doi: 10.1016/S0092-8674(01)00243-4

Li, T., Lu, G., Chiang, E. Y., Chernov-Rogan, T., Grogan, J. L., and Chen, J. (2017). High-throughput electrophysiological assays for voltage gated ion channels using SyncroPatch 768PE. *PLoS ONE* 12, e0180154. doi: 10.1371/journal.pone.0180154

Liu, P. W., Blair, N. T., and Bean, B. P. (2017). Action potential broadening in capsaicin-sensitive DRG neurons from frequency-dependent reduction of Kv3 current. *J. Neurosci.* 37, 9705–9714. doi: 10.1523/JNEUROSCI.1703-17.2017

McDonnell, A., Collins, S., Ali, Z., Iavarone, L., Surujbally, R., Kirby, S., et al. (2018). Efficacy of the Nav1.7 blocker PF-05089771 in a randomised, placebo-controlled, double-blind clinical study in subjects with painful diabetic peripheral neuropathy. *Pain* 159, 1465–1476. doi: 10.1097/j.pain.0000000000001227

McManus, O. B. (2014). HTS assays for developing the molecular pharmacology of ion channels. *Curr. Opin. Pharmacol.* 15, 91–96. doi: 10.1016/j.coph.2014.01.004

Millard, D., Dang, Q., Shi, H., Zhang, X., Strock, C., Kraushaar, U., et al. (2018). Cross-site reliability of human induced pluripotent stem cell-derived cardiomyocyte based safety assays using microelectrode arrays: results from a blinded cipa pilot study. *Toxicol. Sci.* 164, 550–562. doi: 10.1093/toxsci/kfy110

Moran, O., Nizzari, M., and Conti, F. (2000). Endogenous expression of the beta1A sodium channel subunit in HEK-293 cells. *FEBS Lett.* 473, 132–134. doi: 10.1016/S0014-5793(00)01518-0

Mulcahy, J. V., Pajouhesh, H., Beckley, J. T., Delwig, A., du Bois, J., and Hunter, J. C. (2019). Challenges and opportunities for therapeutics targeting the voltage-gated sodium channel isoform NaV1.7. *J. Med. Chem.* 62, 8695–8710. doi: 10.1021/acs.jmedchem.8b01906

Ogiwara, I., Ito, K., Sawaishi, Y., Osaka, H., Mazaki, E., Inoue, I., et al. (2009). De novo mutations of voltage-gated sodium channel alphaII gene SCN2A in intractable epilepsies. *Neurology* 73, 1046–1053. doi: 10.1212/WNL.0b013e3181b9cebc

Ponce, A., Castillo, A., Hinojosa, L., Martinez-Rendon, J., and Cereijido, M. (2018). The expression of endogenous voltage-gated potassium channels in HEK293 cells is affected by culture conditions. *Physiol. Rep.* 6, e13663. doi: 10.14814/phy2.13663

Reid, C. A., Maljevic, S., Petrou, S., Oyrer, J., Scheffer, I. E., and Berkovic, S. F. (2017). Ion channels in genetic epilepsy: from genes and mechanisms to disease-targeted therapies. *Pharmacol. Rev.* 70, 142–173. doi: 10.1124/pr.117.014456

Schoepp, D. D. (2011). Where will new neuroscience therapies come from? *Nat. Rev. Drug Discov.* 10, 715–716. doi: 10.1038/nrd3559

Schroeder, K., Neagle, B., Trezise, D. J., and Worley, J. (2003). IonWorksTM HT: a new high-throughput electrophysiology measurement platform. *J. Biomol. Screen.* 8, 50–64. doi: 10.1177/1087057102239667

Schroeder, K. S. (1996). FLIPR: a new instrument for accurate, high throughput optical screening. *J. Biomol. Screen.* 1, 75–80. doi: 10.1177/108705719600100205

Shields, S. D., Deng, L., Reese, R. M., Dourado, M., Tao, J., Foreman, O., et al. (2018). Insensitivity to pain upon adult-onset deletion of Nav1.7 or its blockade with selective inhibitors. *J. Neurosci.* 38, 10180–10201. doi: 10.1523/JNEUROSCI.1049-18.2018

Snowball, A., and Schorge, S. (2015). Changing channels in pain and epilepsy: exploiting ion channel gene therapy for disorders of neuronal hyperexcitability. *FEBS Lett.* 589, 1620–1634. doi: 10.1016/J.FEBSLET.2015.05.004

Song, C., and Knöpfel, T. (2016). Optogenetics enlightens neuroscience drug discovery. *Nat. Rev. Drug Discov.* 15, 97–109. doi: 10.1038/nrd.2015.15

Splawski, I., Timothy, K. W., Tateyama, M., Clancy, C. E., Malhotra, A., Beggs, A. H., et al. (2002). Variant of SCN5A sodium channel implicated in risk of cardiac arrhythmia. *Science* 297, 1333–1336. doi: 10.1126/SCIENCE.1073569

Stierl, M., Stumpf, P., Udwari, D., Gueta, R., Hagedorn, R., Losi, A., et al. (2011). Light modulation of cellular cAMP by a small bacterial photoactivated adenylyl cyclase, bPAC, of the soil bacterium Beggiatoa. *J. Biol. Chem.* 286, 1181–1188. doi: 10.1074/JBC.M110.185496

Trivedi, S., Dekermendjian, K., Julien, R., Huang, J., Lund, P. E., Krupp, J., et al. (2008). Cellular HTS assays for pharmacological characterization of Na V1.7 modulators. *Assay Drug Dev. Technol.* 6, 167–179. doi: 10.1089/adt.2007.090

Tsukamoto, T., Chiba, Y., Wakamori, M., Yamada, T., Tsunogae, S., Cho, Y., et al. (2017). Differential binding of tetrodotoxin and its derivatives to voltage-sensitive sodium channel subtypes (Nav1. 1 to Nav1. 7). *Brit. J. Pharmacol.* 174, 3881–3892. doi: 10.1111/bph.13985

Veerman, C. C., Wilde, A. A. M., and Lodder, E. M. (2015). The cardiac sodium channel gene SCN5A and its gene product NaV1.5: role in physiology and pathophysiology. *Gene* 573, 177–187. doi: 10.1016/J.GENE.2015.08.062

Vilin, Y. Y., Peters, C. H., and Ruben, P. C. (2012). Acidosis differentially modulates inactivation in Nav1.2, Nav1.4, and Nav1.5 channels. *Front. Pharmacol.* 3, 109. doi: 10.3389/fphar.2012.00109

Walther, F., Feind, D., vom Dahl, C., Müller, C. E., Kukaj, T., Sattler, C., et al. (2020). Action potentials in *Xenopus* oocytes triggered by blue light. *J. Gen. Physiol.* 152, e201912489. doi: 10.1085/JGP.201912489/151581

Wang, J., Ou, S. W., and Wang, Y. J. (2017). Distribution and function of voltage-gated sodium channels in the nervous system. *Channels* 11, 534–554. doi: 10.1080/19336950.2017.1380758

Wang, Y., Mi, J., Lu, K., Lu, Y., and Wang, K. W. (2015). Comparison of gating properties and use-dependent block of Nav1.5 and Nav1.7 channels by anti-arrhythmics mexiletine and lidocaine. *PLoS ONE* 10, e0128653. doi: 10.1371/journal.pone.0128653

Waszkielewicz, A. M., Gunia, A., Szkaradek, N., Soczyska, K., Krupiska, S., and Marona, H. (2013). Ion channels as drug targets in central nervous system disorders. *Curr. Med. Chem.* 20, 1241–1285. doi: 10.2174/0929867311320100005

Werley, C. A., Chien, M.-P., and Cohen, A. E. (2017). An ultrawidefield microscope for high-speed fluorescence imaging and targeted optogenetic stimulation. *Biomed. Opt. Express* 8, 5794. doi: 10.1364/BOE.8.005794

Zhang, H., and Cohen, A. E. (2017). Optogenetic approaches to drug discovery in neuroscience and beyond. *Trends Biotechnol.* 35, 625–639. doi: 10.1016/j.tibtech.2017.04.002

Zhang, H., Moyer, B. D., Yu, V., McGivern, J. G., Jarosh, M., Werley, C. A., et al. (2020). Correlation of optical and automated patch clamp electrophysiology for identification of NaV1.7 inhibitors. *SLAS Discov.* 25, 434–446. doi: 10.1177/2472555220914532

Zhang, H., Reichert, E., and Cohen, A. E. (2016). Optical electrophysiology for probing function and pharmacology of voltagegated ion channels. *eLife* 5, e15202. doi: 10.7554/eLife.15202

Zhang, H., Zou, B., Du, F., Xu, K., and Li, M. (2014). Reporting sodium channel activity using calcium flux: pharmacological promiscuity of cardiac Nav1.5. *Mol. Pharmacol.* 9, 251–258. doi: 10.1124/mol.114.094789

Conflict of Interest: GB, HZ, BH, JJ, JG, RC, DZ, AB, CW, YL, SN, OM, and GD are current or former employees of Q-State Biosciences and may hold stock options in Q-State Biosciences.

Publisher's Note: All claims expressed in this article are solely those of the authors and do not necessarily represent those of their affiliated organizations, or those of the publisher, the editors and the reviewers. Any product that may be evaluated in this article, or claim that may be made by its manufacturer, is not guaranteed or endorsed by the publisher.

frontiers | Frontiers in Molecular Neuroscience

TYPE Original Research
PUBLISHED 09 August 2022
DOI 10.3389/fnmol.2022.976910

OPEN ACCESS

EDITED BY
Tim Strassmaier,
Nanion Technologies GmbH, Germany

REVIEWED BY
Andreas Reiner,
Ruhr University Bochum, Germany
Ludovic Tricoire,
Sorbonne Universités, France
Paul Slesinger,
Icahn School of Medicine at Mount Sinai, United States

*CORRESPONDENCE
John L. Spudich
John.L.Spudich@uth.tmc.edu

SPECIALTY SECTION
This article was submitted to Molecular Signalling and Pathways, a section of the journal Frontiers in Molecular Neuroscience

RECEIVED 23 June 2022
ACCEPTED 21 July 2022
PUBLISHED 09 August 2022

CITATION
Govorunova EG, Sineshchekov OA, Brown LS and Spudich JL (2022) Biophysical characterization of light-gated ion channels using planar automated patch clamp. *Front. Mol. Neurosci.* 15:976910. doi: 10.3389/fnmol.2022.976910

Biophysical characterization of light-gated ion channels using planar automated patch clamp

Elena G. Govorunova[1], Oleg A. Sineshchekov[1], Leonid S. Brown[2] and John L. Spudich[1]*

[1]Department of Biochemistry and Molecular Biology, Center for Membrane Biology, The University of Texas Health Science Center at Houston McGovern Medical School, Houston, TX, United States, [2]Biophysics Interdepartmental Group, Department of Physics, University of Guelph, Guelph, ON, Canada

Channelrhodopsins (ChRs) are proteins that guide phototaxis in protists and exhibit light-gated channel conductance when their genes are heterologously expressed in mammalian cells. ChRs are widely used as molecular tools to control neurons and cardiomyocytes with light (optogenetics). Cation- and anion-selective ChRs (CCRs and ACRs, respectively) enable stimulation and inhibition of neuronal activity by depolarization and hyperpolarization of the membrane, respectively. More than 400 natural ChR variants have been identified so far, and high-throughput polynucleotide sequencing projects add many more each year. However, electrophysiological characterization of new ChRs lags behind because it is mostly done by time-consuming manual patch clamp (MPC). Here we report using a high-throughput automated patch clamp (APC) platform, SyncroPatch 384i from Nanion Technologies, for ChR research. We find that this instrument can be used for determination of the light intensity dependence and current-voltage relationships in ChRs and discuss its advantages and limitations.

KEYWORDS

channelrhodopsins, optogenetics, potassium channels, kalium channelrhodopsins, automated patch clamp, light-gated channels

Introduction

For control of neural circuitry, light provides a much higher spatial and temporal resolution than conventional pharmacological interventions. Microbial rhodopsins are photoactive proteins, in which photon absorption triggers diverse molecular functions, from protein-protein interaction to ion transport (Govorunova et al., 2017; Rozenberg et al., 2021). Expression of microbial rhodopsin genes in animal and human cells enables photocontrol of their biochemical and physiological properties, which is now referred to as optogenetics (Deisseroth, 2015). So far, the most impactful optogenetic application has been manipulation of the electrical activity of neurons and cardiomyocytes using

channelrhodopsins (ChRs), photoactivation of which results in passive transmembrane conductance. ChRs are widely used in neuroscience and cardiology research, and their potential to treat Alzheimer's disease (Cui et al., 2020), Parkinson's disease (Yu et al., 2020), epilepsy (Paschen et al., 2020), cardiac arrythmias (Cheng et al., 2020), and many other neurological, psychiatric and cardiological disorders has been demonstrated in animal models. A report of successful partial vision restoration in a blind human patient using a ChR was published last year (Sahel et al., 2021).

Different optogenetic applications require ChR variants with different properties, most important of which is ion selectivity. ChRs that generate H^+ and Na^+ influx in mammalian cells (cation-conducting ChRs, or CCRs) have been found as phototaxis receptors in chlorophyte algae (Nagel et al., 2002, 2003; Sineshchekov et al., 2002) and are used to stimulate neuronal spiking with light (Boyden et al., 2005; Deisseroth, 2011). ChR2 from the green alga *Chlamydomonas reinhardtii* (*Cr*ChR2) and its mutants are the most frequently used tools for this purpose (Wietek and Prigge, 2016). Anion-conducting ChRs (ACRs), found in cryptophyte algae and some other marine protists (Govorunova et al., 2015, 2020; Oppermann et al., 2019; Rozenberg et al., 2020), are used to inhibit neuronal activity. Very recently, KCRs, a new family of ChRs with a high selectivity for K^+ over Na^+ has been discovered and used to silence neurons with light (Govorunova et al., 2022). ChRs with red-shifted absorption spectra are generally preferable for optogenetics (Klapoetke et al., 2014; Govorunova et al., 2020), because red light more deeply penetrates biological tissue. However, use of ChRs in combination with fluorescent voltage sensors for all-optical electrophysiology creates a demand also for blue light-absorbing ChRs (Fan et al., 2020). Finally, precise optical control of neurons firing at high frequencies (Keppeler et al., 2018) and prolonged inhibition of neuronal activity (Stahlberg et al., 2019) need ChRs with fast or slow photocurrent kinetics, respectively. These requirements call for novel ChRs variants with the desired properties either identified in nature or engineered in the laboratory.

Several hundred natural ChRs variants have been identified (Rozenberg et al., 2020; Govorunova et al., 2021), and many more are reported each year in ongoing genome/transcriptome sequencing projects (Bork et al., 2015). Conventional manual patch clamp (MPC), generally used for electrophysiological characterization of ChRs, requires considerable expertise and is time-consuming. Recently, high-throughput, automated patch clamp (APC) platforms have become increasingly popular in ion channel research and drug discovery (Bell and Fermini, 2021; Obergrussberger et al., 2021). The SyncroPatch 384i platform from Nanion Technologies uses a "bottom-up" planar configuration to allow compatibility with a multiwell plate format to enable simultaneous recording from 384 wells (in a one-module configuration) or 768 wells (in a two-module configuration). Each well of a multiwell plate has one or several small apertures (holes) in the bottom surface made of borosilicate glass. A suspension of target cells is introduced into the wells, after which a negative pressure is applied to capture the cells in the apertures and form Gigaohm (GΩ) seals. Integrated robotic operation for handling of cells, solutions, and compounds provides standardization of all procedures. The SyncroPatch 384i offers unprecedented high throughput close to that of non-electrophysiological screening techniques such as ion-flux measurements and fluorescence assays, with the added benefit of real-time monitoring of channel activity. This instrument and its earlier modifications have already been used to probe voltage- and ligand-gated ion channels in a variety of cell types (Brinkwirth et al., 2020; Potet et al., 2020; Obergrussberger et al., 2022).

We were granted access by Nanion to a SyncroPatch 384 for a 9-months pilot program to evaluate its utility for ChR research. We used this APC platform to characterize photocurrents from three ChR variants. *Hc*KCR1 from *Hyphochytrium catenoides* is a member of a recently discovered class of ChRs that exhibit higher relative permeability to K^+ than to Na^+ detected by MPC (Govorunova et al., 2022). *Hc*CCR is a previously uncharacterized paralog from the same organism, and *Cr*ChR2, the most-studied CCR, was included for comparison. Here we report the results obtained with these three ChRs and discuss the advantages and disadvantages of the SyncroPatch system for ChR research.

Materials and methods

The genes encoding the three *H. catenoides* rhodopsins were identified by Leonard et al. (2018), and refinement of the sequences of *Hc*KCR1 and *Hc*KCR2 has been described by us recently (Govorunova et al., 2022). Initially, we obtained the predicted protein sequence for *Hc*CCR from the database provided by Leonard and Richards,[1] the file hyphochytrium_catenoides_predicted_proteins_renamed _modified. Upon close inspection of an alignment of the predicted transmembrane (TM) domains of these rhodopsins it became clear that the *Hc*CCR sequence is missing part of helix 5. This prompted us to reconfirm the sequence of its TM domain by performing a TBLASTN search of the whole-genome sequencing (WGS) data for *H. catenoides* (Accession FLMG00000000.1 and CAFC00000000.2) at the National Center for Biotechnology Information (NCBI), using the *Hc*CCR sequence provided by Leonard et al. (2018) as the query. The resultant alignments allowed us to build the full sequence for the TM regions of *Hc*CCR with high confidence.

Mammalian codon-adapted polynucleotides encoding the TM domains of *Hc*KCR1, *Hc*CCR and *Cr*ChR2 were synthesized

1 https://www.ebi.ac.uk/biostudies/studies/S-BSST46

and cloned by Genscript Biotech Corporation into the mammalian expression vector pcDNA3.1 (Invitrogen, Cat. #V790-20) in frame with a C-terminal mCherry (*Hc*KCR1 and *Hc*CCR) or EYFP (enhanced yellow fluorescent protein, *Cr*ChR2) tag. The expression construct encoding the TM domain of *Hc*CCR has been deposited in Genbank (accession # OL692497). HEK293 (human embryonic kidney) cells (ATCC, Cat. #CRL-1573; RRID: CVCL_0045) were transfected using the ScreenFect A plus transfection reagent (Fujifilm Waco Chemicals, Cat. #297-77104). All-*trans*-retinal (Sigma-Aldrich, Cat. # R2500) was added from a stock solution in ethanol at the final concentration of 5 μM. Measurements were performed 48–72 h after transfection at room temperature.

Automated whole-cell patch clamp recording was conducted with a SyncroPatch 384i (Nanion Technologies) using planar borosilicate glass medium-resistance chips in a 384-microtiter plate format with one hole per well and Nanion Standard solutions (for their compositions see **Supplementary Table 1**). Transfected cells were dissociated using TrypLE^{TM} Express, diluted with CHO-S-SFM-II medium (both from ThermoFisher, Cat.# 12604013 and 31033020, respectively) and resuspended in External Physiological solution (Nanion Technologies) at 10^5-4 × 10^5 cells ml^{-1}. Each well was filled with 30 μl Chip Fill solution, to which 20 μl of the cell suspension was added. Seal formation was enhanced by the addition of 40 μl of the External Physiological solution supplemented with 10 mM $CaCl_2$ (final concentration). After formation of GΩ seals, 50 μl of the external solution mixture was replaced with 40 μl of External Physiological solution to reduce the Ca^{2+} concentration. For measurements of the pH dependence, the pH of all solutions except that used for resuspension of the cells was adjusted prior to the experiment to 5.4 or 9.4. The final pH during recording was 5.8 or 8.6, as measured in a solution mixture that mimicked that produced by the SyncroPatch. The internal solution in all experiments was KF 110 Internal (Nanion Technologies). All measurements were carried out at room temperature (25°C). Calculation of the series resistance (R_s) was automatically performed during all recordings, and the recordings with R_s > 10 MΩ were not included in the analysis.

Photostimulation was provided with LUXEON Z Color Line light-emitting diodes (LEDs) (Lumileds), Cat.# LXZ1-PB01 (470 ± 20 nm, 38 lm at 500 mA, 25°C) or Cat.# LXZ1-PM01 (530 ± 30 nm, 118 lm at 500 mA, 25°C) arranged in a 6 × 16 matrix that covered a quarter of the 384-well chip. The 10–90% rise time for both LED types was < 100 ns. Other technical characteristics of the LEDs, such as spectral power distribution, radiation patterns, color bin structure and mechanical dimensions are provided on the manufacturer's website.[2] For green LEDs (LXZ1-PM01), two prototype modifications of the photostimulation hardware were tested. In the first modification (**Supplementary Figure 1A**), the LED matrix was simply placed on top of the amplifier grid. In the second modification (**Supplementary Figure 1B**), the matrix was encapsulated in an adaptor that could be fixed on top of the grid in a precise position. Furthermore, a thin class IP68 light guide with a counterbore round head (Mentor, Cat. #1292.1601; length 11.5 mm, diameter 2.2 mm) was attached to each LED to bring the light closer to the cells. In the first modification, the maximal available forward current was 475 mA, in the second, 900 mA. The blue LEDs (LXZ1-PB01) were available only in the first modification of hardware. With both modifications, the matrix had to be repositioned four times during each experiment to cover the entire chip. According to the manufacturer's data, the dependence of luminosity on the forward LED current was close to linear (**Supplementary Figure 1C**). The LEDs were driven by a derivative of the CardioExcyte 96 SOL (Nanion, Cat. #191003) and controlled by Biomek commands in combination with a custom stand-alone software provided by Nanion. Variation of the time delay between the programmed and actual light onset is shown in **Supplementary Figure 1D**.

For data acquisition, PatchControl384 v. 1.9.0 (Nanion Technologies) software was used. The acquisition rate was 200 μs per point (5 kHz sampling rate). The SyncroPatch output was filtered with an analog Bessel filter at 3 kHz and a digital low-pass Lanzcos filter at 3 kHz. The data were analyzed by DataControl384 software v. 1.9.0 (Nanion Technologies). The current traces were also exported in the text format and analyzed by ClampFit, a subroutine of pClamp 10.7 software (Molecular Devices). The kinetics of the current rise and decay was evaluated, respectively, by single and double exponential approximation in ClampFit. Further analysis was performed by Origin Pro 2016 software (OriginLab Corporation). Desensitization was calculated as the difference between the peak and desensitized current divided by the peak current (in %).

Control MPC measurements were performed with an Axopatch 200B amplifier (Molecular Devices) using the same solutions as in the SyncroPatch experiments. The low-pass filter of the amplifier output was set to 2 kHz. The signals were digitized with a Digidata 1440A (Molecular Devices) at 5 kHz sampling rate (200 μs per point) using pClamp 10. Patch pipettes with resistances of 2–4 MΩ were fabricated from borosilicate glass. Continuous light pulses were provided by a Polychrome IV light source (T.I.L.L. Photonics GmbH) in combination with a mechanical shutter (Uniblitz Model LS6, Vincent Associates; half-opening time 0.5 ms). Maximal irradiance at the focal plane of the 40 × objective lens was ∼6.4 mW mm^{-2} at 530 nm and was attenuated using neutral density filters.

Descriptive statistics was calculated by Origin software. The data are presented as mean ± sem values, as indicated in

2 https://lumileds.com/wp-content/uploads/files/DS105-LUXEON-Z-Color-Line-datasheet.pdf

the figure legends; the data from individual replicates are also shown when appropriate. The sample size was estimated from previous experience and published work on similar subjects, as recommended by NIH guidelines. No normal distribution of the data was assumed; when a specific statistics hypothesis was tested, the non-parametric Mann-Whitney test (implemented in Origin software) was used.

Results

Seal quality and stability

To test the quality and stability of the seals obtained using the SyncroPatch, we expressed *Hc*KCR1 in HEK293 cells using chemical transfection (for more detail see section "Materials and methods"). The *H. catenoides* genome encodes three ChR paralogs (Leonard et al., 2018). *Hc*KCR1 and *Hc*KCR2 exhibit higher relative permeability for K^+ over Na^+, as determined by MPC (Govorunova et al., 2022). To the best of our knowledge, the third paralog had not yet been tested by heterologous expression and patch clamp electrophysiology. The SyncroPatch allows monitoring the resistance at predetermined time points during the entire experiment. **Supplementary Figure 2A** shows changes in the seal resistance of four representative wells during the execution of the CellCatch command that applies 10-ms voltage steps (from –20 to –30 mV) to test the seal resistance. As evident from the increase in the resistance starting ∼15 s after the addition of the cells, wells 1–3 had successfully captured the cells, whereas well 4 captured no cell. The success rate of the cell capture (>10 MΩ resistance after the addition of the cells to the wells) was ∼85% in our experiments. **Supplementary Figure 2B** shows the percentage of captured cells that showed a membrane resistance (R_m) > 500 MΩ after the addition of the seal enhancer (10 mM $CaCl_2$), wash with the external solution, formation of the whole-cell configuration, and each of the four applications of the voltage step protocol (from –100 to 20 mV in 20-mV steps) in six independent experiments. The seals demonstrated excellent stability during all these manipulations. The dependence of the R_m on the holding voltage is shown in **Supplementary Figure 2C**. The duration of a typical experiment was ∼20 min from the time of the cell capture, including the time needed to relocate the LED board.

Optimization of photostimulation

The tested version of the SyncroPatch does not have integrated photostimulation capacity, so one of the aims of our study was side-by-side comparison of the two prototypes of the add-on photostimulation unit (**Supplementary Figures 1A,B**; for more detail see section "Materials and methods"). Representative photocurrent traces generated by *Hc*KCR1 in response to light pulses produced by the two modifications of the photostimulation unit are shown in **Supplementary Figures 3A, B**, top traces. The first version of the photostimulation unit, in which the LED array was directly placed on top of the Faraday cage enclosing the chip, produced rapid (one data point, i.e., < 200 μs) light artifacts of variable amplitude accompanying switching the light on and off (**Supplementary Figure 3A**, middle and bottom traces), which could be removed digitally (**Supplementary Figure 3A**, top trace). The second version of the photostimulation unit, with the lightguides attached, produced no such artifacts. Non-transfected cells generated no photoresponses except the abovementioned artifacts with the first version of the photostimulation unit (**Supplementary Figures 3A,B**, bottom traces). Comparison of the current kinetics clearly showed that the second version produced stronger light, as only in this case the current traces exhibited a peak followed by a decrease to a lower steady-state level (a phenomenon known as "desensitization"). In **Supplementary Figures 3C,D** we show the current amplitude at the end of a 200-ms light pulse recorded from all 384 individual wells, and **Supplementary Figures 3E,F**, the corresponding histograms. The cell-to-cell variation of the current amplitude was consistent with variation of the fluorescence and photocurrents measured from similar cultures in MPC experiments. The current amplitude averaged over all 384 wells (including those that captured no cells or non-fluorescent cells) was 28 ± 5 and 81 ± 5 pA with the first and second version, respectively, which confirmed that the second modification of the hardware produced stronger light. Next, we carried out a detailed analysis of the dependence of *Hc*KCR1 photocurrents on the light intensity using the optimized photostimulation unit.

Light intensity dependence

Figure 1A shows a representative series of photocurrent traces recorded from a single cell expressing *Hc*KCR1 at 20 mV holding voltage in response to light pulses at incrementally increased LED forward current and thus light intensity. According to the manufacturer's data, the LED luminosity almost linearly increased upon an increase in the forward current (**Supplementary Figure 1C**). Comparison of the current kinetics recorded with the SyncroPatch with that recorded at the same voltage and ionic conditions by MPC using a calibrated light source (**Figure 1B**) showed that the LED output at 40 mA forward current roughly corresponded to 0.2 mW mm^{-2}. **Figure 1C** shows the dependence of the peak current on the LED forward current for 20 individual cells that generated the largest response. The mean dependence measured when the intensity was increased from low to high closely matched that measured when the intensity was changed in the reversed order (**Figure 1D**), which indicated that the 30-s interval between subsequent light pulses was sufficient for the full recovery of *Hc*KCR1, and that only minimal bleaching/rundown was

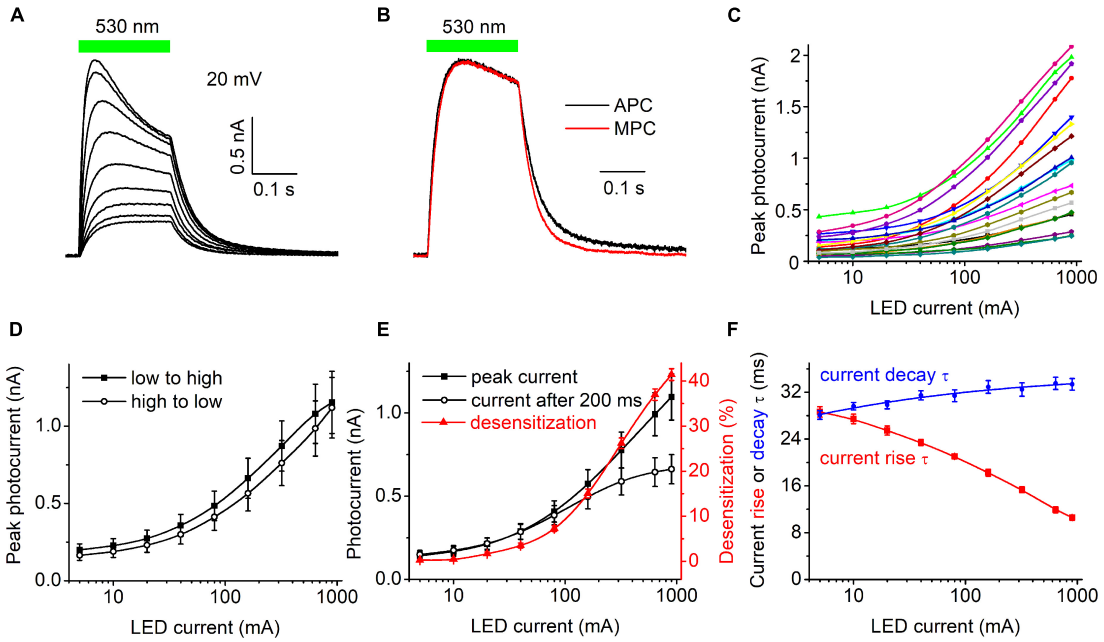

FIGURE 1
(A) A series of photocurrent traces generated by *Hc*KCR1 at 20 mV in response to 200-ms light pulses of incremental intensity. The bar on top shows the duration of illumination. **(B)** Comparison of the normalized photocurrent traces recorded by automated patch clamp (APC, black) at 40 mA forward LED current and by manual patch clamp at 0.2 mW mm^{-2} (MPC, red). **(C)** The dependence of the peak current amplitude on the light intensity (LED current) for 20 individual cells. **(D)** The mean curves for the responses measured upon variation of the LED current from low to high and from high to low values. **(E)** The mean curves for the peak current and desensitized current at the end of the 200-ms light pulse (black symbols and lines, left axis). The red symbols and line (right axis) show the degree of desensitization calculated as the difference between the peak current and the current at the end of 200-ms illumination divided by the peak current and multiplied by 100%. The data points in **(C,E)** are connected with spline lines. **(F)** The dependence of photocurrent rise τ (red) and the main (fast) decay τ (blue) on the light intensity. The data points for the rise τ are connected with a B-spline line; the data for the decay τ are approximated with a logistic function.

observed. The amplitude of the photocurrent measured at the end of 200-ms illumination saturated earlier than the peak (**Figure 1E**), as in other ChRs studied earlier by MPC (Ishizuka et al., 2006; Ernst et al., 2008). The dependence of desensitization on the LED forward current is shown as the red symbols and line in **Figure 1E**. **Figure 1F** shows the dependence of the time constants (τ) of the photocurrent rise (red) and decay (blue) on the LED current.

Current-voltage relationships of three channelrhodopsin variants and their dependence on external pH

Our previous MPC study showed that *Hc*KCR1 exhibits > 100 times less permeability for protons than *Cr*ChR2 (Govorunova et al., 2022). This is very unusual among known CCRs, so we sought to verify this result with the SyncroPatch. Representative series of photocurrent traces generated by *Hc*KCR1 at incrementally increased holding voltages at pH 5.8, 7.4, and 8.6 are shown in **Figures 2A–C**. Our analysis of *Hc*KCR1 photocurrents by MPC showed that its P_K/P_{Na} permeability ratio decreases during continuous illumination (Govorunova et al., 2022). This decrease explains the biphasic (first positive, then negative) photocurrent trace recorded at –60 mV in **Figure 2A**. The current-voltage relationships (*IE* curves) for individual cells that generated the largest response are shown in **Figures 2D–F**. We used well-characterized *Cr*ChR2 as a positive control for proton permeability. Representative series of photocurrent traces generated by *Cr*ChR2 under the same ionic conditions as used for *Hc*KCR1 are shown in **Figures 3A–C**, and the corresponding *IE* curves, in **Figures 3D–F**. In contrast to *Hc*KCR1, alkalization strongly suppressed *Cr*ChR2 photocurrents (in fact, at pH 8.6 only a few cells generated currents that could be resolved from the noise). **Figure 4** shows the results of characterization of the third ChR paralog from *H. catenoides* using the SyncroPatch. Despite its 74.4% primary structure identity and 87% similarity with *Hc*KCR1 (**Supplementary Figure 4**), the E_{rev} of photocurrents generated by this ChR was positive under our conditions (**Figure 4**), which indicated that it was more permeable for Na^+ than K^+. Therefore, we named this protein *Hc*CCR for "*H. catenoides* cation channelrhodopsin."

Comparison of the E_{rev} values for all three tested ChRs are shown in **Figure 5A**. The E_{rev} of *Hc*KCR1 photocurrents was strongly negative and showed no dependence on pH in

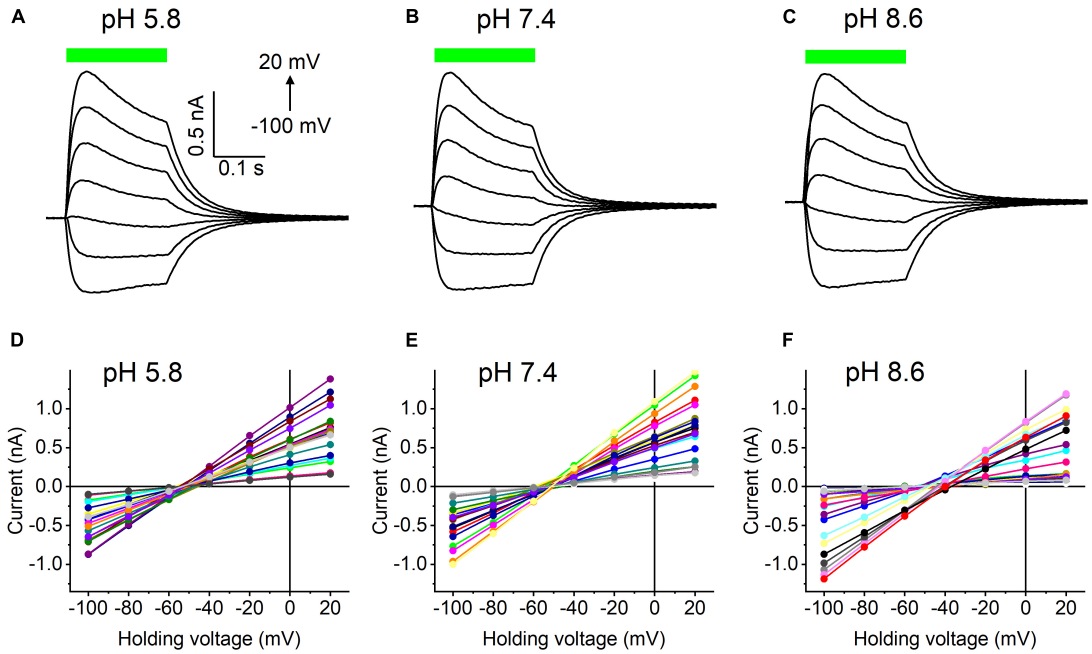

FIGURE 2
(A–C) Photocurrent traces recorded from *Hc*KCR1 at the indicated external pH in response to a 200-ms light pulse (530 nm, 900 mA), the duration of which is shown as a colored bar on top. The holding voltage was varied from −100 to 20 mV in 20-mV steps. **(D–F)** Current-voltage relationships of *Hc*KCR1 measured in individual cells. The current amplitude was measured at the end of a 200-ms light pulse.

the tested range, which was consistent with the results of our previous MPC study (Govorunova et al., 2022). In contrast, the E_{rev} of *Cr*ChR2 shifted upon variation of pH, which matched previous observations by MPC (Nagel et al., 2003; Tsunoda and Hegemann, 2009). The E_{rev} of *Hc*CCR at pH 7.4 was more positive than that of *Cr*ChR2, indicating that *Hc*CCR exhibits a higher Na^+/K^+ permeability ratio than *Cr*ChR2. The E_{rev} of *Hc*CCR exhibited only a small E_{rev} shift upon alkalization, indicating its lower relative permeability for protons than that of *Cr*ChR2.

As shown previously by MPC, the decay kinetics of *Cr*ChR2 photocurrents accelerates upon alkalization (Tsunoda and Hegemann, 2009). The SyncroPatch (**Figure 5B**) recordings reproduced this effect. In contrast to *Cr*ChR2, the decay of *Hc*KCR1 photocurrents was independent of pH, whereas the decay of *Hc*CCR photocurrents slightly slowed at alkaline pH.

Discussion

As of this writing, APC platforms have been used mostly for characterization of mammalian voltage- and ligand-gated ion channels and drug discovery (Brinkwirth et al., 2020; Potet et al., 2020; Bell and Fermini, 2021; Obergrussberger et al., 2021, 2022). Here we tested the SyncroPatch 384i for characterization of ChRs, light-gated ion channels from eukaryotic microbes, expressed in model human cells as C-terminal EYFP or mCherry fusions. Planar APC using the SyncroPatch offers an important advantage over MPC or even pipette-based APC (Kolb et al., 2019), as it completely eliminates the bias introduced by the investigator's selection of fluorescent cells for patching. However, this advantage is relevant only if all cells express the transgene. Stably transfected cell lines have been created for *Cr*ChR2 (Zimmermann et al., 2006), but not for *Hc*KCR1 and *Hc*CCR. Therefore, we used transient chemical transfection to avoid time-consuming generation of stable lines, as we had access to the SyncroPatch 384i for only a limited time. The efficiency of chemical transfection in our experiments, estimated by microscopic observation of tag fluorescence, was 50-70%, which explained the absence of photocurrents in some cells captured in a multiwell plate. Therefore, using chemical transfection saved time, but reduced the throughput. Viral delivery of transgenes yielding higher transfection efficiency may provide a reasonable compromise between time and throughput.

Variability of the time delay between the programmed and actual onset of illumination (**Supplementary Figure 1D**) needs to be taken into account to avoid introducing errors during automatic measurements of photocurrent amplitudes by DataControl384 software. This variability can easily be accounted for if the recorded traces are exported and analyzed individually by ClampFit or other relevant software. According to Nanion engineers, this variability is due to the Biomek command used to trigger the LEDs, not to the LEDs

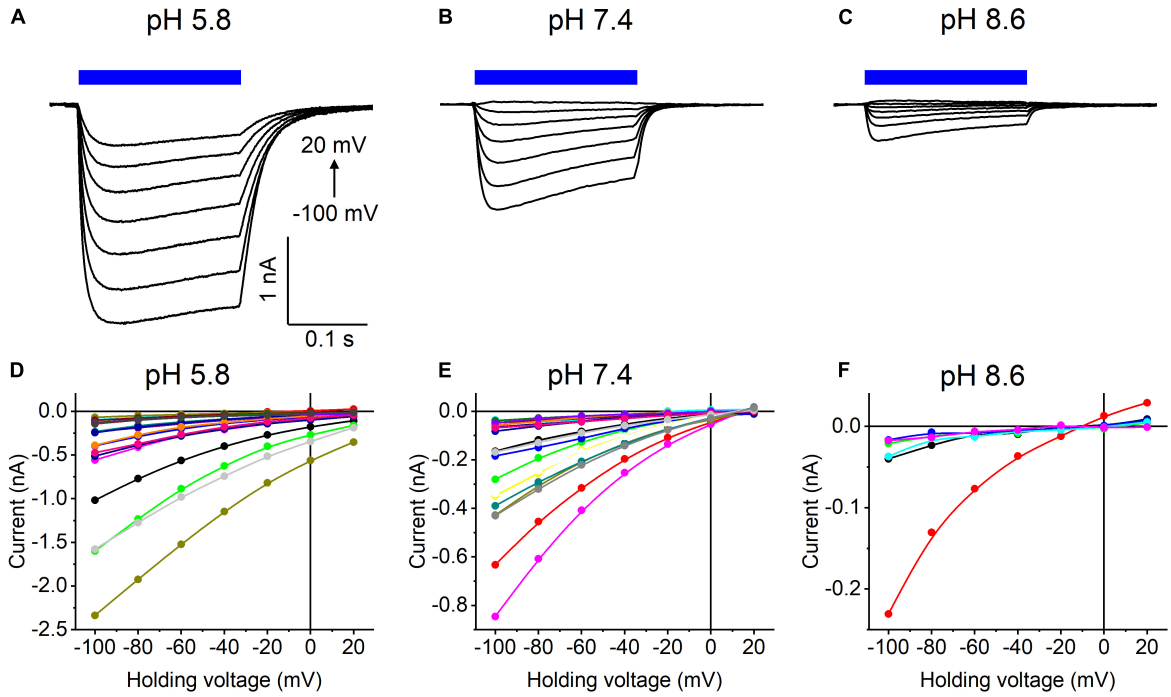

FIGURE 3
(A–C) Photocurrent traces recorded from *Cr*ChR2 at the indicated external pH in response to a 200-ms light pulse (470 nm, 475 mA), the duration of which is shown as a colored bar on top. The holding voltage was varied from −100 to 20 mV in 20-mV steps. **(D–F)** Current-voltage relationships of *Cr*ChR2 measured in individual cells. The current amplitude was measured at the end of a 200-ms light pulse.

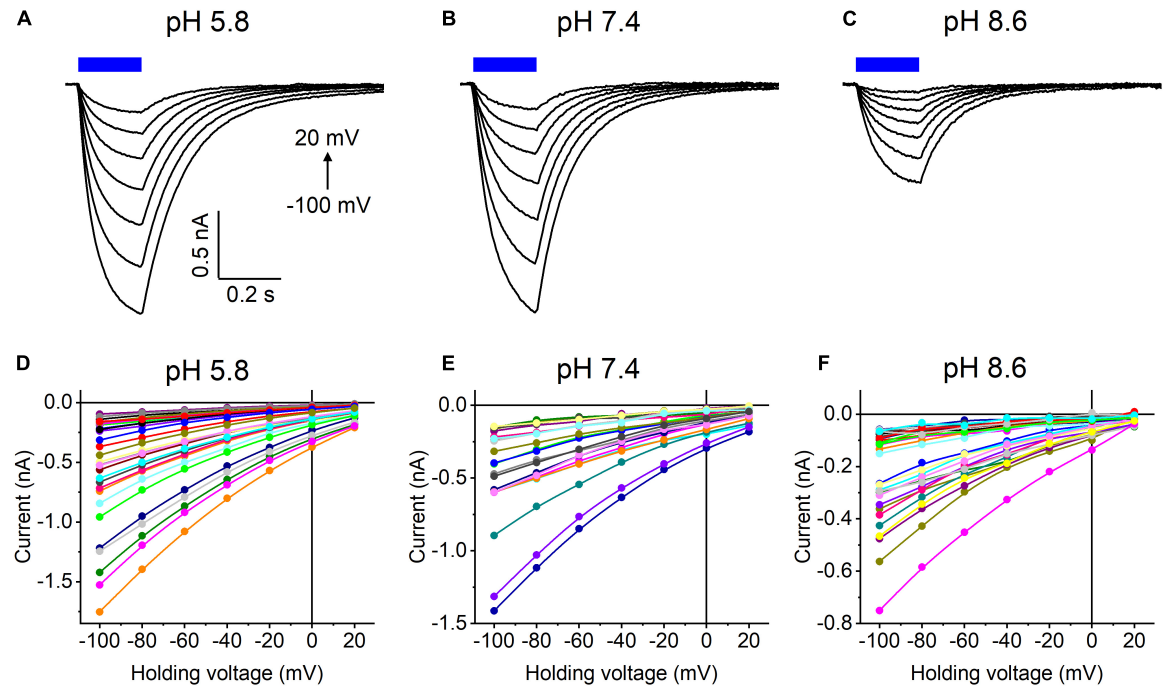

FIGURE 4
(A–C) Photocurrent traces recorded from *Hc*CCR at the indicated external pH in response to a 200-ms light pulse (470 nm, 475 mA), the duration of which is shown as a colored bar on top. The holding voltage was varied from −100 to 20 mV in 20-mV steps. **(D–F)** Current-voltage relationships of *Hc*CCR measured in individual cells. The current amplitude was measured at the end of a 200-ms light pulse.

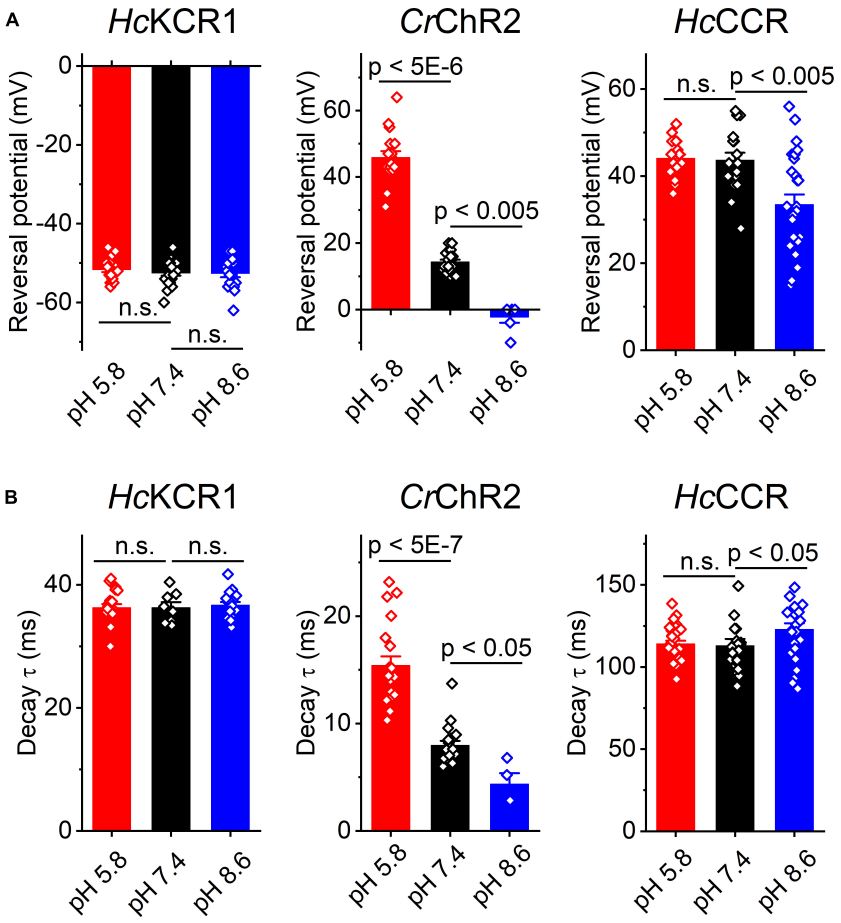

FIGURE 5
The reversal potential of photocurrents **(A)** and the time constant (τ) of the main (fast) component of photocurrent decay **(B)** in *Hc*KCR1, *Cr*ChR2 and *Hc*CCR measured at the indicated external pH. The bars are mean ± sem, the circles are the data from individual cells. Numerical data and full statistical analysis are provided in **Supplementary Datasheet 2**.

themselves. The SyncroPatch 384i platform that we used was based on the Biomek i5 robot, recently replaced with the Biomek 4000 robot. It remains to be seen whether this variability is eliminated in the new SyncroPatch 384 model based on the upgraded robot. We found that the improved photostimulation unit for the SyncroPatch (**Supplementary Figure 1B**) that was available only for 530-nm LEDs produced sufficiently intense light to cause desensitization (attenuation of photocurrent during continuous illumination) of the tested ChRs. Desensitization is observed in all known ChRs and needs to be minimized for optogenetic purposes. Desensitization is caused by accumulation of long-lived non- or less-conductive intermediate(s) of the photocycle, but its molecular mechanisms are poorly understood and appear to be different in different ChRs (Saita et al., 2018; Kuhne et al., 2019; Oppermann et al., 2019; Sineshchekov et al., 2020). The SyncroPatch is expected to be invaluable for high-throughput screening of random ChR mutants for decreased desensitization.

Measurements of the *IE* curves require high seal quality and stability to avoid "seal leakage currents" that develop in response to applied voltage gradients (Wilson et al., 2011). The SyncroPatch provides an excellent seal stability upon application of repetitive voltage steps (**Supplementary Figure 2**). Our results obtained with *Hc*KCR1 and *Cr*ChR2 using this instrument are consistent with those of previous MPC studies (Nagel et al., 2003; Govorunova et al., 2022), which validates using the SyncroPatch for measurements of the *IE* curves and determination of the ionic selectivity of ChRs. In our analysis of the pH dependence of ChR photocurrents and current-voltage relationships, we used external solutions with preadjusted pH. The SyncroPatch also allows rapid exchange of the external and internal solutions without disturbing the gigaohm seals, as shown in experiments with voltage- and ligand-gated channels (Toh et al., 2020; Rotordam et al., 2021; Obergrussberger et al., 2022).

Using the SyncroPatch we found that the third ChR from *H. catenoides*, named here *Hc*CCR, showed no preferred

selectivity for K^+ over Na^+, in contrast to its close relatives *Hc*KCR1 and *Hc*KCR2 from the same organism. In fact, the Na^+/K^+ permeability ratio of *Hc*CCR is even higher than that of *Cr*ChR2, as is evident from the comparison of the corresponding E_{rev} values at pH 7.4 (**Figure 5A**). The close sequence homology of *Hc*KCR1 and *Hc*CCR (**Supplementary Figure 4**) will potentially benefit identification of residue motifs responsible for the high K^+/Na^+ permeability ratio of *Hc*KCR1.

Our conclusion is that the SyncroPatch 384i from Nanion accelerates determination of the basic biophysical characteristics of ChRs, such as their light intensity dependence and current-voltage relationships, and facilitates screening of ChR homologs identified in global polynucleotide sequencing projects. An upgrade of the photostimulation hardware for simultaneous illumination of the entire 384-well chip is expected to further increase its efficiency.

Data availability statement

The datasets presented in this study can be found in online repositories. The names of the repository/repositories and accession number(s) can be found in the article/**Supplementary material**.

Author contributions

EG, OS, and JS conceived the study. LB identified and refined the *Hc*KCR1 and *Hc*CCR sequences in the public databases. EG carried out APC and MPC experiments, analyzed their results, prepared the figures and wrote an original draft. All authors contributed to its review and editing.

Funding

This work was supported by the National Institutes of Health grants R35GM140838 and U01NS118288 (JS), Robert A. Welch Foundation Endowed Chair AU-0009 (JS), and the Natural Sciences and Engineering Research Council of Canada Discovery Grant RGPIN-2018-04397 (LB).

Acknowledgments

We thank Tim Strassmaier, Leo Angelo Morada, Stephan Holzhauser, Rasmus Gönner, Rodolfo Haedo, James Constantin, and Matt Scardina (Nanion Technologies) for their expert help with the SyncroPatch 384i. We also thank Niels Fertig and Andrea Brüggemann for awarding us loaned use of the SyncroPatch 384i in our laboratory in response to our proposal and those of several colleagues to test the system.

Conflict of interest

The authors declare that the research was conducted in the absence of any commercial or financial relationships that could be construed as a potential conflict of interest.

Publisher's note

All claims expressed in this article are solely those of the authors and do not necessarily represent those of their affiliated organizations, or those of the publisher, the editors and the reviewers. Any product that may be evaluated in this article, or claim that may be made by its manufacturer, is not guaranteed or endorsed by the publisher.

Supplementary material

The Supplementary Material for this article can be found online at: https://www.frontiersin.org/articles/10.3389/fnmol.2022.976910/full#supplementary-material

References

Bell, D. C., and Fermini, B. (2021). Use of automated patch clamp in cardiac safety assessment: past, present and future perspectives. *J. Pharmacol. Toxicol. Methods* 110:107072. doi: 10.1016/j.vascn.2021.107072

Bork, P., Bowler, C., de Vargas, C., Gorsky, G., Karsenti, E., and Wincker, P. (2015). Tara Oceans. tara Oceans studies plankton at planetary scale introduction. *Science* 348:873. doi: 10.1126/science.aac5605

Boyden, E. S., Zhang, F., Bamberg, E., Nagel, G., and Deisseroth, K. (2005). Millisecond-timescale, genetically targeted optical control of neural activity. *Nat. Neurosci.* 8, 1263–1268. doi: 10.1038/nn1525

Brinkwirth, N., Takasuna, K., Doi, M., Becker, N., Obergrussberger, A., Friis, S., et al. (2020). Reliable identification of cardiac liability in drug discovery using automated patch clamp: Benchmarking best practices and calibration standards for improved proarrhythmic assessment. *J. Pharmacol. Toxicol. Methods* 105:106884. doi: 10.1016/j.vascn.2020.106884

Cheng, Y., Li, H., Wang, L., Li, J., Kang, W., Rao, P., et al. (2020). Optogenetic approaches for termination of ventricular tachyarrhythmias after myocardial infarction in rats in vivo. *J. Biophotonics* 2020:e202000003. doi: 10.1002/jbio.202000003

Cui, X., Zhang, F., Zhang, H., Huang, X., Wang, K., Huang, T., et al. (2020). Neuroprotective effect of optogenetics varies with distance from channelrhodopsin-2 expression in an amyloid-beta-injected mouse model of Alzheimer's disease. *Front. Neurosci.* 14:583628. doi: 10.3389/fnins.2020.583628

Deisseroth, K. (2011). Optogenetics. *Nat. Methods* 8, 26–29. doi: 10.1038/nmeth.f.324

Deisseroth, K. (2015). Optogenetics: 10 years of microbial opsins in neuroscience. *Nat. Neurosci.* 18, 1213–1225. doi: 10.1038/nn.4091

Ernst, O. P., Sanchez Murcia, P. A., Daldrop, P., Tsunoda, S. P., Kateriya, S., and Hegemann, P. (2008). Photoactivation of channelrhodopsin. *J. Biol. Chem.* 283, 1637–1643. doi: 10.1074/jbc.M708039200

Fan, L. Z., Kheifets, S., Bohm, U. L., Wu, H., Piatkevich, K. D., Xie, M. E., et al. (2020). All-optical electrophysiology reveals the role of lateral inhibition in sensory processing in cortical layer 1. *Cell* 180, 521–535e518. doi: 10.1016/j.cell.2020.01.001

Govorunova, E. G., Gou, Y., Sineshchekov, O. A., Li, H., Lu, X., Wang, Y., et al. (2022). Kalium channelrhodopsins are natural light-gated potassium channels that mediate optogenetic inhibition. *Nat. Neurosci.* accepted doi: 10.1038/s41593-022-01094-6

Govorunova, E. G., Sineshchekov, O. A., Li, H., and Spudich, J. L. (2017). Microbial rhodopsins: Diversity, mechanisms, and optogenetic applications. *Annu. Rev. Biochem.* 86, 845–872. doi: 10.1146/annurev-biochem-101910-144233

Govorunova, E. G., Sineshchekov, O. A., Li, H., Wang, Y., Brown, L. S., Palmateer, A., et al. (2021). Cation and anion channelrhodopsins: Sequence motifs and taxonomic distribution. *MBio* 12:e0165621. doi: 10.1128/mBio.01656-21

Govorunova, E. G., Sineshchekov, O. A., Li, H., Wang, Y., Brown, L. S., and Spudich, J. L. (2020). RubyACRs, non-algal anion channelrhodopsins with highly red-shifted absorption. *Proc. Natl. Acad. Sci. USA* 117, 22833–22840. doi: 10.1073/pnas.2005981117

Govorunova, E. G., Sineshchekov, O. A., Liu, X., Janz, R., and Spudich, J. L. (2015). Natural light-gated anion channels: a family of microbial rhodopsins for advanced optogenetics. *Science* 349, 647–650. doi: 10.1126/science.aaa7484

Ishizuka, T., Kakuda, M., Araki, R., and Yawo, H. (2006). Kinetic evaluation of photosensitivity in genetically engineered neurons expressing green algae light-gated channels. *Neurosci. Res.* 54, 85–94. doi: 10.1016/j.neures.2005.10.009

Keppeler, D., Merino, R. M., Lopez de la Morena, D., Bali, B., Huet, A. T., Gehrt, A., et al. (2018). Ultrafast optogenetic stimulation of the auditory pathway by targeting-optimized Chronos. *EMBO J* 37:24. doi: 10.15252/embj.201899649

Klapoetke, N. C., Murata, Y., Kim, S. S., Pulver, S. R., Birdsey-Benson, A., Cho, Y. K., et al. (2014). Independent optical excitation of distinct neural populations. *Nat. Methods* 11, 338–346. doi: 10.1038/nmeth.2836

Kolb, I., Landry, C. R., Yip, M. C., Lewallen, C. F., Stoy, W. A., Lee, J., et al. (2019). PatcherBot: a single-cell electrophysiology robot for adherent cells and brain slices. *J. Neural. Eng.* 16:046003. doi: 10.1088/1741-2552/ab1834

Kuhne, J., Vierock, J., Tennigkeit, S. A., Dreier, M. A., Wietek, J., Petersen, D., et al. (2019). Unifying photocycle model for light adaptation and temporal evolution of cation conductance in channelrhodopsin-2. *Proc. Natl. Acad. Sci. USA* 116, 9380–9389. doi: 10.1073/pnas.1818707116

Leonard, G., Labarre, A., Milner, D. S., Monier, A., Soanes, D., Wideman, J. G., et al. (2018). Comparative genomic analysis of the 'pseudofungus' *Hyphochytrium catenoides*. *Open Biol.* 8:170184. doi: 10.1098/rsob.170184

Nagel, G., Ollig, D., Fuhrmann, M., Kateriya, S., Musti, A. M., Bamberg, E., et al. (2002). Channelrhodopsin-1: a light-gated proton channel in green algae. *Science* 296, 2395–2398. doi: 10.1126/science.1072068

Nagel, G., Szellas, T., Huhn, W., Kateriya, S., Adeishvili, N., Berthold, P., et al. (2003). Channelrhodopsin-2, a directly light-gated cation-selective membrane channel. *Proc. Natl. Acad. Sci. USA* 100, 13940–13945. doi: 10.1073/pnas.1936192100

Obergrussberger, A., Friis, S., Bruggemann, A., and Fertig, N. (2021). Automated patch clamp in drug discovery: major breakthroughs and innovation in the last decade. *Expert Opin. Drug. Discov.* 16, 1–5. doi: 10.1080/17460441.2020.1791079

Obergrussberger, A., Rinke-Weiss, I., Goetze, T. A., Rapedius, M., Brinkwirth, N., Becker, N., et al. (2022). The suitability of high throughput automated patch clamp for physiological applications. *J. Physiol.* 600, 277–297. doi: 10.1113/JP282107

Oppermann, J., Fischer, P., Silapetere, A., Liepe, B., Rodriguez-Rozada, S., Flores-Uribe, J., et al. (2019). MerMAIDs: a family of metagenomically discovered marine anion-conducting and intensely desensitizing channelrhodopsins. *Nat. Commun.* 10:3315. doi: 10.1038/s41467-019-11322-6

Paschen, E., Elgueta, C., Heining, K., Vieira, D. M., Kleis, P., Orcinha, C., et al. (2020). Hippocampal low-frequency stimulation prevents seizure generation in a mouse model of mesial temporal lobe epilepsy. *Elife* 9:54518. doi: 10.7554/eLife.54518

Potet, F., Egecioglu, D. E., Burridge, P. W., and George, A. L. Jr. (2020). GS-967 and eleclazine block sodium channels in human induced pluripotent stem cell-derived cardiomyocytes. *Mol. Pharmacol.* 98, 540–547. doi: 10.1124/molpharm.120.000048

Rotordam, M. G., Obergrussberger, A., Brinkwirth, N., Takasuna, K., Becker, N., Horvath, A., et al. (2021). Reliable identification of cardiac conduction abnormalities in drug discovery using automated patch clamp II: Best practices for Nav1.5 peak current in a high throughput screening environment. *J. Pharmacol. Toxicol. Methods* 112:107125. doi: 10.1016/j.vascn.2021.107125

Rozenberg, A., Inoue, K., Kandori, H., and Beja, O. (2021). Microbial rhodopsins: the last two decades. *Annu. Rev. Microbiol.* 75, 427–447. doi: 10.1146/annurev-micro-031721-020452

Rozenberg, A., Oppermann, J., Wietek, J., Fernandez Lahore, R. G., Sandaa, R. A., Bratbak, G., et al. (2020). Lateral gene transfer of anion-conducting channelrhodopsins between green algae and giant viruses. *Curr. Biol.* 30, 4910–4920. doi: 10.1016/j.cub.2020.09.056

Sahel, J. A., Boulanger-Scemama, E., Pagot, C., Arleo, A., Galluppi, F., Martel, J. N., et al. (2021). Partial recovery of visual function in a blind patient after optogenetic therapy. *Nat. Med.* 27, 1223–1229. doi: 10.1038/s41591-021-01351-4

Saita, M., Pranga-Sellnau, F., Resler, T., Schlesinger, R., Heberle, J., and Lorenz-Fonfria, V. A. (2018). Photoexcitation of the P4(480) state induces a secondary photocycle that potentially desensitizes channelrhodopsin-2. *J. Am. Chem. Soc.* 140, 9899–9903. doi: 10.1021/jacs.8b03931

Sineshchekov, O. A., Govorunova, E. G., Li, H., Wang, Y., Melkonian, M., Wong, G. K.-S., et al. (2020). Conductance mechanisms of rapidly desensitizing cation channelrhodopsins from cryptophyte algae. *mBio* 11, e657–e620. doi: 10.1128/mBio.00657-20

Sineshchekov, O. A., Jung, K.-H., and Spudich, J. L. (2002). Two rhodopsins mediate phototaxis to low- and high-intensity light in *Chlamydomonas reinhardtii*. *Proc. Natl. Acad. Sci. USA* 99, 8689–8694. doi: 10.1073/pnas.122243399

Stahlberg, M. A., Ramakrishnan, C., Willig, K. I., Boyden, E. S., Deisseroth, K., and Dean, C. (2019). Investigating the feasibility of channelrhodopsin variants for nanoscale optogenetics. *Neurophotonics* 6:015007. doi: 10.1117/1.NPh.6.1.015007

Toh, M. F., Brooks, J. M., Strassmaier, T., Haedo, R. J., Puryear, C. B., Roth, B. L., et al. (2020). Application of high-throughput automated patch-clamp electrophysiology to study voltage-gated ion channel function in primary cortical cultures. *SLAS Discov.* 25, 447–457. doi: 10.1177/2472555220902388

Tsunoda, S. P., and Hegemann, P. (2009). Glu 87 of channelrhodopsin-1 causes pH-dependent color tuning and fast photocurrent inactivation. *Photochem. Photobiol.* 85, 564–569. doi: 10.1111/j.1751-1097.2008.00519.x

Wietek, J., and Prigge, M. (2016). Enhancing channelrhodopsins: An overview. *Methods Mol. Biol.* 1408, 141–165. doi: 10.1007/978-1-4939-3512-3_10

Wilson, J. R., Clark, R. B., Banderali, U., and Giles, W. R. (2011). Measurement of the membrane potential in small cells using patch clamp methods. *Channels* 5, 530–537. doi: 10.4161/chan.5.6.17484

Yu, C., Cassar, I. R., Sambangi, J., and Grill, W. M. (2020). Frequency-specific optogenetic deep brain stimulation of subthalamic nucleus improves parkinsonian motor behaviors. *J. Neurosci.* 40, 4323–4334. doi: 10.1523/JNEUROSCI.3071-19.2020

Zimmermann, D., Terpitz, U., Zhou, A., Reuss, R., Muller, K., Sukhorukov, V. L., et al. (2006). Biophysical characterisation of electrofused giant HEK293-cells as a novel electrophysiological expression system. *Biochem. Biophys. Res. Commun.* 348, 673–681. doi: 10.1016/j.bbrc.2006.07.112

frontiers | Frontiers in Molecular Neuroscience

TYPE Original Research
PUBLISHED 22 August 2022
DOI 10.3389/fnmol.2022.982316

OPEN ACCESS

EDITED BY
Ciria Hernandez,
University of Michigan, United States

REVIEWED BY
Daohua Jiang,
Institute of Physics (CAS), China
Samuel Goodchild,
Xenon Pharmaceuticals Inc., Canada

*CORRESPONDENCE
Markus Rapedius
markus.rapedius@nanion.de

†These authors have contributed equally to this work

SPECIALTY SECTION
This article was submitted to Molecular Signalling and Pathways, a section of the journal Frontiers in Molecular Neuroscience

RECEIVED 30 June 2022
ACCEPTED 26 July 2022
PUBLISHED 22 August 2022

CITATION
Rapedius M, Obergrussberger A, Humphries ESA, Scholz S, Rinke-Weiss I, Goetze TA, Brinkwirth N, Rotordam MG, Strassmaier T, Randolph A, Friis S, Liutkute A, Seibertz F, Voigt N and Fertig N (2022) There is no F in APC: Using physiological fluoride-free solutions for high throughput automated patch clamp experiments. *Front. Mol. Neurosci.* 15:982316. doi: 10.3389/fnmol.2022.982316

There is no F in APC: Using physiological fluoride-free solutions for high throughput automated patch clamp experiments

Markus Rapedius[1*†], Alison Obergrussberger[1†], Edward S. A. Humphries[2], Stephanie Scholz[1], Ilka Rinke-Weiss[1], Tom A. Goetze[1], Nina Brinkwirth[1], Maria Giustina Rotordam[1], Tim Strassmaier[3], Aaron Randolph[3], Søren Friis[1], Aiste Liutkute[4,5,6], Fitzwilliam Seibertz[4,5,6], Niels Voigt[4,5,6] and Niels Fertig[1]

[1]Nanion Technologies GmbH, Munich, Germany, [2]Discovery Sciences, BioPharmaceuticals R&D, AstraZeneca, Cambridge, United Kingdom, [3]Nanion Technologies Inc., Livingston, NJ, United States, [4]Institute of Pharmacology and Toxicology, University Medical Center Göttingen, Georg-August University, Göttingen, Germany, [5]German Center for Cardiovascular Research, Partner Site Göttingen, Göttingen, Germany, [6]Cluster of Excellence "Multiscale Bioimaging: From Molecular Machines to Networks of Excitable Cells", University of Göttingen, Göttingen, Germany

Fluoride has been used in the internal recording solution for manual and automated patch clamp experiments for decades because it helps to improve the seal resistance and promotes longer lasting recordings. In manual patch clamp, fluoride has been used to record voltage-gated Na (Na_V) channels where seal resistance and access resistance are critical for good voltage control. In automated patch clamp, suction is applied from underneath the patch clamp chip to attract a cell to the hole and obtain a good seal. Since the patch clamp aperture cannot be moved to improve the seal like the patch clamp pipette in manual patch clamp, automated patch clamp manufacturers use internal fluoride to improve the success rate for obtaining GΩ seals. However, internal fluoride can affect voltage-dependence of activation and inactivation, as well as affecting internal second messenger systems and therefore, it is desirable to have the option to perform experiments using physiological, fluoride-free internal solution. We have developed an approach for high throughput fluoride-free recordings on a 384-well based automated patch clamp system with success rates >40% for GΩ seals. We demonstrate this method using hERG expressed in HEK cells, as well as $Na_V1.5$, $Na_V1.7$, and

$K_{Ca}3.1$ expressed in CHO cells. We describe the advantages and disadvantages of using fluoride and provide examples of where fluoride can be used, where caution should be exerted and where fluoride-free solutions provide an advantage over fluoride-containing solutions.

KEYWORDS

automated patch clamp, ion channels, hERG, $Na_V1.5$, physiological solutions, $K_{Ca}3.1$, $Na_V1.7$, fluoride

Introduction

Automated patch clamp (APC) instruments are used for a wide variety of applications ranging from basic research into channelopathies and biophysical characteristics of ion channels, through to routine cardiac safety testing (Obergrussberger et al., 2021, 2022). Their use in cardiac safety screening has increased over the years and APC is now an established and accepted technique in most, if not all, safety testing laboratories. It is well-known that fluoride is often used in the internal solution in APC experiments to improve the seal resistance (Zeng et al., 2008) when external calcium (or other divalent cation) are present (Milligan et al., 2009; Obergrussberger et al., 2014, 2018). The mechanism is thought to involve the formation of CaF_2 crystals at the interface between the pipette or micropore and the cell as described in a recent patent application (Lojkner et al., 2019). Even in manual patch clamp experiments, fluoride has been used to record Na_V channels for over 20 years (Cummins et al., 1999; Renganathan et al., 2000; Rugiero et al., 2003), despite known shifts in activation and steady-state inactivation curves of $Na_V1.9$ (Rugiero et al., 2003; Coste et al., 2004), effects on the voltage dependence of conductance and steady-state inactivation of $Na_V1.7$ (Jarecki et al., 2008), shifts in activation and inactivation of $Na_V1.3$ (Meadows et al., 2002), and effects on persistent current of $Na_V1.3$ (Chen et al., 2000). These effects on biophysical properties are not limited to Na_V channels, high concentrations of fluoride have been shown to increase mean open duration, and thereby open probability of L-type calcium channels (Ono and Arita, 1999), and influences current amplitude and inactivation of $K_V1.3$ and K_{2P} channels (Herrmann et al., 2020). In addition to effects on biophysical properties of ion channels, fluoride binds to calcium making its use in experiments involving activation of ion channels by internal free calcium somewhat limited, and itself activates certain ion channels such as CFTR (Berger et al., 1998). It is also well-known that fluoride activates G-proteins when complexed with Al^{3+} present in trace amounts (Li, 2003) and inhibits protein phosphatase (Khatra and Soderling, 1978). Fluoride is used because it improves the seal and allows stable measurements to be performed over long periods of time (Zeng et al., 2008; Föhr et al., 2021). Alternative internal solutions which do not contain fluoride for recording CFTR (Billet et al., 2017; Froux et al., 2020; Becq et al., 2021) or TMEM16A (Obergrussberger et al., 2018) have been used successfully on automated patch clamp devices, but the solutions were not always physiological.

In most experiments run on automated patch clamp instruments, the use of fluoride in the internal solution is no problem, particularly when like is compared with like, i.e., activation and inactivation plots of Na_V channels are always run using internal fluoride. However, there may be some cases where fluoride-free, physiological solutions are required, for example, when comparing data with historical data which was recorded in fluoride-free solutions. Alternatively, it may be the case that fluoride cannot be used because of activation of ion channels, inhibition of phosphatase or binding of calcium ions. For these reasons, we have developed a method for high throughput APC experiments using the SyncroPatch 384 which allow fluoride-free, physiological solutions to be used with good success rates for GΩ and sub-GΩ seals. We demonstrate this using the ion channels $Na_V1.5$ and $Na_V1.7$ expressed in CHO (Charles River), hERG expressed in HEK293 (SB Drug Discovery), and $K_{Ca}3.1$ (SK4) also expressed in CHO cells (Charles River). Additionally, preliminary experiments using human induced pluripotent stem cell-derived cardiomyocytes (hiPSC-CMs) were also performed.

Materials and methods

Cell culture and harvesting

The cell lines used here (hERG stably expressed in HEK 293 cells from SB Drug Discovery, Glasgow, United Kingdom, $hNa_V1.5$; $hNa_V1.7$, and $K_{Ca}3.1$ stably expressed in CHO cells all from Charles River, United States) were cultured as previously described (Brueggemann et al., 2004; Brüggemann et al., 2008; Becker et al., 2013; Obergrussberger et al., 2014). In brief, these cells were cultured in T175 culture flasks in the media recommended by the supplier and passaged every 2–3 days when they were 50–80% confluent. The cells were passaged regularly to ensure that the cells were single when passaged and harvested. The cells were prohibited from reaching 100%

confluency so that they remained healthy, single, and expressed the ion channel of interest when they were harvested into a cell suspension for recordings. hiPSC-derived cardiomyocytes were generated and cultured as previously described (Seibertz et al., 2022). Briefly, hiPSC cell line UMGi014-C.14 was derived from dermal fibroblasts of healthy male donor and the reprogramming to iPSCs was achieved using integration-free CytoTune iPS 2.0 Sendai Reprogramming Kit (Thermo Fisher Scientific) with the reprogramming factors OCT4, KLF4, SOX2, c-MYC. Directed differentiation into ventricular iPSC-CMs was performed *via* WNT signaling modulation and subsequent metabolic selection, as previously described (Kleinsorge and Cyganek, 2020). hiPSC-CMs were cultured at 37°C in 5% CO_2 in a RPMI Medium 1640 (1X) + GlutaMax^{TM} –I [+] 25 mM HEPES (Thermo Fisher Scientific) supplemented with B-27 (Thermo Fisher Scientific). Experiments were performed on hiPSC-CMs at day 41 post differentiation. All protocols were approved by the Ethics Committee of the University Medical Center Göttingen (No. 10/9/15 and 15/2/20). For experiments on the SyncroPatch 384, cells were harvested into suspension and suction was used to attract a cell to the patch clamp aperture of each well. Since it was a blind method for capture, cells had to be single with few clusters and the cell suspension was free from cell debris, as the presence of cell clusters and debris can decrease the success rate. Cell harvesting was performed as described previously (Brueggemann et al., 2004; Brüggemann et al., 2008; Becker et al., 2013; Obergrussberger et al., 2014) using TrypLE, other suitable enzymes, or even enzyme-free detachment protocols. Cells were then resuspended in extracellular recording solution at a density of ∼500,000 cells/ml.

Automated patch clamp electrophysiology

All cells were recorded in the whole cell mode of the patch clamp technique using the SyncroPatch 384 (Nanion Technologies, Munich, Germany). Electrophysiological protocols were constructed, and data digitized using PatchControl 384 (Nanion Technologies, Munich, Germany). Cells were recorded on both single-hole NPC-384 or NPC-384FF chips with medium or high resistance (4–5.5 or 5–7 MΩ, respectively). In a subset of experiments involving $K_{Ca}3.1$ multi-hole chips with 4 holes (NPC-384/NPC-384FF) 4X high resistance (2.2–3.2 MΩ) per well were used. Cells were harvested into suspension and added to the CellHotel of the SyncroPatch 384 where they were kept at 10°C, shaking at 200 rpm, until used for the experiment. The NPC-384 or NPC-384FF chips were filled with internal solution as indicated in **Table 1** and ChipFill external solution. After cells were captured (indicated by an increase in R_{Seal} > 10 MΩ), a brief, transient addition of external solution containing 6 mM Ca^{2+} was made when standard internal solution and NPC-384 chips were used which was then exchanged to external recording solution before commencement of recordings. When fluoride-free internal solution and NPC-384FF chips were used, the ChipFill external solution was replaced by external recording solution (**Table 1**) after cells were captured.

hERG currents were recorded using a double step voltage protocol from a holding potential of −80 mV to +60 mV for 500 ms followed by a step to −40 mV for 500 ms repeated every 15 s. Peak amplitude was measured at the start of the second voltage step (I_{Tail}). Current-voltage relationships were recorded using the same voltage-step to +60 mV, but then followed by voltage steps from −120 to 60 mV with 10 mV increments.

$Na_V1.5$ currents were measured using a 3-step protocol, the first step from −120 to 0 mV, the second step from −100 to 0 mV and the 3rd step from −80 to 0 mV, repeated every 10 s. Current-voltage (IV) relationships were recorded using the voltage-step protocol: For the activation IV, a step pulse of 30 ms was applied, starting from −70 mV and increasing in 10 mV increments up to 40 mV with every sweep, at a sweep interval of 2 s. For analysis, the current response to each step was normalized to the cell's peak current before averaging across all cells. Holding potential was −120 mV.

The inactivation IV pulse protocol consisted of a 500 ms pre-pulse, starting from −100 mV and increasing in 5 mV increments with every sweep up to 20 mV, followed by a 50 ms depolarizing step to 0 mV, at a sweep interval of 5 s. For analysis, each of the current responses to the 50 ms step to 0 mV was normalized to the current response to the 0 mV step following the 500 ms pre-pulse at −120 mV before averaging across all cells. Holding potential was −120 mV.

$K_{Ca}3.1$ was recorded using a voltage ramp protocol from −120 to +60 mV over 198 ms, intersweep holding potential was −80 mV and sweep interval was 5 s. $K_{Ca}3.1$ was activated by internal perfusion of free calcium at 0.3, 1, or 3 μM calculated using Cabuf (freeware from KU Leuven, Belgium).

Ca_V currents from hiPSC-CMs were recorded using a voltage ramp-step protocol, with a ramp from −80 to −40 mV over 300 ms followed by a step from −40 to 0 mV for 100 ms, holding potential was −80 mV. The ramp section of the protocol was used to inactivate Na_V currents. Only the current response to the step to 0 mV is shown in the figure for hiPSC-CMs.

Each well of the SyncroPatch 384 has an individual headstage of the amplifier and, therefore, each well is denoted as n = 1. For success rate and IC_{50} values across plates, n represents results from 1 NPC-384 chip. With PatchControl 384, parameters such as seal resistance, capacitance and series resistance were determined from each well after application of a test pulse. All parameters are monitored over time and can be recorded for individual experiments.

Method of using fluoride-free physiological solutions on the SyncroPatch 384

To allow for fluoride-free recordings, a combinatory approach is adopted on the SyncroPatch 384 consisting

TABLE 1 Composition of recording solutions for fluoride-containing (referred to as standard internal) and fluoride-free (referred to as FF internal) experiments.

Constituent	Internal recording solution			External recording solution	ChipFill external solution (divalent-free)
	Standard	Standard-$K_{Ca}3.1$*	FF	Standard (incl. $K_{Ca}3.1$)/FF	Standard (incl. $K_{Ca}3.1$)/FF
K-gluconate		30	120		
K-Fluoride	120	80			
NaCl	10	10	10	80	140
NMDG-Cl				60	
KCl	10	10	10	4	4
$CaCl_2$				2	
$MgCl_2$				1	
EGTA	5	10	5		
Glucose				5	5
HEPES	10	10	10	10	10
pH	7.2	7.2	7.2	7.4	7.4
Osmolarity (mOsm)	~285	~285	~285	~289	~289

Concentrations are given in mM. Note that for experiments involving $K_{Ca}3.1$, $CaCl_2$ was added to the internal solution as described in Section "Automated patch clamp electrophysiology."
*In recordings with free [Ca^{2+} > 1 μM] 10 mM HEDTA was used instead of EGTA.

of the usage of a specialized, fluoride-free consumable called NPC-384FF in combination with a proprietary, fully automated method for preparing the NPC-384FF prior to execution of the fluoride-free recording. The automated method of NPC-384FF preparation is available on all SyncroPatch 384 devices.

Quality control parameters

Cells had to pass quality control (QC) parameters to be included in the analysis. For some experiments R_{Seal} > 1 GΩ whereas for other experiments R_{Seal} > 0.25 GΩ was used for single- or equivalent in multi-hole chips. In addition to this, I_{Peak} > 150 pA for hERG; I_{Peak} < −100 pA for $Na_V1.5$ or $Na_V1.7$ and I_{Peak} > 350 pA for single-hole chips and I_{Peak} > 1000 pA for multi-hole chips (4X) for $K_{Ca}3.1$ was also used. In order to guarantee appropriate voltage clamp in our comparisons, the analysis of IV-relationships for $Na_V1.5$ and $Na_V1.7$ recordings included additional quality control parameters on capacitance > 2 pF, current size as well as R_{series} that was constrained to −3.0 nA and 20 MΩ, respectively.

Automated patch clamp solutions

See Table 1.

Data analysis

The SyncroPatch 384 platforms have a software package consisting of PatchControl 384 (for data acquisition) and DataControl 384 (for data analysis; both Nanion Technologies, Munich, Germany). Current-voltage plots were calculated using DataControl 384 and fit with Boltzmann equations: $I(V) = Imin + \frac{Imax-Imin}{1+e^{-\frac{V-Vhalf}{Slope}}}$ for a sigmoidal fit for hERG IV and inactivation $Na_V1.5$ and $Na_V1.7$ IVs. In addition, an extended Boltzmann equation was used: $G(V) = \frac{I(V)}{V-Erev} = \left(Gmin + \frac{Gmax-Gmin}{1+e^{-\frac{V-Vhalf}{Slope}}}\right)$ to obtain V_{half} values for activation protocols for $Na_V1.5$ and $Na_V1.7$ where *I(V)* is the amplitude of the current and *G(V)* the conductance at voltage *V*, *Erev* is the reversal potential. *Vhalf* is the membrane potential at half-maximal activation or inactivation and *Slope* is the slope factor.

Concentration response curves were calculated using either cumulative additions or a single point addition approach. When cumulative additions were done, all concentrations of compound were added to each well, in increasing concentrations, and concentration response curves were calculated individually for each well. When single point additions were done, a single concentration of compound was added to each well and the IC_{50} was calculated across multiple wells. IC_{50} analysis was done with DataControl 384, concentration response curves were fit with a Hill equation:

$$Response = Min + \frac{Max-Min}{1 + \left(\frac{EC50}{Conc.}\right)^{Hill}}.$$

Statistics

Data are presented as means ± S.D or means ± S.E.M. Differences between groups were tested using the Student's

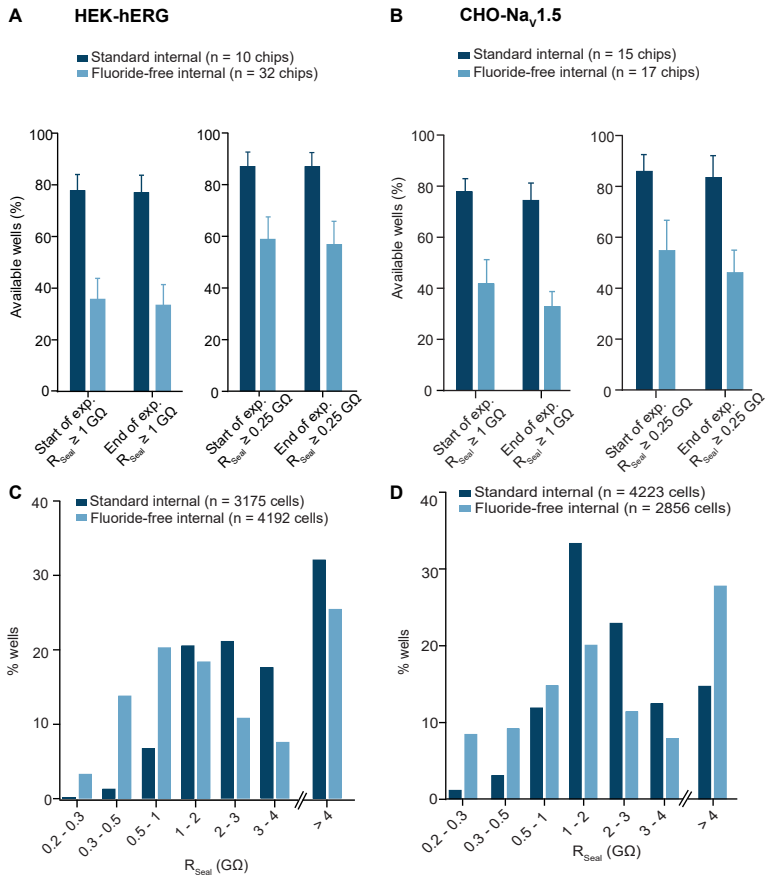

FIGURE 1
HEK and CHO cells recorded in standard and fluoride-free internal solution. **(A)** HEK cells expressing hERG were captured with almost 80% success rate for $R_{Seal} \geq 1$ GΩ + $I_{Tail} > 150$ pA and almost 40% success rate for $R_{Seal} \geq 1$ GΩ in fluoride-free internal solution (left). If a QC cutoff of $R_{Seal} \geq 0.25$ GΩ + $I_{Tail} > 150$ pA was used, the success rate was increased in both conditions (right). **(B)** CHO cells expressing $Na_V1.5$ were captured with almost 80% success rate for $R_{Seal} \geq 1$ GΩ + $I_{Peak} < -100$ pA and over 40% success rate for $R_{Seal} \geq 1$ GΩ in fluoride-free internal solution (left). If a QC cutoff of $R_{Seal} \geq 0.25$ GΩ + $I_{Peak} < -100$ pA was used, the success rate was increased in both conditions (right). **(C)** Histogram plot of the R_{Seal} values for HEK-hERG cells in standard and fluoride-free internal solution. For $R_{Seal} > 4$ GΩ, although they are high giga-seals, the seal resistance is not accurately calculated and is therefore shown as an extra bar and these R_{Seal} values were not included in the calculation for R_{Seal} (**Table 2**). **(D)** Histogram plot of the R_{Seal} values for CHO-$Na_V1.5$ cells in standard and fluoride-free internal. For $R_{Seal} > 4$ GΩ, although they are high giga-seals, the seal resistance is not accurately calculated and is therefore shown as an extra bar and these R_{Seal} values were not included in the calculation for R_{Seal} (**Table 3**).

TABLE 2 Parameters for R_{Seal}, I_{Tail}, cell capacitance, R_{Series}, Rundown, V_{half}, and IC_{50} values for HEK cells expressing hERG for standard internal and fluoride-free internal solution.

Parameter	Standard internal	Fluoride-free internal
R_{Seal} (GΩ)	2.23 ± 0.02 (2155)	1.36 ± 0.02 (3123)*
I_{Tail} (nA)	0.70 ± 0.01 (3175)	0.99 ± 0.01 (4192)***
Capacitance (pF)	16.2 ± 0.3 (387)	15.9 ± 0.4 (313)
R_{Series} (MΩ)	8.6 ± 0.2 (379)	10.2 ± 0.2 (317)***
Rundown over 18 min (%/min)	0.10 ± 0.05 (58)	0.07 ± 0.07 (42)
V_{half} (mV)	−93.0 ± 0.5 (190)	−92.1 ± 2.3 (261)
IC_{50} Terfenadine (nM)	237 ± 26 (52)	337 ± 53 (17)
IC_{50} Verapamil (nM)	394 ± 17 (54)	457 ± 37 (29)

R_{Seal} values > 4 GΩ could not be accurately calculated, therefore only $R_{Seal} \leq 4$ GΩ were used for the calculation of the mean. Shown are mean ± S.E.M, number of cells shown in parentheses.
*$P < 0.05$, ***$P < 0.001$, unpaired Student's *t*-test.

TABLE 3 Parameters for R_{Seal}, I_{Peak}, rundown, V_{half} Activation, V_{half} Inactivation, and tetracaine IC_{50} for CHO cells expressing $Na_V1.5$ for standard internal and fluoride-free internal solution.

Parameter	Standard internal	Fluoride-free internal
R_{Seal} (GΩ)	1.89 ± 0.02 (3598)	1.39 ± 0.02 (2061)***
I_{Peak} (nA)	−1.56 ± 0.01 (4537)	−1.53 ± 0.01 (3336)
Capacitance (pF)	13.9 ± 0.2 (1043)	13.8 ± 0.4 (491)
R_{Series} (MΩ)	7.6 ± 0.1 (1043)	9.8 ± 0.1 (491)***
Rundown over 12 min (%/min; V_{hold} −120 mV)	0.5 ± 0.1 (133)	0.4 ± 0.1 (52)
V_{half} Activation (mV)	−37.5 ± 0.4 (484)	−25.2 ± 0.5 (241)***
V_{half} Inactivation (mV)	−68.4 ± 0.4 (728)	−53.6 ± 0.6 (165)***
IC_{50} Tetracaine (μM, V_{hold} −120 mV)	35.6 ± 9.4 (4 chips)	41.8 ± 9.3 (3 chips)

R_{Seal} values > 4 GΩ could not be accurately calculated, therefore only $R_{Seal} \leq 4$ GΩ were used for the calculation. Shown are mean ± S.E.M, number of cells shown in parentheses. For tetracaine concentration response curves, single point additions were made and the concentration response curve calculated across the whole chip. Shown are mean ± S.E.M for the number of chips given in parentheses.
***$P < 0.001$, unpaired Student's *t*-test.

t-test for normally distributed data. *P*-values are reported in the figures. N represents the number of wells examined or the number of chips as indicated in the figures and/or figure legends.

Results

High throughput automated patch clamp to assess effects of internal fluoride on success rate and seal resistance

In APC experiments, high success rates have been reported using internal solutions without fluoride for several targets, such as CFTR, with success rates for completed experiments > 80% (Billet et al., 2017; Brüggemann et al., 2017; Froux et al., 2020; Becq et al., 2021). However, when switching to more physiological solutions, such as K-chloride or K-gluconate-based internal solutions, success rates very rarely reach acceptable ranges for high throughput APC. In fact, under these conditions we observed 9.3 ± 6.1% (R_{Seal} > 1 GΩ + I_{Tail} > 150 pA) and 18.6 ± 6.3% (R_{Seal} > 0.25 GΩ + I_{Tail} > 150 pA) using hERG expressed in HEK cells (n = 16 NPC-384 chips), in agreement with success rates reported by Zeng et al. (2008). This has posed a limitation in the use of fluoride-free, physiological internal solutions for high throughput APC and was the basis for the development of a special type of consumable, the NPC-384FF, which we have used throughout this study to allow the usage of K-gluconate (or K-chloride) or fluoride-based internal solutions under the same experimental conditions.

First, we evaluated the success rates for seal formation for fluoride-free internal solution compared with standard, fluoride-containing, internal solution using two standard cell culture cell lines. HEK cells expressing hERG as wells as CHO cells expressing $Na_V1.5$ channels were used on the SyncroPatch 384 using either NPC-384 chips and standard internal solution containing fluoride, or NPC-384FF chips with fluoride-free internal solution. For hERG, a classical double voltage-step protocol was used to record hERG tail currents and we determined the number of wells available for recording under both conditions. Using single-hole chips, HEK cells expressing hERG were recorded with a success rate of 77.9 ± 6.1% (n = 10 NPC-384 chips) for R_{Seal} > 1 GΩ + I_{Tail} > 150 pA (at the start of the experiment) when standard K-fluoride was used in the internal solution and 35.9 ± 7.9% (n = 32 NPC-384FF chips) when K-gluconate was used in the internal solution (Figure 1A). The success rate increased to 87.2 ± 5.4% (n = 10 NPC-384 chips) in K-fluoride and 59.0 ± 8.5% (n = 32 NPC-384FF chips) in K-gluconate when a QC cutoff for R_{Seal} > 0.25 GΩ + I_{Tail} > 150 pA was used. Despite the reduced number of available wells when fluoride-free solution was used, the sealing properties of the recorded cells only slightly differed in their R_{Seal} distribution pattern as illustrated in the histograms (Figure 1C), however, a small, but significant reduction for mean R_{Seal} values was observed (Table 2). Importantly, this did not have a large impact on the stability of the recording over time as only few cells were lost during the experiments and the success rate was similar at the end of the experiment (t = 15 min) as at the start of the experiment (Figure 1A). The differences in mean R_{Seal} might be due to the fact that for the fluoride-free approach, the formation of CaF_2 crystals is absent and no elevated external Ca^{2+} levels are used throughout the entire recording resulting in a reduced success rate. Similar results were observed using CHO cells expressing $Na_V1.5$ channels where a 1-step voltage protocol was used to elicit $Na_V1.5$ peak currents. Again, we first determined the number of available wells in single-hole chips (i.e., the number that passed the QC parameters for R_{Seal} and I_{Peak}) and for $Na_V1.5$-CHO we observed a success rate of 78.0 ± 4.9% (n = 15 NPC-384 chips) for R_{Seal} > 1 GΩ + I_{Peak} < −100 pA (at the start of the experiment) when K-fluoride was used in the internal solution

and 41.9 ± 8.6% (n = 17 NPC-384FF chips) when K-gluconate was used in the internal solution (Figure 1B). The success rate increased to 86.1 ± 6.4% (n = 15 NPC-384 chips) in K-fluoride and 55.0 ± 11.7% (n = 17 NPC-384FF chips) in K-gluconate when a QC cutoff R_{Seal} > 0.25 GΩ + I_{Peak} < −100 pA was used. In line with our results with hERG-HEK cells, we observed a similar R_{Seal} distribution pattern for both conditions as illustrated in the histogram (Figure 1D) and a significant difference in mean R_{Seal} values for CHO cells in standard and fluoride-free conditions (Table 3). Similar to hERG-HEK, success rates remained stable over the time course of the experiment, any differences can probably be also attributed to the absence of CaF_2 crystal formation as described above. Taken together, the results from both standard cell culture cell lines (HEK293 or CHO) expressing either $Na_V1.5$ or hERG channels suggest that the fluoride-free approach can be used as an alternative to fluoride-containing internal solution in automated patch clamp experiments with reduced, but acceptable success rates. Therefore, our aim was to minimize experimental variability (such as recording solutions, voltage protocols, recording temperature, expression system, and culturing conditions) and provide a systematic comparison of biophysical and pharmacological parameters for four different targets depending on the internal solutions used.

Effect of internal fluoride on currents, biophysical properties, and pharmacology of hERG expressed in HEK cells

From the hERG-HEK recordings shown in Figures 1A,C we also extracted peak current levels from available wells as displayed in the histogram (Figure 2A). Interestingly, the data showed a difference in the distribution pattern in line with a significantly higher mean peak current level when using fluoride-free solution (Table 2) and single-hole chips. To further understand this difference, we examined the IV relationship using a classical double step inactivation protocol with increasing voltages after initial depolarization to +60 mV using standard and fluoride-free internal solution (Figure 2B) and found a similar IV-relationship that started to deviate for voltages more positive to −40 mV (Figure 2C). The currents were therefore normalized to −40 mV and fitted with a standard Boltzmann equation and resulted in V_{half} values of −93.0 ± 0.5 mV (n = 190 cells) for standard and −92.1 ± 2.3 mV (n = 201 cells) for fluoride-free internal solution with the data pools found to be not significantly different (Figures 2C,D and Table 2). The results imply that voltage dependence per se does not account for the difference in peak current level observed when fluoride-free solution was used. We can also rule out differences in cell size or access resistance as capacitance values were the same in both conditions and R_{series} values were only slightly (but significantly) different (Table 2). Furthermore, the recordings were always performed in a comparable way on the same day using the same cells, recording temperature, external solution, and voltage protocol, with the only difference being the internal solution (standard or fluoride-free). This excludes any errors that may have arisen due to different recording conditions. Therefore, the reasons for the differences in increased currents in fluoride-free solution is unclear and further studies, such as detailed IV properties and a kinetic analysis, are required to elucidate the underlying reasons.

To investigate the influence of internal fluoride on the pharmacology of hERG channels we compared the IC_{50}s of verapamil and terfenadine in the presence and absence of internal fluoride. Figures 3A,B show traces from an example cell in the presence of increasing concentrations of verapamil in standard and fluoride-free internal solution, respectively. Figures 3C,D show the time course of the experiment for I_{Tail} current (at −40 mV) plotted over time using either standard (Figure 3C) or fluoride-free internal solution (Figure 3D) for an average of 54 and 11 cells, respectively. Also shown in Figures 3C,D is the vehicle control (0.3% DMSO, n = 58 cells for standard internal solution and 12 cells for fluoride-free internal) where rundown was low for both groups, <2% over 18 min (Table 2) indicating I_{Tail} current amplitude was stable regardless of internal solution used (P = 0.7, Student's t-test). hERG was blocked by verapamil in a concentration-dependent manner with similar IC_{50}s and the concentration-response curves overlaid almost exactly (Figure 3E, for terfenadine, see Supplementary Figure 1). The spread of IC_{50}s for terfenadine and verapamil was higher when fluoride-free internal solution was used (Figure 3F) but the IC_{50}s were not different to those recorded in standard internal solution (Figure 3F and Table 2). Taken together, despite differences in tail current amplitude, hERG channel voltage dependence of inactivation, recording stability (rundown) as well as pharmacology for the compounds tested seem independent of whether fluoride-free or standard internal solution was used, which has also been suggested by other studies (Zeng et al., 2008) implying that the effect of internal fluoride might not be generalized per se and rather depends on subtype specific modulation of ion channel activity.

Effect of internal fluoride on seal resistance, stability, biophysics, and pharmacology of $Na_V1.5$ expressed in CHO cells

From the experiments shown in Figures 1B,D, the peak current levels from available wells are displayed in Figure 4A as a histogram. In contrast to experiments involving hERG, the data showed a very similar distribution pattern consistent with a mean peak current amplitude that was not significantly different between the two groups (P = 0.2, Student's t-test; Table 3).

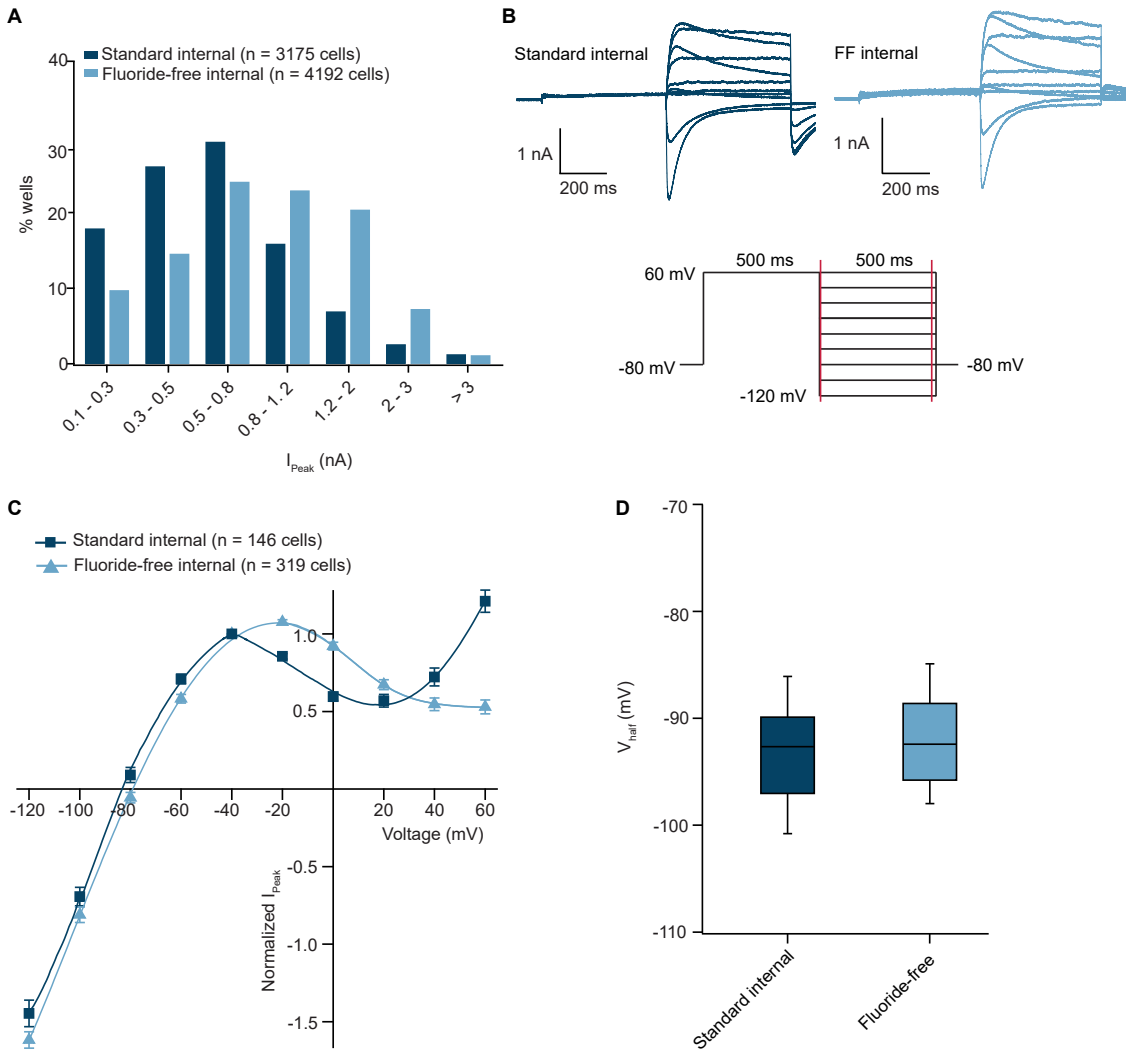

FIGURE 2
hERG currents in standard internal and fluoride-free internal solution. **(A)** Histogram plot of I_{Peak} values for standard internal and fluoride-free internal. There was a tendency to higher peak amplitudes in fluoride-free internal solution vs. standard internal. **(B)** Current-voltage traces of hERG using standard internal (left) and fluoride-free internal (right). The voltage protocol is shown underneath. **(C)** IV curves for an average of 146 cells in standard internal and 319 cells in fluoride-free solution are shown overlaid. A standard Boltzmann equation (see Section "Data analysis") was used to fit the curve from −120 to −20 mV. **(D)** V_{half} values for hERG recorded in standard internal and fluoride-free internal. The V_{half} values of 190 cells in standard internal and 261 cells in fluoride-free internal were not significantly different using a Student's *t*-test ($P > 0.05$).

Furthermore, currents were stable during the time course of the experiment for both groups, with current rundown < 2% over ∼12 min (Table 3). Next, we investigated the effect of internal fluoride on the voltage dependence of activation and fast inactivation. Looking at the literature, there is a relatively large variability in V_{half} values reported for $Na_V1.5$ due to different experimental parameters including voltage protocol, recording solutions, co-expression with β-subunits, recording temperature, holding potential, or cell expression system, the values range from −25 mV (Liu et al., 2003) to −50 mV (McNulty and Hanck, 2004). For this reason, we kept all experimental parameters the same, and only changed the internal solution in order to examine only the effect of fluoride on the V_{half} of activation and inactivation of $Na_V1.5$. Figure 4B shows the voltage protocols used for activation and inactivation of $Na_V1.5$ channels with example traces for both conditions. The results of these experiments are illustrated in Figures 4C,D where the V_{half} of activation was −25.2 ± 0.5 mV (n = 241) for fluoride-free and -37.5 ± 0.4 mV (n = 484) for standard internal solution. A similar difference was observed for the V_{half} of inactivation with −53.6 ± 0.6 mV (n = 165) in fluoride-free and −68.4 ± 0.4 mV (n = 728) using standard internal

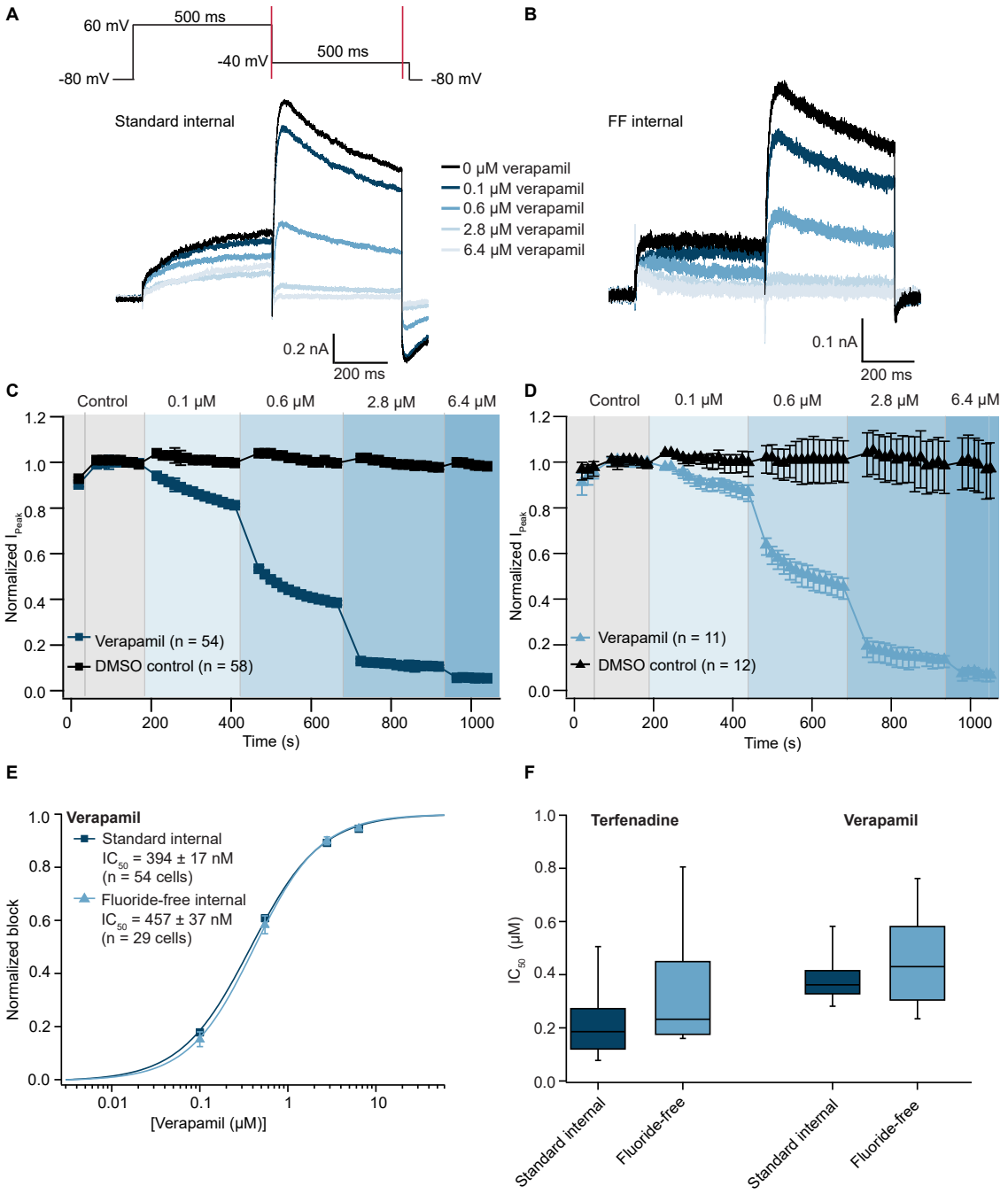

FIGURE 3
Pharmacology of hERG recorded in standard and fluoride-free internal solution. **(A,B)** Raw current traces from an example HEK cell expressing hERG recorded in standard internal **(A)** and fluoride-free internal **(B)** solution was blocked by increasing concentrations of verapamil [voltage protocol is shown at the top of panel **(A)**]. **(C)** Corresponding time course of block by verapamil in standard internal **(C)** and fluoride-free internal **(D)**, 54 or 11 cells, respectively. Time course of 58/12 cells in DMSO control is also shown within panels **(C,D)**. **(E)** Concentration response curve for verapamil in standard internal solution or fluoride-free solution are shown overlaid. **(F)** IC_{50}s for terfenadine and verapamil recorded using standard internal or fluoride-free internal solution are shown as a box plot. The IC_{50}s for verapamil and terfenadine recorded in standard internal or fluoride-free internal solution were not significantly different using a Student's *t*-test ($P > 0.05$).

solution. There is a clear hyperpolarizing effect of fluoride on the voltage sensitivity of $Na_V1.5$ channels which is highlighted in the boxplots shown in Figure 4D with ~12 mV difference for V_{half} of activation and ~15 mV for V_{half} of inactivation. Using the same voltage protocols as highlighted in Figure 4B we observed a similar hyperpolarizing shift for voltage activation/inactivation

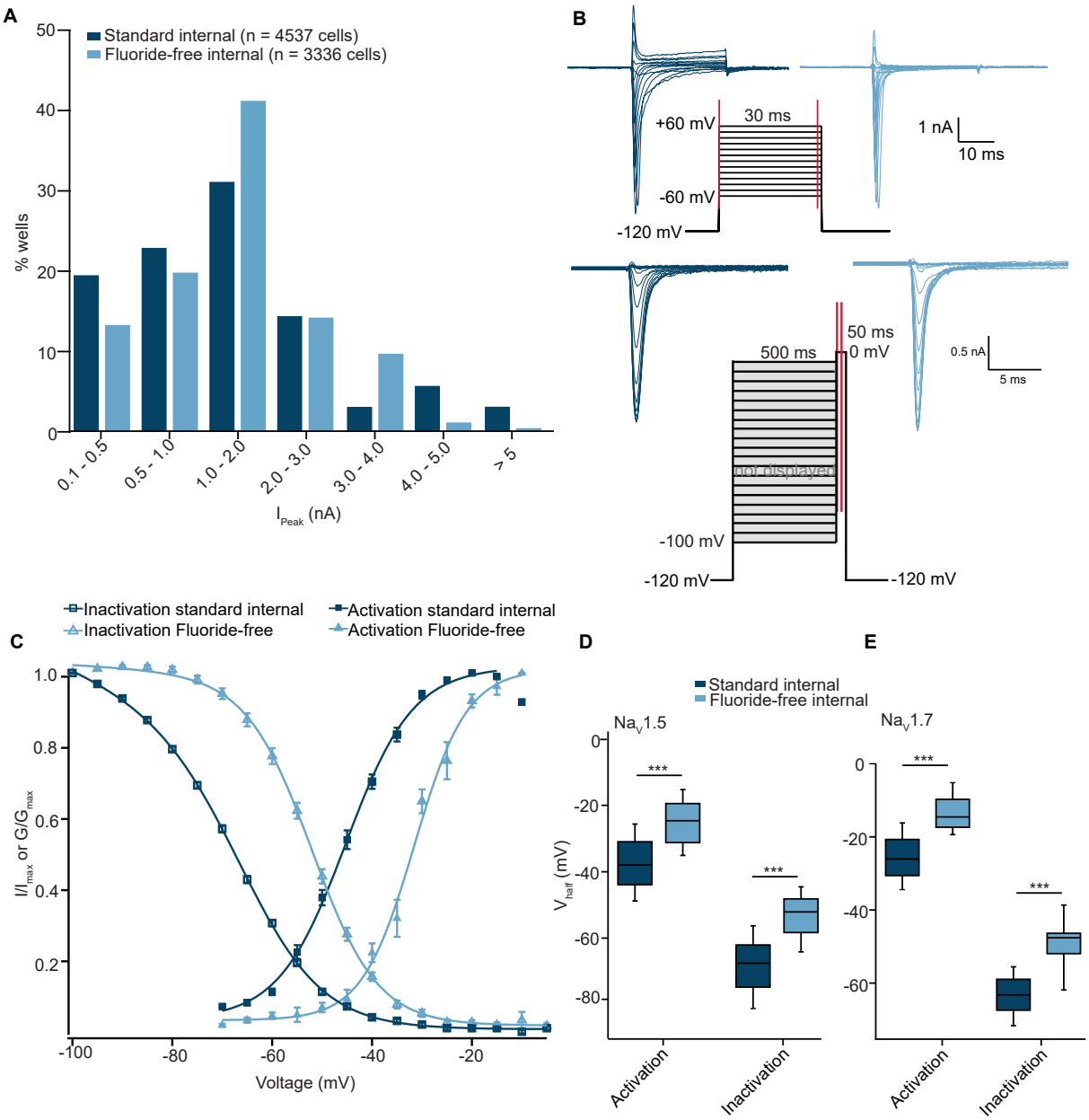

FIGURE 4
$Na_V1.5$ recorded in standard and fluoride-free internal solution. **(A)** Histogram plot of I_{Peak} values recorded using standard internal and fluoride-free internal solution. **(B)** Current-voltage traces of $Na_V1.5$ expressed in CHO cells using an activation protocol (top) and inactivation protocol (bottom) for both conditions. **(C)** Activation (fit with an extended Boltzmann equation, see Section "Data analysis") and inactivation IV curves (fit with a Boltzmann equation, see Section "Data analysis") for $Na_V1.5$ in standard internal and fluoride-free solution are shown overlaid. **(D)** The V_{half} values of activation of 484 cells in standard internal were significantly more negative compared with 241 cells in fluoride-free internal. The same shift to more negative V_{half} of inactivation was also found for 728 in standard internal fluoride compared with 165 cells in fluoride-free internal (Student's *t*-test, $^{***}P < 0.001$). **(E)** A shift in the V_{half} values of activation and inactivation was also observed for $Na_V1.7$ where V_{half} values for activation of 433 cells in standard internal were significantly more negative compared with 29 cells in fluoride-free internal and the V_{half} of inactivation for 493 in standard internal fluoride were significantly more negative compared with 14 cells recorded in fluoride-free internal solution (Student's *t*-test, $^{***}P < 0.001$).

of $Na_V1.7$ expressed in CHO cells when standard K-fluoride internal solution was used. This suggests a common phenotype for the shift of voltage activation/inactivation in $Na_V1.5$ and $Na_V1.7$ channels, however, further studies would be required to confirm whether other members of the Na_V family are affected in a same manner. In fact, a previous report indicates sub-type

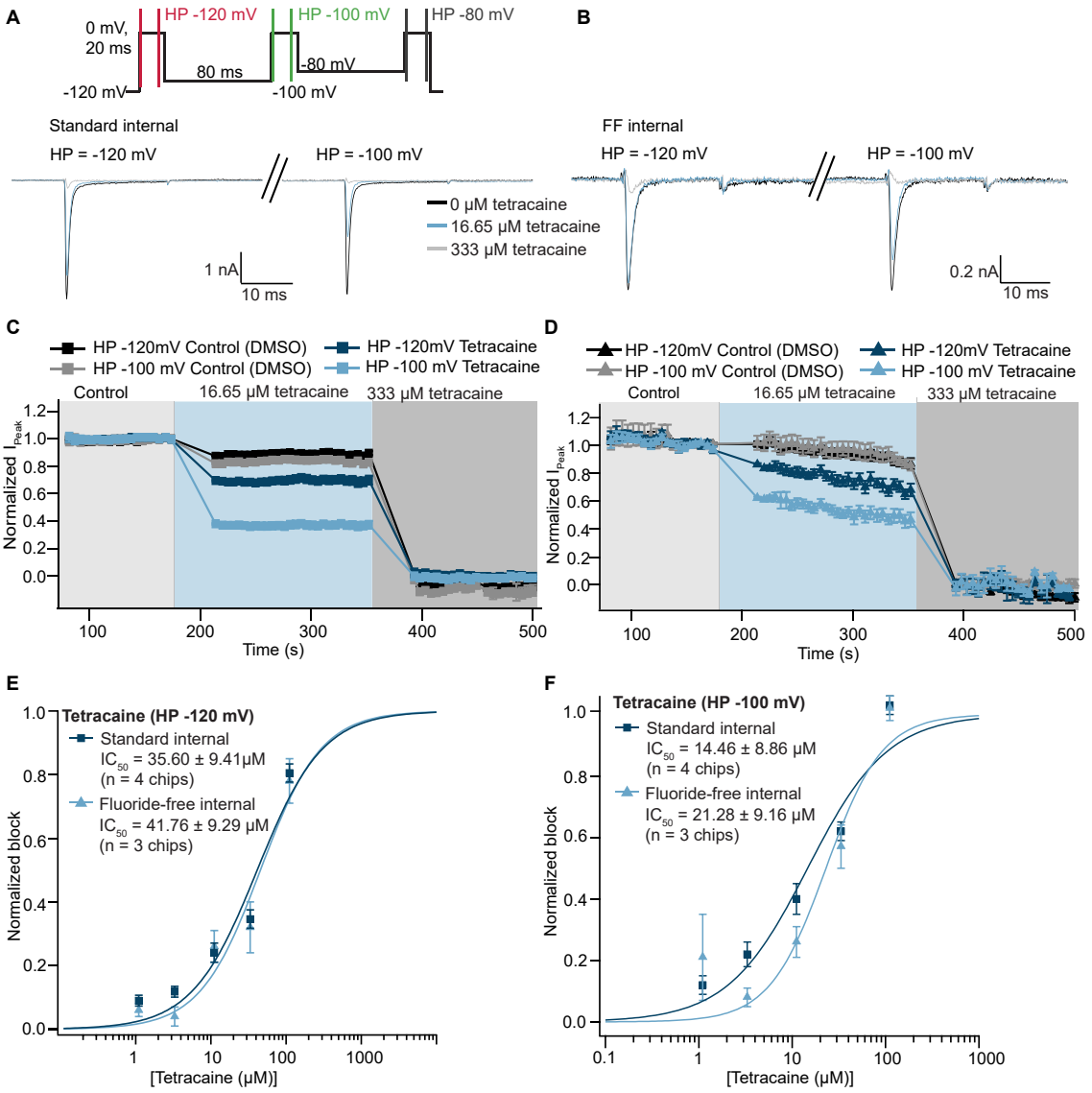

FIGURE 5
Pharmacology of $Na_V1.5$ recorded in standard and fluoride-free internal solution. **(A)** Raw current traces from an example CHO cell expressing $Na_V1.5$ recorded in standard internal solution were blocked by tetracaine using a 3-step protocol (voltage protocol shown at the top). Traces elicited by the first (holding potential −120 mV) and second (holding potential −100 mV) step are shown. **(B)** Raw current traces from an example CHO cell expressing $Na_V1.5$ recorded in fluoride-free internal solution were blocked by tetracaine. **(C)** Corresponding time course of block by tetracaine in standard internal solution for an average of 23 wells (at different holding potentials), time course in DMSO for an average of 41 wells is also shown. **(D)** Corresponding time course of block by tetracaine in fluoride-free internal solution for an average of 10 wells (at different holding potentials), time course in DMSO for an average of 35 wells is also shown. **(E)** Concentration response curves for tetracaine in standard internal solution or fluoride-free solution at a holding potential of −120 mV are shown overlaid. **(F)** Concentration response curves for tetracaine in standard internal solution or fluoride-free solution at a holding potential of −100 mV are shown overlaid.

specific differences associated with the use of internal fluoride solutions (Coste et al., 2004).

To test whether fluoride influences pharmacology of $Na_V1.5$ we used the known Na_V channel blocker, tetracaine. This was applied as a single concentration of compound to each well, followed by a full block concentration (333 µM). Using a 3-Pulse protocol we were able to compare the block of $Na_V1.5$-mediated currents by tetracaine at three different holding potentials as shown in Figures 5A,B (example traces are shown for the first two pulses only, corresponding to a holding potential of −120 and −100 mV). Figures 5C,D shows the peak current at 0 mV over time using two different holding potentials and tetracaine concentrations as well as vehicle only (0.3% DMSO) applied from the extracellular side. As expected, the potency of inhibition increased with a more depolarized holding potential for both conditions consistent with local

anesthetics preferably binding to the inactivated states (Hille, 1977; Hondeghem and Katzung, 1977; Bean et al., 1983; Li et al., 1999). Importantly, the concentration response curves for tetracaine overlaid almost exactly for individual voltages and were not statistically significantly different (Student's *t*-test, $P > 0.05$) for 4 NPC-384 chips in standard internal and 3 NPC-384FF chips in fluoride-free internal solution. However, the IC_{50}s for tetracaine under both conditions decreased ~4–7 fold from holding potentials of −120 mV compared with −100 and −80 mV (**Figures 5E,F** and **Supplementary Table 1**) comparable with values reported for lidocaine in the literature (Bean et al., 1983; Rapedius et al., 2019). In this way, the IC_{50} of tetracaine on $Na_V1.5$ seems independent of whether fluoride is present or not, which is somewhat surprising given the clear hyperpolarizing effect of internal fluoride on voltage activation/inactivation of $Na_V1.5$ (and $Na_V1.7$) and the dependence of tetracaine IC_{50} on holding potential. Further studies are needed to elucidate the molecular mechanisms of these differences and how they apply to other compounds.

Using fluoride-free solution to record $K_{Ca}3.1$ (SK4) channels in the presence of internal Ca^{2+}

We also tested the effect of internal fluoride for an ion channel activated by internal Ca^{2+} and used the internal perfusion of free Ca^{2+} to activate $K_{Ca}3.1$ (SK4) channels. CHO cells expressing $K_{Ca}3.1$ were captured with almost 50% success rate for $R_{Seal} \geq 1$ GΩ with standard and fluoride-free internal solution (**Figure 6A**), if a QC cutoff of $R_{Seal} \geq 0.25$ GΩ was used, the success rate was increased in both conditions (**Figure 6A**). As automated patch clamp recordings are sometimes performed using multi-hole chips to improve success of experiments, we also used multi-hole NPC-384 and NPC-384FF chips with 4 holes per well (4X). The success rates for cell capture and sealing were similar using 4X chips compared with single hole (1X) chips for both standard internal and fluoride-free internal solution (**Figure 6A**). Note that when 4X chips were used, $R_{Seal} > 0.25$ GΩ is equivalent to $R_{Seal} > 1$ GΩ with 1X chips and $R_{Seal} > 0.05$ GΩ is equivalent to $R_{Seal} > 0.25$ GΩ with 1X chips. A ramp voltage protocol from −120 to 60 mV was applied from a holding potential of −80 mV (**Figure 6B**). After exchange of the intracellular solution from 0 to 1 μM free intracellular Ca^{2+} an outwardly rectifying current was observed that was inhibited by external application of 1 mM Ba^{2+} (**Figures 6B,D**) when standard internal or fluoride-free internal solution was used. In fact, we observed a slightly higher success rate for available wells that passed the quality control criteria for current ($I > 350$ pA at 60 mV) after internal free Ca^{2+} application and $R_{Seal} > 0.25$ GΩ before internal free Ca^{2+} application when fluoride-free solution was used (**Figure 6C**), 70.3 ± 6.9% ($n = 9$ chips) vs. 60.6 ± 9.4 ($n = 8$ chips) when standard internal solution was used. Interestingly, when we repeated the same experiment using 4X NPC-384FF chips (quality check criteria for current $I > 1$ nA at 60 mV) the success rate increased to 94.5 ± 3.5% ($n = 2$ chips) and 91.2 ± 6.6 ($n = 2$ chips) when standard internal solution was used. This confirms the benefit of multi-hole chips for assay development in general, and as additional tool for experiments using fluoride-free internal solution.

Using increasing concentrations of internal free Ca^{2+}, we could estimate the apparent affinity for internal free Ca^{2+} to elicit $K_{Ca}3.1$ currents (**Figure 6E**). Both inward (measured at −120 mV) and outward currents (measured at 60 mV) were analyzed, and concentration response curves constructed for standard and fluoride-free solution at the different potentials. The concentration response curves for internal Ca^{2+} are shown overlaid in **Figure 6E**. The corresponding current analysis shows that when standard or fluoride-free solution was used, significantly larger peak currents were elicited at 0.3, 1, and 3 μM free internal Ca^{2+} compared with control (0 μM free internal Ca^{2+}) recorded at 60 mV ($P < 0.001$), whereas only 1 and 3 μM free internal Ca^{2+} elicited a significantly larger peak amplitude compared with control (0 μM free internal Ca^{2+}) recorded at −120 mV ($P < 0.001$), regardless of the internal solution used (**Supplementary Figure 2**). The data was normalized to the maximum response and fitted using a standard Hill equation (**Figure 6E**). The EC_{50} for internal Ca^{2+} was significantly lower when fluoride-free internal solution was used compared with standard internal solution at both 60 mV (635 ± 20 nM ($n = 121$) vs. 808 ± 50 nM ($n = 66$; $P < 0.01$)) and −120 mV (676 ± 22 nM ($n = 121$) in fluoride-free solution vs. 773 ± 44 nM ($n = 66$) in standard internal ($P < 0.05$)).

We also determined the IC_{50} for external Ba^{2+} using either standard internal or fluoride-free internal at −120 and 60 mV using 4X NPC-384 and 4X NPC-384FF chips, with the same ramp protocol shown in **Figure 6B**. **Figure 6F** shows the concentration response curves for Ba^{2+} at −120 and 60 mV in standard and fluoride-free solution. Ba^{2+} was added as a single concentration to each well and the concentration response curves were constructed across the whole plate where it blocked the current at −120 mV with a higher potency than at 60 mV. **Figure 6F** shows the average concentration response curves for 2 NPC-384 or 2 NPC-384FF chips. The IC_{50} for Ba^{2+} (mean ± S.D.) was 170 ± 8 μM when standard and 158 ± 15 μM when fluoride-free internal solution was used at a voltage of −120 mV. The IC_{50} increased ~3-fold to 540 ± 105 μM when standard and 728 ± 161 μM at 60 mV when fluoride-free internal solution was used.

From these results we conclude that the recording of Ca^{2+}-activated K-channels is possible under standard as well as fluoride-free conditions with similar success rates, and even higher success rates for available wells after Ca^{2+} activation with 4X chips than with 1X chips, making multi-hole chips a useful tool for recording Ca^{2+}-activated K-channels. Given

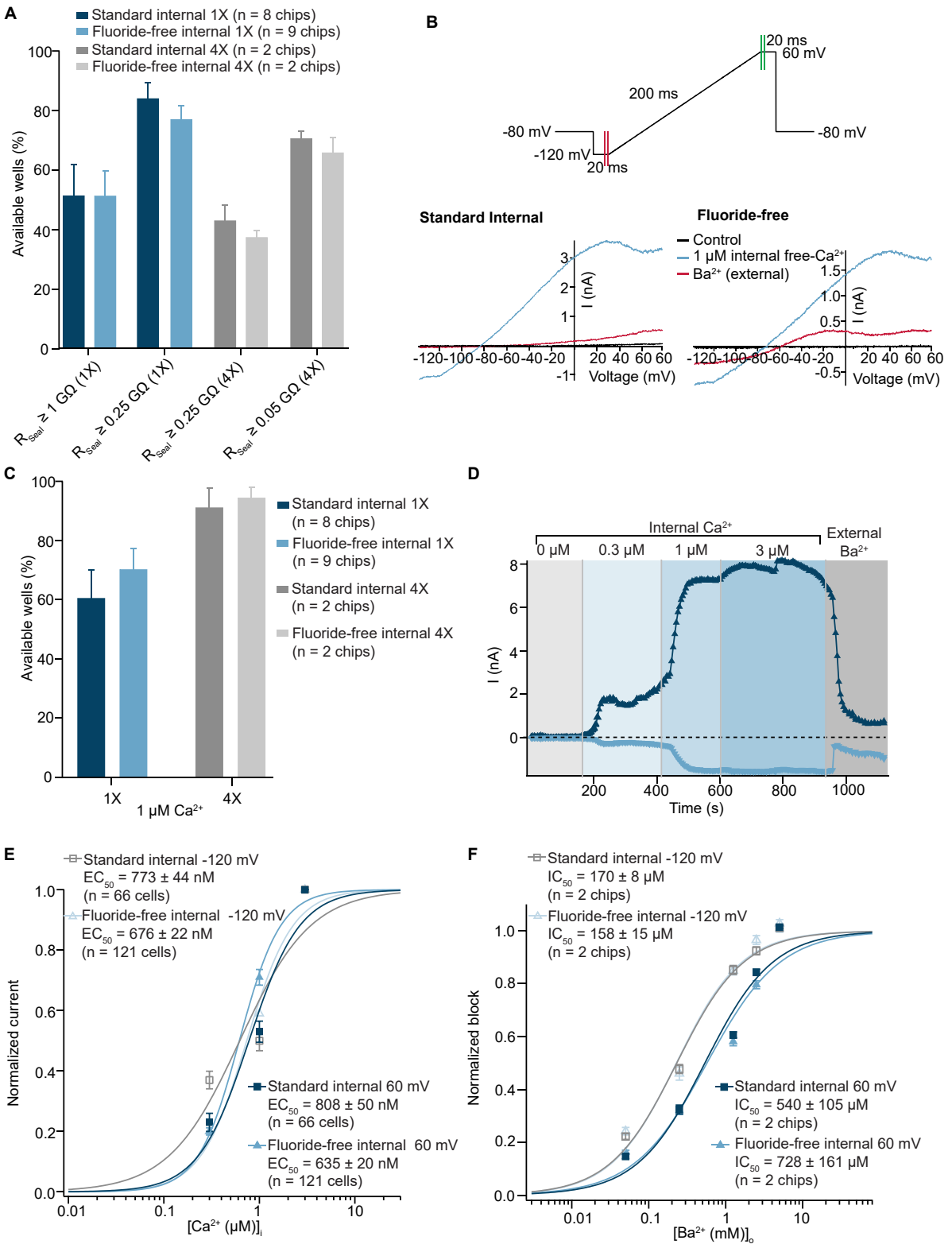

FIGURE 6
Activation by internal free Ca^{2+} of $K_{Ca}3.1$ recorded in standard and fluoride-free internal solution. **(A)** CHO cells expressing $K_{Ca}3.1$ were captured with almost 50% success rate for $R_{Seal} \geq 1$ GΩ with standard and in fluoride-free internal solution (left). If a QC cutoff of $R_{Seal} \geq 0.25$ GΩ was used, the success rate was increased in both conditions (right). Similar success rates were also achieved with multi-hole

(Continued)

FIGURE 6 (Continued)
(4X) chips (gray). **(B)** Raw current traces from example CHO cell expressing $K_{Ca}3.1$ recorded in both standard and fluoride-free internal solution, activated by 1 μM free internal Ca^{2+} and blocked by 1 mM Ba^{2+} (external). **(C)** Success rates after applying initial R_{Seal} (>0.25 GΩ) and current QC plot of I_{Peak} values at −120/60 mV for standard and fluoride-free solutions after internal application of 1 μM free Ca^{2+}. **(D)** IT plot during application of internal free Ca^{2+} with 0.3, 1, and 3 μM free internal Ca^{2+} and subsequent block by external Ba^{2+} (1 mM) at −120/60 mV. **(E)** Current values at −120 or 60 mV in increasing concentrations of internal free Ca^{2+} were normalized to maximum peak amplitude and fit using a Hill equation which shows a slightly increased EC_{50} in standard internal solutions for both voltages. Shown are mean ± S.E.M. **(F)** Current values at −120 or 60 mV in increasing concentrations of external Ba^{2+} were normalized to maximum peak amplitude and fit using a Hill equation which showed no difference in the IC_{50} at −120 mV between standard internal (170 ± 8 μM, n = 2 chips) and fluoride-free internal (158 ± 15 μM, n = 2 chips) or 60 mV, although the IC_{50} was higher at 60 vs. −120 mV for both groups (540 ± 105 μM, n = 2 chips in standard external and 728 ± 161 μM, n = 2 chips in fluoride-free internal solution). IC_{50} values are given as mean of 2 chips ± S.D.

that the EC_{50} for Ca^{2+} was lower with fluoride-free internal solution, and peak currents were larger, we suggest that fluoride-free internal solution may provide an advantage over standard fluoride-containing internal solutions for recording Ca^{2+} activated channels.

Discussion

There is no doubt that automated patch clamp has become an integral part of many electrophysiological assays involving ion channels, including safety pharmacology, lead optimization, target validation, and channelopathy research (Obergrussberger et al., 2021, 2022). Unlike manual patch clamp, the cell cannot be chosen, nor can the patch clamp aperture be moved to improve the seal. In APC, the patch clamp aperture is stationary and solely suction is used to attract the cell to the hole. In both manual and automated patch clamp, suction is then used to further improve the seal and to break into the whole cell configuration. Fluoride has been used in the internal solution in manual and automated patch clamp for years to assist with seal formation (Zeng et al., 2008; Föhr et al., 2021), in particular to record voltage-gated sodium channels where seal resistance and access parameters are critical for good voltage control. The mechanism is thought to involve CaF_2 crystals forming at the aperture (Lojkner et al., 2019). However, it is well-documented that fluoride causes shifts in the activation and inactivation kinetics of Na_V channels (Meadows et al., 2002; Rugiero et al., 2003; Coste et al., 2004; Jarecki et al., 2008), as well as affecting persistent calcium current in neurons (Kay et al., 1986), activating G-proteins through interaction with Al^{3+} (Yatani and Brown, 1991; Li, 2003), and inhibits phosphatase activity (Khatra and Soderling, 1978).

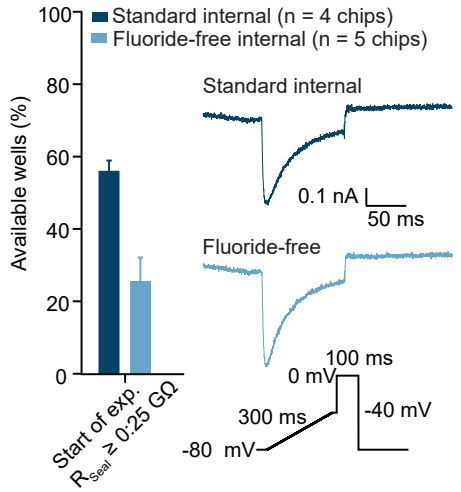

FIGURE 7
hiPSC-CMs recorded in standard and fluoride-free internal solution. hiPSC-CMs were captured with almost 60% success rate for $R_{Seal} \geq 0.25$ GΩ when using standard internal solution and about 25% $R_{Seal} \geq 0.25$ GΩ in fluoride-free internal solution in preliminary experiments. The inset shows an example of a Ca_V current recorded from an example cell in standard (top, dark blue) and fluoride-free (bottom, light blue). The voltage protocol used is also shown and only response to voltage step to 0 mV is shown in the raw trace examples.

Fluoride has little effect on hERG currents

As expected, our data show that success rate as measured by % available wells using strict quality control parameters including R_{Seal} > 1 GΩ or 0.25 GΩ and I_{Peak} > 150 pA was higher when fluoride was used in the internal solution compared with fluoride-free internal solution when HEK cells stably expressing the hERG channel were used. However, with a success rate of around 60% for usable wells (R_{Seal} > 0.25 GΩ) when K-gluconate was used, this results in over 200 usable wells in each experiment lasting approximately 20 min and thus, a vast increase in throughput compared with manual patch clamp. Importantly, there was little change in the number of usable wells at the end of the experiment compared with at the start, indicating that fluoride is not absolutely necessary for long-lasting recordings and 60% for completed experiments is an acceptable success rate for screening.

When fluoride was replaced by gluconate in the internal solution, hERG-mediated currents were slightly,

but statistically significantly, larger than when fluoride was present ($P < 0.05$, unpaired Student's *t*-test). This has not been previously reported and the reasons for the difference are not clear, additional studies are required to elucidate the underlying root cause. In our experiments, we can exclude differences in cell size since the cell capacitance values were unchanged in fluoride and fluoride-free solution, and we have also shown that fluoride does not shift the V_{half} of the hERG tail current. This is in agreement with Zeng et al. (2008, 2013) who also reported no effect on tail current activation parameters by fluoride compared with chloride when using the automated patch clamp system, the PatchXpress, and manual patch clamp, although the fluoride vastly increased success rate on the PatchXpress from 10% in K-chloride to 75% in K-fluoride (Zeng et al., 2008). Indeed, we also found no difference in success rate for K-chloride-containing internal solution compared with K-gluconate-containing internal solution (**Supplementary Table 3**) and can conclude that both gluconate and chloride are suitable alternatives to fluoride for recordings of hERG-HEK on the SyncroPatch 384.

We also compared the IC_{50} values for two compounds, terfenadine and verapamil, obtained using K-fluoride or K-gluconate and found that the IC_{50}s were not different and agreed well with the range found in the literature (Zeng et al., 2008; Kramer et al., 2013; Crumb et al., 2016; Brinkwirth et al., 2020). From our results and those of Zeng et al. (2008, 2013) we can conclude that fluoride does improve the success rate based on R_{Seal} and completed experiments and does not affect V_{half} of hERG tail current nor pharmacology, at least for the two compounds tested. Therefore, we can further conclude that the use of fluoride in the internal solution for hERG screening can be an advantage due to improved success rate, but fluoride-free internal solution can be used on the SyncroPatch 384 with success rates compatible with high throughput screening.

Fluoride shifts V_{half} of activation and inactivation of $Na_V1.5$ and $Na_V1.7$

CHO cells expressing $Na_V1.5$ were also used on the SyncroPatch 384 in fluoride-free internal solution with similar success rates to HEK expressing hERG indicating that this method can be applied to different cell types and different ion channels. Average R_{Seal} values were >1 GΩ regardless of internal solution used, and no difference in I_{Peak} in fluoride-free internal solution compared with standard fluoride internal solution was observed which contrasts to the results observed with hERG.

Our results show that fluoride in the internal solution causes a negative shift in the V_{half} of activation and inactivation of both $Na_V1.5$ (**Figures 4C,D**) and $Na_V1.7$ (**Figure 4E**) which agrees with previous reports that fluoride shifts the V_{half} of activation and inactivation to more negative values of $Na_V1.3$ (Meadows et al., 2002), $Na_V1.7$ (Jarecki et al., 2008), and $Na_V1.9$ (Rugiero et al., 2003; Coste et al., 2004). The values for V_{half} of activation and inactivation for $Na_V1.5$ and $Na_V1.7$ were in good agreement with the literature for fluoride internal (Sheets and Hanck, 1999; Li et al., 2017). Importantly, despite shifts in the V_{half} of activation and inactivation, the IC_{50} of tetracaine block of $Na_V1.5$ was not statistically different in fluoride-free internal solution compared with standard fluoride (**Table 3** and **Figures 5E,F**). Changing the holding potential from −120 to −100 mV or −80 mV resulted in a more potent IC_{50} of tetracaine, regardless of fluoride or fluoride-free internal solution was used (see **Supplementary Table 1**) as expected, as tetracaine and other local anesthetics are state dependent blockers of sodium channels (Hille, 1977; Hondeghem and Katzung, 1977; Bean et al., 1983; Li et al., 1999). The result is somewhat surprising given the fact that internal fluoride acts in a hyperpolarizing fashion and tetracaine is dependent on the holding potential used and may point towards related but independent mechanisms of modulation during transitions between closed, open and inactivated states of $Na_V1.5$ channels as suggested for $Na_V1.8$ and $Na_V1.9$ channels (Coste et al., 2004).

A shift in the activation and inactivation kinetics for cardiac $Na_V1.5$ channels over time has been reported for canine cardiac Purkinje cells (Hanck and Sheets, 1992), rat ventricular cardiac myocytes (Maltsev and Undrovinas, 1997), and rabbit atrial myocytes (Wendt et al., 1992) using manual whole cell patch clamp. In a small study using $Na_V1.5$ expressed in CHO cells, our results also indicate a negative shift in the V_{half} of activation and inactivation over time (data not shown) as previously reported (Hanck and Sheets, 1992; Wendt et al., 1992; Maltsev and Undrovinas, 1997) when activation and inactivation IVs were measured after 10 min compared with immediately after achieving the whole cell configuration. The V_{half} of activation shifted by −0.78 mV/min in fluoride internal and −0.43 mV/min in fluoride-free internal solution. The V_{half} of inactivation shifted by −1.22 mV/min in fluoride and −0.38 mV/min in fluoride-free. In this respect, although the shift in parameters appeared to be more pronounced when fluoride was present, the absence of fluoride did not completely abolish this shift in agreement with Wendt et al. (1992) who also reported a shift in the activation and inactivation parameters regardless of whether fluoride, chloride, aspartate, or glutamate were present in the internal solution. It has been proposed that the shift in activation is dependent on the cytoskeleton (Maltsev and Undrovinas, 1997) and is prevented using the perforated patch technique (Wendt et al., 1992). All our experiments were performed in the whole cell mode of the

patch clamp technique, but the use of a perforator in the internal solution would allow perforated patch experiments to be performed.

Temperature has also been shown to affect activation and inactivation of Na_V channels where cooled temperatures cause a depolarizing shift in the V_{half} of activation of $Na_V1.3$, 1.5, 1.6, and 1.7 (Kriegeskorte et al., 2022). Increasing the temperature to physiological temperature (36 ± 1°C) can also mildly shift the V_{half} of inactivation to more hyperpolarized potentials (Rotordam et al., 2021). Increased temperatures have also been shown to affect IC_{50}s on hERG current, e.g., erythromycin (Kirsch et al., 2004; Stoelzle et al., 2011) and $Na_V1.5$, e.g., mexiletine (Rotordam et al., 2021). For these reasons, it may be desirable to perform automated patch clamp experiments at physiological temperature. Recording at physiological temperature is more challenging and can result in a lower success rate and shorter recordings. In preliminary experiments at physiological temperature, we found that there was little change in the success rate when fluoride was used in the internal solution (see **Supplementary Table 2**) but the success rate in fluoride-free solution was slightly lower compared with room temperature [30.0 ± 7.1 (6 chips) for R_{Seal} > 1 GΩ at physiological temperature vs. 41.9 ± 8.6% (17 chips) at room temperature see **Supplementary Table 2** and Section "High throughput APC to assess effects of internal fluoride on success rate and seal resistance"], nevertheless, and average R_{Seal} was > 1 GΩ in both conditions (**Supplementary Table 2**) and recordings lasted approximately 20 min (data not shown).

In conclusion for Na_V channels, we could confirm that fluoride shifts the V_{half} of activation and inactivation of $Na_V1.5$ and $Na_V1.7$ as has been reported for other Na_V channels (Meadows et al., 2002; Rugiero et al., 2003; Coste et al., 2004; Jarecki et al., 2008) but does not alter the IC_{50} of tetracaine on Nav1.5 channels. Success rates are higher when using fluoride in the internal solution, as expected, and many labs using both conventional and automated patch clamp use internal fluoride when recording Na_V channels and this must be taken into consideration when comparing kinetic parameters with the literature.

Experiments involving Ca^{2+}-activated ion channels

Intracellular Ca^{2+} activated ion channels pose a challenge to APC devices given the use of internal fluoride solutions and the very low solubility of CaF_2 ($K_{sp} = 3.5 \times 10^{-11}$) resulting in unstable amounts of free internal Ca^{2+} concentrations. Nevertheless, the use of appropriate buffer solutions and chelating agents do allow for the development of high throughput drug discovery on Ca^{2+}-activated K-Channels [please see Section "Materials and methods" (see **Table 1**) or Srinivasan et al. (2022)]. Our aim was to compare this approach to our recently developed fluoride-free method using a Ca^{2+}-activated K-channel.

When single hole chips were used, the success rate based on seal resistance did not differ much between standard and fluoride-free solutions, which contrasts to the success rate for cells expressing hERG or $Na_V1.5$, however, the success rate based on current amplitude after activation with 1 μM internal free-Ca^{2+} was increased in experiments where fluoride-free solution was used (**Figures 6A,C**). Additionally, current amplitudes were larger in fluoride-free internal solution (**Supplementary Figure 2**) and the EC_{50} for Ca^{2+} slightly lower (**Figure 6E**). Taken together, it would appear, for Ca^{2+}-activated ion channels at least, fluoride-free internal solution should be recommended. When fluoride is present, there is most probably an unknown amount of precipitation of CaF_2, even if this is not visible, and this can affect the apparent Ca^{2+} affinity, not to mention fluoride interfering with intracellular signaling process involving, for example, phosphorylation (Khatra and Soderling, 1978; Li, 2003). Activation of Ca^{2+}-activated K-channels using fluoride is possible on high throughput APC devices, as shown recently for the BK channel by Srinivasan et al. (2022), however, the free internal Ca^{2+} may be more stable in fluoride-free conditions, especially over time/during the course of the day where precipitation cannot be completely prevented. The use of multi-hole chips with four holes per well (4X) is also possible thus improving the success rate based on current amplitude for both standard and fluoride-free internal solution to over 90%.

Conclusion

In keeping with the topic of this special issue: "Targeting Ion Channels for Drug Discovery: Emerging Challenges for High Throughput Screening Technologies," we have overcome the challenge of low success rates and low seal resistances on high throughput automated patch clamp devices when using fluoride-free physiological internal solution. Implementation of specialized consumables (NPC-384FF) enables us to report success rates for fluoride-free recordings of approximately 60–80% for $R_{Seal} \geq 0.25$ GΩ and 40–50% for $R_{Seal} \geq 1$ GΩ. We mainly used a K-gluconate-based internal solution, but we observed similar success rates using K-chloride-based internal solution (**Supplementary Table 3**). Recordings were also stable, typically lasting around 20 min where cumulative additions of compound or single additions of compound and incubation times of 5 min in compound were used, as per best practice considerations recommended previously for hERG and $Na_V1.5$ (Brinkwirth et al., 2020; Rotordam et al., 2021). In the case of hERG, since fluoride does not appear to exert an obvious influence over inactivation parameters or IC_{50} values, the user

is free to choose whether to use fluoride or fluoride-free internal solution and may prefer fluoride-containing solutions to maximize success rates and minimize cost per data point. For experiments involving Na_V channels, the user should be aware that fluoride causes shifts in activation and inactivation parameters and caution should be used when comparing data generated in different solutions. For recording Ca^{2+}-activated channels, success rates for completed experiments are similar under both conditions, however, the response to internal free Ca^{2+} and estimation of its apparent affinity may be more favorable to pursue when fluoride-free internal solution is used due to complete absence of CaF_2 precipitation and, therefore, there is an advantage for the user to be able to utilize fluoride-free solution with success rates exceeding 50% for completed experiments. Coupling fluoride-free internal solution with multi-hole chips increases the success rate for available wells to >90% and is, therefore, also a consideration when designing the experiment in ion channel drug screening.

Additionally, in preliminary recordings we could successfully use the fluoride-free approach for experiments involving stem cell-derived cardiomyocytes (**Figure 7**). Therefore, the approach is not limited to standard cell lines but could be adopted for a wide range of cell types and experiments to bring conditions used to generate high throughput APC data closer and more comparable to recordings done using manual patch clamp and physiological solutions. Ultimately, this will enhance ion channel characterization and compound testing when using not only cell lines, but also induced pluripotent stem cells and primary cells.

Data availability statement

The raw data supporting the conclusions of this article will be made available by the authors, without undue reservation.

Author contributions

MR designed the study, performed the experiments and analysis, and contributed to writing and proofreading the manuscript. AO designed the experiments, analyzed the data, made the figures, and wrote and proofreading the manuscript. SS, TG, NB, and MGR performed the experiments and contributed to writing and proofreading the manuscript. IR-W, TS, and AR performed the experiments and analysis and contributed to writing and proofreading the manuscript. SF designed the study, performed analysis, and contributed to writing and proofreading the manuscript. NF contributed to writing and proofreading the manuscript. AL, FS, and NV provided the iPSC derived cardiomyocytes, helped with the design of experiments, and contributed to writing and proofreading the manuscript. All authors contributed to the article and approved the submitted version.

Funding

This work was supported by grants from the Deutsche Forschungsgemeinschaft (DFG) to NV (VO1568/3-1, VO1568/4-1, IRTG1816, and SFB1002 project A13 and under Germany's Excellence Strategy—EXC 2067/1—390729940) and from the German Center for Cardiovascular Research to NV (DZHK, 81X2300189, 81X4300102, 81X4300115, and 81X4300112).

Acknowledgments

We thank SB Drug Discovery for kindly providing the hERG-HEK cell line and Charles River Laboratories for kindly providing the $Na_V1.5$-CHO, $Na_V1.7$-CHO, and $K_{Ca}3.1$-CHO cell lines used to compile this manuscript.

Conflict of interest

MR, AO, SS, IR-W, TG, NB, MGR, TS, AR, SF, and NF were employed by Nanion Technologies, the manufacturers of the SyncroPatch 384 used to compile this manuscript. NF was a shareholder in Nanion Technologies. EH was employed by BioPharmaceuticals R&D, AstraZeneca.

The remaining authors declare that the research was conducted in the absence of any commercial or financial relationships that could be construed as a potential conflict of interest.

Publisher's note

Supplementary material

The Supplementary Material for this article can be found online at: https://www.frontiersin.org/articles/10.3389/fnmol.2022.982316/full#supplementary-material

References

Bean, B. P., Cohen, C. J., and Tsien, R. W. (1983). 'Lidocaine block of cardiac sodium channels.'. *J. Gen. Physiol.* 81, 613–642. doi: 10.1085/jgp.81.5.613

Becker, N., Stoelzle, S., Göpel, S., Guinot, D., Mumm, P., Haarmann, C., et al. (2013). 'Minimized cell usage for stem cell-derived and primary cells on an automated patch clamp system'. *J. Pharmacol. Toxicol. Methods* 68, 82–87. doi: 10.1016/j.vascn.2013.03.009

Becq, F., Mirval, S., Carrez, T., Lévêque, M., Billet., A, Coraux, C., et al. (2021). 'The rescue of F508del-CFTR by elexacaftor/tezacaftor/ivacaftor (Trikafta) in human airway epithelial cells is underestimated due to the presence of ivacaftor'. *Eur. Respir. J.* 59:2100671. doi: 10.1183/13993003.00671-2021

Berger, H. A., Travis, S. M., and Welsh, M. J. (1998). 'Fluoride stimulates cystic fibrosis transmembrane conductance regulator Cl- channel activity'. *Am. J. Physiol.Lung Cell. Mol. Physiol.* 274, L305–L312.

Billet, A., Froux, L., Hanrahan, J. W., and Becq, F. (2017). 'Development of automated patch clamp technique to investigate CFTR chloride channel function'. *Front. Pharmacol.* 8:195. doi: 10.3389/fphar.2017.00195

Brinkwirth, N., Takasuna, K., Doi, M., Becker, N., Obergrussberger, A., Friis, S., et al. (2020). 'Reliable identification of cardiac liability in drug discovery using automated patch clamp: Benchmarking best practices and calibration standards for improved proarrhythmic assessment'. *J. Pharmacol. Toxicol. Methods* 105:106884. doi: 10.1016/j.vascn.2020.106884

Brueggemann, A., George, M., Klau, M., Beckler, M., Steindl, J., Behrends, J. C., et al. (2004). 'Ion channel drug discovery and research : The automated nano-patch–clamp © technology'. *Curr. Drug Discov. Technol.* 1, 91–96. doi: 10.2174/1570163043484833

Brüggemann, A., Farre, C., Haarmann, C., Haythornthwaite, A., Kreir, M., Stoelzle, S., et al. (2008). "Planar patch clamp: Advances in electrophysiology," in *Methods in molecular biology, potassium channels*, ed. J. D. Lippiat (Totowa, NJ: Humana Press, a part of Springer Science & Business Media), 165–176. doi: 10.1007/978-1-59745-526-8

Brüggemann, A., Friis, S., Strassmeier, T., Goetze, T., Haarmann, C., Fertig, N., et al. (2017). Characterization of CFTR activators and inhibitors by the use of a planar patch clamp system. *Biophys. J.* 112:411a. doi: 10.1016/j.bpj.2016.11.2561

Chen, Y. H., Dale, T. J., Xie, X. M., Clare, J. J., Romanos, M. A., Whitaker, W. R., et al. (2000). 'Cloning, distribution and functional analysis of the type III sodium channel from human brain'. *Eur. J. Neurosci.* 12, 4281–4289. doi: 10.1111/j.1460-9568.2000.01336.x

Coste, B., Osorio, N., Padilla, F., Crest, M., and Delmas, P. (2004). 'Gating and modulation of presumptive NaV1.9 channels in enteric and spinal sensory neurons'. *Mol. Cell. Neurosci.* 26, 123–134. doi: 10.1016/j.mcn.2004.01.015

Crumb, W. J., Vicente, J., Johannesen, L., and Strauss, D. G. (2016). 'An evaluation of 30 clinical drugs against the comprehensive in vitro proarrhythmia assay (CiPA) proposed ion channel panel'. *J. Pharmacol. Toxicol. Methods* 81, 251–262. doi: 10.1016/j.vascn.2016.03.009

Cummins, T. R., Dib-Hajj, S. D., Black, J. A., Akopian, A. N., Waxman, S. G., Wood, J. N., et al. (1999). A novel persistent tetrodotoxin-resistant sodium current in SNS-null and wild-type small primary sensory neurons. *J. Neurosci.* 19:RC43. doi: 10.1523/jneurosci.19-24-j0001.1999

Föhr, K. J., Nastos, A., Zimmer, T., Jungwirth, B., Messerer, D. A. C., Fauler, M., et al. (2021). 'Block of voltage-gated sodium channels by atomoxetine in a state- and use-dependent manner'. *Front. Pharmacol.* 12:622489. doi: 10.3389/fphar.2021.622489

Froux, L., Elbahnsi, A., Boucherle, B., Billet, A., Baatallah, N., Hoffmann, B., et al. (2020). 'Targeting different binding sites in the CFTR structures allows to synergistically potentiate channel activity'. *Eur. J. Med. Chem.* 190:112116. doi: 10.1016/j.ejmech.2020.112116

Hanck, D. A., and Sheets, M. F. (1992). Time-dependent changes in kinetics of Na+ current in single canine cardiac Purkinje cells'. *Am. J. Physiol. Heart Circ. Physiol.* 262(4 Pt 2), H1197–H1207. doi: 10.1152/ajpheart.1992.262.4.h1197

Herrmann, A. M., Cerina, M., Bittner, S., Meuth, S. G., and Budde, T. (2020). 'Intracellular fluoride influences TASK mediated currents in human T cells'. *J. Immunol. Methods* 487:112875. doi: 10.1016/j.jim.2020.112875

Hille, B. (1977). 'Local anesthetics: Hydrophilic and hydrophobic pathways for the drug-receptor reaction.'. *J. Gen. Physiol.* 69, 497–515. doi: 10.1085/jgp.69.4.497

Hondeghem, L. M., and Katzung, B. G. (1977). 'Time- and voltage-dependent interactions of antiarrhythmic drugs with cardiac sodium channels'. *BBA Rev. Biomembr.* 472, 373–398. doi: 10.1016/0304-4157(77)90003-X

Jarecki, B. W., Jackson, J. O. II, Cummins, T. R., and Sheets, P. L. (2008). 'Paroxysmal extreme pain disorder mutations within the D3/S4-S5 linker of Nav1.7 cause moderate destabilization of fast inactivation'. *J. Physiol.* 586, 4137–4153. doi: 10.1113/jphysiol.2008.154906

Kay, A. R., Miles, R., and Wong, R. K. S. (1986). 'Intracellular fluoride alters the kinetic properties of calcium currents facilitating the investigation of synaptic events in hippocampal neurons'. *J. Neurosci.* 6, 2915–2920. doi: 10.1523/jneurosci.06-10-02915.1986

Khatra, B. S., and Soderling, T. R. (1978). 'Reversible inhibition of skeletal muscle phosphoprotein phosphatase by ATP, phosphate and fluoride'. *Biochem. Biophys. Res. Commun.* 85, 647–654. doi: 10.1016/0006-291X(78)91211-1

Kirsch, G. E., Trepakova, E. S., Brimecombe, J. C., Erickson, H. D., Kochan, M. C., Shyjka, L. M., et al. (2004). 'Variability in the measurement of hERG potassium channel inhibition: Effects of temperature and stimulus pattern'. *J. Pharmacol. Toxicol. Methods* 50, 93–101. doi: 10.1016/j.vascn.2004.06.003

Kleinsorge, M., and Cyganek, L. (2020). 'Subtype-directed differentiation of human iPSCs into atrial and ventricular cardiomyocytes'. *STAR Protoc.* 1:100026. doi: 10.1016/j.xpro.2020.100026

Kramer, J., Obejero-Paz, C. A., Myatt, G., Kuryshev, Y. A., Bruening-Wright, A., Verducci, J. S., et al. (2013). 'MICE models: Superior to the HERG model in predicting Torsade de Pointes.'. *Sci. Rep.* 3:2100. doi: 10.1038/srep02100

Kriegeskorte, S., Raya, B., Martin, H., Ralf, H., and Angelika, L. (2022). High-throughput electrophysiology reveals subtype specific temperature dependence of sodium channel activation and inactivation. *Biophys. J.* 121:95A. doi: 10.1016/j.bpj.2021.11.2249

Li, H. L., Galue, A., Meadows, L., and Ragsdale, D. S. (1999). 'A molecular basis for the different local anesthetic affinities of resting versus open and inactivated states of the sodium channel'. *Mol. Pharmacol.* 55, 134–141. doi: 10.1124/mol.55.1.134

Li, L. (2003). 'The Biochemistry and Physiology of Metallic Fluoride: Action, Mechanism, and Implications'. *Crit. Rev. Oral Biol. Med.* 14, 100–114. doi: 10.1177/154411130301400204

Li, T., Lu, G., Chiang, E. Y., Chernov-Rogan, T., Chen, J., Grogan, J. L., et al. (2017). 'High-throughput electrophysiological assays for voltage gated ion channels using Syncro Patch 768PE'. *PLoS One* 12:e0180154. doi: 10.1371/journal.pone.0180154

Liu, H., Atkins, J., and Kass, R. S. (2003). 'Common molecular determinants of flecainide and lidocaine block of heart Na+ channels: Evidence from experiments with neutral and quaternary flecainide analogues'. *J. Gen. Physiol.* 121, 199–214. doi: 10.1085/jgp.20028723

Lojkner, L. D., Anders, L., Rafael, S. D., and Roskva, R. K. (2019). *Seal Enhancer'. Copenhagen*. Available online at: https://uspto.report/patent/app/20190383792 (accessed August 4, 2022).

Maltsev, V. A., and Undrovinas, A. I. (1997). 'Cytoskeleton modulates coupling between availability and activation of cardiac sodium channel'. *Am. J. Physiol. Heart Circ. Physiol.* 273, H1832–H1840. doi: 10.1152/ajpheart.1997.273.4.h1832

McNulty, M. M., and Hanck, D. A. (2004). 'State-dependent mibefradil block of Na+ channels'. *Mol. Pharmacol.* 66, 1652–1661. doi: 10.1124/mol.66.6.1652

Meadows, L. S., Chen, Y. H., Powell, A. J., Clare, J. J., and Ragsdale, D. S. (2002). 'Functional modulation of human brain Nav1.3 sodium channels, expressed in mammalian cells, by auxiliary β1, β2 and β3 subunits'. *Neuroscience* 114, 745–753. doi: 10.1016/S0306-4522(02)00242-7

Milligan, C. J., Li, J., Sukumar, P., Majeed, Y., Dallas, M. L., English, A., et al. (2009). 'Robotic multiwell planar patch-clamp for native and primary mammalian cells.'. *Nat. Protoc.* 4, 244–255. doi: 10.1038/nprot.2008.230

Obergrussberger, A., Friis, S., Brüggemann, A., and Fertig, N. (2021). 'Automated patch clamp in drug discovery: Major breakthroughs and innovation in the last decade'. *Exp. Opin. Drug Discov.* 16, 1–5. doi: 10.1080/17460441.2020.1791079

Obergrussberger, A., Goetze, T. A., Brinkwirth, N., Becker, N., Friis, S., Rapedius, M., et al. (2018). 'An update on the advancing high-throughput screening techniques for patch clamp-based ion channel screens: Implications for drug discovery'. *Exp. Opin. Drug Discov.* 13, 269–277. doi: 10.1080/17460441.2018.1428555

Obergrussberger, A., Haarmann, C., Rinke, I., Becker, N., Guinot, N., Brueggemann, A., et al. (2014). "Automated patch clamp analysis of nACha7 and NaV 1.7 channels," in *Current protocols in pharmacology*, ed. S. J. Enna (Hoboken, NJ: John Wiley & Sons Inc). doi: 10.1002/0471141755.ph1113s65

Obergrussberger, A., Rinke-Weiß, I., Goetze, T. A., Rapedius, M., Brinkwirth, N., Becker, N., et al. (2022). 'The suitability of high throughput automated

patch clamp for physiological applications'. *J. Physiol.* 600, 277–297. doi: 10.1113/JP282107

Ono, K., and Arita, M. (1999). 'Mechanism of fluoride action on the L-type calcium channel in cardiac ventricular myocytes.'. *Cell Calcium* 26, 37–47. doi: 10.1054/ceca.1999.0050

Rapedius, M., Obergrussberger, A., Becker, N., Rinke-Weiß, I., Rotordam, M. G., et al. (2019) *High throughput pharmacology of NaV 1.5 channels on nanion's SyncroPatch 384PE*. Available online at: https://www.nanion.de/images/phocadownloadpap/Application_Notes/Nanion_APP_Note_384PE_NaV1_5_06003.pdf (accessed June 27, 2022).

Renganathan, M., Cummins, T. R., Hormuzdiar, W. N., and Waxman, S. G. (2000). 'α-SNS Produces the slow TTX-resistant sodium current in large cutaneous afferent DRG neurons'. *J. Neurophysiol.* 84, 710–718. doi: 10.1152/jn.2000.84.2.710

Rotordam, M. G., Obergrussberger, A., Brinkwirth, N., Takasuna, K., Becker, N., Horváth, A., et al. (2021). 'Reliable identification of cardiac conduction abnormalities in drug discovery using automated patch clamp II: Best practices for Nav1.5 peak current in a high throughput screening environment'. *J. Pharmacol. Toxicol. Methods* 112:107125. doi: 10.1016/j.vascn.2021.107125

Rugiero, F., Mistry, M., Sage, D., Black, J. A., Waxman, S. G., Crest, M., et al. (2003). 'Selective expression of a persistent tetrodotoxin-resistant Na+ current and Nav1.9 Subunit in myenteric sensory neurons'. *J. Neurosci.* 23, 2715–2725. doi: 10.1523/jneurosci.23-07-02715.2003

Seibertz, F., Rapedius, M., Fakuade, F. E., Tomsits, P., Cyganek, L., Becker, N., et al. (2022). A modern automated patch-clamp approach for high throughput electrophysiology recordings in native cardiomyocytes. *Commun Biol.* (in press).

Sheets, M. F., and Hanck, D. A. (1999). 'Gating of skeletal and cardiac muscle sodium channels in mammalian cells'. *J. Physiol.* 514(Pt 2), 425–436.

Srinivasan, S. R., Huang, H., Chang, W.-C., Nasburg, J. A., Nguyen, H. M., Strassmaier, T., et al. (2022). Discovery of novel activators of large-conductance calcium-activated potassium channels for the treatment of cerebellar ataxia'. *Mol. Pharmacol.* 102, 17–28. doi: 10.1124/molpharm.121.000478

Stoelzle, S., Obergrussberger, A., Brüggemann, A., Haarmann, C., George, M., Kettenhofen, R., et al. (2011). 'State-of-the-art automated patch clamp devices: Heat activation, action potentials, and high throughput in ion channel screening'. *Front. Pharmacol.* 2:76. doi: 10.3389/fphar.2011.00076

Wendt, D. J., Starmer, C. F., and Grant, A. O. (1992). 'Na channel kinetics remain stable during perforated-patch recordings'. *Am. J. Physiol. Cell Physiol.* 263, C1234–C1240. doi: 10.1152/ajpcell.1992.263.6.c1234

Yatani, A., and Brown, A. M. (1991). 'Mechanism of fluoride activation of G protein-gated muscarinic atrial K+ channels'. *J. Biol. Chem.* 266, 22872–22877. doi: 10.1016/s0021-9258(18)54435-5

Zeng, H., Balasubramanian, B., Penniman, J. R., Kinose, F., Salata, J. J., and Lagrutta, A. (2013). 'Halide ion effects on human ether-à-go-go related gene potassium channel properties'. *Assay Drug Dev. Technol.* 11, 544–550. doi: 10.1089/adt.2013.531

Zeng, H., Penniman, J. R., Kinose, F., Kim, D., Trepakova, E. S., Malik, M. G., et al. (2008). 'Improved throughput of PatchXpress hERG assay using intracellular potassium fluoride'. *Assay Drug Dev. Technol.* 6, 235–241. doi: 10.1089/adt.2007.116

frontiers | Frontiers in Molecular Neuroscience

TYPE Original Research
PUBLISHED 19 October 2022
DOI 10.3389/fnmol.2022.982689

OPEN ACCESS

EDITED BY
Stephan Kellenberger,
Université de Lausanne, Switzerland

REVIEWED BY
Timothy Lynagh,
University of Bergen, Norway
Dominik Wiemuth,
University Hospital RWTH Aachen, Germany

*CORRESPONDENCE
Marc Rogers
channelogist@gmail.com

SPECIALTY SECTION
This article was submitted to Molecular Signalling and Pathways, a section of the journal Frontiers in Molecular Neuroscience

RECEIVED 30 June 2022
ACCEPTED 12 September 2022
PUBLISHED 19 October 2022

CITATION
Ridley J, Manyweathers S, Tang R, Goetze T, Becker N, Rinke-Weiß I, Kirby R, Obergrussberger A and Rogers M (2022) Development of ASIC1a ligand-gated ion channel drug screening assays across multiple automated patch clamp platforms. *Front. Mol. Neurosci.* 15:982689. doi: 10.3389/fnmol.2022.982689

Development of ASIC1a ligand-gated ion channel drug screening assays across multiple automated patch clamp platforms

John Ridley[1], Sam Manyweathers[1], Raymond Tang[1], Tom Goetze[2], Nadine Becker[2], Ilka Rinke-Weiß[2], Robert Kirby[1], Alison Obergrussberger[2] and Marc Rogers[1]*

[1]Metrion Biosciences Ltd., Cambridge, United Kingdom, [2]Nanion Technologies GmbH, Munich, Germany

Human acid-sensing ion channels (ASIC) are ligand-gated ionotropic receptors expressed widely in peripheral tissues as well as sensory and central neurons and implicated in detection of inflammation, tissue injury, and hypoxia-induced acidosis. This makes ASIC channels promising targets for drug discovery in oncology, pain and ischemia, and several modulators have progressed into clinical trials. We describe the use of hASIC1a as a case study for the development and validation of low, medium and high throughput automated patch clamp (APC) assays suitable for the screening and mechanistic profiling of new ligands for this important class of ligand-gated ion channel. Initial efforts to expand on previous manual patch work describing an endogenous hASIC1a response in HEK cells were thwarted by low current expression and unusual pharmacology, so subsequent work utilized stable hASIC1a CHO cell lines. Ligand-gated application protocols and screening assays on the Patchliner, QPatch 48, and SyncroPatch 384 were optimized and validated based on pH activation and nM-μM potency of reference antagonists (e.g., Amiloride, Benzamil, Memantine, Mambalgin-3, A-317567, PcTx1). By optimizing single and stacked pipette tip applications available on each APC platform, stable pH-evoked currents during multiple ligand applications enabled cumulative EC_{50} and IC_{50} determinations with minimized receptor desensitization. Finally, we successfully demonstrated for the first time on an APC platform the ability to use current clamp to implement the historical technique of input resistance tracking to measure ligand-gated changes in membrane conductance on the Patchliner platform.

KEYWORDS

automated patch clamp, ligand-gated ionotropic receptor, acid-sensitive ion channel, drug discovery, screening assay

Introduction

Acid-sensing ion channels (ASICs) are proton-gated cation ion channels which are highly sensitive to extracellular acidosis and variably permeable to Na^+, Ca^{2+} and other cations (Lingueglia and Lazdunski, 2013). To date six different ASIC subunits and splice variants have been described (ASIC1a, 1b, 2a, 2b, 3, and 4) encoded by four genes (Wemmie et al., 2013). ASIC subunits assemble to form homomeric or heteromeric trimers which exhibit different sensitivities to pH activation and modulation by toxins and small molecules, and differential expression across the central nervous system (CNS) and peripheral nervous system (reviewed in Gründer and Chen, 2010; Lingueglia and Lazdunski, 2013; Heusser and Pless, 2021).

ASIC1a is expressed in various regions of the brain, including the hippocampus, cerebral cortex, cerebellum, and amygdala (Wemmie et al., 2013). Elevated neural activity can lower extracellular pH that activates ASIC1a channels, leading to influx of Na^+ and membrane depolarization which underlies their involvement in synaptic learning and memory and fear conditioning (Gründer and Chen, 2010). Homomeric ASIC1a channels are also permeable to Ca^{2+} so excessive activation can contribute to neurotoxicity (Bässler et al., 2001; Xiong et al., 2004; Chassagnon et al., 2017). Consequently, ASIC1a is implicated as a therapeutic target in neurological indications associated with pathophysiological extracellular acidification such as ischemia, stroke, inflammation, multiple sclerosis and seizures.

Peripheral ASIC1 ion channels are involved in nociception as they are expressed in dorsal root ganglia neurons and peripheral nerve terminals where they respond to inflammatory-mediated changes in extracellular pH (Gründer and Chen, 2010). Involvement of ASIC1 channels in pain is evidenced by effects of peptide toxins; the ASIC1 activator MitTx evokes intense, long-lasting pain in patients envenomated by the Texas coral snake (Bohlen et al., 2011), whilst the ASIC1a inhibitors PcTx1 (from tarantula venom) and Mambalgins (from mamba snake venom) reduce thermal and mechanical hyperalgesia (Mazzuca et al., 2007; Diochot et al., 2012). Clinical validation of ASIC-mediated nociception was obtained by PainCeptor, whose inhibitors PPC 5650 and PPC 5692 reduced heat threshold and mechanical sensitivity and pain biomarkers in Phase I clinical trials (Heusser and Pless, 2021 and references therein).

The interest in ASIC1a channels as CNS injury and pain targets creates demand for reliable assays to support drug discovery efforts. Ion channel drug discovery now relies on high throughput electrophysiology assays as automated patch clamp platforms (APC) have come to replace plate-based imaging assays (Obergrussberger et al., 2022), but the development of APC ligand-gated ion channel assays has lagged behind that of voltage-gated ion channels. Ligand-gated ion channels with rapid activation kinetics and desensitization present specific challenges on APC systems due to low channel expression, the need for rapid liquid addition and effective wash-off of ligands, and loss of responsiveness due to short- and long-term desensitization. We therefore used hASIC1a as an exemplar ionotropic receptor target to validate, optimize and compare fast ligand-gated receptor channel assays across multiple APC platforms, and assess their suitability for drug discovery screening.

The trigger for our project was work from GlaxoSmithKline describing endogenous pH-gated ASIC responses in HEK cells (Gunthorpe et al., 2001). RT-PCR analysis and manual patch clamp biophysics and pharmacology indicated that functional human ASIC1a channels were present in untransfected parental HEK cells. We sought to replicate this finding and try to extend it to use the innate HEK cell ASIC1a receptor channel in APC drug screening assays. This work highlights the advantages and disadvantages of exploiting the endogenous expression of ion channels in common cell expression systems (e.g., Rogers et al., 2016; Borg et al., 2020). For example, the use of HEK cell parentals to express mutated hASIC1a and other human and species ortholog ASIC channels (Kuduk et al., 2010; Wolkenberg et al., 2011; Goehring et al., 2014; Cullinan et al., 2019) may be compromised by contamination from background ASIC1a channels.

Historically, activity of ionotropic and metabotropic neurotransmitter receptors was studied in native systems and isolated cells using single microelectrode current clamp tracking of input resistance in response to presynaptic, bath or iontophoretic application of agonists (e.g., Hiruma and Bourque, 1995). Receptor stimulation triggers ion channel activity that produces a change in membrane conductance (e.g., opening of $GABA_A$ receptor Cl^- channels or activation of $GABA_B$ G-protein coupled K^+ channels), which can be monitored by applying small current injections to measure changes in input resistance and membrane conductance. Our interest in demonstrating this traditional technique on APC was triggered by a recent study with a low throughput single well electro-optical version of the input resistance tracking method (Menegon et al., 2017). A field electrode system applied current pulses to populations of heterologous cell lines and membrane potential responses were measured with fast voltage-sensing dyes. We reasoned that input resistance tracking with single cell resolution could be achieved at higher throughput using the current clamp features available on most APC platforms. We used the Patchliner for this proof-of-concept study, enabling comparison of automated input resistance current clamp alongside modern voltage clamp methods of ligand-gated ion channel screening.

Although we confirmed an endogenous HEK cell pH-gated response mediated by hASIC1 and transferred the assay to an APC platform, issues with current expression and reference pharmacology indicated it was not suitable for use in drug discovery screening. Subsequent experiments with human ASIC1a channels stably expressed in CHO cells

allowed successful validation of reliable ligand-gated receptor ion channel screening assays on low (Patchliner), medium (QPatch 48) and high throughput (SyncroPatch 384) APC devices. ASIC1a current responses were reproducible and repetitively activated in the same cell using single pipette and stacked tip techniques which minimize agonist exposure time through rapid liquid application and effective wash-off. ASIC1a channels exhibited expected pH sensitivity and were inhibited by a selection of non-selective (Benzamil, Amiloride, Memantine) and selective antagonists (PcTx1, Mambalgin-3). Finally, we used the current clamp capability available on most APC platforms to successfully implement the traditional input resistance/conductance-tracking technique to measure ligand-gated ASIC1a current activation on the Patchliner.

Materials and methods

Cell lines and cell culture

The HEK parental cell line (ECACC) was grown at 37°C in 5% CO_2 in MEM with addition of 10% foetal calf serum and 1% MEM non-essential amino acids and 2 mM L-Glutamine (all from Thermo Fisher Scientific). Cells were plated in Corning cell culture flasks and passaged after reaching 60–80% confluency using GIBCO TrypLE (Thermo Fisher Scientific). For QPatch experiments, aliquots of dissociated cell suspension were plated into T-175 flasks (Corning) and grown as above in a 5% CO_2 incubator at 37°C for 1–2 days, and in some cases switched to a 30°C incubator for 12–24 h, with plating densities adjusted for the expected doubling time under each condition.

The B-SYS (GmbH) CHO cell line constitutively expressing human ASIC1a was grown by continuous passaging according to vendor instructions. Briefly, cells were grown at 37°C in 5% CO_2 in Ham's F12 media with addition of 10% foetal calf serum (both from Thermo Fisher Scientific) and 250 mg/ml of Geneticin selection antibiotic (Thermo Fisher Scientific). Cells were plated in Corning cell culture flasks and passaged after reaching 70–80% confluency using StemPro Accutase dissociation reagent (Thermo Fisher Scientific). For QPatch experiments, aliquots of dissociated cell suspension were plated into T-175 flasks (Corning) and grown in a 5% CO_2 incubator at 37°C for 1–3 days, with plating densities adjusted for the expected doubling time to avoid excessive confluency.

The Charles River CHO cell line CT6012 was cultured at Nanion Technologies GmbH (Munich) according to vendor instructions. Expression was induced by application of 1 mg/ml tetracycline 3–6 h prior to each SyncroPatch 384i experiment. For harvesting, cells were rinsed twice in HBSS (room temperature) and incubated in TrypLE (Thermo Fisher Scientific) for 7 min at 37°C. Following this, cells were rinsed and triturated 4–6× in cooled HBSS. Cells were allowed to rest at 10°C for 20 min in external recording solution in the Cell Hotel. The cells were kept at 10°C in the Cell Hotel of the SyncroPatch 384i and shaken at 200 rpm prior to use in the experiments.

Automated patch clamp

Table 1 outlines the external and internal solutions used on each APC platform. External solutions were prepared from concentrated stocks kept at 4°C or room temperature, whereas internal solution stocks were aliquoted and stored at −20°C prior to thawing on the day of each experiment. All solutions were filtered and checked for final osmolality and pH before use.

Patchliner methods

CHO cells were cultured according to vendor instructions (B-SYS GmbH) and harvested using optimized protocols before transfer of the cell suspension to the automated cell hotel on the Patchliner where cells are stored at RT (∼20°C) in a small Teflon vessel and repetitively aspirated every 30 s using a 1 ml plastic pipette tip to prevent aggregation. The cell hotel parameters can be adjusted (interval, speed and volume of aspiration) depending on the cell type to maintain viability for 2–3 h. Cell sealing was conducted in the presence of elevated divalent cations and lowered Na^+, which were washed off after whole-cell access was achieved and replaced with external solution while cells were voltage clamped at a holding potential of −60 mV. For current clamp recordings, current was injected to achieve a notional membrane potential of 0 mV (using HEKA "gentleswitch" protocol) and a series of incrementally positive current injections (100 to 200 pA, 100 msec) were applied to measure input resistance under control and pH activating conditions.

ASIC1a currents were elicited under voltage clamp at a holding potential of −60 mV by rapid application (and wash-off) of external solution (with or without compounds) of varied pH (typically 7.0. 6.8, 6.5, 6.0, and 5.5 to enable full range of pH activation). Cells were washed three times with external solution between applications of activating external solution to establish a stable baseline. Cells were then stimulated with repeated applications of either pH 6.5 (screening mode) or varied pH (EC_{50}), and concentrations of reference compounds were applied before and during each pH stimulus (IC_{50} mode). The timing, volume and application speed of these liquid applications were varied to obtain optimum ASIC1a current activation during repeated activation. A 2 min period of rest in pH 7.4 solution (and pre-incubation in test compound as appropriate) between each pH challenge was used to aid recovery from desensitization and allow pre-equilibration of modulatory compounds.

For the input resistance tracking experiments, cells were held at 0 mV under current clamp and a train of incrementing current injections (from 100 to 200 pA in 20 pA increments, 200 msec step duration) were applied to monitor membrane

TABLE 1 APC internal and external solutions.

Constituent	External (mM)			Internal (mM)		
	PL	QP 48	SP384i	PL	QP 48	SP384i
NaCl	140	140	140	10	10	10
KCl	4	5	4	50	40	10
KF	–	–	–	60	–	110
KGluc	–	–	–	–	90	–
HEPES	10	10	10	10	5	10
MES*	10	10	10	–	–	–
$MgCl_2$	1	1.2	1	–	3.2	–
$CaCl_2$	2	1	2	–	–	–
Glucose	5	11.1	5	–	–	–
EGTA	–	–	–	20	3.2	10

All external solutions with pH below 7.0 used for activating ASIC1 responses had MES substituted for HEPES.

resistance (using Ohm's Law V = I*R). This pulse protocol was repeated as cells were exposed to solutions of decreasing pH from 7.3 to 6.0, and changes in membrane resistance were converted into conductance and normalized to the maximum conductance change seen in each cell (G/G_{max}) to enable construction of a pH EC_{50} curve.

QPatch 48 methods

CHO hASIC1a cells were cultured according to vendor instructions (B-SYS GmbH) and HEK cells using standard in-house methods. Both cell lines were harvested using optimized protocols and re-suspended in serum-free media (Gibco CHO-S-SFM from Thermo Fisher Scientific for CHO cells, and Ex-Cell 302 from Merck Sigma-Aldrich for HEK cells) to obtain a suspension of cells with smooth membranes and little debris, before transfer to the automated cell hotel consisting of a 60 ml plastic container (Sophion SB2050) and a magnetic stir bar to prevent cell clumping. An aliquot of cells is then aspirated into a 1 ml microcentrifuge tube and spun down (typically 150 g for 2.5 min) and the supernatant discarded before a user-defined volume of external solution is added by the robot and the cells re-suspended to achieve the desired final cell suspension density before application to primed QPlates. Cell capture, sealing and whole-cell access was achieved using optimized QPatch protocols before currents were recorded using a holding potential of −60 mV. ASIC1a currents were elicited by rapid application (and wash-off) of external solution of varied pH (typically 7.0. 6.8, 6.5, 6.0, and 5.5) to enable full measure of activation around the expected EC_{50} of ∼ 6.5. Cells were washed three times with external pH 7.3 solution (5 μl) between applications of activating acidic solution to establish a stable ASIC1a current baseline. Cells were then stimulated with repeated 3 s applications (5 μl) of either pH 6.5 (screening mode) or varied pH (EC_{50} mode); each ligand application cycle was repeated every 2 min. Each concentration of reference compound was applied to each cell before (i.e., during each pH 7.3 application period) and during each pH stimulus (IC_{50} mode). Thus, each concentration of test compound was pre-incubated with cells for at least 2 min before, and then during each acidic solution challenge, before wash-off in a neutral pH 7.3 solution that contained the next concentration of the same compound. Cells were allowed at least 2 min between applications of acidic solution to enable ASIC1a receptors to recover from desensitization.

SyncroPatch 384i methods

CHO cells expressing ASIC1a (Charles River) were induced using tetracycline 3–6 h prior to dissociation into a cell suspension. Cells were kept in the cell hotel of the SyncroPatch 384i with a set temperature of 10°C and shaking of the plastic reservoir at 200 rpm to prevent aggregation prior to addition to the NPC-384 chip for each experiment. NPC-384 chips were filled with internal and external solutions (see Table 1) followed by the cell suspension. Suction was used to capture and seal the cells on the NPC-384 chip using optimized protocols.

Two different liquid application protocols were utilized on the SyncroPatch 384i platform to assess optimum methods to study ligand-gated ASIC1a responses. For recordings of stability and pharmacology using a bolus or "puff" application of ligand, 5 μl of the agonist solution was aspirated and applied to the cell; liquid dispense speed can be set between 1 and 100 μl/s, and a setting of 40 μl/s was used in these experiments. Following agonist addition, 50 μl of the total 90 μl volume in each well is then taken up by the tip to remove most of the agonist solution from the cell. Final recovery of the ASIC1a receptor response is achieved by taking up wash solution into each tip from a reservoir and applying it to individual cells on the NPC-384 chip, washing the ligand away. For stability experiments, pH 6.5 was applied to each cell followed by a wash with pH 7.4 solution and a wait of 140 s to remove agonist and reverse any desensitization, before a second application of pH 6.5 was made. This sequence was repeated 6–7 times on each cell. For

pharmacology experiments, ASIC1a responses were evoked 3 times by pH 6.5 application followed by pre-incubation in the inhibitor for 140 s, after which the inhibitor was co-applied with a pH 6.5 stimulus. Cumulative concentration responses were obtained for each well using 3–4 incrementing concentrations of inhibitor. Concentration response curves for each well were constructed and mean ± S.E.M values for IC_{50} are given.

In the second ligand-gated protocol, "stacked puff" recordings were made whereby a single [agonist_wash] experiment was sequentially aspirated into each tip prior to flowing the layered liquid array onto each cell across the NPC-384 chip. To assess the pH sensitivity of ASIC1a responses, pipette tips were loaded with 5 μl of pH 7.4 wash solution followed by 5 μl of activating extracellular solution (pH 7.2 to 4.8). For each sweep, the baseline current was recorded for 1 s in pH 7.4 control solution before the application of the 5-μl activating solution, and then the pH 7.4 wash solution was dispensed with a delay of 1 s to allow for recording of channel opening and desensitization in the presence of ligand before ligand wash-off. Application of the wash solution was followed by aspiration of liquid (50 μl of 90 μl total volume) from each well after a delay of 4 s, before a second wash step with pH 7.4 was performed prior to the application of the next activating pH (interval between stimuli 140 s). Each well received an addition of pH 6.5 solution followed by application of a test pH, and this sequence was repeated a second time to enable data from each cell to be normalized to the control pH 6.5 addition. The pH response curve was constructed across multiple wells with replicates of 48. Pharmacology experiments were performed as described above in "puff" application.

Chemicals and reagents

All chemicals were of analytical grade and sourced from Merck Sigma Aldrich. Amiloride and Benzamil were purchased from Merck (Sigma-Aldrich), Mambalgin-3 from Alomone Labs, and PcTx-1 from Tocris. A-317567, Amantadine and Memantine were kind gifts from Vernalis (UK), a Hitgen company (see Rogers et al., 2021b).

Data analysis

Concentration-response xC_{50} curves from Patchliner and QPatch 48 experiments were calculated by plotting %inhibition (antagonists) or activation (pH) data against concentration in Prism software (GraphPad), using the variable sigmoidal dose-response function to fit the Hill equation with theoretical minimum block of 0% and maximum block of 100% and a free constant for Hill slope. Inward current amplitudes were compared to the response to a control pH application (typically pH 6.5) prior to antagonist application or excitation by solutions of different pH to enable calculation of %inhibition or %activation for each cell.

Data was analyzed on the SyncroPatch 384 using DataControl 384 software (Nanion Technologies GmbH, Germany). Concentration response curves were fit using a Hill Equation. Statistical comparison of IC_{50} values for Benzamil was performed using a Student's *t* test in Igor Pro 8 (Wavemetrics). For statistical analysis of SyncroPatch 384 plate and assay quality we used the Z' value typical for HTS evaluation (Zhang et al., 1999; Iversen et al., 2006). Z-Factor (Z') is calculated using the equation:

$$Z' = 1 - \frac{(3 \times SD_{Max} + 3 \times SD_{Min})}{AVG_{Max} - AVG_{Min}} \quad (1)$$

where AVG is the mean and SD the Standard Deviation. The indices Max and Min in the formula for Z' refer to the control measurements with maximum current (i.e., response to negative control) and the minimum current (i.e., response to positive control), respectively. Z' values > 0.5 are considered to correspond to an excellent assay for screening (Zhang et al., 1999; Iversen et al., 2006).

Results

We initially sought to determine if the reported endogenous ASIC1a currents in HEK cells would be amenable for development of ligand-gated ionotropic receptor screening assays on an APC platform. Further work to develop, validate and optimize ASIC1a screening assays suitable for drug discovery applications on low, medium and high throughput microfluidic chip and 384 well-based APC platforms was carried out using CHO cell lines stably expressing the human ASIC1a channel.

Characterizing endogenous acid-sensing ion channels in HEK cells

To quickly confirm a previous publication that HEK cells express endogenous ASIC1a receptor channels and assess the suitability of this cell system for drug discovery screening on APC platforms, we utilized the medium throughput QPatch 48 device. The QPatch uses 48 well microfluidic planar borosilicate chips and coated titanium pipette tips to make whole-cell recordings and sequentially apply small liquid volumes to enable rapid activation followed by slower deactivation (wash-off) of ligand-gated ionotropic responses. HEK cells were voltage-clamped at −60 mV and maintained in external solution at pH 7.4 to avoid steady-state desensitization of ASIC1 receptor channels. Cells were stimulated by external solutions with pH values ranging between 7.0 and 5.5 that evoked rapidly activating inward currents, followed by wash-off in pH 7.4 solution.

Consistent with previous manual patch clamp recordings (Gunthorpe et al., 2001), most HEK cells responded to proton challenge on the QPatch 48 with rapidly activating and slowly deactivating inward currents (**Figure 1A**). As there was a delay in application of the pH 7.4 wash-off solution to each cell, the decay in peak current toward baseline is likely a combination of receptor desensitization followed by ligand removal. Mean inward current amplitude was −567 ± 78 pA (mean ± S.E.M, n = 37; **Figure 1B**), compared to an average amplitude of −334 pA from 47/48 cells in the original manual patch clamp study. The proton sensitivity of endogenous HEK pH-gated currents yielded a pEC_{50} of 6.65 (**Figures 1C,D**), similar to the published manual patch clamp value of 6.45 (Gunthorpe et al., 2001). The Hill slope of pH activation was very steep (8.2), a common feature of ASIC1 receptor activation attributed to a complex gating mechanism involving proton-binding sites in the extracellular domains which interact with other residues in the acidic pocket and pore (Gründer and Chen, 2010). However, there was considerable variability in the magnitude of pH-evoked responses in HEK cells grown under standard cell culture conditions of 37°C, with a significant fraction (24%) of cells failing to exceed our standard minimum current threshold for APC recordings (dashed line in **Figure 1B**). APC users frequently assess the success rate (or "patchability") of an assay by calculating the percentage of cells that pass through each stage of the cell capture and recording process and typical QC filters of seal quality, series resistance. For example, our optimized conditions for endogenous pH-activated responses in HEK cells revealed assay metrics of [100% priming/92% cell-attached/78% seals > 100 MΩ/67% whole-cells/63% completed xC_{50} experiment/48% QC success rate].

In an effort to improve the signal window of endogenous HEK pH-gated responses, cells were incubated for 12 – 48 h at 30°C to induce heat shock and boost protein translocation to the cell membrane. This was moderately successful (**Figure 1B**), increasing the fraction of expressors to 98% and mean current amplitude to −841 ± 61 pA (mean ± S.E.M, n = 53). There was no change in the proton sensitivity of cells grown at 30°C, as the pEC_{50} value of 6.66 at 30°C was identical to that measured in HEK cells grown at 37°C (**Figure 1D**). Although 30°C treatment improved signal window and initial success rate, there was a corresponding decrease in the stability of pH-evoked inward currents compared to that seen in cells grown at 37°C (**Figures 1E,F**). We observed significant current rundown during repeated pH challenges in cells grown at 30°C (**Figure 1F**) leading to poor completion rates of experiments. Best practice in APC ion channel recordings suggests that a rundown rate < 2%/minute is desirable, but various methodological variations and cell biology and biochemical treatments we tested to reduce the rundown rate in cells grown at 30°C to boost current amplitude were unsuccessful (data not shown).

Nevertheless, we sought to confirm that HEK cells express endogenous ASIC1a responses and validate this APC assay using a small toolbox of reference antagonists.

The tarantula toxin PcTx1 is the most selective antagonist for ASIC1a, with an IC_{50} for the human ortholog of ∼ 3 nM (Cristofori-Armstrong et al., 2019). We observed inconsistent and variable effects of PcTx1 in HEK cells across multiple experimental runs (including in the presence of BSA to avoid protein adherence to glass and plastic surfaces). Many cells showed < 20% inhibition of proton-gated currents by concentrations of PcTx1 from 100 pM to 30 nM (**Figure 2A**), and mean data fell below 50% inhibition at the highest concentration tested of 30 nM so no IC_{50} value could be reliably extracted from this data. PcTx1 also potentiates ASIC1b and ASIC1a/2a channels under certain conditions (i.e., desensitizing acidic pH) with ∼10 fold lower potency than ASIC1a inhibition (Liu et al., 2018; Cristofori-Armstrong et al., 2019), but we saw no evidence for such modulation in our experiments on endogenous pH-evoked responses in HEK cells.

The green mamba snake toxin Mambalgin-3 is a moderately selective inhibitor of ASIC1-containing receptor channels with an IC_{50} potency of 127 nM for human ASIC1a and 17 – 55 nM for the rat ortholog (Diochot et al., 2012), and its potency against other ASIC homomers and heteromers ranges between 50 and 250 nM (Baron et al., 2013). The endogenous proton-activated currents in HEK cells were effectively inhibited by Mambalgin-3, with ∼75% block at 300 nM and a cumulative IC_{50} value of 119 nM on the QPatch 48 (**Figures 2B,C**). Mambalgins can also potentiate ASIC1b channels under certain (i.e., acidic) conditions (Cristofori-Armstrong et al., 2021), but we saw no evidence for such modulation in our experiments in HEK cells.

Surprisingly, the benchmark non-selective ASIC1a antagonist Amiloride proved to be a relatively potent but variable inhibitor of pH-evoked responses in HEK cells, frequently exhibiting antagonism at sub-μM concentrations. For example, in some cells 300 nM Amiloride produced ∼25% inhibition of pH-evoked current, whereas in other cells there was no effect until Amiloride concentrations exceeded 10 μM. The mean IC_{50} value obtained for Amiloride in HEK cells was 2.82 μM (**Figure 2D**), and proton activated currents were completely abolished by 100 μM Amiloride (**Figure 2E**). Gunthorpe et al. (2001) also reported a relatively high affinity of 2.2 μM for Amiloride inhibition of endogenous pH-gated responses in HEK cells using manual patch clamp. Our and their values are higher than those typically reported for Amiloride inhibition of heterologously expressed hASIC1a, which range from 10 to 30 μM (Leng and Xiong, 2013, and see below). Together with the weak and variable PcTx1 efficacy, these observations suggest that an additional pH-gated ionic conductance may be functionally expressed in HEK cells which

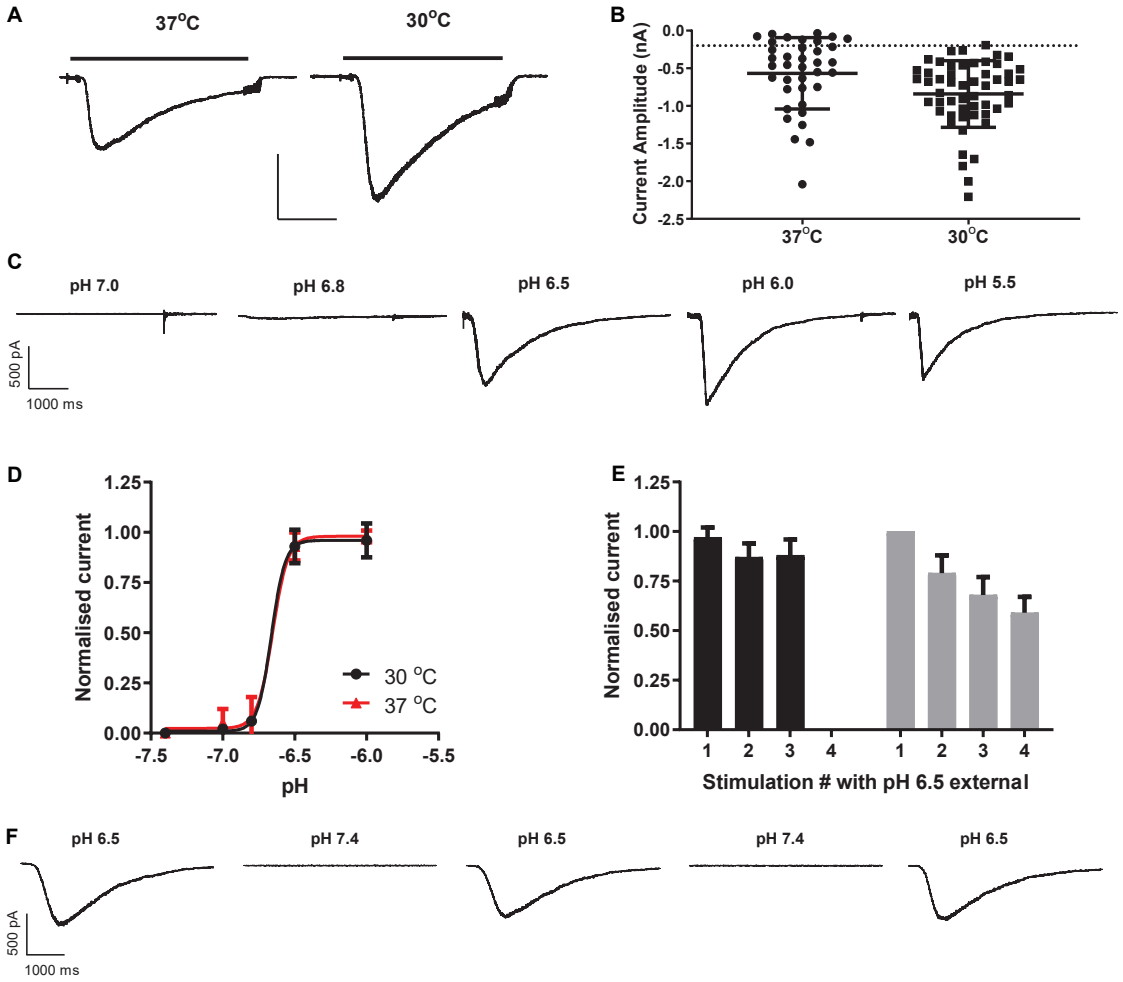

FIGURE 1
Properties of endogenous proton-activated currents in HEK cells on QPatch 48 APC platform. **(A)** Ligand-gated current responses in cells grown at 37°C or 30°C, showing rapid activation by pH 6.5 solution application (solid bar) followed by slower desensitization and then more rapid wash-off. Scale bar 0.5 nA and 1 s. **(B)** Current amplitude distribution in HEK cells grown at 37°C (n = 37) and 30°C (n = 53). Mean ± S.D shown by black line and error bars, and minimum current amplitude of −200 pA as dashed line. **(C)** pH-dependency of endogenous proton-activated currents demonstrated by a series of inward current traces in response to rapid application of solutions of increasing acidity. **(D)** Average pH EC_{50} curves from HEK cells grown at 37°C or 30°C (mean ± S.D, n = 18 and 26, respectively). **(E)** pH-activated currents in HEK cells grown at 37°C are relatively stable during repeated pH 6.5 stimulation (black bars) but exhibit rundown in cells grown at 30°C to boost current expression (gray bars). Mean ± S.D for n = 7 and 11 cells, respectively. **(F)** Stability of inward currents in a HEK cell grown at 37°C during repeated pH 6.5 stimulation, interspersed with application of control pH 7.4 solution.

could contaminate responses attributed to ASIC1 receptor activation.

TRP channels represent another prominent pH-gated ligand-gated ionotropic receptor family, some of which are expressed endogenously in HEK cells (Wu et al., 2000). Application of 1 μM Ruthenium Red, a non-specific inhibitor of a wide range of TRP channels, failed to significantly reduce the amplitude (12 ± 7% inhibition) of currents activated by pH 6.5 in HEK cells (**Figure 2E**), suggesting little or no endogenous TRP receptor function under our experimental conditions.

We conclude from these pharmacology experiments using both broad spectrum and more selective ASIC1 antagonists that the endogenous pH-gated response in HEK cells cannot be clearly and unequivocally attributed to ASIC1a (or TRPx) channels, even though ASIC1a is the only member of the ASIC family detected by PCR (Gunthorpe et al., 2001). Along with issues of low current expression and assay stability of the endogenous pH response in HEK cells, all further ASIC1a APC assay development and validation was carried out using CHO cell lines stably expressing sequence-verified hASIC1a, as there is no endogenous pH-gated response in CHO cells and they

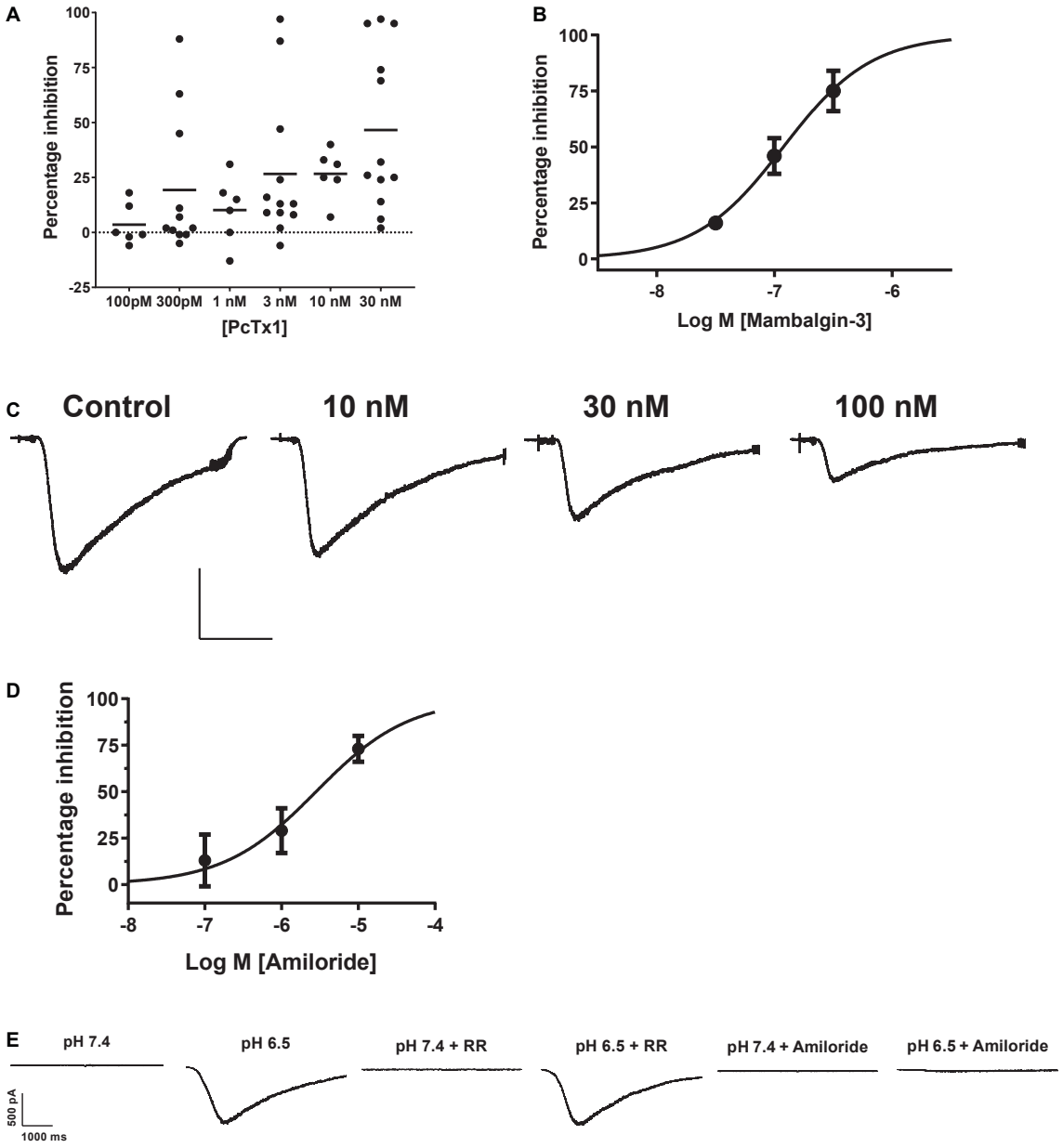

FIGURE 2
Pharmacology of endogenous proton-activated currents in HEK cells. **(A)** Individual % inhibition values plotted against concentration of PcTx1 applied during QPatch 48 recordings, with mean shown by horizontal black lines. Data was obtained from cumulative IC_{50} assays where each cell was exposed to three concentrations of PcTx1, typically in half log unit increments. **(B)** Potency of Mambalgin-3 to inhibit pH-activated currents plotted as a cumulative concentration-response IC_{50} curve. Symbols are mean ± S.D (n = 2 or 3). **(C)** Exemplar current traces from a HEK cell in response to pH 6.5 activation before and after pre-incubation in increasing concentrations of Mambalgin-3. Scale bar is 500 pA and 1 s. **(D)** Inhibition of proton-activated currents in HEK cells by Amiloride. Data was obtained in a similar fashion to C, with each cell stimulated by pH 6.5 solution and then pre-incubated in increasing concentrations of Amiloride to construct a cumulative mini-IC_{50} curve. Symbols are mean ± S.D (n = 3). **(E)** Endogenous proton-activated currents are insensitive to Ruthenium Red (RR, 1 μM) but completely inhibited by a non-selective concentration of the ASIC/ENaC/Degenerin antagonist Amiloride (100 μM). The HEK cell was stimulated by pH 6.5 solution and then pre-incubated (at pH 7.4) in RR or Amiloride followed by consecutive stimulation with pH 6.5 solution containing RR or Amiloride.

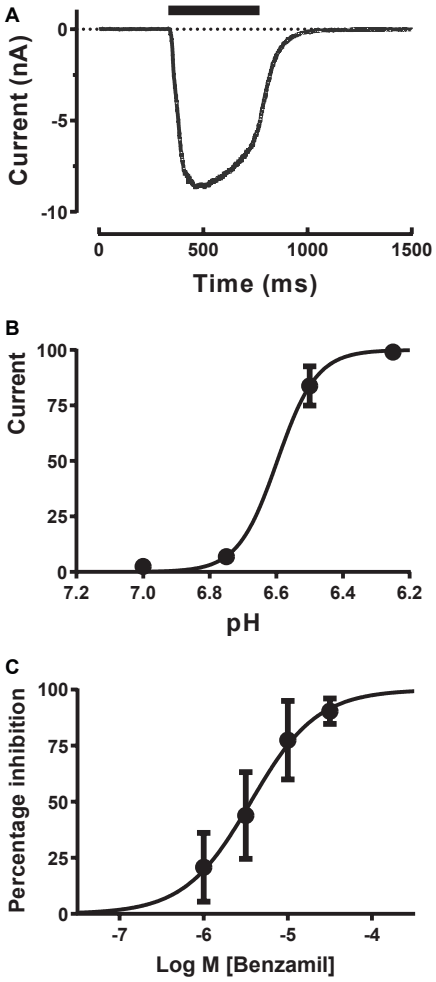

FIGURE 3
Pharmacology of CHO ASIC1a currents using stacked tip application on Patchliner. **(A)** Rapid activation of inward current during pH 6.5 application, followed by desensitization and then rapid wash-off. **(B)** pH activation reveals an EC_{50} of 6.6 ± 0.01 (mean ± S.D, *n* = 3) with a Hill slope of 7.3. **(C)** ASIC1a current inhibition by Benzamil. Cumulative application of increasing concentrations of Benzamil before and during repeated stimulus with pH 6.5 solution reveal an IC_{50} of 3.65 ± 1.18 μM (mean ± S.D, *n* = 3).

also lack Amiloride-sensitive EnaC currents (Meltzer et al., 2007; Hoagland et al., 2010).

Ligand-gated ASIC1a assays on Patchliner automated patch clamp platform

We started development and validation of an APC ligand-gated ASIC1a ion channel assay on the 4 channel Patchliner device as it enables flexible user interaction and cost-effective scale-up from manual patch systems. The Patchliner is a low throughput multi-well APC platform utilizing microfluidic planar borosilicate chips to record whole-cell currents and coated metal pipette tips for solution and compound application. A large range of liquid volumes (10 – 250 μl) can be added to the inflow channels at various speeds (from 1 to 857 μl/sec, typically 4 – 171 μl/sec) to optimize ligand-gated ionotropic receptor activation and wash-off under whole-cell voltage or current clamp. The Patchliner also offers the opportunity to compare and optimize ligand-gated assays using conventional, sequential pipette tip liquid applications or stacked-tip applications.

Initial experiments using sequential single pipette additions of external solution followed by acidic pH solutions elicited rapidly activating ASIC1a currents (−1.0 to −10 nA amplitude, single hole/cell recordings) followed by slower mono-exponential decay back to baseline due, suggestive of receptor desensitization rather than agonist wash-off (data not shown), consistent with previous ligand-gated receptor ion channel experiments on the Patchliner (Nanion, 2013). Such desensitizing ligand-gated ionotropic receptors can make it difficult to distinguish if true peak current (activation) is achieved and resolvable by measurements of maximum amplitude, or if rapid desensitization has begun to erode the peak and affect estimates of agonist EC_{50} and inhibitor IC_{50} values.

To obtain more reliable estimates of ASIC1a activation and modulation we switched to using stacked tip applications. Each pipette took up a set volume of external solution (wash), agonist (pH solution) and external solution (baseline) and then applied these sequentially in reverse order in a continuous manner to each cell under voltage clamp to rapidly evoke inward currents with minimal desensitization. Starting with the recommended settings from the manufacturer (agonist and wash volumes of 50–200 μl applied at speeds of 12–20 μl/sec), we adjusted the volume and speed of each liquid component application to obtain rapidly activating ASIC1a inward currents which exhibited a clear peak before a slower phase of desensitization occurred, followed by a rapid wash-off back to baseline (**Figure 3A**). These pH-evoked responses were stable over multiple applications, allowing the construction of cumulative EC_{50} and IC_{50} concentration-response curves. The pH EC_{50} for proton activation was 6.65 with a Hill slope of 7.3 (**Figure 3B**), and the IC_{50} for Benzamil inhibition was 3.65 μM (**Figure 3C**), in accordance with literature values for human ASIC1a (Leng et al., 2016).

Input resistance measurements of ASIC1a activation on the Patchliner

Most marketed APC platforms now offer the option to carry out current clamp recordings, but this capability has not been widely used for drug discovery screening

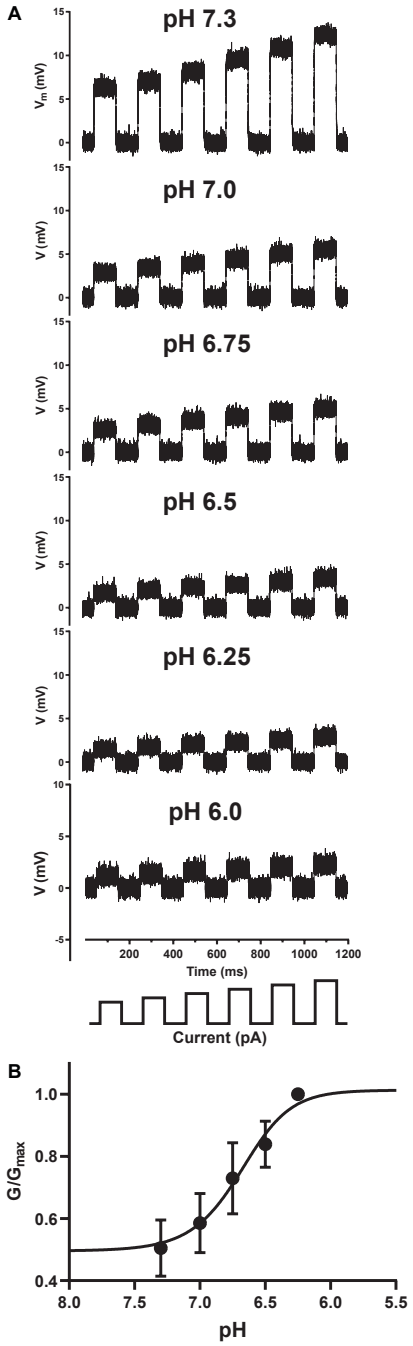

FIGURE 4
Current clamp input resistance tracking of ASIC1a activation on the Patchliner. **(A)** Under control conditions (pH 7.3), positive current injections of 100 to 200 pA (in 20 pA increments, schematic at bottom) from a holding potential of 0 mV elicit membrane depolarizations. Input resistance in response to the same current injection protocol is gradually decreased after application of increasing pH solutions indicated in each panel. **(B)** Converting membrane resistance to conductance and normalizing the change in conductance for each pH concentration by the maximum conductance change (G/G_{max}) in each cell allowed plotting of the pH activation curve obtained under current clamp to yield an EC_{50} value of 6.68 ± 0.01 (mean ± S.D, n = 3).

apart from experiments to record action potentials from iPSC cardiomyocytes and neurons (Stoelzle et al., 2011a,b; Haythornthwaite et al., 2012; Goversen et al., 2018; Li et al., 2019, 2021; Becker et al., 2020). We therefore sought to apply a historical current clamp method used to study ligand-gated ionotropic receptor responses to a modern APC platform, utilizing the same CHO ASIC1a cell line employed in our voltage clamp experiments.

Traditional sharp microelectrode and whole-cell manual patch clamp recordings would apply activating ligand by iontophoresis or bath perfusion, and measure changes in passive membrane resistance during agonist exposure by applying a train of small current injections under current clamp. The size of the membrane voltage excursions in response to a set current injection should decrease as channels open and membrane conductance increases and resistance decreases, in accordance with Ohm's Law (V = I*R). We successfully transferred this ligand-gated current clamp assay paradigm to the Patchliner by holding CHO cells at a membrane potential positive to the net reversal potential for cation flux through the pore, and applied a series of small, incrementing current injections to measure input resistance (**Figure 4A**). Under control conditions (pH 7.3) this protocol elicited large depolarizing membrane potential responses, which were reduced in amplitude when solutions of increasingly acidic pH were applied to individual cells under current clamp. Using this technique, we could then simply convert membrane resistance to conductance and plot these values against pH to obtain a pH EC_{50} value of 6.68 for ASIC1a receptor channel activation (**Figure 4B**), identical to the value obtained using voltage clamp (**Figure 3B**).

Medium throughput ASIC1a automated patch clamp assay on QPatch 48

Like the Patchliner, the QPatch 48 is a microfluidic planar chip-based APC platform that utilizes metal pipette tips to rapidly add and remove solution from individual wells containing single or multiple cells under whole-cell patch clamp. The QPatch 48 used in this study does not offer the ability to stack solutions in the tips (this has subsequently been introduced to newer QPatch systems), so our challenge in implementing a ligand-gated ASIC1a ion channel assay was the coordination of the scheduling of pipette movements and liquid additions so that agonist solutions are applied quickly and consistently for each cell, and acidic solutions were then washed off effectively to avoid desensitization and current rundown. We therefore limited our ASIC1a experiments to a single "insert" of 16 QPlate wells, and designed the experimental timings to optimize the speed and consistency of liquid additions for each cell or well.

Using similar voltage clamp and liquid handling protocols to the initial HEK cell QPatch 48 experiments (except for a

small change to pH 7.3 control solution), we established a stable CHO hASIC1a cell response by implementing three pH 6.5 application cycles to obtain a stable current response before applying a four-point cumulative xC_{50} screening paradigm (**Figure 5A**). Peak current amplitude decreased slightly between the 1st and 2nd pH 6.5 application and then maintained a stable level (and current kinetics) as a steady-state was achieved during subsequent pH activation (**Figure 5B**). We surmise that steady state current reflects equilibrium between ASIC1a receptor activation, desensitization, and recovery back to the resting closed state after agonist wash-off during each pH challenge cycle, the latter achieved using three washes in pH 7.3 solution and a 2 min recovery period at pH 7.3 between each agonist application.

In contrast to untransfected HEK cells, the stable hASIC1a CHO cell line exhibited robust current expression when cells were grown at 37°C and did not require low temperature treatment to achieve the desired 1–2 nA peak current amplitude or > 50% expressor level that is optimal for APC recordings (**Figure 5C**). Mean current amplitude was −1.8 ± 0.2 nA (mean ± S.E.M, $n = 56$) after 1 day at 37°C, increasing slightly to −1.84 ± 0.36 nA ($n = 52$) after 2 days in culture and decreasing to −1.34 ± 0.49 nA ($n = 14$) after 3 days at 37°C. Optimal % expressor levels (> −200 pA minimum current) were seen after 1 day *in vitro*.

Inward currents evoked by application of solutions with pH ranging from 7.0 to 5.5 activated with increasingly rapid kinetics and amplitude followed by a slow phase of desensitization during the 3 s agonist epoch (**Figure 6A**) and recovery back to baseline after ligand wash-off. Mean data indicate a pH EC_{50} of 6.62 (equivalent to 219 nM H^+) with a steep Hill slope of 6.9 typical of the co-operative activation of ASIC1 receptor channels (**Figure 6B**); these values are in good agreement with the literature and results obtained by others on manual and APC platforms (Gunthorpe et al., 2001; Borg et al., 2020; B'Sys, 2022).

The remaining QPatch 48 pharmacology experiments were conducted using pH 6.5 extracellular solution as the agonist to moderately activate ASIC1a currents, as it is close to the calculated EC_{50} value. In addition, this protocol is designed to avoid tachyphylaxis associated with a more acidic pH stimulus, and it allows the development of a ligand-gated ASIC1a channel assay that can distinguish between agonists, partial agonists and antagonists. We used a diverse toolbox of ASIC1 inhibitors to pharmacologically validate the QPatch 48 CHO hASIC1a assay. Reference compounds included the small molecule inhibitors Amiloride, Benzamil, Memantine, Amantadine and A-317567, and the selective peptide toxins Mambalgin-3 and PcTx1 (Dubé et al., 2005; Leng et al., 2016; Nagaeva et al., 2016). Compounds were tested using the cumulative concentration-response assay format shown in **Figure 5A**, which includes a 2 min pre-incubation period for each concentration to allow test samples to reach and equilibrate with their binding site(s) in the pore or large extracellular binding domain of ASIC1 receptor trimers. Agonist effects can also be detected during this period as membrane current data is recorded after every liquid addition. **Figure 6C** summarizes the potency of reference compounds against hASIC1a responses on the QPatch 48, covering 5 orders of concentration. Mean inhibition data for each test sample is plotted against Log[compound] and fit with a concentration-response function. The half-maximal inhibitory (IC_{50}) values and Hill slopes derived from the fits are listed in **Table 2**, which are consistent with values obtained from the literature.

The non-selective degenerin family antagonists Amiloride and Benzamil inhibit hASIC1a responses on the QPatch 48 with expected potencies between 5 and 10 μM (**Table 2**), in contrast to the higher potency of Amiloride against the endogenous proton-activated response in HEK cells (∼2 – 3 μM). A-317567 is a small molecule originally developed by Abbott and found to be a more potent antagonist of ASIC3 and ASIC1a channels (Dubé et al., 2005; Kuduk et al., 2010). We found that this compound worked well on the QPatch 48 and therefore it was used as the positive control as it routinely produced potent and complete inhibition, with an IC_{50} of 660 nM; a close analogue of A-317567 developed by Merck and Co., Inc., (Kuduk et al., 2010) was found to inhibit ASIC1a currents with an IC_{50} of 450 nM. Various low molecular weight hydrophobic amines have been found to modulate ASIC receptor channels, including the clinical drugs Amantadine and Memantine (Nagaeva et al., 2016; Shteinikov et al., 2018). We confirmed their low potency inhibition of ASIC1a with IC_{50} values of 510 and 315 μM, respectively (**Table 2**).

Finally, the QPatch 48 ASIC1a APC assay successfully replicated the published species-specific potency of the hASIC1a-preferring spider venom peptide PcTx1 and the pan-ASIC1 snake toxin Mambalgin-3. The PcTx1 IC_{50} of 2.96 nM we report here (**Figure 6D**) exactly matches that obtained against hASIC1a in *Xenopus* oocytes by Cristofori-Armstrong et al. (2019), and the Hill slope of 2.2 (**Table 2**) is consistent with cryo-EM binding and modeling studies that indicate multiple interactions with distinct residues in the acidic pocket and "thumb" regions of the extracellular ligand-binding domain (Cristofori-Armstrong and Rash, 2017). Similarly, the IC_{50} of 160 nM found for Mambalgin-3 inhibition of hASIC1a on the QPatch 48 is very close to the value of 127 nM reported for human ASIC1a in the original publication on this family of snake toxins (Diochot et al., 2012). Importantly, the Hill slopes of the IC_{50} fits for all the reference compounds tested on the QPatch 48 match expected results, with all but PcTx1 exhibiting a non-cooperative binding mode (**Table 2**) in accordance with previously published data. Overall, this pharmacology data confirms that the QPatch 48 APC ASIC1a assay is capable of accurately identifying antagonists across a wide range of potencies and modalities.

Most APC platforms have the option of using multi-hole plates or chips, where 4–10 apertures are present in each well to allow recordings from multiple cells in parallel. This technique

10.3389/fnmol.2022.982689

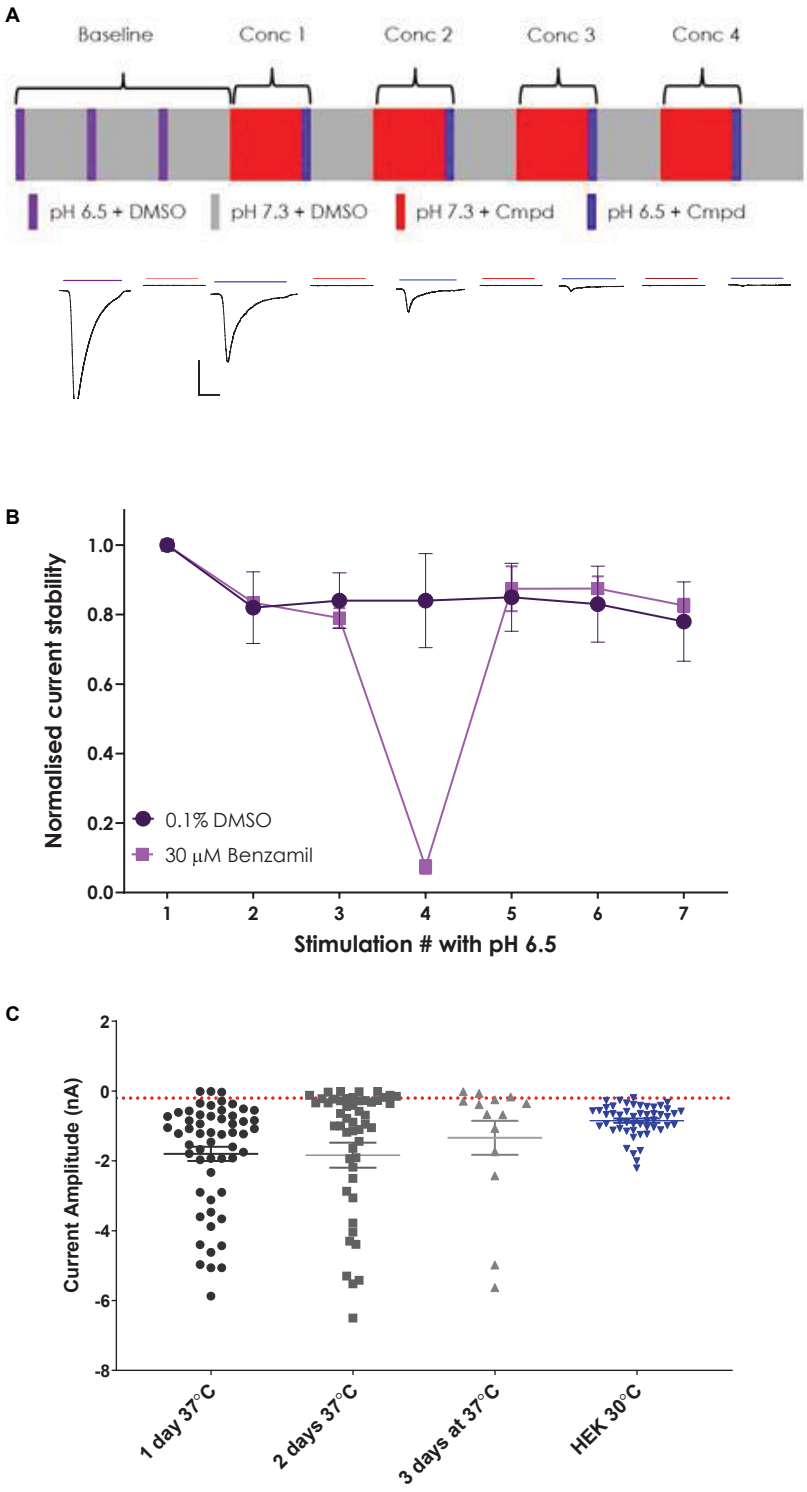

FIGURE 5
Establishing a stable and robust CHO hASIC1a assay format on QPatch 48. **(A)** Schematic of liquid applications and pre-incubations for a cumulative xC_{50} assay format (upper panel) and exemplar current traces with color-coded application bars (lower panel). Scale bar is 500 pA and 1 s. Minimum and maximum period between applications was 2–3 min. **(B)** Normalized current amplitude during repeated pH 6.5 stimulations in 0.1% DMSO vehicle (circles) or interspersed with a 30 μM Benzamil pre-incubation (squares). Mean ± S.D from n = 7 and 2 cells, respectively. **(C)** Comparison of ASIC1a current expression in stable CHO and parental HEK cell lines. CHO cells grown at 37°C for 1–3 days, and HEK cells grown at 30°C. Mean ± S.E.M whole-cell current values shown by whisker graph. Red line is minimum QC current (−200 pA).

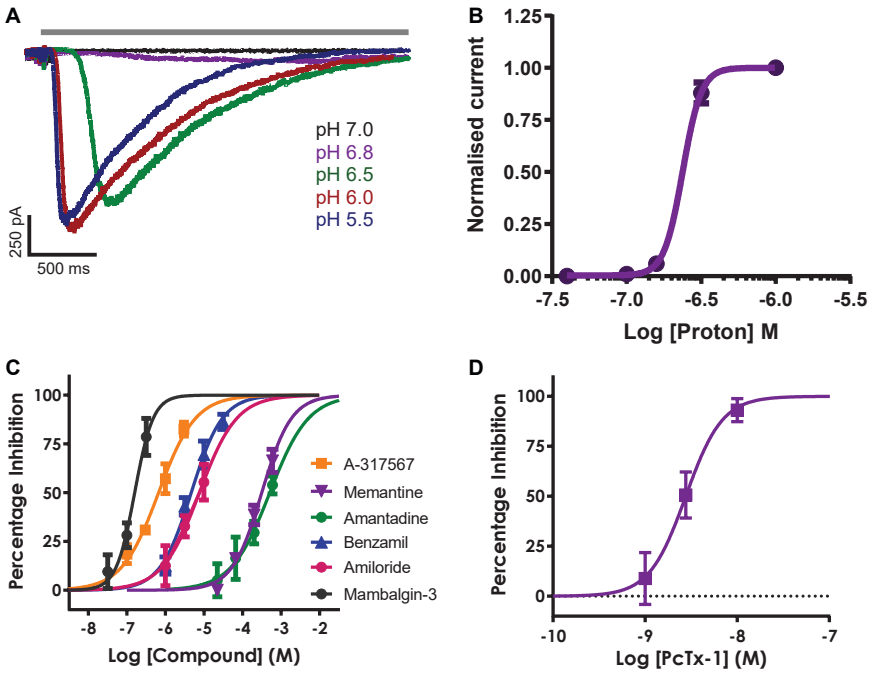

FIGURE 6
Pharmacology of hASIC1a responses in CHO cell line on QPatch 48. **(A)** Current traces in response to application of solutions (solid gray bar) with indicated acidity. **(B)** pH activation curve indicates an EC_{50} of 6.62 (mean ± S.D, n = 5). **(C)** Concentration-response curves for indicated reference antagonists spanning 5 log orders of magnitude. **(D)** Concentration-response data for PcTx1 inhibition indicates an IC_{50} of 2.96 nM. Mean ± S.D, n = 3–6 for each compound in **(C,D)**.

TABLE 2 ASIC1a pharmacology on QPatch 48.

Compound	IC_{50} potency (μM)	Hill slope	Literature IC_{50} (μM)	References
Amiloride	7.62	0.9	13.5	Leng et al., 2016
Benzamil	4.66	1.1	3.50	Leng et al., 2016
A-317567	0.66	0.9	2.00	Dubé et al., 2005
Amantadine	510.4	0.9	25% at 500 μM	Nagaeva et al., 2016
Memantine	315.3	1.1	31% at 500 μM	Nagaeva et al., 2016
PcTx1	0.003	2.2	0.0032	Cristofori-Armstrong et al., 2019
Mambalgin-3	0.16	1.8	0.127	Diochot et al., 2012

IC_{50} values and Hill slopes derived from the concentration-response fits in Figures 6C,D are compared against values reported from the indicated references.

is usually used when target ion channel expression is low (as it sums individual cell current levels), or the assay quality is compromised by issues such as current rundown or other variable parameters. However, multi-hole recordings can also be used to produce a high success rate assay which is very useful when carrying out a HTS with n = 1 or n = 2 samples, as we did recently for an ASIC1a fragment library screen on the QPatch 48 (Rogers et al., 2021b).

Although the single hole/single cell ASIC1a assay on QPatch 48 exceeded our 50% minimum cut-off level in terms of completed recordings (Figure 7A), the final QC pass rate fell below this level due to cells failing our strict QC criteria (−200 pA minimum current, Rseal > 200 MΩ and Rseries < 15 MΩ and stable during the 12–20 min whole-cell recording). In multi-hole mode there was a noticeable increase in the success rate for all parameters to > 90% during the different stages of the experiment, and a significant improvement in the final QC rate to 65%.

Before employing a more efficient multi-hole assay it is important to establish that this variant of the APC whole-cell recording format returns the same biophysics and pharmacology as single cell recordings. To this end we ran some of the reference compounds detailed above in 10 hole "X-plate" mode on the QPatch 48. The potency of the small molecule antagonists Amiloride and Benzamil and the peptide toxin Mambalgin-3 obtained in multi-hole recordings were in

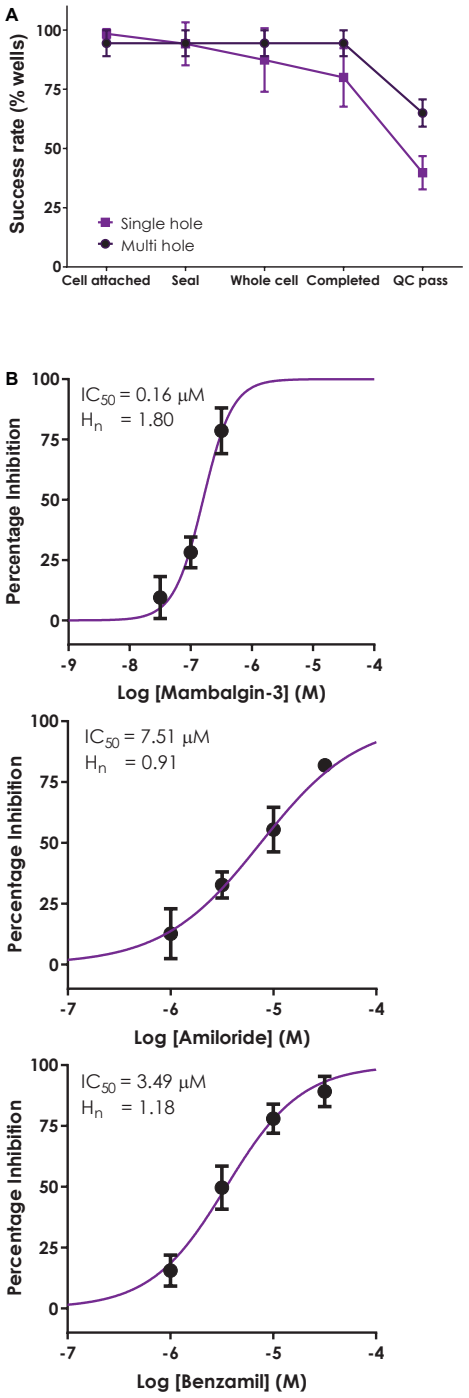

FIGURE 7
Validation of a multi-hole ASIC1a assay on QPatch 48. **(A)** Comparison of efficiency and success rate of single vs. multi-hole QPlate assay format. Mean (± S.D) data for the percentage of wells that passed various quality control (QC) criteria during and after whole-cell recordings in single hole (n = 4 plates, black squares) or multi-hole mode (n = 5 plates, filled circles). **(B)** ASIC1a assay pharmacology in multi-hole mode. Mean (± S.D) concentration-response data for inhibition of ASIC1a currents by Mambalgin-3 (n = 12), Amiloride (n = 8) and Benzamil (n = 4) in multi-hole recordings, with indicated IC_{50} and Hill slope values.

very good alignment with values obtained in single hole/single cell mode (Figure 7B and Table 2), confirming the equivalence of each APC recording format.

High throughput ASIC1a assay on SyncroPatch 384i

The SyncroPatch 384i (SP384i) employs a different design format to the Patchliner and QPatch 48, with plastic tips dispensing liquid straight into individual wells rather than through microfluidic flow channels. While this well-hole layout may not affect drug screening against voltage-gated targets, it may influence ligand-gated recordings in experiments with rapidly activating ionotropic channels prone to desensitization, and in multi-hole recordings receiving liquid applications from a single tip onto multiple cells in the same well, so we also validated the hASIC1a assay on the SP384i.

Initial SP384i experiments applied a series of single bolus applications (5 µl "puff") of pH 6.5 solution with intervening periods in pH 7.4 solution to enable agonist wash-off and ASIC1a receptor recovery from desensitization. This was repeated several times in the same cell to ensure reproducible activation which is critical for subsequent pharmacology experiments. In single hole recordings from a stable CHO hASIC1a cell line grown for several days at 37°C, we observed robust inward current responses in most cells across the 384 well plate after 3–6 h of tetracycline induction, with an average current amplitude of −5 nA (Figure 8A and Table 3). Currents activated rapidly after liquid exchange and then exhibited a mono-exponential decay to baseline, likely due to a mixture of initial ligand removal and receptor desensitization in the single "puff" application format, as subsequent full wash-off occurred several seconds after pH stimulus due to the delay in moving the 384 tip assembly between liquid reservoirs and the recording site. Nevertheless, acid-induced responses were stable, as shown by a sequence of seven pH 6.5 applications followed by washout and recovery at pH 7.4 (for 2 min), evidence of the complete recovery from ASIC1a receptor desensitization in this assay paradigm (Figure 8A). Across two 384 single hole plates tested with single bolus "puff" pH applications we observed a QC success rate of 80.2 and 85.4% based on filters of > -500 pA peak current and > 100 MΩ whole-cell seal resistance at the end of the experiment. It is important to note that actual seal quality was far higher than the minimum cut-off value, with average values of 1.29 ± 0.62 GΩ and 1.12 ± 0.06 GΩ calculated at the end of each experiment from 308 to 328 cells on each test NPC-384 chip, respectively.

Very similar ASIC1a biophysics, current characteristics and pharmacology were obtained with single "puff" pH responses on multi-hole NPC-384 chips with four holes (cells)

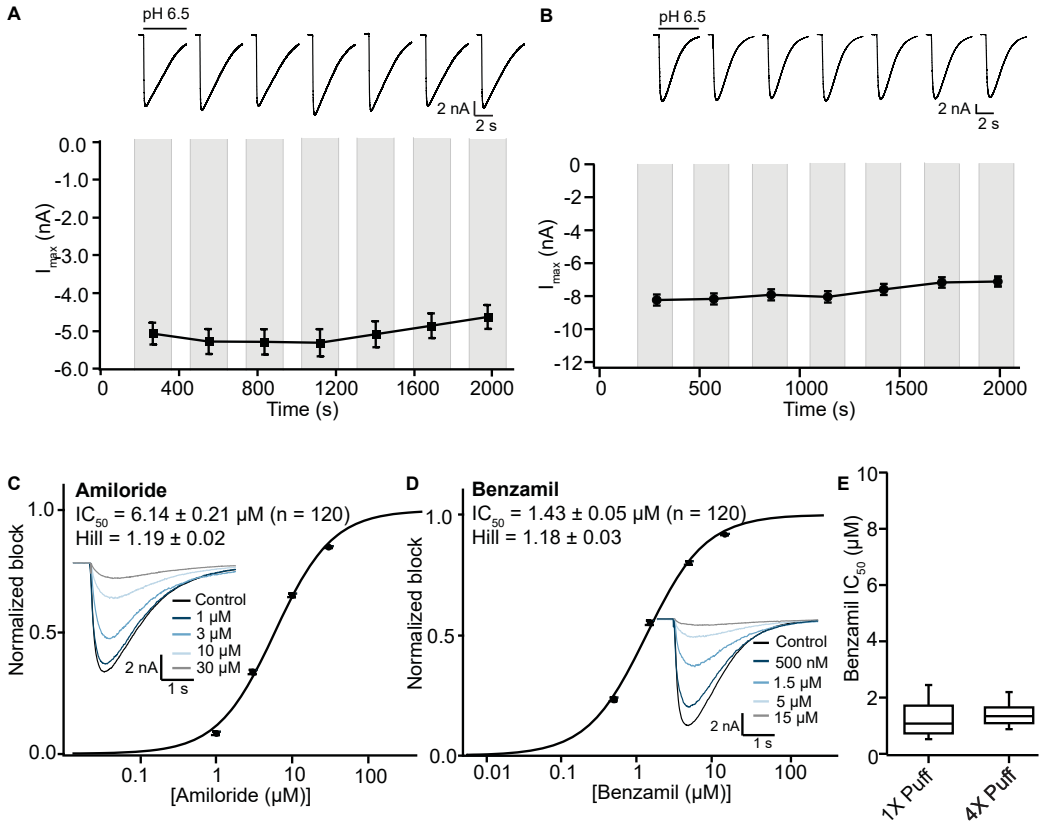

FIGURE 8
Stable ASIC1a responses in single and multi-hole recordings on SP384i enable pharmacological screening. **(A)** Stable responses in a single hole well to repeated "puff" applications of pH 6.5 solution (top), and average current stability data from n = 50 wells (bottom; mean ± S.E.M). **(B)** Stable responses in a multi-hole well (4X) to repeated "puff" applications of pH 6.5 solution (top), and average current stability data from n = 60 wells (bottom; mean ± S.E.M). **(C,D)** Inhibition of ASIC1a responses on SP384i by Amiloride and Benzamil. Raw current traces (insets) in response to pH 6.5 "puff" activation after pre-incubation in indicated concentrations of drug enable construction of cumulative IC_{50} curves for Amiloride **(C)** and Benzamil **(D)**, with indicated mean, S.E.M and n values and Hill slopes of 1.19 and 1.18, respectively. Multi-hole chips (4X) were used. **(E)** There is a wider spread of IC_{50} values for Benzamil on 1X chips compared with 4X chips using the "puff" ligand application method, although the mean values were not statistically different ($P > 0.05$, unpaired Student's t test).

TABLE 3 **Cell parameters, pH 6.5-evoked current expression and success rates for single and multi-hole chips using different liquid addition regimes.**

Chip type	Pipetting technique	Rseal (GΩ)	Cm (pF)	Imax (nA)	Success rate
1X	Puff	1.12 ± 0.06	13.5 ± 0.4	−5.3 ± 0.1	328/384 (85%)
4X	Puff	0.38 ± 0.02	49 ± 1	−8.2 ± 0.1	342/384 (89%)
1X	Stacked Puff	3.65 ± 0.23	13.2 ± 0.6	−5.4 ± 0.2	289/384 (75%)

Shown are parameters for Rseal (for last sweep of the experiment), cell capacitance (Cm) and current amplitude (Imax) of the 1st sweep to pH 6.5. Success rate is calculated for fraction of cells across each 384 well plate meeting or exceeding minimum quality criteria. Using single "puff" applications of pH 6.5 solution in single hole chips, we obtained small molecule reference pharmacology data on the SP384i that were very similar to potencies seen on the other APC platforms in this study and from the literature. Amiloride inhibited peak current with an IC_{50} of 5.90 ± 0.31 μM (Mean ± S.E.M, n = 193) and a Hill slope of 1.20 ± 0.05, while Benzamil exhibited a slightly higher potency of 1.37 ± 0.07 μM (Mean ± S.E.M, n = 224) and a Hill slope of 1.07 ± 0.02 (Table 4).

per well. Current amplitude was obviously increased due to summation of current from multiple cells (Table 3), but ASIC1a current kinetics and assay stability were unchanged using a series of single bolus application of pH 6.5 (Figure 8B). The potencies of Amiloride and Benzamil (6.01 and 1.47 μM, respectively; Figures 8C,D) were similar to those obtained for Amiloride and Benzamil using single hole chips (Table 4).

Assay performance was consistently high across three multi-hole NPC chips, with a QC pass rate of 93.8, 92.2, and 82.6% based on a minimum current amplitude of −500 pA and seal resistance > 25 MΩ at the end of each experiment. As the

TABLE 4 IC_{50} values for Amiloride and Benzamil using different pipetting regimes and chip types (1X single hole and 4X multi-hole).

Chip type	Pipetting technique	Amiloride		Benzamil	
		IC_{50} (μM) and n	Hill slope	IC_{50} (μM) and n	Hill slope
1X	Puff	5.90 ± 0.31 (193)	1.20 ± 0.05	1.37 ± 0.07 (224)	1.07 ± 0.02
4X	Puff	6.01 ± 0.14 (328)	1.14 ± 0.01	1.47 ± 0.03 (357)	1.12 ± 0.02
1X	Stacked Puff	10.9 ± 0.6 (192)	1.39 ± 0.02	2.48 ± 0.18 (191)	1.26 ± 0.03
4X	Stacked Puff	8.31 ± 0.23 (113)	1.24 ± 0.02	2.20 ± 0.08 (112)	1.12 ± 0.02

Shown are mean ± S.E.M, number of wells shown in parentheses. For some conditions, results from multiple plates are given.

average seal resistance value is divided across all 4 sites in each well, this QC parameter is similar to the 100 MΩ cut-off used for single hole recordings. Actual seal resistances were significantly higher in the majority of cells and averaged 0.38 GΩ (Table 3), which as explained previously is equivalent to a mean single cell seal four times this value. As expected, the QC pass rate is improved when using multi-hole chips, mainly due to fewer sites falling below the minimum current amplitude. In addition, more consistent pharmacological data can be obtained across multiple recording sites (Figure 8E). Assay performance as measured by Z' analysis is equally good, and both APC recording formats deliver excellent plate-based screening assay statistics above the industry standard z' cut-off of 0.5 (Table 5).

We next wanted to validate the stacked tip ligand-gated application format on the SP384i using the same CHO ASIC1a cell line and experimental conditions as above, to find the optimal protocol for studying this class of ion channel. Previous stacked tip ligand-gated receptor ion channel experiments on the Patchliner and SP384i typically use a small volume of agonist (5–10 μl) aspirated below a relatively large volume of extracellular buffer (200 or 35–45 μl, respectively) to wash-off the ligand (Milligan and Jiang, 2020; Braun et al., 2021; Obergrussberger et al., 2022). However, more recent work by us and others on the SP384 family of platforms has revealed that a counter-intuitive approach can be more effective, whereby a smaller wash-off volume (i.e., 5 μl) used to reduce bulk mixing in the well achieves faster and more complete wash-off above the recording site and reduces slow desensitization of ligand-gated ionotropic receptor responses (Figure 9A).

Using this optimized small volume "stacked" puff configuration on single hole chips revealed different current decay kinetics but identical pharmacology when compared with the "puff" addition. pH-activated currents rapidly reached a peak and then desensitized slowly, before rapidly returning to baseline upon washout and removal of the ligand (Figure 9A). Thus, it is possible to more reliably estimate peak amplitude and assess receptor desensitization rates with the stacked puff technique compared to a single puff application (e.g., Figures 8, 9A). Using the stacked puff method, ASIC1a currents were repetitively activated with pH 6.5 solution 7 times in the same cell, revealing reproducible and stable results suitable for pharmacological and drug screening (Figure 9B). The peak amplitude of ASIC1a-mediated currents evoked with the stacked puff approach was similar to that obtained with the puff approach using the same chip type (Table 3). Additionally, the reference inhibitors Amiloride and Benzamil blocked ASIC1a-mediated responses in a concentration-dependent manner (Figures 9C,D) with similar potency to that seen using single puff applications of pH on single hole and 4X multi-hole chips (Table 4), and were in excellent agreement with the literature (Leng et al., 2016). As seen with the puff addition (Figure 8E) the spread of IC_{50} values for Benzamil using 1X chips and the stacked puff application was higher than when 4X chips were used (Figure 9E).

Using the optimal stacked puff format and 4X chips, application of increasingly acidic pH evoked rapidly activating and deactivating inward currents (Figure 10A), enabling a pH activation plot to be constructed (Figure 10B). To obtain the composite pH EC_{50} data, a stable current response was obtained with three applications of pH 6.5 to each well. Following this the test pH for each well was then applied, and this cycle was repeated twice with a washout at pH 7.4 between each pH stimulus to acquire a reliable pH response. For each well the test pH response was normalized to the current elicited by pH 6.5, and the pH concentration-response curve calculated from all QC-passed wells across the whole plate. In these experiments the pH which elicited half-maximal current ($pH_{0.5}$) was 6.44 ± 0.08 (mean ± S.D., n = 378), in excellent agreement with literature values from manual patch clamp (Gunthorpe et al., 2001), other SP384 studies (Braun et al., 2021) and other APC platforms (data above and references herein).

Discussion

The results from this collaborative project demonstrate the successful implementation of technically challenging ligand-gated ion channel assays on a range of low, medium and high throughput APC platforms using human ASIC1a channels as a representative target of current interest for drug discovery screening. These data offer examples of how to overcome common problems in making such recordings, such as

TABLE 5 Comparison of SP384i ASIC1a assay performance in single vs. multi-hole chips.

Chip type	Pipetting technique	Z' value				
		$n = 1$	$n = 2$	$n = 3$	$n = 4$	$n = 8$
1X	Puff	0.62 ± 0.08	0.73 ± 0.05	0.78 ± 0.04	0.81 ± 0.04	0.86 ± 0.03
4X	Puff	0.60 ± 0.03	0.72 ± 0.02	0.77 ± 0.02	0.80 ± 0.02	0.86 ± 0.01
1X	Stacked Puff	0.63 ± 0.05	0.73 ± 0.03	0.78 ± 0.03	0.81 ± 0.02	0.87 ± 0.02
4X	Stacked Puff	0.69 ± 0.03	0.78 ± 0.02	0.82 ± 0.02	0.84 ± 0.01	0.89 ± 0.01

For each plate there were 64 wells (four columns) of positive control (incubation in pH 6.5 solution, fully desensitized response) and negative control (0.1% DMSO) solution. Z' values were calculated with replicate number 1, 2, 3, 4 or 8 and the mean ± S.E.M of the 4 pairs of controls for each plate are shown.

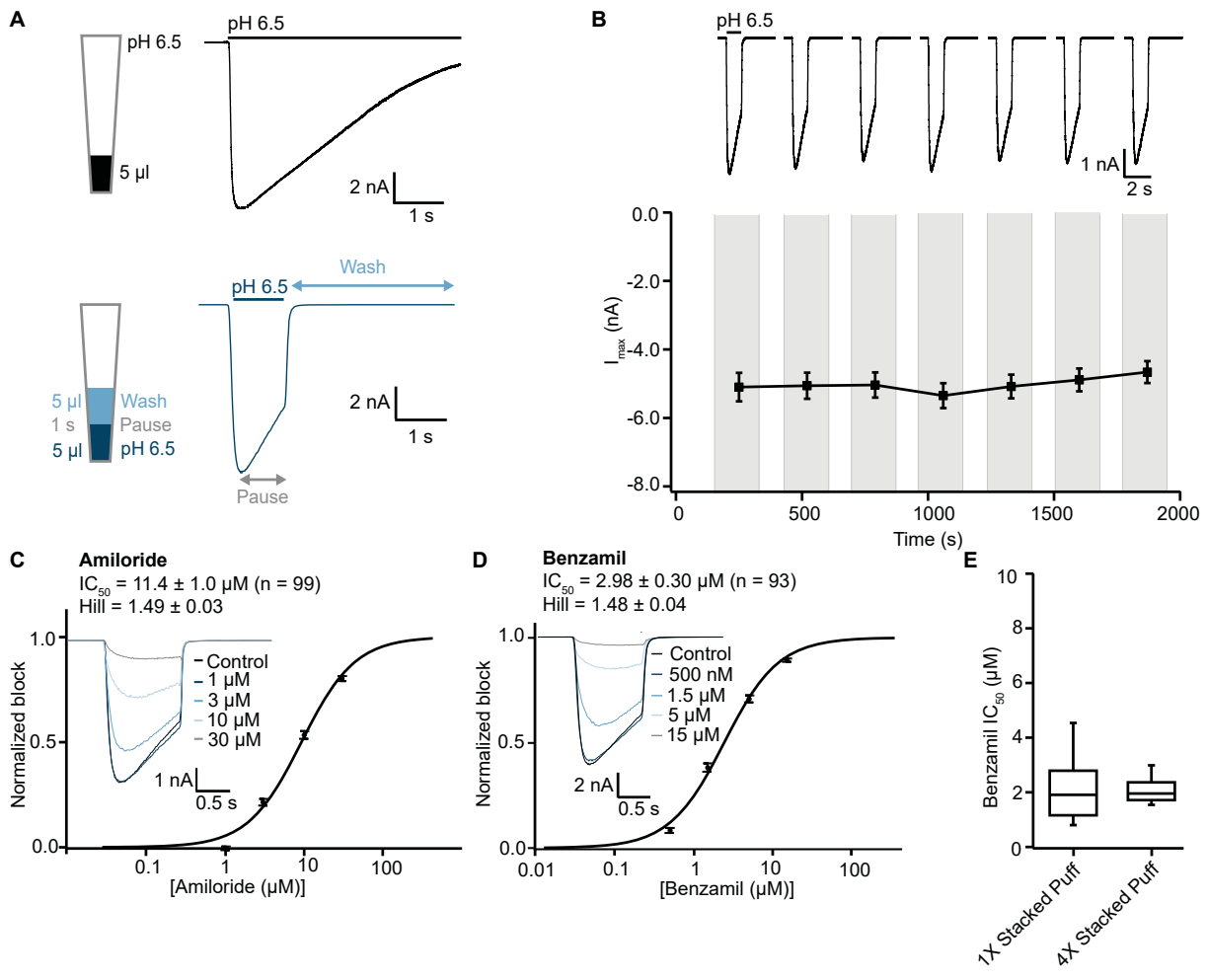

FIGURE 9

Validation of ASIC1a stacked tip assay format on SP384i. **(A)** Comparison of "puff" ligand application versus "stacked puff" format. Top left shows a schematic of the "puff" solution in the pipette tip and corresponding example of ASIC1a-mediated current with slow desensitizing phase. Bottom left shows the schematic of the "stacked puff" solutions in the pipette and an exemplar ASIC1a-mediated current with slow desensitization followed by rapid wash-off. **(B)** Stable responses in a single hole well to repeated "stacked puff" applications of pH 6.5 (top), and average current stability data from n = 48 wells (bottom; mean ± S.E.M). **(C,D)** Inhibition of ASIC1a responses using "stacked puff" approach by Amiloride and Benzamil with single hole chips. Raw current traces (insets) in response to pH 6.5 "stacked puff" activation after pre-incubation in indicated concentrations of drug enable construction of cumulative IC_{50} curves for Amiloride **(C)** and Benzamil **(D)**, with indicated mean, S.E.M and n values, and Hill slopes of 1.49 and 1.48, respectively. **(E)** There is a wider spread of IC_{50} values for Benzamil for 1X chips compared with 4X chips using the "stacked puff" application of ligand, although the mean values were not statistically different ($P > 0.05$, unpaired Student's t test).

improving current amplitude with cell culture protocols and the use of multi-hole chips and plates. We also offer a comparison of different ligand application techniques such as stacked tips that are available on different pipette and tip-based APC platforms. Importantly, the agonist (pH EC_{50}) and antagonist sensitivity of ASIC1a responses are very similar across multiple APC platforms using different ligand-gated application protocols. We also utilize the current clamp capabilities available on most APC platforms to validate a traditional input resistance tracking method on the Patchliner. Finally, our data demonstrate the advantages and risks of using endogenous responses in parental cell lines as the basis for screening assays. Although we successfully replicated a manual patch clamp study of endogenous pH-gated responses in HEK cells attributed to human ASIC1a channels on APC, our extensive validation of this assay indicated an atypical pharmacological profile and low current expression which precluded its use for drug discovery screening.

Endogenous proton-activated currents in HEK cells

It is relatively common in ion channel drug discovery to use native and immortalized cell lines, either for their endogenous human or mammalian ion channel proteins (e.g., Vetter et al., 2012) or as a system for heterologous expression of human orthologs (Rogers et al., 2016). However, the endogenous voltage- and ligand-gated ion channels in the chosen cell line are not always determined before drug discovery screening or mechanistic studies take place, raising questions over the accuracy of subsequent work. It is therefore wise to test for functional responses of the ion channel target family of interest (Gunthorpe et al., 2001; Rogers et al., 2016), profile the cell line system using molecular biology techniques (Gunthorpe et al., 2001), and if necessary knockdown the endogenous target before expressing the functional protein or mutant of interest (Vanoye et al., 2016; Borg et al., 2020; Braun et al., 2021). In the case of ASIC drug screening, the use of parental HEK cells to express mutated hASIC1a (Cullinan et al., 2019) and other human and species orthologs (Kuduk et al., 2010; Wolkenberg et al., 2011; Goehring et al., 2014) may be compromised by contamination from the innate ASIC1a channels we and others have characterized in HEK cells.

Although we were able to confirm the original manual patch clamp publication that native HEK cells express an endogenous ASIC1-like response (Gunthorpe et al., 2001), there are several features of these pH-activated currents that do not make them sufficient for a drug discovery screening assay, especially on APC platforms. Firstly, we found that pH-activated current amplitude was relatively low and that treatments to increase it led to unstable responses unsuitable for pharmacological screening. With HEK cells grown under standard 37°C conditions the mean peak inward current amplitude ranged between −334 and −567 pA for single cell manual and automated patch clamp recordings, respectively (Gunthorpe et al., 2001; **Figure 1**), leaving a small assay window once a minimum current threshold is applied. The lower current amplitude (and % expressors) in APC experiments may be due to loss of neuronal-like processes of adherent HEK cells that express functional ASIC1a receptor channels when cells are dissociated and suspended for use on APC platforms. In order to induce current amplitudes of sufficient size for single hole QPatch 48 experiments cells must be incubated for at least 24 h at 30°C, but this mild heat shock treatment affects ASIC1 current stability and may also trigger surface translocation of other ion channels, thereby reducing assay success rates and specificity. Thus, the trade-off between a treatment to increase current expression and maintain overall assay stability and quality failed to yield a set of experimental conditions in HEK cells that met our goal of achieving a $\geq$ 50% final QC success rate at the end of every single cell cumulative xC_{50} ASIC1a screening experiment. Multi-hole recordings from untransfected HEK cells proved problematic, removing an alternate approach to overcome low current amplitudes and expression rates. Although many APC users now adopt multi-hole recordings as standard, this may mask underlying issues with poorly expressing transient transfections or stable cell lines and sub-optimal cell culture, and also precludes the application of some useful QC filters such as seal resistance and Rseries monitoring. We treated single-hole and multi-hole recordings of hASIC1a currents as separate experiments to enable comparison of recording modes on the APC platforms used in this study, so that an appropriate choice of assay and chip format can be made by other users.

Secondly, we found that the pharmacological profile of the endogenous pH-gated response in HEK cells was not typical for hASIC1a receptors. Amiloride was surprisingly potent, and the moderately selective toxin Mambalgin-3 was more effective than the selective ASIC1 antagonist PcTx-1. Although we were able to replicate the low μM potency of Amiloride seen in the original manual patch clamp study (Gunthorpe et al., 2001) in our QPatch 48 recordings (2.2 vs. 2.8 μM, respectively), both values are more potent than the 10–20 μM values typically obtained in other electrophysiological studies of human and rodent ASIC1a receptors (Baron and Lingueglia, 2015; Leng et al., 2016). In contrast, the potency of 119 nM for Mambalgin-3 inhibition of endogenous pH-gated responses was close to values for human ASIC1a in previous studies (Diochot et al., 2012; Sun et al., 2018), although mambalgins are only moderately selective for ASIC1a channels, exhibiting 1.2 – 5 fold selectivity for rat ASIC1a over other ASIC1 and ASIC2 homomers, heteromers and splice variants. Also, the highly ASIC1a-selective toxin PcTx1 was only moderately effective against pH-activated currents in HEK cells, exhibiting weak, variable and inconsistent inhibition. Mean inhibition by PcTx1

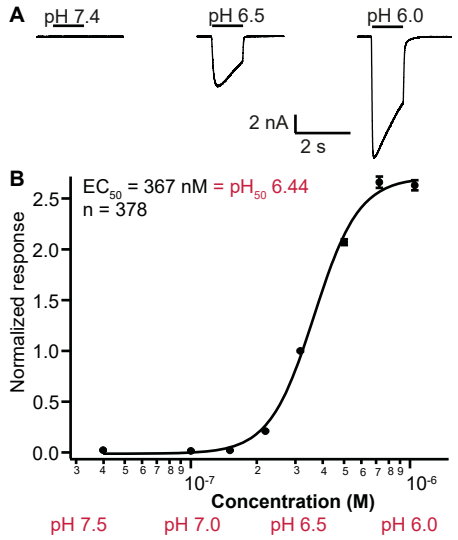

FIGURE 10
pH sensitivity of ASIC1a responses on SP384i using stacked puff format. **(A)** pH was used to activate ASIC1a responses, and decreasing pH led to increased peak amplitude (exemplar traces from different cells shown on the same scale). The pH concentration-response curve was calculated across multiple wells (each well received 1 × pH 6.5 followed by the test pH so the data was normalized to the pH 6.5 response in each well). **(B)** The pH_{50} was calculated to be 6.44. Mean ± S.E.M for each pH is shown by symbols from a maximum of 48 wells per pH concentration. 4X chips were used.

at the highest tested concentration of 30 nM was < 50%, whereas the published potency against human ASIC1a is ∼3 – 13 nM (Baron et al., 2013; Cristofori-Armstrong et al., 2019). Despite the fact it can be difficult to replicate manual patch data for sticky compounds, peptides and other biological ligands on APC platforms, we followed best practice and employ protocols to minimize compound absorption or loss (e.g., glass-lined consumables throughout, BSA in final experimental solutions). As our pharmacology data faithfully replicates the known potency of Mambalgin-3 and PcTx1 against human ASIC1a responses in CHO cells on the same APC platform (**Table 2**), this suggests that the relative potency and efficacy of non-selective vs. selective ASIC1a ligands in HEK cells is evidence for functional expression of an atypical pH-gated receptor complex in this parental cell line.

Whilst TRP channels are present in HEK cells (Wu et al., 2000), our data rules out their contribution to endogenous pH-gated responses in HEK cells; there was no effect of the pan-TRP antagonist Ruthenium Red (**Figure 2E**), and Mambalgin-3 produced over 75% inhibition of whole-cell current (**Figure 2B**) but does not inhibit TRPV1 receptor channels (Diochot et al., 2012). Interestingly, co-assembly of ASIC1 and ENaC subunits in *Xenopus* oocytes increases the potency of Amiloride (Meltzer et al., 2007), and ENaC channels are more sensitive to inhibition by Amiloride (100 nM, Canessa et al., 1994) than ASIC1 channels, perhaps explaining the relatively high sensitivity of endogenous proton-gated responses in HEK cells to Amiloride inhibition found in this study (2.8 μM) and the 2.2 μM value reported by Gunthorpe et al. (2001). As all of the pharmacology testing was done in HEK cells grown at 30°C it is important to note that heat shock induction of intracellular chaperones may facilitate the expression of various endogenous pH-gated conductances in HEK cells, potentially leading to alterations in agonist and antagonist pharmacology. However, we observed no change in the pH EC_{50} values in HEK cells (**Figure 1D**) or CHO cells (data not shown) after 30°C treatment, suggesting that low temperature treatment of HEK cells predominantly upregulated ASIC1-containing receptor channel complexes, or alternatively that ASIC and other degenerin family ion channels such as ENaC may have been increased but all share a similar pH sensitivity (Meltzer et al., 2007).

Application of conductance-tracking in a ligand-gated ion channel automated patch clamp assay

Prior to the development and widespread utilization of whole-cell patch clamp techniques in ion channel research, neurotransmitter-gated receptor responses were often studied using sharp microelectrodes and current clamp monitoring of cell input resistance to track changes in conductance in response to agonist application by iontophoresis or bath application (e.g., Hiruma and Bourque, 1995). This technique has now been supplanted but a recent study from an industry group detailed a low throughput electro-optical version of the input resistance tracking method using field electrodes to apply current pulses and fast voltage-sensing dyes to measure membrane potential changes in populations of heterologous cell lines (Menegon et al., 2017). In theory this optical approach could be scaled up to 96 and 384 well plate-based imaging systems used in ion channel drug discovery, but we wanted to demonstrate that the current clamp features available on most APC platforms could be used to design a higher throughput conductance-tracking assay to study ligand-gated ionotropic receptor targets relevant to ion channel drug discovery.

Using the Patchliner as our proof-of-concept platform, we successfully developed and validated an APC input resistance tracking assay for the fast ligand-gated ASIC1a receptor channel (**Figure 4**). After careful optimization of current clamp protocols and choice of a holding potential that allowed for reliable detection of changes in input resistance in response to a series of current injections, it was possible to accurately track changes in membrane conductance after the application of pH agonist. Our current clamp data reveal pH EC_{50} and Benzamil IC_{50} values in close agreement with those obtained using fast ligand application under voltage clamp

on the Patchliner and other APC platforms. This is the first demonstration to our knowledge for implementation of the traditional current clamp conductance tracking technique to study a ligand-gated receptor channel on a multi-well APC platform, demonstrating the untapped utility of these devices.

ASIC1a ligand-gated screening assay validation on automated patch clamp platforms

While voltage-gated ion channel screening is well served by the gigaseal recording qualities and sophisticated biophysical features of current APC platforms, successful implementation of robust pharmacological assays for ligand-gated receptor channels has been more challenging. Early protocols on low and medium throughput platforms and initial models of 384 devices utilized slow and sequential additions of agonist and wash-off solutions due to the need for the tip or pipette to return to a reservoir of external solution and then back to the recording site to wash-off the agonist, which can lead to profound receptor desensitization. Such assays run the risk of screening against a non-physiological state of the ligand-gated ionotropic receptor of interest, and can also flatter users by revealing an agonist EC_{50} for the desensitized state which is more potent than the activated state. Numerous ligand-gated receptor channels of therapeutic interest exhibit such desensitization, including ASIC channels, α7 and other nAChRs, as well as $GABA_A$ receptors, NMDA, kainate and AMPA GluRs, and $P2_X$ receptors. APC vendors have now developed new ligand-gated assay features with faster application speeds and the ability to stack different solutions within each tip, so we sought to compare the same ligand-gated hASIC1a receptor channel assay across multiple APC platforms and test the efficacy of various optimization strategies.

A key parameter for the accuracy and reliability of a ligand-gated ionotropic receptor assay is the agonist EC_{50}, as this value can be compromised by compound absorption, slow or partial access to the ligand-binding pocket, and receptor desensitization. In the case of ASIC1a the pH dependence is steep (Hill slope > 5) so even small deficits in the assay format and liquid application and wash-off protocols can significantly affect this value. It was therefore reassuring to see very similar pH EC_{50} values obtained using the same CHO ASIC1a cell line on the Patchliner with stacked pipette tips (6.68) and on the QPatch 48 using a bolus pipette application (6.62). These values are comparable to pH EC_{50} potencies published for hASIC1a on the QPatch and SP384 family of APC platforms (Braun et al., 2021; B'Sys, 2022). A slightly more acidic pH EC_{50} of 6.44 was obtained on the SP384i with a stacked puff application from plastic tips, but it should be noted that multi-hole chips and a different CHO cell line were used in these experiments. It was clear that ASIC1a receptor desensitization occurred over a second or so after current activation and prior to ligand wash-off with the bolus applications on the SP384i, and that this could be minimized using the various stacked tip protocols now available on most APC platforms. All of these APC pH EC_{50} values are significantly different from the much more acidic EC_{50} value of 5.6 obtained for hASIC1a in *Xenopus* oocytes where fast perfusion and complete solution washout is problematic (Borg et al., 2020).

Although there is significant desensitization of hASIC1a responses during more prolonged and acidic pH applications, seen in both bolus or "puff" applications (e.g., **Figures 1A**, **3A**, **6A**, **9**), ASIC1a receptor ion channels recover quickly from desensitization upon return to neutral pH. Thus, we saw no obvious differences in pH EC_{50} values across the Patchliner, QPatch 48 and SP384 APC platforms as care was taken to effectively remove acidic solution during wash-off and allow the receptors to recover from desensitization with repeated periods in pH 7.4. The same rapid recovery from desensitization may not be true for other types of ligand-gated ion channels (e.g., α7 nAChR, neuronal $P2_X$ receptors, GluRs), in which case it becomes useful and perhaps essential to employ APC assays with stacked ligand and wash solutions to achieve effective ligand-gated assays with reduced desensitization, current rundown and altered pharmacology.

Once we had established the correct pH EC_{50} value for each APC platform and ASIC1a cell line it was possible to pharmacologically validate the assay using a toolbox of reference compounds, including both small molecules and peptide toxins that are common ligand modalities in ion channel drug discovery. Benzamil was tested across all APC platforms and exhibited very consistent potencies when tested using a bolus pipette application (QPatch 48) or stacked tip application (Patchliner, SP384i). Focusing on data from single hole recordings, we obtained an IC_{50} for Benzamil of 3.65 μM on Patchliner (**Figure 3C**), 4.66 μM on QPatch 48 (**Figure 6C** and **Table 2**), and 1.37 and 2.48 μM on SP384i using puff or stacked puff applications (**Table 4**), respectively. Amiloride was used as a positive control for the medium throughput QPatch 48 and high throughput SP384i platforms, exhibiting an IC_{50} of 7.62 μM on the former (**Figure 6C** and **Table 2**) and values of 5.90 and 10.9 μM on the latter with puff or stacked puff applications (**Table 4**), respectively. The potencies of Amiloride and Benzamil across these APC platforms (**Tables 2**, **4**) align well with published values of 3.5 and 13.5 μM, respectively (Leng et al., 2016).

A comprehensive ASIC compound toolbox was tested on the QPatch 48 as we wanted to validate the CHO ASIC1a cell line on this platform prior to a fragment screen

(Rogers et al., 2021b). We found excellent agreement between the nM potencies of the selective ASIC1a toxins PcTx1 and Mambalgin-3 on the QPatch 48 compared to literature values (**Table 2**), confirming the ability to reliably detect the activity of biological ligands in APC assays if suitable steps are taken to minimize peptide absorption. PcTx1 binds within the "acidic pocket" in the extracellular domain of ASIC channels, and as such is a state-dependent modulator as its affinity can be strongly affected by local pH (Baron et al., 2013). Pre-incubating CHO cells in the presence of PcTx1 at pH 7.3 was sufficient to allow efficient binding, and the potency of 3 nM we obtained on the QPatch 48 (**Figure 6D** and **Table 2**) was nearly identical to published values of 0.9 – 3 nM for human ASIC1a channels (Escoubas et al., 2000; Cristofori-Armstrong et al., 2019; Braun et al., 2021). Whilst there is a paucity of data for Mambalgin-3 against human ASIC1a channels as most published data utilized mammalian orthologs (Diochot et al., 2012; Sun et al., 2018), this toxin only differs from Mambalgin-1 at one non-critical amino acid residue and it is assumed to exhibit similar potency. Indeed, the very similar potencies of Mambalgin-3 on QPatch 48 of 119 and 160 nM against endogenous pH-gated responses in HEK cells (**Figure 2B**) and human ASIC1a stably expressed in a CHO cell line (**Table 2**) align very closely with quoted values of 127 or 197 nM for Mambalgin-1 tested against human ASIC1a channels (Diochot et al., 2012; Sun et al., 2018). Unlike PcTx1, Mambalgins are no longer thought to bind within the "acidic pocket" of the ASIC1a receptor but nearby on the "thumb," and thereby disrupt (reduce) proton sensitivity of activation (Baron et al., 2013; Cristofori-Armstrong and Rash, 2017). In this way Mambalgins may bind to both the closed and desensitized/inactivated states of ASIC1 receptor channels but don't alter their desensitization pH sensitivity.

Several small molecule antagonists of ASIC receptor channels were also tested on the QPatch 48 in preparation for a drug discovery screen. The clinical drugs Amantadine and Memantine are low molecular weight hydrophobic amines that inhibit various ASIC receptor channels with low potency (Nagaeva et al., 2016; Shteinikov et al., 2018), and we found IC_{50} values of 510 and 315 μM against human ASIC1a, respectively (**Table 2**). Although A-317567 is not selective for ASIC1a as it was originally designed by Abbott as an ASIC3 modulator (Dubé et al., 2005) and used as a scaffold to develop further analogues against this target by Merck and Co., Inc., (Kuduk et al., 2010), A-317567 is a relatively potent drug discovery compound that can be used to benchmark screening assays designed to discover new selective and potent inhibitors of ASIC1a receptor channels. Compared to published data that A-317567 inhibits "ASIC1-like" pH-activated currents in rat dorsal root ganglion neurons with a potency of 2 μM (Dubé et al., 2005), we found that human ASIC1a channels exhibited an IC_{50} of 660 nM (**Figure 6C** and **Table 2**), with the small difference in activity likely attributable to differences in activating pH and cell type. Significantly, a close analogue of A-317567 developed by Merck and Co., Inc., was found to inhibit ASIC1a currents with an IC_{50} of 450 nM (Kuduk et al., 2010). In summary, our pharmacological validation data highlights the current lack of potent and selective small molecule inhibitors of hASIC1a, and demonstrate the need for further virtual and compound library screens to discover novel and effective ASIC1a receptor channel modulators to treat peripheral and CNS diseases.

All APC platforms offer the choice between single hole well/single cell recording chips, and multi-hole or population patch clamp recordings. Single hole chips and plates are preferred for rigorous biophysical recordings of voltage-gated ion channels as they allow for application of compensation circuits and tracking of single cell properties for QC purposes, and enable an accurate assessment of variation in cell line characteristics during assay optimization. Multi-hole recordings are favored as they increase assay success rate and reduce screening costs, and can compensate for sub-par cells or difficult-to-express ion channel targets. We were interested to assess what difference, if any, that single vs. multi-hole APC recordings would make for a ligand-gated receptor channel such as ASIC1a due to potential differences in liquid application and wash-off for a single cell compared to an array of cells across the bottom of a multi-hole recording well. Significantly, we did not find any obvious differences in the pharmacological potency of reference small molecule compounds and peptide toxins tested in single vs. multi-hole format on the QPatch 48 (**Figure 7**) and SP384i (**Table 4**). Also, multi-hole recordings can deliver ligand-gated receptor ion channel assays with a higher success rate (**Figure 7**) and thus improved screening efficiency and lower costs, as well as more consistent pharmacological results (**Figures 8E**, **9E**).

In summary, we demonstrated that it is possible to implement robust and reliable medium and high throughput APC screening assays for a challenging ligand-gated receptor ion channel. This was achieved on three different APC instruments, Patchliner, QPatch 48 and SP384i, by careful design of an ASIC1a assay format that maximized current stability and minimized desensitization during repeated pH activations (**Figures 5B**, **8A,B**, **9B**), enabling accurate pharmacological sensitivity. The need for a more efficient and cost-effective ASIC1a drug screening assay is topical (Bordon et al., 2020), as previous efforts to bring ASIC modulators to the clinic for various therapeutic indications have failed for various reasons (Wolkenberg et al., 2011; Heusser and Pless, 2021). Previous screening efforts used manual patch techniques and low throughput 16 channel APC devices, and traditional 384 plate-based fluorescence imaging assays to detect cation flux through ASIC1a receptor channels has proven challenging due to the rapid activation and profound desensitization of these channels that is hard to overcome on systems with slow or limited liquid

addition and washout capabilities. Thus, our demonstration of improved, robust and efficient ligand-gated ionotropic receptor screening assays on a range of APC platforms may foster renewed efforts to discover potent, selective and efficacious modulators of human ASIC1a channels.

Data availability statement

The original contributions presented in this study are included in the article, further inquiries can be directed to the corresponding author.

Author contributions

SM carried out the Patchliner experiments designed by MR, and undertook the data analysis and figure creation. RT, JR, and RK designed and carried out the QPatch 48 experiments and data analysis and helped prepare the figures. TG and NB carried out the SP384i experiments and data analysis, supported by IR-W. AO and NB prepared the figures. AO and MR collected, organized, and interpreted the results, and co-wrote the manuscript. MR conceptualized the study and coordinated the project and dissemination of the results. All authors contributed to the article and approved the submitted version.

Acknowledgments

We would like to thank the cell and tissue culture staff at Metrion Biosciences and Nanion Technologies for their important contribution to these studies, as well as Charles River Laboratories for use of the CHO human ASIC1a cell line (CT6012). Metrion Biosciences acknowledge the work of Ian Witton and our collaborators at Vernalis (UK) for their part in a fragment screen that utilized the QPatch 48 ASIC1a assay. MR and AO would also like to acknowledge the support and insight offered by past and present colleagues at Metrion Biosciences and Nanion Technologies, respectively, and thank Niels Fertig (Nanion Technologies) for his contribution to writing and proofreading the manuscript and supporting this collaborative project. Some of these results were previously published online (as abstracts) and available publicly as virtual posters at the Biophysical Society 65th annual meeting in February 2021 (Rogers et al., 2021a,b).

Conflict of interest

JR, RT, RK, and MR are employees and shareholders of Metrion Biosciences Ltd., and SM was an employee of Metrion Biosciences when he conducted these experiments. TG, NB, IR-W, and AO are employees of Nanion Technologies GmbH. The employer companies were not involved in the study design, collection, analysis, or interpretation of data, the writing of this article, or the decision to submit it for publication.

Publisher's note

References

B'Sys (2022). *CHO ASIC1a Cell Line, Specification Sheet.* Available online at: https://www.bsys.ch/media/cho_asic_1a.pdf (accessed April 19, 2022).

Baron, A., and Lingueglia, E. (2015). Pharmacology of acid-sensing ion channels – Physiological and therapeutical perspectives. *Neuropharmacology* 94, 19–35. doi: 10.1016/j.neuropharm.2015.01.005

Baron, A., Diochot, S., Salinas, M., Deval, E., Noël, J., and Lingueglia, E. (2013). Venom toxins in the exploration of molecular, physiological and pathophysiological functions of acid-sensing ion channels. *Toxicon* 75, 187–204. doi: 10.1016/j.toxicon.2013.04.008

Bässler, E. L., Ngo-Anh, T. J., Geisler, H. S., Ruppersberg, J. P., and Gründer, S. (2001). Molecular and Functional characterization of Acid-sensing Ion Channel (ASIC) 1b. *J. Biol. Chem.* 276, 33782–33787. doi: 10.1074/jbc.M1040 30200

Becker, N., Horváth, A., De Boer, T., Fabbri, A., Grad, C., Fertig, N., et al. (2020). Automated Dynamic clamp for simulation of IK1 in Human induced pluripotent stem cell-derived cardiomyocytes in real time using patchliner Dynamite8. *Curr. Protoc. Pharmacol.* 88:e70. doi: 10.1002/cpph.70

Bohlen, C. J., Chesler, A. T., Sharif-Naeini, R., Medzihradszky, K. F., Zhou, S., King, D., et al. (2011). A heteromeric Texas coral snake toxin targets acid-sensing ion channels to produce pain. *Nature* 479, 410–414. doi: 10.1038/nature10607.A

Bordon, K., de, C. F., Cologna, C. T., Fornari-Baldo, E. C., Pinheiro-Júnior, E. L., Cerni, F. A., et al. (2020). From Animal poisons and venoms to medicines: Achievements, Challenges and Perspectives in drug discovery. *Front. Pharmacol.* 11:1132. doi: 10.3389/fphar.2020.01132

Borg, C. B., Braun, N., Heusser, S. A., Bay, Y., Weis, D., Galleano, I., et al. (2020). Mechanism and site of action of big dynorphin on ASIC1a. *Proc. Natl. Acad. Sci. U.S.A.* 117, 7447–7454. doi: 10.1073/pnas.1919323117

Braun, N., Friis, S., Ihling, C., Sinz, A., Andersen, J., and Pless, S. A. (2021). High-throughput characterization of 309 photocrosslinker-bearing ASIC1a variants maps residues critical for channel function and pharmacology. *PLoS Biol.* 19:e3001321. doi: 10.1371/journal.pbio.3001321

Canessa, C. M., Schild, L., Buell, G., Thorens, B., Gautschi, I., Horisberger, J. D., et al. (1994). Amiloride-sensitive epithelial Na+ channel is made of three homologous subunits. *Nature* 367, 463–467. doi: 10.1038/367463a0

Chassagnon, I. R., McCarthy, C. A., Chin, Y. K. Y., Pineda, S. S., Keramidas, A., Mobli, M., et al. (2017). Potent neuroprotection after stroke afforded by a double-knot spider-venom peptide that inhibits acid-sensing ion channel 1a. *Proc. Natl. Acad. Sci. U.S.A.* 114, 3750–3755. doi: 10.1073/pnas.1614728114

Cristofori-Armstrong, B., and Rash, L. D. (2017). Acid-sensing ion channel (ASIC) structure and function: Insights from spider, snake and sea anemone venoms. *Neuropharmacology* 127, 173–184. doi: 10.1016/j.neuropharm.2017.04.042

Cristofori-Armstrong, B., Budusan, E., and Rash, L. D. (2021). Mambalgin-3 potentiates human acid-sensing ion channel 1b under mild to moderate acidosis: Implications as an analgesic lead. *Proc. Natl. Acad. Sci. U.S.A.* 118:e2021581118. doi: 10.1073/pnas.2021581118

Cristofori-Armstrong, B., Saez, N. J., Chassagnon, I. R., King, G. F., and Rash, L. D. (2019). The modulation of acid-sensing ion channel 1 by PcTx1 is pH-, subtype- and species-dependent: Importance of interactions at the channel subunit interface and potential for engineering selective analogues. *Biochem. Pharmacol.* 163, 381–390. doi: 10.1016/j.bcp.2019.03.004

Cullinan, M., Aryal, P., and Bankston, J. (2019). Measuring Dynamics of the acid-sensing ion channel N-Terminus using transition metal Ion FRET. *Biophys. J.* 116, 35–36. doi: 10.1016/j.bpj.2018.11.236

Diochot, S., Baron, A., Salinas, M., Douguet, D., Scarzello, S., Dabert-Gay, A. S., et al. (2012). Black mamba venom peptides target acid-sensing ion channels to abolish pain. *Nature* 490, 552–555. doi: 10.1038/nature11494

Dubé, G. R., Lehto, S. G., Breese, N. M., Baker, S. J., Wang, X., Matulenko, M. A., et al. (2005). Electrophysiological and in vivo characterization of A-317567, a novel blocker of acid sensing ion channels. *Pain* 117, 88–96. doi: 10.1016/j.pain.2005.05.021

Escoubas, P., De Weille, J. R., Lecoq, A., Diochot, S., Waldmann, R., Champigny, G., et al. (2000). Isolation of a tarantula toxin specific for a class of proton-gated Na+ channels. *J. Biol. Chem.* 275, 25116–25121. doi: 10.1074/jbc.M003643200

Goehring, A., Lee, C. H., Wang, K. H., Michel, J. C., Claxton, D. P., Baconguis, I., et al. (2014). Screening and large-scale expression of membrane proteins in mammalian cells for structural studies. *Nature Protocols* 9, 2574–2585. doi: 10.1038/nprot.2014.173

Goversen, B., Becker, N., Stoelzle-Feix, S., Obergrussberger, A., Vos, M. A., van Veen, T. A. B., et al. (2018). A hybrid model for safety pharmacology on an automated patch clamp platform: Using dynamic clamp to join iPSC-derived cardiomyocytes and simulations of Ik1 ion channels in real-time. *Front. Physiol.* 8:1094. doi: 10.3389/fphys.2017.01094

Gründer, S., and Chen, X. (2010). Structure, function, and pharmacology of acid-sensing ion channels (ASICs): Focus on ASIC1a. *Int. J. Physiol. Pathophysiol. Pharmacol.* 2, 73–94.

Gunthorpe, M. J., Smith, G. D., Davis, J. B., and Randall, A. D. (2001). Characterisation of a human acid-sensing ion channel (hASIC1a) endogenously expressed in HEK293 cells. *Pflugers Arch. Eur. J. Physiol.* 442, 668–674. doi: 10.1007/s004240100584

Haythornthwaite, A., Stoelzle, S., Hasler, A., Kiss, A., Mosbacher, J., George, M., et al. (2012). Characterizing Human ion channels in induced pluripotent stem cell-derived neurons. *J. Biomol. Screen.* 17, 1264–1272. doi: 10.1177/1087057112457821

Heusser, S. A., and Pless, S. A. (2021). Acid-sensing ion channels as potential therapeutic targets. *Trends Pharmacol. Sci.* 42, 1035–1050. doi: 10.1016/j.tips.2021.09.008

Hiruma, H., and Bourque, C. W. (1995). P2 purinoceptor-mediated depolarization of rat supraoptic neurosecretory cells *in vitro*. *J. Physiol.* 489, 805–811. doi: 10.1113/jphysiol.1995.sp021093

Hoagland, E. N., Sherwood, T. W., Lee, K. G., Walker, C. J., and Askwith, C. C. (2010). Identification of a calcium permeable human acid-sensing ion channel 1 transcript variant. *J. Biol. Chem.* 285, 41852–41862. doi: 10.1074/jbc.M110.171330

Iversen, P. W., Eastwood, B. J., Sittampalam, G. S., and Cox, K. L. (2006). A comparison of assay performance measures in screening assays: Signal window, Z' factor, and assay variability ratio. *J. Biomol. Screen.* 11, 247–252. doi: 10.1177/1087057105285610

Kuduk, S. D., Di Marco, C. N., Bodmer-Narkevitch, V., Cook, S. P., Cato, M. J., Jovanovska, A., et al. (2010). Synthesis, structure-activity relationship, and pharmacological profile of analogs of the ASIC-3 inhibitor A-317567. *ACS Chem. Neurosci.* 1, 19–24. doi: 10.1021/cn9000186

Leng, T. D., and Xiong, Z. G. (2013). The pharmacology and therapeutic potential of small molecule inhibitors of acid-sensing ion channels in stroke intervention. *Acta Pharmacol. Sin.* 34, 33–38. doi: 10.1038/aps.2012.81

Leng, T. D., Si, H. F., Li, J., Yang, T., Zhu, M., Wang, B., et al. (2016). Amiloride Analogs as ASIC1a Inhibitors. *CNS Neurosci. Ther.* 22, 468–476. doi: 10.1111/cns.12524

Li, W., Luo, X., Ulbricht, Y., and Guan, K. (2021). Blebbistatin protects iPSC-CMs from hypercontraction and facilitates automated patch-clamp based electrophysiological study. *Stem Cell Res.* 56, 102565. doi: 10.1016/j.scr.2021.102565

Li, W., Luo, X., Ulbricht, Y., Wagner, M., Piorkowski, C., El-Armouche, A., et al. (2019). Establishment of an automated patch-clamp platform for electrophysiological and pharmacological evaluation of hiPSC-CMs. *Stem Cell Res.* 41:101662. doi: 10.1016/j.scr.2019.101662

Lingueglia, E., and Lazdunski, M. (2013). Pharmacology of ASIC channels. *Wiley Interdiscip. Rev.* 2, 155–171. doi: 10.1002/wmts.88

Liu, Y., Hagan, R., and Schoellerman, J. (2018). Dual actions of Psalmotoxin at ASIC1a and ASIC2a heteromeric channels (ASIC1a/2a) /631/154/436/2387/631/378/2586 /9/74 article. *Sci. Rep.* 8:7179. doi: 10.1038/s41598-018-25386-9

Mazzuca, M., Heurteaux, C., Alloui, A., Diochot, S., Baron, A., Voilley, N., et al. (2007). A tarantula peptide against pain via ASIC1a channels and opioid mechanisms. *Nat. Neurosci.* 10, 943–945. doi: 10.1038/nn1940

Meltzer, R. H., Kapoor, N., Qadri, Y. J., Anderson, S. J., Fuller, C. M., and Benos, D. J. (2007). Heteromeric assembly of acid-sensitive ion channel and epithelial sodium channel subunits. *J. Biol. Chem.* 282, 25548–25559. doi: 10.1074/jbc.M703825200

Menegon, A., Pitassi, S., Mazzocchi, N., Redaelli, L., Rizzetto, R., Rolland, J. F., et al. (2017). A new electro-optical approach for conductance measurement: An assay for the study of drugs acting on ligand-gated ion channels. *Sci. Rep.* 7:44843. doi: 10.1038/srep44843

Milligan, C. J., and Jiang, L. H. (2020). Automated planar patch-clamp recording of P2X receptors. *Methods Mol. Biol.* 2041, 285–300. doi: 10.1007/978-1-4939-9717-6_21

Nagaeva, E. I., Potapieva, N. N., Nikolaev, M. V., Gmiro, V. E., Magazanik, L. G., and Tikhonov, D. B. (2016). Determinants of action of hydrophobic amines on ASIC1a and ASIC2a. *Eur. J. Pharmacol.* 788, 75–83. doi: 10.1016/j.ejphar.2016.06.013

Nanion (2013). *Characterization of hASIC3 (HEK) on Nanion's Patchliner, Application Note.* Available online at: https://www.nanion.de/images/phocadownloadpap/Application_Notes/Nanion_APP_Note_PL_ASIC3_02019.pdf (accessed April 19, 2022).

Obergrussberger, A., Rinke-Weiß, I., Goetze, T. A., Rapedius, M., Brinkwirth, N., Becker, N., et al. (2022). The suitability of high throughput automated patch clamp for physiological applications. *J. Physiol.* 600, 277–297. doi: 10.1113/JP282107

Rogers, M., Manyweathers, S., Götze, T., Becker, N., Rinke, I., George, M., et al. (2021a). Development and Validation of ASIC1a ligand-gated ion channel drug discovery assays on automated patch clamp platforms. *Biophys. J.* 120:338. doi: 10.1016/j.bpj.2020.11.2115

Rogers, M., Ridley, J., Witton, I., Tang, R., and Kirby, R. W. (2021b). Validation of an ASIC1a ligand-gated assay on an automated patch clamp platform and its use for novel ligand screening. *Biophys. J.* 120:337. doi: 10.1016/j.bpj.2020.11.2111

Rogers, M., Zidar, N., Kikelj, D., and Kirby, R. W. (2016). Characterization of endogenous sodium channels in the ND7-23 neuroblastoma cell line: Implications for use as a heterologous ion channel expression system suitable for automated patch clamp screening. *Assay Drug Dev. Technol.* 14, 109–130. doi: 10.1089/adt.2016.704

Shteinikov, V. Y., Tikhonova, T. B., Korkosh, V. S., and Tikhonov, D. B. (2018). Potentiation and Block of ASIC1a by Memantine. *Cell. Mol. Neurobiol.* 38, 869–881. doi: 10.1007/s10571-017-0561-6

Stoelzle, S., Haythornthwaite, A., Kettenhofen, R., Kolossov, E., Bohlen, H., George, M., et al. (2011a). Automated Patch Clamp on mESC-derived cardiomyocytes for cardiotoxicity prediction. *J. Biomol. Screen.* 16, 910–916. doi: 10.1177/1087057111413924

Stoelzle, S., Obergrussberger, A., Brüggemann, A., Haarmann, C., George, M., Kettenhofen, R., et al. (2011b). State-of-the-art automated patch clamp devices: Heat activation, action potentials, and high throughput in ion channel screening. *Front. Pharmacol.* 2:76. doi: 10.3389/fphar.2011.00076

Sun, D., Yu, Y., Xue, X., Pan, M., Wen, M., Li, S., et al. (2018). Cryo-EM structure of the ASIC1a-mambalgin-1 complex reveals that the peptide toxin mambalgin-1 inhibits acid-sensing ion channels through an unusual allosteric effect. *Cell Discov.* 4:27. doi: 10.1038/s41421-018-0026-1

Vanoye, C. G., Abramova, T. V., DeKeyser, J.-M. L., and George, A. L. (2016). A modified neuronal cell line for high throughput analysis of voltage-gated sodium channels. *Biophys. J.* 110:437. doi: 10.1016/j.bpj.2015.11.2356

Vetter, I., Mozar, C. A., Durek, T., Wingerd, J. S., Alewood, P. F., Christie, M. J., et al. (2012). Characterisation of Na v types endogenously expressed in human SH-SY5Y neuroblastoma cells. *Biochem. Pharmacol.* 83, 1562–1571. doi: 10.1016/j.bcp.2012.02.022

Wemmie, J. A., Taugher, R. J., and Kreple, C. J. (2013). Acid-sensing ion channels in pain and disease. *Nat. Rev. Neurosci.* 14, 461–471. doi: 10.1038/nrn3529

Wolkenberg, S. E., Zhao, Z., Mulhearn, J. J., Harrison, S. T., Sanders, J. M., Cato, M. J., et al. (2011). High concentration electrophysiology-based fragment screen: Discovery of novel acid-sensing ion channel 3 (ASIC3) inhibitors. *Bioorg. Med. Chem. Lett.* 21, 2646–2649. doi: 10.1016/j.bmcl.2010.12.115

Wu, X., Babnigg, G., and Villereal, M. L. (2000). Functional significance of human trp1 and trp3 in store-operated Ca2+ entry in HEK-293 cells. *Am. J. Physiol. Cell Physiol.* 278, C526–C536. doi: 10.1152/ajpcell.2000.278.3.c526

Xiong, Z. G., Zhu, X. M., Chu, X. P., Minami, M., Hey, J., Wei, W. L., et al. (2004). Neuroprotection in ischemia: Blocking calcium-permeable acid-sensing ion channels. *Cell* 118, 687–698. doi: 10.1016/j.cell.2004.08.026

Zhang, J.-H. H., Chung, T. D., and Oldenburg, K. R. (1999). A Simple statistical parameter for use in evaluation and validation of high throughput screening assays. *J. Biomol. Screen.* 4, 67–73. doi: 10.1177/108705719900400206

frontiers | Frontiers in Molecular Neuroscience

TYPE Mini Review
PUBLISHED 29 June 2023
DOI 10.3389/fnmol.2023.1182515

OPEN ACCESS

EDITED BY
Anan Srikiatkhachorn,
King Mongkut's Institute of Technology Ladkrabang, Thailand

REVIEWED BY
Daniela Pietrobon,
University of Padua, Italy

*CORRESPONDENCE
Song Guo
✉ song.guo@regionh.dk

RECEIVED 08 March 2023
ACCEPTED 15 June 2023
PUBLISHED 29 June 2023

CITATION
Clement A, Christensen SL, Jansen-Olesen I, Olesen J and Guo S (2023) The ATP sensitive potassium channel (K_{ATP}) is a novel target for migraine drug development.
Front. Mol. Neurosci. 16:1182515.
doi: 10.3389/fnmol.2023.1182515

The ATP sensitive potassium channel (K_{ATP}) is a novel target for migraine drug development

Amalie Clement[1], Sarah Louise Christensen[1], Inger Jansen-Olesen[1], Jes Olesen[1] and Song Guo[1,2]*

[1]Glostrup Research Institute, Department of Neurology, Danish Headache Center, Copenhagen University Hospital – Rigshospitalet, Copenhagen, Denmark, [2]Department of Odontology, Panum Institute, Faculty of Health, University of Copenhagen, Copenhagen, Denmark

Migraine is one of the leading causes of disability worldwide, affecting work and social life. It has been estimated that sales of migraine medicines will reach 12.9 billion USD in 2027. To reduce social impact, migraine treatments must improve, and the ATP-sensitive potassium (K_{ATP}) channel is a promising target because of the growing evidence of its implications in the pathogenesis of migraine. Strong human data show that opening of the K_{ATP} channel using levcromakalim is the most potent headache and migraine trigger ever tested as it induces headache in almost all healthy subjects and migraine attacks in 100% of migraine sufferers. This review will address the basics of the K_{ATP} channel together with clinical and preclinical data on migraine implications. We argue that K_{ATP} channel blocking, especially the Kir6.1/SUR2B subtype, may be a target for migraine drug development, however translational issues remain. There are no human data on the closure of the K_{ATP} channel, although blocking the channel is effective in animal models of migraine. We believe there is a good likelihood that an antagonist of the Kir6.1/SUR2B subtype of the K_{ATP} channel will be effective in the treatment of migraine. The side effects of such a blocker may be an issue for clinical use, but the risk is likely only moderate. Future clinical trials of a selective Kir6.1/SUR2B blocker will answer these questions.

KEYWORDS

K_{ATP} antagonist, potassium channel, migraine, headache, levcromakalim, drug target

1. Introduction

Migraine is by far the most prevalent neurological disease with a lifetime prevalence of 15–20% (Stovner et al., 2018). It is sexually dimorphic with a sex ratio of 2.5 women for each man and greater severity in women. Thus, approximately 80% of the total burden of migraine is on women (Steiner et al., 2020). According to WHO migraine is number two out of all diseases causing disability and the disease has huge socioeconomic costs to society in addition to the personal costs and suffering afflicted (Abbafati et al., 2020). It is obvious that a disease of these dimensions for which no cure exists requires effective drug therapy at each acute attack and as prophylaxis in those most affected. This was illustrated by the huge success of the triptans with a peak sale at several billion USD. They are still the dominant treatment for acute migraine attacks but now mostly off patent and inexpensive. The picture was further cemented by the advent of human monoclonal antibodies against CGRP or its receptor which in a very short time has obtained impressive sales. It has been estimated that total sales of migraine medicines will reach 15.6 billion USD in 2029 (IHealthcareAnalyst I, 2023).

Growing evidence suggests that ATP-sensitive potassium (K_{ATP}) channels are implicated in the pathogenesis of migraine as opening of the channel using levcromakalim is the most potent headache and migraine trigger ever tested. It has been suggested that the K_{ATP} channel may be the unifying mechanism for signaling pathways of established migraine triggers including calcitonin gene-related peptide (CGRP), pituitary adenylate cyclase-activating peptide-38 (PACAP38) and nitroglycerine (GTN) leading to migraine attacks (Figure 1). We have recently published a comprehensive review on the K_{ATP} channels (Clement et al., 2022), whereas this shorter review has a more general perspective on the basics of the K_{ATP} channel together with clinical and preclinical data on migraine implications. We argue that K_{ATP} channel blocking may be a novel promising target for migraine drug development.

2. How are migraine patients served by current drugs?

The so-called triptan wave rolled 20 years ago, and it was widely believed that the triptans had solved the migraine problem (Loder, 2010). Huge sales efforts by the pharmaceutical industry and enthusiastic doctors helped to promote this picture. Later, it turned out that the picture was not that rosy. The efficacy of triptans was originally based on rather soft success criteria, and when much stricter and more relevant criteria were applied the triptan response was much less satisfactory (Tfelt-Hansen and Olesen, 2012). A recent study showed that only 1/7 of all Danes with migraine currently uses a triptan (Davidsson et al., 2021). Whether this is due to lack of long-term efficacy or side effects is unclear, but it is not due to cost since medical service including prescriptions is free in Denmark. Thus, the treatment of migraine attacks is far from ideal. Better drugs or drugs working by a different mechanism are needed. The latter was fulfilled by the advent of small molecule CGRP receptor antagonists (Lipton and Dodick, 2004). They are less effective than the triptans but work *via* a different mechanism (Tfelt-Hansen and Loder, 2019). In prophylaxis the human antibodies against CGRP or its receptor and small molecule CGRP receptor antagonists are likewise not more effective than existing drugs but have fewer side effects than former prophylactic drugs (Charles and Pozo-Rosich, 2019; Tfelt-Hansen and Loder, 2019). Importantly, they work by a very specific mechanism and therefore have few side effects. They are also effective in non-responders to existing drugs (Ferrari et al., 2019). In conclusion, CGRP based therapies are valuable new drugs. However, these drugs are effective only in 50–60% of patients (Dodick et al., 2014a,b; Bigal et al., 2015; Sun et al., 2016) which illustrates the importance of developing more therapies with novel mechanisms of action.

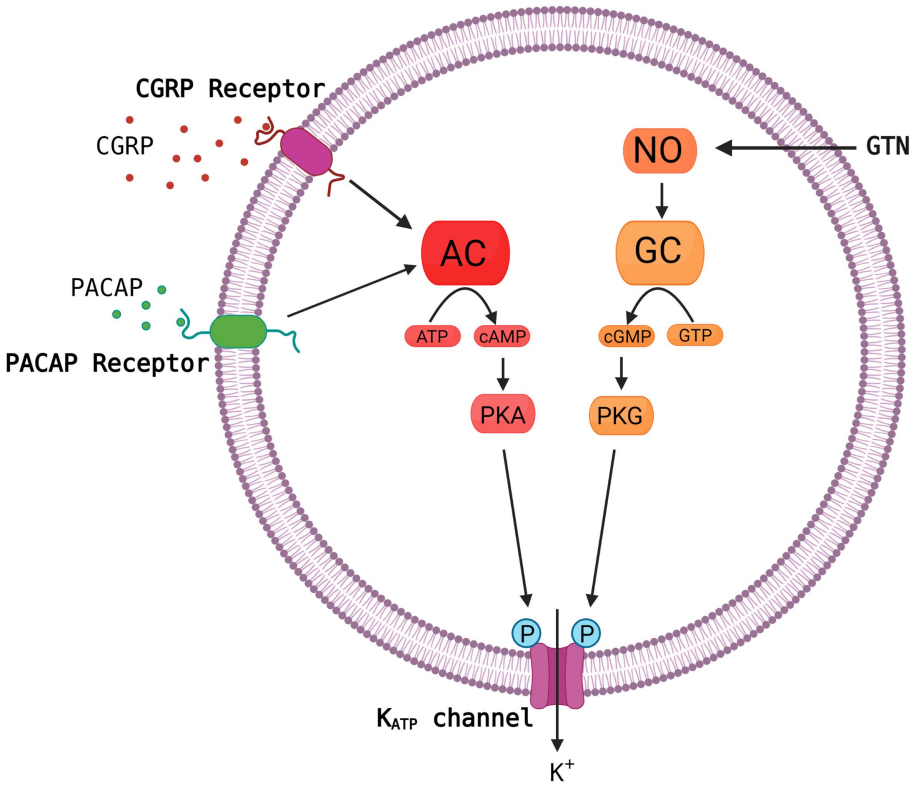

FIGURE 1
Common molecular pathways resulting in activation of the K_{ATP} channel. The migraine triggers CGRP, PACAP and nitroglycerine (GTN) are hypothesized to activate the K_{ATP} channel *via* cyclic adenosine monophosphate (cAMP) or cyclic guanosine monophosphate (cGMP) and downstream pathways. This is a simplified and hypothetical model describing the potential signaling pathways of migraine triggers and is based mainly on human experimental provocation studies (Ashina et al., 2013). More complex interactive processes and yet unknown mechanisms between signaling molecules are probably involved. AC, adenylate cyclase; NO, nitric oxide; PKA, protein kinase A; GC, guanylate cyclase; GTP, guanosine triphosphate; PKG, protein kinase G. Created with BioRender.com.

3. Migraine heterogeneity suggests a need for precision medicine

Novel drugs such as the CGRP antagonists have been developed against unspecified migraine. In the international classification of headache disorder both the first, second and third edition (ICHD-3) subdivides migraine. The primary division is into migraine without aura and migraine with aura, but no study in recent years has focused specifically on migraine with aura which is less prevalent than migraine without aura and rarely has a high attack frequency indicating prophylactic treatment (Hauge et al., 2009). More understandably, no studies have focused on the rare sub-forms: migraine with brainstem aura, retinal migraine and familial hemiplegic migraine (Russell and Ducros, 2011). Finally, chronic migraine is the most severe form of migraine, but it represents a conglomerate of migraine without aura, migraine with aura and tension-type headache. It seems unlikely therefore, that a drug would ever be specific for chronic migraine. It has been suggested to subdivide migraine without aura and migraine with typical aura according to autonomic symptoms (Christensen et al., 2022), osmophobia (Chalmer et al., 2019), menstrual relation (Vetvik and MacGregor, 2021), genetics (Kogelman et al., 2019) and ability to sensitize during attacks (Bernstein and Burstein, 2012). But so far, there has been little correlation between these features and drug response. The huge prevalence of migraine and the known clinical and genetic heterogeneity suggest, however, that migraine in future will be best served by a multitude of drugs with a multitude of different mechanisms of action. Antagonists of the K_{ATP} channel, if effective, would be a needed addition to our current therapeutic armamentarium.

4. K_{ATP} channel building blocks and channel sub-types

The K_{ATP} channels belong to one of seven families of inwardly rectifying potassium channels (Kir), namely the Kir6 (Hibino et al., 2010). Kir is the building block of the ion pore which consists of an aggregation of four units (Figure 2). The Kir6 subfamily is divided into Kir6.1 and Kir6.2, and around the ion pore is the modifying unit sulfonylurea receptor called SUR, which exists in three sub-forms, SUR1, SUR2A and SUR2B (Babenko et al., 1998). Thus, many configurations of the K_{ATP} channel can exist depending on the combination of inner and outer building blocks. Drugs can either target the SUR unit or the pore itself. The distribution of the different types of K_{ATP} channels in different tissues is shown in Table 1.

5. K_{ATP} channel agonists in other diseases cause headache

Several K_{ATP} channel agonists have been developed for clinical practice including levcromakalim, nicorandil, tifenazoxide, pinacidil, minoxidil, diazoxide and with indications for asthma, ischemic heart disease, hypertension, hair loss and hypoglycaemia. Except for nicorandil, none of these drugs is widely used in clinical practice but headache is reported as a common side effect for all these K_{ATP} agonists probably due to their vasodilating effects of cranial arteries (Table 2; Jahangir and Terzic, 2005). Notably, the most frequent side effect reported for levcromakalim, nicorandil and pinacidil treatment was headache (Kidney et al., 1993) - mostly as mild to moderate in intensity that generally occurred early in treatment. Headache was also often responsible for patients discontinuing their treatment (Simpson and Wellington, 2004). Altogether, these findings sparked curiosity in investigating the role of K_{ATP} channels in basic science and human experimental models of migraine.

6. Cephalic localization and function of K_{ATP} channels (*in vitro*)

6.1. Cranio-vascular

In intracranial arteries from rat, pig and human Kir6.1 and SUR2B mRNA and protein are predominantly expressed. Only low levels of Kir6.2 and SUR1 and no SUR2A are detected (Ploug et al., 2006). The subdivided location of K_{ATP} channels in cephalic arterial smooth muscle cells and endothelial cells have not yet been examined. However, K_{ATP} channels in endothelial and smooth muscle cells of peripheral arteries are of the Kir6.1/SUR2B subtype (Aziz et al., 2017; Li et al., 2020). Activation of K_{ATP} channels leads to hyperpolarization of smooth muscle cells (Brayden, 2002) that prevents the opening of depolarization activated Ca^{2+} channels. This causes a decrease in Ca^{2+} entry to the cell leading to vasodilatation (Quast, 1996). In endothelial cells activation of K_{ATP} channels elevate intracellular calcium by inducing hyperpolarization and augmenting the driving force for potential dependent Ca^{2+} influx. In this way, the K_{ATP} channel agonist may promote Ca^{2+}-dependent formation of endothelium-derived relaxing factors such as nitric oxide (Lückhoff and Busse, 1990).

Pharmacological *ex vivo* and *in vivo* studies show vasodilatory effects of K_{ATP} channel openers in rat and pig intracranial arteries. These responses are inhibited by high doses of the non-selective K_{ATP} channel blocker glibenclamide and lower doses of the Kir6.1 blocker PNU-37883A supporting involvement of Kir6.1/SUR2B K_{ATP} channels in cranio-vascular responses (Gozalov et al., 2005; Ploug et al., 2006, 2008). Removal of rat basilar artery endothelium slightly but significantly, inhibited K_{ATP} channel opener induced vasodilation, suggesting a partial involvement of endothelial K_{ATP} channels (Jansen-Olesen et al., 2005). *In vivo* studies have shown CGRP to activate K_{ATP} channels and thereby participate in CGRP mediated dilation of rat meningeal arteries (Gozalov et al., 2008). Interestingly, glibenclamide attenuated this CGRP-induced vasodilation *in vivo* but was without effect *ex vivo* (Gozalov et al., 2008).

6.2. Neuronal

In the nervous system, K_{ATP} channels are highly expressed in neurons, where they cause hyperpolarization resulting in reduced excitability, potassium efflux (Babenko et al., 1998; Seino and Miki, 2003; Hibino et al., 2010) and consequently reduced neurotransmitter release (Soundarapandian et al., 2007; Yildirim et al., 2021; Clement et al., 2022). Furthermore, K_{ATP} channels of the nervous system are suggested to mediate neuroprotection in different scenarios like hypoxia and oxidative stress (Zoga et al., 2010; Country and Jonz, 2021; Clement et al., 2022). Especially the mitochondrial K_{ATP} channels have been highlighted in neuroprotection during excitatory

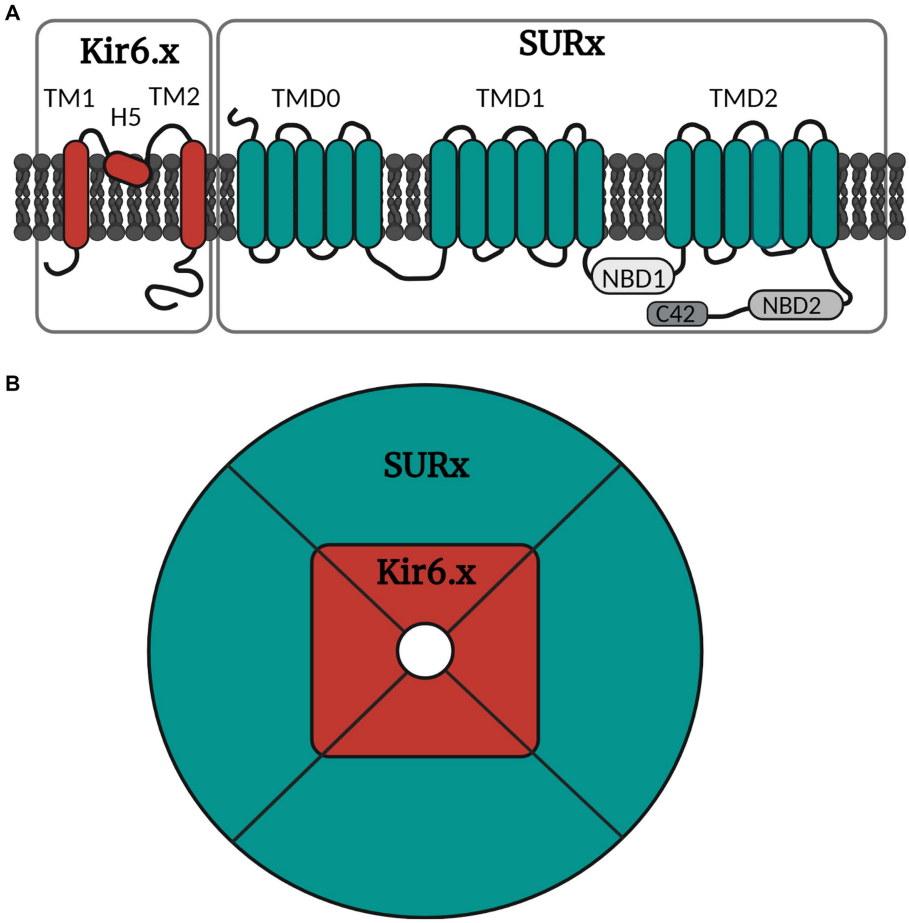

FIGURE 2
Simple illustration of the molecular and octameric K_{ATP} channel structure. **(A)** The K_{ATP} channel is arranged into subunits of Kir6.x and SURx. Kir6.x is composed of two transmembrane regions (TM1 and TM2) linked by the pore forming region H5. SURx is divided into three domains, where TMD0 consists of five transmembrane regions, while TMD1 and TMD2 consist of six transmembrane regions. SURx also holds the nucleotide binding domains (NBD1 and NBD2) and lastly the C42 C-terminal. **(B)** The channel is organized in four inner Kir6.x subunits and four outer SURx units. The Kir6.x subunits form the ion pore, while the SURx subunits form the outer structure of the channel, and these are necessary for channel activity. Created with BioRender.com.

toxicity stimulation (Soundarapandian et al., 2007), as activation of mitochondrial K_{ATP} channels cause depolarization and reduces neuronal death probably by decreasing influx of Ca^{2+} which lowers mitochondrial Ca^{2+} levels (Soundarapandian et al., 2007). This process hinders loss of oxidative phosphorylation and ATP depletion (Country and Jonz, 2021; Clement et al., 2022), but overall the mechanisms underlying the mitochondrial K_{ATP} channel-related neuroprotective effects remain unclear.

K_{ATP} channels have been found on nerve terminals of rat hippocampal slices, likely on both noradrenergic and glutamatergic nerve endings (Freiman et al., 2001). Likewise, K_{ATP} channels are found on nerve terminals prepared from rat motor cortex (Lee et al., 1995). K_{ATP} channels (Kir6.2/SUR1 and Kir6.2/SUR2) were also identified on neurons, glial satellite cells and Schwann cells of dorsal root ganglion isolated from rat (Zoga et al., 2010). In this study, K_{ATP} channel expression was reduced after painful axotomy, suggesting an involvement in pain perception and a potential target for therapeutic intervention.

Lastly, both Kir6.1 and Kir6.2 expression (using RT-PCR studies) are found in pure glial cultures of rat midbrain (Toulorge et al., 2010). Interestingly, expression of K_{ATP} channels was not found on the migraine relevant trigeminal ganglia isolated from mouse, using both RT-PCR and Western blotting, but high expression on dura mater and brain arteries (Christensen et al., 2022). This pattern is supported by RNAseq data from human and mouse trigeminal ganglion (Yang et al., 2022).

7. Human K_{ATP} agonist and antagonist studies

Both levcromakalim (K_{ATP} channel agonist) and glibenclamide (K_{ATP} channel blocker) have been tested in human experimental studies of headache.

Intravenous infusion of levcromakalim induced migraine attacks in 100% of migraine patients without aura ($n = 16$) making it the most potent migraine-triggering compound to date ever tested (Al-Karagholi et al., 2019). The provoked headache developed very quickly with a median time to onset of 20 min after infusion, and for that reason, no prodrome symptoms were registered. Interestingly,

TABLE 1 Subunit composition and tissue expression of K_{ATP} channels in different species.

Channel structure	Tissue	Species	References
Kir6.1/SUR1	Retina	Frog + tadpole	Skatchkov et al. (2002)
	Nervous system	Frog	Eaton et al. (2002)
Kir6.1/SUR2B	Vascular smooth muscle	Human + pig	Ploug et al. (2008)
		Rat	Ploug et al. (2006), Ploug et al. (2010), and Li et al. (2003)
		Mouse	Christensen et al. (2022) and Yamada et al. (1997)
	Connective tissue	Mouse	Christensen et al. (2022)
	Conduction system of the heart	Mouse	Bao et al. (2011)
Kir6.2/SUR1	Pancreas	Rat	Ploug et al. (2010)
		Mouse	Isomoto et al. (1996)
		Dog	Donley et al. (2005)
	Heart	Rat	Ploug et al. (2010)
		Mouse	Isomoto et al. (1996) and Flagg et al. (2008)
	Nervous system	Rat	Zoga et al. (2010) and Ploug et al. (2010)
	Skeletal muscle	Mouse	Mele et al. (2014)
Kir6.2/SUR2A	Heart	Mouse	Bao et al. (2011), Isomoto et al. (1996), and Flagg et al. (2008)
	Skeletal muscle	Rat	Inagaki et al. (1996)
Kir6.2/SUR2B	Non-vascular smooth muscle	Mouse	Isomoto et al. (1996) and Koh et al. (1998)
	Nervous system	Rat	Zoga et al. (2010)
	Conduction system of the heart	Mouse	Bao et al. (2011)
	Skeletal muscle	Rat	Inagaki et al. (1996)
		Mouse	Mele et al. (2014)

TABLE 2 Headache incidences registered during clinical trials with K_{ATP} channel agonists.

K_{ATP} agonist	Study design	Indication	Headache	Ref.
Levcromakalim	RCT	Asthma	76%	Kidney et al. (1993)
Nicorandil	Review (4 RCTs)	Ischaemic heart disease	36%	Simpson and Wellington (2004)
Tifenazoxide (NN414)	RCT	Healthy subjects	Up to 33% depending on dose	Zdravkovic et al. (2007)
Pinacidil	RCT	Hypertension	21%	Goldberg (1988)
Minoxidil	Open label	Hypertension and hair loss	21%	Sanabria et al. (2022)
Diazoxide	RCT	Hypoglycaemia	Yes (frequency not reported)	Product Information (2015)

when levcromakalim was given to migraine patients with visual aura ($n = 17$), 59% developed migraine attacks with visual aura (Al-Karagholi et al., 2021). These findings suggest that levcromakalim is a migraine aura-inducing compound and that the K_{ATP} channel may play a role in both migraine aura and migraine headache. It has been argued that levcromakalim most likely induces visual aura and migraine headache through distinct mechanisms, because it very potently triggers migraine without aura, and no aura symptoms, in migraine patients who have never experienced aura. Also, levcromakalim was also able to induce migraine without aura in some patients who previously have only experienced visual aura symptoms not accompanied by headache or migraine (Al-Karagholi et al., 2021). A possible underlying mechanism may be that levcromakalim increases extracellular potassium concentrations in neurons, glial cells, and brain vasculature, which depolarizes neighboring cells thereby triggering a wave of cortical spreading depression (CSD) underlying the visual aura. Nevertheless, it is unclear whether levcromakalim can cross the blood–brain barrier (BBB) but based on its small molecular weight (286.33 Da) and probable lipophilic properties, a central effect cannot be ruled out.

In healthy volunteers ($n = 14$), levcromakalim induced headache in 86% of participants and dilated the middle meningeal arteries (MMA). The dilatation was reversed by sumatriptan injection (Al-Karagholi et al., 2019). Notably, 14% of the healthy participants reported migraine-like attacks after levcromakalim. Also, the headache-associated dilatation of MMA is noteworthy, as the MMA is the only cranial artery with dilation on the pain side during the early phase of experimentally induced migraine attacks (Khan et al., 2019). However, intradermal and intramuscular levcromakalim injections did not produce more pain than placebo (Al-Karagholi et al., 2019) indicating that levcromakalim-induced headache pain is unlikely to be the result of direct activation of peripheral nociceptors.

Glibenclamide is a non-specific K_{ATP} channel blocker widely used for the treatment of diabetes mellitus type 2 to increase insulin

secretion. It belongs to the second generation of sulfonylureas (Gribble and Reimann, 2003; Mannhold, 2004). It is yet unknown whether glibenclamide can prevent migraine attacks in adults with migraine. Nevertheless, in healthy volunteers, pre-treatment with glibenclamide did not prevent levcromakalim-induced headache (Al-Karagholi et al., 2020) and did not attenuate levcromakalim-induced vascular changes, e.g., mean global CBF, intracranial artery circumferences, mean arterial blood pressure and heart rate (Al-Karagholi et al., 2021). However, glibenclamide seemingly delayed the onset of levcromakalim-induced headache with median time to headache onset 180 min (Al-Karagholi et al., 2020) versus 20 min (Al-Karagholi et al., 2019). As previously mentioned, glibenclamide is a non-selective K_{ATP} channel blocker with a higher affinity for the SUR1 subunit compared to the SUR2 subunits. The K_{ATP} channel opener levcromakalim which is one of the most effective drugs to induce headache in humans, has a high affinity to the SUR2B subtype. The high expression of SUR1 in pancreas mediate an increase in insulin secretion which limits the maximum tolerated dose of glibenclamide in humans due to severe risk of hypoglycaemia. Although the blood glucose levels were stabilised by infusion of glucose the dose of glibenclamide could still be too low to inhibit the SUR2B subtype of the K_{ATP} channel upon which levcromakalim acts. Glibenclamide did not prevent CGRP- and PACAP-induced headache and hemodynamic changes in healthy volunteers (Coskun et al., 2021; Kokoti et al., 2022). Collectively, these findings imply that glibenclamide does not inhibit the headache-inducing effects of K_{ATP} channel activation, probably because glibenclamide is non-specific and primarily inhibits the SUR1 subunit of the K_{ATP} channel. Thus, more selective K_{ATP} channel blockers selective for the Kir6.1/SUR2B subtype are needed to further examine the therapeutic potential of K_{ATP} channel inhibitors in migraine.

8. Preclinical K_{ATP} channel agonist and antagonist studies

A range of migraine triggering substances identified in studies of human experimental migraine have also been studied in rodent models where they induce a state of hypersensitivity to various sensory stimuli (Bates et al., 2010; Pradhan et al., 2014; Rea et al., 2018; Demartini et al., 2019; Christensen et al., 2021; Kuburas et al., 2021; Ernstsen et al., 2022). Repeated systemic administration of levcromakalim induced hypersensitivity to tactile stimulation with von Frey filaments (Christensen et al., 2020, 2021; Wu et al., 2022), heat (Christensen et al., 2022), and increased c-Fos expression in the spinal trigeminal nucleus (Wu et al., 2022). In contrast, local intraplantar and intracerebroventricular administration did not lower sensory threshold (Wu et al., 2011; Christensen et al., 2022).

Tactile hypersensitivity induced by migraine triggers GTN, cilostazol, levcromakalim and PACAP38 was fully or partially prevented by pre-administration of glibenclamide (Christensen et al., 2020, 2021; Ernstsen et al., 2022). In a distinct rat model of migraine presenting with spontaneous (inheritable) hypersensitivity in cephalic dermatomes (Oshinsky et al., 2012; Munro et al., 2018), both glibenclamide and gliquidone treatment normalized cephalic sensitivity thresholds, but did not increase the otherwise normal hind-paw threshold (Christensen et al., 2020). These findings initiated further investigation of K_{ATP} channel subtype specificity. Significant contribution of the vascular Kir6.1/SUR2B channel subtype to migraine pain generation was indicated as mice lacking Kir6.1 specifically in smooth muscle cells did not sensitize to the same degree as controls following repeated dosing of neither GTN nor levcromakalim (Christensen et al., 2022). Although, vasodilation seems to play a role in the levcromakalim-induced hypersensitivity, it alone may not explain it. Other unclear non-vascular mechanisms are likely to be at play as well. Because glibenclamide in high doses only partially blocked the hypersensitivity induced by PACAP38, whereas the relatively low dose of glibenclamide inhibited levcromakalim-induced hypersensitivity in rodents without affecting the vasodilation produced by levcromakalim *in vivo* and *ex-vivo* (Christensen et al., 2020, 2021; Ernstsen et al., 2022). Also, the levcromakalim-induced hypersensitivity can be abolished by CGRP-antagonizing drugs, suggesting that levcromakalim causes CGRP release *via* an unknown mechanism. The CGRP release may also not be secondary to vasodilation produced by K_{ATP} activation because the vasodilation is not inhibited by glibenclamide at concentrations that inhibit the hypersensitivity. In *ex vivo* organ preparations of dura mater and trigeminal ganglion glibenclamide inhibited capsaicin induced CGRP release (Christensen et al., 2020) which also supports the fact that K_{ATP} channel blockers may have a positive effect on migraine *via* non-vascular mechanisms. Opening of K_{ATP} channels does not directly cause CGRP release in the isolated tissue (Ploug et al., 2012; Christensen et al., 2021).

9. Likelihood of effectiveness of K_{ATP} antagonists

There are many examples of therapeutic efficacy of antagonists of migraine provocation (Ashina et al., 2017). Angiography provoked attacks of migraine with aura and studies of regional cerebral blood flow demonstrated that cortical spreading depression is the likely mechanism of the aura (Olesen et al., 1981, 1990). A blocker of cortical spreading depression, tonabersat, was effective in the prophylaxis of migraine with aura (Hauge et al., 2009). GTN, *via* liberation of nitric oxide, was effective in provoking migraine without aura attacks and the non-selective blocker of nitric oxide synthases L-NMMA was effective in treating acute attacks of migraine without aura (Lassen et al., 1997). Finally, and most convincingly, CGRP was effective in inducing migraine attacks without aura in patients (Lassen et al., 2002) and this was crucial for developing brain non-penetrant small molecule CGRP receptor antagonists as well as non-penetrant human monoclonal antibodies against CGRP or its receptor. Antagonism to a migraine provoking substance is therefore often predictive of clinical efficacy but not always. Histamine is equally effective to nitroglycerin in inducing migraine attacks (Lassen et al., 1995), but antihistamines have been on the market for more the 50 years and have received several trials in migraine without convincing results (Lassen et al., 1996; Vollesen et al., 2019). It makes sense that migraine can be experimentally induced by mechanisms that also occur during spontaneous attacks but, likewise, it can be induced by mechanisms that are not part of the mechanisms of spontaneous migraine attacks. Therefore, it cannot be concluded that the strong migraine-provoking effect of

levcromakalim in adults with migraine proofs that an antagonist of the K_{ATP} channel will effectively prevent or resolve migraine attacks. However, we believe it to be likely. But there are other caveats. K_{ATP} channels are abundant in the heart and knockout of specific K_{ATP} subfamilies in rodent models have been lethal in mice (Miki et al., 2002). To date, there are no studies of a selective Kir6.1/SUR2B knockout model, which is less abundant in the heart. If opening of the channel is important for migraine attack development, then the opening would primarily be in K_{ATP} channel subtypes localized in the cephalic vasculature or other cephalic structures and therefore a selective blocker would selectively affect these structures and not the heart.

10. Conclusion

K_{ATP} channels are acknowledged as viable therapeutic targets for migraine treatment as human data show that opening of the K_{ATP} channel induces headache in healthy subjects and migraine in migraine sufferers. Still, drug discovery remains a formidable obstacle. Currently, only data from migraine rodent models has illustrated a migraine-relevant effect of blocking the K_{ATP} channel activity. To move forward, additional research must be conducted on the specific subtypes of the K_{ATP} channel to gain a deeper comprehension of their structures, functions, and distribution for the development of more selective and effective drugs. We believe there is a likelihood that an antagonist of the Kir6.1/SUR2B sub-type will be effective in migraine. Only development and clinical testing of a future selective K_{ATP} channel blocker with attention on side effects can answer these questions.

Author contributions

All authors listed have made a substantial, direct, and intellectual contribution to the work, and approved it for publication.

Funding

SG is supported by the BRIDGE – Translational Excellence Programme (bridge.ku.dk) at the Faculty of Health and Medical Sciences, University of Copenhagen, funded by the Novo Nordisk Foundation. Grant agreement no. NNF20SA0064340 (2021 fellows). Also, this work was supported by Candys Foundation.

Conflict of interest

JO owns shares in the start-up company Cephagenix.

The remaining authors declare that the research was conducted in the absence of any commercial or financial relationships that could be construed as a potential conflict of interest.

Publisher's note

References

Abbafati, C., Abbas, K. M., Abbasi-Kangevari, M., Abd-Allah, F., Abdelalim, A., Abdollahi, M., et al. (2020). Global burden of 369 diseases and injuries in 204 countries and territories, 1990-2019: a systematic analysis for the global burden of disease study 2019. *Lancet* 396, 1204–1222. doi: 10.1016/S0140-6736(20)30925-9

al-Karagholi, M. A. M., Ghanizada, H., Hansen, J. M., Aghazadeh, S., Skovgaard, L. T., Olesen, J., et al. (2019). Extracranial activation of ATP-sensitive potassium channels induces vasodilation without nociceptive effects. *Cephalalgia* 39, 1789–1797. doi: 10.1177/0333102419888490

al-Karagholi, M. A. M., Ghanizada, H., Hansen, J. M., Skovgaard, L. T., Olesen, J., Larsson, H. B. W., et al. (2019). Levcromakalim, an adenosine triphosphate-sensitive Potassium Channel opener, dilates Extracerebral but not cerebral arteries. *Headache* 59, 1468–1480. doi: 10.1111/head.13634

Al-Karagholi, M. A. M., Ghanizada, H., Kokoti, L., Paulsen, J. S., Hansen, J. M., and Ashina, M. (2020). Effect of KATP channel blocker glibenclamide on levcromakalim-induced headache. *Cephalalgia* 40, 1045–1054. doi: 10.1177/0333102420949863

al-Karagholi, M. A. M., Ghanizada, H., Nielsen, C. A. W., Ansari, A., Gram, C., Younis, S., et al. (2021). Cerebrovascular effects of glibenclamide investigated using high-resolution magnetic resonance imaging in healthy volunteers. *J. Cereb. Blood Flow Metab.* 41, 1328–1337. doi: 10.1177/0271678X20959294

Al-Karagholi, M. A. M., Ghanizada, H., Nielsen, C. A. W., Hougaard, A., and Ashina, M. (2021). Opening of ATP sensitive potassium channels causes migraine attacks with aura. *Brain* 144, 2322–2332. doi: 10.1093/brain/awab136

Al-Karagholi, M. A. M., Hansen, J. M., Guo, S., Olesen, J., and Ashina, M. (2019). Opening of ATP-sensitive potassium channels causes migraine attacks: a new target for the treatment of migraine. *Brain* 142, 2644–2654. doi: 10.1093/brain/awz199

Ashina, M., Hansen, J. M., á Dunga, B. O., and Olesen, J. (2017). Human models of migraine-short-term pain for long-term gain. *Nat. Clin. Pract. Neurol.* 13, 713–724. doi: 10.1038/nrneurol.2017.137

Ashina, M., Hansen, J. M., and Olesen, J. (2013). Pearls and pitfalls in human pharmacological models of migraine: 30 years' experience. *Cephalalgia* 33, 540–553. doi: 10.1177/0333102412475234

Aziz, Q., Li, Y., Anderson, N., Ojake, L., Tsisanova, E., and Tinker, A. (2017). Molecular and functional characterization of the endothelial ATP-sensitive potassium channel. *J. Biol. Chem.* 292, 17587–17597. doi: 10.1074/jbc.M117.810325

Babenko, A. P., Aguilar-Bryan, L., and Bryan, J. (1998). A view of Sur/Kir6.X, KATP channels. *Annu. Rev. Physiol.* 60, 667–687. doi: 10.1146/annurev.physiol.60.1.667

Bao, L., Kefaloyianni, E., Lader, J., Hong, M., Morley, G., Fishman, G. I., et al. (2011). Unique properties of the ATP-sensitive K^+ channel in the mouse ventricular cardiac conduction system. *Circ. Arrhythm. Electrophysiol.* 4, 926–935. doi: 10.1161/CIRCEP.111.964643

Bates, E. A., Nikai, T., Brennan, K. C., Fu, Y. H., Charles, A. C., Basbaum, A. I., et al. (2010). Sumatriptan alleviates nitroglycerin-induced mechanical and thermal allodynia in mice. *Cephalalgia* 30, 170–178. doi: 10.1111/j.1468-2982.2009.01864.x

Bernstein, C., and Burstein, R. (2012). Sensitization of the trigeminovascular pathway: perspective and implications to migraine pathophysiology. *J Clin Neurol* 8, 89–99. doi: 10.3988/jcn.2012.8.2.89

Bigal, M. E., Edvinsson, L., Rapoport, A. M., Lipton, R. B., Spierings, E. L. H., Diener, H.-C., et al. (2015). Safety, tolerability, and efficacy of TEV-48125 for preventive treatment of chronic migraine: a multicentre, randomised, double-blind, placebo-controlled, phase 2b study. *Lancet Neurol.* 14, 1091–1100. doi: 10.1016/S1474-4422(15)00245-8

Brayden, J. E. (2002). Functional roles of KATP channels in vascular smooth muscle. *Clin. Exp. Pharmacol. Physiol.* 29, 312–316. doi: 10.1046/j.1440-1681.2002.03650.x

Chalmer, M. A., Hansen, T. F., and Olesen, J. (2019). Nosographic analysis of osmophobia and field testing of diagnostic criteria including osmophobia. *Cephalalgia* 39, 38–43. doi: 10.1177/0333102418771375

Charles, A., and Pozo-Rosich, P. (2019). Targeting calcitonin gene-related peptide: a new era in migraine therapy. *Lancet* 394, 1765–1774. doi: 10.1016/S0140-6736(19)32504-8

Christensen, S. L., Munro, G., Petersen, S., Shabir, A., Jansen-Olesen, I., Kristensen, D. M., et al. (2020). ATP sensitive potassium (KATP) channel inhibition: a promising new drug target for migraine. *Cephalalgia* 40, 650–664. doi: 10.1177/0333102420925513

Christensen, S. L., Rasmussen, R. H., Cour, S. L., Ernstsen, C., Hansen, T. F., Kogelman, L. J., et al. (2022). Smooth muscle ATP-sensitive potassium channels mediate

migraine-relevant hypersensitivity in mouse models. *Cephalalgia* 42, 93–107. doi: 10.1177/03331024211053570

Christensen, S. L., Rasmussen, R. H., Ernstsen, C., la Cour, S., David, A., Chaker, J., et al. (2021). CGRP-dependent signalling pathways involved in mouse models of GTN-cilostazol- and levcromakalim-induced migraine. *Cephalalgia* 41, 1413–1426. doi: 10.1177/03331024211038884

Christensen, C. G., Techlo, T. R., Kogelman, L. J. A., Wegner Thørner, L., Nissen, J., Sørensen, E., et al. (2022). Population-based prevalence of cranial autonomic symptoms in migraine and proposed diagnostic appendix criteria. *Cephalalgia* 42, 1160–1171. doi: 10.1177/03331024221094548

Clement, A., Guo, S., Jansen-Olesen, I., and Christensen, S. L. (2022). ATP-sensitive potassium channels in migraine: translational findings and therapeutic potential. *Cells* 11, 1–23. doi: 10.3390/cells11152406

Coskun, H., Elbahi, F. A., Al-Karagholi, M. A. M., Ghanizada, H., Sheykhzade, M., and Ashina, M. (2021). The effect of K ATP Channel blocker Glibenclamide on CGRP-induced headache and hemodynamic in healthy volunteers. *Front. Physiol.* 12:12. doi: 10.3389/fphys.2021.652136

Country, M. W., and Jonz, M. G. (2021). Mitochondrial KATP channels stabilize intracellular Ca2+ during hypoxia in retinal horizontal cells of goldfish (*Carassius auratus*). *J. Exp. Biol.* 224:jeb242634. doi: 10.1242/jeb.242634

Davidsson, O. B., Olofsson, I. A., Kogelman, L. J. A., Andersen, M. A., Rostgaard, K., Hjalgrim, H., et al. (2021). Twenty-five years of triptans - a nationwide population study. *Cephalalgia* 41, 894–904. doi: 10.1177/0333102421991809

Demartini, C., Greco, R., Zanaboni, A. M., Sances, G., de Icco, R., Borsook, D., et al. (2019). Nitroglycerin as a comparative experimental model of migraine pain: from animal to human and back. *Prog. Neurobiol.* 177, 15–32. doi: 10.1016/j.pneurobio.2019.02.002

Dodick, D. W., Goadsby, P. J., Silberstein, S. D., Lipton, R. B., Olesen, J., Ashina, M., et al. (2014a). Safety and efficacy of ALD403, an antibody to calcitonin gene-related peptide, for the prevention of frequent episodic migraine: a randomised, double-blind, placebo-controlled, exploratory phase 2 trial. *Lancet Neurol.* 13, 1100–1107. doi: 10.1016/S1474-4422(14)70209-1

Dodick, D. W., Goadsby, P. J., Spierings, E. L. H., Scherer, J. C., Sweeney, S. P., and Grayzel, D. S. (2014b). Safety and efficacy of LY2951742, a monoclonal antibody to calcitonin gene-related peptide, for the prevention of migraine: a phase 2, randomised, double-blind, placebo-controlled study. *Lancet Neurol.* 13, 885–892. doi: 10.1016/S1474-4422(14)70128-0

Donley, V. R., Hiskett, E. K., Kidder, A. C., and Schermerhorn, T. (2005). ATP-sensitive potassium channel (KATP channel) expression in the normal canine pancreas and in canine insulinomas. *BMC Vet. Res.* 1:8. doi: 10.1186/1746-6148-1-8

Eaton, M. J., Skatchkov, S. N., Brune, A., Biedermann, B., Veh, R. W., and Reichenbach, A. (2002). SURI and Kir6.1 subunits of K(ATP)-channels are co-localized in retinal glial (Müller) cells. *Neuroreport* 13, 57–60. doi: 10.1097/00001756-200201210-00016

Ernstsen, C., Christensen, S. L., Rasmussen, R. H., Nielsen, B. S., Jansen-Olesen, I., Olesen, J., et al. (2022). The PACAP pathway is independent of CGRP in mouse models of migraine: possible new drug target? *Brain* 145, 2450–2460. doi: 10.1093/brain/awac040

Ferrari, M. D., Diener, H. C., Ning, X., Galic, M., Cohen, J. M., Yang, R., et al. (2019). Fremanezumab versus placebo for migraine prevention in patients with documented failure to up to four migraine preventive medication classes (FOCUS): a randomised, double-blind, placebo-controlled, phase 3b trial. *Lancet* 394, 1030–1040. doi: 10.1016/S0140-6736(19)31946-4

Flagg, T. P., Kurata, H. T., Masia, R., Caputa, G., Magnuson, M. A., Lefer, D. J., et al. (2008). Differential structure of atrial and ventricular KATP: atrial KATP channels require SUR1. *Circ. Res.* 103, 1458–1465. doi: 10.1161/CIRCRESAHA.108.178186

Freiman, T. M., Kukolja, J., Heinemeyer, J., Eckhardt, K., Aranda, H., Rominger, A., et al. (2001). Modulation of K+-evoked [3H]-noradrenaline release from rat and human brain slices by gabapentin: involvement of KATP channels. *Naunyn-Schmiedeberg's Arch Pharmacol* 363, 537–542. doi: 10.1007/s002100100408

Goldberg, M. R. (1988). Clinical pharmacology of pinacidil, a prototype for drugs that affect potassium channels. *J. Cardiovasc. Pharmacol.* 12, S41–S47. doi: 10.1097/00005344-198812002-00008

Gozalov, A., Jansen-Olesen, I., Klaerke, D., and Olesen, J. (2008). Role of KATP channels in cephalic vasodilatation induced by calcitonin gene-related peptide, nitric oxide, and transcranial electrical stimulation in the rat. *Headache* 48, 1202–1213. doi: 10.1111/j.1526-4610.2008.01205.x

Gozalov, A., Petersen, K. A., Mortensen, C., Jansen-Olesen, I., Klaerke, D., and Olesen, J. (2005). Role of KATP channels in the regulation of rat dura and pia artery diameter. *Cephalalgia* 25, 249–260. doi: 10.1111/j.1468-2982.2004.00848.x

Gribble, F. M., and Reimann, F. (2003). Sulphonylurea action revisited: the post-cloning era. *Diabetologia* 46, 875–891. doi: 10.1007/s00125-003-1143-3

Hauge, A. W., Asghar, M. S., Schytz, H. W., Christensen, K., and Olesen, J. (2009). Effects of tonabersat on migraine with aura: a randomised, double-blind, placebo-controlled crossover study. *Lancet Neurol.* 8, 718–723. doi: 10.1016/S1474-4422(09)70135-8

Hibino, H., Inanobe, A., Furutani, K., Murakami, S., Findlay, I., and Kurachi, Y. (2010). Inwardly rectifying potassium channels: their structure, function, and physiological roles. *Physiol. Rev.* 90, 291–366. doi: 10.1152/physrev.00021.2009

IHealthcareAnalyst I. (2023). Global Anti-migraine Drugs Market $15.6 Billion by 2029. Available at: https://www.ihealthcareanalyst.com/global-anti-migraine-drugs-market/ (Accessed January 30, 2023).

Inagaki, N., Gonoi, T., Iv, J. P. C., Wang, C. Z., Aguilar-Bryan, L., Bryan, J., et al. (1996). A family of sulfonylurea receptors determines the pharmacological properties of ATP-sensitive K+ channels. *Neuron* 16, 1011–1017. doi: 10.1016/S0896-6273(00)80124-5

Isomoto, S., Kondo, C., Yamada, M., Matsumoto, S., Higashiguchi, O., Horio, Y., et al. (1996). A novel sulfonylurea receptor forms with BIR (Kir6.2) a smooth muscle type ATP-sensitive K+ channel. *J. Biol. Chem.* 271, 24321–24324. doi: 10.1074/jbc.271.40.24321

Jahangir, A., and Terzic, A. (2005). K(ATP) channel therapeutics at the bedside. *J. Mol. Cell. Cardiol.* 39, 99–112. doi: 10.1016/j.yjmcc.2005.04.006

Jansen-Olesen, I., Mortensen, C. H., El-Bariaki, N., and Ploug, K. B. (2005). Characterization of KATP-channels in rat basilar and middle cerebral arteries: studies of vasomotor responses and mRNA expression. *Eur. J. Pharmacol.* 523, 109–118. doi: 10.1016/j.ejphar.2005.08.028

Khan, S., Amin, F. M., Christensen, C. E., Ghanizada, H., Younis, S., Olinger, A. C. R., et al. (2019). Meningeal contribution to migraine pain: a magnetic resonance angiography study. *Brain* 142, 93–102. doi: 10.1093/brain/awy300

Kidney, J. C., Fuller, R. W., Worsdell, Y. M., Lavender, E. A., Chung, K. F., and Barnes, P. J. (1993). Effect of an oral potassium channel activator, BRL 38227, on airway function and responsiveness in asthmatic patients: comparison with oral salbutamol. *Thorax* 48, 130–133. doi: 10.1136/thx.48.2.130

Kogelman, L. J. A., Esserlind, A.-L., Francke Christensen, A., Awasthi, S., Ripke, S., Ingason, A., et al. (2019). Migraine polygenic risk score associates with efficacy of migraine-specific drugs. *Neurol Genet.* 5:e364. doi: 10.1212/NXG.0000000000000364

Koh, S. D., Bradley, K. K., Rae, M. G., Keef, K. D., Horowitz, B., and Sanders, K. M. (1998). Basal activation of ATP-sensitive potassium channels in murine colonic smooth muscle cell. *Biophys. J.* 75, 1793–1800. doi: 10.1016/S0006-3495(98)77621-0

Kokoti, L., al-Karagholi, M. A. M., Elbahi, F. A., Coskun, H., Ghanizada, H., Amin, F. M., et al. (2022). Effect of KATPchannel blocker glibenclamide on PACAP38-induced headache and hemodynamic. *Cephalalgia* 42, 846–858. doi: 10.1177/03331024221080574

Kuburas, A., Mason, B. N., Hing, B., Wattiez, A.-S., Reis, A. S., Sowers, L. P., et al. (2021). PACAP induces light aversion in mice by an inheritable mechanism independent of CGRP. *J. Neurosci.* 41, 4697–4715. doi: 10.1523/JNEUROSCI.2200-20.2021

Lassen, L. H., Ashina, M., Christiansen, I., Ulrich, V., and Olesen, J. (1997). Nitric oxide synthase inhibition in migraine. *Lancet* 349, 401–402. doi: 10.1016/S0140-6736(97)80021-9

Lassen, L. H., Haderslev, P. A., Jacobsen, V. B., Iversen, H. K., Sperling, B., and Olesen, J. (2002). CGRP may play a causative role in migraine. *Cephalalgia* 22, 54–61. doi: 10.1046/j.1468-2982.2002.00310.x

Lassen, L. H., Thomsen, L. L., Kruuse, C., Iversen, H. K., and Olesen, J. (1996). Histamine-1 receptor blockade does not prevent nitroglycerin induced migraine. Support for the NO-hypothesis of migraine. *Eur. J. Clin. Pharmacol.* 49, 335–339. doi: 10.1007/BF00203773

Lassen, L. H., Thomsen, L. L., and Olesen, J. (1995). Histamine induces migraine via the H1-receptor. Support for the NO hypothesis of migraine. *Neuroreport* 6, 1475–1479. doi: 10.1097/00001756-199507310-00003

Lee, K., Dixon, A. K., Rowe, I. C. M., Ashford, M. L. J., and Richardson, P. J. (1995). Direct demonstration of sulphonylurea-sensitive KATP channels on nerve terminals of the rat motor cortex. *Br. J. Pharmacol.* 115, 385–388. doi: 10.1111/j.1476-5381.1995.tb16344.x

Li, Y., Aziz, Q., Anderson, N., Ojake, L., and Tinker, A. (2020). Endothelial ATP-sensitive Potassium Channel protects against the development of hypertension and atherosclerosis. *Hypertens* 76, 776–784. doi: 10.1161/HYPERTENSIONAHA.120.15355

Li, L., Wu, J., and Jiang, C. (2003). Differential expression of Kir6.1 and SUR2B mRNAs in the vasculature of various tissues in rats. *J. Membr. Biol.* 196, 61–69. doi: 10.1007/s00232-003-0625-z

Lipton, R. B., and Dodick, D. W. (2004). CGRP antagonists in the acute treatment of migraine. *Lancet Neurol.* 3:332. doi: 10.1016/S1474-4422(04)00764-1

Loder, E. (2010). Triptan therapy in migraine. *N. Engl. J. Med.* 363, 63–70. doi: 10.1056/NEJMct0910887

Lückhoff, A., and Busse, R. (1990). Activators of potassium channels enhance calcium influx into endothelial cells as a consequence of potassium currents. *Naunyn Schmiedeberg's Arch. Pharmacol.* 342, 94–99. doi: 10.1007/BF00178979

Mannhold, R. (2004). KATP channel openers: structure-activity relationships and therapeutic potential. *Med. Res. Rev.* 24, 213–266. doi: 10.1002/med.10060

Mele, A., Camerino, G. M., Calzolaro, S., Cannone, M., Conte, D., and Tricarico, D. (2014). Dual response of the KATP channels to staurosporine: a novel role of SUR2B, SUR1 and Kir6.2 subunits in the regulation of the atrophy in different skeletal muscle phenotypes. *Biochem. Pharmacol.* 91, 266–275. doi: 10.1016/j.bcp.2014.06.023

Miki, T., Suzuki, M., Shibasaki, T., Uemura, H., Sato, T., Yamaguchi, K., et al. (2002). Mouse model of Prinzmetal angina by disruption of the inward rectifier Kir6.1. *Nat. Med.* 8, 466–472. doi: 10.1038/nm0502-466

Munro, G., Petersen, S., Jansen-Olesen, I., and Olesen, J. (2018). A unique inbred rat strain with sustained cephalic hypersensitivity as a model of chronic migraine-like pain. *Sci. Rep.* 8:1836. doi: 10.1038/s41598-018-19901-1

Olesen, J., Friberg, L., Olsen, T. S., Iversen, H. K., Lassen, N. A., Andersen, A. R., et al. (1990). Timing and topography of cerebral blood flow, aura, and headache during migraine attacks. *Ann. Neurol.* 28, 791–798. doi: 10.1002/ana.410280610

Olesen, J., Larsen, B., and Lauritzen, M. (1981). Focal hyperemia followed by spreading oligemia and impaired activation of rCBF in classic migraine. *Ann. Neurol.* 9, 344–352. doi: 10.1002/ana.410090406

Oshinsky, M. L., Sanghvi, M. M., Maxwell, C. R., Gonzalez, D., Spangenberg, R. J., Cooper, M., et al. (2012). Spontaneous trigeminal allodynia in rats: a model of primary headache. *Headache* 52, 1336–1349. doi: 10.1111/j.1526-4610.2012.02247.x

Ploug, K. B., Amrutkar, D. V., Baun, M., Ramachandran, R., Iversen, A., Lund, T. M., et al. (2012). K ATP channel openers in the trigeminovascular system. *Cephalalgia* 32, 55–65. doi: 10.1177/0333102411430266

Ploug, K. B., Baun, M., Hay-Schmidt, A., Olesen, J., and Jansen-Olesen, I. (2010). Presence and vascular pharmacology of KATP channel subtypes in rat central and peripheral tissues. *Eur. J. Pharmacol.* 637, 109–117. doi: 10.1016/j.ejphar.2010.03.027

Ploug, K. B., Edvinsson, L., Olesen, J., and Jansen-Olesen, I. (2006). Pharmacological and molecular comparison of KATP channels in rat basilar and middle cerebral arteries. *Eur. J. Pharmacol.* 553, 254–262. doi: 10.1016/j.ejphar.2006.09.053

Ploug, K. B., Sørensen, M. A., Strøbech, L., Klaerke, D. A., Hay-Schmidt, A., Sheykhzade, M., et al. (2008). KATP channels in pig and human intracranial arteries. *Eur. J. Pharmacol.* 601, 43–49. doi: 10.1016/j.ejphar.2008.10.041

Pradhan, A. A., Smith, M. L., McGuire, B., Tarash, I., Evans, C. J., and Charles, A. (2014). Characterization of a novel model of chronic migraine. *Pain* 155, 269–274. doi: 10.1016/j.pain.2013.10.004

Product Information. *Proglycem (Diazoxide)*. Teva Pharmaceuticals USA (2015).

Quast, U. (1996). ATP-sensitive K+ channels in the kidney. *Naunyn Schmiedeberg's Arch. Pharmacol.* 354, 213–225. doi: 10.1007/BF00171051

Rea, B. J., Wattiez, A.-S., Waite, J. S., Castonguay, W. C., Schmidt, C. M., Fairbanks, A. M., et al. (2018). Peripherally administered calcitonin gene-related peptide induces spontaneous pain in mice: implications for migraine. *Pain* 159, 2306–2317. doi: 10.1097/j.pain.0000000000001337

Russell, M. B., and Ducros, A. (2011). Sporadic and familial hemiplegic migraine: pathophysiological mechanisms, clinical characteristics, diagnosis, and management. *Lancet Neurol.* 10, 457–470. doi: 10.1016/S1474-4422(11)70048-5

Sanabria, B. D., Palmegiani, E., Seron, A. F., Perdomo, Y. C., Miot, H. A., and Müller, R. P. (2022). Prospective cardiovascular evaluation with 24-hour Holter and 24-hour ambulatory blood pressure monitoring in men using 5-mg oral minoxidil for androgenetic alopecia. *J. Am. Acad. Dermatol.* 88, 436–437. doi: 10.1016/j.jaad.2022.05.026

Seino, S., and Miki, T. (2003). Physiological and pathophysiological roles of ATP-sensitive K+ channels. *Prog. Biophys. Mol. Biol.* 81, 133–176. doi: 10.1016/S0079-6107(02)00053-6

Simpson, D., and Wellington, K. (2004). Nicorandil: a review of its use in the management of stable angina pectoris, including high-risk patients. *Drugs* 64, 1941–1955. doi: 10.2165/00003495-200464170-00012

Skatchkov, S. N., Rojas, L., Eaton, M. J., Orkand, R. K., Biedermann, B., Bringmann, A., et al. (2002). Functional expression of Kir 6.1/SUR1-KATP channels in frog retinal Müller glial cells. *Glia* 38, 256–267. doi: 10.1002/glia.10073

Soundarapandian, M. M., Zhong, X., Peng, L., Wu, D., and Lu, Y. (2007). Role of K ATP channels in protection against neuronal excitatory insults. *J. Neurochem.* 103, 1721–1729. doi: 10.1111/j.1471-4159.2007.04963.x

Steiner, T. J., Stovner, L. J., Jensen, R., Uluduz, D., and Katsarava, Z. (2020). Migraine remains second among the world's causes of disability, and first among young women: findings from GBD2019. *J. Headache Pain* 21, 4–7. doi: 10.1186/s10194-020-01208-0

Stovner, L. J., Nichols, E., Steiner, T. J., Abd-Allah, F., Abdelalim, A., al-Raddadi, R. M., et al. (2018). Global, regional, and national burden of migraine and tension-type headache, 1990-2016: a systematic analysis for the global burden of disease study 2016. *Lancet Neurol.* 17, 954–976. doi: 10.1016/S1474-4422(18)30322-3

Sun, H., Dodick, D. W., Silberstein, S., Goadsby, P. J., Reuter, U., Ashina, M., et al. (2016). Safety and efficacy of AMG 334 for prevention of episodic migraine: a randomised, double-blind, placebo-controlled, phase 2 trial. *Lancet Neurol.* 15, 382–390. doi: 10.1016/S1474-4422(16)00019-3

Tfelt-Hansen, P., and Loder, E. (2019). The Emperor's new Gepants: are the effects of the new Oral CGRP antagonists clinically meaningful? *Headache* 59, 113–117. doi: 10.1111/head.13444

Tfelt-Hansen, P., and Olesen, J. (2012). Taking the negative view of current migraine treatments: the unmet needs. *CNS Drugs* 26, 375–382. doi: 10.2165/11630590-000000000-00000

Toulorge, D., Guerreiro, S., Hirsch, E. C., and Michel, P. P. (2010). KATP channel blockade protects midbrain dopamine neurons by repressing a glia-to-neuron signaling cascade that ultimately disrupts mitochondrial calcium homeostasis. *J. Neurochem.* 114, 553–564. doi: 10.1111/j.1471-4159.2010.06785.x

Vetvik, K. G., and MacGregor, E. A. (2021). Menstrual migraine: a distinct disorder needing greater recognition. *Lancet Neurol.* 20, 304–315. doi: 10.1016/S1474-4422(20)30482-8

Vollesen, L. H., Guo, S., Andersen, M. R., and Ashina, M. (2019). Effect of the H 1-antihistamine clemastine on PACAP38 induced migraine. *Cephalalgia* 39, 597–607. doi: 10.1177/0333102418798611

Wu, X. F., Liu, W. T., Liu, Y. P., Huang, Z. J., Zhang, Y. K., and Song, X. J. (2011). Reopening of ATP-sensitive potassium channels reduces neuropathic pain and regulates astroglial gap junctions in the rat spinal cord. *Pain* 152, 2605–2615. doi: 10.1016/j.pain.2011.08.003

Wu, S., Ren, X., Zhu, C., Wang, W., Zhang, K., Li, Z., et al. (2022). A c-Fos activation map in nitroglycerin/levcromakalim-induced models of migraine. *J. Headache Pain* 23:128. doi: 10.1186/s10194-022-01496-8

Yamada, M., Isomoto, S., Matsumoto, S., Kondo, C., Shindo, T., Horio, Y., et al. (1997). Sulphonylurea receptor 2B and Kir6.1 form a sulphonylurea-sensitive but ATP-insensitive K+ channel. *J. Physiol.* 499, 715–720. doi: 10.1113/jphysiol.1997.sp021963

Yang, L., Xu, M., Bhuiyan, S. A., Li, J., Zhao, J., Cohrs, R. J., et al. (2022). Human and mouse trigeminal ganglia cell atlas implicates multiple cell types in migraine. *Neuron* 110, 1806–1821.e8. doi: 10.1016/j.neuron.2022.03.003

Yildirim, C., Özkaya, B., and Bal, R. (2021). KATP and TRPM2-like channels couple metabolic status to resting membrane potential of octopus neurons in the mouse ventral cochlear nucleus. *Brain Res. Bull.* 170, 115–128. doi: 10.1016/j.brainresbull.2021.02.009

Zdravkovic, M., Kruse, M., Rost, K. L., Møss, J., and Kecskes, A. (2007). The effects of NN414, a SUR1/Kir6.2 selective potassium channel opener in subjects with type 2 diabetes. *Exp. Clin. Endocrinol. Diabetes* 115, 405–406. doi: 10.1055/s-2007-973062

Zoga, V., Kawano, T., Liang, M. Y., Bienengraeber, M., Weihrauch, D., McCallum, B., et al. (2010). KATP channel subunits in rat dorsal root ganglia: alterations by painful axotomy. *Mol. Pain* 6:1744-8069-6-6. doi: 10.1186/1744-8069-6-6

frontiers | Frontiers in Molecular Neuroscience

TYPE Original Research
PUBLISHED 11 July 2023
DOI 10.3389/fnmol.2023.1205265

OPEN ACCESS

EDITED BY
Corrado Romano,
University of Catania, Italy

REVIEWED BY
Snezana Maljevic,
University of Melbourne, Australia
Katrine M. Johannesen,
Rigshospitalet, Denmark

*CORRESPONDENCE
Jianhua Feng
✉ hzhz87083886@zju.edu.cn
Yuezhou Li
✉ Yuezhou-Li@zju.edu.cn

†These authors have contributed equally to this work and share first authorship

RECEIVED 13 April 2023
ACCEPTED 19 June 2023
PUBLISHED 11 July 2023

CITATION
Ye J, Tang S, Miao P, Gong Z, Shu Q, Feng J and Li Y (2023) Clinical analysis and functional characterization of KCNQ2-related developmental and epileptic encephalopathy. *Front. Mol. Neurosci.* 16:1205265. doi: 10.3389/fnmol.2023.1205265

Clinical analysis and functional characterization of KCNQ2-related developmental and epileptic encephalopathy

Jia Ye[1†], Siyang Tang[2†], Pu Miao[2†], Zhefeng Gong[3], Qiang Shu[2], Jianhua Feng[3*] and Yuezhou Li[1*]

[1]National Clinical Research Center for Child Health, The Children's Hospital, Zhejiang University School of Medicine, Hangzhou, China, [2]Pediatric Department, Second Affiliated Hospital, Zhejiang University School of Medicine, Hangzhou, China, [3]School of Brain Science and Brain Medicine, Zhejiang University School of Medicine, Hangzhou, China

Background: Developmental and epileptic encephalopathy (DEE) is a condition characterized by severe seizures and a range of developmental impairments. Pathogenic variants in *KCNQ2*, encoding for potassium channel subunit, cause *KCNQ2*-related DEE. This study aimed to examine the relationships between genotype and phenotype in *KCNQ2*-related DEE.

Methods: In total, 12 patients were enrolled in this study for genetic testing, clinical analysis, and developmental evaluation. Pathogenic variants of KCNQ2 were characterized through a whole-cell electrophysiological recording expressed in Chinese hamster ovary (CHO) cells. The expression levels of the KCNQ2 subunit and its localization at the plasma membrane were determined using Western blot analysis.

Results: Seizures were detected in all patients. All DEE patients showed evidence of developmental delay. In total, 11 *de novo* KCNQ2 variants were identified, including 10 missense variants from DEE patients and one truncating variant from a patient with self-limited neonatal epilepsy (SeLNE). All variants were found to be loss of function through analysis of M-currents using patch-clamp recordings. The functional impact of variants on M-current in heteromericKCNQ2/3 channels may be associated with the severity of developmental disorders in DEE. The variants with dominant-negative effects in heteromeric channels may be responsible for the profound developmental phenotype.

Conclusion: The mechanism underlying *KCNQ2*-related DEE involves a reduction of the M-current through dominant-negative effects, and the severity of developmental disorders in DEE may be predicted by the impact of variants on the M-current of heteromericKCNQ2/3 channels.

KEYWORDS

developmental and epileptic encephalopathy, dominant-negative effects, developmental delay, KCNQ2, pediatrics

Introduction

Voltage-gated potassium channels Kv7.2 encoded by the *KCNQ2* gene have been recognized as a common genetic cause of epileptic disorders (Lerche et al., 2001; Armijo et al., 2005; Errington et al., 2005). The subunit Kv7.2 combines with the KCNQ3 subunit to form a heterotetrameric potassium channel that underlies the M-current (Brown and Adams, 1980; Wang et al., 1998; Shapiro et al., 2000). The M-current plays a critical role in controlling

the threshold of neuronal excitability by stabilizing the resting potential and suppressing the repetitive firing of action potentials (Delmas and Brown, 2005; Tzingounis and Nicoll, 2008). Pathogenic variants in KCNQ2 have been linked to a range of neonatal epileptic disorders from self-limited neonatal epilepsy (SeLNE) to more severe neonatal-onset developmental and epileptic encephalopathy (DEE) (Kato et al., 2013). SeLNE is characterized by seizures that occur in the first days of life but typically disappear spontaneously after a few weeks to months (Steinlein et al., 2007; Maljevic and Lerche, 2014; Millichap et al., 2016). DEE, on the other hand, is characterized by severe seizures, developmental delay, and a poor prognosis (Berg et al., 2021; Specchio and Curatolo, 2021). Furthermore, a recent study has indicated that KCNQ2 may be linked to intellectual disability in the absence of epilepsy (Mary et al., 2021).

The relationship between genotype and phenotype in KCNQ2-related epilepsy is not fully understood. However, patch-clamp recordings have improved our understanding of KCNQ2 channel dysfunction and the spectrum of clinical severity (Miceli et al., 2013; Soldovieri et al., 2014; Vanoye et al., 2022). SeLNE is due to haploinsufficiency as the majority of SeLNE variants have only a subtle loss-of-function (LOF) effect on the current amplitude of expressed heteromeric channels, leading to a small reduction in current (Schroeder et al., 1998). Most variants associated with DEE lead to a more significant reduction in total current, suggesting a dominant-negative effect as the primary pathogenic mechanism for the severe epilepsy phenotype (Orhan et al., 2014; Gomis-Perez et al., 2019). The recent studies on a mouse model carrying the DEE variant p.T274M showed that spontaneous seizures occurred more frequently at postweaning stages than at juvenile stages and were associated with reduced M-current density and hyperexcitability of pyramidal cells in motor cortical slices (Milh et al., 2020; Biba-Maazou et al., 2022). However, cognitive development and behavior are often impaired in most patients with DEE, even if epilepsy is well-controlled. In these cases, controlling seizures does not necessarily lead to good cognitive outcomes (Berg et al., 2021; Specchio and Curatolo, 2021). The question of whether KCNQ2 variants are functionally associated with the developmental impairment of DEE and how to predict prognosis remains unanswered.

In this study, we identified 11 *de novo* KCNQ2 variants including 10 missense variants from DEE patients and one truncating variant from a SeLNE patient. Combining clinical analysis and whole-cell electrophysiological recording of M-currents resulting from homomericKCNQ2 or heteromericKCNQ2/3 channels, we investigated the functional consequence of pathogenic variants that were correlated with developmental impairment. Our findings expanded the variants associated with the spectrum of clinical/functional diversity and provided insights into the phenotype–genotype relationships of KCNQ2-related DEE.

Materials and methods

Patients

A total of 12 patients including eight female patients and four male patients diagnosed in the Second Affiliated Hospital, Zhejiang University School of Medicine, with neonatal-onset epilepsy were enrolled in this study. No underlying non-genetic factors, such as acquired brain injury, were identified in any of the participants. Out of the 12 patients, 11 exhibited mild-to-profound developmental delay, with only one patient exhibiting normal development. Clinical data including demographic information, seizure history, developmental history, EEG results, cranial imaging results, and treatment information were collected and evaluated by two pediatric neurologists. Developmental milestones, such as eye contact, head control, sitting, standing, walking, and language ability, as well as neurologic and behavioral features, were assessed using the composite neurodevelopmental score system of *STXBP1*-DEE for patients who were at least 3 years of age at the time of the study (Balagura et al., 2022). Genetic sequencing was performed, and the pathogenicity of the identified variants was evaluated by a clinical geneticist according to the guidelines of the American College of Medical Genetics.

Mutagenesis and heterologous expression of KCNQ2

The wild-type (WT) KCNQ2 was subcloned into a pIRES2-EGFP vector, and the variants were introduced using a ClonExpress II One Step Cloning Kit (vazyme). KCNQ3 was subcloned into a pIRES2-mCherry vector. The ORFs of all plasmids were confirmed by sequencing full length before transfection. Channel subunits were expressed in Chinese hamster ovary (CHO) cells by transient transfection. CHO cells were maintained in DMEM (Gibco), containing 10% fetal bovine serum (Gibco), penicillin (100 U/ml), and streptomycin (100 μg/ml) at 37°C with 5% CO_2. For electrophysiological experiments, the cells were seeded on glass coverslips and transfected on the next day with a certain ratio of plasmids using Lipofectamine 2000; the total cDNA in the transfection mixture was kept constant at 3 μg. Transfection-positive cells were identified by the fluorescent protein and were used for whole-cell patch-clamp recording.

Cell surface biotinylation and Western blotting

The expression of KCNQ2 subunits in CHO cells was investigated as previously described (Maljevic et al., 2011; Miceli et al., 2015). After 24 h of transfection, the CHO cells were treated with Sulfo–NHS–LC–Biotin (Thermo) following the manufacturer protocol and then lysed. The cell lysates were then reacted with Streptavidin UltraLink Resin (Thermo). The channel subunits in total lysates and streptavidin precipitates were analyzed by Western blotting using rabbit monoclonal anti-KCNQ2 primary antibodies (D9L5S, dilution 1:1,000; Cell Signaling Technology, 14752), followed by secondary antibodies (Alexa Fluor 680 Conjugate; dilution 1:5000; Abcam, 175773). An anti-beta actin antibody (dilution 1:5,000; GenScript) was used to check for equal protein loading.

Electrophysiology

Macroscopic currents were recorded at room temperature (20–22°C) 1 day after transfection with an Axon MultiClamp 700B amplifier (Axon Instruments). Patch pipettes were pulled to a pipette resistance of 3–5MΩ. The pipette solution (intracellular) contained 140 mM KCl, 2 mM $MgCl_2$, 10 mM EGTA, 10 mM HEPES, and 5 mM Mg-ATP, and the pH was adjusted to 7.4 with KOH. The bath solution contained 138 Mm NaCl, 2 mM $CaCl_2$, 5.4 mMKCl, 1 mM $MgCl_2$, 10 mM d-(+) glucose, and 10 mM HEPES, and the pH was adjusted to 7.4 with NaOH. Current densities were calculated as peak K+ currents at +40 mV. To generate conductance–voltage (G/V) curves, the cells were held at −80 mV and then depolarized for 1.5 s from −80 to +50 mV using an incremental pulse of 10 mV, followed by an isopotential pulse at −10 mV of 400 ms. The current values recorded at the beginning of the−10 mV pulse were normalized and fitted using the Boltzmann function: $y = \max/[1 + \exp(V_{0.5} - V)/k]$, to obtain the half-maximum activation voltage ($V_{0.5}$) and the slope factor (k).

Statistics

All data were expressed as mean ± SEM, and statistically significant differences between the data were evaluated with one-way ANOVA by Bonferroni *post hoc* test, with the threshold set at a *p*-value of <0.05.

Results

Clinical features

A total of 12 patients, consisting of eight female patients and four male patients, were included in this study (see Table 1 for detailed clinical features). All patients were born without any acquired brain injury, such as those related to encephalitis, hypoxia, neoplasm, metabolic disturbance, traumatic brain injury, or toxicity.

Patients 1–11 were detected with DEE phenotypes, while patient 12 was diagnosed with SeLNE. All the patients had neonatal-onset epilepsy, with onset ranging from 1 day to 14 days after birth. Seizure onset within the first 3 days of life was observed in nine patients. Tonic seizures were found in nearly all patients as the initial seizure type, with burst suppression and multiple spikes being the most common EEG patterns at the early stage of the disease.

Although seizures were controlled within 3–9 months, all DEE patients exhibited varying degrees of developmental delay, most of them (>3 years old) being followed up with profound developmental delay by using the composite neurodevelopmental score system of DEE patients. Developmental delay became the primary symptom after 1 year of age in all DEE patients, and no drugs or other therapies were found to improve the impairments. The SeLNE patient presented seizure-free 2 months after birth and demonstrated normal subsequent development.

Two DEE patients died during the follow-up period. Patient 10 had tonic seizure onset 8 h after birth, which was frequently refractory to multiple antiseizure medications (ASMs). At 2 months of age, he had difficulty swallowing milk and died from suffocation by choking. Patient 8 had tonic seizure onset 1 day after birth and was also refractory to multiple ASMs. At 2 years old, she suffered frequent vomiting and developed food intolerance gradually, leading to her death from suffocation by choking.

In all patients, seizures were found to be drug resistant to multiple ASMs, either used alone or in combination. Valproate (VPA) and topiramate (TPM) were the most frequently used ASMs in this study, followed by phenobarbital (PB), levetiracetam (LEV), and oxcarbazepine (OXC). Of these, OXC was the most effective drug, effectively controlling seizures in five out of six patients, followed by TPM (two out of eight patients) and LEV (one out of six patients). PB was used in eight patients but was found to be ineffective in each case. After unsuccessful trials of multiple ASMs, lacosamide (LCM) was effectively used in patients 2 and 5. PB, TPM, VPA, nitrazepam (NZP), and methylprednisolone (M) were tried in patient 6, but none were found to be effective. Her seizures resolved spontaneously at the age of 9 months.

Genetic analysis

Genetic analysis revealed 11 *de novo* KCNQ2 variants including 10 missense variants from DEE patients and one truncating variant from SeLNE patients. The variants identified include (NM_172107.4) the following: c.553G>A (p.A185T) in Patient 1; c.643G>A (p.G215R) in Patient 2; c.712A>C (p.I238L) in Patient 3; c.794C>T (p.A265V) in Patient 4; c.829A>G (p.T277A) in Patient 5; c.853C>T (p.P285S) in Patient 6; c.868G>A (p.G290S) in Patient 7; c.901G>A (p.G301S) in Patients 8 and 9; c.1687G>A (p.D563N) in Patient 10; c.1734G>A (p.M578I) in Patient 11; and c.1816A>T (p.K606X) in Patient 12.

Among these variants, p.G215R, p.A265V, p.T277A, p.P285S, p.G290S, p.G301S, and p.M578I have been previously reported in patients with neonatal seizures and developmental delay but without functional characterization (Weckhuysen et al., 2012; Milh et al., 2013; Dalen Meurs-Van der Schoor et al., 2014; Numis et al., 2014; Parrini et al., 2017; Miao et al., 2018). P.D563N has been previously reported in a case report and functionally characterized in an article (Milh et al., 2015; Ambrosino et al., 2018). The remaining variants (p.A185T, p.I238L, and p.K606X) have not been reported previously.

These variants are located throughout the KCNQ2 channel (Figure 1), with one located in the S3-S4 linker (p.A185T), one in the S4-S5 linker (p.G215R), six in the pore-forming S5-S6 region (p.I238L, p.A265V, p.T277A, p.P285S, p.G290S, and p.G301S), and three in the C terminus (p.D563N, p.M578I, and p.K606X). The p.K606X variant creates a stop code and results in a truncated channel with a partial deletion from K606 in the C terminus.

Functional studies

To determine the effects of the variants on the KCNQ2 channel, we conducted whole-cell recordings on transiently expressed WT and mutated KCNQ2 channels in CHO cells. The results showed

TABLE 1 Clinical features of patients.

	Patient 1	Patient 2	Patient 3	Patient 4	Patient 5	Patient 6	Patient 7	Patient 8	Patient 9	Patient 10	Patient 11	Patient 12
Sex	Female	Female	Female	Male	Female	Female	Male	Female	Female	Male	Female	Male
Age	3y	3y 9m	5m	4y 2m	3y	5y	5y	died at 2y	3y	died at 2m	3y	2y 2m
Variants	c.553G>A p.A185T[a]	c.643G>A p.G215R[b]	c.712A>C p.I238L[a]	c.794C>T A265V[c]	c.829A>G p.T277A[d]	c.853C>T p.P285S[d]	c.868G>A; p.G290S[e]	c.901G>A; p.G301S[f]	c.901G>A; p.G301S[f]	c.1687G>A; p.D563N[g]	c.1734G>A; p.M578I[h]	c.1816A>T; p.K606X[a]
Location	S3	S4-S5	S5	Pore loop	Pore loop	Pore loop	S6	S6	S6	C-term	C-term	C- truncating
Inheritance	De novo	De novo	De novo	De novo	De novo	De novo	De novo	De novo	De novo	De novo	De novo	De novo
Seizure onset	2d	14d	1d	2d	1d	1d	3d	1d	7d	1d	7d	3d
Seizure types	Tonic	Spasms, focal, GTCS	Focal, GTCS	Tonic, spams	Tonic, spasms, focal	Tonic, spasms, focal	Tonic	Tonic	Tonic	Tonic	Tonic, spams	Tonic
EEG	BUS	BUS->H	BUS	BUS->H	BUS->H	BUS->H	BUS	MS	BUS	MS	BUS->H	Normal
Diagnosis	OS	OS->IS	OS	OS->IS	OS->IS	OS->IS	OS	EIMFS	OS	EIMFS	OS->IS	SeLNE
ASMs used	PB, LEV	PB, TPM, LEV, VGB, OXC, ACTH, LEV, CZP, CLB, LCM	LEV, OXC	PB, VPA	LEV, PB, TPM, NZP, OXC, CLB, LCM, CBZ	PB, TPM, VPA, NZP, M	PB, TPM, OXC,	OXC, VPA	VPA, TPM, CZP, CBZ	PB, TPM, OXC, NZP	TPM, VPA, OXC	PB, LEV, TPM
Effective ASMs	LEV	LCM	OXC	VPA	OXC, LCM	/	OXC	OXC	CBZ, TPM	OXC	OXC	TPM
Seizure free	6 m	9 m	3 m	3 m	6 m	9 m	1.5 m	Died	5 m	Died	8 m	2 m
Developmental delay	Head control, eye contact walking, and no language	Poor eye contact, no head control, and hypotonia	Poor head Control and poor eye contact	No eye contact, no head control, difficulty in swallowing, and hypotonia	Poor head control, poor eye contact, unable to sit, and hypotonia	Head control, unable to sit, poor eye contact, and hypotonia	Poor head control, poor eye contact, unable to sit, and pyramidal signs	Died at 2 y due todysphagia and asphyxia	Poor eye contact, no head control, and hypotonia	Died at 2 m due to dysphagia and asphyxia	Head control, eye contact, walking, no language, and hypotonia	normal
Composite developmental Score*	6	2	/	1.5	2.5	3	2.5	/	1.5	/	5.5	10
Developmental ratings	Moderate	Profound	/	Profound	Profound	Severe	Profound	/	Profound	/	Moderate	Normal

[a]Mutations are new; [b]Dalen Meurs-Van der Schoor et al., 2014; [c]Weckhuysen et al., 2012; [d]Miao et al., 2018; [e]Milh et al., 2013; [f]Parrini et al., 2017; [g]Milh et al., 2015; [h]Numis et al., 2014. ACTH, adrenocorticotropic hormone; ASMs, antiseizure medications; BUS, burst-suppression; CBZ, carbamazepine; CLB, clobazam; CZP, clonazepam; EIMFS, epilepsy of infancy with migrating focal seizures; GTCS, generalized tonic–clonic seizure; H, hypsarrhythmia; IS, infantile spasms; LCM, lacosamide; LEV, levetiracetam; M, methylprednisolone; MS, Multiple spikes; NZP, nitrazepam; OS, Ohtahara syndrome; OXC, oxcarbazepine; PB, phenobarbital; SeLNE, Self-limited neonatal epilepsy; TPM, topiramate; VGB, vigabatrin; VPA, valproic acid. *According to STXBP1 composite developmental score (>3 y): mild ≥7, moderate: ≥5 and <7, severe: ≥3 and <5, and profound: <3.

10.3389/fnmol.2023.1205265

TABLE 2 Biophysical properties of mutant KCNQ2/3 channel.

	Current density (pA/pF)	$V_{0.5}$ (mV)	K (mV/e-Fold)
Q2 WT	81.0 ± 6.7	−23.1 ± 0.5	11.8 ± 0.4
A185T	45.7 ± 10.2[a]	−11.8 ± 0.7[a]	11.6 ± 0.6
G215R	3.1 ± 1.2[a]	—	—
I238L	73.6 ± 8.0	−6.4 ± 1.0[a]	11.0 ± 0.8
A265V	2.0 ± 0.9[a]	—	—
T277A	5.5 ± 1.2[a]	—	—
P285S	4.0 ± 1.1[a]	—	—
G290S	3.4 ± 1.7[a]	—	—
G301S	2.3 ± 1.0[a]	—	—
D563N	6.4 ± 1.3[a]	—	—
M578I	7.2 ± 2.2[a]	—	—
K606X	2.4 ± 1.0[a]	—	—
Q2+A185T	52.0 ± 9.1[a]	−12.4 ± 1.0[a]	11.7 ± 0.6
Q2+G215R	29.4 ± 6.4[a]	−16.4 ± 1.2[a]	11.4 ± 0.5
Q2+I238L	73.9 ± 8.2	−15.5 ± 1.1[a]	10.3 ± 1.0
Q2+A265V	24.7 ± 6.9[a]	−11.2 ± 1.2[a]	12.5 ± 0.8
Q2+T277A	26.5 ± 8.2[a]	−17.3 ± 0.8[a]	10.1 ± 0.5
Q2+P285S	23.5 ± 3.6[a]	−19.0 ± 0.8[a]	8.2 ± 0.5[a]
Q2+G290S	11.3 ± 4.5[a]	−16.8 ± 1.4[a]	9.4 ± 0.6
Q2+G301S	20.6 ± 5.0[a]	−17.9 ± 0.9[a]	9.5 ± 0.6
Q2+D563N	15.1 ± 4.0[a]	−10.0 ± 1.4[a]	11.5 ± 0.6
Q2+M578I	20.8 ± 1.3[a]	−16.0 ± 1.0[a]	9.7 ± 1.0
Q2+K606X	51.1 ± 11.3[a]	−16.7 ± 0.9[a]	7.1 ± 0.6[a]
Q2 WT+Q3 WT (1:1)	281.6 ± 18.7	−24.9 ± 0.6	10.7 ± 0.4
Q2 WT+Q3 WT (0.5:1)	202.9 ± 35.3[b]	−26.3 ± 0.9	9.7 ± 0.6
Q2+A185T+Q3	200.9 ± 23.1[b]	−21.2 ± 1.0[c]	8.6 ± 0.7
Q2+G215R+Q3	139.6 ± 9.6[b,c]	−17.7 ± 0.9[b,c]	9.0 ± 1.0
Q2+I238L+Q3	270.4 ± 23.5[c]	−20.5 ± 0.8[b,c]	10.8 ± 0.6
Q2+A265V+Q3	145.2 ± 26.3[b,c]	−12.1 ± 1.2[b,c]	11.8 ± 0.9
Q2+T277A+Q3	195.3 ± 35.8[b]	−15.4 ± 0.8[b,c]	10.0 ± 1.0
Q2+P285S+Q3	205.2 ± 20.9[b]	−21.8 ± 1.0[c]	9.2 ± 0.8
Q2+G290S+Q3	71.6 ± 12.3[b,c]	−18.7 ± 0.6[b,c]	9.6 ± 0.6
Q2+G301S+Q3	191.8 ± 25.2[b]	−18.4 ± 0.7[b,c]	11.9 ± 0.5
Q2+D563N+Q3	150.5 ± 17.3[b,c]	−17.4 ± 1.0[b,c]	9.4 ± 1.0
Q2+M578I+Q3	268.2 ± 32.2[c]	−22.0 ± 0.8[c]	8.4 ± 0.8
Q2+K606X+Q3	294.3 ± 30.5[c]	−21.0 ± 0.7[b,c]	9.6 ± 0.9

Current densities were calculated as peak current at +40 mV. $V_{0.5}$ is the voltage of half-maximal activation; k is the slope factor. Data are presented as means ± SEM, n = 8–15. [a]$P < 0.05$ vs. Q2. [b]$P < 0.05$ vs. Q2/Q3 (1:1). [c]$P < 0.05$ versus Q2/Q3 (0.5:1).

that the homomeric WT KCNQ2 channels generated potassium-selective currents that activated at a threshold potential of around −50 mV and did not inactivate. However, the variants p.G215R, p.A265V, p.T277A, p.P285S, p.G290S, p.G301S, p.D563N, p.M578I, or p.K606X showed barely detectable or negligible currents (Figure 2A). The variant p.A185T resulted in reduced current amplitudes, while p.I238L showed 91% current density compared to WT (Figure 2B). Both p.A185T and p.I238L significantly shifted the activation curve to more positive potentials than WT (Figures 2C, D). The results demonstrated the LOF phenotype of the variants.

The tetrameric KCNQ2 channel assembled with variant and WT subunits reduced more than 50% current, not merely haploinsufficiency, namely dominate-negative effects. To evaluate these effects, we coexpressed each variant with the WT in a 1:1 ratio (1.5 ug: 1.5 ug) to simulate the heterozygous genotype (Figure 3). Compared to homomeric WT KCNQ2 (3 ug), variants p.G215R, p.A265V, p.T277A, p.P285S, p.G290S, p.G301S, p.D563N, and p.M578I were each assembled with WT in a 1:1 ratio that presented a drastically reduced current (reduced more than 50% of the relative WT channel current amplitudes), indicating a dominant-negative effect. Variants p.A185T, p.I238L, and K606X showed <50% reduction in current when coexpressed with the WT channel, suggesting a partial current-suppressing effect without a dominant-negative effect (Figures 3A, B) (Table 2). All of the variants' heteromeric channels showed significant positive shifts in $V_{0.5}$ compared to the WT (Figures 3C, D).

The heteromeric assembly of KCNQ2 and KCNQ3 subunits gives rise to larger currents and underlies most of the neuronal M-currents. Thus, the functional consequences of the variants were assessed in heteromeric channels formed upon coexpression of WT KCNQ2, variant KCNQ2, and WT KCNQ3 in a 0.5:0.5:1 (0.75 ug:0.75 ug:1.5 ug) ratio to simulate the heteromeric subunit composition and proportion in an affected individual (Figure 4A). Compared to their homomeric channels, most heteromeric variant channels were rescued by KCNQ3 and showed larger current sizes. Variants p.I238L, p.M578I, and p.K606X showed similar current density to the WT. The current amplitudes of p.A185T, p.T277A, p.P285S, and p.G301S were reduced by 20–30%, similar to that of cells transfected with Q2/Q3 at a 0.5:1 ratio, indicating a partial LOF. Notably, the current density in cells expressing p.G215R, p.A265V, p.G290S, and p.D563N with WT Q2/Q3 was significantly smaller than that cell expressed Q2/Q3 at a 0.5:1 ratio, therefore suggesting a strong dominant-negative effect on Q2/Q3 heteromeric channel currents exerted by the mutant subunits (Figure 3B). A significant rightward shift in the $V_{0.5}$ was observed for p.G215R, p.I238L, p.A265V, p.T277A, p.G290S, p.G301S, and p.D563N, indicating that these variants require a more positive potential to reach their maximum currents and may not evoke enough currents to control the action potential at negative potentials (Figures 4C, D).

Reduced KCNQ2 variant expression or impaired trafficking to the plasma membrane may be the potential underlying mechanisms leading to the LOF effect of the KCNQ2 channel. To examine the effect of variants on the expression of KCNQ2 subunits, we used Western blots to assess the total KCNQ2

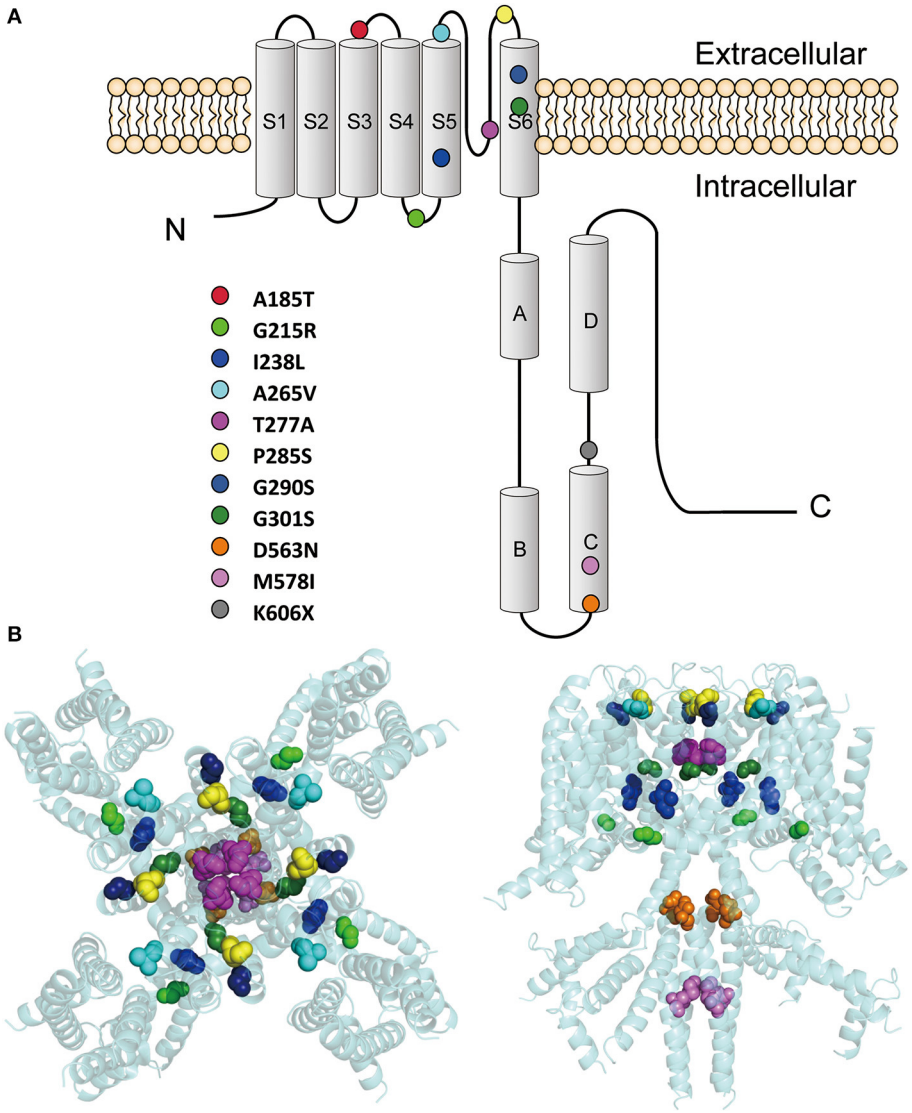

FIGURE 1
Locations of the pathogenic KCNQ2 variants. **(A)** Topology diagram of the KCNQ2 channel. The KCNQ2 subunits possess six transmembrane segment regions (S1-S6) and a long intracellular C terminus. Segments S1–S3 and S4 form the voltage-sensing domain. S5–S6 in conjunction with their extracellular linker constitute the channel pore. C-terminal helices A and B indicate the sites for interaction with calmodulin. Helices C and D are involved in subunit–subunit interactions. The locations of the variants described in the present report are shown as circles in different colors. **(B)** Structure of the human KCNQ2 (PDB:7CR3) (Li et al., 2021). The side view is shown on the left and the top view is on the right. The variants are shown as sphere styles in different colors. The p.A185T and p.K606X are not shown because they are not resolved in the original structure.

protein levels. As shown in Figure 5A, the expected 92 kDa bands were shown by using an anti-KCNQ2 antibody. The Western blot analysis of the total cell lysates from WT or variant KCNQ2 expressing CHO cells revealed that all the variants' expression levels were similar to WT (Figure 5B). Next, we investigated whether the presence of these variants was able to interfere with the trafficking of KCNQ2 subunits to the plasma membrane. The Western blot analysis of membrane protein fraction from CHO cells is presented in Figure 5C. The quantification of the bands from four different experiments showed no significant differences between WT and the variants in membrane expression levels.

Discussion

In this study, we reported 11 *de novo* KCNQ2 variants including 10 DEE variants and 1 SeLNE variant. Among the 10 DEE variants, six of them were found to be located in the S5–S6 pore domain, which is consistent with previously identified hotspots (Goto et al., 2019). All of the DEE patients in this study we investigated showed neonatal-onset epilepsy in the first few days or weeks of birth, with tonic seizures as the initial seizure type. Despite seizure control occurring between 3 months and 9 months old, all DEE patients developed moderate-to-profound developmental delay after their first year of life.

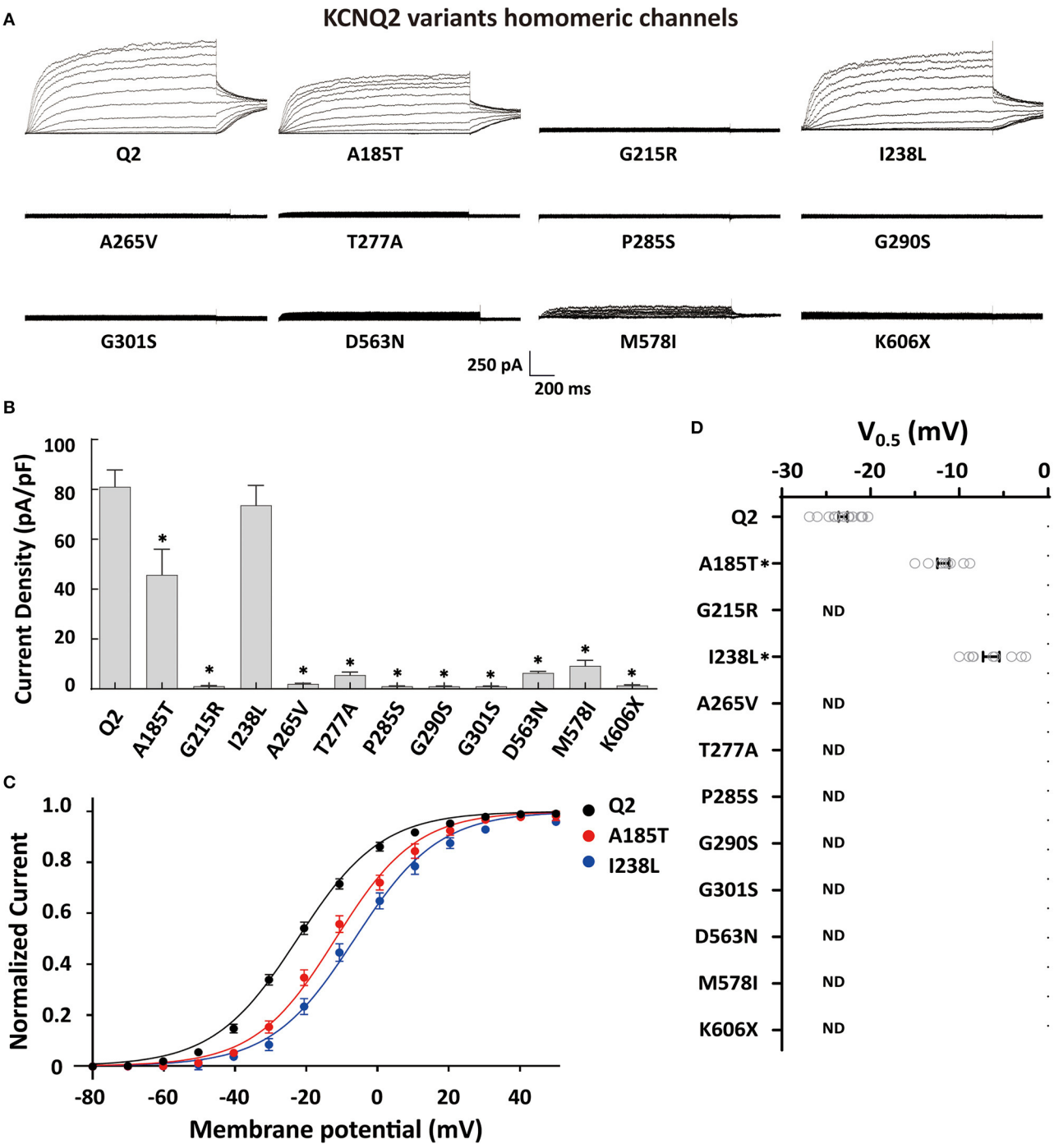

FIGURE 2
Functional properties of the homomericKCNQ2 variants. **(A)** Macroscopic current traces recorded in CHO cells transfected with KCNQ2 variants (3μg) in homomeric configuration. Current scale, 250 pA; time scale, 200 ms. **(B)** Mean current densities of KCNQ2 channel at +40 mV in the homozygous state. **(C)** Current–voltage relationships of the KCNQ2 homomeric channel were determined from tail current amplitudes. Lines represent fits of a Boltzmann function. **(D)** Differences in activation of $V_{0.5}$ were determined for the KCNQ2 channel expressed in the homozygous state ($n = 8–15$). Statistically significant differences *$p < 0.05$ versus WT KCNQ2.

To investigate a potential genotype–phenotype correlation, we performed functional characterization of the variants using whole-cell electrophysiological recordings from homomericKCNQ2 or heteromericKCNQ2/3 channels. Most homomeric variants showed significant LOF, with barely detectable or negligible currents. Interestingly, two novel variants, p.A185T and p.I238L, retained 56% and 91% current density relative to the WT channel, respectively. It is worth noting that both p.A185T and p.I238L significantly shifted the activation curve to more positive potentials leading to a significant current reduction in

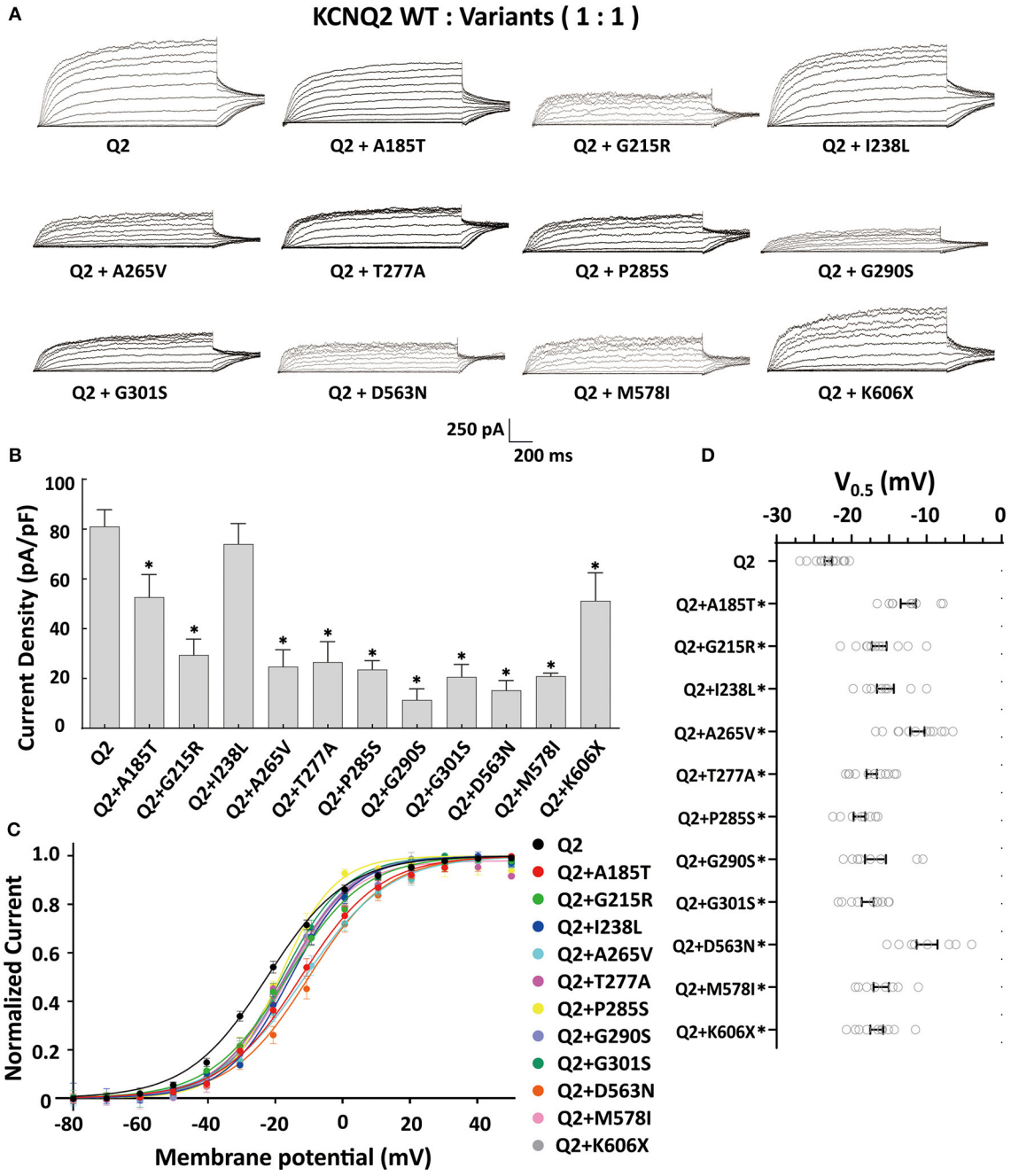

FIGURE 3
Functional properties of the KCNQ2 variants coexpressed with WTKCNQ2. **(A)** Macroscopic current traces recorded in CHO cells transfected KCNQ2 variants with WTKCNQ2in a 1:1 ratio (1.5 μg:1.5 μg). Current scale, 250 pA; time scale, 200 ms. **(B)** The mean current densities of the KCNQ2 variants coexpressed with WT in a 1:1 ratio at +40mV. **(C)** Current–voltage relationships of KCNQ2 variants coexpressed with WTKCNQ2 in a 1:1 ratio determined from tail current amplitudes. Lines represent fits of a Boltzmann function. **(D)** Differences in activation of V0.5 were determined for the KCNQ2 variants and WTKCNQ2 in a 1:1 ratio ($n = 8–15$). Statistically significant differences *$p < 0.05$ versus WT KCNQ2.

the subthreshold range of an action potential, supporting the LOF properties.

When assembled with a WT KCNQ2 subunit in a 1:1 ratio, most DEE variants showed a drastically reduced current, with over 50% reduction in relative WT channel current amplitudes, consistent with the dominant-negative effect as the primary pathogenic mechanism for the severe epileptic phenotype. Not surprisingly, the SeLNE variant K606X exhibited haploinsufficiency effects, with a 37% reduction in current amplitude. The p.A185T and p.I238L variants retained partial heteromeric channel currents when incorporated with WT KCNQ2. However, the altered gating kinetics with a significant depolarizing shift of the activation curve observed in these variants may contribute to the clinical severity of DEE. Despite not exerting dominant-negative effects, these variants

10.3389/fnmol.2023.1205265

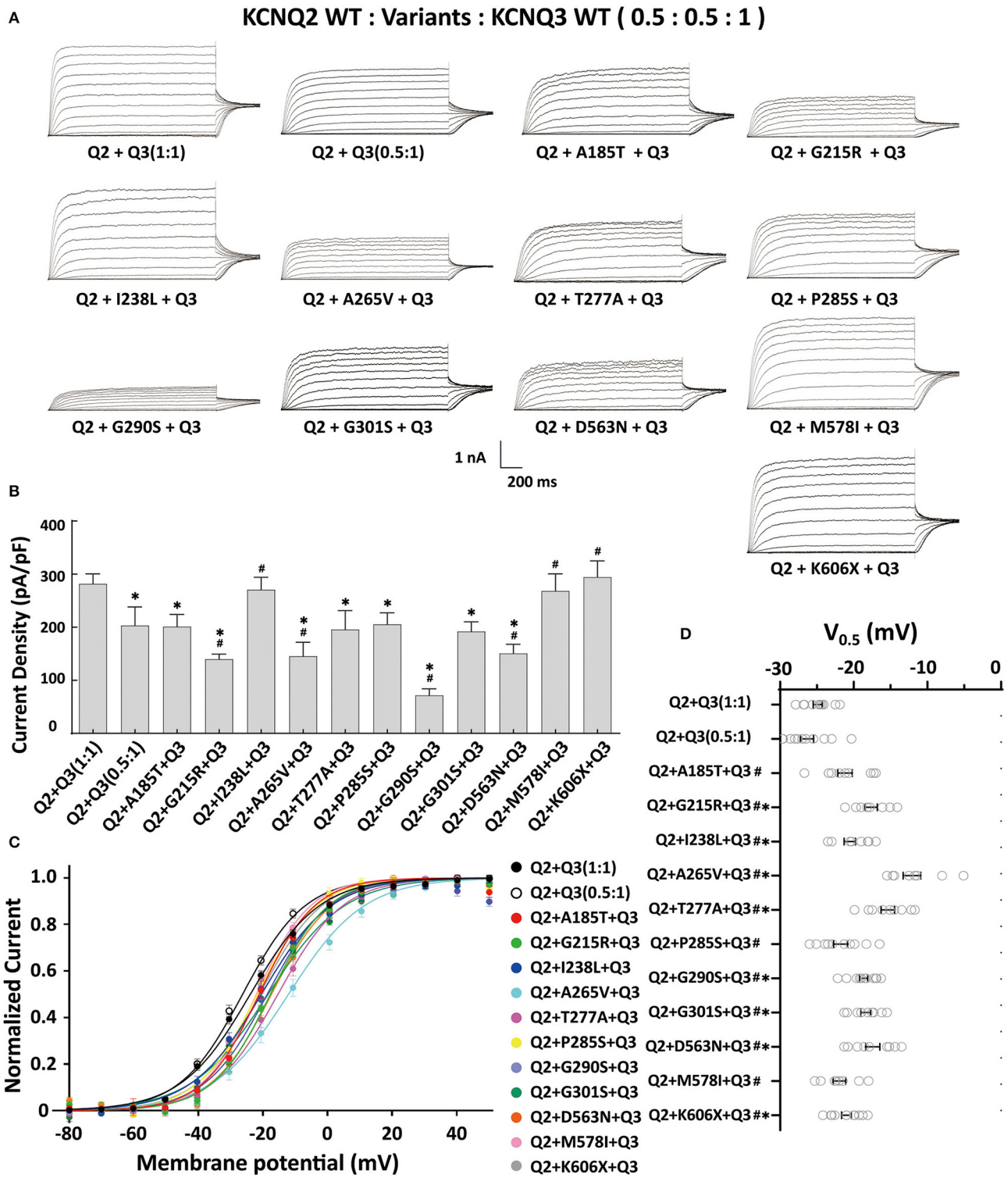

FIGURE 4
Functional properties of the KCNQ2 variants coexpressed with WTKCNQ2 and WTKCNQ3. **(A)** Macroscopic current traces recorded in CHO cells transfected KCNQ2 variants with WTKCNQ2 and WTKCNQ3 in 0.5:0.5:1 ratio (0.75 μg:0.75 μg:1.5 μg). Current scale, 1 nA; time scale, 200 ms. **(B)** The mean current densities of the KCNQ2variants coexpressed with WTKCNQ2 and WTKCNQ3 in a 0.5:0.5:1 ratio at +40 mV. **(C)** Current–voltage relationships of KCNQ2 variants coexpressed with WTKCNQ2 and WTKCNQ3 in a 0.5:0.5:1 ratio determined from tail current amplitudes. Lines represent fits of a Boltzmann function. **(D)** Differences in activation of $V_{0.5}$ were determined for the KCNQ2 variants, WTKCNQ2 and WTKCNQ3in a 0.5:0.5:1 ratio orWTKCNQ2 and WTKCNQ3in a 0.5:1ratio ($n = 8–11$). Statistically significant differences $^{*}p < 0.05$ versus WTKCNQ2/WTKCNQ3 in a 1:1 ratio. $^{\#}p < 0.05$ vs. WTKCNQ2/WTKCNQ3 in a 0.5:1 ratio.

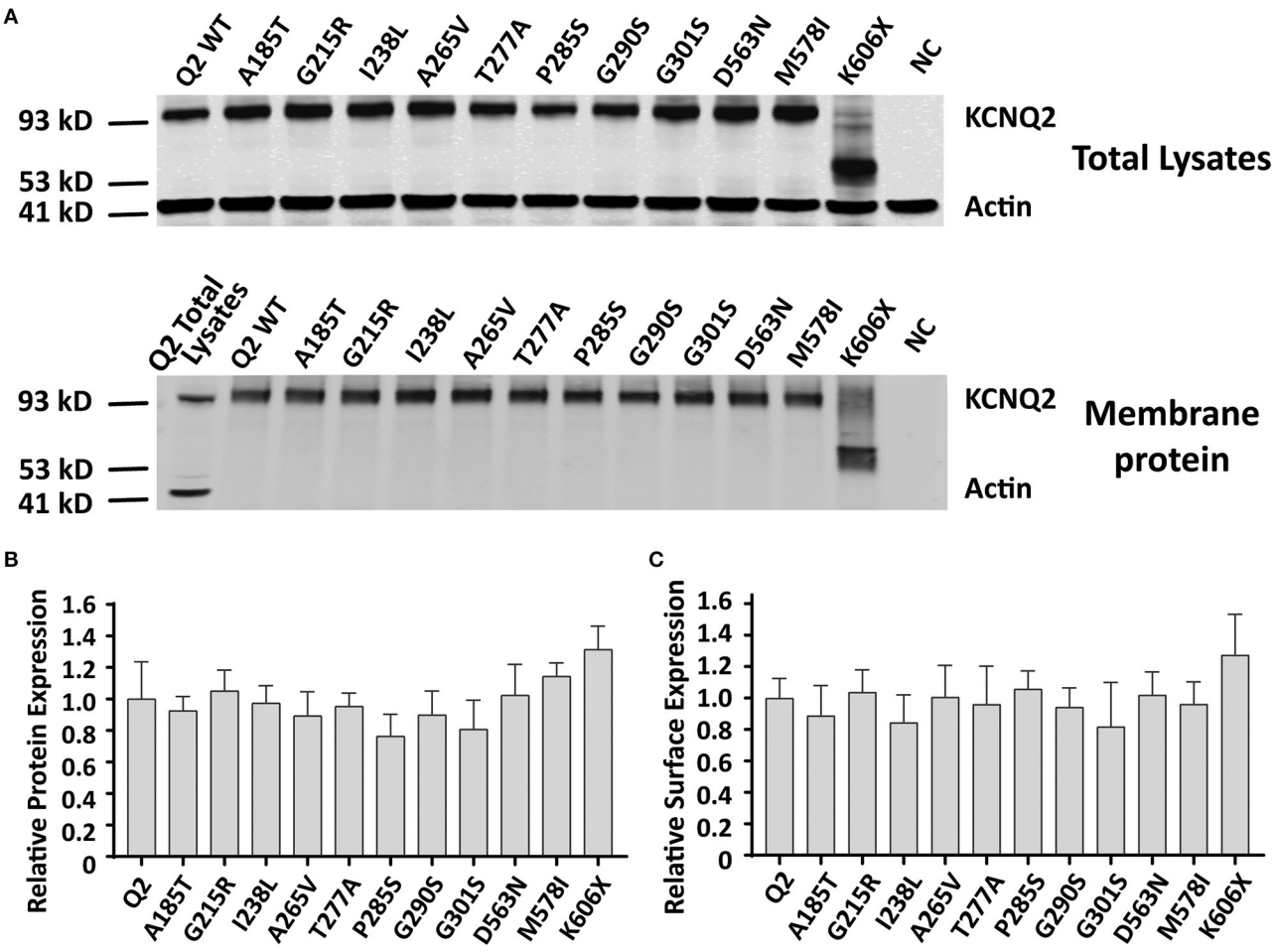

FIGURE 5
Total expression and surface expression of KCNQ2 channel. **(A)** Western blot analysis of proteins from total lysates **(top)** or plasma membrane fractions **(bottom)** from the negative control (NC, non-transfected CHO cells) or the CHO cells transfected with KCNQ2 variants. **(B)** Protein expression levels in total lysates obtained from transfected CHO cells were determined by normalizing KCNQ2 variants to the corresponding actin signals in four independent experiments. **(C)** Surface expression levels of the KCNQ2 variants normalized to WTKCNQ2 from four independent experiments. Statistically significant differences $*p < 0.05$ versus WT KCNQ2.

might still have a detrimental impact on M-current, resulting in developmental delay and other neurologic impairments.

Most of the variants we studied were rescued by KCNQ3 and showed larger currents in the heteromeric assembly of KCNQ2 and KCNQ3 subunits. The homomeric KCNQ3 channel exhibited a more negative V0.5 (−10 to −20 mV) compared to KCNQ2 (Miceli et al., 2015; Ambrosino et al., 2018). Therefore, when combining Q2:Q3 in a 1:1 ratio, the heteromeric channel would demonstrate a negative shift in $V_{0.5}$ relative to the homomeric KCNQ2 channel. When transfected with Q2:Q3 in a ratio of 0.5:1, where Q3 subunits constitute a larger proportion, a more pronounced negative shift in $V_{0.5}$ would be observed compared to the heteromeric Q2/Q3 channel in a 1:1 ratio (Soldovieri et al., 2014). As a result, the $V_{0.5}$ values of all 11 variants showed significant differences compared to Q2:Q3 in a ratio of 0.5:1. However, it is worth noting that we typically compare the differences in current density to the 0.5:1 ratio, while we rarely compare the differences in $V_{0.5}$ to the 0.5:1 ratio. Typically, we compare the $V_{0.5}$ values to Q2:Q3 in a ratio of 1:1. Under these conditions, variants A185T, P285S, and M578I showed no significant differences in $V_{0.5}$ compared to Q2:Q3 in a ratio of 1:1.

Variants p.I238L, p.M578I, and p.K606X had a current density close to WT KCNQ2/3. The current amplitude of p.A185T, p.T277A, p.P285S, and p.G301S had less reduction, ∼30%, similar to cells transfected with Q2/Q3 at a 0.5:1 ratio. Patients with variants p.A185T, p.P285S, and p.M578I, presenting with moderate-to-severe developmental delay, may be due to a partial loss of function (LOF) without dominant-negative effects on Q2/Q3 heteromeric channels. An mRNA molecule encoding a truncated variant may decay and fail to be translated into protein (Goto et al., 2019; Mary et al., 2021). However, our Western blot results demonstrated that the K606X variant could be translated into protein. The expression level of the K606X variant was comparable to that of the wild-type and other variants. Despite losing the intracellular helices D and the C-terminal, the K606X variant may still retain some functionality when combined with WT subunits and potentially influence the heteromeric channel, so when combining the K606X variant with Q2:Q3 in a 0.5:0.5:1 ratio,

we observed a positive shift in V0.5 compared to Q2:Q3 in a ratio of 1:1 ($0.01 < p < 0.05$). However, there was no significant difference in current density compared to Q2:Q3 in a ratio of 1:1. The K606X variants did not exhibit dominant-negative effects when combined with Q2 in a ratio of 1:1 or with Q2/Q3 in a ratio of 0.5:0.5:1, which may contribute to the SeLNE phenotype. As a SeLNE variant, the patient carrying the p.K606X variant was expected to have normal development. Variants p.G215R, p.A265V, p.G290S, and p.D563N had nearly 50% reduction in current and showed dominant-negative effects in heteromeric channels when incorporated with WT Q2/Q3. Patients carrying these variants presented profound developmental impairment without even head control. p.A265 is a high-frequency mutational site located in the pore domain, and different substitutions (p.A265V, p.A265P, and p.A265T) at this site have been reported previously in patients with encephalopathy and severe or profound developmental disorders (Weckhuysen et al., 2012; Kato et al., 2013; Orhan et al., 2014). In this study, the patient with p.A265V had seizures stopped at the earliest age but had the most profound developmental delay. These results suggest that the functional consequence of the M-current of heteromericKCNQ2/3 channels caused by dominant-negative effects may be a common mechanism associated with the severity of developmental disorders in DEE. The variants with dominant-negative effects in heteromeric channels, such as p.G215R, p.A265V, and p.G290S, may be responsible for the profound developmental phenotype.

Interestingly, variants p.I238L, p.T277A, and p.G301S did not show dominant-negative effects in heteromeric channels with WTKCNQ2/Q3, while the patients carrying these variants still presented profound developmental impairment. All these three variants were located in the pore-forming domain. There were some missense mutations in this region such as KCNQ2p.Y284C, p.A294V, p.A306T, and KCNQ3 p.G310V (corresponding to the G271V mutation in KCNQ2), which showed no effects on the surface expression of the protein in the Xenopus oocyte or the CHO cell expression system (Schwake et al., 2000; Abidi et al., 2015). However, these variants were altered in total protein levels, surface expressions, or subcellular localization in hippocampal neurons (Chung et al., 2006; Abidi et al., 2015). Variants p.I238L, p.T277A, and p.G301S may also exhibit changes in the expression levels or subcellular localization in neurons and may affect motor axon excitability and transmitter release (Martire et al., 2004; Schwarz et al., 2006). The mechanisms of KCNQ2 variants associated with developmental phenotype were complex, and further studies with these variants using neuron or animal models may help us explain KCNQ2-related developmental disorders.

All variants in this study were identified as LOF, indicating a decrease in M-current amplitude from moderate to strong. This is consistent with the previous findings that most pathogenic KCNQ2 variants cause LOF and lead to severe DEE with neonatal-onset seizures (Orhan et al., 2014; Gomis-Perez et al., 2019). However, a few gain-of-function (GOF) cases have also been reported (Miceli et al., 2015; Devaux et al., 2016; Millichap et al., 2017; Xiong et al., 2022). *De novo* GOF variants in the KCNQ2 gene, such as p.R201C and p.R201H, are associated with a distinct neonatal syndrome characterized by non-epileptic myoclonus and a suppression-burst EEG pattern without seizures. On the other hand, the KCNQ2p.R198Q variant has been frequently observed in patients with West syndrome who did not have neonatal seizures. Nonetheless, all patients with GOF variants had significant developmental delays. KCNQ2/3 channels are expressed in both pyramidal neurons and interneurons (Cooper et al., 2001; Uchida et al., 2017; Springer et al., 2021). The hypothesis is that GOF variants preferentially dampen the excitability of interneurons, disrupting the balance of the excitatory network. Despite reports of homeostatic potentiation of excitatory transmission as a result of loss of KCNQ2/KCNQ3 function in interneurons, the imbalance in the excitatory network and interneurons may play a crucial role in the pathogenesis of both LOF and GOF variants in the KCNQ2 gene (Soh et al., 2018).

KCNQ3 variants affecting residues p.R230 (p.R230C, p.R230H, and p.R230S) and p.R227 (p.R227Q), which are homologous to the KCNQ2 GOF site at p.R201 and R198, respectively, are also GOF and lead to neurodevelopmental disabilities without neonatal seizures (Barro-Soria, 2019; Sands et al., 2019). Given that developmental and behavioral impairments in DEE patients exist independently of epilepsy onset, the relationship between KCNQ3 and developmental disorders is an important question to consider. While variants may alter the gating, trafficking, or subcellular localization of KCNQ2 and KCNQ3, the expression pattern of these channels in the nervous system during development may provide insight. Recent data from large transcriptomic studies and single-cell RNA sequencing indicate that the expression of both channels begins early in development and varies depending on the brain region and cell type, with KCNQ2 expression starting slightly earlier (Springer et al., 2021). Comprehensive considerations should be taken to associate the various clinical phenotypes with the ongoing exploration of mechanisms.

There are several limitations to this study. Although clinical analysis and functional characterization of 11 *de novo* KCNQ2 variants in this study suggest an association between the functional consequence and the severity of the developmental disorders, more variants need to be investigated to validate the relationships between genotypes and phenotypes in KCNQ2-related DEE. Automated patch-clamp recordings enable high-throughput evaluation of epilepsy-associated KCNQ2 variants, expanding our understanding of the molecular basis of KCNQ2-related epilepsy (Vanoye et al., 2022). Future studies using neural networks and animal models may help explain KCNQ2-related DEE from a mechanism perspective.

In summary, this study combined clinical analysis and functional characterization to investigate a group of patients carrying pathogenic KCNQ2 variants who exhibited neonatal epileptic onset and developmental delay ranging from moderate to profound. The findings support that the reduction of M-current due to dominant-negative effects underlies the mechanism of KCNQ2-related DEE. The functional impact of variants on M-current in heteromericKCNQ2/3 channels may be associated with the severity of developmental disorders in DEE, potentially serving as a predictor of neurologic prognosis.

Data availability statement

The original contributions presented in the study are included in the article/supplementary material, further inquiries can be directed to the corresponding authors.

Ethics statement

Ethical approval of the study was provided by the Second Affiliated Hospital of Zhejiang University (2018-080) and the study procedures have been performed in accordance with the Declaration of Helsinki and its later ethical standards. Informed consents were obtained from the parents of patients.

Author contributions

JY, ST, and PM designed research, performed research, analyzed data, and wrote the manuscript. ZG and QS performed research and reviewed the manuscript. JF and YL drafted and critically revised the study. All authors contributed to the article and approved the submitted version.

Funding

This project was supported by the National Natural Science Foundation of China (31871060 and 82101515), the Ministry of Science and Technology of China (2018YFE0112900), and the Key Research and Development Project of Science and Technology Department of Zhejiang Province (2021C03104).

Acknowledgments

We are grateful to Lan Yu at Children's Hospital, Zhejiang University School of Medicine, and core facilities of Zhejiang University School of Medicine, the Center of Cryo-Electron Microscopy of Zhejiang University, the Laboratory Animal Center of Zhejiang University, for the technical support.

Conflict of interest

The authors declare that the research was conducted in the absence of any commercial or financial relationships that could be construed as a potential conflict of interest.

Publisher's note

References

Abidi, A., Devaux, J. J., Molinari, F., Alcaraz, G., Michon, F. X., Sutera-Sardo, J., et al. (2015). A recurrent KCNQ2 pore mutation causing early onset epileptic encephalopathy has a moderate effect on M current but alters subcellular localization of Kv7 channels. *Neurobiol. Dis.* 80, 80–92. doi: 10.1016/j.nbd.04017

Ambrosino, P., Freri, E., Castellotti, B., Soldovieri, M. V., Mosca, I., Manocchio, L., et al. (2018). Kv7.3 compound heterozygous variants in early onset encephalopathy reveal additive contribution of C-terminal residues to PIP2-dependent K+ channel gating. *Mol. Neurobiol.* 55, 7009–7024. doi: 10.1007/s12035-018-0883-5

Armijo, J. A., Shushtarian, M., Valdizan, E. M., Cuadrado, A., Las Cuevas, D. e. I., and Adin, J. (2005). Ion channels and epilepsy. *Curr. Pharm. Des.* 11, 1975–2003. doi: 10.2174/1381612054021006.

Balagura, G., Xian, J., Riva, A., Marchese, F., Ben Zeev, B., Rios, L., et al. (2022). Epilepsy course and developmental trajectories in STXBP1-DEE. *Neurol. Genet.* 8, e676. doi: 10.1212/nxg.0000000000000676

Barro-Soria, R. (2019). Epilepsy-associated mutations in the voltage sensor of KCNQ3 affect voltage dependence of channel opening. *J. Gen. Physiol.* 151, 247–257. doi: 10.1085/jgp.201812221

Berg, A. T., Mahida, S., and Poduri, A. (2021). KCNQ2-DEE: developmental or epileptic encephalopathy? *Ann. Clin. Transl. Neurol.* 8, 666–676. doi: 10.1002/acn3.51316

Biba-Maazou, N., Becq, H., Pallesi-Pocachard, E., Sarno, S., Granjeaud, S., Montheil, A., et al. (2022). Time-limited alterations in cortical activity of a knock-in mouse model of KCNQ2-related developmental and epileptic encephalopathy. *J. Physiol. London* 600, 2429–2460. doi: 10.1113/jp282536

Brown, D. A., and Adams, P. R. (1980). Muscarinic suppression of a novel voltage-sensitive K+ current in a vertebrate neuron. *Nature* 283, 673–676. doi: 10.1038/283673a0

Chung, H. J., Jan, Y. N., and Jan, L. Y. (2006). Polarized axonal surface expression of neuronal KCNQ channels is mediated by multiple signals in the KCNQ2 and KCNQ3 C-terminal domains. *Proceed. Nat. Acad. Sci. USA* 103, 8870–8875. doi: 10.1073/pnas.0603376103

Cooper, E. C., Harrington, E., Jan, Y. N., and Jan, L. Y. (2001). M channel KCNQ2 subunits are localized to key sites for control of neuronal network oscillations and synchronization in mouse brain. *J. Neurosci.* 21, 9529–9540. doi: 10.1523/jneurosci.21-24-09529.2001

Dalen Meurs-Van der Schoor, C., Van Weissenbruch, M., Van Kempen, M., Bugiani, M., Aronica, E., Ronner, H., et al. (2014). Severe neonatal epileptic encephalopathy and KCNQ2 mutation: neuropathological substrate? *Front. Pediatr.* 2, 136. doi: 10.3389/fped.2014.00136

Delmas, P., and Brown, D. A. (2005). Pathways modulating neural KCNQ/M (Kv7) potassium channels. *Nat. Rev. Neurosci.* 6, 850–862. doi: 10.1038/nrn1785

Devaux, J., Abidi, A., Roubertie, A., Molinari, F., Becq, H., Lacoste, C., et al. (2016). A Kv7.2 mutation associated with early onset epileptic encephalopathy with suppression-burst enhances Kv7/M channel activity. *Epilepsia* 57, E87–E93. doi: 10.1111/epi.13366

Errington, A. C., Stohr, T., and Lees, G. (2005). Voltage gated ion channels: Targets for anticonvulsant drugs. *Curr. Top. Med. Chem.* 5, 15–30. doi: 10.2174/1568026053386872

Gomis-Perez, C., Urrutia, J., Marce-Grau, A., Malo, C., Lopez-Laso, E., Felipe-Rucian, A., et al. (2019). Homomeric Kv7.2 current suppression is a common feature in KCNQ2 epileptic encephalopathy. *Epilepsia* 60, 139–148. doi: 10.1111/epi.14609

Goto, A., Ishii, A., Shibata, M., Ihara, Y., Cooper, E. C., and Hirose, S. (2019). Characteristics of KCNQ2 variants causing either benign neonatal epilepsy or developmental and epileptic encephalopathy. *Epilepsia* 60, 1870–1880. doi: 10.1111/epi.16314

Kato, M., Yamagata, T., Kubota, M., Arai, H., Yamashita, S., Nakagawa, T., et al. (2013). Clinical spectrum of early onset epileptic encephalopathies caused by KCNQ2 mutation. *Epilepsia* 54, 1282–1287. doi: 10.1111/epi.12200

Lerche, H., Jurkat-Rott, K., and Lehmann-Horn, F. (2001). Ion channels and epilepsy. *Am. J. Med. Genet.* 106, 146–159. doi: 10.1002/ajmg.1582

Li, X., Zhang, Q., Guo, P., Fu, J., Mei, L., Lv, D., et al. (2021). Molecular basis for ligand activation of the human KCNQ2 channel. *Cell Res.* 31, 52–61. doi: 10.1038/s41422-020-00410-8

Maljevic, S., and Lerche, H. (2014). *Potassium Channel Genes and benign familial neonatal* epilepsy. In: Steinlein, O. K. (ed.) Genetics of Epilepsy.

Maljevic, S., Naros, G., Yalcin, O., Blazevic, D., Loeffler, H., Caglayan, H., et al. (2011). Temperature and pharmacological rescue of a folding-defective, dominant-negative K(V)7.2 mutation associated with neonatal seizures. *Hum. Mutat.* 32, E2283–E2293. doi: 10.1002/humu.21554

Martire, M., Castaldo, P. D'amico, M., Preziosi, P., Annunziato, L., and Taglialatela, M. (2004). M channels containing KCNQ2 subunits modulate norepinephrine, aspartate, and GABA release from hippocampal nerve terminals. *J Neurosci.* 24, 592–7. doi: 10.1523/jneurosci.3143-03.2004

Mary, L., Nourisson, E., Feger, C., Laugel, V., Chaigne, D., Keren, B., et al. (2021). Pathogenic variants in KCNQ2 cause intellectual deficiency without epilepsy: broadening the phenotypic spectrum of a potassium channelopathy. *Am. J. Med. Genet. A* 185, 1803–1815. doi: 10.1002/ajmg.a.62181

Miao, P., Feng, J., Guo, Y., Wang, J., Xu, X., Wang, Y., et al. (2018). Genotype and phenotype analysis using an epilepsy-associated gene panel in Chinese pediatric epilepsy patients. *Clin. Genet.* 94, 512–520. doi: 10.1111/cge.13441

Miceli, F., Soldovieri, M. V., Ambrosino, P., Barrese, V., Migliore, M., Cilio, M. R., et al. (2013). Genotype-phenotype correlations in neonatal epilepsies caused by mutations in the voltage sensor of K(v)7.2 potassium channel subunits. *Proceed. Nat. Acad. Sci. USA* 110, 4386–4391. doi: 10.1073/pnas.1216867110

Miceli, F., Soldovieri, M. V., Ambrosino, P., Maria, De., Migliore, M., Migliore, M., et al. (2015). Early-onset epileptic encephalopathy caused by gain-of-function mutations in the voltage sensor of K(v)7.2 and K(v)7.3 potassium channel subunits. *J. Neurosci.* 35, 3782–3793. doi: 10.1523/jneurosci.4423-14.2015

Milh, M., Boutry-Kryza, N., Sutera-Sardo, J., Mignot, C., Auvin, S., Lacoste, C., et al. (2013). Similar early characteristics but variable neurological outcome of patients with a de novo mutation of KCNQ2. *Orphanet. J. Rare Dis.* 8, 80. doi: 10.1186/1750-1172-8-80

Milh, M., Lacoste, C., Cacciagli, P., Abidi, A., Sutera-Sardo, J., Tzelepis, I., et al. (2015). Variable clinical expression in patients with mosaicism for KCNQ2 mutations. *Am. J. Med. Genet. Part A* 167, 2314–2318. doi: 10.1002/ajmg.a.37152

Milh, M., Roubertoux, P., Biba, N., Chavany, J., Ghata, A. S., Fulachier, C., et al. (2020). A knock-in mouse model for KCNQ2-related epileptic encephalopathy displays spontaneous generalized seizures and cognitive impairment. *Epilepsia* 61, 868–878. doi: 10.1111/epi.16494

Millichap, J. J., Miceli, F., Maria, D. e., Keator, M., Joshi, C., Tran, N., et al. (2017). Infantile spasms and encephalopathy without preceding neonatal seizures caused by KCNQ2 R198Q, a gain-of-function variant. *Epilepsia* 58, e10–e15. doi: 10.1111/epi.13601

Millichap, J. J., Park, K. L., Tsuchida, T., Ben-Zeev, B., Carmant, L., Flamini, R., et al. (2016). KCNQ2 encephalopathy: features, mutational hot spots, and ezogabine treatment of 11 patients. *Neurol. Gen.* 2, e96. doi: 10.1212/nxg.0000000000000096

Numis, A. L., Angriman, M., Sullivan, J. E., Lewis, A. J., Striano, P., Nabbout, R., et al. (2014). KCNQ2 encephalopathy: delineation of the electroclinical phenotype and treatment response. *Neurology* 82, 368–70. doi: 10.1212/wnl.0000000000000060

Orhan, G., Bock, M., Schepers, D., Ilina, E. I., Reichel, S. N., Loeffler, H., et al. (2014). Dominant-negative effects of KCNQ2 mutations are associated with epileptic encephalopathy. *Ann. Neurol.* 75, 382–394. doi: 10.1002/ana.24080

Parrini, E., Marini, C., Mei, D., Galuppi, A., Cellini, E., Pucatti, D., et al. (2017). Diagnostic targeted resequencing in 349 patients with drug-resistant pediatric epilepsies identifies causative mutations in 30 different genes. *Hum. Mutat.* 38, 216–225. doi: 10.1002/humu.23149

Sands, T. T., Miceli, F., Lesca, G., Beck, A. E., Sadleir, L. G., Arrington, D. K., et al. (2019). Autism and developmental disability caused by KCNQ3 gain-of-function variants. *Ann. Neurol.* 86, 181–192. doi: 10.1002/ana.25522

Schroeder, B. C., Kubisch, C., Stein, V., and Jentsch, T. J. (1998). Moderate loss of function of cyclic-AMP-modulated KCNQ2/KCNQ3 K+ channels causes epilepsy. *Nature* 396, 687–690. doi: 10.1038/25367

Schwake, M., Pusch, M., and Kharkovets, T., and Jentsch, T. J. (2000). Surface expression and single channel properties of KCNQ2/KCNQ3, M-type K+ channels involved in epilepsy. *J. Biol. Chem.* 275, 13343–8. doi: 10.1074/jbc.275.18.13343

Schwarz, J. R., Glassmeier, G., Cooper, E. C., Kao, T. C., Nodera, H., Tabuena, D., et al. (2006). KCNQ channels mediate IKs, a slow K+ current regulating excitability in the rat node of Ranvier. *J. Physiol.* 573, 17–34. doi: 10.1113/jphysiol.2006.106815

Shapiro, M. S., Roche, J. P., Kaftan, E. J., Cruzblanca, H., Mackie, K., and Hille, B. (2000). Reconstitution of muscarinic modulation of the KCNQ2/KCNQ3 K+ channels that underlie the neuronal M current. *J. Neurosci.* 20, 1710–1721.

Soh, H., Park, S., Ryan, K., Springer, K., Maheshwari, A., and Tzingounis, A. V. (2018). Deletion of KCNQ2/3 potassium channels from PV plus interneurons leads to homeostatic potentiation of excitatory transmission. *Elife* 7, 38617. doi: 10.7554./eLife.38617

Soldovieri, M. V., Boutry-Kryza, N., Milh, M., Doummar, D., Heron, B., Bourel, E., et al. (2014). Novel KCNQ2 and KCNQ3 mutations in a large cohort of families with benign neonatal epilepsy: first evidence for an altered channel regulation by syntaxin-1A. *Hum. Mutat.* 35, 356–367. doi: 10.1002/humu.22500

Specchio, N., and Curatolo, P. (2021). Developmental and epileptic encephalopathies: what we do and do not know. *Brain* 144, 32–43. doi: 10.1093/brain/awaa371

Springer, K., Varghese, N., and Tzingounis, A. V. (2021). Flexible stoichiometry: implications for KCNQ2-and KCNQ3-associated neurodevelopmental disorders. *Dev. Neurosci.* 43, 191–200. doi: 10.1159/000515495

Steinlein, O. K., Conrad, C., and Weidner, B. (2007). Benign familial neonatal convulsions: always benign? *Epilepsy Res.* 73, 245–249. doi: 10.1016/j.eplepsyres.10010

Tzingounis, A. V., and Nicoll, R. A. (2008). Contribution of KCNQ2 and KCNQ3 to the medium and slow afterhyperpolarization currents. *Proceed. Nat. Acad. Sci. USA* 105, 19974–19979. doi: 10.1073/pnas.0810535105

Uchida, T., Lossin, C., Ihara, Y., Deshimaru, M., Yanagawa, Y., Koyama, S., et al. (2017). Abnormal gamma-aminobutyric acid neurotransmission in a Kcnq2 model of early onset epilepsy. *Epilepsia* 58, 1430–1439. doi: 10.1111/epi.13807

Vanoye, C. G., Desai, R. R., Ji, Z., Adusumilli, S., Jairam, N., Ghabra, N., et al. (2022). High-throughput evaluation of epilepsy-associated KCNQ2 variants reveals functional and pharmacological heterogeneity. *Jci Insight,* 7, 6314. doi: 10.1172./jci.insight.156314

Wang, H. S., Pan, Z. M., Shi, W. M., Brown, B. S., Wymore, R. S., Cohen, I. S., et al. (1998). KCNQ2 and KCNQ3 potassium channel subunits: molecular correlates of the M-channel. *Science,* 282, 1890–1893. doi: 10.1126/science.282.5395.1890

Weckhuysen, S., Mandelstam, S., Suls, A., Audenaert, D., Deconinck, T., Claes, L. R. F., et al. (2012). KCNQ2 encephalopathy: emerging phenotype of a neonatal epileptic encephalopathy. *Ann. Neurol.* 71, 15–25. doi: 10.1002/ana.22644

Xiong, J., Chen, S., Chen, B., Zhang, W., Chen, C., Deng, X., et al. (2022). A novel KCNQ2 missense variant in non-syndromic intellectual disability causes mild gain-of-function of Kv7.2 channel. *Clin. Chim. Acta* 530, 74–80. doi: 10.1016/j.cca.03001

frontiers | Frontiers in Molecular Neuroscience

TYPE Review
PUBLISHED 05 January 2024
DOI 10.3389/fnmol.2023.1336004

OPEN ACCESS

EDITED BY
Jean-Marc Taymans,
Institut National de la Santé et de la Recherche Médicale (INSERM), France

REVIEWED BY
Xianjin Xu,
University of Missouri, United States
Zhiguang Jia,
University of Massachusetts Amherst, United States

*CORRESPONDENCE
Jens Meiler
✉ jens@meilerlab.org
Georg Künze
✉ georg.kuenze@uni-leipzig.de

†These authors have contributed equally to this work

RECEIVED 09 November 2023
ACCEPTED 05 December 2023
PUBLISHED 05 January 2024

CITATION
Melancon K, Pliushcheuskaya P, Meiler J and Künze G (2024) Targeting ion channels with ultra-large library screening for hit discovery. *Front. Mol. Neurosci.* 16:1336004. doi: 10.3389/fnmol.2023.1336004

Targeting ion channels with ultra-large library screening for hit discovery

Kortney Melancon[1,2†], Palina Pliushcheuskaya[3†], Jens Meiler[1,2,3,4*] and Georg Künze[3,4,5*]

[1]Department of Chemistry, Vanderbilt University, Nashville, TN, United States, [2]Center for Structural Biology, Vanderbilt University, Nashville, TN, United States, [3]Medical Faculty, Institute for Drug Discovery, Leipzig University, Leipzig, Germany, [4]Center for Scalable Data Analytics and Artificial Intelligence, Leipzig University, Leipzig, Germany, [5]Interdisciplinary Center for Bioinformatics, Leipzig University, Leipzig, Germany

Ion channels play a crucial role in a variety of physiological and pathological processes, making them attractive targets for drug development in diseases such as diabetes, epilepsy, hypertension, cancer, and chronic pain. Despite the importance of ion channels in drug discovery, the vastness of chemical space and the complexity of ion channels pose significant challenges for identifying drug candidates. The use of *in silico* methods in drug discovery has dramatically reduced the time and cost of drug development and has the potential to revolutionize the field of medicine. Recent advances in computer hardware and software have enabled the screening of ultra-large compound libraries. Integration of different methods at various scales and dimensions is becoming an inevitable trend in drug development. In this review, we provide an overview of current state-of-the-art computational chemistry methodologies for ultra-large compound library screening and their application to ion channel drug discovery research. We discuss the advantages and limitations of various *in silico* techniques, including virtual screening, molecular mechanics/dynamics simulations, and machine learning-based approaches. We also highlight several successful applications of computational chemistry methodologies in ion channel drug discovery and provide insights into future directions and challenges in this field.

KEYWORDS

virtual screening, ion channels, drug design, deep learning, chemical library

Introduction

Ion channels are widely expressed in living cells and play critical roles in the generation of the cell membrane potential and in additional diverse cellular functions, such as signal transduction, neurotransmitter release, muscle contraction, hormone secretion, cell volume regulation, growth, mobility, and apoptosis. Dysfunction of ion channels due to mutations in ion channel genes are associated with numerous diseases collectively known as channelopathies, which include cardiac arrhythmias, ataxias, migraine headaches, muscle paralysis, epilepsy, deafness and cancer. More than 60 channelopathies have been identified in human diseases, and clinical sequencing results often discover novel mutations in ion channel genes (Cannon, 2007; Kim, 2014). Because of the high pathophysiological importance of ion channels and their involvement in several human diseases, they are the target of diverse drugs, from antiepileptics to analgesics. Ion channels are the second largest group of drug targets with approximately 130 drugs on the market that act on ion channels.

Examples include voltage-gated sodium channel blockers for the treatment of arrhythmia and local anesthesia, calcium channel blockers for the treatment of angina and hypertension, and ATP-sensitive potassium channel blockers for the therapy of type II diabetes (Ford et al., 2016; Imbrici et al., 2016; Santos et al., 2016; Li et al., 2017; Wolkenberg et al., 2017; Hutchings et al., 2019; Chen et al., 2023). Despite this large number of existing drugs, ion channels remain relatively underexploited for therapeutic interventions. It is notable that the major chemical classes of ion channel modulators were identified through serendipity and have been in clinical use for many years, pre-dating major milestones in ion channel research such as the development of patch clamp physiology, molecular cloning of ion channels and their structure determination by cryogenic electron microscopy (cryo-EM).

The rapid growth in structural information of ion channels has fueled the use of computer-assisted drug discovery approaches. At the time of writing (as of October 2023), approximately 100 unique human ion channel protein structures have been deposited in the Protein Data Bank (PDB), ∼81% of these structures were determined by cryo-EM (Lau et al., 2018; Rao et al., 2019; Chen et al., 2023; mpstruc database, n.d.). In recent decades, the increasing numbers of high-quality ion channel structures, along with advances in computer-assisted drug discovery, have led to a number of successful virtual screening (VS) campaigns (Kang, 2001; Urbahns et al., 2003; Kenyon et al., 2006; Liu et al., 2007; Etkins, 2018; Llanos et al., 2022; Pasqualetto et al., 2023). Among ion channels, L-type calcium channels and hERG channels have received the most extensive research attention to date (Ekins et al., 2007). In contrast, there are very few examples of successful applications for more ion-selective channels (K, Na) and less selective channels such as nicotinic acetylcholine receptors (nAChR) or acid-sensing ion channels (ASICs).

Most recently, the utility of VS for lead discovery has also been boosted by the expansion of accessible chemical space through make-on-demand compound libraries like Enamine REAL Space library (Grygorenko et al., 2020; Enamine, n.d.). Since 2016, these libraries have witnessed a remarkable expansion, scaling up the availability of molecules from 11 million to an astonishing 38 billion, and there is still potential for further growth (Lyu et al., 2023). While such libraries cannot be empirically screened, molecules within them can be computational prioritized for synthesis and testing using VS and machine learning approaches. Combining *in silico* approaches with conventional high-throughput screening techniques greatly enhances ion channel drug discovery. Methods of computer-aided drug discovery (CADD) can significantly speed up screening and can drastically improve hit rates. Molecular docking is routinely used to process virtual libraries containing millions of molecules against a variety of drug targets with known structures.

Recent strides in automated synthesis and the proliferation of available chemicals present significant opportunities for VS methods overall, and especially for docking. However, they also introduce entirely new challenges to contend with (Gentile et al., 2020). The widely used ZINC library has grown from 7,000 entries in 2005 to over 1.3 billion constituent molecules in 2020, a remarkable 1,000-fold increase (Irwin and Shoichet, 2005; Irwin et al., 2020; ZINC Database, n.d.). In the past two years alone, the Enamine REAL database has grown from 11 billion molecules to 38 billion make-on-demand molecules (Grygorenko et al., 2020). Recently published works seem to advocate for expanding VS to ultra-large chemical libraries. In a recent groundbreaking study, Lyu et al. conducted docking experiments with 170 million on-demand molecular structures (Lyu et al., 2019). Their findings demonstrated that VS of such extensive databases not only enables the discovery of highly potent inhibitors but also uncovers novel chemical classes that are typically absent from routinely screened, readily available chemical libraries (Lyu et al., 2019). Other docking studies involving large collections of molecules led to similar conclusions (Gorgulla et al., 2020; Stein et al., 2020).

Progress in high-throughput docking programs, computational resources, and the accessibility of more and more ion channel structures, promote a paradigm shift in drug discovery research toward faster *in silico* lead compound generation. Despite these advancements, it's worth noting that the chemical space remains so vast that it often remains beyond practical reach. A common approach to mitigate these challenges is to filter these large chemical collections to manageable subsets based on parameters set forth by Lipinski and others (Lipinski et al., 2001; Lipinski, 2004). While this approach can effectively reduce an ultra-large database to smaller, more accessible subsets, many potentially useful compounds and novel or unconventional chemotypes could be overlooked. It is essential to maximize the number of database entries tangibly evaluated against a target of interest. Additionally, a vast majority of docking data is not being utilized while it could represent a very relevant, well-formatted, and content-rich landscape for machine learning algorithms. Typical docking campaigns rely on completing a full docking run and selecting only an extremely narrow subset (∼1%) of favorably docked molecules for future evaluation.

Ultra-large VS in ion channel drug discovery offers numerous advantages compared to conventional experimental high throughput screening methods. VS enables the exploration of a vast chemical space, including millions of potential ion channel modulators, increasing the likelihood of discovering novel hit compounds with unique structures. It is cost and time-efficient, allowing for rapid evaluation of compounds *in silico*, reducing the need for expensive and time-consuming experimental synthesis and testing. VS enables early hit identification, helping researchers prioritize the most promising compounds and saving resources by excluding less viable candidates. It provides mechanistic insights into ion channel interactions and facilitates rational design and optimization of modulators. Additionally, VS allows evaluation of rare or challenging-to-source compounds, such as natural products or derivatives, enhancing the probability of discovering valuable hits. VS serves as a complement to experimental screening, and computational predictions can guide subsequent experimental validation and optimization of identified hits.

In this review we will introduce basic principles of VS and methodology behind it. We will give an overview of the knowledge base of ion channel structures and how they can be generated. We will describe chemical libraries of small molecules that are used to screen ion channel structures and we will go through several real VS campaigns on ion channels utilizing different docking-based, ligand-based, and deep learning VS techniques.

Overview of virtual screening methods

Ultra-large VS technologies refer to computational methods and techniques used to screen large chemical libraries against a target of interest in drug discovery. VS is a firmly established technique in computational drug design which can greatly reduce the costs of discovering a new drug. In general, VS aims to identify potential drug candidates by simulating and predicting their interactions with a target protein or biological system. Ultra-large VS technologies take this concept to a larger scale, enabling the screening of massive chemical libraries containing millions or even billions of compounds. The methodology of ultra-large VS will be reviewed below in the sections devoted to each of the methods and their applications in ion channel drug discovery campaigns will be illustrated. The primary goal of ultra-large VS is to narrow down the chemical space and prioritize the most promising compounds for further experimental validation. It is an important tool in the early stages of drug discovery where large-scale screening can significantly reduce the time and cost associated with traditional high-throughput screening methods.

VS methods can be divided into two main categories: ligand-based and structure-based approaches (Figure 1). Ligand-based methods rely on the similarity of identified molecules to the known actives, whereas structure-based methods aim to predict the binding pose of molecules based on the known 3D protein target (Lavecchia and Di Giovanni, 2013).

Ligand-based VS (LBVS) approach is less computationally expensive than the structure-based method because it does not rely on macromolecular structure in calculations. LBVS methods are usually performed by comparing fingerprints of tested molecules with the ones from the active set. These fingerprints can be of various types, such as topological descriptors, circular and pharmacophore-based fingerprints, etc. Similarity searching and quantitative structure-activity relationship (QSAR) modeling can be applied to compare the fingerprints and derive the underlying relationship between molecules and their activities (Gimeno et al., 2019).

The analysis and recognition of QSAR has also become an essential component of ligand-based VS techniques and the pharmacology of ion channels. QSAR is an attempt to establish a correlation between the chemical structure of a molecule and the biological effect. The representation of chemical structures can be described through molecular descriptors: 1-D descriptors encode generic properties such as molecular weight, hydrophobic/hydrophilic partition coefficient, and molar refractivity, commonly related to a basic description of drug-likeness; 2-D descriptors predict physicochemical properties, and provide quantitative estimates of biological activity from topological representations of the molecules; 3-D descriptors are derived as the name implies, from the 3-D structures of the molecules, depending on the conformation used and the flexible superposition of the molecules. 3-D QSAR offers a better representation of molecules interacting with proteins and leads to statistically improved models. QSAR analysis builds on mathematical models, e.g., random forest, decision trees, naive Bayes classifier, support vector machines, k-nearest neighbors, and artificial neural networks, to find some statistical correlation between the biological parameters of tested molecules derived from various assays (pEC_{50}, Ki, activity, toxicity, etc.) and their chemical structures (Hansch and Fujita, 1953). Regression and classification techniques are applied to derive the relationship between molecules, which can be substantiated by machine learning (Neves et al., 2018) and pharmacophore modeling.

Structure-based VS (SBVS) methods require a 3D structure of a protein of interest, and tested molecules are ranked according to their activity toward a receptor obtained from calculations (Maia et al., 2020). Docking is the main approach used in SBVS (Kuntz et al., 1982), which can be also supported by machine learning to derive scoring functions, which evaluate the binding orientations of molecules, as well as deep learning that speeds up the docking protocol and allows to screen billions of molecules in much shorter time (Pereira et al., 2016; Gentile et al., 2022). SBVS can also utilize pharmacophore modeling, which does not focus on a specific ligand structure, but rather defines necessary functional groups that a molecule should possess to create interactions in a receptor's binding pocket (Giordano et al., 2022). Another approach in SBVS is fragment-based virtual screening, which involves screening small molecular fragments against a target protein, followed by growing, merging or linking fragments into larger drug-like molecules (Doak et al., 2016). Since the key aspect of fragment-based VS requires the availability of the 3D structure of the protein target, this technology is directly related to SBVS (Murray and Rees, 2009). By employing fragment docking or fragment-based *de novo* design techniques, millions or billions of molecules can be computationally screened against a target. One advantage is that the small size of the fragments allows a more efficient search of chemical space and recovers more protein binding information than in traditional high-throughput screens, allowing the size of the library to be much smaller. Furthermore, the combination of fragment-based and combinatorial chemistry approaches allows designing target-focused and diverse chemical libraries (Liu et al., 2017). Hits obtained from this screening can be expanded and optimized to develop more potent drug candidates (Li, 2020).

In the following sections we will introduce the concepts of several VS methods and review their applications in recent ion channel drug discovery campaigns.

Ion channel structures for virtual screening

Ultra-large VS efforts benefit from the quickly growing number of protein target structures. For instance, for the largest group of drug targets, G protein-coupled receptors (GPCRs), VS experiments have flourished because of a larger number of available GPCR structures (Luttens et al., 2022; Matricon et al., 2023). Similarly, the number of ion channel structures has increased tremendously over the last 25 years; from the determination of the first ion channel structure, the KcsA channel from Streptomyces lividans, in 1998 (Doyle et al., 1998) to more than 1,500 structures nowadays. This includes ca. 200 ion channel structures from the human proteome, with almost 100 of them being unique human ion channel structures (Figure 2) (Pliushcheuskaya and Künze, 2023).

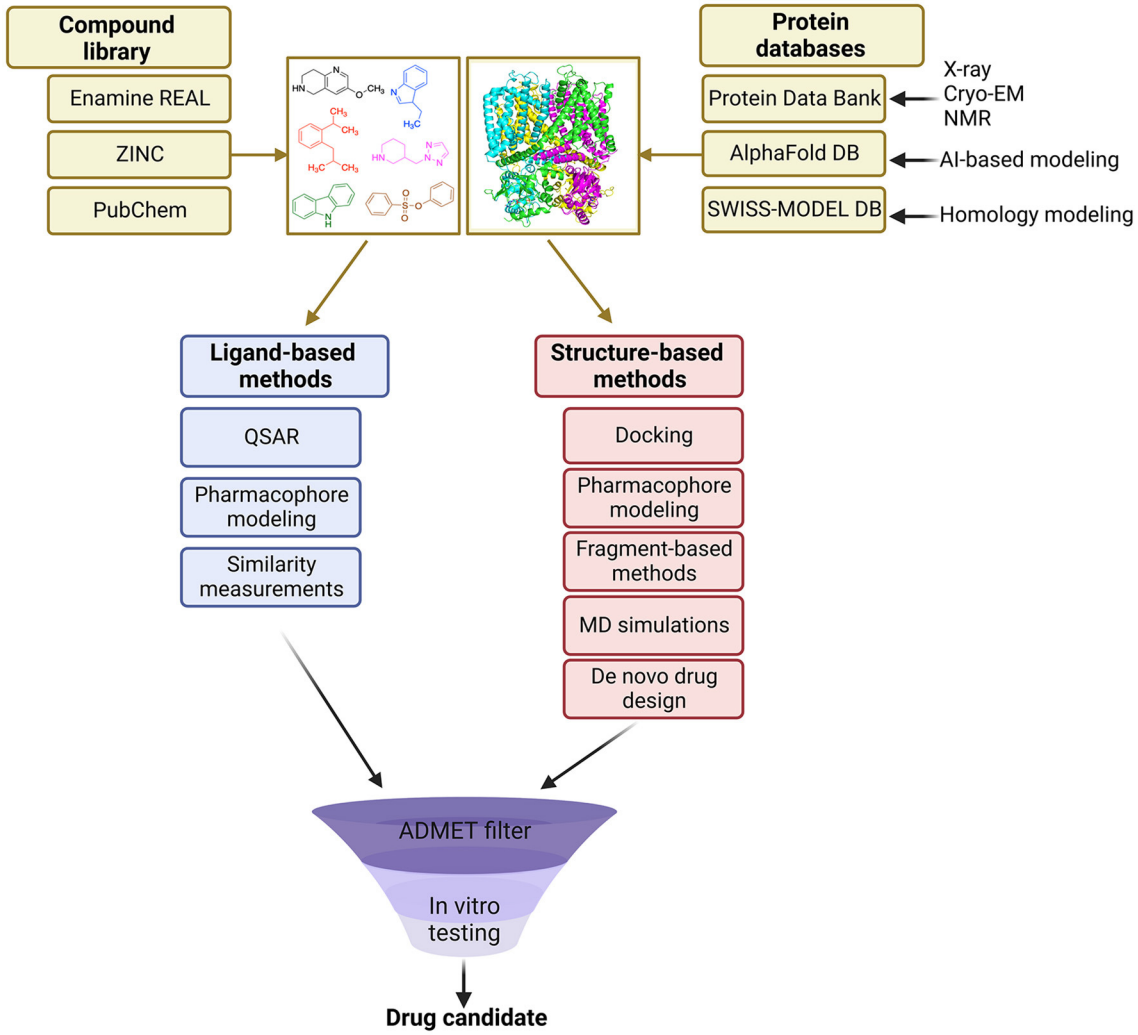

FIGURE 1
Overview of the general VS workflow.

This progress was primarily due to technological advancements in X-ray crystallography and cryo-EM.

If an experimental structure for an ion channel of interest is lacking, structure prediction methods like AlphaFold (Jumper et al., 2021), RoseTTAFold (Baek et al., 2021), or ESMFold (Lin et al., 2023) offer a solution. For instance, The AlphaFold database estimates more than 290 non-redundant structures for ion channels for the human proteome (Varadi et al., 2022). These artificial intelligence-based prediction methods can provide highly accurate model structures which are often suitable for VS applications.

Another use case of AlphaFold structure prediction is to aid interpretation of low-resolution electron density maps of ion channels. For instance, Huang et al. (2022a) studied the voltage-gated sodium ion channel $Na_V1.7$, which is highly expressed in nociceptive neurons and is a drug target for pain relief (Hameed, 2019). Specifically, structures of $Na_V1.7$ in combination with pore blockers are of high interest to better understand the mechanism of $Na_V1.7$ modulation and develop effective analgesics (Zhang et al., 2022b). In the study of Huang et al. (2022a), various wild-type and mutant structures of $Na_V1.7$ with and without small-molecule ligands were determined. The use of AlphaFold was key to facilitate interpretation of intracellular low-resolution regions of the cryo-EM map, which are of direct interest for designing inhibitors of $Na_V1.7$. Eventually, the authors were able to identify determinants of the $Na_V1.7$ channel modulation, which was enabled by the accurate structure determination of $Na_V1.7$ (Figure 3).

Chemical libraries for ultra-large virtual high-throughput screening

Physically available compound collections in academic and industrial research institutions typically range from thousands to millions of compounds (Sadybekov and Katritch, 2023). In contrast, virtual compound libraries can be much larger, reaching

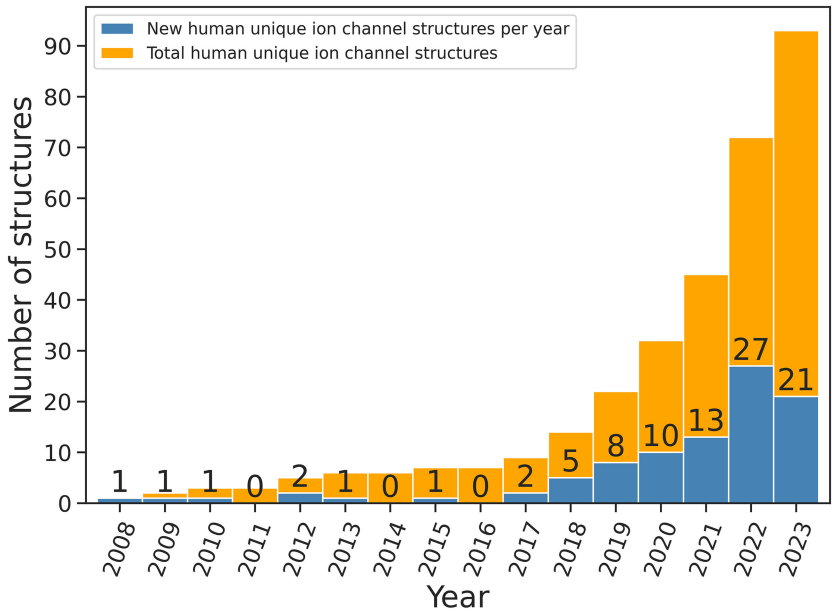

FIGURE 2
Number of unique structures of human ion channels released every year since 2011 (data were obtained from mpstruc database, source: mpstruc database: Available at: https://blanco.biomol.uci.edu/mpstruc/, accessed on 23 October 2023). Values on top of blue bars indicate the number of new human ion channel structures released every year.

billions of compounds, with the aim of enhancing chemical diversity coverage (Grygorenko et al., 2020; Huang et al., 2022b; Kuan et al., 2023; Lyu et al., 2023). Chemical space encompasses all possible organic molecules, estimated to be around 10^{60} or more. This vastness offers an opportunity to discover unique biological activities and mechanisms of action not found in general screenings.

Enamine is a chemical supplier that offers diverse small molecule collections for screening and hit expansion, focusing on synthetically accessible molecules. The REAL (Readily Accessible) database, popular among researchers, contains over 38 billion compounds with varied chemical scaffolds (REAL Compounds, n.d.). Widely used in drug discovery stages such as hit identification, lead optimization, and fragment-based screening, the REAL library is a significant advancement in combinatorial chemistry. It features simple fragments and building blocks connected through efficient one- or two-step reactions, allowing for a vast number of unique combinations. This versatility makes it valuable for diverse molecular structure generation in VS and positions it as a crucial resource in drug discovery and material science. Similar extensive libraries are offered now also by other vendors like eMolecules (eMolecules, n.d.).

The ZINC database is a widely used resource that provides a vast collection of commercially available compounds for VS and drug discovery. It contains over 230 million small molecules with diverse chemical structures (Irwin and Shoichet, 2005), of which approximately 34 million predictions belong to the ion channel major class. Regarding the number of reactions, the ZINC database primarily focuses on providing commercially available compounds, while the Enamine REAL database emphasizes synthetically accessible compounds. As a result, Enamine's REAL database may have a larger number of enumerated reactions available for the compounds within its library (Saldívar-González et al., 2020). However, it is worth noting that the exact number of compounds in each database can vary over time due to updates and additions.

PubChem is a free chemical database maintained by the National Center for Biotechnology Information (NCBI). It offers a vast collection of chemical substances (over 293 million), small molecules (over 110 million), bioassays (over 1.25 million), and their associated data (Kim et al., 2016). PubChem is extensively used in drug discovery research. PubChem primarily focuses on aggregating and curating chemical data from various sources, while the Enamine REAL database specifically emphasizes synthetically accessible compounds.

ChEMBL is a large database of over 2.4 million bioactive compounds and their associated biological activities (Gaulton et al., 2012) where approximately 190,000 are associated with an ion channel family major class. It provides access to chemical structures, target information, and bioactivity data extracted from scientific literature. ChEMBL is commonly used for drug discovery, lead optimization, and target identification. It primarily focuses on capturing and curating bioactivity data and target information rather than enumerating chemical reactions.

Another type of VS libraries are combinatorial libraries which consist of related molecules systematically generated by altering structural scaffolds or through parallel synthesis methods. These libraries efficiently explore chemical space and save time in drug discovery and other applications. Scaffold hopping and reaction-based scheme are two common approaches to create such libraries, enabling the generation of structurally related compounds with potential variations in biological activity. By defining the main substituents that molecules should possess, combinatorial libraries

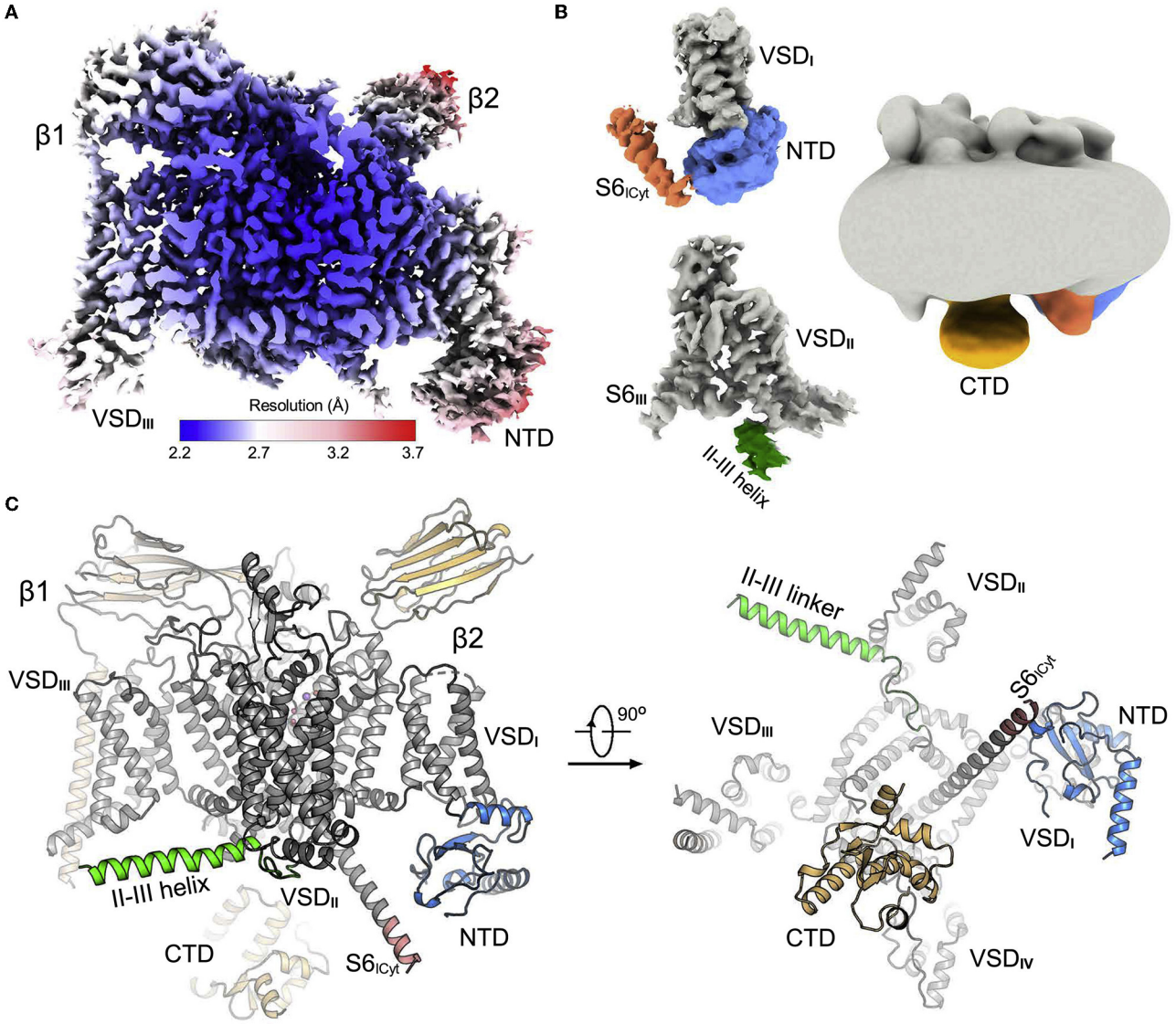

FIGURE 3
Cryo-EM structure of wild-type human $Na_V1.7$. **(A)** EM map of wild-type $Na_V1.7$-β1-β2 complex. **(B)** EM maps of previously unresolved cytosolic regions. **(C)** Structure of $Na_V1.7$-β1-β2 complex. The core domain is gray, previously unresolved regions are colored correspondingly to those in **(B)**. VSD, voltage-sensing domain; NTD, amino-terminal domain, CTD, carboxy-terminal domain. Reprinted (adapted) from Huang et al. (2022a). Copyright 2022, Elsevier.

can be generated by a scaffold mining with addition of these substituents to varying chemical cores (Varin et al., 2011; Hu et al., 2017). This approach is usually applied when a specific protein target is known and pharmacophoric elements are of importance for a potential drug to be active (Karthikeyan et al., 2015). The other way of generating combinatorial libraries involves defining a set of chemical reactions that should be followed in order to generate final molecules by connecting building blocks (Podlewska et al., 2017; Suay-García et al., 2022). Several pharmaceutical companies develop their own reaction-based combinatorial libraries, such as Eli Lilly's Proximal Collection (Nicolaou et al., 2016) and Pfizer global virtual library (Hu et al., 2012).

There are also ion channel-focused combinatorial libraries, like the IONCore library developed by ChemBridge (n.d.). This is an ion channel-focused library consisting of ca. 6000 small molecules, which were compiled based on 3D similarity to published compounds with activity against ion channels. SelleckChem developed an ion channel ligand library consisting of 745 small molecules to target a diverse set of ion channels (Ion Channel Ligand Library, n.d.). Furthermore, Enamine provides an ion channel-targeted library containing ca. 40,000 compounds, subdivided into collections for major ion channel families, e.g., the calcium ion channel library with 10,560 compounds and the sodium ion channel library with 5440 molecules, respectively (Ion Channel Library, n.d.).

Other commercial vendors provide chemical additional databases, e.g., MolPort (n.d.). MolPort aggregates compounds from various suppliers and contains ca. four million entities,

including molecules generated via combinatorial methods and reaction-based approaches.

Challenges of CADD on ion channels compared to soluble protein targets

CADD encounters distinctive challenges when targeting ion channels in comparison to soluble protein targets. The lipid membrane environment, in which ion channels reside, poses complexities in accurately predicting ion channel-ligand interactions due to the unique physicochemical properties of the membrane and additional interactions that are formed between the small molecule compound and lipids. Furthermore, the involvement of ion channels in regulating ion concentration gradients and changing the electrical field properties across the membrane emphasizes the significance of considering electrostatic interactions for modeling ligand binding. Additionally, the narrow and deep binding sites in ion channels, particularly in the pore region, present challenges in designing ligands that can efficiently navigate these confined spaces. This can be further complicated by the fact that ion channels switch between multiple conformational states during gating and that experimentally determined structures are available for only a handful of these states, also underscoring the intricacies of CADD in this context. Growing evidence from biophysical and structural investigations suggest association of many small-molecule drugs with the membrane-exposed surface of ion channels (Payandeh and Volgraf, 2021). The absence of a direct path from bulk solvent to the binding site entails an initial partitioning into the membrane, fundamentally shaping the drug's interaction with the protein target. This membrane access mechanism imparts a critical influence on potency data, structure-activity relationships, pharmacokinetics and physicochemical properties.

MD simulations can be an accurate method for simulating ion channel-ligand binding events within the membrane region (Gumbart et al., 2005; Goossens and De Winter, 2018), because the dynamic behavior of both the protein and the surrounding lipid bilayer can be explicitly modeled. While MD approaches can provide valuable insights, they are usually time-consuming, limiting their applicability to a small number of ligands. The intractability of MD for extensive ligand sets has led to the exploration of alternative techniques such as free energy perturbation (FEP) (Kuhn et al., 2020). In a recent study, Dickson et al. (2021), applied FEP to calculate the relative binding energies of a series of antagonists that target the lipid-exposed, extra-helical site of a membrane protein. By constructing an appropriate thermodynamic cycle, the authors were able to uncouple the membrane partitioning of the drug from the drug binding at the lipid-exposed site and could calculate the free energy for each step. Because of its promising performance the protocol might be applied in a predictive manner on larger datasets of ligands targeting protein-membrane interfaces. This approach holds potential for enhancing the efficiency and scalability of computational studies focused on membrane protein-ligand interactions.

The hydrophobic environment of the lipid bilayer poses a challenge for CADD due to its impact on the energetics of ligand binding. The dynamics of the lipid bilayer further complicates matters, influencing conformational changes in ion channels, which are crucial for their function. Incorporating these aspects into computational protocols presents a complex task, requiring ongoing computational protocol development and optimization of force fields. One such specialized protocol was devised within the Rosetta framework for the docking of cholesterol to integral membrane proteins (Marlow et al., 2023). The so-called RosettaCholesterol protocol, based on RosettaLigand (Meiler and Baker, 2006), adapts the sampling and scoring steps to improve docking of the cholesterol ligand and adds an additional filtering step to predict the cholesterol binding site specificity. The RosettaCholesterol protocol improved sampling and scoring of native poses over the RosettaLigand baseline in 91% of cases. Furthermore, the authors were able to recapitulate experimentally validated specific sites on the β2 adrenergic receptor. It proves to be a computationally fast and inexpensive tool that can screen many possible protein-cholesterol complexes. Future studies may further refine Rosetta-based protocols to explore a broader spectrum of lipid-protein interactions, paving the way for a more comprehensive understanding of membrane biology and protein-lipid dynamics.

Some lipids also have pharmacological effects and can be utilized to inform drug design. Notably, polyunsaturated fatty acids (PUFAs) can serve as signaling molecules with pharmacological effects, influencing cellular processes and modulating ion channels and inflammation (Xiao et al., 2005). Understanding the roles of bioactive lipids in cellular signaling informs the rational design of compounds targeting the protein-lipid surface. For example, Yazdi et al. (2021) studied PUFAs-modulated activation and mode of binding on KCNQ1 channels. Utilizing MD and electrophysiological experiments, they observed that PUFAs bind to the KCNQ1 voltage sensor and pore domain. The positively charged amino acid residues in these regions favorably stabilize the electronegative head group of PUFAs, while the tail group maintains the open position of KCNQ1 upon interaction with the hydrophobic residues. Different PUFA analogs produce a range of modulatory effects in ion channels (Bohannon et al., 2020a,b) which can be a useful information to guide the design of anti-epileptic and anti-arrhythmic drugs.

There exists still much uncertainty about the location of possible druggable sites in ion channels and new binding sites have been often discovered at unexpected locations (Wright et al., 2020; Sridhar et al., 2021; Botte et al., 2022; Kschonsak et al., 2023). Hence, methods that can accurately predict ligand binding sites on membrane proteins will significantly improve drug discovery. Lu et al. (2019) described a machine learning-based classifier tailored to the prediction of ligand binding sites on membrane protein surfaces. The MPLs-Pred method uses evolutionary profiles, topological features, physicochemical properties, and primary sequence segment descriptors as combined features in a random forest classifier. MPLs-Pred achieved an appreciable performance with Matthew's correlation coefficients of 0.597 and 0.356 on cross-validation and independent test sets, respectively. Ligand-specific predictive models that classify ligands into drugs, metal ions and

biomacromolecules further improved the prediction performance. Notably, the versatility inherent in the approach above suggests the potential for its extension to accommodate the prediction of various other ligand species.

The characteristics of ion channel binding sites, particularly the narrow and deep pores, requires molecules that can efficiently navigate and bind within these confined spaces. CaverDock, developed by Vavra et al. (2019), is a docking tool based on AutoDock Vina (Eberhardt et al., 2021) which can simulate the binding and unbinding of ligands to protein tunnels like ion channel pores. This tool uses the optimized docking algorithm of AutoDock Vina for ligand placement and implements a parallel heuristic algorithm to search the space of possible trajectories. In comparison with MD simulations, CaverDock does not require extensive knowledge of the studied system. CaverDock can sample the binding energy throughout the whole protein tunnel and identify unfavorable binding interactions, which can then be optimized by site-directed mutagenesis.

Ligand docking scoring functions used in CADD may be less accurate for membrane proteins because of the unique physicochemical environment of lipid membranes and because scoring functions have been usually optimized for soluble protein-ligand systems (Li et al., 2019; Rudden and Degiacomi, 2021), emphasizing the need for refinement and validation of scoring approaches tailored to ion channels. The presence of charged residues in the membrane surface region necessitates careful consideration of electrostatic interactions. Therefore, tuning the scoring function may involve emphasizing terms related to electrostatic forces, including charged interactions between the ligand and the protein. This is also observed in the hydrophobic deep membrane region, where the lipid bilayer provides a nonpolar environment, requiring adjustments of the solvation and electrostatic score terms. Unfortunately, the availability of tools tailored for ligand docking scoring functions is relatively limited, with a predominant focus on the development and benchmarking of ligand docking scoring functions for soluble receptors (Li et al., 2019). Very few docking programs have incorporated membrane scoring functions to address the challenges associated with modeling interactions at the protein-membrane interface. Usually these computational frameworks are intended for protein docking but can be adapted to ligand docking as well. MEMDOCK is an algorithm designed specifically for docking alpha-helical membrane proteins within the membrane. The method models both side chain and backbone flexibility and performs rigid body optimization of the ligand orientation using modified Patchdock and Fiberdock (Hurwitz et al., 2016). Furthermore, HADDOCK (Dominguez et al., 2003), LightDock (Jiménez-García et al., 2018), and Rosetta (Leman et al., 2020) also offer the possibility for protein and ligand docking in an implicit membrane model. Within the Schrödinger suite of tools, Glide (Halgren et al., 2004) and Desmond (Desmond Software, n.d.) allow for an integrated workflow in which researchers can first conduct MD simulations on membrane proteins using Desmond and subsequently transition the resulting structures to Glide for ligand docking experiments. This offers a holistic exploration of membrane protein dynamics and facilitates a detailed examination of ligand binding within the context of the lipid bilayer environment. While other common docking programs such as ZDOCK (Pierce et al., 2014) and AutoDock (Eberhardt et al., 2021) traditionally lack built-in membrane protein scoring functions for ligand binding, noteworthy adaptations and integrations have been introduced to enable their functionality in the context of docking ligands into transmembrane domains (Greene et al., 2016; Kobeissy Stanley M Stevens and editors, 2017). These modifications often involve specialized considerations for the hydrophobic and electrical properties of membrane environments.

Docking-based ultra-large virtual screening

In docking-based VS a panel of protein targets is screened with various molecular docking software to model the binding mode and interactions with small molecules in the binding pocket. The top-ranked small molecules are prioritized for further studies (Lazar et al., 2017). Software tools and platforms like AutoDock, DOCK, Glide, DiffDock, and Deep Docking (DD) facilitate high-throughput docking by employing diverse scoring functions and algorithms to predict compound binding affinity and orientation within the target's binding site (Kuntz et al., 1982; Halgren et al., 2004; Trott and Olson, 2009; Gentile et al., 2020; Corso et al., 2022).

Hughes et al. (2019) applied docking-based VS to discover new modulators of transient receptor potential vanilloid 5 (TRPV5) ion channels. TRPV5 is a calcium-selected ion channel, which plays an important role in renal calcium homeostasis in the human organism (Dang et al., 2019). TRPV5-knockout mice were shown to exhibit hypercalciuria and nephrolithiasis proving its critical role in calcium levels maintenance (De Groot et al., 2008). There are several existing TRPV5 modulators (Nilius et al., 2001; Hughes et al., 2018), but they lack selectivity over TRPV6 subtype, which is the closest homolog of TRPV5. In this regard, Hughes et al. (2019) conducted a VS experiment at the inhibitor binding site of TRPV5 utilizing the ZINC15 library with over 12 million molecules. The library was docked into TRPV5 using the Glide software package from the Schrödinger suite (Friesner et al., 2004), and top-100 best decoys were clustered into 65 groups with unique scaffolds based on the Tanimoto similarity score. 43 were proceeded to physiological testing by means of whole cell patch clamp experiments. Several compounds from this set were shown to inhibit TRPV5-induced currents, with two of them, ZINC9155420 and ZINC17988990, exhibiting additionally selectivity for TRPV5 over TRPV6. The authors also determined cryo-EM structures of these two ligands bound to the TRPV5 channels and identified new binding sites that provided insights into the ligand mode of specificity.

Wacker et al. (2012) studied heteromultimeric K_V channels in VS experiments. Particularly, K_V1.1–1.2 represents the most abundant potassium channel multimer in central and peripheral nervous systems (Coleman et al., 1999). K_V1.1–1.2 channels are highly expressed in the hippocampus and are an important target in epileptic seizures and multiple sclerosis (D'adamo et al., 2020). The known K_V1.1–1.2 inhibitor, 4-aminopyridine, however, has limited potency and also inhibits other K_V channels (K_V1.4, K_V4.2 subtypes), which compromises cardiac safety (Goodman et al., 2009, 2010). Wacker et al. (2012) conducted docking-based VS

with Autodock-Vina (Trott and Olson, 2009) on K_V1.1-1.2 using the ZINC library containing ∼10 million molecules. From 200 top scored compounds 89 compounds were tested using patch clamp experiments. Fourteen of 89 compounds showed some inhibitory activity ranging from 0.6 to 6 μM on K_V1.1–1.2 channels (compared to 4-aminopyridine with IC_{50} = 170 μM on K_V1.1 and IC_{50} = 230 μM on K_V1.2), and two of them also showed a higher potency toward inhibition of K_V1.1–1.2 in respect to other channels (hERG, Ca_V1.2, Na_V1.5).

Docking-based VS was also utilized in the study of Oddsson et al. (2020), aiming at identifying new dual target molecules against Alzheimer's disease, acting via nicotinic acetylcholine receptors (nAChRs). The same research group showed that a combination acetylcholinesterase (AChE) inhibitors and activators of nAChRs can lead to beneficial effects in the symptomatic treatment of Alzheimer's disease (Zoli et al., 2015; Kowal et al., 2019). The research group speculated that the increased activity of α7 nAChR, which is a ligand-gated ion channel, may improve treatment in Alzheimer's disease. Correspondingly, Oddsson et al. (2020) performed VS on both target proteins using the ZINC15 dataset with a total number of ∼four million compounds. All molecules were docked into AChE and nAChRs, and from the top-scored ligands in both proteins a common subset was selected that was encountered in both screening runs. One of the identified hit molecules showed the desirable inhibitory effect on AChE and agonistic activity on nAChR when evaluated in voltage-clamp electrophysiological testing. The identified compound represented the first example of a multitarget compound for the treatment of Alzheimer's disease.

Additional notable docking-based VS studies on ion channels include the discovery of small-molecule activators of the KCNQ1 channel (Liu et al., 2020; Lin et al., 2021) and of allosteric modulators of BK channels (Zhang et al., 2022a). All of these studies used the MDock docking software (Yan and Zou, 2015) and the Available Chemical Database (ACD) for screening. Interestingly, the identified compounds were found to affect their ion channel targets via different modes of action. The KCNQ1 activator molecule CP1 mimics the lipid PIP2 in mediation of voltage sensor-pore coupling and thereby enhances KCNQ1 activation (Liu et al., 2020). C28 is another KCNQ1 activator molecule but binds to and stabilizes the voltage sensor domain, thereby decreasing the voltage required for voltage-dependent KCNQ1 activation (Lin et al., 2021). The authors found that C28 can effectively reverse drug-induced lengthening of the action potential duration in ventricular myocytes. The small-molecule BK channel allosteric modulator BC5 binds at the voltage sensor-cytosolic tail domain interface and specifically enhances Ca^{2+}-dependent activation by perturbing the pathway for coupling between Ca^{2+} binding and pore opening (Zhang et al., 2022a). This mode of action was corroborated by mutagenesis and atomistic simulations and suggested that the interface between voltage sensor and cytosolic tail domain in BK channels is an important site for allosteric modulation.

Ultra-large VS requires fast algorithms that are able to predict the activity or binding affinity of billions of compounds in reasonable time. Deep Docking (DD), is a novel deep learning platform that is suitable for docking billions of molecular structures in a rapid, yet accurate fashion (Gentile et al., 2020). The DD approach employs sophisticated deep neural network models rooted in QSAR principles. These models are trained using docking scores from a small subset of a molecule library. The primary goal is to predict the docking results for new entries and iteratively exclude unfavorable molecules. By integrating the DD methodology with the FRED docking program, Gentile et al. achieved rapid and precise computation of docking scores for 1.36 billion molecules sourced from the ZINC15 library (Gentile et al., 2020). This extensive analysis covered 12 notable target proteins. Notably, this approach led to an impressive data reduction of up to 100-fold and a remarkable enrichment of high-scoring molecules by a factor of 6,000. Importantly, these advancements were attained without any substantial loss in the successful docking of molecules. The DD protocol can be seamlessly incorporated into many docking programs and is publicly available (Gentile et al., 2020).

In a recent study conducted by Yang et al. (2023), the researchers utilized deep docking-facilitated VS in conjunction with the VirtualFlow platform to screen ligands targeting the inward rectifier potassium channel 5.1 (Kir5.1, KCNJ16). VirtualFlow is a flexible and parallel workflow platform designed to execute VS tasks on Linux-based computer clusters of various sizes and types, all seamlessly managed by a batch system. The author's gene profiling and enrichment analyses revealed that KCNJ16 exhibited downregulation in thyroid tumor tissues compared to normal ones, implicating a pivotal role for KCNJ16 in cell growth and differentiation. Consequently, Kir5.1, encoded by KCNJ16, emerged as an appealing target in thyroid cancer research. To narrow down their selection of compounds, Yang et al. employed the DD protocol and executed the final docking run using VirtualFlow. They relied on the AlphaFold predicted structure of Kir5.1 for docking. Employing the DD protocol, the authors identified several molecules, including Z2087256678_2, Z2211139111_1, Z2211139111_2, and PV-000592319198_1, as potent ligands for Kir5.1. Unfortunately, the computationally identified hit molecules were not further tested and, therefore, should be regarded as suggestive.

V-SYNTHES (virtual synthon hierarchical enumeration screening), developed by Sadybekov et al., represents another approach aimed at efficiently screening ultra-large compound libraries for potential hit compounds using a modular synthon-based strategy (Sadybekov et al., 2022). Essentially, a synthon represents a fragment of a molecule that can be used as a building block for synthesizing more complex molecules. In this pioneering study, the algorithm enabled efficient screening of the Enamine REAL library and its REAL Space extension containing over 11 billion drug-like compounds.

V-SYNTHES involves several iterative steps (Figure 4), starting with the creation of a fragment-like compound library representing all possible scaffold-synthon combinations. In the first step, compounds are constructed by combining reaction scaffolds with corresponding synthons at one position, while other positions are capped. Capping refers to the process of modifying or blocking certain positions on a molecule while allowing chemical reactions to occur at specific, chosen positions. This results in a library of ∼600,000 compounds, corresponding to the number of synthons. In the second step, docking simulations are used to predict the binding affinity of these fragments to a target protein. The

top-scoring candidates (1,000–10,000) undergo further rounds of enumeration and docking in steps three and four. The final set of 50–100 compounds for experimental testing is selected based on post-processing filters e.g., synthesizability.

In the original V-SYNTHES paper (Sadybekov et al., 2022), the Enamine REAL Space library was screened for cannabinoid receptor antagonists using a receptor-template-based approach. V-SYNTHES significantly accelerated the screening process, requiring docking of only ca. 2 million compounds, while screening a much larger chemical space. Furthermore, V-SYNTHES outperformed traditional brute force VS approaches by identifying more high-scoring compounds. The approach yielded 80 hit candidates, with 60 synthesized and functionally characterized. Notably, 33% of these hits had K_i values better than 10 μM. This hit rate was twice as high as the hit rate achieved in standard docking of a representative subset of the Enamine REAL library.

The hit compounds showed diverse structures, containing new scaffolds and fully occupying the receptor's orthosteric binding pocket. Application of V-SYNTHES to the kinase target ROCK1 also led to successful results, with a 28.5% hit rate containing compounds with nanomolar affinity. Overall, V-SYNTHES provides a practical and efficient method for rapidly screening ultra-large modular virtual libraries. It can be adapted to various docking-based screening platforms and applied to ion channels and other target proteins, which demonstrates the broad applicability of the method in drug discovery efforts.

Ligand-based virtual screening

Ligand-based VS techniques play a crucial role in the field of ion channel drug discovery by aiding in the identification of potential compounds that could modulate ion channel activity. Ligand-based VS focuses on identifying molecules with structural and chemical properties similar to known ion channel modulators. This approach is particularly useful when experimental structural information about the target ion channel is limited or unavailable. The ligand-based methods include approaches like similarity and substructure searching, QSAR modeling, pharmacophore-based search, and 3D shape matching supported by machine learning and molecular modeling techniques.

Ligand-based VS enables the efficient exploration of large compound databases, identifying molecules that exhibit potential ion channel modulatory effects. This approach helps prioritize compounds for experimental testing, reducing the time and resources required in early stages of drug discovery. Overall, ligand-based VS techniques complement experimental approaches in ion channel drug discovery and contribute significantly to the identification of novel therapeutic candidates targeting ion channels, potentially leading to the development of innovative treatments for various diseases (Sharma et al., 2021).

Ijjaali et al. (2007) focused on the use of ligand-based VS techniques for the discovery of novel T-type calcium channel inhibitors. T-type calcium channels are implicated in various neural disorders such as epilepsy and neuropathic pain. To identify new inhibitors, the researchers employed a pharmacophore-based VS approach using 2D pharmacophoric fingerprints. They collected a dataset of known active compounds from the AurSCOPE Ion Channels knowledgebase (AurSCOPE Ion Channel Database, n.d.), which was used as a query to screen an external molecular database. A total of 38 compounds were selected for biological evaluation, and functional patch clamp assays were conducted on the $Ca_V3.2$ isoform. Interestingly, 16 out of the 38 compounds showed more than 50% blockade of $Ca_V3.2$-mediated T-type current. These findings demonstrate the effectiveness of ligand-based VS in identifying potential T-type calcium channel inhibitors for further investigation in drug discovery efforts.

Mohan et al. conducted a study aiming to identify compounds with N-type calcium channel blocking activity (Mungalpara et al., 2010). They utilized multiple descriptors such as structure, ADME/Tox, thermodynamics, and electrotopological properties to train a QSAR model for predicting blocking activity. The resultant descriptors offered insights into the physico-chemical attributes influencing N-type calcium channel blocking activity.

The team led by Noskov evaluated a collection of hERG pore domain blockers through a combination of 3D-QSAR and receptor-based molecular docking techniques (Durdagi et al., 2011). They also designed a pharmacophore model that enabled swift assessment of compound channel-blocking capability. The outcomes were corroborated by docking hits into a hERG homology model and through *in silico* mutagenesis, aligning closely with experimental data.

Pharmacophore-based screening methods represent another powerful approach for ligand-based VS. Pharmacophore models represent the critical chemical features of the ligand molecule and their spatial arrangement required for compound-target interactions. These methods can swiftly search large chemical databases for compounds that conform to the pharmacophoric constraints of the target (Urbahns et al., 2003; Dror et al., 2009; Seidel et al., 2010; Giordano et al., 2022). Pharmacophore-based screening is particularly useful when the protein target structure is challenging to obtain (Kaserer et al., 2015; Schaller et al., 2020).

Sehgal et al. (2014) performed pharmacophore-based screening experiments to identify inhibitors of the potassium channel subfamily K member 18 (KCNK18). KCNK18 is one of the determinant factors of migraine-associated pain. A large number of mutations in the KCNK18 gene exist that are associated with excessive neuronal excitability and severe headaches (Grangeon et al., 2023). Sehgal et al. (2014) used pharmacophore models created based on other anti-migraine drugs and the LigandScout tool (Wolber and Langer, 2005) to screen the ZINC database and two other custom-made compound libraries for new KCNK18 inhibitors. The top-ranked compounds were subsequently analyzed using docking with the AutoDock software (Trott and Olson, 2009; Eberhardt et al., 2021), and the top four molecules were chosen for further assessment in binding experiments. Based on docking and drug likeness analysis, newly identified compounds (PB-408318540, PB-415019010, PB-414901730, PB-414901692) were proposed as potential drug molecules to target KCNK18, opening up a therapeutic option for the treatment of migraine occurrences.

In another study, Krueger et al. (2009) tested various ligand-based VS procedures to discover new hits for the N-Methyl-D-Aspartate (NMDA) receptor. NMDA receptor is an ion channel that is found in neurons and activated upon binding

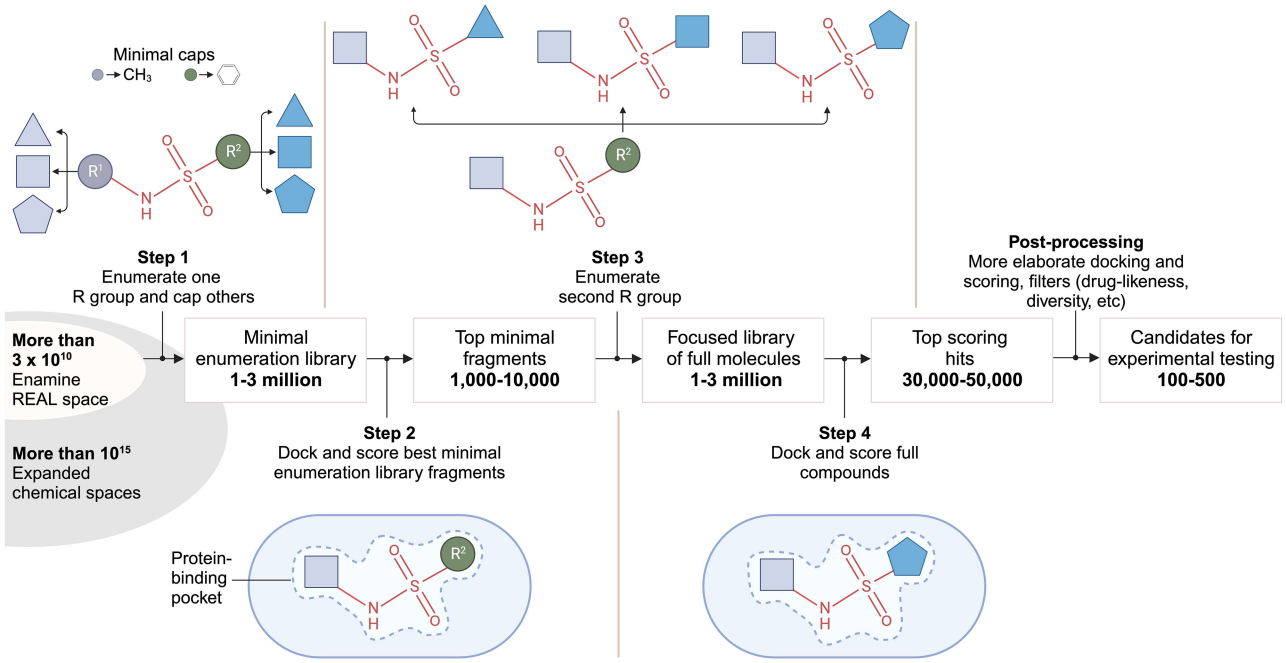

FIGURE 4
V-SYNTHES approach to modular screening of Enamine REAL Space. The flow chart from left to right provides a broad outline of the 4-step algorithm developed by Sadybekov et al. (2022).

of glutamate and glycine. Both the hypo- and hyperfunctioning of NMDA is involved in various neurodegenerative diseases, such as schizophrenia, Parkinson's disease, and Alzheimer's disease (Lin and Lane, 2019). The glycine binding site of the NMDA receptor represents a promising strategy for inhibitor design (Parsons, 2001). Thus, after analyzing all commercially available compound libraries, Krueger et al. (2009) obtained ~4.6 million molecules to screen against the NMDA receptor's glycine site. The authors used 2D and 3D descriptors for screening as well as ligand docking with Glide SP (Friesner et al., 2004) and Glide XP (Friesner et al., 2006), pharmacophore-based and QSAR-based models, and 3D shape search strategies. From each method 500 molecules were extracted, and 201 of them proceeded into *in vitro* testing. While most of the newly identified molecules exhibited a low activity in the micromolar range, all the applied methods were able to derive compounds with novel scaffolds and a high percentage of true actives.

Ion channel researchers have also harnessed machine learning techniques during the early stages of analgesic discovery. This includes identifying novel genes and pathways linked to both acute and chronic pain (Chidambaran et al., 2020), as well as predicting inhibitors for the $Na_V1.7$ sodium channel, an important target for the treatment of pain. To simplify the prediction of novel multi-target analgesics or drug combinations for pain management, an extensive pain-focused chemogenomics knowledge base has been established. This comprehensive resource incorporates existing analgesics, the 3D structures of pain-related targets, and compounds associated with these target proteins (Kong et al., 2020).

Virtual drug discovery with deep generative models

Deep learning is not only used for speeding up VS methods, but is also a driver for the field of generative drug design (also referred to as de novo drug design). In generative drug design, novel chemical molecules with desired chemical and biological properties are generated from scratch, aiming to find new bioactive and synthesizable molecules in a time- and cost-efficient manner. Briefly, the essence of a generative model is to learn the distribution of molecules presented in a training set and generate new molecules for one or multiple targets which are different from those in the training set (Zeng et al., 2022). Combined with evolutionary algorithms or reinforcement learning, the properties of the generated molecules can be further optimized to satisfy different design objectives (Tan et al., 2022). Generative drug design is a relatively new field but could offer advantages compared to conventional VS with regard to the time and cost required for navigating the large chemical space. In a remarkable study by Zhavoronkov et al. (2019) deep generative drug design enabled the discovery of novel potent small molecule inhibitors of the discoidin domain receptor 1 (DDR1) with nanomolar inhibitory efficacy in only 21 days.

The representation of molecules employed by the generative model can be in many forms (David et al., 2020). Many methods use the Simplified Molecular Input Line Entry System (SMILES) (Weininger, 1988) to represent molecules as sequence of characters. From the sequences of SMILES characters as input, language processing neural networks such as recurrent neural networks (RNNs) learn to predict one character at a time, based on the

proceeding portion of the sequence and a probability distribution. From the learnt probability distribution new SMILES strings can be sampled (Gupta et al., 2018). However, this approach has one or more limitations. The generated SMILES may not represent a chemically feasible structure, and even a single character change in a SMILES code can change the underlying molecular structure significantly. To overcome these limitations, approaches using graph-based (Li et al., 2018; Xia et al., 2019) and 3D molecule representations (Xie et al., 2022) have been developed. In addition to RNNs (Gupta et al., 2018; Segler et al., 2018), other generative design algorithms include variational autoencoder (VAE) (Gómez-Bombarelli et al., 2018), generative adversarial network (GAN) (Abbasi et al., 2022), transformer models (Liu et al., 2023), and generative models combined with reinforcement learning (RL) (Popova et al., 2018; Liu et al., 2021; Govinda Bhisetti, 2022).

Since drug-likeness and synthetic accessibility are critical parameters that decide about the success of drug candidates, generative models have been trained to yield molecules with specific properties. For example, RL with policy gradient for forward synthesis (PGFS) was proposed as a method to generate molecules that can be feasibly synthesized (Krishna Gottipati et al., 2020). Furthermore, RationaleRL is a graph-based RL model that tries to optimize a multi-objective target function, including properties such as bioactivity against multiple proteins, drug-likeness, and synthetic accessibility (Jin et al., 2020).

The application of deep generative drug design to ion channels is still in its infancy. Schultz et al. (2021) reported the use of deep generative models to design novel antagonists targeting the phencyclidine (PCP) site of the N-methyl D-aspartate receptor (NMDAR). NMDAR antagonists have demonstrated therapeutic benefit in the treatment of neurological diseases such as Parkinson's and Alzheimer's disease (Liu et al., 2019). The authors applied a VAE-based method, called DarkChem (Colby et al., 2020), for NMDAR antagonist design and developed a library of potential NMDAR PCP site-targeting molecules. From ~200,000 compounds designed by DarkChem, 12 novel compounds were found that passed all subsequent *in silico* filtering techniques, including ligand docking, ADMET and synthesizability predictions, drug-likeness filter, substructure and similarity analyses, and were not available in existing public chemical databases. This study provided an example of what generative drug design on ion channels can achieve, although chemical synthesis and experimental validation of the AI-generated compounds were not performed.

To better meet the requirements of drug discovery, deep drug design models are able to consider multiple design objectives. Liu et al. (2021) demonstrated a RNN- and RL-based algorithm, DrugEx, which achieves multi-objective molecule optimization to generate molecules which are active toward one or multiple specific targets while avoiding off-target effects with other proteins. DrugEx was tested for the generation of molecules that should have high affinity for adenosine receptor subtypes A_1 and A_{2A} but low or zero affinity for the hERG potassium ion channel. Because drug-induced blockage of the hERG ion channel can lead to severe cardiotoxicity,

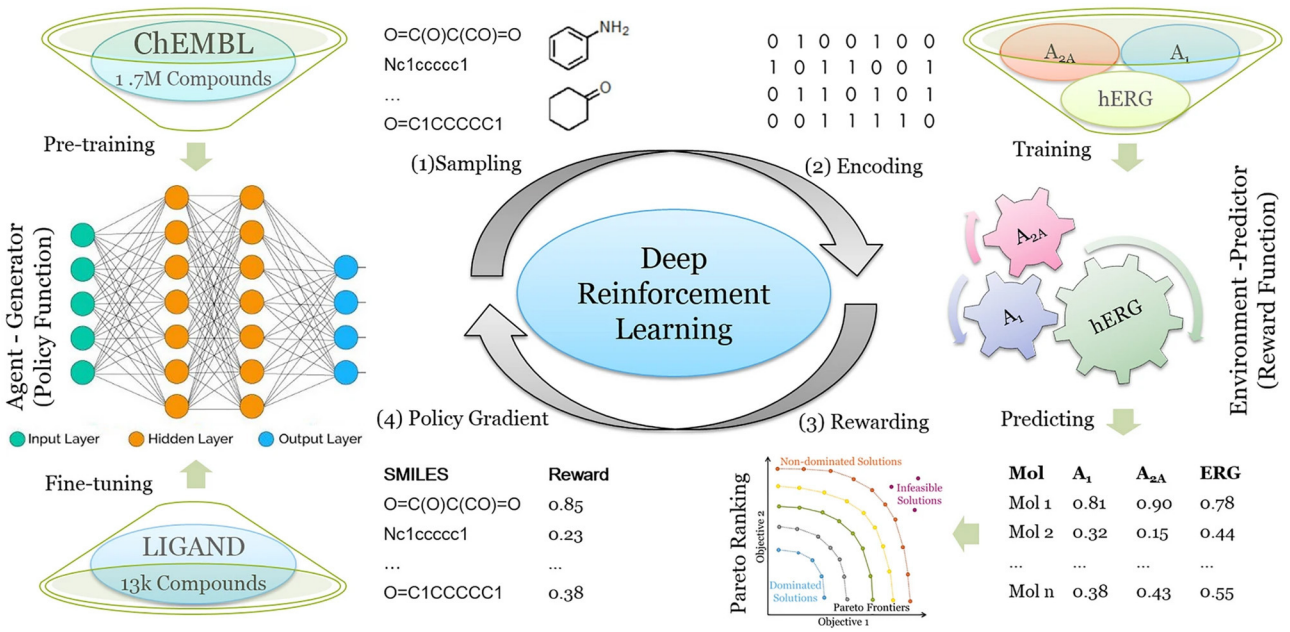

FIGURE 5
Workflow of the DrugEx method for designing molecules with selectivity to A_1 and A_{2A} adenosine receptors but no affinity for hERG. (1) New molecules are sampled as SMILES based on the probability calculated by the RNN-based agent generator. (2) The SMILES are encoded into descriptors and their affinity for A_1, A_{2A} and hERG is predicted. (3) The predicted affinities are transformed into a single value as the reward for each molecule based on Pareto optimization. (4) For training the generative model, the SMILES and their rewards are sent back to the generator. Steps (1) to (4) are repeated until convergence of the training process is reached. Reproduced from Liu et al. (2021) under permission of Creative Commons Attribution 4.0 International License (http://creativecommons.org/licenses/by/4.0/).

which has been one of the most common reasons for the withdrawal of drugs from the market, hERG toxicity assessment methods have been implemented in the early stages of drug discovery. In the conceptualization of DrugEx, the authors used an RNN as the agent and several machine learning prediction models as environment which operate together in the RL framework. The reward of each molecule is calculated from the Pareto ranking obtained by considering the ML scores for all objectives in the environment as well as a metric representing molecule chemical diversity (Figure 5). The molecules generated by DrugEx covered a larger chemical space compared to other drug design methods and bore some similarity to known adenosine receptor ligands. The approach can be relevant also for developing more selective ion channel modulators.

Molecule design with deep generative models has brought new momentum for drug discovery. If constantly improved and further developed, these methods may be increasingly used for ion channel drug discovery. However, current bottlenecks of AI technologies, such as lack of availability of high-quality data and limited interpretability of the model, currently restrict their application and affect their performance.

Conclusion and perspective

The integration of computational methods such as VS and deep learning holds great promise in revolutionizing the landscape of drug discovery. These methods, by augmenting traditional experimental high-throughput screening (HTS) techniques, offer a multifaceted approach to drug development. VS techniques, including hit expansion, scaffold hopping, and exploration of uncharted chemical space, demonstrate the potential to uncover novel lead compounds that might have been overlooked within conventional screening libraries. Additionally, the predictive power of computational methods in estimating essential pharmacokinetic and toxicological properties facilitates early identification of promising candidates, significantly streamlining the drug discovery pipeline.

While computational methods offer remarkable insights, it is crucial to acknowledge their synergy with experimental HTS methods. The amalgamation of computational and physical screening tests enriches our understanding of compound behavior in complex biological systems. Physical tests provide indispensable data, especially in relevant biological contexts, aiding in the assessment of properties such as absorption, distribution, metabolism, excretion, and toxicity (ADMET), which remain challenging to simulate accurately computationally.

The continuous evolution of computational techniques prompts us to consider the future of drug discovery. While computational simulations are powerful tools offering valuable insights, they are not yet poised to entirely replace traditional physical screening tests. Instead, the synergy between computational and experimental methods represents the most potent approach. Combining computational and experimental approaches in an iterative and integrative manner often leads to the most effective and comprehensive results. As computational methods advance, the question arises: will they eventually supplant or significantly reduce the need for conventional physical screening tests? This intriguing prospect awaits further exploration, marking an exciting chapter in the ongoing narrative of scientific progress in drug discovery.

Author contributions

KM: Writing—original draft, Writing—review & editing. PP: Writing—original draft, Writing—review & editing. JM: Writing—review & editing. GK: Writing—review & editing.

Funding

The author(s) declare financial support was received for the research, authorship, and/or publication of this article. JM acknowledges funding by the Deutsche Forschungsgemeinschaft (DFG) through SFB1423 (421152132), SFB 1052 (209933838), and SPP 2363 (460865652) and by the National Institutes of Health (grant numbers R01 DA046138, R01 HL122010, and R01 GM080403). JM was further supported by a Humboldt Professorship of the Alexander von Humboldt Foundation and by the BMBF (Federal Ministry of Education and Research) through the Center for Scalable Data Analytics and Artificial Intelligence (ScaDS.AI). This work was partly supported by the BMBF through DAAD project 57616814 (SECAI, School of Embedded Composite AI). GK acknowledges funding by the DFG through TRR-386 (subprojects A2 and B2) and by the BMBF through ScaDS.AI.

Acknowledgments

The authors acknowledge support from the German Research Foundation (DFG) and Universität Leipzig within the program of Open Access Publishing.

Conflict of interest

The authors declare that the research was conducted in the absence of any commercial or financial relationships that could be construed as a potential conflict of interest.

Publisher's note

References

Abbasi, M., Santos, B. P., Pereira, T. C., Sofia, R., Monteiro, N. R. C., Simões, C. J. V., et al. (2022). Designing optimized drug candidates with Generative Adversarial Network. *J. Cheminform.* 14. doi: 10.1186/s13321-022-00623-6

AurSCOPE Ion Channel Database (n.d.). Available online at: https://www.aureus-pharma.com (accessed October 27, 2023).

Baek, M., DiMaio, F., Anishchenko, I., Dauparas, J., Ovchinnikov, S., Lee, G. R., et al. (2021). Accurate prediction of protein structures and interactions using a three-track neural network. *Science (1979).* 373, 871–876. doi: 10.1126/science.abj8754

Bohannon, B. M., de la Cruz, A., Wu, X., Jowais, J. J., Perez, M. E., Liin, S. I., et al. (2020a). Polyunsaturated fatty acid analogues differentially affect cardiac nav, cav, and kv channels through unique mechanisms. *Elife* 9, e51453. doi: 10.7554/eLife.51453

Bohannon, B. M., Wu, X., Wu, X., Perez, M. E., Liin, S. I., and Peter Larsson, H. (2020b). Polyunsaturated fatty acids produce a range of activators for heterogeneous IKs channel dysfunction. *J. General Physiol.* 152, 12396. doi: 10.1085/jgp.201912396

Botte, M., Huber, S., Bucher, D., Klint, J. K., Rodríguez, D., Tagmose, L., et al. (2022). Apo and ligand-bound high resolution Cryo-EM structures of the human Kv3.1 channel reveal a novel binding site for positive modulators. *PNAS Nexus* 1, 83. doi: 10.1093/pnasnexus/pgac083

Cannon, S. C. (2007). Physiologic principles underlying ion channelopathies. *Neurotherapeutics* 4, 174–183. doi: 10.1016/j.nurt.2007.01.015

ChemBridge (n.d.). Available online at: https://chembridge.com (accessed October 27, 2023).

Chen, G. L., Li, J., Zhang, J., and Zeng, B. (2023). To be or not to be an ion channel: cryo-EM structures have a say. *Cells* 12. doi: 10.3390/cells12141870

Chidambaran, V., Ashton, M., Martin, L. J., and Jegga, A. G. (2020). Systems biology-based approaches to summarize and identify novel genes and pathways associated with acute and chronic postsurgical pain. *J. Clin. Anesth.* 62. doi: 10.1016/j.jclinane.2020.109738

Colby, S. M., Nuñez, J. R., Hodas, N. O., Corley, C. D., and Renslow, R. R. (2020). Deep learning to generate *in silico* chemical property libraries and candidate molecules for small molecule identification in complex samples. *Anal. Chem.* 92, 1720–1729. doi: 10.1021/acs.analchem.9b02348

Coleman, S. K., Newcombe, J., Pryke, J., and Dolly, J. O. (1999). Subunit composition of Kv1 channels in human CNS. *J. Neurochem.* 73, 849–858. doi: 10.1046/j.1471-4159.1999.0730849.x

Corso, G., Stärk, H., Jing, B., Barzilay, R., and Jaakkola, T. (2022). DiffDock: diffusion steps, twists, and turns for molecular docking. *arXiv[Preprint]. arXiv:* 2210.01776. doi: 10.48550/arXiv.2210.01776

D'adamo, M. C., Liantonio, A., Rolland, J. F., Pessia, M., and Imbrici, P. (2020). Kv1.1 channelopathies: pathophysiological mechanisms and therapeutic approaches. *Int. J. Mol. Sci.* 21, 2935. doi: 10.3390/ijms21082935

Dang, S., Van Goor, M. K., Asarnow, D., Wang, Y. Q., Julius, D., Cheng, Y., et al. (2019). Structural insight into TRPV5 channel function and modulation. *Proc. Natl. Acad. Sci. USA.* 116, 8869–8878. doi: 10.1073/pnas.1820323116

David, L., Thakkar, A., Mercado, R., and Engkvist, O. (2020). Molecular representations in AI-driven drug discovery: a review and practical guide. *J. Cheminform.* 12, 5. doi: 10.1186/s13321-020-00460-5

De Groot, T., Bindels, R. J. M., and Hoenderop, J. G. J. (2008). TRPV5: An ingeniously controlled calcium channel. *Kidney Int.* 74, 1241–1246. doi: 10.1038/ki.2008.320

Desmond Software (n.d.). Available online at: https://www.schrodinger.com/products/desmond (accessed November 28, 2023).

Dickson, C. J., Hornak, V., and Duca, J. S. (2021). Relative binding free-energy calculations at lipid-exposed sites: deciphering hot spots. *J. Chem. Inf. Model.* 61, 5923–5930. doi: 10.1021/acs.jcim.1c01147

Doak, B. C., Norton, R. S., and Scanlon, M. J. (2016). The ways and means of fragment-based drug design. *Pharmacol. Ther.* 167, 28–37. doi: 10.1016/j.pharmthera.2016.07.003

Dominguez, C., Boelens, R., and Bonvin, A. M. J. J. (2003). HADDOCK: a protein-protein docking approach based on biochemical or biophysical information. *J. Am. Chem. Soc.* 125, 1731–1737. doi: 10.1021/ja026939x

Doyle, D. A., Cabral, M., Pfuetzner, R. A., Kuo, A., Gulbis, J. M., Cohen, S. L., et al. (1998). The structure of the potassium channel: molecular basis of K+ conduction and selectivity. *Science* 280, 1–9. doi: 10.1126/science.280.5360.69

Dror, O., Schneidman-Duhovny, D., Inbar, Y., Nussinov, R., and Wolfson, H. J. (2009). Novel approach for efficient pharmacophore-based virtual screening: method and applications. *J. Chem. Inf. Model.* 49, 2333–2343. doi: 10.1021/ci900263d

Durdagi, S., Duff, H. J., and Noskov, S. Y. (2011). Combined receptor and ligand-based approach to the universal pharmacophore model development for studies of drug blockade to the hERG1 pore domain. *J. Chem. Inf. Model.* 51, 463–474. doi: 10.1021/ci100409y

Eberhardt, J., Santos-Martins, D., Tillack, A. F., and Forli, S. (2021). AutoDock vina 1.2.0: new docking methods, expanded force field, and python bindings. *J. Chem. Inf. Model.* 61, 3891–3898. doi: 10.1021/acs.jcim.1c00203

Ekins, S., Mestres, J., and Testa, B. (2007). *In silico* pharmacology for drug discovery: Applications to targets and beyond. *Br. J. Pharmacol.* 152, 21–37. doi: 10.1038/sj.bjp.0707306

eMolecules (n.d.). Available online at: https://www.emolecules.com (accessed October 27, 2023).

Enamine (n.d.). Available online at: https://enamine.net (accessed October 27, 2023).

Etkins, S. (2018). *Computational Toxicology: Risk Assessment for Chemicals.* Hoboken: John Wiley and Sons. doi: 10.1002/9781119282594

Ford, J., Milnes, J., El Haou, S., Wettwer, E., Loose, S., Matschke, K., et al. (2016). The positive frequency-dependent electrophysiological effects of the IKur inhibitor XEN-D0103 are desirable for the treatment of atrial fibrillation. *Heart Rhythm* 13, 555–564. doi: 10.1016/j.hrthm.2015.10.003

Friesner, R. A., Banks, J. L., Murphy, R. B., Halgren, T. A., Klicic, J. J., Mainz, D. T., et al. (2004). Glide: a new approach for rapid, accurate docking and scoring. 1. method and assessment of docking accuracy. *J. Med. Chem.* 47, 1739–1749. doi: 10.1021/jm0306430

Friesner, R. A., Murphy, R. B., Repasky, M. P., Frye, L. L., Greenwood, J. R., Halgren, T. A., et al. (2006). Extra precision glide: Docking and scoring incorporating a model of hydrophobic enclosure for protein-ligand complexes. *J. Med. Chem.* 49, 6177–6196. doi: 10.1021/jm051256o

Gaulton, A., Bellis, L. J., Bento, A. P., Chambers, J., Davies, M., Hersey, A., et al. (2012). ChEMBL: A large-scale bioactivity database for drug discovery. *Nucleic Acids Res.* 40. doi: 10.1093/nar/gkr777

Gentile, F., Agrawal, V., Hsing, M., Ton, A. T., Ban, F., Norinder, U., et al. (2020). Deep docking: a deep learning platform for augmentation of structure based drug discovery. *ACS Cent. Sci.* 6, 939–949. doi: 10.1021/acscentsci.0c00229

Gentile, F., Yaacoub, J. C., Gleave, J., Fernandez, M., Ton, A. T., Ban, F., et al. (2022). Artificial intelligence–enabled virtual screening of ultra-large chemical libraries with deep docking. *Nat. Protoc.* 17, 672–697. doi: 10.1038/s41596-021-00659-2

Gimeno, A., Ojeda-Montes, M. J., Tomás-Hernández, S., Cereto-Massagué, A., Beltrán-Debón, R., Mulero, M., et al. (2019). The light and dark sides of virtual screening: what is there to know? *Int. J. Mol. Sci.* 20. doi: 10.3390/ijms20061375

Giordano, D., Biancaniello, C., Argenio, M. A., and Facchiano, A. (2022). Drug design by pharmacophore and virtual screening approach. *Pharmaceuticals* 15, 646. doi: 10.3390/ph15050646

Gómez-Bombarelli, R., Wei, J. N., Duvenaud, D., Hernández-Lobato, J. M., Sánchez-Lengeling, B., Sheberla, D., et al. (2018). Automatic chemical design using a data-driven continuous representation of molecules. *ACS Cent. Sci.* 4, 268–276. doi: 10.1021/acscentsci.7b00572

Goodman, A. D., Brown, T. R., Edwards, K. R., Krupp, L. B., Schapiro, R. T., Cohen, R., et al. (2010). A phase 3 trial of extended release oral dalfampridine in multiple sclerosis. *Ann. Neurol.* 68, 494–502. doi: 10.1002/ana.22240

Goodman, A. D., Brown, T. R., Krupp, L. B., Schapiro, R. T., Schwid, S. R., Cohen, R., et al. (2009). Sustained-release oral fampridine in multiple sclerosis: a randomised, double-blind, controlled trial. *Lancet* 373, 732–738. doi: 10.1016/S0140-6736(09)60442-6

Goossens, K., and De Winter, H. (2018). Molecular dynamics simulations of membrane proteins: an overview. *J. Chem. Inf. Model.* 58, 2193–2202. doi: 10.1021/acs.jcim.8b00639

Gorgulla, C., Boeszoermenyi, A., Wang, Z. F., Fischer, P. D., Coote, P. W., Padmanabha Das, K. M., et al. (2020). An open-source drug discovery platform enables ultra-large virtual screens. *Nature* 580, 663–668. doi: 10.1038/s41586-020-2117-z

Govinda Bhisetti, C. F. (2022). Artificial intelligence-enabled de novo design of novel compounds that are synthesizable. *Meth. Mol. Biol.* 2390, 409–419. doi: 10.1007/978-1-0716-1787-8_17

Grangeon, L., Lange, K. S., Waliszewska-Prosół, M., Onan, D., Marschollek, K., Wiels, W., et al. (2023). Genetics of migraine: where are we now? *J. Headache Pain* 24, 8. doi: 10.1186/s10194-023-01547-8

Greene, D., Botello-Smith, W. M., Follmer, A., Xiao, L., Lambros, E., and Luo, R. (2016). Modeling membrane protein-ligand binding interactions: the human purinergic platelet receptor. *J. Physi. Chemi. B* 120, 12293–12304. doi: 10.1021/acs.jpcb.6b09535

Grygorenko, O. O., Radchenko, D. S., Dziuba, I., Chuprina, A., Gubina, K. E., and Moroz, Y. S. (2020). Generating multibillion chemical space of readily

accessible screening compounds. *iScience* 23, 101681. doi: 10.1016/j.isci.2020.101681

Gumbart, J., Aksimentiev, A., Tajkhorshid, E., Wang, Y., and Schulten, K. (2005). Molecular dynamics simulations of proteins in lipid bilayers. *Curr. Opin. Struct. Biol.* 15, 423–431. doi: 10.1016/j.sbi.2005.07.007

Gupta, A., Müller, A. T., Huisman, B. J. H., Fuchs, J. A., Schneider, P., and Schneider, G. (2018). Generative recurrent networks for de novo drug design. *Mol. Inform.* 37. doi: 10.1002/minf.201700111

Halgren, T. A., Murphy, R. B., Friesner, R. A., Beard, H. S., Frye, L. L., Pollard, W. T., et al. (2004). Glide: a new approach for rapid, accurate docking and scoring. 2. Enrichment factors in database screening. *J. Med. Chem.* 47, 1750–1759. doi: 10.1021/jm030644s

Hameed, S. (2019). Nav1.7 and Nav1.8: role in the pathophysiology of pain. *Mol. Pain* 15, 1744806919858801. doi: 10.1177/1744806919858801

Hansch, C., and Fujita, T. (1964). p-σ-π Analysis. A method for the correlation of biological activity and chemical structure. *J. Am. Chem. Soc.* 86, 1616–1626. doi: 10.1021/ja01062a035

Hu, Q., Peng, Z., Sutton, S. C., Na, J., Kostrowicki, J., Yang, B., et al. (2012). Pfizer global virtual library (PGVL): a chemistry design tool powered by experimentally validated parallel synthesis information. *ACS Comb. Sci.* 14, 579–589. doi: 10.1021/co300096q

Hu, Y., Stumpfe, D., and Bajorath, J. (2017). Recent advances in scaffold hopping. *J. Med. Chem.* 60, 1238–1246. doi: 10.1021/acs.jmedchem.6b01437

Huang, G., Liu, D., Wang, W., Wu, Q., Chen, J., Pan, X., et al. (2022a). High-resolution structures of human Nav1.7 reveal gating modulation through α-π helical transition of S6IV. *Cell Rep.* 39. doi: 10.1016/j.celrep.2022.110735

Huang, L., Bai, J., Zong, R., Zhou, J., Zuo, Z., Chai, X., et al. (2022b). Sodium MRI at 7T for early response evaluation of intracranial tumors following stereotactic radiotherapy using the cyberknife. *Am. J. Neuroradiol.* 43, 181–187. doi: 10.3174/ajnr.A7404

Hughes, T. E. T., Pumroy, R. A., Yazici, A. T., Kasimova, M. A., Fluck, E. C., Huynh, K. W., et al. (2018). Structural insights on TRPV5 gating by endogenous modulators. *Nat. Commun.* 9, 6. doi: 10.1038/s41467-018-06753-6

Hughes, T. E. T., Rosario, J. S., Del, K. A., Yazici, A. T., Yudin, Y., Fluck, E. C., et al. (2019). Structure-based characterization of novel TRPV5 inhibitors. *Elife* 8, 1–21. doi: 10.7554/eLife.49572

Hurwitz, N., Schneidman-Duhovny, D.i., and Wolfson, H. J. (2016). Memdock: an α-helical membrane protein docking algorithm. *Bioinformatics* 32, 2444–2450. doi: 10.1093/bioinformatics/btw184

Hutchings, C. J., Colussi, P., and Clark, T. G. (2019). Ion channels as therapeutic antibody targets. *MAbs* 11, 265–296. doi: 10.1080/19420862.2018.1548232

Ijjaali, I., Barrere, C., Nargeot, J., Petitet, F., and Bourinet, E. (2007). Ligand-based virtual screening to identify new T-type calcium channel blockers. *Channels* 1, 300–304. doi: 10.4161/chan.4999

Imbrici, P., Liantonio, A., Camerino, G. M., De Bellis, M., Camerino, C., Mele, A., et al. (2016). Therapeutic approaches to genetic ion channelopathies and perspectives in drug discovery. *Front. Pharmacol.* 7, 121. doi: 10.3389/fphar.2016.00121

Ion Channel Library (n.d.). Available online at: https://enamine.net/compound-libraries/targeted-libraries/ion-channel-library (accessed October 27, 2023).

Ion Channel Ligand Library (n.d.). Available online at: https://www.selleckchem.com/screening/ion-channel-ligand-library.html (accessed October 27, 2023).

Irwin, J. J., and Shoichet, B. K. (2005). ZINC-a free database of commercially available compounds for virtual screening. *J. Chem. Inf. Model.* 45, 177–82. doi: 10.1002/chin.200516215

Irwin, J. J., Tang, K. G., Young, J., Dandarchuluun, C., Wong, B. R., Khurelbaatar, M., et al. (2020). ZINC20 - a free ultralarge-scale chemical database for ligand discovery. *J. Chem. Inf. Model.* 60, 6065–6073. doi: 10.1021/acs.jcim.0c00675

Jiménez-García, B., Roel-Touris, J., Romero-Durana, M., Vidal, M., Jiménez-González, D., and Fernández-Recio, J. (2018). LightDock: a new multi-scale approach to protein-protein docking. *Bioinformatics* 34, 49–55. doi: 10.1093/bioinformatics/btx555

Jin, W., Barzilay, R., and Jaakkola, T. (2020). "Multi-objective molecule generation using interpretable substructures," in *Proceedings of the 37th International Conference on Machine Learning (PLMR)*. Available online at: https://proceedings.mlr.press/v119/jin20b.html

Jumper, J., Evans, R., Pritzel, A., Green, T., Figurnov, M., Ronneberger, O., et al. (2021). Highly accurate protein structure prediction with AlphaFold. *Nature* 596, 583–589. doi: 10.1038/s41586-021-03819-2

Kang, J. (2001). Interactions of a series of fluoroquinolone antibacterial drugs with the human cardiac K+ channel HERG. *Mol. Pharmacol.* 59, 122–126. doi: 10.1124/mol.59.1.122

Karthikeyan, M., Pandit, D., and Vyas, R. (2015). ChemScreener: a distributed computing tool for scaffold based virtual screening. *Comb. Chem. High Throughput Screen.* 18, 544–561. doi: 10.2174/1386207318666150703112242

Kaserer, T., Beck, K. R., Akram, M., Odermatt, A., Schuster, D., and Willett, P. (2015). Pharmacophore models and pharmacophore-based virtual screening: concepts and applications exemplified on hydroxysteroid dehydrogenases. *Molecules* 20, 22799–22832. doi: 10.3390/molecules201219880

Kenyon, V., Chorny, I., Carvajal, W. J., Holman, T. R., and Jacobson, M. P. (2006). Novel human lipoxygenase inhibitors discovered using virtual screening with homology models. *J. Med. Chem.* 49, 1356–1363. doi: 10.1021/jm050639j

Kim, J. B. (2014). Channelopathies. *Korean J. Pediatr.* 57, 1–18. doi: 10.3345/kjp.2014.57.1.1

Kim, S., Thiessen, P. A., Bolton, E. E., Chen, J., Fu, G., Gindulyte, A., et al. (2016). PubChem substance and compound databases. *Nucleic Acids Res.* 44, D1202–D1213. doi: 10.1093/nar/gkv951

Kobeissy Firas, H., and Stevens Stanley, M. Jr (2017). "Neuroproteomics: methods and protocols," in *Methods in Molecular Biology* (New York, NY), 1598. doi: 10.1007/978-1-4939-6952-4

Kong, W., Tu, X., Huang, W., Yang, Y., Xie, Z., and Huang, Z. (2020). Prediction and optimization of NaV1.7 sodium channel inhibitors based on machine learning and simulated annealing. *J. Chem. Inf. Model.* 60, 2739–2753. doi: 10.1021/acs.jcim.9b01180

Kowal, N. M., Indurthi, D. C., Ahring, P. K., Chebib, M., Olafsdottir, E. S., and Balle, T. (2019). Novel approach for the search for chemical scaffolds with dual activity with acetylcholinesterase and the α7 nicotinic acetylcholine receptor—a perspective for the treatment of neurodegenerative disorders. *Molecules* 24, 446. doi: 10.3390/molecules24030446

Krishna Gottipati, S., Sattarov, B., Niu, S., Pathak, Y., Wei, H., Liu, S., et al. (2020). "Learning to navigate the synthetically accessible chemical space using reinforcement learning," in *Proceedings of the 37th International Conference on Machine Leaning (PMLR)*. Available online at: https://proceedings.mlr.press/v119/gottipati20a.html

Krueger, B. A., Weil, T., and Schneider, G. (2009). Comparative virtual screening and novelty detection for NMDA-Glycine B antagonists. *J. Comput. Aided Mol. Des.* 23, 869–881. doi: 10.1007/s10822-009-9304-1

Kschonsak, M., Jao, C. C., Arthur, C. P., Rohou, A. L., Bergeron, P., Ortwine, D. F., et al. (2023). Cryo-EM reveals an unprecedented binding site for NaV1.7 inhibitors enabling rational design of potent hybrid inhibitors. *Elife* 12, e84151. doi: 10.7554/eLife.84151

Kuan, J., Radaeva, M., Avenido, A., Cherkasov, A., and Gentile, F. (2023). Keeping pace with the explosive growth of chemical libraries with structure-based virtual screening. *Wiley Interdiscip. Rev. Comput. Mol. Sci.* 13, e1678. doi: 10.1002/wcms.1678

Kuhn, M., Firth-Clark, S., Tosco, P., Mey, A. S. J. S., MacKey, M., and Michel, J. (2020). Assessment of binding affinity via alchemical free-energy calculations. *J. Chem. Inf. Model.* 60, 3120–3130. doi: 10.1021/acs.jcim.0c00165

Kuntz, I. D., Blaney, J. M., Oatley, S. J., Langridge, R., and Ferrin, T. E. (1982). A geometric approach to macromolecule-ligand interactions. *J. Mol. Biol.* 161, 269–288. doi: 10.1016/0022-2836(82)90153-X

Lau, C., Hunter, M. J., Stewart, A., Perozo, E., and Vandenberg, J. I. (2018). Never at rest: insights into the conformational dynamics of ion channels from cryo-electron microscopy. *J. Physiol.* 596, 1107–1119. doi: 10.1113/JP274888

Lavecchia, A., and Di Giovanni, C. (2013). Virtual screening strategies in drug discovery: a critical review. *Curr. Med. Chem.* 20, 2839–2860. doi: 10.2174/09298673113209990001

Lazar, I. M., Kontoyianni, M., and Lazar, A. C. (2017). *Proteomics for Drug Discovery Methods and Protocols Methods in Molecular Biology 1647*. New York: Springer.

Leman, J. K., Weitzner, B. D., Lewis, S. M., Adolf-Bryfogle, J., Alam, N., Alford, R. F., et al. (2020). Macromolecular modeling and design in Rosetta: recent methods and frameworks. *Nat. Methods* 17, 665–680. doi: 10.1038/s41592-020-0848-2

Li, J., Fu, A., and Zhang, L. (2019). An overview of scoring functions used for protein–ligand interactions in molecular docking. *Interdiscip. Sci.* 11, 320–328. doi: 10.1007/s12539-019-00327-w

Li, Q. (2020). Application of fragment-based drug discovery to versatile targets. *Front. Mol. Biosci.* 7, 180. doi: 10.3389/fmolb.2020.00180

Li, T., Lu, G., Chiang, E. Y., Chernov-Rogan, T., Grogan, J. L., and Chen, J. (2017). High-throughput electrophysiological assays for voltage gated ion channels using SyncroPatch 768PE. *PLoS ONE* 12, e0180154. doi: 10.1371/journal.pone.0180154

Li, Y., Zhang, L., and Liu, Z. (2018). Multi-objective de novo drug design with conditional graph generative model. *J. Cheminform.* 10, 6. doi: 10.1186/s13321-018-0287-6

Lin, C. H., and Lane, H. Y. (2019). The role of N-methyl-D-aspartate receptor neurotransmission and precision medicine in behavioral and psychological symptoms of dementia. *Front. Pharmacol.* 10, 540. doi: 10.3389/fphar.2019.00540

Lin, Y., Grinter, S., Lu, Z., Xu, X., Zhan Wang, H., Liang, H., et al. (2021). Modulating the voltage sensor of a cardiac potassium channel shows antiarrhythmic effects. *Proc. Natl. Acad. Sci. USA.* 118, 2024215118. doi: 10.1073/pnas.2024215118

Lin, Z., Akin, H., Rao, R., Hie, B., Zhu, Z., Lu, W., et al. (2023). Evolutionary-scale prediction of atomic-level protein structure with a language model. *Science (1979).* 379, 1123–1130. doi: 10.1126/science.ade2574

Lipinski, C. A. (2004). Lead- and drug-like compounds: the rule-of-five revolution. *Drug Discov. Today Technol.* 1, 337–341. doi: 10.1016/j.ddtec.2004.11.007

Lipinski, C. A., Lombardo, F., Dominy, B. W., and Feeney, P. J. (2001). Experimental and computational approaches to estimate solubility and permeability in drug discovery and development settings. *Adv. Drug Deliv. Rev.* 46, 3–26. doi: 10.1016/S0169-409X(00)00129-0

Liu, H., Gao, Z. B., Yao, Z., Zheng, S., Li, Y., Zhu, W., et al. (2007). Discovering potassium channel blockers from synthetic compound database by using structure-based virtual screening in conjunction with electrophysiological assay. *J. Med. Chem.* 50, 83–93. doi: 10.1021/jm060414o

Liu, J., Chang, L., Song, Y., Li, H., and Wu, Y. (2019). The role of NMDA receptors in Alzheimer's disease. *Front. Neurosci.* 13:43. doi: 10.3389/fnins.2019.00043

Liu, R., Li, X., and Lam, K. S. (2017). Combinatorial chemistry in drug discovery. *Curr. Opin. Chem. Biol.* 38, 117–126. doi: 10.1016/j.cbpa.2017.03.017

Liu, X., Ye, K., van Vlijmen, H. W. T., Emmerich, M. T. M., IJzerman, A. P., and van Westen, G. J. P. (2021). DrugEx v2: de novo design of drug molecules by Pareto-based multi-objective reinforcement learning in polypharmacology. *J. Cheminform.* 13. doi: 10.1186/s13321-021-00561-9

Liu, X., Ye, K., van Vlijmen, H. W. T., IJzerman, A. P., and van Westen, G. J. P. (2023). DrugEx v3: scaffold-constrained drug design with graph transformer-based reinforcement learning. *J. Cheminform.* 15. doi: 10.1186/s13321-023-00694-z

Liu, Y., Xu, X., Gao, J., Naffaa, M. M., Liang, H., Shi, J., et al. (2020). A PIP2 substitute mediates voltage sensor-pore coupling in KCNQ activation. *Commun. Biol.* 3, 385. doi: 10.1038/s42003-020-1104-0

Llanos, M. A., Sbaraglini, L., Garofalo, F. M., Talevi, A., Gavernet, L., and Mart, P. (2022). Structure-based virtual screening identifies novobiocin, montelukast, and cinnarizine as TRPV1 modulators with anticonvulsant activity *in vivo*. *J. Chem. Inf. Model.* 62, 3008–22. doi: 10.1021/acs.jcim.2c00312

Lu, C., Liu, Z., Zhang, E., He, F., Ma, Z., and Wang, H. (2019). MPLS-pred: Predicting membrane protein-ligand binding sites using hybrid sequence-based features and ligand-specific models. *Int. J. Mol. Sci.* 20, 3120. doi: 10.3390/ijms20133120

Luttens, A., Gullberg, H., Abdurakhmanov, E., Vo, D. D., Akaberi, D., Talibov, V. O., et al. (2022). Ultralarge virtual screening identifies SARS-CoV-2 main protease inhibitors with broad-spectrum activity against coronaviruses. *J. Am. Chem. Soc.* 144, 2905–2920. doi: 10.1021/jacs.1c08402

Lyu, J., Irwin, J. J., and Shoichet, B. K. (2023). Modeling the expansion of virtual screening libraries. *Nat. Chem. Biol.* 19, 712–718. doi: 10.1038/s41589-022-01234-w

Lyu, J., Wang, S., Balius, T. E., Singh, I., Levit, A., Moroz, Y. S., et al. (2019). Ultra-large library docking for discovering new chemotypes. *Nature* 566, 224–229. doi: 10.1038/s41586-019-0917-9

Maia, E. H. B., Assis, L. C., de Oliveira, T. A., da Silva, A. M., and Taranto, A. G. (2020). Structure-based virtual screening: from classical to artificial intelligence. *Front. Chem.* 8, 343. doi: 10.3389/fchem.2020.00343

Marlow, B., Kuenze, G., Meiler, J., and Leman, J. K. (2023). Docking cholesterol to integral membrane proteins with Rosetta. *PLoS Comput. Biol.* 19, 1010947. doi: 10.1371/journal.pcbi.1010947

Matricon, P., Nguyen, A. T., Vo, D. D., Baltos, J. A., Jaiteh, M., Luttens, A., et al. (2023). Structure-based virtual screening discovers potent and selective adenosine A1 receptor antagonists. *Eur. J. Med. Chem.* 257, 115419. doi: 10.1016/j.ejmech.2023.115419

Meiler, J., and Baker, D. (2006). ROSETTALIGAND: Protein-small molecule docking with full side-chain flexibility. *Proteins* 65, 538–548. doi: 10.1002/prot.21086

MolPort (n.d.). Available online at: https://www.molport.com/shop/index (accessed November 21, 2023).

mpstruc database (n.d.). Available online at: https://blanco.biomol.uci.edu/mpstruc/ (accessed October 27, 2023).

Mungalpara, J., Pandey, A., Jain, V., and Mohan, C. G. (2010). Molecular modelling and QSAR analysis of some structurally diverse N-type calcium channel blockers. *J. Mol. Model.* 16, 629–644. doi: 10.1007/s00894-009-0591-1

Murray, C. W., and Rees, D. C. (2009). The rise of fragment-based drug discovery. *Nat. Chem.* 1, 187–192. doi: 10.1038/nchem.217

Neves, B. J., Braga, R. C., Melo-Filho, C. C., Moreira-Filho, J. T., Muratov, E. N., and Andrade, C. H. (2018). QSAR-based virtual screening: advances and applications in drug discovery. *Front. Pharmacol.* 9, 1275. doi: 10.3389/fphar.2018.01275

Nicolaou, C. A., Watson, I. A., Hu, H., and Wang, J. (2016). The proximal lilly collection: mapping, exploring and exploiting feasible chemical space. *J. Chem. Inf. Model.* 56, 1253–1266. doi: 10.1021/acs.jcim.6b00173

Nilius, B., Prenen, J., Vennekens, R., Hoenderop, J. G. J., Bindels, R. J. M., and Droogmans, G. (2001). Pharmacological modulation of monovalent cation currents through the epithelial Ca2+ channel ECac1. *Br. J. Pharmacol.* 134, 453–462. doi: 10.1038/sj.bjp.0704272

Oddsson, S., Kowal, N. M., Ahring, P. K., Olafsdottir, E. S., and Balle, T. (2020). Structure-based discovery of dual-target hits for acetylcholinesterase and the α7 nicotinic acetylcholine receptors: *in silico* studies and *in vitro* confirmation. *Molecules* 25, 2872. doi: 10.3390/molecules25122872

Parsons, C. G. (2001). NMDA receptors as targets for drug action in neuropathic pain. *Eur. J. Pharmacol.* 429, 71–78. doi: 10.1016/S0014-2999(01)01307-3

Pasqualetto, G., Zuanon, M., Brancale, A., and Young, M. T. (2023). Identification of a novel P2X7 antagonist using structure-based virtual screening. *Front. Pharmacol.* 13, 1094607. doi: 10.3389/fphar.2022.1094607

Payandeh, J., and Volgraf, M. (2021). Ligand binding at the protein–lipid interface: strategic considerations for drug design. *Nat. Rev. Drug Discov.* 20, 710–722. doi: 10.1038/s41573-021-00240-2

Pereira, J. C., Caffarena, E. R., and Dos Santos, C. N. (2016). Boosting docking-based virtual screening with deep learning. *J. Chem. Inf. Model.* 56, 2495–2506. doi: 10.1021/acs.jcim.6b00355

Pierce, B. G., Wiehe, K., Hwang, H., Kim, B. H., Vreven, T., and Weng, Z. (2014). ZDOCK server: Interactive docking prediction of protein-protein complexes and symmetric multimers. *Bioinformatics* 30, 1771–1773. doi: 10.1093/bioinformatics/btu097

Pliushcheuskaya, P., and Künze, G. (2023). Recent advances in computer-aided structure-based drug design on ion channels. *Int. J. Mol. Sci.* 24, 9226. doi: 10.3390/ijms24119226

Podlewska, S., Czarnecki, W. M., Kafel, R., and Bojarski, A. J. (2017). Creating the new from the old: combinatorial libraries generation with machine-learning-based compound structure optimization. *J. Chem. Inf. Model.* 57, 133–147. doi: 10.1021/acs.jcim.6b00426

Popova, M., Isayev, O., and Tropsha, A. (2018). Deep reinforcement learning for de novo drug design. *Sci Adv* 4, 7885. doi: 10.1126/sciadv.aap7885

Rao, S., Klesse, G., Stansfeld, P. J., Tucker, S. J., and Sansom, M. S. P. (2019). A heuristic derived from analysis of the ion channel structural proteome permits the rapid identification of hydrophobic gates. *Proc. Natl. Acad. Sci. USA.* 116, 13989–13995. doi: 10.1073/pnas.1902702116

REAL Compounds (n.d.). Available online at: https://enamine.net/compound-collections/real-compounds (accessed October 27, 2023).

Rudden, L. S. P., and Degiacomi, M. T. (2021). Transmembrane Protein Docking with JabberDock. *J. Chem. Inf. Model.* 61, 1493–1499. doi: 10.1021/acs.jcim.0c01315

Sadybekov, A. A., Sadybekov, A. V., Liu, Y., Iliopoulos-Tsoutsouvas, C., Huang, X. P., Pickett, J., et al. (2022). Synthon-based ligand discovery in virtual libraries of over 11 billion compounds. *Nature* 601, 452–459. doi: 10.1038/s41586-021-04220-9

Sadybekov, A. V., and Katritch, V. (2023). Computational approaches streamlining drug discovery. *Nature* 616, 673–685. doi: 10.1038/s41586-023-05905-z

Saldívar-González, F. I., Huerta-García, C. S., and Medina-Franco, J. L. (2020). Chemoinformatics-based enumeration of chemical libraries: a tutorial. *J. Cheminform.* 12, 64. doi: 10.1186/s13321-020-00466-z

Santos, R., Ursu, O., Gaulton, A., Bento, A. P., Donadi, R. S., Bologa, C. G., et al. (2016). A comprehensive map of molecular drug targets. *Nat. Rev. Drug Discov.* 16, 19–34. doi: 10.1038/nrd.2016.230

Schaller, D., Šribar, D., Noonan, T., Deng, L., and Nguyen, T. N., Pach, S., et al. (2020). Next generation 3D pharmacophore modeling. *Wiley Interdiscip. Rev. Comput. Mol. Sci.* 10, 1468. doi: 10.1002/wcms.1468

Schultz, K. J., Colby, S. M., Yesiltepe, Y., Nuñez, J. R., McGrady, M. Y., and Renslow, R. S. (2021). Application and assessment of deep learning for the generation of potential NMDA receptor antagonists. *Phys. Chem. Chem. Phys.* 23, 1197–1214. doi: 10.1039/D0CP03620J

Segler, M. H. S., Kogej, T., Tyrchan, C., and Waller, M. P. (2018). Generating focused molecule libraries for drug discovery with recurrent neural networks. *ACS Cent. Sci.* 4, 120–131. doi: 10.1021/acscentsci.7b00512

Sehgal, S. A., Hassan, M., and Rashid, S. (2014). Pharmacoinformatics elucidation of potential drug targets against migraine to target ion channel protein KCNK18. *Drug Des. Devel. Ther.* 8, 571–581. doi: 10.2147/DDDT.S63096

Seidel, T., Ibis, G., Bendix, F., and Wolber, G. (2010). Strategies for 3D pharmacophore-based virtual screening. *Drug Discov. Today Technol.* 7, 4. doi: 10.1016/j.ddtec.2010.11.004

Sharma, V., Wakode, S., and Kumar, H. (2021). "Structure- and ligand-based drug design: Concepts, approaches, and challenges," in *Chemoinformatics and Bioinformatics in the Pharmaceutical Sciences* (London: Elsevier), 27–53.

Sridhar, A., Lummis, S. C. R., Pasini, D., Mehregan, A., Brams, M., Kambara, K., et al. (2021). Regulation of a pentameric ligand-gated ion channel by a semiconserved cationic lipid-binding site. *J. Biol. Chem.* 297, 100899. doi: 10.1016/j.jbc.2021.100899

Stein, R. M., Kang, H. J., McCorvy, J. D., Glatfelter, G. C., Jones, A. J., Che, T., et al. (2020). Virtual discovery of melatonin receptor ligands to modulate circadian rhythms. *Nature* 579, 609–614. doi: 10.1038/s41586-020-2027-0

Suay-García, B., Bueso-Bordils, J. I., Falcó, A., Antón-Fos, G. M., and Alemán-López, P. A. (2022). Virtual combinatorial chemistry and pharmacological screening: a short guide to drug design. *Int. J. Mol. Sci.* 23, 1620. doi: 10.3390/ijms23031620

Tan, X., Li, C., Yang, R., Zhao, S., Li, F., Li, X., et al. (2022). Discovery of pyrazolo[3,4- d]pyridazinone derivatives as selective DDR1 inhibitors via deep learning based design, synthesis, and biological evaluation. *J. Med. Chem.* 65, 103–119. doi: 10.1021/acs.jmedchem.1c01205

Trott, O., and Olson, A. J. (2009). AutoDock Vina: improving the speed and accuracy of docking with a new scoring function, efficient optimization, and multithreading. *J. Comput. Chem.* 31, 455–61. doi: 10.1002/jcc.21334

Urbahns, K., Horváth, E., Stasch, J. P., and Mauler, F. (2003). 4-Phenyl-4H-pyrans as IKCa channel blockers. *Bioorg. Med. Chem. Lett.* 13, 2637–2639. doi: 10.1016/S0960-894X(03)00560-2

Varadi, M., Anyango, S., Deshpande, M., Nair, S., Natassia, C., Yordanova, G., et al. (2022). AlphaFold Protein Structure Database: massively expanding the structural coverage of protein-sequence space with high-accuracy models. *Nucleic Acids Res.* 50, D439–D444. doi: 10.1093/nar/gkab1061

Varin, T., Schuffenhauer, A., Ertl, P., and Renner, S. (2011). Mining for bioactive scaffolds with scaffold networks: Improved compound set enrichment from primary screening data. *J. Chem. Inf. Model.* 51, 1528–1538. doi: 10.1021/ci2000924

Vavra, O., Filipovic, J., Plhak, J., Bednar, D., Marques, S. M., Brezovsky, J., et al. (2019). CaverDock: a molecular docking-based tool to analyse ligand transport through protein tunnels and channels. *Bioinformatics* 35, 4986–4993. doi: 10.1093/bioinformatics/btz386

Wacker, S. J., Jurkowski, W., Simmons, K. J., Fishwick, C. W. G., Johnson, A. P., Madge, D., et al. (2012). Identification of selective inhibitors of the potassium channel Kv1.1-1.2(3) by high-throughput virtual screening and automated patch clamp. *Chem. Med. Chem.* 7, 1775–1783. doi: 10.1002/cmdc.201100600

Weininger, D. (1988). SMILES, a chemical language and information system. 1. Introduction to methodology and encoding rules. *J. Chem. Inf. Comput. Sci* 28, 31–36. doi: 10.1021/ci00057a005

Wolber, G., and Langer, T. (2005). LigandScout: 3-D pharmacophores derived from protein-bound ligands and their use as virtual screening filters. *J. Chem. Inf. Model.* 45, 160–169. doi: 10.1021/ci049885e

Wolkenberg, S. E., Nolt, M. B., Bilodeau, M. T., Trotter, B. W., Manley, P. J., Kett, N. R., et al. (2017). Discovery of MK-1832, a Kv1.5 inhibitor with improved selectivity and pharmacokinetics. *Bioorg. Med. Chem. Lett.* 27, 1062–1069. doi: 10.1016/j.bmcl.2016.12.054

Wright, D. J., Simmons, K. J., Johnson, R. M., Beech, D. J., Muench, S. P., and Bon, R. S. (2020). Human TRPC5 structures reveal interaction of a xanthine-based TRPC1/4/5 inhibitor with a conserved lipid binding site. *Commun. Biol.* 3, 8. doi: 10.1038/s42003-020-01437-8

Xia, X., Hu, J., Wang, Y., Zhang, L., and Liu, Z. (2019). Graph-based generative models for de Novo drug design. *Drug Discov Today Technol* 32–33, 45–53. doi: 10.1016/j.ddtec.2020.11.004

Xiao, Y. F., Sigg, D. C., and Leaf, A. (2005). The antiarrhythmic effect of n-3 polyunsaturated fatty acids: Modulation of cardiac ion channels as a potential mechanism. *J. Memb. Biol.* 206, 141–154. doi: 10.1007/s00232-005-0786-z

Xie, W., Wang, F., Li, Y., Lai, L., and Pei, J. (2022). Advances and challenges in de novo drug design using three-dimensional deep generative models. *J. Chem. Inf. Model.* 62, 2269–2279. doi: 10.1021/acs.jcim.2c00042

Yan, C., and Zou, X. (2015). "MDock: An Ensemble Docking Suite for Molecular Docking, Scoring and *In silico* Screening," in *Methods in Pharmacology and Toxicology* (Totowa: Humana Press Inc.)

Yang, X., Wu, Y., Xu, S., Li, H., Peng, C., Cui, X., et al. (2023). Targeting the inward rectifier potassium channel 5.1 in thyroid cancer: artificial intelligence-facilitated molecular docking for drug discovery. *BMC Endocr. Disord.* 23, 113. doi: 10.1186/s12902-023-01360-z

Yazdi, S., Nikesj,ö, J., Miranda, W., Corradi, V., Peter Tieleman, D., Noskov, S. Y., et al. (2021). Identification of pufa interaction sites on the cardiac potassium channel kcnq1. *J. General Physiol.* 153. doi: 10.1085/jgp.202012850

Zeng, X., Wang, F., Luo, Y., Kang, S., gu, Tang, J., Lightstone, F. C., et al. (2022). Deep generative molecular design reshapes drug discovery. *Cell Rep. Med.* 3, 100794. doi: 10.1016/j.xcrm.2022.100794

Zhang, G., Xu, X., Jia, Z., Geng, Y., Liang, H., Shi, J., et al. (2022a). An allosteric modulator activates BK channels by perturbing coupling between Ca2+ binding and pore opening. *Nat. Commun.* 13, 6. doi: 10.1038/s41467-022-34359-6

Zhang, J., Shi, Y., Huang, Z., Li, Y., Yang, B., Gong, J., et al. (2022b). Structural basis for NaV1.7 inhibition by pore blockers. *Nat. Struct. Mol. Biol.* 29, 1208–1216. doi: 10.1038/s41594-022-00860-1

Zhavoronkov, A., Ivanenkov, Y. A., Aliper, A., Veselov, M. S., Aladinskiy, V. A., Aladinskaya, A. V., et al. (2019). Deep learning enables rapid identification of potent DDR1 kinase inhibitors. *Nat. Biotechnol.* 37, 1038–1040. doi: 10.1038/s41587-019-0224-x

ZINC Database (n.d.). Available online at: https://zinc.docking.org (accessed October 27, 2023).

Zoli, M., Pistillo, F., and Gotti, C. (2015). Diversity of native nicotinic receptor subtypes in mammalian brain. *Neuropharmacology* 96, 302–311. doi: 10.1016/j.neuropharm.2014.11.003

Frontiers in
Molecular Neuroscience

Leading research into the brain's molecular structure, design and function

Part of the most cited neuroscience series, this journal explores and identifies key molecules underlying the structure, design and function of the brain across all levels.

Discover the latest Research Topics

See more →

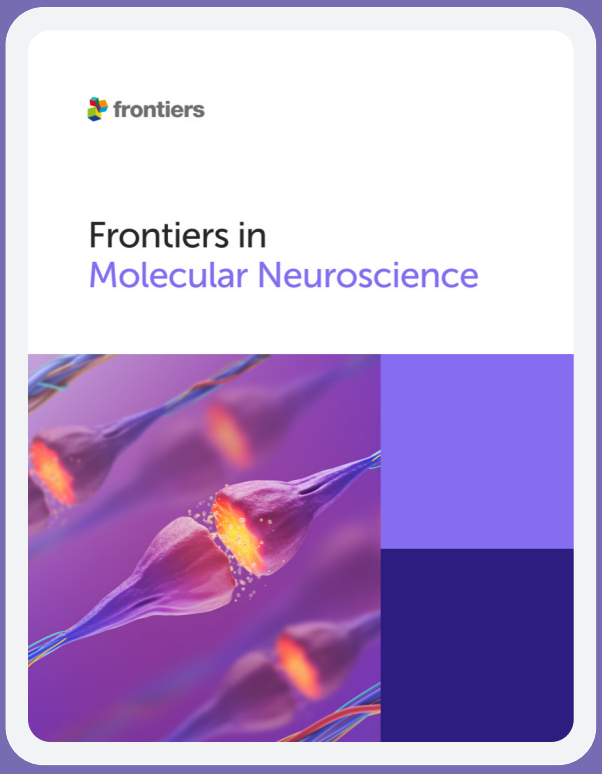

Frontiers

Avenue du Tribunal-Fédéral 34
1005 Lausanne, Switzerland
frontiersin.org

Contact us

+41 (0)21 510 17 00
frontiersin.org/about/contact